ENDOMMAGEMENT, RUPTURE ET CHANGEMENTS D'ÉCHELLES DANS LES MATÉRIAUX HÉTÉROGÈNES

François Hild

MÉMOIRE D'HABILITATION À DIRIGER DES RECHERCHES

Spécialité :

MÉCANIQUE

Présenté
à l'Université Pierre et Marie Curie
– Paris 6 –

par **François HILD**

Sujet :

ENDOMMAGEMENT, RUPTURE ET CHANGEMENTS D'ÉCHELLES DANS LES MATÉRIAUX HÉTÉROGÈNES

Soutenu le 10 juin 1998 devant le jury composé de

André ZAOUI	Président
Thierry BRETHEAU	Rapporteur
André DRAGON	Rapporteur
Dominique JEULIN	Rapporteur
Didier BAPTISTE	Examinateur
Jean LEMAITRE	Examinateur
André PINEAU	Examinateur

LMT-CACHAN
ENS de Cachan / CNRS / Université Paris 6
61, avenue du Président Wilson - 94235 CACHAN CEDEX (FRANCE)

RÉSUMÉ

Les analyses présentées dans ce mémoire portent sur l'endommagement et la rupture de matériaux hétérogènes. Le mécanisme principal de dégradation est la fissuration à l'échelle la plus petite. Une approche probabiliste s'avère être un outil efficace. Ceci concerne des matériaux à comportement fragile (céramiques, fontes GS sous sollicitation cyclique) ou quasi-fragile (céramiques monolithiques impactées ou renforcées par des fibres longues, ciments renforcés par des fibres longues ou courtes). Le dialogue entre les différentes échelles a d'une part permis de construire des modèles de prévision de l'endommagement et de la rupture. D'autre part, diverses stratégies d'identification des paramètres du matériau ont été mises en oeuvre.

ABSTRACT

The analyses presented in this dissertation deal with damage and failure of heterogeneous materials. The main degradation mechanism is cracking at the lowest level. A probabilistic approach constitutes a useful tool. Brittle materials (such as ceramics, SG cast iron under cyclic loadings) or quasi-brittle materials (*e.g.*, impacted ceramics, fiber-reinforced ceramics, cementitious matrices reinforced by short or continuous fibers) are concerned. The dialogue between different scales is used to build models predicting damage and failure. On the other hand, different identification strategies are developed to identify the material parameters.

DISCIPLINE :
Mécanique.

MOTS-CLÉS :
Comportement fragile, Comportement quasi-fragile, Identification, Localisation, Loi de comportement, Probabilité de rupture.

ADRESSE DU LABORATOIRE :
LMT-Cachan, ENS de Cachan / CNRS / Université Paris 6
61, avenue du Président Wilson - 94235 CACHAN CEDEX (FRANCE).

À Anne, Elisabeth, Guillaume...
À Lucien.

Mes remerciements s'adressent à :

- MM. DRAGON, JEULIN et BRETHEAU, rapporteurs ;
- M. ZAOUI, président du jury ;
- MM. BAPTISTE et PINEAU, examinateurs ;
- Jean LEMAITRE dont les conseils et les encouragements m'ont été particulièrement utiles ;
- Fred LECKIE qui par sa grande compétence, sa disponibilité et sa paternelle sollicitude a créé un environnement scientifique et humain hors du commun.

J'exprime ma reconnaissance toute particulière à Ahmed BENALLAL, René BILLARDON, Pippo GEYMONAT et Didier MARQUIS dont les échanges tout au long de ce travail ont été très appréciables.

Les résultats présentés dans ce mémoire sont le fruit de discussions et travaux en collaboration avec de nombreuses personnes tant en France et aux États-Unis que dans d'autres parties du monde. Je ne puis toutes les citer nommément, mais je les prie de trouver, ici, l'expression de ma gratitude.

J'ai ainsi vécu seul [...] jusqu'à cette panne dans le désert du Sahara il y a six ans. Quelque chose s'était cassé dans mon moteur. Et comme je n'avais avec moi ni mécanicien, ni passagers, je me préparai à essayer de réussir une réparation difficile. C'était pour moi une question de vie ou de mort. J'avais à peine de l'eau à boire pour huit jours.

Le premier soir je me suis donc endormi sur le sable à mille miles de toute terre habitée. [...] Vous imaginez ma surprise, au lever du jour, quand une drôle de petite voix m'a réveillé. Elle disait :

— S'il vous plaît... dessine-moi un mouton !

— Hein !

— Dessine-moi un mouton...

A. DE SAINT-EXUPÉRY (1946), *Le Petit Prince*, Gallimard.

Ce mémoire présente une synthèse des travaux de recherche que l'auteur a effectués durant les années 1989-1998. Cette recherche a débuté par une thèse de l'Université Pierre et Marie Curie (Paris 6) co-encadrée par Didier MARQUIS et Jean LEMAITRE, soutenue en décembre 1992. Cette thèse a porté sur l'étude de la rupture des matériaux à comportement fragile (céramiques monolithiques et microbétons). Les aspects expérimentaux et théoriques liés à la présence de défauts initiaux ont été abordés et discutés en utilisant l'hypothèse du maillon le plus faible. Cette étude s'est inscrite dans le cadre d'un contrat de recherche entre Renault et le LMT-Cachan, et d'une action thématique programmée du CNRS « matériaux hétérogènes ». Ce travail a donné lieu à deux extensions directes :

- la première a consisté à développer la prise en compte des défauts initiaux dans le cas où l'on peut observer une propagation stable. Ces concepts ont été appliqués

à une fonte à graphite sphéroïdal soumise à des sollicitations de fatigue à grand nombre de cycles (contrat de recherche entre Renault et le LMT-Cachan). Cette étude a fait l'objet de la thèse de Hassan YAACOUB AGHA soutenue en novembre 1996 ;

- la seconde, utilisant la même méthodologie, a été employée pour l'étude de la fissuration sous-critique de céramiques (collaboration entre le CEA et le LMT-Cachan).

Toutes ces analyses consistent à évaluer la sensibilité des matériaux aux défauts initiaux. Cette notion fait partie du concept dit « de tolérance au dommage » développé dans le domaine aéronautique et son utilisation est actuellement envisagée, entre autres, dans l'industrie automobile.

Si ces études reposent sur une hypothèse principale, celle du maillon le plus faible, un autre axe de recherche a été développé : la multifissuration de matériaux hétérogènes. Ce travail a été mené en plusieurs phases :

1. l'analyse de la résistance ultime de composites à matrice céramique renforcés par des fibres longues en constituait la première et fut le sujet du « PhD » de l'Université de Californie à Santa Barbara (UCSB) encadré par Frederick A. LECKIE et soutenu par l'auteur en janvier 1995. Il faisait l'objet d'un contrat de recherche entre l'US Air Force et l'UCSB ;
2. ce travail a été poursuivi au LMT-Cachan en collaboration avec Pascal FEILLARD pour analyser la multifragmentation de fibres ;
3. parallèlement fut entreprise l'analyse de la fissuration matricielle de composites à matrice céramique renforcée par des fibres longues avec Alain BURR en collaboration avec Frederick A. LECKIE dans le cadre du programme « University Research Initiative » dont l'UCSB est le leader ;
4. des outils similaires ont été utilisés pour la modélisation du comportement mécanique de bétons renforcés par des fibres courtes en acier. Cette étude a constitué le travail de thèse de Dorothée BOUDON-CUSSAC soutenue en novembre 1996 ;
5. enfin, des méthodes voisines peuvent être employées dans l'analyse du comportement de blindages bicouches céramique/métal. Dans ce cas, il s'agit principalement d'étudier le comportement mécanique de céramiques sous impact. Ce travail fait l'objet de la thèse de Christophe DENOUAL (collaboration entre la DGA/DCE/CTA et le LMT-Cachan) dont la soutenance est prévue en 1998.

Tous ces travaux ont pour but d'étudier l'endommagement et la rupture de matériaux hétérogènes. L'un des concepts développés dans ce travail est l'analyse à différentes échelles des phénomènes de dégradation pour, ensuite, discuter de la manière dont les informations peuvent être transmises d'une échelle à une autre. En particulier, les problèmes liés à l'identification des paramètres représentatifs du comportement des matériaux hétérogènes sont discutés et illustrés sur différents exemples.

Table des matières

Liste des figures

Liste des tableaux

Introduction

Qu'est-ce que l'homme dans la nature ? Un néant à l'égard de l'infini, un tout à l'égard du néant, un milieu entre rien et tout.
B. PASCAL (1670), *Pensées*, édition de Port-Royal.

La notion d'échelle est utilisée dans différentes disciplines. Le choix d'une échelle « adéquate » est souvent lié à l'apparition de nouveaux moyens d'observation et de mesure des phénomènes :

- la perception de la planète comme une sphère fragile (notion globale) apparaît durant la révolution spatiale des années 1960 au détriment d'une vision (locale) galiléenne et copernicienne [WEBER, 1996]. L'apparition du concept de « biosphère » est souvent rapprochée de l'observation de la terre depuis les engins spatiaux. La naissance des mouvements écologiques qui oeuvrent pour la protection de la terre (effet de serre, pollution, notion de développement durable...) a ainsi été causée par une révolution technologique !

- en démographie, la croissance de la population mondiale est un phénomène global qui masque bien des disparités entre les différents continents. De même au niveau des continents, de forts contrastes peuvent s'expliquer par des différences géographiques et de développement économique. À des échelles plus fines, la survie d'une communauté humaine de quelques âmes est tributaire de son environnement immédiat (par exemple, l'assèchement d'une oasis peut conduire à la disparition d'un village en Afrique) alors que la survie d'une mégapole ne dépend pratiquement pas de son écosystème immédiat.

- en science économique, une des grandes interrogations est la suivante : l'économie est-elle fondamentalement de type microscopique ou de type macroscopique ? C'est une question qui met en jeu une idée déjà connue des Grecs : pour connaître l'univers, faut-il aller de la partie vers le tout ou, inversement, du tout vers la partie ? Les rapports entre le macrocosme (l'univers) et le microcosme (l'homme) ont évolué au cours des siècles avec l'émergence de nouvelles pensées philosophiques, fréquemment liées à des découvertes scientifiques. Aujourd'hui la priorité est souvent donnée à l'analyse macro-économique. Bien qu'opposées, les pensées marxistes et keynésiennes utilisent la même méthode d'analyse en raisonnant sur des quantités globales. L'idée de globalité ne supprime pas le passage de la micro-économie à la macro-économie : a-t-on le droit d'additionner des données hétérogènes ?

Dans de nombreuses disciplines, les visions à différentes échelles sont généralement antagonistes et aboutissent à la « domination » d'une des échelles par rapport aux autres ; des débats très « animés » ont eu lieu dans les exemples mentionnés précédemment. La Mécanique des Matériaux est née du rapprochement entre des visions à différentes échelles. Plus qu'une opposition entre descriptions nanoscopique, microscopique, mésoscopique ou macroscopique, la complémentarité est souvent de mise. Aujourd'hui, la modélisation du comportement mécanique de matériaux fait

souvent appel à un dialogue entre des descriptions à différentes échelles. Par exemple, la courbe non-linéaire contrainte/déformation mesurée à l'échelle macroscopique lors d'un essai de traction cache plusieurs mécanismes actifs très différents à l'échelle microscopique. Les techniques modernes d'observation microscopique (optique ou électronique) ont là encore constitué une avancée dans le domaine de l'appréhension de ces phénomènes microscopiques. Ainsi les modélisations sont de plus en plus confrontées à des mesures à une échelle microscopique. À titre d'illustration, les essais *in situ* (dans un microscope électronique à balayage) sont devenus possibles et pratiqués dans différents laboratoires. Cependant, un calcul de structure s'effectue généralement à partir de la description du comportement du matériau à l'échelle de l'élément de volume de la mécanique des milieux continus (passage qui reste, actuellement, encore nécessaire).

En élasticité linéaire, l'étude de la réponse contrainte/déformation de nombreux matériaux hétérogènes fait appel à des notions d'homogénéisation à partir d'études du comportement de phases à des échelles inférieures. L'émergence des matériaux hétérogènes (composites à particules, à fibres) n'est pas étrangère à l'apparition de cette technique. Le comportement non-linéaire a également été traité avec des développements encore un peu plus complexes (cf. par exemple [SUQUET, 1996]). Tous les problèmes sont loin d'avoir été résolus [GILORMINI, 1995], même si, de plus en plus de modèles intègrent des ingrédients de la théorie de l'homogénéisation. Citons par exemple les modèles polycristallins pour déterminer les limites d'écoulement et prévoir l'évolution des textures cristallographiques. L'école française initiée par MANDEL [ZARKA, 1968 ; BUI, 1969 ; ZAOUI, 1970] a permis de nombreuses avancées notamment dans le domaine de la (visco)plasticité. La plasticité cyclique a également été abordée en tirant profit de moyens de calcul performants [CAILLETAUD, 1987 ; PILVIN, 1990 ; 1995].

Quant aux problèmes d'endommagement et de rupture, leur résolution n'est pas toujours aussi « simple », c'est-à-dire réductible à des études sur des volumes élémentaires représentatifs du comportement du matériau. Au-delà d'une certaine limite, point qui sera abordé dans ce document, cette démarche n'est plus applicable. Cependant les changements d'échelle peuvent être utilisés et constituent un des outils privilégiés pour l'étude de l'endommagement et de la rupture de matériaux hétérogènes. Le cadre de la mécanique de l'endommagement se prête bien à ce genre d'études. Là encore, l'école française initiée par J. LEMAITRE [CORDEBOIS, 1976 ; CHABOCHE, 1978 ; DUFAILLY, 1980 ; MAZARS, 1984] et plus généralement l'école européenne [KACHANOV, 1958 ; 1961 ; ODQVIST et HULT, 1961 ; ODQVIST, 1966 ; RABOTNOV, 1969 ; LECKIE et HAYHURST, 1974 ; KRAJCINOVIC et LEMAITRE, 1987] a produit de nombreux résultats.

Dans ce qui suit, un seul type de dégradation est envisagé : la fissuration de matériaux hétérogènes. Ceci sous-entend la présence d'au moins un composé à *comportement fragile*, que le matériau soit une céramique, une fonte ou un béton. Le choix d'un type de mécanisme est lié au choix de l'échelle de description des phénomènes de dégradation et des moyens d'observation mis en oeuvre. Bien entendu des analyses à des échelles les plus fines constituent un apport non négligeable auquel on fait de plus en plus appel. Il ne faut cependant pas occulter des informations plus « traditionnelles » (telles qu'un essai de traction) pour compléter la base de données qui servira à construire une loi de comportement ; la complémentarité est plus profitable que l'exclusion. Ainsi à une démarche hypothético-déductive, rêve (illusoire ?) de certains, nous préférerons une démarche inductive.

Le chapitre 1 a pour but de décrire de manière générale le formalisme qui va être utilisé tout au long de ce mémoire. En particulier, les outils de la thermodynamique des milieux continus vont être couplés à ceux des changements d'échelle. Différentes approches de l'endommagement et de la rupture des matériaux sont discutées dans le cas de matériaux contenant des hétérogénéités initiales susceptibles de créer des fissures pouvant se propager de manière instable ou stable. On notera qu'il existe toujours une échelle où le matériau est intrinsèquement hétérogène. Nous nous efforcerons de choisir l'échelle la plus grossière qui permette de prendre en compte ces hétérogénéités en vue d'analyser l'endommagement et la rupture de matériaux. Ainsi l'échelle nanoscopique ne sera jamais envisagée, car le caractère opérationnel risque d'être compromis (pour les problèmes que nous nous sommes posés). Le choix de l'échelle d'étude est dicté par un double soucis de simplicité et d'efficacité et conduit donc à trouver un compromis « acceptable ». Les différents exemples traités dans les chapitres qui suivent illustrent le compromis recherché par l'auteur.

Si l'on admet que la rupture à un niveau local entraîne la rupture au niveau global, l'hypothèse du maillon le plus faible est applicable. Dans ce cas, toute concentration de contrainte (*e.g.*, défauts mésoscopiques) peut être fatale à la tenue du matériau ou de la structure. Ces défauts sont souvent distribués de manière aléatoire : un traitement probabiliste de la présence des défauts devient indispensable. Ces concepts sont appliqués dans le chapitre 2 à des céramiques monolithiques sous chargements monotone, « statique », « dynamique » ou cyclique, et à des fontes à graphite sphéroïdal sous sollicitations de fatigue à grand nombre de cycles.

Cependant, l'hypothèse du maillon le plus faible est souvent très forte. Dans le chapitre 3, elle est levée. Dans ces conditions, plusieurs ruptures peuvent se produire au

niveau microscopique ou mésoscopique avant qu'elles n'entraînent une rupture macroscopique. La multifissuration et la rupture de matériaux à comportement quasi-fragile est analysée à l'échelle microscopique et mésoscopique. Ceci concerne notamment le comportement des céramiques à l'impact, la fissuration matricielle et la rupture de fibres dans des composites à matrice fragile. Les conditions de rupture sont également discutées et analysées à différentes échelles.

Chapitre 1

Comportement mécanique et rupture d'un élément de volume endommagé

La cinquième planète était très curieuse. C'était la plus petite de toutes. Il y avait là juste assez de place pour loger un réverbère et un allumeur de réverbères. Le petit prince ne parvenait pas à s'expliquer à quoi pouvait servir, quelque part dans le ciel, sur une planète sans maison, ni population, un réverbère et un allumeur de réverbères. Cependant il se dit en lui-même :

— Peut-être bien que cet homme est absurde. Cependant il est moins absurde que le roi, que le vaniteux, que le businessman et que le buveur. Au moins son travail a-t-il un sens. Quand il allume son réverbère, c'est comme s'il faisait naître une étoile de plus, ou une fleur. Quand il éteint son réverbère ça endort la fleur ou l'étoile. C'est véritablement utile puisque c'est joli...

A. DE SAINT-EXUPÉRY (1946), *Le Petit Prince*, Gallimard.

L'objet de ce chapitre est l'étude générale du comportement mécanique et de la rupture d'un élément de volume endommagé. Par endommagé, nous entendons la présence de discontinuités de matière (par exemple une fissure). Cette étude sera faite à un niveau *mésoscopique*, c'est-à-dire à une échelle où la taille caractéristique est supérieure à celle de la microstructure de la matière (grains, cristaux). C'est l'échelle « habituelle » de l'élément de volume de la mécanique des milieux continus. Nous nous laisserons cependant la possibilité d'avoir plusieurs phases mais dont la taille sera supérieure à celle de la microstructure de chaque composé. Ce dernier cas nécessite des études au niveau *microscopique*. À cette échelle, nous supposerons que les concepts de mécanique des milieux continus sont encore applicables. On notera que même à des niveaux *nanoscopiques*, les hypothèses de la mécanique des milieux continus peuvent être utilisées [DELOBELLE, 1997 ; SIDOROFF, 1997] bien que, dans certains cas, des études soient faites à l'aide de notions discontinues. Enfin, l'échelle *macroscopique* désigne celle de la structure constituée d'un ou plusieurs matériaux. Cette définition des échelles est conventionnelle et peut être complétée dans certaines situations. Cependant, dans ce qui suit, on fera principalement appel aux échelles microscopiques, mésoscopiques et macroscopiques.

Dans une première partie (paragraphe 1.1), une étude générale des lois de comportement est écrite. Il s'agit en particulier de discuter de l'apport d'études à différentes échelles par rapport à une approche purement mésoscopique, qui analyse le comportement mécanique d'un volume élémentaire dans le cadre de la mécanique des milieux continus. Après la discussion d'un formalisme général, quelques exemples de volumes élémentaires endommagés sont développés :

1° un modèle rhéologique simple est tout d'abord analysé. Il a pour but de montrer comment l'apport de la « micromécanique » peut aider à construire un potentiel d'état ;

2° l'effet d'un champ de contraintes résiduelles lié à l'élaboration sur la fissuration d'un composite est ensuite étudié. La liaison avec des résultats de la mécanique de l'endommagement (paragraphe 1.1.1) est montrée ;

3° le calcul de la densité d'énergie irrécupérable est ensuite mené pour étudier le comportement mécanique d'un composite subissant de la décohésion et du frottement. Un parallèle peut être fait entre cet exemple et le premier.

Le choix des variables décrivant l'état d'un volume endommagé et le calcul du potentiel d'état associé sont présentés pour tous ces exemples. Les différentes contri-

butions énergétiques sont tracées sur les courbes contrainte/déformation mésoscopiques.

Les conditions de rupture sont ensuite analysées (paragraphe 1.2). On suppose étudier ces conditions à un niveau mésoscopique, c'est-à-dire très supérieur au niveau nanoscopique pour lequel une description atomique est nécessaire [KANNINEN et POPELAR, 1985]. On distingue deux cas :

- le premier concerne le comportement fragile, c'est-à-dire celui où la rupture est brutale (paragraphe 1.2.1). D'un point de vue mésoscopique et macroscopique, cette rupture n'est pas précédée de phénomènes d'alerte (typiquement une non-linéarité). Ceci conduit à un traitement particulier de la tenue des structures en matériau à comportement fragile. De plus, les causes de la rupture (*i.e.*, défauts initiaux) sont souvent réparties de manière aléatoire ce qui nécessite une analyse probabiliste de la rupture. Ce problème particulier est traité dans le chapitre 2 ;

- le deuxième nous met en présence d'un comportement quasi-fragile (paragraphe 1.2.2). On peut alors avoir une progression lente de la dégradation à une échelle mésoscopique, bien qu'elle puisse être brutale à une échelle microscopique. Il en est ainsi, notamment, des composites à matrice fragile. On observe alors un comportement non-linéaire mais les amplitudes des déformations et des déplacements permettent de conserver l'hypothèse des petites perturbations. La loi de comportement en déformation peut être suffisante pour étudier les conditions de rupture. Dans ce cas, le critère d'amorçage (*i.e.*, de rupture au niveau mésoscopique) fait appel aux résultats de la théorie de la localisation des déformations. Il est utilisé dans le chapitre 3 pour l'étude de la rupture de composites.

1.1 Loi de comportement et changement d'échelle

Cette étude est faite à un niveau mésoscopique (homogène ou non). Considérons un élément de volume Ω_0 soumis à des efforts associés à un état homogène de contraintes $\underline{\underline{\overline{\sigma}}}$. Soit $\underline{\underline{\overline{\epsilon}}}$ l'état de déformation homogène associé. L'état de contrainte mésoscopique $\underline{\underline{\overline{\sigma}}}$ est uniforme bien que les contraintes $\underline{\underline{\sigma}}$ et les déformations $\underline{\underline{\epsilon}}$ locales (ou microscopiques) varient d'un point à l'autre des constituants.

Après application d'un chargement extérieur, toutes les composantes de déformations sont supposées rester petites de telle manière que la décomposition additive en déformation élastique ($\underline{\underline{\epsilon}}^{\mathrm{e}}$) et inélastique ($\underline{\underline{\epsilon}}^{\mathrm{i}}$) reste valable

$$\underline{\underline{\epsilon}} = \underline{\underline{\epsilon}}^{\mathrm{e}} + \underline{\underline{\epsilon}}^{\mathrm{i}} \tag{1.1}$$

Les déformations inélastiques peuvent être plastiques pour les métaux et les alliages métalliques. Ce cas a été étudié de manière intensive dans le passé. Dans le cas de matériaux à comportement fragile (par exemple des céramiques), ces déformations peuvent correspondre à un mécanisme de fluage. Ce phénomène mérite d'être considéré dans le cas de composites à application thermostructurale (cf. par exemple [SURESH et BROCKENBROUGH, 1990 ; WEBER *et al.*, 1994 ; BEGLEY *et al.*, 1995]).

On suppose le comportement des constituants élastique linéaire

$$\underline{\underline{\sigma}} = \underline{\underline{\underline{\underline{E}}}} : \underline{\underline{\epsilon}}^{\mathrm{e}} + \underline{\underline{\rho}} \tag{1.2}$$

où $\underline{\underline{\sigma}}$ est le tenseur des contraintes de Cauchy, $\underline{\underline{\underline{\underline{E}}}}$ le tenseur d'élasticité (local) avec toutes les symétries usuelles (majeure et mineures), $\underline{\underline{\rho}}$ le tenseur des contraintes résiduelles (*i.e.*, auto-équilibrées à l'échelle mésoscopique) initiales, et « : » le produit contracté sur deux indices.

Nous supposons également la présence de discontinuités de déplacement à l'échelle microscopique (*i.e.*, des fissures) $[\![\underline{u}]\!]$ au travers de surfaces $\partial\Omega_{\mathrm{f}}$ caractérisées par une normale $\underline{n}$. Les discontinuités de déplacement sont également décomposées en une partie élastique $[\![\underline{u}]\!]^{\mathrm{e}}$ et inélastique $[\![\underline{u}]\!]^{\mathrm{i}}$

$$[\![\underline{u}]\!] = [\![\underline{u}]\!]^{\mathrm{e}} + [\![\underline{u}]\!]^{\mathrm{i}} \tag{1.3}$$

Des illustrations de différents comportements étudiés durant les années 1970 et au début des années 1980 sont consignés dans [SUQUET, 1982]. Dans les exemples qui suivent, la partie élastique du saut de déplacement sera traitée dans le cadre de la mécanique de l'endommagement. Quant à la partie inélastique, elle est créée par des glissements d'autres fissures interagissant avec la fissure considérée. C'est le cas, notamment, de

composites subissant de la fissuration matricielle (fissure principale) qui induit de la décohésion et du frottement le long de l'interface fibre/matrice (dans la direction perpendiculaire à la fissure matricielle). Ces deux derniers mécanismes de dégradation conduisent à un saut de déplacement inélastique de la fissure matricielle (cf. paragraphe 1.1.2.iii).

Les irréversibilités microscopiques telles que les fissures ou le fluage influencent le comportement mécanique d'un élément de volume (endommagé). Cette influence peut se traduire à l'aide de grandeurs énergétiques. D'un point de vue énergétique, on peut définir, à l'échelle mésoscopique, deux potentiels « complémentaires » au sens de la transformée (partielle) de LEGENDRE-FENCHEL. Ce sont la densité d'énergie libre (de HELMHOLTZ) $\overline{\psi}$ et la densité d'enthalpie libre (de GIBBS) $\overline{\varphi}$

$$\overline{\psi} + \overline{\varphi} = \underline{\underline{\bar{\varepsilon}}} : \underline{\underline{\bar{\sigma}}} \tag{1.4}$$

Les potentiels $\overline{\psi}$ et $\overline{\varphi}$ sont des potentiels d'état, donc indépendants du chemin suivi. Ces potentiels comprennent une partie élastique *récupérable* ($\overline{\psi}^{e}$ ou $\overline{\varphi}^{e}$) et une partie élastique *irrécupérable* ($\overline{\psi}^{i}$ ou $\overline{\varphi}^{i}$) qui est associée aux champs de contraintes résiduelles dans le matériau. La densité d'énergie irrécupérable peut être soit stockée (terme souvent employé pour les matériaux à comportement ductile), soit restituée (cf. paragraphe 1.1.2.ii) lorsqu'il existe initialement un champ de contraintes résiduelles (d'élaboration).

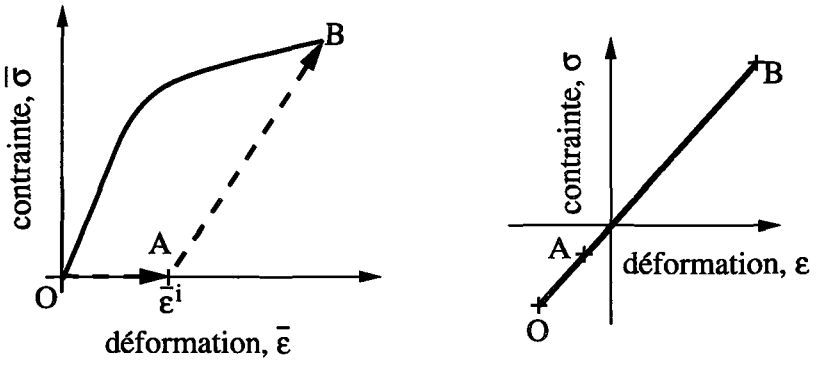

FIG. 1.1 - Construction des deux étapes pour le calcul des parties irrécupérable et récupérable du potentiel d'état (à l'échelle mésoscopique et microscopique).

La construction du potentiel d'état peut être obtenue en considérant deux étapes différentes de celle que subit le matériau (de l'état O à l'état B à l'échelle mésoscopique, trait plein de la figure 1.1) en utilisant la propriété d'indépendance de chemin suivi. La première étape (de l'état O à l'état A, cf. figure 1.1) consiste à effectuer tous les changements et dégradations microstructuraux sans charge extérieure. On peut ainsi calculer la partie irrécupérable du potentiel d'état. Soient $\underline{\underline{\sigma}}^{r}$ le champ de contraintes

résiduelles induit par cette transformation (qui peut être différent du champ de contraintes résiduelles initiales $\underline{\underline{\rho}}$) et $\underline{\underline{\epsilon}}^{\mathrm{r}}$ les déformations associées. La création (ou la disparition) de contraintes résiduelles induit des déformations permanentes (ou inélastiques) $\underline{\underline{\epsilon}}^{\mathrm{i}}$ au niveau mésoscopique.

La seconde étape (de l'état A à l'état B, cf. figure 1.1) considère un chargement élastique du matériau (éventuellement dégradé). On peut ainsi évaluer la partie réversible du potentiel d'état. Soient $\underline{\underline{\epsilon}}^*$ et $\underline{\underline{\sigma}}^*$ les déformations et contraintes (dans le matériau élastique « de comparaison », c'est-à-dire pour lequel tous les changements et dégradations microstructuraux sont figés) permettant d'atteindre, depuis le point A, le niveau de chargement du point B. On a ainsi

$$\underline{\underline{\epsilon}}^{\mathrm{r}} = \underline{\underline{\epsilon}}_{\mathrm{B}} - \underline{\underline{\epsilon}}^* \tag{1.5}$$

$$\underline{\underline{\sigma}}^{\mathrm{r}} = \underline{\underline{\sigma}}_{\mathrm{B}} - \underline{\underline{\sigma}}^* \tag{1.6}$$

En appliquant le principe des puissances virtuelles, et en remarquant que $\underline{\underline{\sigma}}^{\mathrm{r}}$ est un champ de contraintes auto-équilibré et que $\underline{\underline{\epsilon}}^*$ est un champ de déformation compatible, on peut montrer que [MANDEL, 1977 ; ARAVAS *et al.*, 1990]

$$\overline{\psi}_{\mathrm{OB}} = \overline{\psi}^{\mathrm{e}}_{\mathrm{OB}} + \overline{\psi}^{\mathrm{i}}_{\mathrm{OB}} \tag{1.7}$$

avec

$$\overline{\psi}^{\mathrm{e}}_{\mathrm{OB}} = \overline{\psi}^{\mathrm{e}}_{\mathrm{AB}} = \frac{1}{2}\int_{\Omega_0} \underline{\underline{\sigma}}^* : \underline{\underline{\underline{\underline{E}}}}^{-1} : \underline{\underline{\sigma}}^* \, dV \tag{1.8}$$

$$\overline{\psi}^{\mathrm{i}}_{\mathrm{OB}} = \overline{\psi}^{\mathrm{i}}_{\mathrm{OA}} = \frac{1}{2}\int_{\Omega_0} \underline{\underline{\sigma}}^{\mathrm{r}} : \underline{\underline{\underline{\underline{E}}}}^{-1} : \underline{\underline{\sigma}}^{\mathrm{r}} \, dV - \frac{1}{2}\int_{\Omega_0} \underline{\underline{\rho}} : \underline{\underline{\underline{\underline{E}}}}^{-1} : \underline{\underline{\rho}} \, dV \tag{1.9}$$

Le calcul de la partie récupérable a été longuement traité au début des années 1980 à l'aide de la résolution par une formulation variationnelle *ad hoc* (cf. par exemple [BUI *et al.*, 1981a ; 1981b ; 1982 ; SUQUET, 1982]). La traduction dans le cadre de la mécanique des milieux continus a été faite par la mécanique de l'endommagement qui s'est considérablement développée à cette époque (cf. paragraphe 1.1.1). Par contre, la partie irrécupérable a été moins analysée. Citons cependant les études de ANDRIEUX *et al.* [1981 ; 1986] dans le cas de fissures frottantes.

De même, on a

$$\overline{\varphi}_{\mathrm{OB}} = \overline{\varphi}^{\mathrm{e}}_{\mathrm{OB}} + \overline{\varphi}^{\mathrm{i}}_{\mathrm{OB}} \tag{1.10}$$

avec

$$\overline{\varphi}^{e}_{OB} = \underline{\underline{\overline{\sigma}}}_{B} : \underline{\underline{\overline{\varepsilon}}}_{B} - \overline{\psi}^{e}_{OB} \tag{1.11}$$

$$\overline{\varphi}^{i}_{OB} = -\overline{\psi}^{i}_{OB} \tag{1.12}$$

Ce type d'approche en deux étapes a été introduit par VOLTERRA [1907], et utilisé pour analyser le comportement élastique de matériaux homogènes et isotropes [VOLTERRA, 1907 ; LOVE, 1927], l'influence d'inclusions dans un milieu infini [ESHELBY, 1957 ; 1959]. En utilisant cette méthode, la partie irrécupérable peut être calculée, ce qui évite de la postuler comme cela est fait classiquement [LEMAITRE et CHABOCHE, 1985].

La prise en compte de toutes ces dégradations peut être effectuée au niveau mésoscopique par l'introduction de variables *internes* qui caractérisent de manière globale toutes les dégradations et changements microstructuraux. On peut ainsi remarquer que la partie récupérable de la densité d'énergie libre dépend de la partie élastique des discontinuités de déplacement $[\![\underline{u}]\!]^{e}$. Le moyen le plus naturel de les traiter de manière mésoscopique est d'utiliser une variable d'endommagement (cf. paragraphe 1.1.1). Elle peut aussi, sous certaines conditions, influencer la partie irrécupérable de la densité d'énergie libre dans le cas où il existe un champ de contraintes résiduelles dans le matériau non endommagé (cf. paragraphe 1.1.2.ii). La dégradation conduit alors à une relaxation du champ de contraintes résiduelles au voisinage de la fissure et à l'apparition de déformations « inélastiques ». La partie inélastique des discontinuités de déplacement $[\![\underline{u}]\!]^{i}$ influence également la partie irrécupérable de la densité d'énergie libre par la modification du champ de contraintes résiduelles (cf. paragraphe 1.1.2.iii). Le choix des variables internes est différent de celui qui a été fait dans le cas de la prise en compte des discontinuités élastiques de déplacement.

Les résultats précédents peuvent être utilisés dans le cadre de la thermodynamique des milieux continus [GERMAIN *et al.*, 1983]. Pour simplifier les calculs, on supposera des conditions isothermes. Sous cette hypothèse, la seule source de dissipation est d'origine « mécanique » (dissipation intrinsèque $\overline{p}^{d}$). La densité d'énergie de HELMHOLTZ $\overline{\psi}$ est une fonction de la déformation mésoscopique $\underline{\underline{\overline{\varepsilon}}}$ et d'un ensemble de variables internes notées collectivement $\widetilde{\mathbf{V}}$. L'application du premier principe de la thermodynamique conduit à

$$\underline{\underline{\overline{\sigma}}} : \dot{\underline{\underline{\overline{\varepsilon}}}} = \dot{\overline{\psi}}\,(\underline{\underline{\overline{\varepsilon}}}, \widetilde{\mathbf{V}}) + \overline{p}^{d}(\underline{\underline{\overline{\varepsilon}}}, \widetilde{\mathbf{V}}, \dot{\widetilde{\mathbf{V}}}) \tag{1.13}$$

où $\dot{\star}$ désigne la dérivée temporelle de la grandeur $\star$.

Le second principe de la thermodynamique stipule que la dissipation soit positive

pour toute transformation infinitésimale (inégalité de CLAUSIUS-DUHEM). Dans le cas particulier (isotherme) considéré, ceci revient à écrire

$$\overline{p}^{\mathrm{d}} \geq 0 \tag{1.14}$$

La dernière étape de la démarche consiste en l'identification des variables d'état $\widetilde{\mathbf{V}}$, leurs forces associées ainsi que leurs lois d'évolution. Les forces associées aux variables internes sont définies par

$$\overline{\underline{\underline{\sigma}}} = \frac{\partial \overline{\psi}}{\partial \overline{\underline{\underline{\epsilon}}}} \ , \ \widetilde{\mathbf{W}} = -\frac{\partial \overline{\psi}}{\partial \widetilde{\mathbf{V}}} \tag{1.15}$$

où $\widetilde{\mathbf{W}}$ sont les forces associées aux variables internes $\widetilde{\mathbf{V}}$. La puissance dissipée peut alors être réécrite comme suit

$$\overline{p}^{\mathrm{d}} = \widetilde{\mathbf{W}} \bullet \dot{\widetilde{\mathbf{V}}} \tag{1.16}$$

où « $\bullet$ » représente la contraction sur le nombre approprié d'indices. De même, de manière duale, on obtient

$$\overline{\underline{\underline{\epsilon}}} = \frac{\partial \overline{\varphi}}{\partial \overline{\underline{\underline{\sigma}}}} \ , \ \widetilde{\mathbf{W}} = \frac{\partial \overline{\varphi}}{\partial \widetilde{\mathbf{V}}} \tag{1.17}$$

L'obtention et l'identification des lois d'évolution des variables internes constitue la dernière étape de la construction d'une loi de comportement. Le choix des variables internes et le calcul du potentiel d'état sont un préalable important. En effet, la (bonne) connaissance d'une variable d'état et de sa force associée est un atout de taille dans la mesure où l'écriture des lois d'évolution est généralement facilitée. C'est pourquoi une grande partie du chapitre 3 est consacrée à l'étude du potentiel d'état. Une autre partie de ce chapitre est consacrée à l'écriture des lois d'évolution et à l'identification des paramètres inconnus. Ces lois d'évolution sont obtenues, soit sous forme différentielle

$$\dot{\widetilde{\mathbf{V}}} = \eta(\widetilde{\mathbf{V}}, \widetilde{\mathbf{W}}, \dot{\widetilde{\mathbf{W}}}, ...) \tag{1.18}$$

soit sous forme entière

$$\widetilde{\mathbf{V}} = \zeta(\widetilde{\mathbf{W}}, ...) \tag{1.19}$$

où η et ζ sont des fonctions à identifier. On notera que le cadre du « milieu standard généralisé » [HALPHEN et NGUYEN, 1975] est souvent utilisé (mais non obligatoire)

$$\dot{\widetilde{\mathbf{V}}} \in \partial\phi(\widetilde{\mathbf{V}}, \widetilde{\mathbf{W}}, \dot{\widetilde{\mathbf{W}}}, ...) \tag{1.20}$$

où $\partial\phi$ est le sous-différentiel du (pseudo-)potentiel de dissipation ϕ. Outre son caractère opérationnel [LEMAITRE et CHABOCHE, 1985], un des avantages (non négligeables) est de vérifier automatiquement l'inégalité de CLAUSIUS-DUHEM (1.14) lorsque ϕ est une fonction convexe de ses arguments, positive et nulle à l'origine (condition suffisante mais non nécessaire). Une comparaison entre les deux écritures (1.20) et (1.19) est faite dans le paragraphe 3.3.1.i.

Le choix d'échelles judicieusement identifiées rend l'écriture d'une loi d'évolution plus « naturelle » voire simplifiée par rapport à une démarche à une échelle unique. Des lois d'évolution sont présentées dans le paragraphe 3.1.3 dans le cas de chargements dynamiques de céramiques monolithiques, dans le paragraphe 3.2.2 pour l'analyse de la fissuration matricielle de composites à matrice fragile et dans le paragraphe 3.2.3 pour la rupture de fibres. Elles seront toutes basées sur la prise en compte de dégradations à l'échelle microscopique.

Reste enfin l'identification des paramètres des lois d'évolution. Différentes stratégies peuvent être considérées :

- la première consiste à identifier les paramètres à l'échelle à laquelle les lois sont écrites. Dans le passé, cette méthode a été utilisée avec succès pour les modèles à l'échelle mésoscopique. Les modèles « micromécaniques » font également appel à des mesures à l'échelle microscopique. La démarche sera illustrée dans le paragraphe 3.2.3 dans le cas d'un composite SiC/SiC [0/90]. On remarquera que la base du modèle (écrit à l'échelle mésoscopique) est microscopique (en particulier pour la construction du potentiel d'état), bien que les lois d'évolution soïent écrites et identifiées à une échelle mésoscopique ;

- la seconde utilise le changement d'échelle comme partie intégrante de l'identification. On peut ainsi corréler des paramètres mesurables à une échelle (grossière) à ceux correspondant à une autre échelle (plus fine). Ce point est discuté dans le paragraphe 2.3 pour des matériaux à comportement fragile. Dans le paragraphe 3.2.2, on montre comment une loi d'évolution identifiée à une échelle mésoscopique est plus « efficace » que celle qui aurait nécessité une étude détaillée au niveau microscopique (paragraphe 3.2.1).

Dans la suite de ce paragraphe, quelques exemples de calculs de densités d'énergies sont donnés. L'apport d'analyses à l'échelle microscopique est illustré pour le calcul des quantités énergétiques à l'échelle mésoscopique.

1.1.1 Calcul de la densité d'énergie élastique récupérable

Le comportement élastique d'un élément de volume endommagé est « affaibli » par rapport à un élément sain (non endommagé sans contrainte résiduelle). Ceci conduit à un couplage (classique [LEMAITRE et CHABOCHE, 1985 ; LEMAITRE, 1992a]) entre l'élasticité et l'endommagement. Dans la classification des différents couplages, celui-ci correspond à un couplage d'état, c'est-à-dire portant directement sur le potentiel d'état [MARQUIS, 1989]. La densité d'énergie libre récupérable $\overline{\psi}^{e}$ ne dépend que du tenseur de déformation élastique $\underline{\underline{\varepsilon}}^{e} = \underline{\underline{\varepsilon}} - \underline{\underline{\varepsilon}}^{i}$ et de la variable d'endommagement $\mathbf{D}$ dont la nature mathématique n'est pas précisée pour le moment. On suppose que la densité d'énergie irrécupérable ne dépend ni de la déformation totale $\underline{\underline{\varepsilon}}$, ni de la variable d'endommagement $\mathbf{D}$. Les forces associées aux variables d'état $\underline{\underline{\varepsilon}}$ et $\mathbf{D}$ sont respectivement définies par

$$\underline{\underline{\sigma}} = \frac{\partial \overline{\psi}^{e}}{\partial \underline{\underline{\varepsilon}}} \quad , \quad \mathbf{Y} = -\frac{\partial \overline{\psi}^{e}}{\partial \mathbf{D}} \tag{1.21}$$

où $\mathbf{Y}$ est le taux de restitution de densité d'énergie [CHABOCHE, 1977]. La conséquence du couplage d'état entre l'élasticité et l'endommagement est la suivante

$$\frac{\partial^2 \overline{\psi}^{e}}{\partial \mathbf{D} \partial \underline{\underline{\varepsilon}}} \neq 0 \quad \text{et} \quad \frac{\partial^2 \overline{\psi}^{e}}{\partial \underline{\underline{\varepsilon}} \partial \mathbf{D}} \neq 0 \tag{1.22}$$

De manière équivalente, la densité d'enthalpie libre récupérable $\overline{\varphi}^{e}$ dépend alors du tenseur des contraintes $\underline{\underline{\sigma}}$ et de la variable d'endommagement $\mathbf{D}$ et on obtient

$$\frac{\partial^2 \overline{\varphi}^{e}}{\partial \mathbf{D} \partial \underline{\underline{\sigma}}} \neq 0 \quad \text{et} \quad \frac{\partial^2 \overline{\varphi}^{e}}{\partial \underline{\underline{\sigma}} \partial \mathbf{D}} \neq 0 \tag{1.23}$$

Ce couplage d'état est mis à profit pour mesurer la variable d'endommagement $\mathbf{D}$ de manière indirecte par l'intermédiaire de la perte de raideur [LEMAITRE et DUFAILLY, 1977 ; 1987]. Ceci revient à écrire la partie réversible de la densité d'énergie libre sous la forme

$$\overline{\psi}^{e} = \frac{1}{2} (\underline{\underline{\varepsilon}} - \underline{\underline{\varepsilon}}^{i}) : \underline{\underline{\underline{\underline{E}}}}(\mathbf{D}) : (\underline{\underline{\varepsilon}} - \underline{\underline{\varepsilon}}^{i}) \tag{1.24}$$

où $\underline{\underline{\underline{\underline{E}}}}(\mathbf{D})$ est le tenseur de HOOKE du matériau endommagé.

Cette technique est couramment employée au LMT-Cachan dans le cas des matériaux métalliques [LEMAITRE et DUFAILLY, 1977 ; DUFAILLY, 1980 ; 1995] mais aussi pour les matériaux composites [POSS, 1982 ; GILETTA, 1985 ; LADEVÈZE *et al.*, 1994] ou des bétons [MAZARS, 1984 ; COLLOMBET, 1985 ; PIJAUDIER-CABOT, 1985]. Cette méthode peut être délicate dans le cas où l'endommagement est très dilué ou lorsque des phénomènes de refermeture de fissure sont observés. Dans ces conditions, le

caractère (quasi-)unilatéral de l'endommagement a également été analysé de manière diverse et variée au LMT-Cachan [LADEVÈZE, 1983 ; LADEVÈZE et LEMAITRE, 1984 ; LIÉNARD, 1989 ; MAZARS *et al.*, 1990 ; RAMTANI, 1990 ; LA BORDERIE, 1991]. Le caractère unilatéral de l'endommagement est liée à un mécanisme de fissuration au niveau mésoscopique ou microscopique dans le cas des composites [LADEVÈZE *et al.*, 1994] (ce dernier mécanisme sera analysé dans le chapitre 3). Les études récentes sur ce sujet intègrent cette notion de manière plus ou moins sophistiquée [CHABOCHE, 1992 ; DRAGON et HALM, 1995 ; 1996].

La prise en compte explicite des hétérogénéités microscopiques a été considérée de diverses manières dès l'émergence de la mécanique de l'endommagement. Citons par exemple les travaux de M. KACHANOV [VAKULENKO et KACHANOV, 1971 ; KACHANOV, 1994], ceux de BUDIANSKY [1965 ; 1976] qui ne font pas explicitement référence à la mécanique de l'endommagement mais qui peuvent être reformulés dans ce cadre [KRAJCINOVIC, 1987 ; KRAJCINOVIC et SUMARAC, 1987 ; KRAJCINOVIC, 1989 ; BURR *et al.*, 1995]. Ces analyses conduisent à des descriptions tensorielles de l'endommagement d'ordre pair et peuvent être rapprochées des travaux de décomposition de tenseurs symétriques d'ordre 4 (tenseur d'élasticité) en tenseurs d'ordre 0, 2 et 4 [LECKIE et ONAT, 1980 ; ONAT, 1984 ; ONAT et LECKIE, 1988]. Ce type de décomposition permet également de justifier le choix d'un tenseur du second ordre pour décrire un mécanisme d'endommagement par fissuration dans lequel les fissures restent ouvertes [DRAGON et HALM, 1995]. On remarquera que si les conditions unilatérales sont explicitement prises en compte et si les faces des fissures fermées peuvent glisser sans frotter, l'approximation précédente n'est plus justifiée et l'introduction d'un tenseur du quatrième ordre est nécessaire. Une prise en compte du frottement ne change pas fondamentalement ce résultat [KRAJCINOVIC, 1987 ; KRAJCINOVIC et SUMARAC, 1987]. Un autre type de décomposition peut être employé en étudiant les valeurs propres du tenseur de HOOKE ou des souplesses [FRANÇOIS, 1995]. Le lien entre les deux approches reste encore à faire.

Remarquons que le couplage d'état entre élasticité et endommagement a été d'abord envisagé en terme de contrainte effective unidimensionnelle [RABOTNOV, 1969] puis tridimensionnelle à l'aide du principe d'équivalence en déformation [LEMAITRE, 1978] dans le cas d'une description isotrope de l'endommagement. L'extension de la notion de contrainte effective au cas anisotrope n'est pas aisée car la symétrie majeure du tenseur de HOOKE peut être perdue. D'autre part, la condition de symétrie peut s'avérer trop restrictive quant à la forme du tenseur des contraintes effectives [CORDEBOIS et SIDOROFF, 1982]. CORDEBOIS et SIDOROFF proposent d'étudier directement le couplage entre l'élasticité et l'endommagement au niveau de l'enthalpie libre d'un

matériau endommagé par l'introduction de la contrainte effective, ce qui garantit automatiquement la symétrie du tenseur des souplesses (et donc du tenseur de HOOKE) sans préjuger de la relation liant le tenseur des contraintes effectives (microscopiques) au tenseur des contraintes appliquées (mésoscopiques). Finalement la manière la plus simple d'étudier ce couplage est d'en analyser les conséquences sur les propriétés élastiques ce qui est fait couramment depuis le milieu des années 1970 d'un point de vue expérimental [LEMAITRE et DUFAILLY, 1977]. Cependant, les études micromécaniques des années 1980 et 1990 ne font appel ni à la notion de contrainte effective, ni au principe d'équivalence en déformation. Les différents auteurs étudient davantage les variations du tenseur des souplesses (cf. par exemple [ONAT, 1984 ; KRAJCINOVIC, 1989 ; KACHANOV, 1994]) en calculant la densité d'enthalpie libre récupérable

$$\overline{\varphi}^{\mathrm{e}} = \frac{1}{2}\,\underline{\underline{\overline{\sigma}}} : \underline{\underline{\underline{\underline{\overline{S}}}}}(\mathbf{D}) : \underline{\underline{\overline{\sigma}}} + \underline{\underline{\overline{\sigma}}} : \underline{\underline{\overline{\epsilon}}}^{\mathrm{i}} \tag{1.25}$$

où $\underline{\underline{\underline{\underline{\overline{S}}}}}(\mathbf{D})$ est le tenseur des souplesses (ou complaisances). Ce type de raisonnement sera utilisé dans le paragraphe 3.1.1 avec $\underline{\underline{\overline{\epsilon}}}^{\mathrm{i}} = 0$. Les forces associées aux variables d'état $\underline{\underline{\overline{\sigma}}}$ et $\mathbf{D}$ sont définies par

$$\underline{\underline{\overline{\epsilon}}} = \frac{\partial \overline{\varphi}^{\mathrm{e}}}{\partial \underline{\underline{\overline{\sigma}}}} \quad , \quad \mathbf{Y} = \frac{\partial \overline{\varphi}^{\mathrm{e}}}{\partial \mathbf{D}} \tag{1.26}$$

en supposant que la partie irrécupérable de l'enthalpie libre ne dépend ni de $\underline{\underline{\overline{\sigma}}}$, ni de $\mathbf{D}$.

Enfin, la notion d'endommagement initial est fondamentale pour l'étude de matériaux hétérogènes contenant des phases à comportement ductile [CORDEBOIS, 1979 ; BENALLAL *et al.*, 1987]. Cette notion a également été développée pour des matériaux à comportement fragile [HILD, 1992 ; YAACOUB AGHA et HILD, 1995]. Se pose néanmoins la question de la nature de l'endommagement initial par rapport à celle de l'endommagement induit par le chargement extérieur. Cette question est partiellement traitée dans le paragraphe 1.2.2.

1.1.2 Calcul de la densité d'énergie élastique irrécupérable

L'objet de ce paragraphe est de calculer la densité d'énergie irrécupérable en utilisant les résultats évoqués ci-dessus. On montre le lien que l'on peut établir entre les calculs à partir de considérations microscopiques et le choix de variables internes à l'échelle mésoscopique. Les exemples (très simples) qui suivent ont pour but d'introduire des concepts qui sont réutilisés et généralisés dans le chapitre 3. Dans le premier exemple, deux méthodes différentes seront présentées pour le calcul de la déformation inélastique mésoscopique. Les deuxième et troisième exemples utiliseront

chacun l'une d'entre elles.

i Modèle rhéologique d'un matériau biphasé écrouissable

Ce premier exemple est certainement le modèle le plus simple pour calculer une densité d'énergie irrécupérable (cf. par exemple [MANDEL, 1978a] dans une version légèrement modifiée de l'association d'éléments rhéologiques). La figure 1.2 montre un ressort S_1 de raideur E_1 et de fraction volumique f en parallèle avec un ressort S_2 de raideur E_2 et de fraction volumique $(1-f)$ en série avec un patin Y_2 caractérisé par un glissement γ_2^{p}. On suppose qu'initialement le composite est libre de toute contrainte.

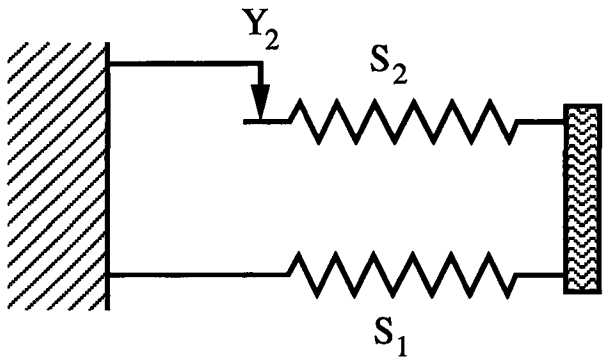

FIG. 1.2 - Modèle rhéologique d'un matériau biphasé écrouissable.

La raideur initiale du composite est $E = fE_1 + (1-f)E_2$. Le calcul de la densité d'énergie irrécupérable nécessite le calcul du champ de contraintes résiduelles σ^{r} qui a pour expression dans chaque ressort

$$\sigma_1^{\mathrm{r}} = \frac{(1-f)E_2E_1}{E}\gamma_2^{\mathrm{p}} \quad , \quad \sigma_2^{\mathrm{r}} = -\frac{fE_1E_2}{E}\gamma_2^{\mathrm{p}} \tag{1.27}$$

Ce champ de contraintes résiduelles correspond au passage d'un état « non plastifié » (point O de la figure 1.1) à un état « plastifié » (point A de la figure 1.1) sans chargement extérieur. La densité d'énergie irrécupérable s'exprime par (cf. équation (1.9))

$$\overline{\psi}^{\mathrm{i}} = \frac{1}{2}\left[\frac{f(\sigma_1^{\mathrm{r}})^2}{E_1} + \frac{(1-f)(\sigma_2^{\mathrm{r}})^2}{E_2}\right] = \frac{f(1-f)E_1E_2}{2E}\left(\gamma_2^{\mathrm{p}}\right)^2 \tag{1.28}$$

Cette densité d'énergie (1.28) peut aussi s'écrire en fonction de la déformation plastique mésoscopique $\overline{\epsilon}^{\mathrm{p}}$. Pour calculer cette déformation plastique, deux approches équivalentes peuvent être employées :

- la première consiste à utiliser le principe des travaux virtuels. On considère le champ de déplacement associé au modèle rhéologique et le champ de contrainte associé au système de deux ressorts en parallèle sans patin ($\gamma_2^{\mathrm{p}} = 0$). Soit $\hat{\overline{\sigma}}$ la contrainte mésoscopique (virtuelle), les contraintes microscopiques (virtuelles) s'expriment de la manière suivante

$$\hat{\sigma}_1 = \frac{E_1}{E}\hat{\overline{\sigma}} \ , \ \hat{\sigma}_2 = \frac{E_2}{E}\hat{\overline{\sigma}} \tag{1.29}$$

  Par application du principe des travaux virtuels, et en remarquant que le champ de contraintes résiduelles σ_1^{r} et σ_2^{r} est auto-équilibré, on obtient

$$\hat{\overline{\sigma}}\,\overline{\epsilon}^{\mathrm{p}} = (1-f)\hat{\sigma}_2\gamma_2^{\mathrm{p}} \ \text{ soit } \ \overline{\epsilon}^{\mathrm{p}} = \frac{(1-f)E_2}{E}\gamma_2^{\mathrm{p}} \tag{1.30}$$

  Cette méthode a pour avantage de ne pas nécessiter la connaissance exacte du champ de contraintes résiduelles pour évaluer la déformation plastique mésoscopique [Cocks et Leckie, 1987 ; Burr *et al.*, 1995]. Elle sera réutilisée dans le paragraphe 1.1.2.iii.

- la seconde revient à remarquer que la déformation dans le ressort S_1, $\sigma_1^{\mathrm{r}}/E_1$, correspond à la déformation mésoscopique $\overline{\epsilon}^{\mathrm{p}}$. On obtient à nouveau le résultat (1.30). Elle sera réutilisée dans le paragraphe 1.1.2.ii.

La densité d'énergie irrécupérable s'exprime alors par

$$\overline{\psi}^{\mathrm{i}} = \frac{E}{2}\frac{fE_1}{(1-f)E_2}\left(\overline{\epsilon}^{\mathrm{p}}\right)^2 \tag{1.31}$$

Cette expression ne dépend pas du comportement exact du patin. La variable interne caractérisant ce problème est la déformation $\overline{\epsilon}^{\mathrm{p}}$ et la force associée est obtenue à partir de l'expression du potentiel d'état $\overline{\psi}$

$$\overline{\psi} = \frac{E}{2}\left(\overline{\epsilon} - \overline{\epsilon}^{\mathrm{p}}\right)^2 + \frac{E}{2}\frac{fE_1}{(1-f)E_2}\left(\overline{\epsilon}^{\mathrm{p}}\right)^2 \tag{1.32}$$

et s'écrit

$$X = -\frac{\partial\overline{\psi}}{\partial\overline{\epsilon}^{\mathrm{p}}} = \overline{\sigma} - E\frac{fE_1}{(1-f)E_2}\overline{\epsilon}^{\mathrm{p}} \tag{1.33}$$

de telle manière que la puissance dissipée devient

$$\overline{p}^{\mathrm{d}} = X\,\dot{\overline{\epsilon}}^{\mathrm{p}} \tag{1.34}$$

Si l'on suppose que ce patin modélise un mécanisme de plasticité parfaite au niveau microscopique (cission critique τ_2^{c}), le comportement mésoscopique est celui d'un

matériau à écrouissage cinématique linéaire et on peut calculer la puissance dissipée ($\dot{\gamma}_2^{\mathrm{p}} \geq 0, \dot{\bar{\epsilon}}^{\mathrm{p}} \geq 0$)

$$\overline{p}^{\mathrm{d}} = (1-f)\tau_2^{\mathrm{c}}\,\dot{\gamma}_2^{\mathrm{p}} = \frac{E}{E_2}\tau_2^{\mathrm{c}}\,\dot{\bar{\epsilon}}^{\mathrm{p}} \tag{1.35}$$

Cette quantité est positive et vérifie donc l'inégalité de CLAUSIUS DUHEM (*i.e.*, le second principe de la thermodynamique).

Sur un graphe contrainte/déformation mésoscopique on peut facilement tracer les différentes énergies mises en jeu pour passer d'un point O à un point B (en passant par le point F). La figure 1.3 représente les différents termes dans le cas d'un écrouissage cinématique linéaire. Sur cette figure on remarquera que l'on n'a pas utilisé la représentation classique de l'énergie irrécupérable (cf. par exemple [SUQUET, 1982 ; LEMAITRE et CHABOCHE, 1985]) mais l'aire $FEBF$. Ce type de raisonnement pour calculer l'énergie irrécupérable va être explicité ci-dessous. Il peut être conduit pour des associations plus complexes de ressorts et de patins [MANDEL, 1978a] ou dans le cas de champs de contraintes hétérogènes [ARAVAS *et al.*, 1990].

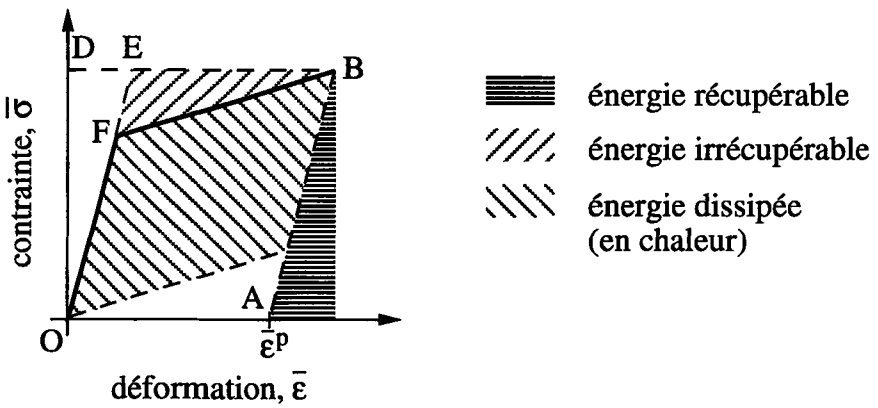

FIG. 1.3 - Bilan énergétique pour un matériau à écrouissage cinématique linéaire.

En suivant le raisonnement de ARAVAS *et al.* [1990], l'aire $ODEBFO$, $\mathcal{A}_{\mathrm{ODEBFO}}$, correspond à

$$\mathcal{A}_{\mathrm{ODEBFO}} = \int_O^B \bar{\epsilon}\, d\bar{\sigma} \tag{1.36}$$

Or l'aire $ODEFO$ représente $\overline{\psi}^{\mathrm{e}}_{\mathrm{OB}}$, de telle sorte que l'aire $FEBF$ devient

$$\mathcal{A}_{\mathrm{FEBF}} = \overline{\psi}^{\mathrm{i}}_{\mathrm{OB}} + (1-f)\int_O^B \gamma_2^{\mathrm{p}}\, d\tau_2 \tag{1.37}$$

La loi de normalité implique que $\gamma_2^{\mathrm{p}}\ d\tau_2 = 0$ d'où le résultat énoncé. Un raisonnement équivalent peut être trouvé dans [MANDEL, 1978a]. On remarquera enfin que, lorsque le principe du travail maximal est satisfait [HILL, 1950] (*i.e.*, $[\tau_2(B) - \tau_2]\ d\gamma_2^{\mathrm{p}} \geq 0$), l'aire $FEBF$ est un *majorant* de l'énergie irrécupérable [ARAVAS *et al.*, 1990].

ii Composite endommageable

La figure 1.4 montre une cellule de longueur $2L$ avec une fibre (f) de raideur E_{f} et de fraction volumique f entourée de matrice (m) de raideur E_{m} et de fraction volumique $(1-f)$. La fissuration matricielle se produit au milieu de la cellule (la longueur $2L$ caractérise la distance entre fissures matricielles, donc l'état de dégradation du matériau).

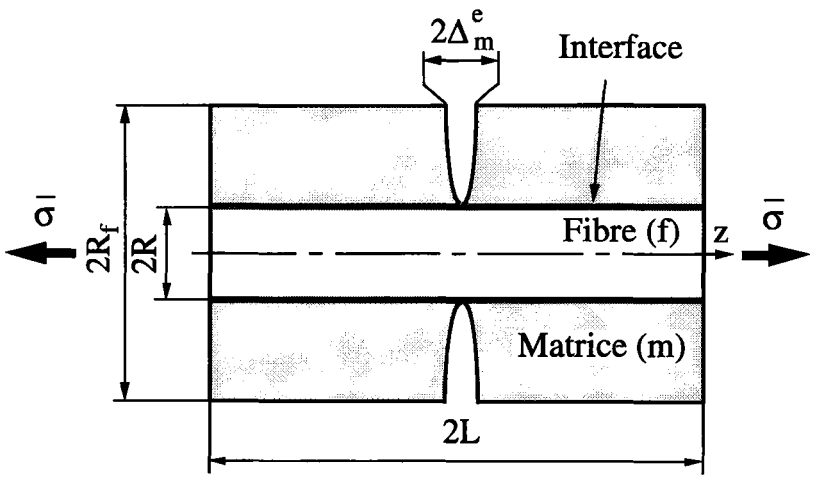

FIG. 1.4 - Cellule élémentaire pour l'étude de la fissuration d'un composite endommageable.

On note ρ_{f} et ρ_{m} les contraintes résiduelles initiales dans chaque constituant. Ce champ est auto-équilibré

$$f\rho_{\mathrm{f}} + (1-f)\rho_{\mathrm{m}} = 0 \tag{1.38}$$

Pour déterminer les contraintes dans la fibre et la matrice, on utilise le modèle de COX [1952] dont les hypothèses statiques et cinématiques sont assez voisines de celles utilisées dans l'étude d'assemblages rivetés [VOLKERSEN, 1938]. D'autres modèles peuvent être utilisés (cf. par exemple [BUDIANSKY *et al.*, 1986]). Les hypothèses sont assez proches de celles utilisées par COX [1952]. La contrainte longitudinale dans la fibre $\sigma_{\mathrm{f}}(z)$, solution d'une équation différentielle du second ordre, s'écrit

$$\sigma_{\mathrm{f}}(z) = \frac{(1-f)E_{\mathrm{m}}}{fE}\frac{\cosh[B(L-z)]}{\cosh BL}(\overline{\sigma}+\rho) + \frac{E_{\mathrm{f}}}{E}\overline{\sigma} + \rho_{\mathrm{f}} \tag{1.39}$$

avec

$$\frac{\rho}{E} = \frac{\rho_{\mathrm{m}}}{E_{\mathrm{m}}} \tag{1.40}$$

où z est la coordonnée longitudinale et B est une constante dépendant des propriétés élastiques et géométriques de la fibre et de la matrice (le paramètre B est inversement proportionnel au rayon R de la fibre). La contrainte longitudinale dans la matrice $\sigma_{\mathrm{m}}(z)$ s'obtient par la condition d'équilibre globale

$$f\sigma_{\mathrm{f}}(z) + (1-f)\sigma_{\mathrm{m}}(z) = \overline{\sigma} \tag{1.41}$$

Enfin la contrainte de cisaillement dans la matrice $\tau_{\mathrm{m}}(r,z)$ s'obtient à l'aide de l'intégration de l'équation d'équilibre locale dans la matrice

$$\tau_{\mathrm{m}}(r,z) = \frac{R\tau_{\mathrm{i}}(z)}{r} \tag{1.42}$$

où r est le rayon au point courant, et $\tau_{\mathrm{i}}(z)$ est la contrainte de cisaillement agissant sur la fibre, qui vérifie l'équilibre longitudinal de la fibre

$$\frac{d\sigma_{\mathrm{f}}}{dz}(z) + \frac{2\tau_{\mathrm{i}}(z)}{R} = 0 \tag{1.43}$$

En notant que le point de référence de calcul des déformations est le composite dans son état initial (avec contraintes résiduelles), la déformation longitudinale mésoscopique s'exprime par

$$\overline{\epsilon} = \frac{1}{2L}\int_{-L}^{L} \frac{\sigma_{\mathrm{f}}(z) - \rho_{\mathrm{f}}}{E_{\mathrm{f}}}\, dz = \frac{\overline{\sigma}}{E} + \delta\overline{\epsilon} \tag{1.44}$$

où $\delta\overline{\epsilon}$ est la déformation additionnelle liée à l'ouverture élastique $\Delta_{\mathrm{m}}^{\mathrm{e}}$ de la fissure matricielle

$$\delta\overline{\epsilon} = \frac{(1-f)E_{\mathrm{m}}}{E}\frac{\Delta_{\mathrm{m}}^{\mathrm{e}}}{L} \tag{1.45}$$

$$= \frac{(1-f)E_{\mathrm{m}}}{fE_{\mathrm{f}}}\frac{\tanh(BL)}{BL}\frac{\overline{\sigma}+\rho}{E} \tag{1.46}$$

En utilisant la méthode développée par BUDIANSKY *et al.* [1986], on peut calculer la variation d'énergie de GIBBS $\Delta\overline{\varphi}$

$$\Delta\overline{\varphi} = \frac{(1-f)E_{\mathrm{m}}}{fE_{\mathrm{f}}}\frac{\tanh(BL)}{BL}\frac{(\overline{\sigma}+\rho)^2}{2E} \tag{1.47}$$

Tous ces résultats sont la traduction au niveau mésoscopique du modèle micromécanique choisi (ici le modèle de COX [1952]). Voyons maintenant comment ces résultats peuvent être retraduits dans le cadre de la thermodynamique des milieux continus. Pour cela,

remarquons que seul le paramètre BL intervient dans les équations (1.46) et (1.47). La variable naturelle prenant en compte ce paramètre (adimensionnel) est une variable d'endommagement D que l'on peut définir de la manière suivante

$$\frac{D}{1-D} = \frac{(1-f)E_{\mathrm{m}}}{fE_{\mathrm{f}}}\frac{\tanh(BL)}{BL} \tag{1.48}$$

de telle manière que la variation de densité d'énergie de GIBBS s'écrit

$$\overline{\varphi} = \frac{\overline{\sigma}^2}{2E} + \frac{(\overline{\sigma}+\rho)^2 D}{2E(1-D)} \tag{1.49}$$

et la relation déformation/contrainte (1.44) devient

$$\overline{\epsilon} = \frac{\overline{\sigma}}{E} + \frac{(\overline{\sigma}+\rho)D}{E(1-D)} \tag{1.50}$$

Si l'on veut calculer la densité d'énergie de HELMHOLTZ, on peut utiliser la méthode générale en deux étapes. La première étape consiste à créer une fissure dans un composite sans chargement extérieur et soumis à un champ de contraintes résiduelles. On suppose que $\rho_{\mathrm{f}} \geq 0$ de telle manière que la fissure créée sans charge extérieure puisse effectivement s'ouvrir. Dans le cas général cette condition (restrictive) peut être levée sans aucun problème (la refermeture pouvant avoir lieu dans le premier quadrant du diagramme contrainte/déformation). En remarquant que : $\overline{\psi}^{\mathrm{i}} = -\Delta\overline{\varphi}(\overline{\sigma}=0)$, on obtient en utilisant l'équation (1.47)

$$\overline{\psi}^{\mathrm{i}} = -\frac{\rho^2 D}{2E(1-D)} \tag{1.51}$$

On notera que ce résultat peut également être obtenu en appliquant l'équation (1.9)

$$\begin{aligned}\overline{\psi}^{\mathrm{i}} &= \frac{1}{2L}\int_{-L}^{L}\left[\frac{f\{\sigma_{\mathrm{f}}^{\mathrm{r}}(z)\}^2}{2E_{\mathrm{f}}} + \frac{(1-f)\{\sigma_{\mathrm{m}}^{\mathrm{r}}(z)\}^2}{2E_{\mathrm{m}}}\right] dz \\ &+ \frac{1}{2LR_{\mathrm{m}}^2}\int_{-L}^{L}\int_{R}^{R_{\mathrm{m}}}\frac{\tau_{\mathrm{m}}^2(r,z)}{G_{\mathrm{mf}}}\, r dr\, dz\end{aligned} \tag{1.52}$$

pour le champ de contraintes résiduelles suivant

$$\sigma_{\mathrm{f}}^{\mathrm{r}}(z) = \frac{(1-f)E_{\mathrm{m}}}{fE}\left[\frac{\cosh[B(L-z)]}{\cosh BL} - 1\right]\rho \tag{1.53}$$

$$\sigma_{\mathrm{m}}^{\mathrm{r}}(z) = -\frac{f\sigma_{\mathrm{f}}^{\mathrm{r}}(z)}{1-f} \tag{1.54}$$

$$\tau_{\mathrm{m}}^{\mathrm{r}}(r,z) = -\frac{2R^2}{r}\frac{d\sigma_{\mathrm{f}}^{\mathrm{r}}}{dz}(z) \tag{1.55}$$

Cette restitution d'énergie s'accompagne de déformations inélastiques $\overline{\epsilon}^{\mathrm{i}}(D)$ causées par la relaxation des contraintes résiduelles. Cette déformation inélastique dépend de la variable d'endommagement D (ce n'est pas une variable interne supplémentaire)

$$\overline{\epsilon}^{\mathrm{i}}(D) = \frac{1}{2L}\int_{-L}^{L} \frac{\sigma_{\mathrm{f}}^{\mathrm{r}}(z) - \rho_{\mathrm{f}}}{E_{\mathrm{f}}}\, dz = \frac{\rho D}{E(1-D)} \tag{1.56}$$

La deuxième étape consiste à appliquer une charge extérieure sur un matériau endommagé. La densité d'énergie récupérable $\overline{\psi}^{\mathrm{e}}$ s'écrit donc de manière classique (cf. paragraphe 1.1.1)

$$\overline{\psi}^{\mathrm{e}} = \frac{E(1-D)}{2}\left[\overline{\epsilon} - \overline{\epsilon}^{\mathrm{i}}(D)\right]^2 \tag{1.57}$$

de telle manière que la densité d'énergie de HELMHOLTZ s'exprime par

$$\overline{\psi} = \frac{E(1-D)}{2}\left[\overline{\epsilon} - \overline{\epsilon}^{\mathrm{i}}(D)\right]^2 - \frac{\rho^2 D}{2E(1-D)} \tag{1.58}$$

La force associée Y à la variable d'endommagement D devient

$$Y = -\frac{\partial \overline{\psi}}{\partial D} = \frac{(\overline{\sigma} + \rho)^2}{2E(1-D)^2} \tag{1.59}$$

de telle manière que la puissance dissipée s'écrit

$$\overline{p}^{\mathrm{d}} = Y\, \dot{D} \tag{1.60}$$

Cette quantité est positive (car $Y \geq 0$) lorsque $\dot{D} \geq 0$. On remarquera que la contrainte « effective » $\tilde{\sigma} = (\overline{\sigma} + \rho)/(1-D)$ est modifiée par rapport à sa forme classique ($\tilde{\sigma} = \overline{\sigma}/(1-D)$) [RABOTNOV, 1969 ; LEMAITRE et CHABOCHE, 1985] du fait de la présence d'un champ de contraintes résiduelles initiales. Tous ces résultats auraient pu être obtenus (plus rapidement) en utilisant la transformée de LEGENDRE-FENCHEL (cf. équation (1.4)) à partir de l'équation (1.49).

On peut à nouveau tracer les différentes énergies mises en jeu pour passer d'un état O à un état B. La figure 1.5 représente les différentes contributions dans le cas d'un chargement à contrainte $\overline{\sigma}$ croissante. Le tracé de l'énergie élastique récupérable ne pose pas de problème particulier. Pour tracer l'énergie irrécupérable, on remarquera que l'on peut considérer un chemin différent de celui passant de O à B. Pour cela, notons que si l'on applique une contrainte mésoscopique $\overline{\sigma} = -\rho$, la contrainte dans la matrice est nulle (point C). On peut alors créer une fissure sans occasionner de déformations inélastiques. Ensuite on peut charger cet élément endommagé qui se comporte comme un solide élastique avec une raideur dégradée $E(1-D)$ jusqu'au point B. À partir du point C, on se retrouve dans la situation classique pour un élément endommageable

[LEMAITRE et CHABOCHE, 1985]. L'énergie dissipée (en chaleur) correspond à l'aire *OBACO*. Quant à l'opposé de l'énergie irrécupérable, elle correspond à l'aire *OACO*.

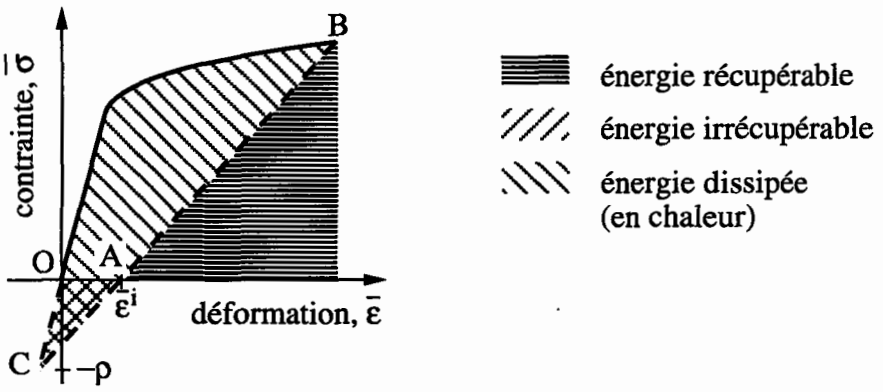

FIG. 1.5 - Bilan énergétique pour un composite endommageable avec contraintes résiduelles initiales.

iii Fissure frottante

Ce dernier exemple concerne une cellule élémentaire qui sera réutilisée pour l'étude de la dégradation de composites unidirectionnels (cf. paragraphe 3.2.2) et bidirectionnels (cf. paragraphe 3.2.3). Une généralisation peut également être trouvée dans [BURR *et al.*, 1995]. La base de cette cellule est celle du paragraphe précédent (cf. figure 1.4).

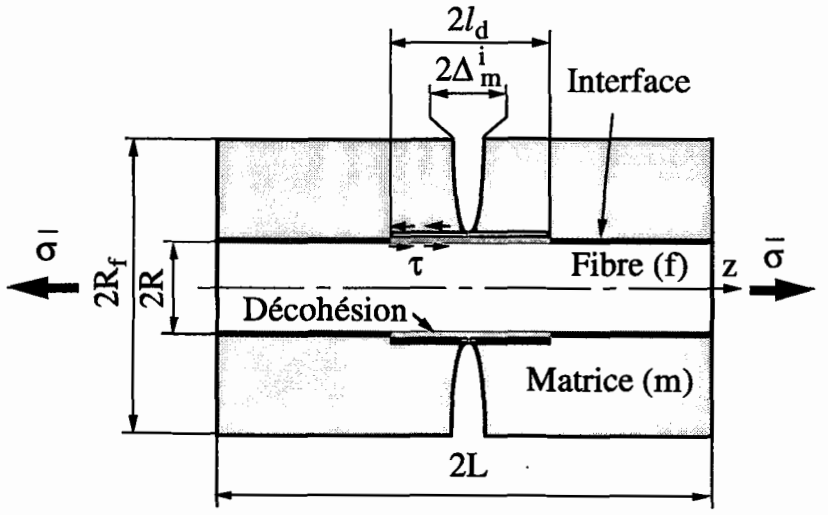

FIG. 1.6 - Cellule élémentaire d'un composite subissant de la décohésion et du frottement.

La fissuration matricielle (non décrite dans ce paragraphe) engendre une décohésion sur une longueur $2l_{\mathrm{d}}$. On suppose que cette fissure subit un frottement sur une longueur $2l_{\mathrm{f}}$, prise égale à $2l_{\mathrm{d}}$. Pour simplifier les calculs, seuls les phénomènes de décohésion et de glissement sont pris en compte ($L \gg l_{\mathrm{f}}$). Aucune variable d'endommagement de fissuration (matricielle) ne sera utilisée ($BL \gg 1$).

Le calcul de la densité d'énergie irrécupérable nécessite la connaissance du champ de contraintes résiduelles $\underline{\underline{\sigma}}^{\mathrm{r}}$ induit par le frottement. On note $\sigma_{\mathrm{f}}^{\mathrm{r}}(z)$ et $\sigma_{\mathrm{m}}^{\mathrm{r}}(z)$ les contraintes uniaxiales résiduelles dans la fibre et la matrice qui vérifient

$$f\sigma_{\mathrm{f}}^{\mathrm{r}}(z) + (1-f)\sigma_{\mathrm{m}}^{\mathrm{r}}(z) = 0 \quad \forall\, z \in [-L, L] \tag{1.61}$$

La densité d'énergie irrécupérable s'exprime par (cf. équation (1.9))

$$\begin{aligned} \overline{\psi}^{\mathrm{i}} &= \frac{1}{2L}\int_{-L}^{L}\left[\frac{f\{\sigma_{\mathrm{f}}^{\mathrm{r}}(z)\}^2}{2E_{\mathrm{f}}} + \frac{(1-f)\{\sigma_{\mathrm{m}}^{\mathrm{r}}(z)\}^2}{2E_{\mathrm{m}}}\right] dz \\ &= \frac{EfE_{\mathrm{f}}}{4L(1-f)E_{\mathrm{m}}}\int_{-L}^{L}\left[\frac{\sigma_{\mathrm{f}}^{\mathrm{r}}(z)}{E_{\mathrm{f}}}\right]^2 dz \end{aligned} \tag{1.62}$$

Cette densité d'énergie (1.62) peut aussi s'écrire en fonction de la déformation inélastique mésoscopique $\overline{\epsilon}^{\mathrm{i}}$. Pour calculer cette déformation inélastique, on utilisera le principe des travaux virtuels (de la même manière que dans le paragraphe 1.1.2.i). On considère le champ de déplacement associé au problème de la fissure frottante et le champ de contrainte associé au système non fissuré. On note $\hat{\overline{\sigma}}$ la contrainte mésoscopique uniaxiale, les contraintes uniaxiales microscopiques s'expriment de la manière suivante

$$\hat{\sigma}_{\mathrm{f}} = \frac{E_{\mathrm{f}}}{E}\hat{\overline{\sigma}} \ , \ \hat{\sigma}_{\mathrm{m}} = \frac{E_{\mathrm{m}}}{E}\hat{\overline{\sigma}} \tag{1.63}$$

Par application du principe des travaux virtuels on obtient

$$\begin{aligned} 2L\pi R_{\mathrm{f}}^2\, \hat{\overline{\sigma}}\, \overline{\epsilon}^{\mathrm{i}} &= \pi R_{\mathrm{f}}^2 \int_{-L}^{L}\left[\frac{f\hat{\sigma}_{\mathrm{f}}\sigma_{\mathrm{f}}^{\mathrm{r}}(z)}{E_{\mathrm{f}}} + \frac{(1-f)\hat{\sigma}_{\mathrm{m}}\sigma_{\mathrm{m}}^{\mathrm{r}}(z)}{E_{\mathrm{m}}}\right] dz \\ &+ 2\pi\int_{R}^{R_{\mathrm{f}}} \hat{\sigma}_{\mathrm{m}}\, [\![u_{\mathrm{m}}(r)]\!]^{\mathrm{i}}\, r dr \end{aligned} \tag{1.64}$$

et en remarquant que le champ de contraintes résiduelles $\sigma_{\mathrm{f}}^{\mathrm{r}}(z)$ et $\sigma_{\mathrm{m}}^{\mathrm{r}}(z)$ est auto-équilibré (équation (1.61)), on obtient

$$\overline{\epsilon}^{\mathrm{i}} = \frac{(1-f)E_{\mathrm{m}}}{E}\frac{\Delta_{\mathrm{m}}^{\mathrm{i}}}{L} \tag{1.65}$$

avec

$$\Delta_{\mathrm{m}}^{\mathrm{i}} = \frac{1}{R_{\mathrm{f}}^2 - R^2} \int_R^{R_{\mathrm{f}}} [\![u_{\mathrm{m}}(r)]\!]^{\mathrm{i}} \, r dr = \int_{-L}^{L} \left[\frac{\sigma_{\mathrm{f}}^{\mathrm{r}}(z)}{E_{\mathrm{f}}} - \frac{\sigma_{\mathrm{m}}^{\mathrm{r}}(z)}{E_{\mathrm{m}}} \right] dz \tag{1.66}$$

On notera à nouveau la similitude entre les équations (1.30.2), (1.45) et (1.65). La quantité $\Delta_{\mathrm{m}}^{\mathrm{i}}$ représente la demi-ouverture de la fissure matricielle liée à la décohésion et au frottement. La densité d'énergie libre irrécupérable s'exprime par

$$\overline{\psi}^{\mathrm{i}} = \frac{E}{2} \frac{\left(\overline{\epsilon}^{\mathrm{i}}\right)^2}{d} \tag{1.67}$$

où la variable d'endommagement d s'écrit

$$d = \frac{(1-f)E_{\mathrm{m}}}{fE_{\mathrm{f}}} \frac{\left[\frac{1}{2L}\int_{-L}^{L} \frac{\sigma_{\mathrm{f}}^{\mathrm{r}}(z)}{E_{\mathrm{f}}} \, dz\right]^2}{\frac{1}{2L}\int_{-L}^{L} \left[\frac{\sigma_{\mathrm{f}}^{\mathrm{r}}(z)}{E_{\mathrm{f}}}\right]^2 dz} \tag{1.68}$$

La variable d'endommagement d est encadrée par

$$0 \leq d \leq \frac{(1-f)E_{\mathrm{m}}}{fE_{\mathrm{f}}} \tag{1.69}$$

On remarquera que ce type d'expression a également été utilisé par ANDRIEUX *et al.* [1981 ; 1986] dans l'étude de milieux microfissurés.

Les variables internes caractérisant ce problème sont la déformation inélastique $\overline{\epsilon}^{\mathrm{i}}$ et la variable d'endommagement d. Les forces associées sont obtenues à partir de l'expression du potentiel d'état $\overline{\psi}$

$$\overline{\psi} = \frac{E}{2}\left(\overline{\epsilon} - \overline{\epsilon}^{\mathrm{i}}\right)^2 + \frac{E}{2}\frac{\left(\overline{\epsilon}^{\mathrm{i}}\right)^2}{d} \tag{1.70}$$

et s'écrivent

$$X = -\frac{\partial \overline{\psi}}{\partial \overline{\epsilon}^{\mathrm{i}}} = \overline{\sigma} - E\frac{\overline{\epsilon}^{\mathrm{i}}}{d} \quad , \quad y = -\frac{\partial \overline{\psi}}{\partial d} = \frac{E}{2}\left(\frac{\overline{\epsilon}^{\mathrm{i}}}{d}\right)^2 \tag{1.71}$$

de telle manière que la puissance dissipée s'écrit

$$\overline{p}^{\mathrm{d}} = X \overset{\bullet}{\overline{\epsilon}}^{\mathrm{i}} + y \overset{\bullet}{d} \tag{1.72}$$

Par définition on a : $\overset{\bullet}{d} \geq 0$ et $\overset{\bullet}{\overline{\epsilon}}^{\mathrm{i}} \geq 0$ en chargement. La force associée à l'endommagement d vérifie : $y \geq 0$ (cf. équation (1.71.2)). Par contre, le calcul de la force X nécessite la connaissance du modèle d'interface. Si l'on suppose que le glissement interfacial obéit au modèle (très simple voire simpliste) à contrainte de cisaillement constante τ [KELLY et TYSON, 1965 ; AVESTON *et al.*, 1971] on peut expliciter les résultats précédents. Le champ de contraintes résiduelles s'écrit

$$\sigma_{\rm f}^{\rm r}(z) = \frac{2\tau}{R}(l_{\rm f} - |z|) \ , \ \sigma_{\rm m}^{\rm r}(z) = -\frac{2f\tau}{(1-f)R}(l_{\rm f} - |z|) \quad \forall\, |z| \in [0, l_{\rm f}] \tag{1.73}$$

$$\sigma_{\rm f}^{\rm r}(z) = 0 \ , \ \sigma_{\rm m}^{\rm r}(z) = 0 \quad \forall\, |z| \in [l_{\rm f}, L] \tag{1.74}$$

de telle manière que la variable d'endommagement d et les déformations inélastiques $\overline{\epsilon}^{\rm i}$ s'expriment par

$$d = \frac{3(1-f)E_{\rm m}}{4fE_{\rm f}}\frac{l_{\rm d}}{L} \ , \ \overline{\epsilon}^{\rm i} = \frac{\tau l_{\rm d}^2}{RE_{\rm f}L} \tag{1.75}$$

avec

$$\frac{\tau l_{\rm f}}{RE_{\rm f}} = \frac{\overline{\sigma}}{2E}\frac{(1-f)E_{\rm m}}{fE_{\rm f}} \tag{1.76}$$

d'où $X = \overline{\sigma}/3$ et $y = 2\overline{\sigma}^2/9E$. La dissipation est positive et vérifie donc le second principe de la thermodynamique.

Sur un graphe contrainte/déformation mésoscopiques on considère un chemin de chargement d'un état O à un état B (trait gras de la figure 1.7). La figure 1.7 représente les différentes énergies mises en jeu.

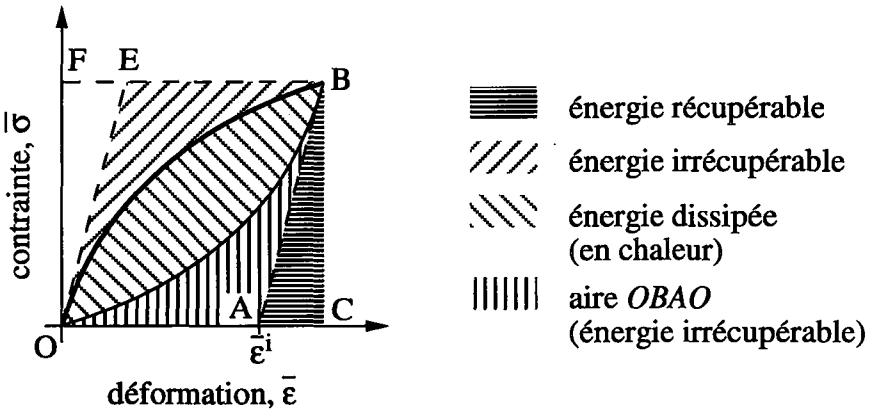

FIG. 1.7 - Bilan énergétique pour un composite (en chargement monotone) subissant de la décohésion et du frottement.

On applique le principe des travaux virtuels (ici réels) sous la forme suivante

$$\int_O^B \overline{\epsilon}\, d\overline{\sigma} = \overline{\psi}_{\rm OB}^{\rm e} + \overline{\psi}_{\rm OB}^{\rm i} + \frac{f}{L}\int_O^B \int_{-l_{\rm d}}^{l_{\rm d}} \frac{[\![u(z)]\!]^{\rm i}}{R}\, d\tau(z)\, dz \tag{1.77}$$

L'aire $OFBO$ correspond au premier terme de l'équation (1.77). L'aire $OEFO$ est l'énergie élastique récupérable ($\overline{\psi}_{\rm OB}^{\rm e}$). Avec le modèle d'interface utilisé, le dernier terme

de l'équation (1.77) est nul car $[\![u(z)]\!]^{\mathrm{i}}\ d\tau(z) = 0$ (loi de « normalité »). On montre ainsi que l'aire $OEBO$ est égale à $\overline{\psi}^{\mathrm{i}}_{\mathrm{OB}} = -\overline{\varphi}^{\mathrm{i}}_{\mathrm{OB}}$. Par application du premier principe de la thermodynamique on obtient l'énergie dissipée (en chaleur) $\overline{q}^{\mathrm{d}}_{\mathrm{OB}}$

$$\int_O^B \overline{\sigma}\ d\overline{\epsilon} = \overline{\psi}^{\mathrm{e}}_{\mathrm{OB}} + \overline{\psi}^{\mathrm{i}}_{\mathrm{OB}} + \overline{q}^{\mathrm{d}}_{\mathrm{OB}} \tag{1.78}$$

avec

$$\overline{q}^{\mathrm{d}}_{\mathrm{OB}} = -\frac{f}{L}\int_O^B \int_{-l_{\mathrm{d}}}^{l_{\mathrm{d}}} \tau(z)\ \frac{d\,[\![u(z)]\!]^{\mathrm{i}}}{R}\ dz \tag{1.79}$$

L'aire $OBCO$ correspond au membre de gauche de l'équation (1.78). L'aire $ABCA$ (égale à l'aire $OFEO$) est égale à $\overline{\psi}^{\mathrm{e}}_{\mathrm{OB}}$. La densité d'énergie irrécupérable représentée par l'aire $OEBO$ est aussi égale à l'aire $OBAO$. On obtient ainsi l'énergie dissipée (en chaleur) au cours du chemin OB (aire du fuseau OB, cf. figure 1.7).

les deux derniers exemples traités servent de base aux études sur l'endommagement de composites à matrice fragile dans le cas de la fissuration matricielle. Ils seront généralisés dans le paragraphe 3.2.

1.2 Rupture d'un volume élémentaire endommagé et changement d'échelle

Dans ce paragraphe, il s'agit d'étudier les conditions de rupture d'un élément de volume contenant un défaut initial. Deux cas vont être envisagés. Le premier traite de la rupture d'un élément de volume d'un matériau à comportement fragile. Le second traite de la rupture d'un matériau à comportement quasi-fragile : les résultats développés pour des matériaux à comportement ductile sont encore applicables dans la mesure où la loi de comportement est également non-linéaire. En revanche, contrairement au cas du comportement ductile, les non-linéarités géométriques ne sont pas prises en compte car l'hypothèse des petites perturbations peut encore être faite. Des non-linéarités matérielles (ou physiques), et en particulier l'adoucissement, peuvent se produire à cause de l'endommagement (et plus particulièrement du couplage d'état entre élasticité et endommagement).

1.2.1 Rupture fragile

Le niveau de contrainte (mésoscopique) à rupture d'un élément endommagé est, en général, très inférieur à celui qui résulterait des actions moléculaires (celui-ci étant de l'ordre du dixième du module d'YOUNG). Cette borne supérieure (correspondant à l'échelle nanoscopique) est rarement atteinte car les matériaux contiennent des défauts à l'échelle microscopique (défauts aux joints de grains ou phases secondaires par exemple) qui conduisent à des contraintes de rupture de l'ordre du centième du module d'YOUNG (ceci est le cas des fibres dans les matériaux composites). Enfin, des défauts encore plus grands (à échelle mésoscopique) peuvent exister et à ce moment les contraintes de rupture sont de l'ordre du millième du module d'YOUNG. Dans les deux derniers cas des concepts liés à la mécanique (linéaire) de la rupture ou à la mécanique de l'endommagement peuvent être utilisés. Cet « effet d'échelle » a été reconnu depuis le début des années 1920 [GRIFFITH, 1921 ; 1924] en Génie Mécanique et est couramment enseigné depuis les années 1960-70 (cf. par exemple [BUI, 1978 ; MANDEL, 1978b]). On remarquera que la décroissance de la contrainte de rupture avec la taille des hétérogénéités est aussi observée pour des ciments et bétons. Il est également appelé « effet d'échelle » dans la littérature du Génie Civil [BAZANT, 1986 ; MAZARS, 1989]. À l'échelle de la structure, la propagation de macrofissures est, en général, analysée à l'aide de la mécanique linéaire (ou non-linéaire) de la rupture.

La mécanique (linéaire) de la rupture est très souvent choisie car elle fait explicite-

ment référence à la présence de défauts (fissures) dans un matériau à comportement fragile. Un des critères les plus couramment employés fait référence à une valeur critique $\mathcal{G}_c$ du taux de restitution d'énergie $\mathcal{G}$ [GRIFFITH, 1921 ; 1924], force associée à la surface de la fissure,

$$\mathcal{G} \geq \mathcal{G}_c \tag{1.80}$$

Ce critère est la base de l'étude des conditions de rupture de matériaux contenant des défauts initiaux répartis de manière aléatoire présentée dans le chapitre 2. On remarquera que d'autres critères font appel à une valeur critique du facteur d'intensité des contraintes. La relation entre facteur d'intensité des contraintes et taux de restitution d'énergie [IRWIN, 1957] permet de montrer l'équivalence entre les deux critères dans le cadre de la mécanique linéaire de la rupture. Enfin des notions liées aux forces de cohésion au voisinage de la pointe d'une fissure peuvent également être invoquées [DUGDALE, 1960 ; BARENBLATT, 1962]. L'introduction d'une intégrale de contour J [ESHELBY, 1956] a permis de montrer l'équivalence entre tous ces critères [RICE, 1968]. L'intégrale duale I fut introduite par BUI [1973]. D'autres intégrales de contour ont également été déduites des lois de conservation écrites pour différents types de transformations [BUI, 1978]. Les résultats de mécanique linéaire de la rupture peuvent aussi être étendus aux cas non-linéaires. Ceci concerne notamment les situations de plasticité généralisée [DUGDALE, 1960] pour des matériaux à comportement ductile, ou des composites dans lesquels les fissures matricielles sont pontées [AVESTON *et al.*, 1971 ; MARSHALL *et al.*, 1985]. Différentes lois de pontage ont été employées (cf. par exemple [SUO, 1992]) dans un cadre qui est très proche de celui proposé initialement par BARENBLATT [1962]. Les résultats obtenus par RICE peuvent également être appliqués au cas des composites. Une version simplifiée peut être trouvée dans l'étude de cas (DEA Mécanique & Matériaux, 1996-97) sur les matériaux composites renforcés par des fibres [HILD, 1997].

La mécanique de l'endommagement peut également être utilisée, bien qu'elle ne nécessite pas la présence de défauts initiaux. Un critère équivalent au précédent peut être écrit à partir de la force Y associée à la variable d'endommagement D et définie par

$$Y = -\frac{\partial \overline{\psi}}{\partial D} = \frac{\partial \overline{\varphi}}{\partial D} \tag{1.81}$$

de telle manière que le critère de rupture locale peut s'écrire

$$Y \geq Y_c \tag{1.82}$$

où Y_c représente une quantité critique qui dépend du matériau. Au passage, on remarquera que la définition du taux de restitution de densité d'énergie Y [CHABOCHE, 1977] possède la même propriété (cf. équation (1.81)) que celle du taux de restitution d'énergie $\mathcal{G}$. Les équations (1.26.2) et (1.21.2) ont le mérite, entre autres, de « réconcilier » la mécanique de l'endommagement et la mécanique (linéaire) de la rupture. Bien que le critère d'endommagement le plus couramment utilisé corresponde à une valeur critique de l'endommagement D_c [LEMAITRE, 1984 ; 1992b], le critère (1.82) est l'équivalent naturel du critère (1.80).

1.2.2 Rupture quasi-fragile

Le comportement quasi-fragile est caractérisé par une non-linéarité de la relation contrainte/déformation. Cette non-linéarité est supposée décrite par un module tangent « en charge » $\underline{\underline{\underline{\underline{H}}}}$ tel que la loi (linéaire) en vitesse s'écrit

$$\dot{\underline{\underline{\sigma}}} = \underline{\underline{\underline{\underline{H}}}} : \dot{\underline{\underline{\epsilon}}} \tag{1.83}$$

où $\dot{\underline{\underline{\sigma}}}$ est le tenseur des vitesses de contrainte et $\dot{\underline{\underline{\epsilon}}}$ le tenseur des vitesses de déformation.

Les conditions de rupture mésoscopique peuvent être obtenues à l'aide des conditions de localisation des déformations. L'avantage de cette méthode est qu'elle fait explicitement référence à des solutions pour lesquelles il existe au moins une surface au passage de laquelle le saut de vitesse de déformation est discontinu. Les résultats rappelés ci-après sont, *a priori*, uniquement valables pour le solide « linéaire de comparaison » [HILL, 1958]. Ceci revient à considérer un matériau élastique non-linéaire dont le comportement correspond à la partie « en charge » (1.83) de la loi de comportement du matériau non-linéaire réel. On notera qu'on peut montrer qu'il y a bifurcation pour le solide réel dès qu'il y a bifurcation pour le solide linéaire à condition que la zone inélastique soit totalement en charge avant bifurcation [HILL, 1961 ; HUTCHINSON, 1974].

Le problème de base concerne la recherche de solutions discontinues. Les premiers travaux remontent à RIEMANN en 1860 dans l'étude de la propagation de discontinuités dans le mouvement rectiligne des gaz, et à ceux de CHRISTOFFEL en 1877 dans la généralisation à des cas tridimensionnels de l'étude des ondes de choc [HADAMARD, 1903]. Les raisonnements développés ci-dessous partent de la constatation suivante : les discontinuités des diverses dérivées d'une fonction qui reste continue à la traversée d'une onde ne sont pas indépendantes entre elles. Elles doivent vérifier des conditions

particulières appelées « conditions de compatibilité ». L'importance fondamentale de ces conditions a été montrée par HUGONIOT en 1887. La présentation qui suit reprend celle de HADAMARD [1903] et de MANDEL [1966]. On considère une surface isolée dont l'équation s'écrit

$$f(x, y, z) = 0 \tag{1.84}$$

La relation précédente exprime la condition que doivent remplir les coordonnées (x, y, z) d'un point matériel pour que celui-ci soit le siège d'une discontinuité. Nous désignons par S la surface représentée en coordonnées cartésiennes par l'équation (1.84). Soit $\varphi(x, y, z)$ une fonction qui ne subit aucune discontinuité à la traversée de la surface S, c'est-à-dire qui a la même valeur en deux points M_1 et M_2 infiniment voisins situés de part et d'autre de S. On suppose au contraire que les dérivées premières subissent des discontinuités $[\![\varphi_{,\mathrm{x}}]\!]$, $[\![\varphi_{,\mathrm{y}}]\!]$, $[\![\varphi_{,\mathrm{z}}]\!]$ (où $[\![\star]\!]$ est le saut de la grandeur $\star$ au travers de S). Faisons décrire à un point (x, y, z) un chemin quelconque situé sur la surface S et caractérisé par des accroissements dx, dy, dz qui doivent vérifier l'équation différentielle de S

$$f_{,\mathrm{x}}\, dx + f_{,\mathrm{y}}\, dy + f_{,\mathrm{z}}\, dz = 0 \tag{1.85}$$

On peut supposer un point M de S, soit dans la région (1) (position M_1), soit dans la région (2) (position M_2) : cf. figure 1.8.

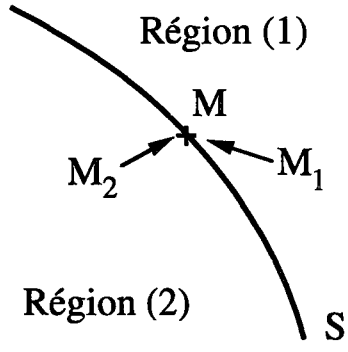

FIG. 1.8 - Surface de discontinuité.

La variation de φ est la même dans les deux cas, de sorte que

$$d\varphi = \varphi_{,\mathrm{x}}\, dx + \varphi_{,\mathrm{y}}\, dy + \varphi_{,\mathrm{z}}\, dz \tag{1.86}$$

a la même valeur. Par soustraction on en déduit que

$$[\![\varphi_{,\mathrm{x}}]\!]\, dx + [\![\varphi_{,\mathrm{y}}]\!]\, dy + [\![\varphi_{,\mathrm{z}}]\!]\, dz = 0 \tag{1.87}$$

L'équation (1.87) est valable pour tout accroissement dx, dy, dz. Par conséquent

$$\frac{[\![\varphi_{,x}]\!]}{f_{,x}} = \frac{[\![\varphi_{,y}]\!]}{f_{,y}} = \frac{[\![\varphi_{,z}]\!]}{f_{,z}} \tag{1.88}$$

Les équations (1.88) constituent les conditions de compatibilité recherchées. Le raisonnement tenu pour une fonction réelle se généralise aisément à des vecteurs. Ainsi, si le champ de vitesses $\underline{V}$ est continu mais le gradient des vitesses est discontinu, il vérifiera

$$[\![\, \underline{\underline{\mathrm{grad}}}(\underline{V}) \,]\!] = \underline{g} \otimes \underline{n} \tag{1.89}$$

de sorte que le saut des vitesses de déformation vérifie

$$[\![\dot{\underline{\underline{\varepsilon}}}]\!] = \frac{1}{2}\left(\underline{g} \otimes \underline{n} + \underline{n} \otimes \underline{g}\right) = \underline{g} \otimes_s \underline{n} \tag{1.90}$$

où $\underline{n}$ est la normale à la surface de discontinuité, $\underline{g}$ le vecteur caractérisant la discontinuité et « $\otimes$ » le produit tensoriel. On a un mode d'ouverture (ou longitudinal [HADAMARD, 1903]) lorsque $\underline{g}$ est parallèle à $\underline{n}$ et une bande de cisaillement (ou un mode transversal [HADAMARD, 1903]) lorsque $\underline{g}$ est orthogonal à $\underline{n}$.

Dans le cas de l'existence d'une surface de discontinuité, la loi de conservation de la quantité de mouvement (*i.e.*, équations d'équilibre dans le cas d'ondes stationnaires) s'écrit [HILL, 1962 ; MANDEL, 1962]

$$[\![\dot{\underline{\underline{\sigma}}}]\!] \,.\, \underline{n} = 0 \tag{1.91}$$

Une condition nécessaire [RUDNICKI et RICE, 1975 ; RICE et RUDNICKI, 1980] et suffisante [BORRÉ et MAIER, 1989] de localisation est de trouver une normale $\underline{n} \neq \underline{0}$ à l'intérieur d'un solide telle que

$$\det\left(\underline{n}.\underline{\underline{\underline{H}}}.\underline{n}\right) = 0 \tag{1.92}$$

où $\underline{n}$ est la normale à la surface de localisation lorsque la condition (1.92) est satisfaite. La forme de la discontinuité du taux de déformation est alors donnée par l'équation (1.90). Ce critère sera utilisé dans la détermination des conditions d'amorçage macroscopique dans des composites renforcés par des fibres longues (cf. paragraphes 3.3.1 et 3.3.2).

On notera que les résultats précédents peuvent être réinterprétés en terme d'ondes stationnaires dans des matériaux non-linéaires. En effet, HADAMARD [1903] a notamment analysé la propagation d'ondes dans des milieux élastiques. Le vecteur de discontinuité $\underline{g}$ peut être considéré comme le vecteur propre du tenseur acoustique

$\underline{n}.\underline{\underline{H}}.\underline{n}$ associé à la valeur propre nulle.

La condition de localisation indique également le moment où les calculs par la méthode aux éléments finis cessent d'être corrects dans le cas où les fonctions de forme des éléments ne permettent pas de rendre compte des discontinuités des déplacements [DOGHRI, 1989]. Le caractère prédictif de l'amorçage par ce critère dans le cadre de la mécanique de l'endommagement appliquée à des matériaux à comportement ductile a été notamment montré par BILLARDON et DOGHRI [1989] et cette théorie a été appliquée dans d'autres cas de figure par RICE et RUDNICKI notamment [RUDNICKI et RICE, 1975 ; RICE, 1976 ; RICE et RUDNICKI, 1980 ; PERRIN et LEBLOND, 1993]. On remarquera enfin qu'un raisonnement par transformation de FOURIER de l'équation d'équilibre homogène (méthode de perturbation) conduit aux mêmes résultats [HACHICH, 1994] et permet de lier la perte d'ellipticité à l'apparition d'ondes d'accélération stationnaires [HILL, 1962 ; MANDEL, 1962].

Dans ce qui suit, on montre des résultats que l'on peut obtenir dans le cadre de la mécanique de l'endommagement en étudiant les conditions de localisations à différentes échelles (microscopique et mésoscopique). Les comportements microscopiques sont décrits par des lois simples d'élasticité couplée à l'endommagement et les cas de chargements sont principalement de la traction mésoscopique. En particulier, les critères microscopiques font référence à une valeur critique Y_c à partir d'études des conditions de localisation (cf. équation (1.82)).

Localisation microscopique et mésoscopique

par H. YAACOUB AGHA, F. HILD et R. BILLARDON (1997).
D.L. MCDOWELL (ed.), *Application of Continuum Damage Mechanics to Fatigue and Fracture* (ASTM STP1315), ASTM, Philadelphia, PA (USA), pp. 119-130.

Hassan Yaacoub Agha,[1] *François Hild,*[1] *and René Billardon*[1]

Microscopic and Mesoscopic Damage Localization

REFERENCE: Yaacoub Agha, H., Hild, F., and Billardon, R., **"Microscopic and Mesoscopic Damage Localization,"** *Applications of Continuum Damage Mechanics to Fatigue and Fracture, ASTM STP 1315*, D. L. McDowell, Ed., American Society for Testing and Materials, 1997, pp. 119–130.

ABSTRACT: Initial defects are the main cause of the failure of structures made of brittle or quasi-brittle materials. The aim of this paper is to model within the framework of continuum damage mechanics these defects and their influence on the mechanical behavior of the structure they lie in by using a strain localization criterion. The microscopic and mesoscopic conditions for localization are studied by utilizing isotropic or anisotropic damage variables. A representative volume element (RVE) containing one defect is defined and the failure criterion of such an RVE is derived. The initial defect is modeled by an initial damage parameter. The evolution law of this damage value depends upon the nature of induced damage. Finally, an extension of this study to the case of high-cycle fatigue is proposed.

KEYWORDS: brittle materials, quasi-brittle materials, initial defects, initial damage parameter, induced damage parameter, continuum damage mechanics, damage localization, high-cycle fatigue, cracking, fatigue (materials), fracture (materials)

Initial defects are usually the cause of failure of structures made of brittle or quasi-brittle materials such as ceramics, concrete, and cast iron under high-cycle fatigue loading conditions. Studying the failure of this kind of material requires information about the initial distribution of these defects as well as their evolution. In the case of brittle materials, failure can be studied at a mesoscopic level where the structure is divided into representative volume elements (RVEs) that contain only one defect. The defects can be modeled by penny-shaped cracks. The failure criterion may be defined by a critical size of the propagating defect. Statistical models may be employed to analyze the failure of these structures [*1*]. For quasi-brittle materials, the details of the defect geometry must be taken into consideration. In this case, studying the failure of the structure requires information at a microscopic level.

Stationary waves were studied by Hadamard [*2*] in elasticity and by Hill [*3*] and Mandel [*4*] in elastoplasticity. Rice [*5*] related the localization of plastic shear bands to jumps of the velocity gradient. Borré and Maier [*6*] gave the conditions necessary for the onset of localized modes inside the body. These conditions are a generalization of the sufficient conditions derived by Rice and Rudnicki [*5,7*]. Strain localization corresponds to the onset of a surface across which the velocity field is discontinuous. In the framework of infinitesimal strain, damage may be one of the mechanisms responsible of such a localization. Localization is due to strain softening. Hence, continuum damage mechanics is an appropriate theory to determine the local failure of an RVE, that is, to define a macrocrack initiation condition. This criterion is then a strain and

[1] Research assistant, research associate professor, and professor, respectively, Laboratoire de Mécanique et Technologie, E.N.S. Cachan/C.N.R.S./Université Paris 6, 61, avenue du Président Wilson, F-94235 Cachan Cedex, France.

damage criterion to predict localization corresponding to the transition from a homogeneous deterioration to a localized one. This approach has successfully been used for ductile materials [8,9].

The aim of this paper is to model, in the framework of continuum damage mechanics, the defects and their influence on the mechanical behavior of the structure they lie in. The first step consists of studying the behavior of a matrix without defects and the corresponding localization conditions by using two different damage models. The first model corresponds to an isotropic description, and the second one to an anisotropic description that describes the creation of cracks in the matrix. In a second step, we define an RVE containing an initial defect and the failure criterion for such an RVE. The defects are modeled by an initial value of a damage variable. The evolution law of this damage parameter depends upon the nature of induced damage due to the loadings. In this paper, monotonic and high-cycle fatigue loadings are considered. Two phenomenological models are introduced: the first one is called an additive model where the induced damage is of the same nature as the initial damage, and the second is a multiplicative model where the induced damage is different from the initial one. Micromechanical analyses are carried out on pre-cracked cells and on volumes containing initial defects that can be modeled as cylindrical holes, and the propagating defects as penny-shaped cracks embedded in an elastic matrix.

State Coupling: Elasticity and Damage

The behavior of the matrix containing initial defects is considered to be elastic-damageable. The degradation mechanism is characterized by one scalar variable, D. This variable can be either isotropic or anisotropic. For the sake of simplicity, we will consider the case of plane stress. In the case of an isotropic damage description, the Helmholtz free energy density, ψ, and the associated force, Y, to the damage variable (that is, the energy release rate density [10]) can be written as [11]

$$\rho\psi = \frac{1}{2}\frac{E(1-D)[\varepsilon_{11}^2 + 2\nu\varepsilon_{11}\varepsilon_{22} + \varepsilon_{22}^2]}{1-\nu^2} + 2\tilde{G}(D)\varepsilon_{12}^2$$

$$Y = -\rho\frac{\partial\psi}{\partial D} = \frac{\sigma_{11}^2 + 2\nu\sigma_{11}\sigma_{22} + \sigma_{22}^2}{2E(1-D)^2} + \frac{\sigma_{12}^2}{2\tilde{G}(D)(1-D)}, \quad \tilde{G}(D) = G(1-D) \tag{1}$$

where

ρ = material density, kg/m^3;
ε_{11}, ε_{22}, ε_{12} = components of the infinitesimal strain tensor;
σ_{11}, σ_{22}, σ_{12} = components of the Cauchy stress tensor, Pa; and
E, ν = Young's modulus, Pa, and Poisson's ratio of the virgin material.

In the case of cracking that is normal to the 1-direction, an anisotropic damage variable is more appropriate. The damage variable, D, then is a function of the crack density (that is, $\pi a^2/S$, where $2a$ is the crack size within a surface, S) and the Helmholtz free energy density, ψ, and the energy release rate density, Y, are the following [12]

$$\rho\psi = \frac{1}{2}\frac{E\{(1-D)\varepsilon_{11}^2 + 2\nu(1-D)\varepsilon_{11}\varepsilon_{22} + \varepsilon_{22}^2\}}{1-\nu^2(1-D)} + 2\tilde{G}(D)\varepsilon_{12}^2$$

$$Y = -\rho\frac{\partial\psi}{\partial D} = \frac{\sigma_{11}^2 + \sigma_{12}^2}{2E(1-D)^2}, \quad \tilde{G}(D) = \frac{E}{2(1+\nu) + \dfrac{D}{1-D}} \tag{2}$$

Damage Evolution Law

In the case of an isotropic or anisotropic description, it was decided to model the damage evolution by a law developed by Marigo [*13*]. In this model the elastic domain is defined as

$$f(Y,D) = Y - (Y_{th} + MD) \leq 0 \tag{3}$$

where

Y_{th} = threshold energy release rate density below which no evolution occurs, J/m^3; and
M = scaling parameter, J/m^3.

For an initially virgin material ($D(t = 0) = 0$), the damage evolution is written as

$$\mathring{D} = \frac{\partial F}{\partial Y}\mathring{\lambda} \tag{4a}$$

where the loading/unloading conditions are formulated in Kuhn-Tucker form as

$$\mathring{\lambda} \geq 0,\ f \leq 0,\ \mathring{\lambda}f = 0 \tag{4b}$$

where

$\mathring{\lambda}$ = damage multiplier derived from the consistency condition $\mathring{\lambda}\mathring{f} = 0$, and
F = damage potential written as $F(Y) = (Y - Y_{th})/M$ so that $\mathring{\lambda} = \mathring{Y}$ and $\mathring{D} = \mathring{D}(\mathring{Y})$.

Microscopic Initiation Conditions

Local failure corresponds to the strain and damage localization in one point of the structure, that is, to the onset of a surface across which the strain rate is discontinuous, in other words, to the failure of the ellipticity condition. The strain rate is related to the stress velocity by

$$\underline{\underline{\mathring{\sigma}}} = \begin{cases} \underline{\underline{\underline{\underline{E}}}} : \underline{\underline{\mathring{\varepsilon}}} \text{ if } \mathring{D} = 0 & \text{(unloading)} \\ \underline{\underline{\underline{\underline{H}}}} : \underline{\underline{\mathring{\varepsilon}}} \text{ if } \mathring{D} \neq 0 & \text{(loading)} \end{cases} \tag{5}$$

where

$\underline{\underline{\underline{\underline{E}}}}$ = fourth order elastic operator, Pa;
$\underline{\underline{\underline{\underline{H}}}}$ = fourth order tangent operator, Pa; and
$\underline{\underline{\mathring{\sigma}}}, \underline{\underline{\mathring{\varepsilon}}}$ = second order stress rate (Pa/s) and strain rate tensors (1/s).

Localization occurs inside the structure if and only if [*6,7*]

$$\det\left(\underline{n}\cdot\underline{\underline{\underline{\underline{H}}}}\cdot\underline{n}\right) = 0 \tag{6}$$

where $\underline{n}$ = vector normal to the localization surface.

In the case of an isotropic damage description, the localization conditions for a plane stress state are depicted in Fig. 1, where k denotes the ratio of the in-plane minimum principal strain,

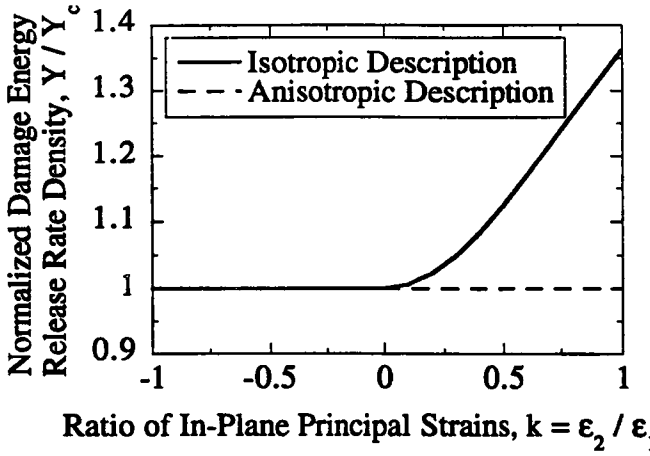

FIG. 1—*Evolution of the normalized energy release rate density at localization as a function of the ratio of in-plane principal strains.*

ε_2, upon the maximum principal strain, ε_1. The orientation of the localization surfaces are given in Figs. 2 and 3. The localization direction is unique and aligned with the maximum principal stress direction when the two principal strains are positive. On the other hand, they vary between 0° and ±45° if the minimum principal strain is negative.

When an anisotropic description is used, a closed-form solution for localization can be found provided the normal to the crack is parallel to the maximum principal strain direction, that is, the 1-direction. Localization occurs when

$$H_{1111} = \nu H_{1122} = \nu H_{2211} = 0 \text{ which leads to } Y = Y_c \tag{7}$$

where H_{1111}, H_{1122}, and H_{2211} are components of the tangent operator $\underline{\underline{\underline{\underline{H}}}}$, Pa.

If $F(Y) = (Y - Y_{th})/M$, then $Y_c = (Y_{th} + M)/3$ and at localization $\sigma_{11} = (1 - F(Y_c))\sqrt{2EY_c}$. This value is the same as that obtained with the isotropic description in the case of

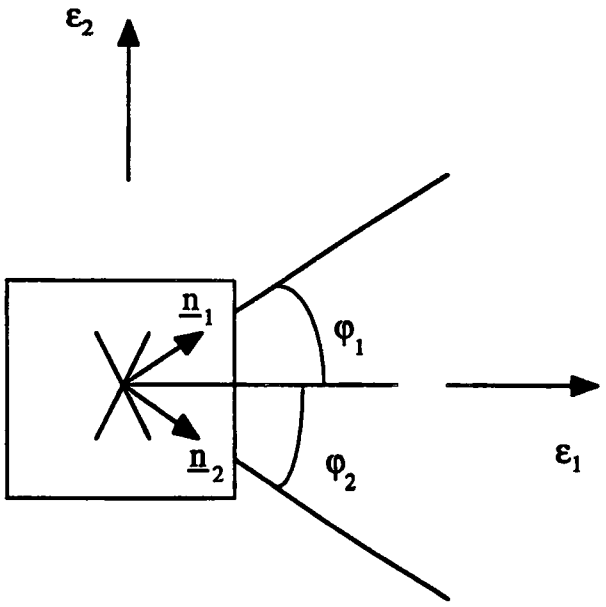

FIG. 2—*Orientation of the localization surfaces.*

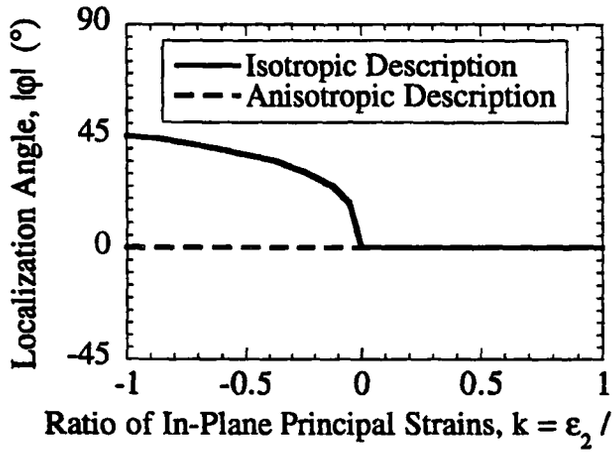

FIG. 3—*Evolution of the orientation of the localization surface as a function of the ratio of in-plane principal strains in plane stress conditions,* $|\varphi| = |\varphi_1|$ *or* $|\varphi| = |\varphi_2|$.

pure tension. In Figs. 1 and 3, the results of the present analysis are shown in dashed lines. It must be noticed that in this case, the localization direction always coincides with that of the cracking direction.

Behavior of a Predamaged RVE

The presence of defects in a considered RVE is modeled on a mesoscopic scale by damage parameters that are chosen uniform in the RVE and dependent on both the RVE size and the defect characteristics (for example, size, orientation). In the case of cylindrical holes, an initial value, D_0, of a mesoscopic isotropic damage variable, D, is assumed to be sufficient to model the influence of that kind of defect distribution. This isotropic damage variable is a function of the volume fraction of voids. In the case of a crack of size $2a$ with its normal aligned along the 1-direction in a cell of surface S, a mesoscopic anisotropic description may be used. It is characterized by a unique mesoscopic damage variable, D, of initial value, D_0, that is a function of the crack density (that is, $\pi a^2/S$).

In both isotropic and anisotropic cases, the question to address is the evolution of damage induced by the load history. When the nature of induced damage, d, is identical to that of the initial damage, D_0, a first approach assumes that

$$\mathring{D} = \frac{\partial F}{\partial Y} \mathring{\lambda} \text{ and } D(t = 0) = D_0 \tag{8}$$

In this case, induced damage, d, is defined by the following relationship

$$D = D_0 + d \tag{9}$$

This kind of approach has been used to model predamaged ductile materials [*14*].

On the other hand, if the induced damage is of a different nature from the initial damage, D_0, other assumptions may be valid. The Helmholtz free energy density must take into account D_0 so that in the case of an isotropic description, the Young's modulus of the material in its initial state (at $t = 0$) is equal to $E(1 - D_0)$. The damage evolution law for the induced damage, d, may be given by

$$\mathring{d} = \frac{\partial F}{\partial Y} \mathring{\lambda} \text{ and } d(t = 0) = 0 \tag{10}$$

In the case of an isotropic description for initial and induced damages, the final damaged elastic stiffness appears as $E(1 - D_0)(1 - d)$ that can be noted $E(1 - D)$ so that the final damage, D, is expressed by

$$D = D_0 + d(1 - D_0) \tag{11}$$

such a multiplicative coupling corresponds to the model proposed by Hayhurst and Perrin to study weldments [*15*].

Initial Damage is a Crack

Let us consider crack propagation of a pre-cracked system constituted of a plate with an initial crack of a size, $2a_0$. It can be shown that if this RVE is subjected to a load such that the maximum principal stress is normal to the initial crack, the final anisotropic damage variable, D, can be written as a function of the initial damage due to the initial crack, D_0, and the induced anisotropic damage, d

$$D = \frac{D_0 + d - 2D_0 d}{1 - D_0 d} \tag{12}$$

In this case, we have an expression corresponding to neither an additive nor a multiplicative model. In particular, the additive model, $D = D_0 + d$, is recovered only in the case of small values of $(D_0 d)$, even though the initial and induced damages are of the same nature.

Let us consider a case where there is an initial anisotropic damage, D_1, corresponding to cracking normal to the 1-direction. If the material is subsequently loaded in the perpendicular 2-direction, an induced damage variable, D_2, may develop so that the Helmholtz free energy density can be written as [*12*]

$$\rho\psi = \frac{1}{2}\frac{E\{(1 - D_1)\varepsilon_{11}^2 + 2\nu(1 - D_1)(1 - D_2)\varepsilon_{11}\varepsilon_{22} + (1 - D_2)\varepsilon_{22}^2\}}{1 - \nu^2(1 - D_1)(1 - D_2)} + 2\tilde{G}(D_1, D_2)\varepsilon_{12}^2$$

$$\tilde{G}(D_1, D_2) = \frac{E}{2(1 + \nu) + \dfrac{D_1}{1 - D_1} + \dfrac{D_2}{1 - D_2}} \tag{13}$$

In that case, the multiplicative effect only appears in the terms modeling the Poisson effect.

Initial Damage is a Hole

In this part, numerical simulations are performed on plates containing holes of different sizes. The value of the initial isotropic damage, D_0, is obtained by computing loss of stiffness due to the presence of a hole of a given diameter.

Simulations are done on six plates of size $2b$ containing holes of diameters, $2r$, so that the ratio b/r varies between 0.1 and 0.6 with a step of 0.1. Plates are subjected to a remote uniaxial displacement. For each displacement, the global reaction force is computed. The value of the mesoscopic damage variable then corresponds to the loss of stiffness. The mesoscopic damage

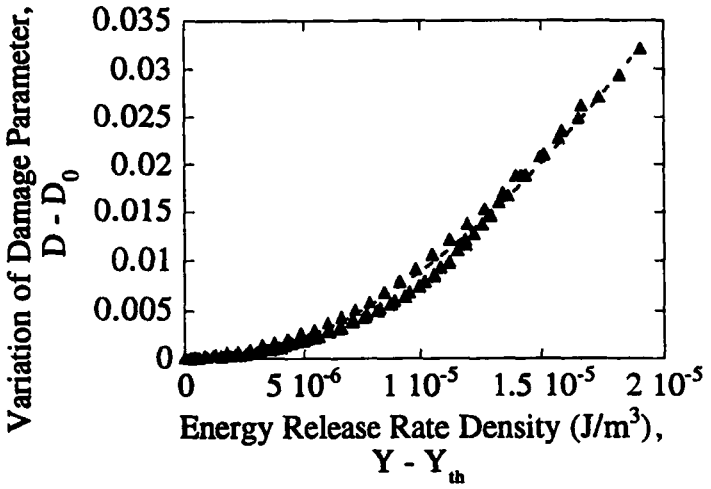

FIG. 4—*Evolution of the variation of the mesoscopic induced damage,* $D - D_0$, *as a function of the mesoscopic energy release rate density,* $Y - Y_{th}$, *for all the analyzed hole diameters with an isotropic damage description at the microscopic level.*

evolution (defined by a damage offset of 0.0001) occurs when the energy release rate density, Y, reaches a threshold value depending upon the initial damage, $Y_{th}(D_0)$. The numerical results can be fitted by the following relationship

$$Y_{th}(D_0) = Y_{th0}(1 - D_0)^2 \tag{14}$$

The mesoscopic damage evolution is plotted as a function of the evolution of the energy release rate density, $Y - Y_{th}(D_0)$, in Fig. 4. The relationship between the two variables can be fitted by

$$D - D_0 = A\left[\frac{Y - Y_{th}(D_0)}{Y_{th0}}\right]^B \tag{15}$$

where A, B = material parameters.

Equation 15 shows again that in this case the damage evolution is neither multiplicative nor additive. However, if one assumes that the evolution of induced damage, d, may be influenced by the initial damage, D_0, then Eq 15 corresponds to an additive model.

Monotonic Failure Conditions of an RVE

In this section, the failure criterion for an RVE containing an initial defect is analyzed in terms of strain and damage localization at a microscopic level. First, the localization conditions are obtained for cells containing cylindrical holes subjected to remote tension, σ_∞, in plane stress conditions. The induced microscopic damage in the surrounding matrix is assumed to be either isotropic or anisotropic.

The influence on the localization conditions of different parameters characteristic of the mesh refinement were studied. Figure 5 shows a typical mesh used for these numerical simulations. After several simulations, it appeared that the parameter that has the most important effect on the localization conditions is the size of the most loaded element, Δ. Figure 6 shows the evolution of the failure stress at localization for one initial damage value ($D_0 = 0.02$) as a function

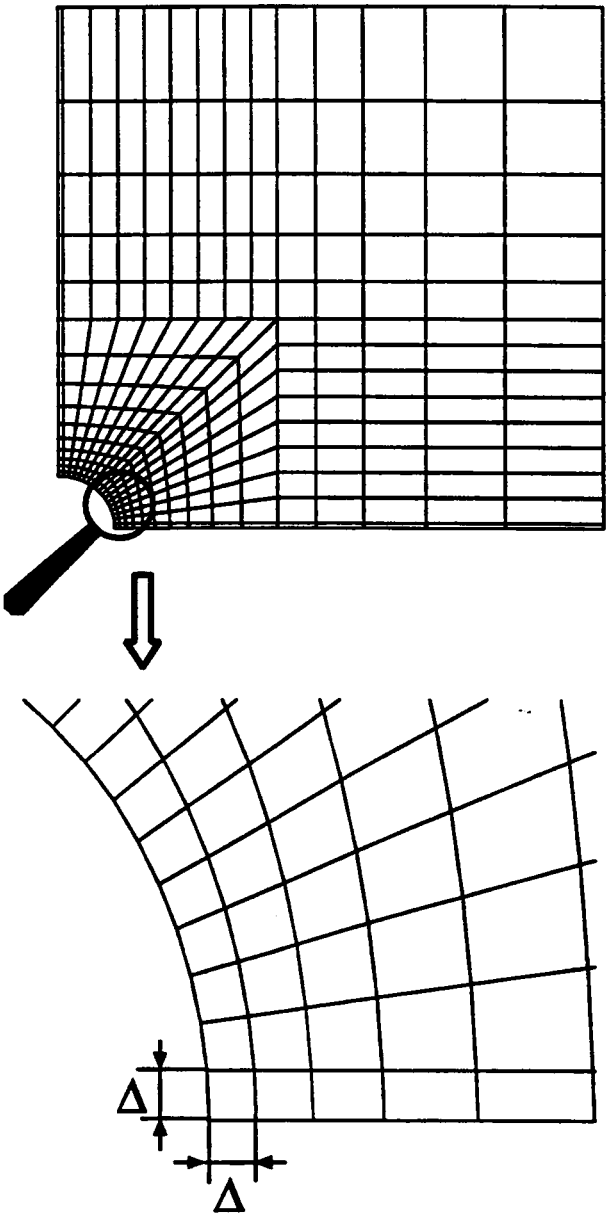

FIG. 5—*Mesh of a plate with a hole corresponding to an initial damage,* $D_0 = 0.02$.

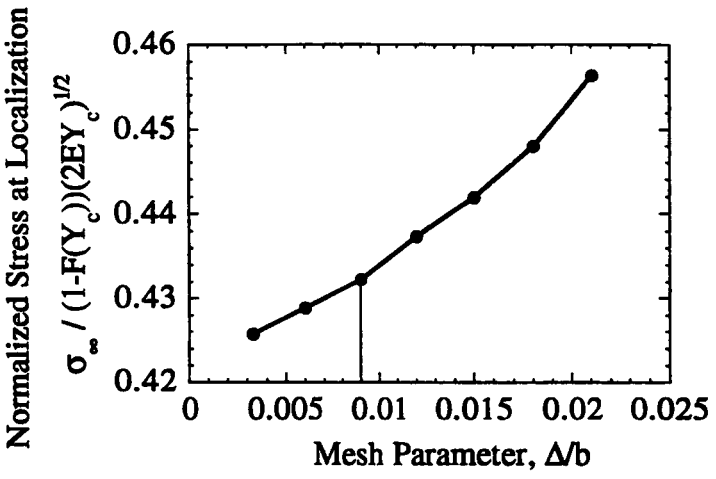

FIG. 6—*Evolution of a mesoscopic stress at localization as a function of the Δ mesh size* ($D_0 = 0.02$).

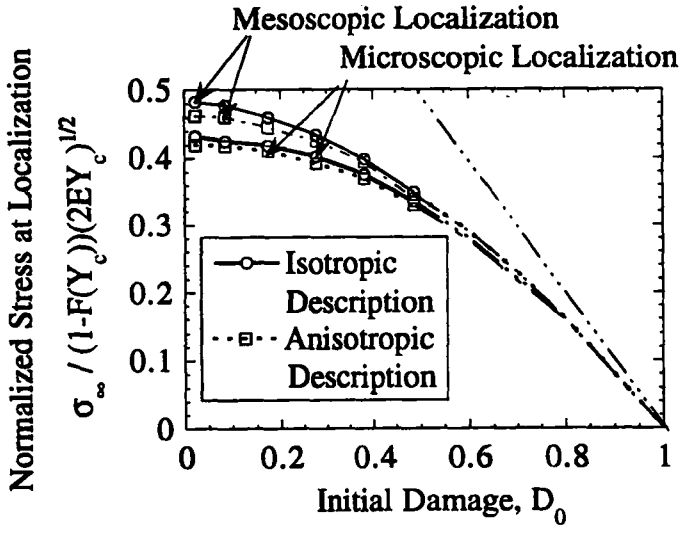

FIG. 7—*Mesoscopic stress at microscopic and mesoscopic damage localization for isotropic and anisotropic damage models at a microscopic level.*

of Δ/b. A fixed value, $\Delta/b = 0.009$, is used for all simulations. The present value is taken as a compromise between mesh sensitivity and computation cost.

Figure 7 shows the mesoscopic stress, σ_∞, at microscopic localization for different values of the initial damage variable, D_0. The difference between the stress values at localization for the two models is not very important, which can be justified by the results of Fig. 1 for which the localization conditions for values of the strain ratio, $k < 0$, are identical for both models. The same conclusion can be drawn for the stress levels at mesoscopic localization, that is, peak of the mesoscopic stress, σ_∞. Besides, it can be shown that all the curves of Fig. 7 can be approximated by the following expression

$$\Sigma = \beta(1 - D_0)^{-1/\beta} + (1 - D_0) \tag{16}$$

where

Σ = normalized stress, and
β = material parameter depending on the damage description.

It is worth noting that in this case the mesoscopic stress levels at microscopic and mesoscopic localization are very close to each other. Similar results have already been found for unidirectional fiber-reinforced composites [*16*]. It is worth remembering that the mesoscopic stress level at mesoscopic localization may be mesh-dependent. Since the latter is very close to that at microscopic localization, it is expected that the mesh-dependence is very weak.

Extension to High-Cycle Fatigue

It is assumed that the damage evolution law has the main features of a macrocrack propagation law based upon a generalized Paris' law [*17*]

$$\frac{1}{(1 - D)^2}\frac{dD}{dN} = C\left(\frac{\sqrt{Y_{max}} - \sqrt{Y_{th}}}{\sqrt{Y_c} - \sqrt{Y_{th}}}\right)^n \tag{17}$$

where

C,n = material parameters;

$Y_{max} = \dfrac{\sigma_{max}^2}{2E(1-D)^2}$, maximum over one cycle of the energy release rate density, Jm^{-3};

Y_c = critical energy release rate corresponding to microscopic failure (localization), Jm^{-3}; and

Y_{th} = threshold energy release rate density below which no damage evolution occurs, Jm^{-3}.

If we consider that the initial damage values are bounded by a maximum damage value, D_{0M}, two threshold stresses can be defined. A monotonic threshold stress, S_c, denoting the minimum value of the applied local stress above which local failure is certain under monotonic loading (that is, when the initial damage value of the RVE is equal to D_{0M}). A cyclic threshold stress, S_{th} denoting the minimum value of the applied local stress below which local failure does not occur. These two stresses are defined by

$$S_c = (1 - D_{0M})\sqrt{2EY_c},\ S_{th} = (1 - D_{0M})\sqrt{2EY_{th}} \tag{18}$$

Integration of Eq 17 gives the relationship between the damage value, D, after N cycles of constant amplitude $Y_{max} - Y_{min} \geq Y_{max} - Y_{th}$ and the initial damage value, D_0

$$\varphi(D) - \varphi(D_0) = \frac{(1-n)C}{\left(\frac{1}{k} - 1\right)^n \frac{1}{(1 - D_{0M})^n}} \left(\frac{\sigma_{max}}{S_{th}}\right)^n N \tag{19}$$

with

$$\varphi(D) = \left(\frac{1}{1-D} - \frac{1}{1 - D_{th}}\right)^{1-n} \text{ if } D_0 \geq D_{th},\ k = \frac{S_{th}}{S_c}$$

where D_{th} = threshold damage value associated to the applied stress σ_{max}: $Y_{th} = \dfrac{\sigma_{max}^2}{2E(1 - D_{th})^2}$.

Microscopic localization occurs when the damage value reaches a critical value, D_c, corresponding to the critical energy release rate density

$$Y_c = \frac{\sigma_{max}^2}{2E(1 - D_c)^2} \tag{20}$$

so that the number of cycles to failure, N_F, is given by

$$\varphi(D_c) - \varphi(D_0) = g\left(N_F; \frac{\sigma_{max}}{S_{th}}\right) \tag{21}$$

where

$$g\left(N_F; \frac{\sigma_{max}}{S_{th}}\right) = \frac{(1-n)C}{\left(\frac{1}{k} - 1\right)^n \frac{1}{(1 - D_{0M})^n}} \left(\frac{\sigma_{max}}{S_{th}}\right)^n \text{ and}$$

N_F represents the effect of induced damage.

Equation 21 shows that in the general case, the effect of induced damage is neither additive nor multiplicative.

Conclusions

An elastic law coupled with damage is introduced to study the behavior of quasi-brittle materials. Two kinds of damage variables are introduced to model the material degradation. The first one is an isotropic damage variable and the second is an anisotropic one able to model microcracking. The local failure criterion is damage localization at one point of the structure. Under plane stress conditions, the isotropic and anisotropic descriptions are equivalent in terms of load level and angle at localization when the ratio between the principal strains is less than zero. Microscopic localization corresponding to local failure appears when the energy release rate density reaches a critical value, Y_c.

The presence of an initial defect in an RVE is modeled by an initial damage value, D_0, measuring stiffness loss due to the presence of the defect. Two models are introduced to study the damage evolution in an RVE containing an initial defect. The first one is an additive model, where the induced damage is of the same nature as the initial damage. The second one is a multiplicative law, which can model the cases where the induced damage is of a different nature from initial damage. A micromechanical study of a pre-cracked system shows that the damage law can be an additive model for small values of induced damage. In the general case, however, the damage law is more complicated as exemplified by a numerical micromechanical study of plates with holes. A mesoscopic damage law evolution can be identified by studying the evolution of the induced damage as a function of the energy release rate density.

An extension to high-cycle fatigue using a damage evolution law deduced from a generalized Paris' law for the case of macrocrack propagation is also proposed. The damage value after N cycles is given as a function of the initial damage value and the maximum applied stress. A critical damage value leading to damage localization is deduced from the critical value of the energy release rate density. This model also shows the complexity of the damage law in the general case.

References

[1] Hild, F., Béranger, A.-S., and Billardon, R., "Fatigue Failure Maps of Heterogeneous Materials," *Mechanics of Materials*, Vol. 22, 1996, pp. 11–21.

[2] Hadamard, J., "Leçon sur la propagation des ondes et les équations de l'hydrodynamique," *Libraries scientifiques A*, Hermann, Paris, 1903.

[3] Hill, R., "Acceleration Waves in Solids," *Journal of the Mechanics and Physics of Solids*, Vol. 10, 1962, pp. 1–16.

[4] Mandel, J., "Ondes plastiques dans un milieu indéfini à trois dimensions," *Journal de Mécanique*, Vol. 1, No. 1, 1962, pp. 3–30.

[5] Rice, J. R., "The Localization of Plastic Deformations," *Theoretical and Applied Mechanics*, W. T. Koiter, Ed., North-Holland, Amsterdam, London, 1976, pp. 207–220.

[6] Borré, G. and Maier, G., "On Linear versus Nonlinear Flaw Rules in Strain Localization Analysis," *Meccanica*, Vol. 24, 1989, pp. 36–41.

[7] Rudnicki, J. W. and Rice, J. R., "Conditions for Localization of Deformation in Pressure-Sensitive Dilatant Materials," *Journal of the Mechanics and Physics of Solids*, Vol. 23, 1975, pp. 371–394.

[8] Billardon, R. and Doghri, I., "Prévision de l'amorçage d'une macro-fissure par la localisation de l'endommagement," *Comptes Rendus de l'Académie des Sciences, Paris*, Vol. 308, Série II, 1989, pp. 347–352.

[9] Doghri, I. and Billardon, R., "Investigation of Localization due to Damage in Elasto-Plastic Materials," *Mechanics of Materials*, Vol. 19, 1995, pp. 129–149.

[10] Chaboche, J.-L., "Description thermodynamique et phénoménologique de la viscoplasticité cyclique avec endommagement," Thèse d'Etat, Université Paris 6, 1978.

[11] Lemaitre, J., *A Course on Damage Mechanics*, Springer-Verlag, Berlin, 1992.

[12] Burr, A., Hild, F., and Leckie, F. A., "Micro-Mechanics and Continuum Damage Mechanics," *Archive of Applied Mechanics*, Vol. 65, No. 7, 1995, pp. 437–456.

[13] Marigo, J.-J., "Formulation d'une loi d'endommagement d'un matériau élastique," *Comptes Rendus de l'Académie des Sciences, Paris*, Vol. 292, Série II, 1981, pp. 1309–1312.

[14] Benallal, A., Billardon, R., Doghri, I., and Moret-Bailly, L., "Crack Initiation and Propagation Analyses Taking into Account Initial Strain Hardening and Damage Fields," *Numerical Methods in Fracture Mechanics*, A. Luxmore, Ed., Pineridge Press, Swansea, UK, 1987, pp. 337–351.

[15] Hayhurst, D. R. and Perrin, I. J., "CDM Analysis of Creep Rupture in Weldments," *Proceedings*, 10th ASCE Engineering Mechanics Conference, S. Sture, Ed., Boulder, CO, American Society of Civil Engineers, New York, 1995, pp. 393–396.

[16] Hild, F. and Burr, A., "Localization and Ultimate Strength of Fiber-Reinforced Ceramic-Matrix Composites," *Mechanics Research Communications*, Vol. 21, No. 4, 1994, pp. 297–302.

[17] Pellas, J., Baudin, G., and Robert, M., "Mesure et calcul du seuil de fissuration après surcharge," *Recherche aérospatiale*, Vol. 3, 1977, pp. 191–201.

Chapitre 2

Rupture de matériaux à comportement fragile

Et maintenant, bien sûr, ça fait six ans déjà... Je n'ai jamais encore raconté cette histoire. Les camarades qui m'ont revu ont été bien contents de me revoir vivant. J'étais triste, mais je leur disais : « c'est la fatigue... »

A. DE SAINT-EXUPÉRY (1946), *Le Petit Prince*, Gallimard.

La rupture fragile est, par expérience, nettement moins reproductible que la rupture ductile (précédée de déformations plastiques). Le caractère non-linéaire du comportement associé à la rupture ductile est un signe avant-coureur de la rupture. Dans le cas de la rupture fragile, le comportement reste élastique jusqu'à rupture ce qui rend sa prévision beaucoup plus délicate. Pour une série d'essais identiques, la contrainte de rupture peut varier de manière non négligeable par rapport à sa valeur moyenne. Ceci oblige à considérer la dispersion de la contrainte de rupture comme un phénomène à part entière qu'il s'agit de traiter à l'aide d'outils probabilistes.

Le comportement du matériau restant élastique, toute concentration de contrainte macroscopique (angles vifs, épaulements...), mésoscopique (inclusions, porosités...) ou microscopique (phase secondaire, joint de grain fissuré...) est néfaste à sa tenue en service. Ceci conduit à une conception de forme qui évite le plus possible les concentrations de contraintes macroscopiques. Des précautions expérimentales particulières sont nécessaires lorsque, par exemple, on veut effectuer un essai de traction [HILD, 1990]. Quant aux défauts (concentration de contrainte mésoscopique ou microscopique), essentiellement créés par le mode d'obtention de ces matériaux (fonderie ou frittage), ils font partie intégrante du matériau. La maîtrise des procédés d'obtention tend à diminuer leur taille. Leur apparition ne peut cependant pas être complètement évitée et requiert l'utilisation de contrôles non-destructifs afin d'en éliminer les plus gros (*i.e.*, les plus facilement observables). De plus, ces défauts sont très souvent répartis de manière aléatoire dans le matériau. Cet aspect est traité à l'aide des statistiques expérimentales qui consistent à collecter et à formaliser les données expérimentales. Lors d'une sollicitation mécanique, l'énergie apportée au matériau est stockée de manière réversible et ne peut être dissipée que par la formation de nouvelles surfaces de rupture. On parlera ainsi de comportement (élastique) fragile [BUI, 1978].

Pour traiter de la rupture des matériaux à comportement fragile, il s'agit de déterminer la probabilité de rupture en fonction du chargement (information mécanique) et de la population de défauts *initiaux* (information physique). Cette deuxième étape consiste à choisir un modèle dans le cadre de la théorie des probabilités. De nombreux modèles existent dans la littérature. Nous en avons retenu trois qui sont le plus couramment rencontrés. Le premier et le plus ancien a été introduit de manière heuristique. C'est le modèle de WEIBULL [1939b ; 1939a ; 1951 ; 1952]. Il a l'avantage, outre ses qualités de modèle macroscopique, de correspondre à l'une des trois lois extrêmes dites « de GUMBEL » [1954]. Les deux modèles suivants se distinguent du premier par leur soucis de prendre en compte la distribution initiale de défauts. BATDORF *et al.* [1974 ; 1977 ; 1978], EVANS et LAMON [1978 ; 1983 ;

1988] ont proposé des modèles basés sur des hypothèses assez voisines, bien que leur équivalence n'ait été démontrée qu'au début des années 1990 [CHAO et SHETTY, 1990 ; FURGIUELE et LAMBERTI, 1991 ; TUCKER et JOHNSON, 1994]. On notera que les études de MCCLINTOCK [1979] sont également assez proches des précédentes. D'autres modèles, basés sur des informations plus fines sur les défauts initiaux sont encore développés actuellement (cf. par exemple [BRINKMAN et DUFFY, 1994 ; WANG, 1997]).

L'étude de la rupture de matériaux à comportement fragile se fait en deux étapes distinctes et à deux échelles différentes (au moins).

Dans un premier temps, il s'agit d'étudier la rupture d'un élément de volume (paragraphe 2.1). Dans ce qui suit, on fera appel aux résultats obtenus dans le chapitre 1 (paragraphe 1.2.1). À partir de l'analyse de la rupture locale, une expression générale de la probabilité de rupture est établie dans le cas de propagation instable (paragraphe 2.1.1) ou stable (paragraphe 2.1.2) au niveau mésoscopique (*i.e.*, à l'échelle du volume élémentaire considéré). À l'aide de considérations simples, l'équivalence des modèles de BATDORF *et al.* et de LAMON-EVANS est montrée. La généralisation à des cas de propagation stable est également présentée et discutée (paragraphes 2.1.3, 2.1.4, 2.1.5, 2.1.6).

Une expression de la probabilité de rupture d'une structure (*i.e.*, à l'échelle macroscopique) est ensuite établie dans le cadre de la théorie du maillon le plus faible (paragraphe 2.2). L'effet d'hétérogénéité des contraintes, initialement développé dans le cas de propagations instables de défauts [HILD *et al.*, 1992] est étendu à la fatigue à grand nombre de cycles (paragraphe 2.2.1) puis appliqué à un bras de suspension automobile (paragraphe 2.2.2). Enfin une dernière étape de l'étude consiste à identifier et à valider le modèle proposé. Cette étape peut se faire par des mesures physiques indépendantes ou par des tests d'hypothèse grâce aux statistiques mathématiques. Seul le premier point évoqué sera traité. L'accent est porté sur la stratégie d'identification à partir d'études à différentes échelles. Quatre applications sont présentées. La première concerne le nitrure de silicium (paragraphe 2.3.1) sous chargements monotone et cyclique. Des ferrites manganèse-zinc sollicités de manière « dynamique » sont ensuite étudiés (paragraphe 2.3.2). La tenue à des sollicitations cycliques de fontes à graphite sphéroïdal est enfin analysée dans le paragraphe 2.3.3.

2.1 Probabilité de rupture d'un volume élémentaire

Le calcul de la fiabilité d'un élément de volume nécessite l'étude de l'évolution de la probabilité de rupture en fonction du niveau de sollicitation et de la durée de la sollicitation. La plupart des modèles traite de la propagation instable de fissures. Dans ce paragraphe, il est proposé d'étudier l'expression de la probabilité de rupture sous condition de propagation instable *et* stable des défauts initiaux, en fonction de la distribution initiale de défauts et de leur loi de propagation. En particulier, on obtient une présentation unifiée des deux cas de propagation [HILD et ROUX, 1991 ; HILD et MARQUIS, 1995].

Dans le cas de sollicitations monotones, cycliques, « statiques » ou « dynamiques », les fissures au sein des matériaux peuvent se propager de manière instable ou stable. Dans certains matériaux à comportement fragile, une propagation stable (ou sous-critique) est observée [EVANS, 1972]. D'autre part, une propagation stable peut également se produire pour des matériaux sous sollicitations cycliques [SURESH, 1991]. Enfin, dans le cas de sollicitations à grand nombre de cycles, la rupture se produit par extension stable puis instable de défauts initiaux distribués de manière aléatoire dans le matériau.

2.1.1 Propagation instable de défauts

Dans ce qui suit, on montre que la plupart des modèles probabilistes de rupture des matériaux à comportement fragile entrent dans le cadre général développé ci-dessous [HILD, 1996]. Il s'agit de déterminer les expressions de la probabilité cumulée de rupture élémentaire P_{F0}. On considère un volume élémentaire occupant un domaine Ω_0 de volume V_0, contenant des défauts initiaux répartis suivant une densité de probabilité f. La densité initiale f_0 dépend de paramètres w qui caractérisent la géométrie du défaut : une taille a, une orientation caractérisée par une normale $\underline{n}$, et éventuellement d'autres paramètres morphologiques ω. Dans le cas où la propagation est instable, la probabilité cumulée de rupture P_{F0} de l'élément de volume Ω_0 pour un chargement Q fixé est donnée par

$$P_{\mathrm{F0}}(Q) = \int_{\mathcal{D}_c} f_0(a, \underline{n}, \omega)\, da d\underline{n} d\omega \tag{2.1}$$

où $\mathcal{D}_c$ est l'ensemble des défauts critiques. Lorsque $\mathcal{D}_c$ est l'ensemble des défauts tels que le taux de restitution d'énergie élastique $\mathcal{G}(a, \underline{n}, \omega; Q)$ est supérieur à une valeur critique $\mathcal{G}_c$ (cf. paragraphe 1.2.1), on peut réécrire $P_{\mathrm{F0}}(Q)$ plus simplement. Tous les modèles présentés ci-après font implicitement ou explicitement cette hypothèse.

On considère une situation tridimensionnelle dans laquelle le critère de rupture peut s'écrire

$$Z\|\underline{\underline{\sigma}}(\overline{\sigma}_1, \overline{\sigma}_2, \overline{\sigma}_3, \underline{n})\|\sqrt{a} \geq \sqrt{E\mathcal{G}_c} \tag{2.2}$$

avec

$$\|\underline{\underline{\sigma}}(\overline{\sigma}_1, \overline{\sigma}_2, \overline{\sigma}_3, \underline{n})\| = \overline{\sigma}_1 G\left(\frac{\overline{\sigma}_2}{\overline{\sigma}_1}, \frac{\overline{\sigma}_3}{\overline{\sigma}_1}, \underline{n}\right)$$

où $\overline{\sigma}_1 \geq \overline{\sigma}_2 \geq \overline{\sigma}_3$ sont les contraintes principales à l'échelle mésoscopique, Z un paramètre de forme du défaut et E le module d'YOUNG du matériau non endommagé. Dans le cas présent, seuls deux paramètres morphologiques sont nécessaires à la définition de la géométrie des défauts initiaux supposés être des fissures circulaires (« *penny shaped cracks* ») : la taille a et l'orientation $\underline{n}$. La première expression de la probabilité de rupture est établie en intégrant d'abord par rapport à la normale, et en faisant apparaître un angle solide contenant toutes les normales pour lesquelles le critère de rupture est atteint. Soit $\Omega_c(\|\underline{\underline{\sigma}}\|, a)$ l'angle solide contenant les défauts dont les normales $\underline{n}$ sont telles que le critère (2.2) est vérifié. Si l'on suppose une équirépartition angulaire indépendante de la taille du défaut, et que la taille maximale du défaut n'est pas bornée, la probabilité cumulée de rupture P_{F0} devient

$$P_{F0} = \int_{a_c(\underline{\underline{\sigma}})}^{+\infty} \frac{\Omega_c(\|\underline{\underline{\sigma}}\|, a)}{4\pi} f_0(a)\, da \tag{2.3}$$

où $a_c(\underline{\underline{\sigma}})$ désigne la plus petite taille de défaut critique. En notant g une fonction telle que

$$-f_0\left[a_c(\Sigma)\right]\, da_c(\Sigma) = g(\Sigma)\, d\Sigma \quad \text{avec} \quad a_c(\Sigma) = \frac{E\mathcal{G}_c}{Z^2\Sigma^2} \tag{2.4}$$

on obtient

$$P_{F0} = \int_0^{\overline{\sigma}} \frac{\Omega_c(\|\underline{\underline{\sigma}}\|, \Sigma)}{4\pi} g(\Sigma)\, d\Sigma \tag{2.5}$$

avec

$$\Omega_c(\|\underline{\underline{\sigma}}\|, \Sigma) = \{\underline{n} \mid \|\underline{\underline{\sigma}}(\overline{\sigma}_1, \overline{\sigma}_2, \overline{\sigma}_3, \underline{n})\| \geq \Sigma\}$$

Lorsque la contrainte équivalente de rupture est définie à partir du taux de restitution d'énergie, la fonction G devient égale à G_B et est définie par

$$G_B\left(\frac{\overline{\sigma}_2}{\overline{\sigma}_1}, \frac{\overline{\sigma}_3}{\overline{\sigma}_1}, \psi, \varphi\right) = \frac{\sqrt{\overline{\sigma}_n^2 + \overline{\tau}^2}}{\overline{\sigma}_1} \tag{2.6}$$

avec

$$\begin{aligned} \overline{\sigma}_{\mathrm{n}} &= \left(\overline{\sigma}_1 \cos^2\psi + \overline{\sigma}_2 \sin^2\psi\right)\cos^2\varphi + \overline{\sigma}_3 \sin^2\varphi \\ \overline{\tau} &= \left[\left(\overline{\sigma}_1^2 \cos^2\psi + \overline{\sigma}_2^2 \sin^2\psi\right)\cos^2\varphi + \overline{\sigma}_3^2 \sin^2\varphi\right] - \overline{\sigma}_{\mathrm{n}}^2 \end{aligned}$$

où les angles ψ et φ définissent les orientations du vecteur $\underline{n}$ dans le repère principal (figure 2.1).

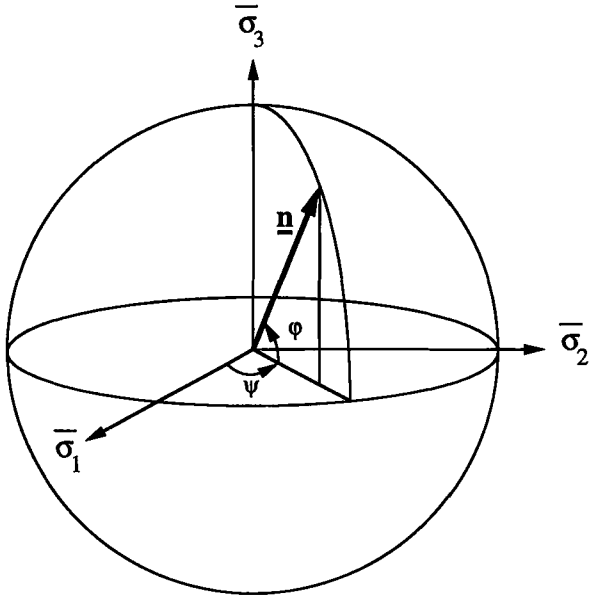

FIG. 2.1 - Définition du vecteur d'orientation dans le repère principal.

Dans le cas où la fonction f_0 est approchée par $\kappa a^{-\mathrm{n}}$ pour des valeurs élevées de a, on obtient la probabilité de rupture élémentaire associée à un modèle de BATDORF *et al.* [1974 ; 1977 ; 1978]. L'inconvénient de ce type de formulation est le calcul de l'angle solide dans le cas général [BERDIN, 1989]. C'est pourquoi une deuxième expression de la probabilité de rupture est établie en intégrant d'abord par rapport à la taille

$$P_{\mathrm{F0}} = \int_0^{4\pi} \frac{1}{4\pi}\left[1 - F_0\left(\frac{E\mathcal{G}_{\mathrm{c}}}{\left\{Z\overline{\sigma}_1 G\left(\frac{\overline{\sigma}_2}{\overline{\sigma}_1}, \frac{\overline{\sigma}_3}{\overline{\sigma}_1}, \underline{n}\right)\right\}^2}\right)\right] d\underline{n} \qquad (2.7)$$

Dans le cas où la fonction f_0 est approchée par $\kappa a^{-\mathrm{n}}$ pour des valeurs élevées de a, la probabilité cumulée de rupture est approchée par une loi de WEIBULL à deux paramètres

$$P_{\mathrm{F0}} = \left(\frac{\langle\overline{\sigma}_1\rangle}{S_0}\right)^{\mathrm{m}} I\left(m, \frac{\overline{\sigma}_2}{\overline{\sigma}_1}, \frac{\overline{\sigma}_3}{\overline{\sigma}_1}\right) \tag{2.8}$$

avec

$$\begin{aligned}
\langle\star\rangle &= \text{partie positive de } \star \\
m &= 2(n-1) \\
S_0 &= \frac{\sqrt{E\mathcal{G}_{\mathrm{c}}}}{Z}\left(\frac{n-1}{\kappa}\right)^{\frac{1}{m}} \\
I\left(m, \frac{\overline{\sigma}_2}{\overline{\sigma}_1}, \frac{\overline{\sigma}_3}{\overline{\sigma}_1}\right) &= \frac{2}{\pi}\int_0^{\frac{\pi}{2}}\int_0^{\frac{\pi}{2}} G^{\mathrm{m}}\left(\frac{\overline{\sigma}_2}{\overline{\sigma}_1}, \frac{\overline{\sigma}_3}{\overline{\sigma}_1}, \varphi, \psi\right)\cos\varphi\, d\varphi d\psi
\end{aligned}$$

Initialement, WEIBULL [1939b] avait proposé de prendre pour contrainte équivalente, la contrainte normale $\overline{\sigma}_{\mathrm{n}}$ au défaut. Avec les outils d'aujourd'hui, cela revient à dire que l'on suppose que seul le mode I est pris en compte dans une formulation à l'aide de la mécanique linéaire de la rupture. Sous ces hypothèses, la fonction I est égale à I_{W} et est définie par

$$\begin{aligned}
&I_{\mathrm{W}}\left(m, \frac{\overline{\sigma}_2}{\overline{\sigma}_1}, \frac{\overline{\sigma}_3}{\overline{\sigma}_1}\right) = \\
&\frac{2}{\pi}\int_0^{\frac{\pi}{2}}\int_0^{\frac{\pi}{2}}\left[\left(\cos^2\psi + \frac{\overline{\sigma}_2}{\overline{\sigma}_1}\sin^2\psi\right)\cos^2\varphi + \frac{\overline{\sigma}_3}{\overline{\sigma}_1}\sin^2\varphi\right]^{\mathrm{m}}\cos\varphi\, d\varphi d\psi
\end{aligned} \tag{2.9}$$

Enfin, on peut utiliser un autre critère de rupture qui fait apparaître une troisième combinaison entre contrainte normale $\overline{\sigma}_{\mathrm{n}}$ et contrainte tangentielle $\overline{\tau}$. Ce critère de rupture correspond à un taux de restitution d'énergie non coplanaire qui permet de définir une autre expression de la fonction G prise égale à G_{LE}

$$G_{\mathrm{LE}}\left(\frac{\overline{\sigma}_2}{\overline{\sigma}_1}, \frac{\overline{\sigma}_3}{\overline{\sigma}_1}, \psi, \varphi\right) = \frac{\left(\overline{\sigma}_{\mathrm{n}}^4 + 6\overline{\tau}^2\overline{\sigma}_{\mathrm{n}}^2 + \overline{\tau}^4\right)^{\frac{1}{4}}}{\overline{\sigma}_1} \tag{2.10}$$

et la probabilité de rupture élémentaire peut être écrite sous la forme suivante

$$P_{\mathrm{F0}} = \int_0^{\overline{\sigma}_1} g(S)\, dS \tag{2.11}$$

avec

$$\begin{aligned}
g(S) &= \frac{m}{S_0}\left(\frac{S}{S_0}\right)^{\mathrm{m}-1} I_{\mathrm{LE}}\left(m, \frac{\overline{\sigma}_2}{\overline{\sigma}_1}, \frac{\overline{\sigma}_3}{\overline{\sigma}_1}\right) \\
I_{\mathrm{LE}}\left(m, \frac{\overline{\sigma}_2}{\overline{\sigma}_1}, \frac{\overline{\sigma}_3}{\overline{\sigma}_1}\right) &= \frac{2}{\pi}\int_0^{\pi}\int_0^{\pi} G_{\mathrm{LE}}^{\mathrm{m}}\left(\frac{\overline{\sigma}_2}{\overline{\sigma}_1}, \frac{\overline{\sigma}_3}{\overline{\sigma}_1}, \underline{n}\right)\cos\varphi\, d\varphi d\psi
\end{aligned}$$

Ce dernier résultat correspond à l'expression de la probabilité de rupture associée à un modèle de LAMON-EVANS [1978 ; 1983 ; 1988]. Enfin, on remarquera que dans des

cas plus simples, cette corrélation entre paramètres de WEIBULL et caractéristiques de distribution de défauts peut être faite dans le cadre de la mécanique linéaire de la rupture ou dans le cadre de la mécanique de l'endommagement [JAYATILAKA et TRUSTRUM, 1977 ; HILD et MARQUIS, 1990].

2.1.2 Propagation stable de défauts

Dans le cas de propagation stable, les paramètres morphologiques initiaux w évoluent pour devenir W après un instant t. En particulier des bifurcations peuvent avoir lieu et conduire à une évolution de ces paramètres morphologiques. On se reportera à la figure 2.3 pour les définitions de $w = \{a, \underline{n}\}$ et $W = \{A, \underline{N}\}$ dans un cas particulier schématique de fissures en milieu plan. Les grandeurs W sont supposées être liées aux grandeurs initiales w de manière unique par des fonctions de classe C^1 telles que

$$W = \zeta(w; Q, t) \tag{2.12}$$

À l'instant t et pour un chargement Q correspond une probabilité de rupture P_{F0} liée à la répartition de défauts modélisée par la densité de probabilité f_t

$$P_{F0}(Q,t) = \int_{\mathcal{D}_c(Q)} f_t(W; Q, t)\, dW \tag{2.13}$$

avec par exemple, $\mathcal{D}_c(Q) = \{W \mid \mathcal{G}(W; Q) \geq \mathcal{G}_c\}$. Si l'on suppose qu'aucun nouveau défaut n'est créé au cours du chargement, c'est-à-dire que seuls les défauts initialement présents conduisent à la rupture, la densité de probabilité f_t est reliée à la densité initiale de probabilité f_0 par

$$f_t[\zeta(w; Q, t)] = J^{-1}(w; Q, t) f_0(w) \tag{2.14}$$

où J désigne le Jacobien de la transformation définie par l'équation (2.12). Cette relation constitue une généralisation de résultats obtenus dans le cas où la distribution initiale de défauts est décrite par un seul paramètre [HILD et ROUX, 1991]. Lorsque plusieurs paramètres sont nécessaires à la modélisation d'un défaut initial, le Jacobien J permet de caractériser la corrélation entre les paramètres lors de leur évolution avec t. En particulier, si les paramètres initiaux sont décorrélés, le Jacobien J donnera directement l'évolution de leur corrélation en fonction de t.

Par l'intermédiaire de l'équation (2.14), la probabilité P_{F0} après une durée t peut être exprimée uniquement en fonction de la répartition initiale f_0

$$P_{F0}(Q,t) = \int_{\mathcal{D}_c^*(Q,t)} f_0(w)\, dw \tag{2.15}$$

où $\mathcal{D}_c^*(Q,t)$ permet de définir les défauts initiaux qui deviennent critiques après un instant t, par exemple $\mathcal{D}_c^*(Q,t) = \{w \mid \mathcal{G}[\zeta(w;Q,t);Q] \geq \mathcal{G}_c\}$. L'équation (2.15) montre qu'il n'est pas nécessaire de calculer l'évolution de la distribution de défauts, mais de simplement écrire l'évolution des bornes d'intégration, c'est-à-dire des frontières du domaine $\mathcal{D}_c^*(Q,t)$. Dans le reste de cette partie, le chargement même triaxial est supposé simple et caractérisé par le seul paramètre Q. On notera que l'équation (2.15) correspond à une écriture *unifiée* de la probabilité de rupture dans le cas de propagations instable ou stable de défauts.

2.1.3 Bornes de probabilité de rupture

Dans ce paragraphe, on suppose l'existence d'un taux de restitution d'énergie seuil $\mathcal{G}_{th}$, valeur en dessous de laquelle les défauts ne se propagent pas, quelle que soit leur orientation. Les grandeurs $\mathcal{G}_{th}$ et $\mathcal{G}_c$ permettent d'introduire deux niveaux de charge Q_{th} (en dessous de laquelle aucune rupture n'est possible pour une probabilité de rupture P_{F0} fixée) et Q_c (en dessous de laquelle aucune rupture sans propagation stable n'est possible pour P_{F0} fixée) : figure 2.2.

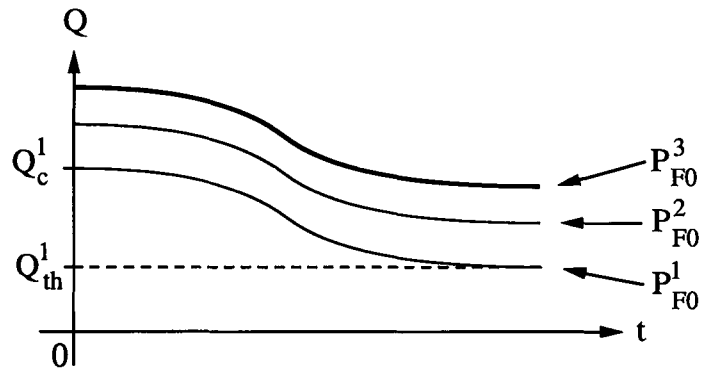

FIG. 2.2 - Isoprobabilités de rupture pour un élément de volume.

Ce raisonnement peut être tenu quelle que soit la valeur de la probabilité de rupture P_{F0}. En conséquence, deux bornes à la probabilité de rupture P_{F0} peuvent être données. Une borne supérieure, P_{F0}^U, qui correspond à $\mathcal{G}(w;Q) \geq \mathcal{G}_c$, et une borne inférieure, P_{F0}^L, faisant appel au critère de non propagation $\mathcal{G}(w;Q) < \mathcal{G}_{th}$

$$P_{F0}^U(Q) = \int_{\mathcal{D}_c(Q)} f_0(w)\,dw \ , \ \mathcal{D}_c(Q) = \{w \mid \mathcal{G}(w;Q) \geq \mathcal{G}_c\} \tag{2.16}$$

$$P_{F0}^L(Q) = \int_{\mathcal{D}_{th}(Q)} f_0(w)\,dw \ , \ \mathcal{D}_{th}(Q) = \{w \mid \mathcal{G}(w;Q) < \mathcal{G}_{th}\} \tag{2.17}$$

où $\mathcal{D}_{\text{th}}$ est l'ensemble des défauts ne se propageant jamais. L'équation (2.17) permet d'obtenir l'évolution des limites d'endurances pour différentes probabilités de rupture. En particulier, ces limites d'endurance sont indépendantes de la loi de propagation. Sachant que le taux de restitution d'énergie $\mathcal{G}(w;Q)$ est une fonction homogène de degré deux du chargement Q, il existe une relation très simple entre ces deux bornes

$$Q_{\text{th0}} = \sqrt{k}\, Q_{\text{c0}} \ , \ P_{\text{F0}}^{\text{U}}(Q) = P_{\text{F0}}^{\text{L}}(\sqrt{k}Q) \ , \ k = \mathcal{G}_{\text{th}}/\mathcal{G}_{\text{c}} \tag{2.18}$$

Ce dernier résultat montre que l'écart type ne peut pas être identique pour $N = 0$ et pour $N \to \infty$. Cette hypothèse est souvent utilisée dans le domaine de la fatigue à grand nombre de cycles depuis les travaux de BASTENAIRE [1960]. Par contre, on peut se convaincre assez facilement que le coefficient de variation est identique dans ces deux cas extrêmes.

2.1.4 Isoprobabilité de rupture

Les résultats du paragraphe précédent montrent qu'une isoprobabilité de rupture (P_{F0}^1) ne peut varier qu'entre deux bornes de chargement Q_{th}^1 et Q_{c}^1 ($Q_{\text{th}}^1 = \sqrt{k}\, Q_{\text{c}}^1$). Grâce à l'équation (2.15), une isoprobabilité de rupture est simplement liée à la densité f_0 et aux bornes du domaine des défauts critiques $\mathcal{D}_{\text{c}}^*$. Les relations générales de l'équation (2.12) permettent de déterminer l'instant de rupture $t(W;Q)$ pour lequel $\mathcal{G}(W;Q) = \mathcal{G}_{\text{c}}$. Ainsi l'équation d'une isoprobabilité est donnée par

$$P_{\text{F0}}(Q, t^1) = P_{\text{F0}}^1 \tag{2.19}$$

À l'aide des bornes précédentes, on en déduit que lorsque t^1 tend vers zéro alors Q tend vers Q_{c}^1, et lorsque t^1 tend vers l'infini Q tend vers Q_{th}^1. La figure 2.2 illustre l'utilisation des résultats précédents lors de la conception ou de la maintenance de pièces : le chargement supportable par un élément de volume est alors déduit pour une durée d'usage et une probabilité de rupture fixées.

Enfin, ce type de résultat permet de développer une procédure d'identification en deux étapes. La première étape consiste à identifier la distribution initiale de défauts en analysant une des bornes. En général, la borne inférieure est facilement accessible dans le cas de propagation stable de défauts. En fatigue à grand nombre de cycles, elle correspond à une information sur les limites d'endurance du matériau. D'autre part, la loi de propagation peut être identifiée par l'analyse d'une isoprobabilité de rupture, qui, dans le cas le plus simple, ne dépend que de la loi de propagation. Quant à la borne supérieure, elle est utilisée dans le cas de la propagation instable de défauts, car elle coïncide avec l'expression de la probabilité de rupture donnée par l'équation (2.1).

2.1.5 Applications à deux cas simples

Dans ce qui suit, on suppose que les défauts sont des fissures en milieu plan de taille initiale a et d'orientation θ ($0 < \theta < \pi/2$). Après un instant t, la fissure est supposée être caractérisée par A et Θ (figure 2.3). On suppose tout d'abord un état de contrainte mésoscopique uniaxial, caractérisé par une contrainte $\overline{\sigma}$, indépendant du temps. Afin de simplifier les calculs, on suppose que la bifurcation d'une fissure s'effectue lorsque $\mathcal{G}(a, \theta; \overline{\sigma}) = \mathcal{G}_{\text{th}}$, et que la direction de propagation est perpendiculaire à la direction de contrainte principale maximale mésoscopique. D'autre part, la loi de propagation est supposée être donnée par l'évolution de la longueur projetée $X = a\cos\theta + B$ de la fissure (figure 2.3)

$$\frac{dX}{dt} = C Z^{\text{n}} \overline{\sigma}^{\text{n}} X^{\text{n}/2} \ , \ E\,\mathcal{G}_{\text{th}} < Z^2\,\overline{\sigma}^2\,X < E\,\mathcal{G}_{\text{c}} \tag{2.20}$$

où C et n sont des paramètres du matériau, Z est un facteur de forme de la fissure supposé constant ; cette hypothèse simplificatrice permet de mener analytiquement les calculs suivants. Cette loi permet de modéliser les phénomènes de fissuration sous-critique [EVANS, 1972 ; EVANS et WIEDERHORN, 1974] ainsi que les phénomènes de sollicitations cycliques [PARIS *et al.*, 1961]. L'intégration de l'équation (2.20) correspond à l'équation (2.12) dans l'exemple particulier considéré.

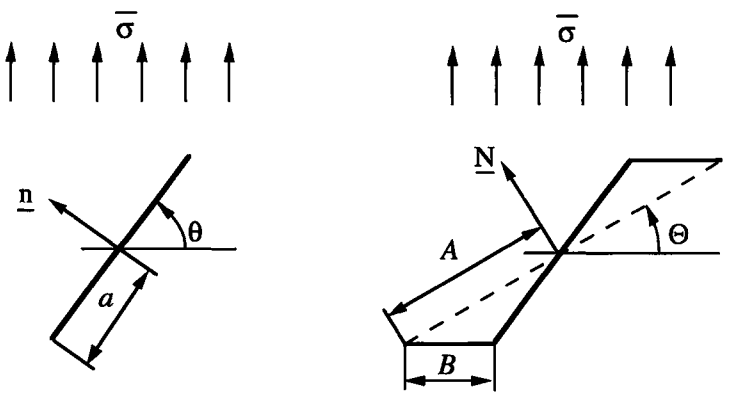

FIG. 2.3 - Fissure initiale (a, θ) et fissure après propagation (A, Θ).

Dans le cas où $f_0(a, \theta) = \frac{2}{\pi} f_0(a)$, et $f_0(a)$ peut être approchée par $k\,p\,a^{-\text{p}-1}$ au voisinage des grandes tailles de défauts, la probabilité de rupture P_{F0} est donnée par

$$P_{\text{F0}}(\overline{\sigma}, t) = \left(\frac{\langle\overline{\sigma}\rangle}{S_0}\right)^{2\text{p}} \left[1 + \frac{n-2}{2} C\,Z^2\,\overline{\sigma}^2\,(E\,\mathcal{G}_{\text{c}})^{(\text{n}-2)/2}\,t\right]^{2\text{p}/(\text{n}-2)} I_{\text{p}} \tag{2.21}$$

$$I_{\text{p}} = \int_0^{\pi/2} \cos^{\text{p}}\theta\,d\theta \ , \ S_0 = \frac{\sqrt{E\mathcal{G}_{\text{c}}}}{Z}\,k^{-1/2\text{p}}$$

Ce résultat correspond à une généralisation d'une loi de WEIBULL à deux paramètres ou de LAMON-EVANS [1983] dans le cas particulier envisagé. Lorsque $f_0(a)$ peut être approchée par $\kappa(\beta+1/2)(a_M-a)^{\beta-1}$ au voisinage d'une taille maximale de défaut a_M, la probabilité de rupture P_{F0} est donnée par

$$P_{F0}(\overline{\sigma},t) = \left[\frac{\langle \overline{\sigma}\left\{1+\frac{n-2}{2}C\,Z^2\overline{\sigma}^2\,(E\,\mathcal{G}_c)^{(n-2)/2}\,t\right\}^{1/(n-2)} - S_u\rangle}{S_0}\right]^{\beta+1/2} \tag{2.22}$$

$$S_u = \frac{\sqrt{E\mathcal{G}_c}}{Z\sqrt{a_M}}\ ,\ S_0 = \frac{S_u}{2}\left(\frac{\pi}{2\sqrt{2}\kappa}\right)^{1/(\beta+1/2)}$$

Les équations (2.21) et (2.22) sont similaires à des résultats obtenus sans propagation stable [HILD et MARQUIS, 1990]. Le seul changement est donné par la contrainte considérée qui est $\overline{\sigma}\left\{1+\frac{n-2}{2}C\,Z^2\overline{\sigma}^2\,(E\,\mathcal{G}_c)^{(n-2)/2}\,t\right\}^{1/(n-2)}$ à la place de $\overline{\sigma}$.

Pour un état de contrainte équibiaxial, caractérisé par une contrainte $\overline{\sigma}$, aucune bifurcation n'a lieu ($\mathcal{G}$ est indépendant de θ, d'où $\Theta=\theta$). D'autre part, la loi de propagation ainsi que les critères d'amorçage et de rupture sont indépendants de l'orientation θ. La probabilité de rupture P_{F0} fait alors référence à la distribution marginale de taille $\mathcal{F}_0(a)$

$$P_{F0}(\overline{\sigma},t) = \int_{a_{c0}(\overline{\sigma},t)}^{+\infty} \mathcal{F}_0(a)\,da\ ,\ \mathcal{F}_0(a) = \int_0^{\pi/2} f_0(a,\theta)\,d\theta \tag{2.23}$$

La taille $a_{c0}(\overline{\sigma},t)$ correspond à la taille initiale de défaut qui devient critique après un instant t

$$a_{c0}(\overline{\sigma},t) = \left(\frac{E\mathcal{G}_c}{Z^2\overline{\sigma}^2}\right)\left[1+\frac{n-2}{2}C\,Z^2\overline{\sigma}^2\,(E\,\mathcal{G}_c)^{(n-2)/2}\,t\right]^{2/(2-n)} \tag{2.24}$$

Dans ce cas, l'équation d'une isoprobabilité de rupture ($a_{c0}(\overline{\sigma},t)$ = constante) est de forme identique à celle donnée dans les équations (2.21) et (2.22).

Enfin, en fatigue à grand nombre de cycles, d'autres applications peuvent être faites à partir des résultats du paragraphe 2.1.2. Ils ont été utilisés, en particulier, dans l'étude de cas (DEA Mécanique & Matériaux, 1995-96) sur les fontes GS [BOMPARD, 1996].

2.1.6 Hypothèses de travail

Dans ce paragraphe, on utilise les résultats précédents dans un cas simplifié pour lequel une procédure d'identification sera mise en place dans le paragraphe 2.3. Ceci

consiste à supposer qu'un seul paramètre, une taille a, est nécessaire pour caractériser la géométrie des défauts initiaux. Cela revient à faire l'hypothèse d'une éventuelle propagation stable en mode I, qui est bien identifiée pour les matériaux que l'on va étudier. Nous supposons qu'en chaque point de la structure l'état de contrainte (mésoscopique) est caractérisé par une contrainte équivalente $\|\underline{\underline{\sigma}}\|$. La probabilité de rupture d'un maillon élémentaire P_{F0} dans le cas de propagation instable de défauts s'écrit

$$P_{\mathrm{F0}}^{\mathrm{U}}(\|\underline{\underline{\sigma}}\|) = \int_{a_{\mathrm{c}}(\|\underline{\underline{\sigma}}\|)}^{+\infty} f_0(a)da \tag{2.25}$$

Cette probabilité est fonction de la distribution de défauts et de la taille critique de défaut a_{c}, qui elle-même dépend du niveau de chargement mesuré par $\|\underline{\underline{\sigma}}\|$. Dans le cas de propagation stable de défauts, l'expression de la probabilité de rupture d'un maillon est donnée par [HILD et ROUX, 1991]

$$P_{\mathrm{F0}}(\|\underline{\underline{\sigma}}\|, t) = \int_{a_{\mathrm{c0}}(\|\underline{\underline{\sigma}}\|, t)}^{+\infty} f_0(a)da \tag{2.26}$$

où a_{c0} est la taille du défaut qui devient critique (*i.e.*, égale à a_{c}) à l'instant t. Cette expression dépend du niveau de chargement au point pour lequel la probabilité de rupture est calculée et de l'instant considéré. Au voisinage des limites d'endurance (*i.e.*, t tend vers l'infini) la probabilité cumulée de rupture devient indépendante de t et s'écrit (cf. paragraphe 2.1.2)

$$P_{\mathrm{F0}}^{\mathrm{L}}(\|\underline{\underline{\sigma}}\|) = \int_{a_{\mathrm{th}}(\|\underline{\underline{\sigma}}\|)}^{+\infty} f_0(a)da \tag{2.27}$$

Cette probabilité dépend de la distribution initiale de défauts et de la taille seuil de défaut a_{th}, elle-même fonction du niveau de chargement mesuré par $\|\underline{\underline{\sigma}}\|$. Tous les raisonnements qui suivent s'appuieront sur les résultats de ce dernier paragraphe.

2.2 Probabilité de rupture d'une structure

Pour établir l'expression de la probabilité de rupture d'une structure, l'hypothèse la plus couramment admise est celle du maillon le plus faible. Cela revient à assimiler une structure à un ensemble de maillons en série (une chaîne) ; la rupture de l'un d'entre eux (le plus faible) entraîne la rupture de toute la chaîne. Cette vision a été introduite en mécanique par PIERCE [1926] dans l'étude de la résistance de fils de coton. Ce concept a été appliqué la première fois à un volume par WEIBULL [1939b]. Cette notion a été formalisée par de nombreux auteurs dont FREUDENTHAL [1968]. Utiliser cette hypothèse suppose également que les interactions entre les différents éléments de volume sont négligeables. La coalescence d'une fissure macroscopique à partir de multiples fissures mésoscopiques n'est pas prise en compte. Pour traiter ce problème, il s'agit en particulier de prendre en compte les interactions entre défauts (cf. par exemple [FOND, 1992 ; KACHANOV, 1994]). On peut alors aboutir à une description non-locale en faisant explicitement référence à ces interactions [PIJAUDIER-CABOT et BERTHAUD, 1990] ou en postulant leur effet [PIJAUDIER-CABOT et BAZANT, 1987].

La modélisation du couplage macroscopique (interactions entre défauts) entre l'élasticité et l'endommagement est importante lorsque l'on veut simuler le comportement de matériaux hétérogènes pour lesquels la distance moyenne entre défauts est du même ordre de grandeur que la taille maximale de défaut que l'on peut observer. Ces simulations peuvent être conduites dans le cadre de la mécanique de l'endommagement par l'introduction d'un endommagement initial réparti de manière aléatoire ou non [HILD, 1992 ; YAACOUB AGHA, 1996] dans le cadre des méthodes dites « entièrement couplées » [BENALLAL *et al.*, 1991]. Dans le cas contraire, ce premier couplage est souvent négligé voire ignoré. D'un point de vue numérique, cela revient à mettre en oeuvre des approches « découplées » dans lesquelles le calcul du champ de contrainte est effectué en supposant que le comportement du matériau est élastique. On remarquera que la distinction entre couplage mésoscopique et macroscopique n'est pas propre au domaine de l'endommagement. On la retrouve également dans l'étude des couplages magnéto-mécaniques [BILLARDON et HIRSINGER, 1997]. Dans ce cas, on fait référence à des couplages locaux et globaux [BILLARDON, 1997]. Les couplages locaux, essentiellement d'état [MARQUIS, 1989], entre variables magnétiques et mécaniques permettent de décrire, par exemple, les déformations de magnétostriction [HIRSINGER, 1994]. Inversement, la prise en compte de ce couplage permet de décrire l'influence de la contrainte sur les courbes d'hystérésis magnétique [GOURDIN *et al.*, 1997]. Il existe aussi des couplages globaux, c'est-à-dire au niveau des lois de conservation. Citons l'effet du magnétisme sur la mécanique par l'intermédiaire des forces surfaciques (à

prendre en compte lors de l'écriture des conditions aux limites) ainsi que des forces de volume (qui constituent autant de termes « sources » dans le problème mécanique).

Les hypothèses de découplage sont raisonnables lorsque les défauts sont suffisamment dilués dans le matériau pour que les interactions initiales (dans le cas de la propagation instable) et induites par le chargement (dans le cas de la propagation stable) restent faibles. Ceci correspond à un passage mésoscopique-macroscopique particulier. Il peut être fait dans le cas des céramiques monolithiques ainsi que dans les cas où la phase de propagation macroscopique est négligeable par rapport à la phase d'amorçage macroscopique (*i.e.*, propagation mésoscopique instable). Le cas de la fatigue à grand nombre de cycles vérifie souvent cette hypothèse. On remarquera enfin que le dimensionnement de structures du Génie Mécanique et du Génie Civil fait souvent, de manière implicite, appel à la notion de maillon le plus faible ce qui conduit à des estimations conservatives de leur tenue en service.

Dans le cadre de l'hypothèse du maillon le plus faible et de non-interaction entre défauts, la probabilité cumulée de rupture d'une structure Ω de volume V est liée à la probabilité de rupture élémentaire P_{F0} par la relation suivante

$$P_F = 1 - \exp\left[\frac{1}{V_0}\int_\Omega \ln\left(1 - P_{F0}\right)\, dV\right] \tag{2.28}$$

où V_0 est le volume du maillon élémentaire. L'équation (2.28) permet de rendre compte de différents effets liés au comportement fragile. L'effet de la distribution des défauts sur la probabilité de rupture (effet D) est directement décrit dans la mesure où les équations (2.1) et (2.15) sont utilisées. La visualisation de cet effet est synthétisée à l'aide de cartes présentées dans le paragraphe 2.3.3 et complétée dans la thèse de H. YAACOUB AGHA [1996]. L'effet de volume (effet V) est pris en compte dès que l'hypothèse du maillon le plus faible est invoquée : plus le volume est grand, plus la probabilité de trouver des gros défauts est grande et plus la contrainte moyenne de rupture est faible. Cet effet a été observé expérimentalement [KADLECEK et SPETLA, 1967 ; L'HERMITE, 1973 ; KATAMAYA et HATTORI, 1982] et décrit analytiquement [FREUDENTHAL, 1968 ; ROUX, 1990 ; JEULIN, 1991]. Enfin l'effet d'hétérogénéité des contraintes (effet H) est également obtenu : plus le champ de contrainte est hétérogène, plus la probabilité de trouver un gros défaut fortement sollicité diminue, plus la contrainte moyenne de rupture augmente. Cet effet a également été observé expérimentalement [L'HERMITE, 1973] et a été étudié analytiquement. De manière générale les effets V et H sont analysés simultanément à l'aide de la notion de volume effectif [DAVIES, 1973]. On fait alors référence aux « effets d'échelle » dans les matériaux à comportement fragile. Cependant on peut découpler ces effets par l'intermédiaire de

facteurs d'hétérogénéité des contraintes [HILD *et al.*, 1992].

En pratique, les effets DVH interviennent simultanément et nécessitent donc d'être décrits de manière aussi fine que possible. Ces effets ont été étudiés par l'auteur de manière expérimentale [HILD, 1992] et numérique [HILD et MARQUIS, 1992] dans des situations de propagation instable de défauts. Ils peuvent être généralisés dans des configurations de propagation stable de défauts [HACHICH, 1990 ; YAACOUB AGHA, 1996]. Dans ce qui suit, on abordera plus particulièrement l'effet d'hétérogénéité des contraintes dans le cas de propagation stable de défauts.

2.2.1 Effet d'hétérogénéité des contraintes en fatigue

Supposons que le volume de la structure Ω est V, et qu'en chaque point de la structure l'état de contrainte est caractérisé par une contrainte équivalente $\|\underline{\underline{\sigma}}\|$. On considère que $\overline{\sigma}_{\mathrm{F}}$ est la plus grande contrainte équivalente appliquée à la structure et qu'elle est strictement positive. La probabilité de rupture d'un maillon élémentaire P_{F0} en chargement monotone est donnée par l'équation (2.25). Cette probabilité est fonction de la distribution de défauts et de la taille critique de défaut a_{c}, qui est elle-même fonction du niveau de chargement mesuré par $\|\underline{\underline{\sigma}}\|$. L'expression $\ln(1 - P_{\mathrm{F0}})$ peut être écrite de la manière suivante

$$\ln\left[1 - P_{\mathrm{F0}}(\|\underline{\underline{\sigma}}\|)\right] = -\sum_{n\geq 1} \alpha_{\mathrm{n}} \left(\frac{\|\underline{\underline{\sigma}}\|}{S_0}\right)^{\mathrm{n}} \tag{2.29}$$

où les constantes n, α_{n} et S_0 dépendent de la modélisation adoptée et de la distribution initiale de défauts. La probabilité cumulée de rupture de la structure peut alors s'écrire

$$P_{\mathrm{F}} = 1 - \exp\left[-\frac{V}{V_0}\sum_{n\geq 1} \alpha_{\mathrm{n}} H_{\mathrm{n}} \left(\frac{\overline{\sigma}_{\mathrm{F}}}{S_0}\right)^{\mathrm{n}}\right] \tag{2.30}$$

Le facteur d'hétérogénéité des contraintes d'ordre n est donné par

$$H_{\mathrm{n}} = \frac{1}{V}\int_{\Omega} \frac{\|\underline{\underline{\sigma}}\|^{\mathrm{n}}}{\overline{\sigma}_{\mathrm{F}}^{\mathrm{n}}}\, dV \tag{2.31}$$

Le facteur H_1 représente le moment d'ordre 1 associé à la fonction de répartition des contraintes dans une structure. Plus H_{n} est petit, plus le champ de contrainte est hétérogène. En élasticité linéaire, le rapport $\|\underline{\underline{\sigma}}\|/\overline{\sigma}_{\mathrm{F}}$ est indépendant de $\overline{\sigma}_{\mathrm{F}}$, les facteurs H_{n} sont donc indépendants du niveau de chargement. On peut remarquer que pour un chargement de traction pure la valeur de H_{n} est égale à 1 quelle que soit la valeur de n.

La notion de volume effectif introduite par DAVIES [1973] peut être généralisée de la manière suivante

$$V_{\text{eff}} = V \frac{\sum_{n\geq 1} \alpha_{\text{n}} H_{\text{n}} \left(\frac{\overline{\sigma}_{\text{F}}}{S_0}\right)^{\text{n}}}{\sum_{n\geq 1} \alpha_{\text{n}} \left(\frac{\overline{\sigma}_{\text{F}}}{S_0}\right)^{\text{n}}} \tag{2.32}$$

Dans le cas de propagation stable de défauts, l'expression de la probabilité de rupture d'un maillon est donnée par l'équation (2.26). Cette expression dépend du niveau de chargement au point pour lequel la probabilité de rupture est calculée et de l'instant considéré. Le même développement permet de définir des facteurs d'hétérogénéité de contraintes $H_{\text{n}}(t)$ qui dépendent de l'instant t. Lorsque t tend vers l'infini, la probabilité cumulée de rupture en fatigue devient indépendante de t : cf. équation (2.27). Les résultats obtenus dans le cas de propagation instable (équation (2.31)) sont applicables. C'est dans cette situation particulière que nous nous plaçons. Une généralisation de la définition de H_{n} est donnée en prenant comme contrainte équivalente en un point M de la structure la contrainte équivalente maximale en ce même point sur un cycle de chargement de période T [HACHICH, 1990]

$$H_{\text{n}} = \frac{1}{V} \int_{\Omega} \frac{\overline{\sigma}^{\text{n}}_{\max}(M)}{\overline{\sigma}^{\text{n}}_{\text{F}}} \, dV \quad , \quad \overline{\sigma}_{\max}(M) = \max_{t\in[0,T]} \|\underline{\underline{\overline{\sigma}}}(M,t)\| \quad , \quad \overline{\sigma}_{\text{F}} = \max_{M\in\Omega} \overline{\sigma}_{\max}(M) \tag{2.33}$$

Ces facteurs d'hétérogénéité de contraintes sont aussi indépendants du niveau de chargement.

Lorsqu'on suppose que la taille maximale de défaut n'est pas bornée, il est possible de supposer la forme suivante pour la distribution de défauts pour des tailles élevées de défauts

$$f_0(a) \cong w a^{-\text{n}} \tag{2.34}$$

La relation entre la taille de défaut seuil a_{th} et la contrainte équivalente maximale $\overline{\sigma}_{\max}$ est donnée par la relation

$$a_{\text{th}}(\overline{\sigma}_{\max}) = \frac{\mathcal{G}_{\text{th}} E}{Z \overline{\sigma}^2_{\max} g(R)^2} \tag{2.35}$$

où $g(R)$ est une fonction qui caractérise l'effet du rapport de charge R sur les conditions de début de propagation stable (cf. paragraphe 2.3.3). La probabilité cumulée de rupture peut être approchée par

$$P_{\text{F0}} = \left(\frac{\langle \overline{\sigma}_{\max} \rangle}{S_0}\right)^{\text{m}} \tag{2.36}$$

où les deux paramètres m et S_0 sont définis par

$$m = 2(n-1) \quad \text{et} \quad S_0 = \sqrt{\frac{\mathcal{G}_{\text{th}} E}{Z}} \frac{1}{g(R)} \left(\frac{n-1}{w}\right)^{\frac{1}{2(n-1)}} \tag{2.37}$$

La probabilité de rupture P_{F}^{L} est alors approchée par une loi de WEIBULL à deux paramètres

$$P_{\text{F}}^{\text{L}} = 1 - \exp\left[-\frac{V}{V_0} H_{\text{m}} \left(\frac{\overline{\sigma}_{\text{F}}}{S_0}\right)^{\text{m}}\right] \tag{2.38}$$

avec

$$H_{\text{m}} = \frac{1}{V} \int_{\Omega} \frac{\overline{\sigma}_{\text{max}}^{\text{m}}(M)}{\overline{\sigma}_{\text{F}}^{\text{m}}} \, dV \tag{2.39}$$

Le facteur H_{m} est indépendant du niveau de chargement et ne dépend que du type de chargement. Le volume effectif V_{eff} est égal à $V H_{\text{m}}$. Ce volume effectif est constant pour un type de chargement donné. De la même manière on peut obtenir l'expression de la contrainte $\overline{\sigma}_{\text{W}}$ dite « de WEIBULL » [BEREMIN, 1983]

$$\overline{\sigma}_{\text{W}} = \overline{\sigma}_{\text{F}} \left(\frac{V H_{\text{m}}}{V_0}\right)^{1/\text{m}} \tag{2.40}$$

La taille maximale de défaut étant bornée par a_{M}, on peut faire l'hypothèse que la fonction de répartition de défauts est équivalente à

$$f_0 = \frac{W(a_{\text{M}} - a)^{\beta}}{a_{\text{M}}^{\beta+1}} \quad \text{avec} \quad W > 0 \quad \text{et} \quad \beta > -1 \tag{2.41}$$

La contrainte seuil est donc fonction de a_{M} et sa valeur est donnée pour $g(R=0) = 1$

$$S_{\text{th}} = \frac{1}{Z} \sqrt{\frac{E \mathcal{G}_{\text{th}}}{a_{\text{M}}}} \tag{2.42}$$

La probabilité cumulée de rupture d'un seul maillon peut être approchée par

$$P_{\text{F0}} \cong \frac{W}{\beta+1} \left[1 - \frac{a_{\text{th}}}{a_{\text{M}}}\right]^{\beta+1} \qquad a_{\text{th}} \leq a_{\text{M}} \tag{2.43}$$

ou encore

$$P_{\text{F0}} = \frac{W}{\beta+1} \left[1 - \left\{\frac{S_{\text{th}}}{\overline{\sigma}_{\text{max}} g(R)}\right\}^2\right]^{\beta+1} \tag{2.44}$$

Lorsque le niveau de chargement $\overline{\sigma}_{\text{max}}$ est proche de $S_{\text{th}}/g(R)$ cette probabilité est écrite

$$P_{\text{F0}} = \left[\frac{\langle \overline{\sigma}_{\text{max}} - \frac{S_{\text{th}}}{g(R)} \rangle}{S_0}\right]^{\beta+1} \quad \text{avec} \quad S_0 = \frac{S_{\text{th}}}{2g(R)} \left[\frac{W}{\beta+1}\right]^{\frac{1}{\beta+1}} \tag{2.45}$$

La probabilité de rupture P_F^L peut alors être approchée par

$$P_F^L = 1 - \exp\left[-\frac{V}{V_0} H_m^* \left(\frac{\langle \overline{\sigma}_R - \frac{S_{th}}{g(R)} \rangle}{\overline{\sigma}_0}\right)^m\right] \tag{2.46}$$

avec

$$H_m^* = \frac{1}{V}\int_\Omega \frac{\langle \overline{\sigma}_{max}(M) g(R) - S_{th} \rangle^m}{\langle \overline{\sigma}_F g(R) - S_{th} \rangle^m} dV \text{ lorsque } \overline{\sigma}_F g(R) > S_{th} \tag{2.47}$$

H_m^* est un facteur d'hétérogénéité de contraintes modifié : il est fonction du type de chargement et du niveau de chargement appliqué. L'équation (2.46) correspond à une loi de WEIBULL à trois paramètres avec $m = \beta + 1$. Le paramètre β donne la tendance de la distribution de défauts initiaux pour les grandes tailles (de l'ordre de a_M). Le volume effectif modifié est donné par

$$V_{eff}^* = H_m^* V \tag{2.48}$$

Ce volume est aussi fonction du niveau de chargement. Pour le cas simple de la traction pure ce volume effectif est égal à zéro lorsque $\sigma_F g(R) \leq S_{th}$ et il est égal à V lorsque $\sigma_F g(R) > S_{th}$. L'exemple de flexion rotative a été traité par BÉRANGER *et al.* [1997].

À partir de ces résultats, une autre expression peut être proposée pour les facteurs d'hétérogénéité de contraintes d'ordre n (cf. équation (2.31)) à prendre en compte lors de sollicitations de fatigue

$$H_n^* = \frac{1}{V}\int_\Omega \frac{\langle \overline{\sigma}_{max}(M) g(R) - S_{th} \rangle^n}{\langle \overline{\sigma}_F g(R) - S_{th} \rangle^n} dV \tag{2.49}$$

Ces facteurs d'hétérogénéité de contraintes modifiés sont donc fonction du niveau de chargement. Le volume effectif modifié d'ordre n est alors donné par

$$V_{eff}^* = H_n^* V \tag{2.50}$$

Ces résultats vont être utilisés dans le paragraphe suivant où l'on étudie la fiabilité d'un bras de suspension.

2.2.2 Application à une structure

Un outil numérique a été développé afin d'effectuer un calcul de fiabilité de pièces de fonderie soumises à des sollicitation cycliques. Ce programme, ASTAR (Approche STAtistique de la Rupture), est un post-processeur qui utilise le résultat d'un calcul de champ de contrainte (par la méthode des éléments finis par exemple) et qui permet de visualiser les probabilités de rupture élémentaires ainsi que de calculer la probabilité

de rupture d'une structure quelconque [YAACOUB AGHA *et al.*, 1997]. Les effets DVH peuvent ainsi être étudiés de manière très systématique en fatigue à grand nombre de cycles. Il est actuellement implanté chez Renault [BILLARDON *et al.*, 1996]. Une application de la démarche est présentée dans ce qui suit.

Le programme ASTAR est écrit en Fortran. Il permet de calculer la valeur de la probabilité de rupture d'une structure à partir des probabilités de rupture des différents maillons (éléments) constituant la structure. Il permet aussi de calculer les facteurs d'hétérogénéité des contraintes correspondant au type de chargement appliqué à cette structure. La figure 2.4 montre l'organigramme de ce programme.

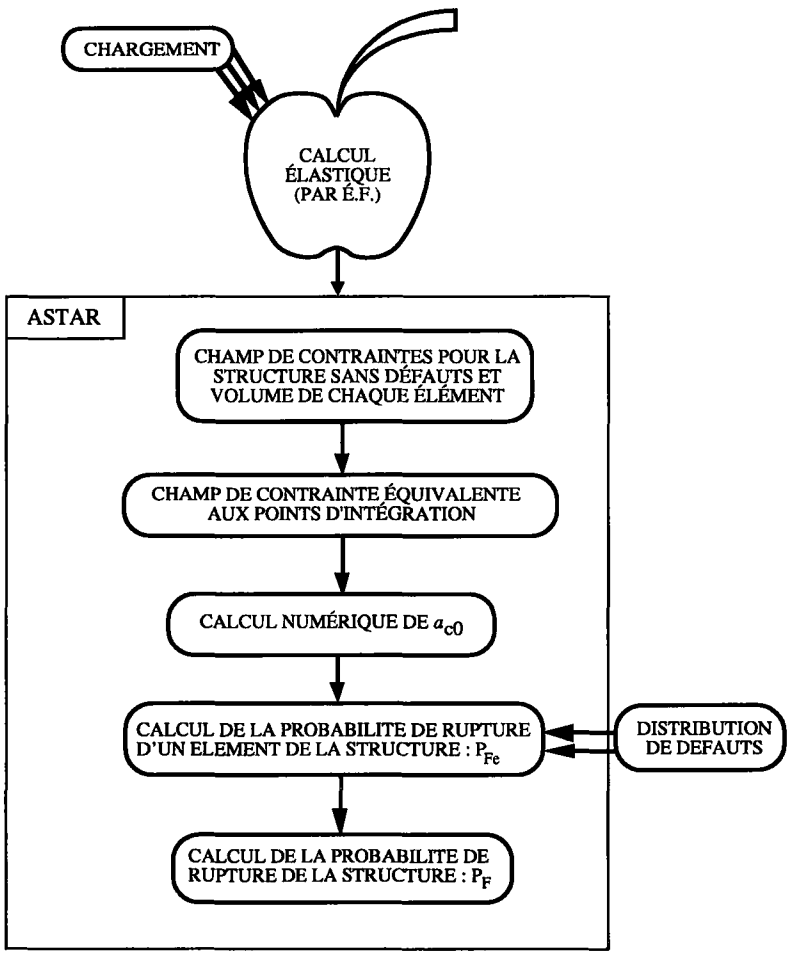

FIG. 2.4 - Organigramme du programme ASTAR.

À partir des résultats d'une analyse élastique de la structure réalisée par un code de calcul par éléments finis, en chaque point de la structure (généralement point de GAUSS), le programme calcule la contrainte équivalente. À cette contrainte équivalente

et à un nombre de cycles N correspond une taille de défaut a_{c0} qui devient critique après N cycles. Cette taille de défaut est calculée en utilisant une méthode de NEWTON.

La probabilité de rupture au point de GAUSS i, P_{F0}^{i} est calculée par intégration numérique. L'intégration par la méthode de GAUSS sur le volume total de l'élément permet de calculer la probabilité de rupture de l'élément j, P_{Fe}^{j} dépend du volume V_e (donc du maillage)

$$\ln(1 - P_{Fe}^{j}) = \frac{V_e^{j}}{V_0} \sum_{i=1}^{n_g} \ln(1 - P_{F0}^{i}) \times w_i \tag{2.51}$$

où n_g représente le nombre de points de GAUSS par élément, V_e^{j} le volume de l'élément j et w_i le poids associé au point de GAUSS i. La probabilité de rupture de la structure P_F est calculée à partir de l'expression suivante

$$P_F = 1 - \exp\left[\sum_{j=1}^{n_e} \ln(1 - P_{Fe}^{j})\right] \tag{2.52}$$

n_e représentant le nombre total d'éléments dans la structure. La dépendance au maillage de P_F est beaucoup plus faible que celle de P_{Fe}^{j}. Une étude de sensibilité au maillage est cependant nécessaire si l'on veut s'affranchir de cette dépendance. Les résultats obtenus sont interprétés en terme d'isoprobabilités de rupture de chaque élément.

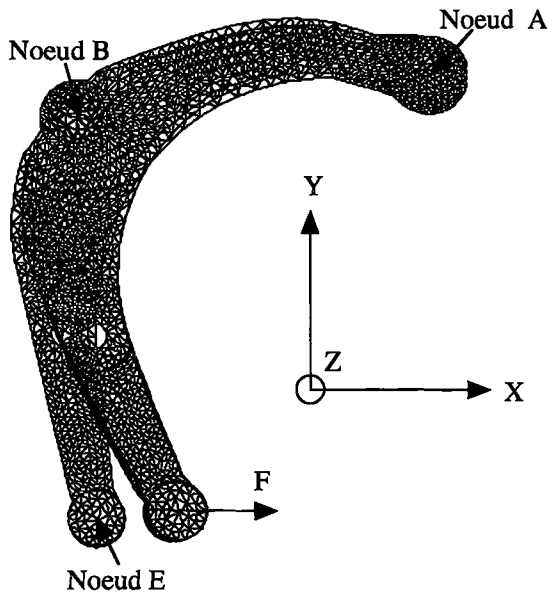

FIG. 2.5 - Maillage du bras X54 avec les conditions aux limites et le maillage déformé.

Une simulation numérique est effectuée sur un bras de suspension conçu par Renault et appelé « bras X54 ». Le maillage est réalisé en éléments coques et a été fourni

en chaque point de GAUSS de la structure ainsi qu'un autre fichier contenant le volume de chaque élément du maillage. Ces deux fichiers constituent les données nécessaires au logiciel de post-traitement ASTAR pour calculer la probabilité de rupture de chaque élément de la structure et la probabilité de rupture de la structure complète. Les valeurs des paramètres de la distribution de défauts et de la loi de propagation utilisés dans ASTAR ont été identifiées à partir de résultats expérimentaux sur une fonte GS à matrice ferritique [YAACOUB AGHA, 1996]. Un nombre de cycles N est fixé pour faire les calculs.

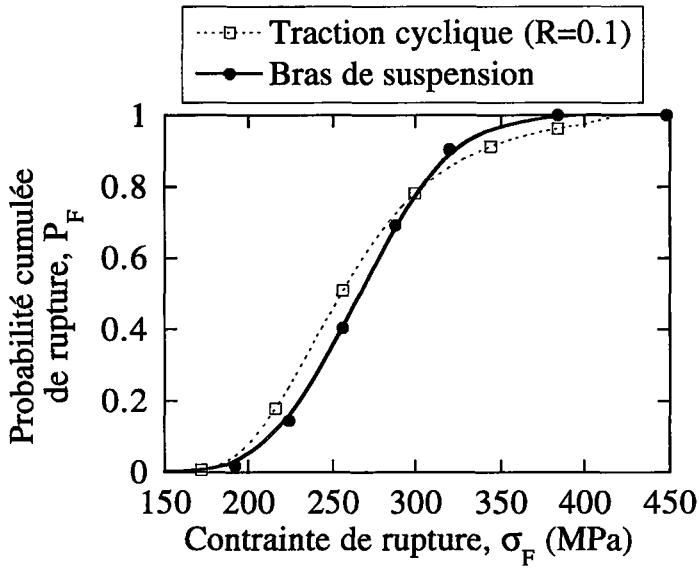

FIG. 2.7 - Probabilité cumulée de rupture du bras X54 en fonction de la contrainte maximale appliquée ($R = 0.1$). Comparaison avec un essai de traction ($R = 0.1$).

D'autres simulations ont été faites avec différentes valeurs de la charge appliquée. Les résultats de ces simulations sont rassemblés sur la figure 2.7, où la probabilité de rupture de la structure est tracée en fonction de la contrainte équivalente maximale. La comparaison de cette courbe avec la courbe tracée en pointillés qui représente la probabilité de rupture en fonction de la limite d'endurance ($N \geq 10^7$ cycles) pour les essais réalisés en traction avec un rapport de charge $R = 0.1$ montre que la différence entre les deux cas est très faible. Ceci peut être interprété en terme de volume effectif.

L'étude d'une loi de WEIBULL à trois paramètres a montré que le volume effectif est du même ordre de grandeur que le volume utile (V_0) de l'éprouvette dans le cas des essais d'identification en traction (paragraphe 2.3.3.ii). Les résultats obtenus sur le bras de suspension par ASTAR montrent que le volume effectif associé au facteur d'hétérogénéité de contraintes $H^*_{\beta+1}$ modifié introduit dans l'équation (2.49) est du même

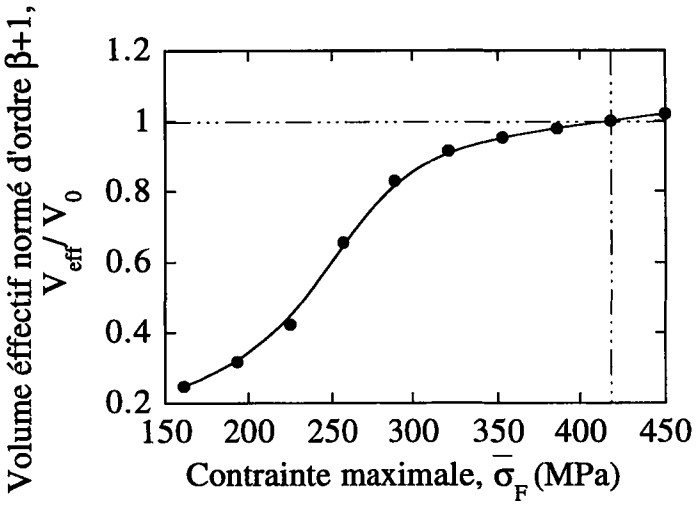

FIG. 2.8 - Évolution du volume effectif en fonction du niveau de chargement appliqué au bras X54 ($\beta = 25$).

ordre de grandeur que V_0 à $\overline{\sigma}_F = 415$ MPa. La figure 2.8 montre l'évolution de ce volume effectif en fonction du niveau de chargement maximal. Cette courbe montre que le volume effectif d'ordre $\beta + 1$ évolue rapidement pour les petites valeurs de contraintes et qu'il se stabilise lorsque le niveau de contrainte augmente. Ceci explique le résultat de la figure 2.8 qui aurait pu apparaître comme pure coïncidence.

2.3 Procédures d'identification : études à différentes échelles

Les paragraphes précédents ont montré que l'une des informations primordiales concerne la distribution initiale de défauts. Suivant le type d'analyse, différentes stratégies peuvent être employées pour identifier la distribution de défauts. La première méthode consiste à mesurer une répartition de défauts par analyse au microscope optique ou électronique à balayage de coupes successives. Elle a notamment été employée dans l'étude du nitrure de silicium par BERDIN [1993]. L'inconvénient de cette méthode, outre sa longueur, est la difficulté de trouver les plus gros défauts présents dans le matériau. Ceci nécessite donc une extrapolation des mesures vers les grandes tailles qui n'est pas toujours admissible. Cette première stratégie peut être qualifiée de « méso-macro ».

Une seconde stratégie revient à corréler la probabilité de rupture à la distribution initiale de défauts en utilisant une simplification des résultats développés dans ce chapitre. Cela peut se faire, par exemple, par l'analyse de la probabilité de rupture à l'aide d'une loi de WEIBULL [JAYATILAKA et TRUSTRUM, 1977 ; HILD et MARQUIS, 1990]. Plus particulièrement, on peut obtenir une corrélation entre les paramètres de la loi de WEIBULL et les paramètres de la distribution initiale de défauts à l'aide de la mécanique linéaire de la rupture ou de la mécanique de l'endommagement. Cette corrélation n'est, en général, valable que pour de grandes tailles de défauts [HILD, 1992]. Elle est donc complémentaire par rapport à la première méthode d'identification. Cette seconde stratégie est appelée « macro-méso ». Appliquée au nitrure de silicium, elle est décrite dans le paragraphe 2.3.1 dans le cas de chargements monotones (propagation instable de défauts) et cycliques (propagation stable de défauts).

Certaines céramiques, notamment celles contenant de l'oxygène, sont sensibles à l'environnement [EVANS, 1972 ; EVANS et WIEDERHORN, 1974]. On observe une propagation stable de fissures qui est liée à l'interaction en pointe de fissure de la microstructure de la céramique avec des agents oxydants de l'atmosphère dans laquelle elle est plongée. Ce phénomène se produit par exemple pour des ferrites spinelles MnZn ou NiZn [KADOUCH, 1993]. La conséquence de cette fissuration sous-critique est une sensibilité du matériau à la vitesse de sollicitation. Le traitement de ce problème rentre dans le cadre du paragraphe 2.1.2 dans lequel la loi de propagation est modélisée par une loi proposée par EVANS et WIEDERHORN [1974]. Les résultats obtenus sont présentés dans le paragraphe 2.3.2 pour des ferrites spinelles MnZn. L'identification de la distribution de défauts n'a pas pu être comparée à celle présente dans le matériau

pour des raisons de confidentialité. Par contre, la loi de propagation est en bon accord avec celle obtenue à l'aide d'essais de double torsion [HILD et MARQUIS, 1994]. Le même type d'approche a été employé pour l'étude du comportement de ferrites spinelles NiZn [KADOUCH, 1993]. Un autre domaine dans lequel le phénomène de propagation sous-critique est utilisé est celui des céramiques vitreuses (cf. par exemple [GRENET, 1899 ; WIEDERHORN, 1967]). L'étude du verre trempé en est un cas particulier. Des techniques assez similaires ont été utilisées pour la prévision de la sensibilité à la vitesse de sollicitation. Dans ce cas, la loi de propagation est supposée être connue pour les défauts et la seule inconnue est la distribution initiale de défauts [CARRÉ, 1996].

La fatigue à grand nombre de cycles est un autre domaine dans lequel on observe une propagation stable de défauts. Le comportement mécanique de structures soumises à ce type de chargement est essentiellement élastique linéaire à l'échelle macroscopique. À l'échelle microscopique, de la plasticité apparaît mais elle reste généralement confinée dans de petites zones au voisinage de la pointe de la fissure. Les lois de propagation de fissures sont décrites par des lois dérivées de celle initialement proposée par PARIS *et al.* [1961]. Les hypothèses de ce chapitre s'appliquent encore, en particulier dans l'étude de la tenue de structures en fonte GS. Le paragraphe 2.3.3.i est consacré à l'étude de l'effet de distribution de défauts sur les propriétés de rupture de matériaux hétérogènes sollicités cycliquement. En particulier, des cartes de rupture sont introduites pour rendre cette analyse plus facilement utilisable par un bureau d'étude. La faisabilité de l'approche est montrée à l'aide d'analyses d'essais de flexion sur fonte GS à matrice bainitique [JOKIPII, 1992]. Aucune comparaison entre distributions expérimentale et identifiée n'a pu être conduite car les essais ont été tirés de la littérature et cette information n'était pas disponible. Dans le paragraphe 2.3.3.ii, des essais de traction cyclique et de traction/compression cyclique ont été conduits au LMT-Cachan [YAACOUB AGHA, 1996] et chez Renault. Une approche de type « méso-macro » a été utilisée. À l'aide d'une technique d'identification en deux étapes, la distribution initiale de défauts a pu être déterminée (par analyse d'image) séparément de la loi de propagation des défauts (obtenue à partir de l'isoprobabilité de rupture 50%). La loi de propagation identifiée est comparée à des mesures indépendantes [CLÉMENT, 1984 ; CLÉMENT *et al.*, 1984 ; CLÉMENT et PINEAU, 1984]. Une approche « macro-méso » est développée dans [YAACOUB AGHA, 1996 ; YAACOUB AGHA *et al.*, 1997] pour laquelle l'identification de la distribution initiale de défauts est obtenue par l'analyse des limites d'endurance. La qualification de la méthode est conduite à l'aide de mesures indépendantes de la distribution initiale de défauts par analyse systématique de 50 faciès de rupture. Dans ce cas, on suppose que le passage classique « 2D-3D » [COSTER, 1974 ; COSTER et CHERMANT, 1989] n'est pas nécessaire car les plus gros défauts sont très vraisemblablement

coupés dans un des plans équatoriaux.

2.3.1 Rupture du nitrure de silicium monolithique

par F. HILD et D. MARQUIS (1994).
C.R. BRINKMAN et S.F. DUFFY (eds.), *Life Prediction Methodologies and Data for Ceramic Materials* (ASTM STP 1201), ASTM, Philadelphia, PA (USA), pp. 112-126.

François HILD,[1] Didier MARQUIS[2]

MONOTONIC AND CYCLIC RUPTURE OF A SILICON NITRIDE CERAMIC

REFERENCE: Hild, F. and Marquis, D., "Monotonic and Cyclic Rupture of a Silicon Nitride Ceramic," Life Prediction Methodologies and Data for Ceramic Materials, ASTM STP 1201, C. R. Brinkman and S. F. Duffy, Eds., American Society for Testing and Materials, Philadelphia, 1994.

ABSTRACT: A testing system was developed to perform tensile tests on monolithic ceramics. Tensile tests under monotonic and cyclic conditions were carried out on a silicon nitride ceramic. Fractographic observations were made to identify the causes of failure. The monotonic tensile tests are compared with three different kinds of monotonic flexural tests. A size effect analysis is performed using a Weibull-type of modeling. An expression of the cumulative failure probability, which takes account of the initial flaw distribution, is derived in the framework of the weakest link assumption and the independent events hypothesis.

KEYWORDS: silicon nitride, failure properties, initial flaws, statistical analysis, size effect, monotonic rupture, cyclic rupture, cumulative failure probability.

A large scatter of failure stress is a common feature of all brittle materials. The strength and data scatter are due to initial flaw size and distribution within the material. These flaws are either intrinsic (porosities, inclusions) from the manufacturing process of the ceramic (sintering, pressing), or extrinsic from grinding of specimen surface.

In this paper, tensile tests are performed in order to analyze the initial flaws under the influence of homogeneous loading conditions. The experiments are carried out at room temperature on specimens made of silicon nitride under monotonic and cyclic loading conditions. Fractographic observations are made to characterize the causes of failure. The monotonic tensile tests are compared with experiments where the stress field profile within the specimen is heterogeneous. A size effect analysis is performed to study the correlation between mean failure stress and effective volume.

[1]Postgraduate researcher, Laboratoire de Mécanique et Technologie, 61 avenue du Président Wilson, F–94235 Cachan Cedex, France.

[2]Professor, Laboratoire de Mécanique et Technologie, 61 avenue du Président Wilson, F–94235 Cachan Cedex, France.

An expression of the cumulative failure probability is given under monotonic and cyclic conditions. It allows a unified approach of the failure probability considering the flaw distribution and its evolution in the case of cyclic loading.

TENSILE TEST SYSTEM

The advantage of a tensile test is the homogeneous macroscopic stress field within the specimen. This test is more complicated to perform on brittle materials than on ductile materials. This is because the failure strains of brittle materials are very small (typically 0.1 %). Therefore, if no particular caution is taken, spurious flexural strains induced by the testing grips can easily reach the magnitude of tensile failure strains.

To avoid such problems, a new testing system is designed [1]. It is composed of four main parts (Fig. 1). The role of the elastic joints (4) is to avoid flexural strains. To obtain an equivalent Cardan joint, the elastic joints are constituted of thin elastic bonds in two orthogonal directions. Because the specimen shape is axisymmetric, the grips (2) are entirely axisymmetric-like. Two half-shells (3) maintain the specimen in the grip and evenly distribute the load onto the cone-shaped surfaces of the specimen. To avoid stress concentration, a smooth axisymmetric specimen (1) without singularities is designed. It is composed of a cylindrical testing volume (1000 mm^3), cone-shaped heads and tore-like connecting parts in the same material.

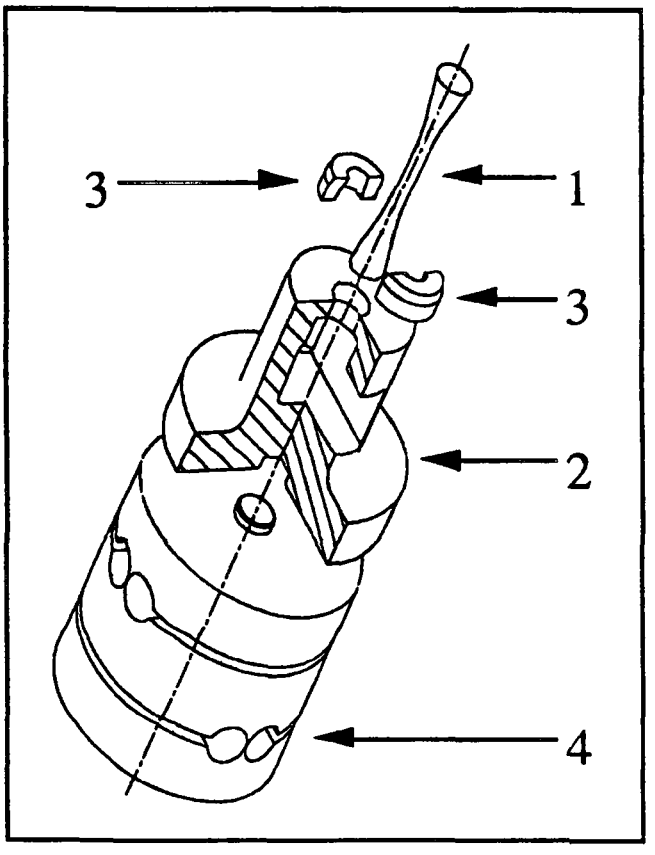

FIG. 1—The gripping system for tensile tests [1]
(1- specimen, 2- grip, 3- half shells, 4- elastic joint).

Some specimens have been tested with four strain gauges on the central section to verify the stress alignment: the maximum difference between the four gauges is less than 1.3×10^{-4} (i.e. 7.4 % of the tensile strain), and we conclude that the flexural strains are small (at maximum about 11%) compared with the tensile strains. As it is shown in the following, the scatter in failure stress induced by the flexural strains is small in comparison with the scatter induced by initial flaws.

MONOTONIC TENSILE TESTS ON SILICON NITRIDE

Eighteen specimens were tested in tension. They were made of isostatically pressed silicon nitride (SN 220M, Kyocera, Japan), density of 3,200 kg/m^3, and cylindrically machined from rods (18 mm in diameter). The value of the effective surface roughness (R_a) of the specimens was less than 0.6 μm. The loading rate was equal to 1.5 MPa/s.

First, the silicon nitride stress-strain behavior is purely linear elastic with brittle failure. Second, the failure stress varied from 374 to 635 MPa , with a mean value of 526 MPa (Fig. 2).

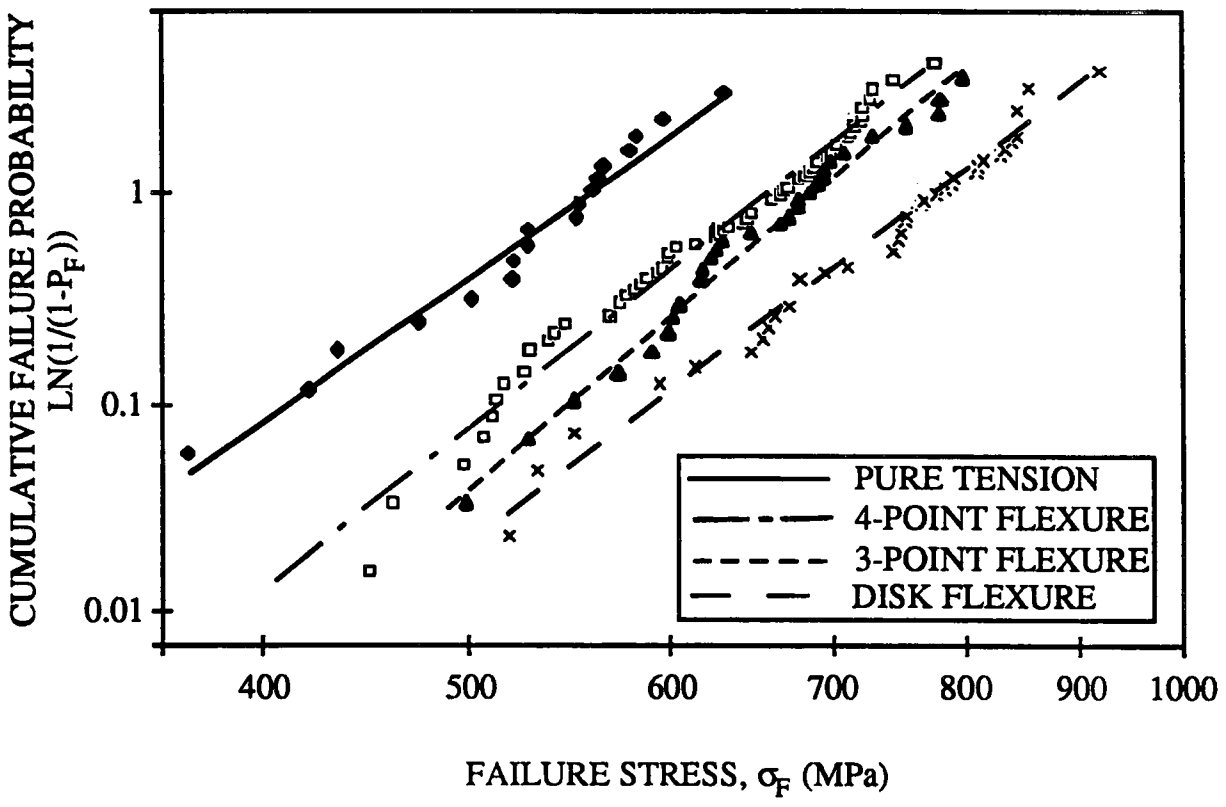

FIG. 2—An experimental data-base for the rupture of silicon nitride specimens subjected to different loading patterns (P_F : cumulative failure probability, σ_F : failure stress).
Tensile tests (◆) and Weibull correlation (——————),
Four-point flexural tests (□) and Weibull correlation (—— · ——),
Three-point flexural tests (▲) and Weibull correlation (– – – – – – –),
Disk flexural tests (×) and Weibull correlation (— — —).

These experimental results can be fitted (with least squares) to a two-parameter Weibull model [2] (Eqn. (1)) with a value of the Weibull modulus m equal to 8.0, the effective volume (V_{eff}) and the reference volume (V_0) are equal to 1000 mm^3 and 1 mm^3, respectively, and the Weibull stress S_0 equals 1360 MPa.

$$\ln\left(\ln\left(\frac{1}{1-P_F}\right)\right) = m\ln(\sigma_F) - m\ln(S_0) + \ln\left(\frac{V_{eff}}{V_0}\right) \quad (1)$$

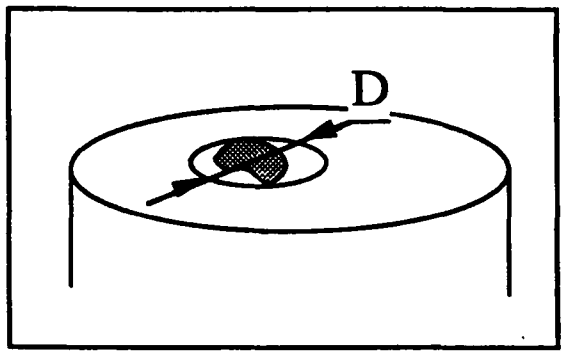

FIG. 3.1—Definition of the flaw size.

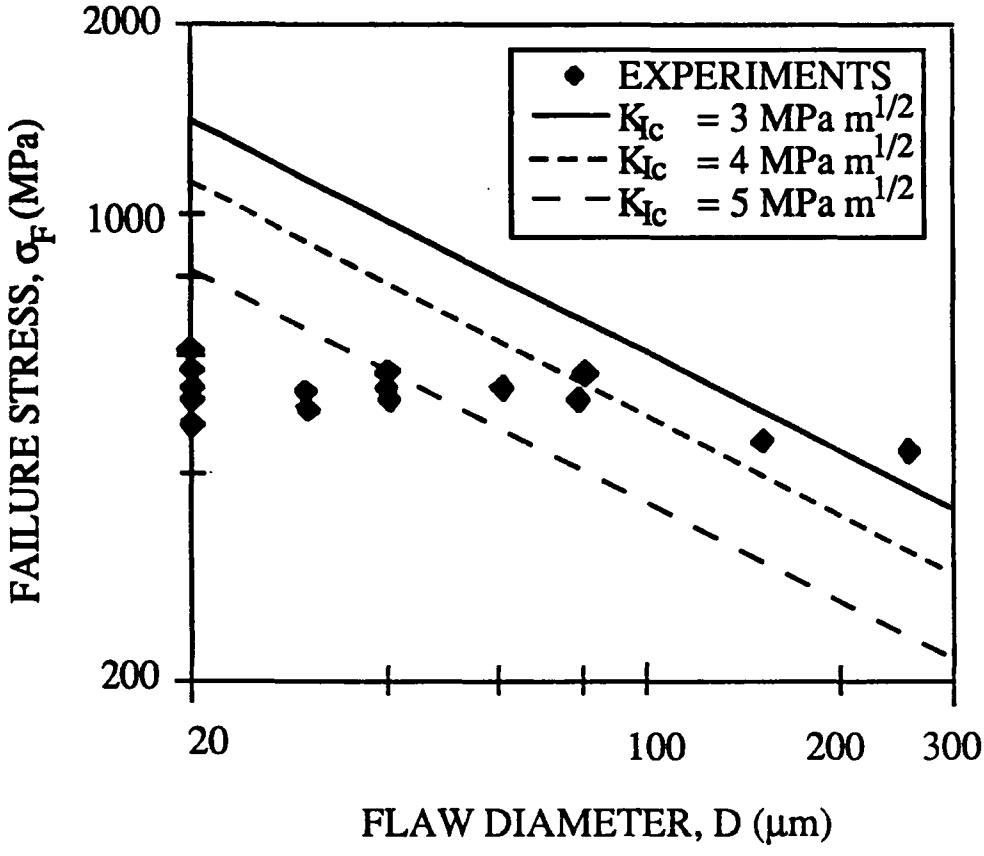

FIG. 3.2—Correlation between failure stress and flaw diameter in pure tension.

The initiation sites observed on the fracture surfaces of the specimens has flaws which size lies between 20 and 250 μm (Fig. 3.1–2). In Fig. 3.2, the experimental failure stresses are compared with failure stresses derived from a calculation where the initial flaws are assumed to be penny-shaped cracks loaded in mode I. For large flaws ($70 \leq D \leq 250$ μm) a correlation given by a Linear Elastic Fracture Mechanics approach with a critical stress intensity factor K_{Ic} on the order of 4–5 MPa$\sqrt{m}$ seems to correlate the experimental data (For SN 220M the value of K_{Ic} is known to be on the order of 5 MPa$\sqrt{m}$). Conversely, for small flaws ($D \leq 70$ μm) a correlation given by a constant failure stress on the order of 550–600 MPa seems better.

Seventeen out of eighteen failures initiated within the volume of the specimen (Fig. 4) and not at the surface. This seems to be an *a posteriori* proof of the quality of the experimental setup that has been designed for these tests: the surface flaws do not play any leading role because of the homogeneity of the stress field that is induced by this setup. Moreover, because of this homogeneity, it is likely that the initiation flaw observed is, whatever its size, the largest flaw, i.e. the weakest link [3], [4], within the specimen.

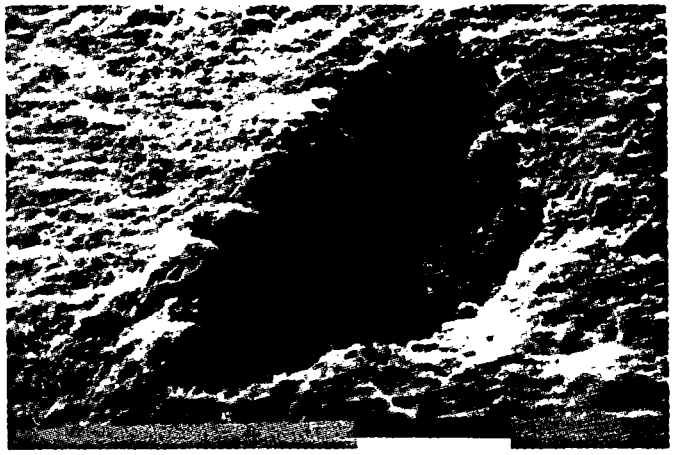

FIG. 4—Fractographic observation in pure tension (bar = 100 μm, σ_F = 425 MPa).

COMPARISON WITH OTHER MONOTONIC TESTS

To analyze the effect of the stress field pattern, the monotonic tensile tests is compared with three different kind of flexural tests (Fig. 2). An effective volume analysis is performed on the four series of tests.

Flexural Tests

4–Point flexural tests—One hundred machined rectangular-type specimens (35 mm x 4 mm x 3 mm) were subjected to four-point flexure. They were made of isostatically

pressed SN 220M and the R_a value was less than 1 μm. The load and support spans were equal to 12.5 and 24 mm, respectively.

The load-displacement curve has the same linear aspect as the curve obtained in pure tension. The failure stress (defined as the maximum stress over the structure and calculated by beam theory) lies between 448 MPa and 780 MPa (Fig. 2). The value of the Weibull modulus m (using a least squares method) is 8.9, the effective volume is equal to 8 mm^3, and the Weibull stress S_0 equals 875 MPa.

Compared to the pure tension case, the size of the initiation flaws is on average smaller (15 to 110 μm) [5], and the mean failure stress is higher (629 MPa instead of 526 MPa). Moreover, the initiation sites are located near the surface of the specimens that is subjected to tensile stresses (97% were in the volume). These observations lead to two conclusions that are valid for this type of loading. First, the highest tensile stress levels play a leading role in the failure process. Second, the initiation flaws located near the surface in tension are not in general the largest flaws within the material.

3–Point flexural tests—Fifty machined rectangle-type specimens (70 mm x 4 mm x 3 mm) were subjected to three-point flexure. The material and the R_a value were the same as for the four-point flexure specimens. The support span was 60 mm. The load-displacement curve has the same linear aspect as the curve obtained in pure tension.

The failure stress (defined as the maximum stress over the structure and calculated by beam theory) lies between 491 MPa and 801 MPa (Fig. 2). The value of m (using a least squares method) is 9.6, the effective volume is equal to 3.2 mm^3, and the Weibull stress S_0 is 780 MPa.

Compared to the four-point flexural case, the size of the initiation flaws is on average similar [5] (90% were located in the volume), and the mean failure stress is higher (660 MPa instead of 629 MPa).

Disk flexural tests—To understand the behavior of silicon nitride when subjected to a multiaxial stress field, a set of fifty disks was subjected to biaxial stress loading using ring on ring. The disk specimens were 30 mm in diameter and 3 mm in thickness. They were made of uniaxially pressed SN 220M and the value, after machining, of R_a was less than 1 μm. The disk-flexural testing setup consisted of a loading and a supporting ring 2.5 mm in diameter and 24 mm in diameter, respectively.

The failure stress, defined as the maximum principal stress over the structure and derived from a finite element analysis, lies between 513 MPa and 918 MPa (Fig. 2). The value of m (using a least squares method) is 8.4, of the effective volume is 0.5 mm^3 (a maximum principal stress criterion is used to compute the effective volume), and of S_0 is 720 MPa.

Compared to the three-point flexure case, the size of the initiation flaws is on average similar [5] (70% were located in the volume), the mean failure stress is higher (721 MPa instead of 660 MPa).

Effective Volume Analysis

Using the results of Davies [6] an effective volume analysis can be performed to correlate mean failure stress and effective volume. It is worth noting that in the framework

of a Weibull model [2], the expression of the effective volume [6] can be related to the Weibull stress heterogeneity factor H_m and to the total volume V of a structure Ω by

$$V_{eff} = V H_m \tag{2}$$

where H_m is defined as [7]

$$H_m = \left\{ \frac{1}{V} \int_{\Omega} \| \sigma \|^m \, dV \right\} / \sigma_F^m \tag{3}$$

where $\| \sigma \|$ is the equivalent stress (we used the maximum principal stress), and σ_F is the failure stress corresponding to the maximum equivalent stress in Ω, $\sigma_F \equiv \underset{\Omega}{\text{Max}} \| \sigma \|$. The mean failure stress, $\overline{\sigma}_F$, is then related to the effective volume by

$$\overline{\sigma}_F = S_0 \left(\frac{V_0}{V_{eff}} \right)^{1/m} \Gamma\left(1 + \frac{1}{m}\right) \tag{4}$$

where Γ is the Euler function of the second kind. Therefore, a Weibull model leads to a linear correlation between mean failure stress and effective volume in a log-log plot with a slope equal to $-1/m$. The correlation between the two quantities (Fig. 5) leads to a slope equal to -0.04 ($=-1/25$) with a coefficient of correlation ρ^2 equal to 0.995. The value of the slope does not correspond to the experimental Weibull modulus.

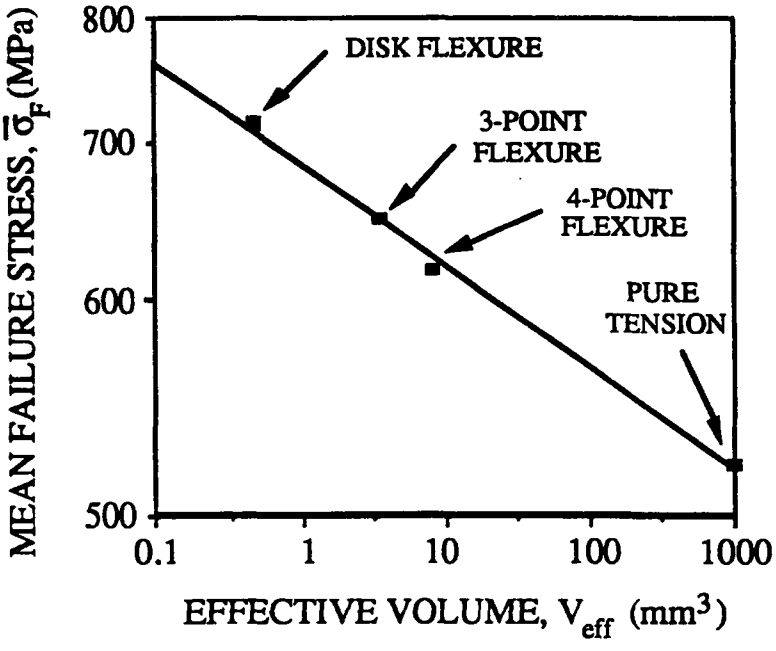

FIG. 5—Correlation between mean failure stress ($\overline{\sigma}_F$) and effective volume (V_{eff}).

Contrary to Katamaya and Hattori [8], for this set of experiments, a correlation in terms of effective volume is not satisfactory. Also, a correlation in terms of effective surface is not satisfactory since it leads to a slope equal to $-1/17$ with ρ^2 equal to 0.983.

In summary, the values of the scale parameter S_0 were found to be different. They lead to a value of the shape parameter m, derived from an effective volume analysis (on the order of 25), different from the values observed experimentally (on the order of 9). The batches of specimens were made by using various processing techniques: therefore the flaw distribution was not the same for the four sets of specimens. It is worth noting that the data plotted in Fig. 2 correspond to the same material but do not correspond to a unique initial flaw distribution.

CYCLIC TENSILE TEST ON SILICON NITRIDE

Testing Procedure

The tensile testing system is also used to perform cyclic tests. These tests were carried out to study the influence of cyclic loadings at different stress levels corresponding to known values experimentally obtained of cumulative failure probabilities under monotonic conditions. The minimum stress is equal to about 20 MPa. The maximum stress is also controlled during a test. The test is divided into series of 10,000 cycles. The first stress level (422 MPa) corresponds to a cumulative failure probability under monotonic conditions equal to 10%, the second stress level (470 MPa) corresponds to a cumulative failure probability under monotonic conditions equal to 20% , and so on. The frequency of the first cycle is equal to 5×10^{-3} Hz and corresponds to a monotonic test. The 9,999 remaining cycles have a frequency equal to 10 Hz. The test stops when the specimen breaks.

Experimental Results

Seventeen specimens were tested from a second batch. Seven out of seventeen failed at a stress level less than 422 MPa (i.e. the number of cycles to rupture is equal to unity). This shows the advantage of having a first cycle of each series with a very low frequency. For one of the specimens, a stiffness analysis is performed each 2,000th cycle. Fifteen analyses were carried out (the number of cycles to rupture was equal to 28,600, and the corresponding failure stress is equal to 507 MPa). The variation of the Young's modulus was less than 1% of the initial value of the Young's modulus. The stress alignment was again checked: the maximum difference between the four gauges was less than 11% (value observed under monotonic conditions). The number of cycles to rupture is plotted against the failure stress in Fig. 6. It is worth noting that all the ruptures do not occur when the load level is increased. The highest number of cycles is equal to 45,000 and corresponds to a failure stress of 545 MPa (i.e. a cumulative failure probability under monotonic conditions equal to 50%).

Fractographic analyses were made and led to observations similar to those found in the case of monotonic tension. In particular the mirror zone is still observed and the initiation sites are within the volume for the tests with a number of cycles to rupture greater than unity. When the number of cycles to rupture is equal to unity, the initiation sites are all at the surface. This may indicate that the grinding of the batch of specimen tested in cyclic tension is of a poorer quality than the batch of specimens tested in monotonic tension. The

initiation sites observed on the fracture surfaces of the specimens are flaws which size is between 60 and 150 μm in diameter.

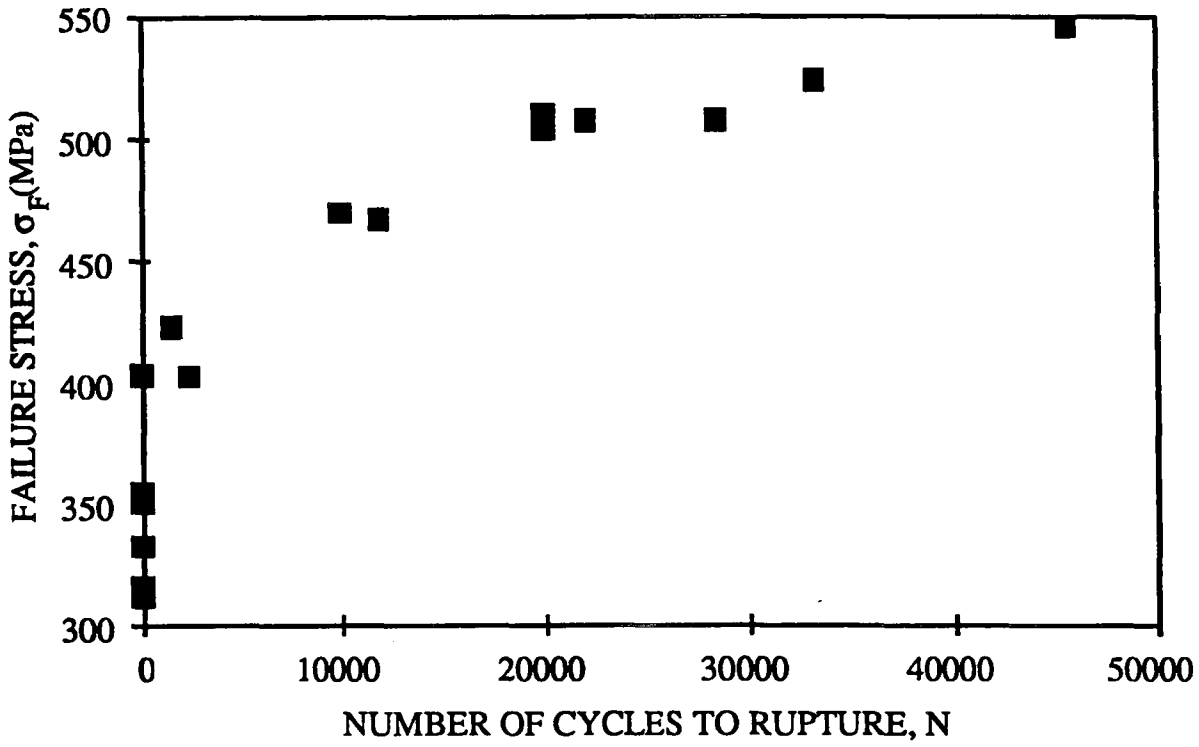

FIG. 6—Number of cycles to rupture versus failure stress.

In Fig. 7, the experimental failure stresses are compared with failure stresses derived from a calculation where the initial flaws are assumed to be penny-shaped cracks loaded in mode I. With this assumption, a Linear Elastic Fracture Mechanics approach indicates that the critical stress intensity factor K_{Ic} is again on the order of 3–5 MPa$\sqrt{m}$.

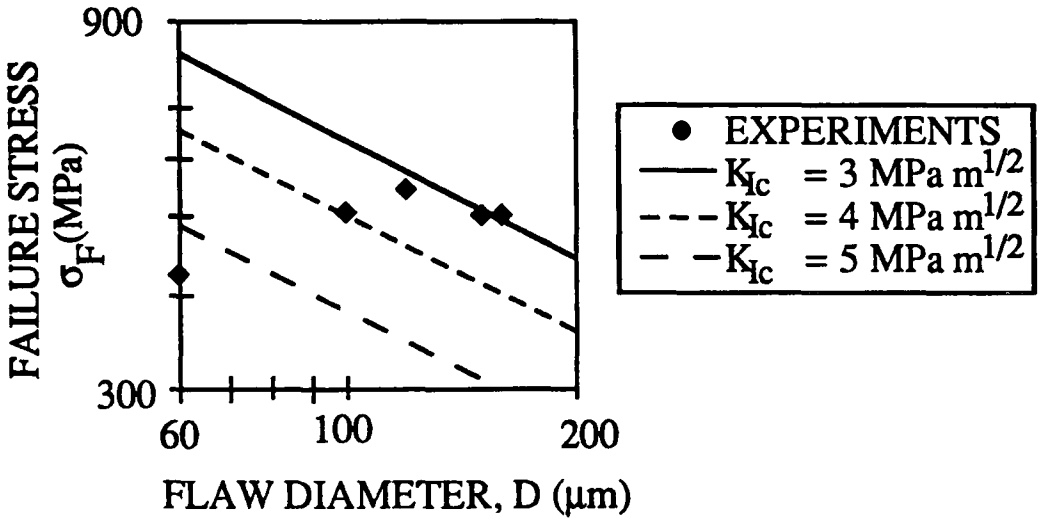

FIG. 7—Correlation between failure stress and flaw diameter in pure tension.

RELIABILITY ANALYSIS UNDER MONOTONIC AND CYCLIC LOADING CONDITIONS

The aim of this section is to analyze the reliability of structures, subjected to monotonic and cyclic loading, by considering initial flaw distributions. The study is conducted in the framework of the weakest link theory. An independent events hypothesis is made.

Expression of the Cumulative Failure Probability

The initial flaws are characterized by an initial flaw distribution density, f_0, which depends only upon their size, a (=D/2). Let us denote a_c the critical flaw size at a given stress level under monotonic and cyclic loading. Its expression is directly related to the type of modeling [9]. The cumulative failure probability P_{F0} is the probability of finding a flaw which size is larger than the critical flaw size a_c

$$P_{F0} = \int_{a_c}^{+\infty} f_0(a)\, da \tag{5}$$

In the case of cyclic loading, the flaws grow with the number of cycles, N (from $a(0)$ to $a(N)$), and the flaw distribution evolves from f_0 to f_N. The cumulative failure probability P_{F0} is then related to the flaw distribution f_N

$$P_{F0} = \int_{a_c}^{+\infty} f_N(a)\, da \tag{6}$$

It is useful to introduce a function ψ such that $a(0)=\psi(a(N))$ given by the evolution law of the flaws. If no new flaw nucleates, f_0 can be related to f_N by [10]

$$f_N(a) = f_0(\psi(a)) \frac{\partial \psi}{\partial a} \tag{7}$$

where the coefficient $(\partial\psi/\partial a)$ comes from the change of measure (from da to $d\psi(a)$). Therefore for monotonic and cyclic loading we have

$$P_{F0} = \int_{\psi(a_c)}^{+\infty} f_0(a)\, da \tag{8}$$

where $\psi(a_c)$ denotes the initial flaw size that, after N cycles of loading with a maximum equivalent stress over a cycle of period T, $\sigma = \underset{0\le t\le T}{\text{Max}} \| \bar{\sigma} \|$, reaches the critical flaw size a_c.

Eqn. (8) constitutes a unified expression of the cumulative failure probability in the case of monotonic and cyclic loading.

On the structural level, the failure occurs when one flaw within the volume becomes critical. It means that if this flaw reaches the critical flaw size, a_c, failure occurs. Determining the failure at a structural level is equivalent to finding the 'weakest link' of the structure. When the interaction between flaws can be neglected, an hypothesis of independent events can be made. We consider a structure Ω of volume V, subjected to any stress field. It can be divided into a large number of elements of volume V_0 (i.e. a representative volume element subjected to a uniform remote stress field characterized by an equivalent stress). The cumulative failure probability, P_F, of a structure Ω can be related to the cumulative failure probability, P_{F0}, of a link by

$$P_F = 1 - \exp\left\{\frac{1}{V_0}\int_{\Omega}\ln\left(1 - P_{F0}\right) dV\right\} \tag{9}$$

By means of expressions (8) and (9), a general relationship between the initial flaw distribution and the cumulative failure probability of a structure Ω can be derived

$$P_F = 1 - \exp\left\{\frac{1}{V_0}\int_{\Omega}\ln\left(1 - \int_{\psi(a_c)}^{+\infty} f_0(a)\, da\right) dV\right\} \tag{10}$$

For monotonic loading, the same equation holds with the substitution $\psi(a_c)$ into a_c.

Correlation with a Weibull Law

In the case of monotonic loading, a correlation can be obtained between the Weibull parameters and the parameters of the flaw size distribution. If we assume that the initial flaws are modeled by cracks, the value of the critical flaw size, a_c, is related to the equivalent applied stress, σ, by

$$Y\sigma\sqrt{a_c} = K_{Ic} \tag{11}$$

where Y is a dimensionless parameter characterizing the shape of the flaw, and K_{Ic} is the critical stress intensity factor. If we assume that the maximum flaw size is bounded by a_M, the flaw size distribution f can be given by a beta distribution [11]

$$f_0(a) = \frac{a_M^{-1-\alpha-\beta}}{B_{\alpha\beta}} a^{\alpha}(a_M - a)^{\beta} \qquad 0 < a < a_M \quad , \quad \alpha > -1, \beta > -1 \tag{12}$$

where α and β are the parameters of the beta function, and $B_{\alpha\beta}$ is equal to $B(\alpha+1,\beta+1)$, where B is the Euler function of the first kind. There exists a threshold stress, S_u, defined as the lowest value of the stress, under which the failure probability has a zero value

$$S_u = \frac{K_{Ic}}{Y\sqrt{a_M}} \tag{13}$$

Assuming that a_c is close to a_M, Eqns. (8) and (12) lead to the following approximation of the cumulative failure probability of a single link, P_{F0}

$$P_{F0} \cong \left\{ \frac{<\|\sigma\| - S_u>}{S_0} \right\}^{\beta+1} \quad \text{with} \quad S_0 = \frac{S_u}{2}\left\{(\beta+1)B_{\alpha\beta}\right\}^{1/(\beta+1)} \tag{14}$$

Using Eqns. (9) and (14), we obtain a Weibull expression where m is related to β (one of the parameters of the flaw distribution f_0) by

$$m = \beta + 1 \tag{15}$$

The β parameter gives the trend of the defect distribution for the large sizes (i.e. a being close to a_M). In that case, large defects are more critical for failure. Eqn. (14) gives a relationship between a parameter of the flaw distribution (i.e. a physical parameter) and m (i.e. a mechanical parameter) that can be obtained through an analysis of a set of macroscopic failure tests.

Analysis of the Monotonic Tests

For the four sets of tests, the identification was performed on the basis of a two parameter Weibull law. A similar correlation as the previous one can be derived [9] in the case of an unbounded flaw distribution. Since the values of m and S_0 are different for the four series of tests, we can conclude that the flaw distribution for small failure stresses is different.

This can also be shown by a direct identification of Eqns. (10) and (12). A good set of values of the parameters is given by $\alpha = -0.81$, $\beta = 7.11$, when $K_{Ic} = 4$ MPa$\sqrt{m}$ ($Y \cong 1$), $a_M = 125$ µm, and $V_0 = 1$ mm^3. Fig. 8 shows the computations compared with the experiments. The difference between experimental and theoretical data in the three other sets of experiments again indicates that the flaw distribution is different. This is due to the difference in processing techniques used to make the various specimen batches.

In summary, we have used two different approaches to show that the initial flaw distribution is different for the four sets of experiments. Another way to prove this difference is to perform direct measurements of the flaw distribution. This work is more tedious and the probability of finding a large flaw is very small.

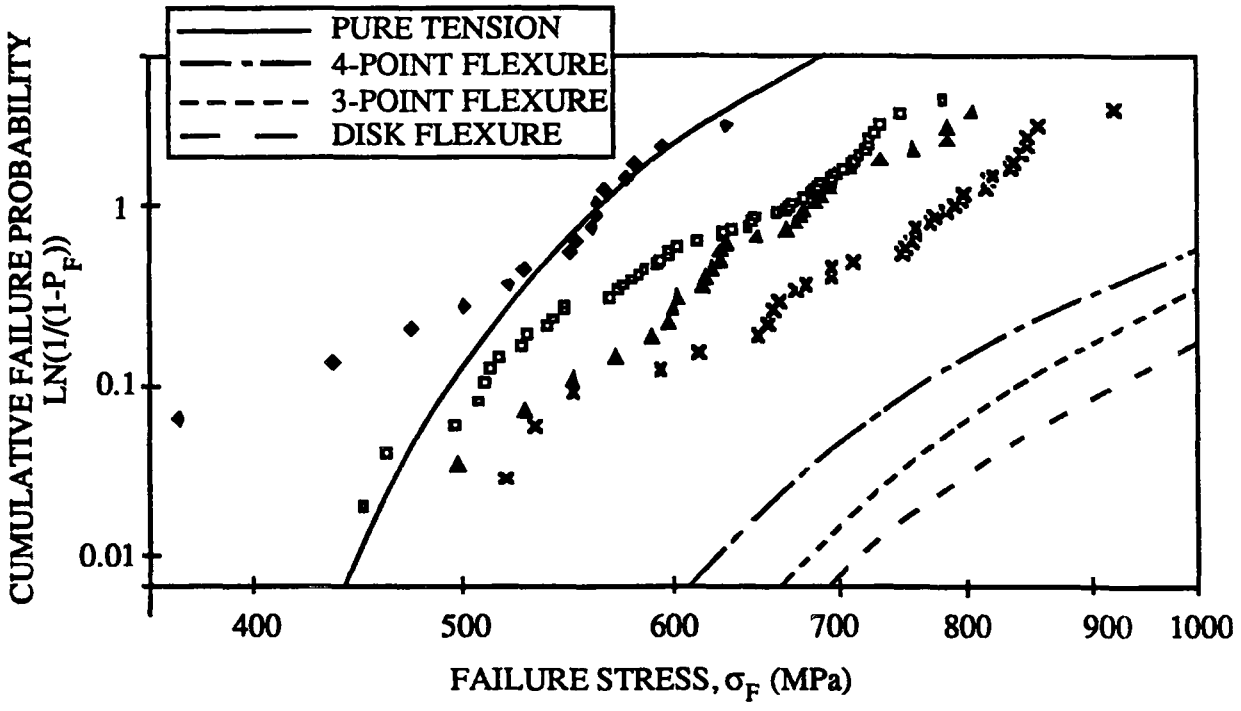

FIG. 8—Comparison between experiments and predictions for the rupture of silicon nitride specimens subjected to different loading patterns.
Experiment (◆) and model (——————) in tension,
Experiment (□) and model (—— · ——) in four-point flexure,
Experiment (▲) and model (– – – – – –) in three-point flexure,
Experiment (×) and model (— — —) in disk flexure.

Analysis of the Cyclic Tests

Eqn. (10) enables a computation of the cumulative failure probability in the case of monotonic and cyclic loading. We can therefore compute the cumulative failure probability when the number of cycles to failure is equal to 1, 10,000, 20,000, and so on. We assume that the critical stress intensity factor K_{Ic} on the order of 4 MPa$\sqrt{m}$ can model the fracture behavior as it is suggested in the fractographic analysis. The evolution law is assumed to be given by the power law regime of a Paris law

$$\frac{da}{dN} = C\, K_{max}^{n} \tag{16}$$

where the constants C and n are taken to be 6.23 x 10^{-24} m (MPa$\sqrt{m}$)$^{-n}$ and 21.1, respectively [12]. For a given load level we can compute the value of $\psi(a_c)$ as a function of the number of cycles N

$$\psi(a_c)/a_M = \left(\frac{\sigma}{S_u}\right)^{-2} \left\{ 1 + \frac{n-2}{2} C^* N \left(\frac{\sigma}{S_u}\right)^{2} \right\}^{2/(2-n)} \tag{17}$$

where $C^* = C K_{Ic}^n / a_M = 2.52 \times 10^{-7}$. When the quantity $\frac{n-2}{2} C^* N \left(\frac{\sigma}{S_u}\right)^2 << 1$, the previous expression can be simplified to become

$$\psi(a_c) / a_M \equiv \left(\frac{S_u}{\sigma}\right)^2 - C^* N \qquad (18)$$

In the considered cases, the value of S_u is 360 MPa ($Y \equiv 1$) and $C^* N << 1$ therefore the cumulative failure probability does not evolve very much during the series of cyclic loading. However it is worth remembering that failures occurred during sequences of constant load levels. This shows that a stable degradation can occur and can lead to a catastrophic failure. Moreover, the fractographic analyses did not spot any micro cracking around initial flaws. This is consistent with the fact that initial flaws grew only very little to reach the critical size. Therefore initial and critical flaws are almost identical and the correlation between initial flaw size and failure stress of Fig. 7 is relevant.

Furthermore, it is possible to compute the stress drop for the same cumulative failure probability after N Cycles. After N cycles, we get the same cumulative failure probability by writing [10]

$$\psi(a_c) / a_M = A \qquad (19)$$

where the constant A depends upon the details of the flaw distribution. Eqn. (19) enables us to get the relationship between the number of cycles to failure and the stress level to give the same cumulative failure probability.

For instance, in the case of the experiments in monotonic tension, a failure stress equal to 515 MPa corresponds to a cumulative failure probability equal to 0.25. Using the material parameters defined earlier, a drop of 10% of the applied stress corresponds to a number of cycles to rupture greater than 1.8 million of cycles.

CONCLUSION

A series of tensile tests was carried out on silicon nitride specimens. The mean strength in tension is less than the mean strength in four-point flexure, in three point flexure and in disk flexure. The Weibull modulus in tension is on the same order as in the different types of flexure. However, the value of the scale parameter changes. A correlation between the size of the flaw leading to rupture and the failure stress is given. In tension, seventeen out of eighteen failures initiated in the volume of the specimen.

The size effect analysis performed for the present results leads to a good correlation in a log-log plot. Yet the slope does not correspond to the experimentally determined Weibull modulus.

In the case of cyclic tension, a stable propagation was observed. Seven out of seventeen failures occurred for number of cycles less than unity. A correlation between the size of the flaw leading to rupture and the failure stress is given.

An expression of the cumulative failure probability taking account of the initial flaw distribution has been derived in the case of monotonic and cyclic loading. It enables us to correlate the reliability of a structure to the initial flaw distribution, which corresponds to the cause of rupture. The cumulative failure probability in the case of cyclic tension is

shown to be on the same order as the cumulative failure probability in the case of monotonic tension.

In this study, it is shown that the failure properties of a structure made of ceramics not only depend upon the volume of structure and the stress field profile, but also upon the flaw distribution. It is therefore important to specify these three quantities to be able to fully describe the failure conditions.

ACKNOWLEDGEMENTS

The authors gratefully acknowledge the financial support of Renault through contract ENSC/24 (H5–25–511) with the Laboratoire de Mécanique et Technologie, Ecole Normale Supérieure de Cachan.

REFERENCES

[1] Hild, F., "Dispositif de traction-compression d'une éprouvette," French Patent, Patent number 90 06848, 1990.

[2] Weibull, W., "A Statistical Theory of the Strength of Materials," Ing. Vetenskap Akad., 153, 1939.

[3] Weibull, W., "A Statistical Distribution Function of Wide Applicability," J. Appl. Mech., Vol. 18, No. 3, 1951, pp 293-297.

[4] Freudenthal, A. M., "Statistical Approach to Brittle Fracture," Fracture (an Advanced Treatrise), Vol. 2, 1968, pp 591-619.

[5] Amar, E., Gauthier, F. and Lamon, J., "Reliability Analysis of a Si_3N_4 Ceramic Piston Pin for Automotive Engines," 3rd Int. Symp. Ceramic Materials and Components for Engines, Las Vegas, Nevada, V. J. Tennery (Edt.), American Ceramic Society, 1989, pp 1334-1356.

[6] Davies, D. G. S., "The Statistical Approach to Engineering Design in Ceramics," Proceeding Brit. Ceram. Soc., Vol. 22, 1973, pp 429-452.

[7] Hild, F., Billardon, R. and Marquis, D., "Stress Heterogeneity versus Failure of Brittle Materials," C. R. Acad. Sci. Paris, tome 315, série II, 1992, pp 1293-1298.

[8] Katamaya, Y. and Hattori, Y., "Effects of Specimen Size on Strength of Sintered Silicon Nitride," J. Am. Ceram. Soc., 1982, pp C-164/C-165.

[9] Hild, F. and Marquis, D., "A Statistical Approach to the Rupture of Brittle Materials," Eur. J. Mech. A/Solids, Vol. 11, No. 6, 1992, pp 753-765.

[10] Hild, F. and Roux, S., "Fatigue Initiation in Heterogeneous Brittle Materials," Mech. Res. Comm., Vol. 18, No. 6, 1991, pp 409-414.

[11] Spanier, J. and Oldham, K. B., An Atlas of Functions, Springer Verlag, 1987.

[12] Hoshide, T., Ohara, T. and Yamada, T., "Fatigue Crack Growth from Indentation Flaw in Ceramics," Int. J. Fract., Vol. 37, 1988, pp 47-59.

2.3.2 Fissuration sous-critique de ferrites manganèse-zinc

par F. HILD, O. KADOUCH, J.-P. LAMBELIN et D. MARQUIS (1996).
ASME J. Eng. Mat. Tech., 118 (3), pp. 343-348.

François Hild
Chargé de Recherche au C.N.R.S.

Didier Marquis
Professor.

*Laboratoire de Mécanique et Technologie,
E.N.S. Cachan/C.N.R.S./Université Paris 6,
61, avenue du Président Wilson,
F-94235 Cachan Cedex, France

Olivier Kadouch
Research Scientist,
Commissariat à l'Energie Atomique,
Centre d'Etudes de Vaujours-Moronvilliers,
B.P. No 7, F-77181 Courtry, France

Jean-Pierre Lambelin
Research Scientist,
Commissariat à l'Energie Atomique,
Centre d'Etudes du C.E.S.T.A., B.P. No 2,
F-33114 Le Barp, France

Analysis of the Failure of Ceramics Due to Subcritical Crack Growth

Failure conditions are assessed when ceramics exhibit Subcritical Crack Growth from preexisting flaws. In the framework of the weakest link theory and independent events hypothesis, a reliability analysis is carried out by modeling flaw distributions and crack growth laws. Experimental data obtained on a spinel Mn Zn ferrite subjected to five different load rates are analyzed by using an expression for the failure probability accounting for Subcritical Crack Growth.

1 Introduction

The need for high performance materials has motivated the use of structures made of brittle materials. Such materials are usually characterized by a large scatter in strength leading to a requirement for a statistical treatment of strength properties. For design purposes, a statistical failure analysis should allow the use of experimental data obtained on small specimens subjected to simple load patterns, to infer the failure probability of structures under complex stress states encountered in service.

It is now well accepted that initial flaws cause catastrophic failure by fracture of structures made of ceramics. These initial flaws are usually randomly distributed, and lead to different strengths, even though the geometry and the loading conditions are identical. The failure condition is given by the probability of finding one critical flaw within a structure. To be critical, a flaw needs to be large enough and located in a sufficiently high loaded region. This critical flaw then represents "the weakest link" of the structure.

To predict failure conditions, various expressions of the failure probability have been proposed. Generally, they are deduced from both the weakest link theory and the independent events hypothesis. The first attempt was made by Weibull (1939), and was based upon an empirical treatment of failure. Yet "this approach does not recognize the flaws as being unique entities operated on by the multiaxial stress and does not, therefore, represent a fundamental way of treating the multiaxial effect (Evans, 1978)." Batdorf and Crose (1974) modeled initial flaws by cracks whose size and orientation are randomly distributed. Evans and Lamon (1978; 1983; 1988) derived another model based upon similar assumptions. The drawback of these approaches is that they are not easily extendable to cases where the material behavior is time-dependent, i.e., exhibiting Subcritical Crack Growth.

In the framework of Linear Elastic Fracture Mechanics, Jayatilaka and Trustrum (1977) showed that under some simplifying assumptions the Weibull parameters can be related to flaw distributions. These results have been extended in the framework of Linear Elastic Fracture Mechanics and Continuum Damage Mechanics (Hild and Marquis, 1992). An expression for the failure probability was obtained, in which the flaw distribution was directly considered. Therefore, when the material is exhibiting Subcritical (or Slow) Crack Growth (SCG), the initial flaw distribution evolves with time, and the previous approach can still be used. Some attempts have been made by Aoki et al. (1980; 1983) but by assuming that the time effects can be decoupled from the stress effects. This assumption is generally not valid: Hild and Roux (1991) obtained an expression for the flaw size distribution after a time t related to the initial flaw size distribution (i.e., $t = 0$). More recent results can be found in (Brinkman and Duffy, 1994); most of the approaches do not explicitly consider the flaw distribution. The aim of this paper is to derive an expression for the failure probability taking account of the evolution of the flaw distribution for materials with a time-dependent behavior.

Section 2 is devoted to deriving an expression for the failure probability of a structure made of a material with a time-dependent behavior. This expression is derived within the framework of the weakest link theory and the independent events hypothesis. It consists in modeling the mechanical behavior of a single link and studying the failure of a structure composed of several links. In Section 3 the general equations governing Subcritical Crack Growth are presented. Approximations are made in order to derive tractable expressions. Based upon the hypotheses of Section 3, Section 4 deals with a simplified expression for the failure probability of a structure made of a material with a time-dependent behavior. The failure probability of a single link is related to an initial flaw size distribution. To assess the reliability of a Representative Volume Element (RVE), one needs to calculate the initial critical flaw size under static and dynamic conditions. An upper bound and a lower bound of the failure probability are then derived. In Section 5, the previous results are studied when the flaw size distribution is modeled by a modified Gamma function. In particular, a Weibull law can be derived by using simplifying assumptions. Lastly, in Section 6, experimental data obtained on a spinel Mn Zn ferrite are compared with predictions using the previous results.

Contributed by the Materials Division for publication in the JOURNAL OF ENGINEERING MATERIALS AND TECHNOLOGY. Manuscript received by the Materials Division March 18, 1995; revised manuscript received January 17, 1996. Associate Technical Editor: K. S. Chan.

2 Reliability of Structures Containing Flaws With a Time-Dependent Failure Behavior

In general, initial flaws are randomly distributed within a structure. We assume that the flaw distribution is characterized by a probability density function f. The function f gives the flaw distribution at a given stage of the load history. The function f may depend upon several morphological parameters w (e.g., a flaw size denoted by a; a flaw direction characterized by a normal $\underline{n}$).

2.1 Failure Probability of a Representative Volume Element. The failure probability, P_{F0}, of an RVE is given by the probability of finding a critical flaw within an element Ω_0 of volume V_0. The probability of finding a critical flaw refers to the *initial* flaw distribution characterized by a probability density function f_0. For a given load level, the set of flaws $\mathcal{D}$ splits into two subsets. The first subset, $\mathcal{D}_c$, is related to the flaws that are critical (e.g., the energy release rate $\mathcal{G}(w, Q) \geq \mathcal{G}_c$, where Q is a loading parameter, and $\mathcal{G}_c$ a critical energy release rate). The second one, $\mathcal{D}_{nc}$, is related to the flaws that are not critical (e.g., $\mathcal{G}(w; Q) < \mathcal{G}_c$). The higher the load level, the larger $\mathcal{D}_c$ becomes with respect to $\mathcal{D}_{nc}$. The determination of the critical flaws depends upon the mechanical modeling of the flaw (Hild and Marquis, 1992). Some particular expressions can be found in the literature: Weibull (1939) used the "mode I" energy release rate, Batdorf and Crose (1974) used the coplanar energy release rate, Lamon and Evans (1983) used the non-coplanar energy release rate. When propagation is unstable, the failure probability $P_{F0}(Q)$ of a volume Ω_0 for a given loading parameter Q is given by

$$P_{F0}(Q) = \int_{\mathcal{D}_c(Q)} f_0(w)dw. \tag{1}$$

with, for instance, $\mathcal{D}_c(Q) = \{w | \mathcal{G}(w; Q) \geq \mathcal{G}_c\}$. In the case of stable propagation, the initial morphological parameters w evolve to become W after an instant τ. In particular, bifurcation may take place (therefore $\underline{N} \neq \underline{n}$, and other morphological parameters may be needed). The morphological parameters W are assumed to be uniquely related to their initial values w through deterministic functions of C^1 class

$$W = \xi(w; Q, \tau) \tag{2}$$

At an instant τ and a fixed Q, the failure probability $P_{F0}(Q, \tau)$ is linked with the flaw density function f_τ

$$P_{F0}(Q, \tau) = \int_{\mathcal{D}_c(Q)} f_\tau(W; Q, \tau)dW \tag{3}$$

e.g., $\mathcal{D}_c(Q) = \{W | \mathcal{G}(W; Q) \geq \mathcal{G}_c\}$. If no new cracks initiate during the loading, f_τ is related to f_0 by (Hild and Marquis, 1995)

$$f_\tau[\xi(w; Q, \tau)] = J^{-1}(w; Q, \tau)f_0(w) \tag{4}$$

where J denotes the Jacobian of the transformation defined in Eq. (2). This relationship is a generalization of the results derived in the case of a flaw size distribution (Hild and Roux, 1991). Through Eq. (4), Eq. (3) can be written as Eq. (5), where $\mathcal{D}_c^*$ defines the initial flaws that become critical after τ

$$P_{F0}(Q, \tau) = \int_{\mathcal{D}_c^*(Q,\tau)} f_0(w)dw \tag{5}$$

e.g., $\mathcal{D}_c^*(Q, \tau) = \{w | \mathcal{G}[\xi(w; Q, \tau); Q] \geq \mathcal{G}_c\}$. Equation (5) constitutes a unified expression for the failure probability with or without SCG. It relates the failure probability to the initial flaw distribution f_0.

2.2 Failure Probability of a Structure Under Time-Dependent Conditions. If we assume that the interaction between flaws is negligible, the expression for the failure probability, P_F, of a structure Ω of volume V can be derived in the framework of the weakest link theory and with the independent events assumption. When the material behavior is either time-dependent or time-independent, the expression for P_F can be related to the failure probability, P_{F0}, of a link by (Freudenthal, 1968)

$$P_F = 1 - \exp\left\{\frac{1}{V_0}\int_\Omega \ln(1 - P_{F0})dV\right\} \tag{6}$$

The failure probability, P_{F0}, as well as the failure probability, P_F is a function of the loading parameter Q and elapsed time τ. By means of Eqs. (5) and (6), a general relationship between the initial flaw distribution and the failure probability of a structure Ω can be derived

$$P_F(Q, \tau) = 1 - \exp\left\{\frac{1}{V_0}\int_\Omega \ln\left(1 - \int_{\mathcal{D}_c^*(Q,\tau)} f_0(w)dw\right)dV\right\} \tag{7}$$

Equation (7) constitutes the main result of this section. The failure probability of a structure can be related to the initial flaw distribution even for materials exhibiting time-dependent behaviors. The time dependence is given in the definition of the set of initial defects that become critical after an instant τ and when the applied load level is equal to Q. Equation (7) constitutes a generalization of the existing failure probabilities only valid under time-independent behavior. It is worth noting that Eq. (7) allows the competition of flaws of different sizes at different locations with different stress levels, and the weakest link is not necessarily a flaw located at the most loaded point(s) but the most critical flaw defined by $\mathcal{G}[\xi(w; Q, \tau); Q] \geq \mathcal{G}_c$.

3 Modeling of Subcritical Crack Growth

In this section, the evolution law of a single flaw is analyzed. The aim of this section is to study different expressions of Eq. (2) obtained experimentally.

3.1 Crack Propagation Under Pure Mode I Conditions. Brittle fracture of ceramic materials is often preceded by SCG. This behavior leads to a time-dependence of the failure strength (Evans, 1972; Evans and Wiederhorn, 1974). This effect is due to the interaction between the environment and the material. A sensitivity of a ceramic to SCG is measured by the evolution of mode I stress intensity factor K versus crack growth rate da/dt. Usually, the $K - da/dt$ curve is schematically described by the curve given in Fig. 1 (Evans, 1972). Region I corresponds to somewhat low stress levels. The chemical reaction at the crack tip controls the crack propagation. Evans and Wiederhorn (1974) proposed to model this region by the following relationship

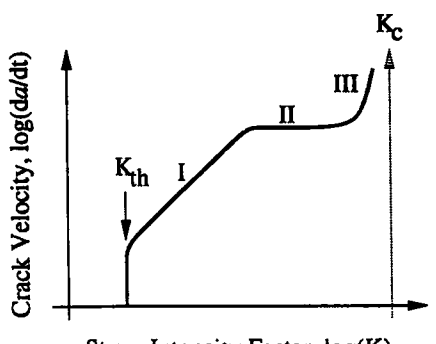

Fig. 1 Schematic representation of the effect of stress intensity factor, K, on crack velocity, da/dt, during Subcritical Crack Growth.

$$\frac{da}{dt} = CK^n, K \geq K_{th} \quad (8)$$

where C, n are material parameters, and a the flaw size. The parameter n can be used as a measure of material sensitivity to SCG: the higher n, the lower the sensitivity to SCG. Region I is characterized by a threshold stress intensity factor K_{th} (or a threshold energy release rate $\mathcal{G}_{th}$) under which no growth occurs. For example, the spinel Mn Zn ferrite exhibits SCG when double torsion experiments are performed in air at room temperature. The value of the parameter n is found equal to 20 (Kadouch, 1993). Region II corresponds to the diffusion of corrosive species to the crack tip. This diffusion controls the crack growth. The characteristic of the region is a constant velocity. Region III sometimes exits. Yet, the crack velocities are very high in the two last regions as compared to the first region. The fracture condition given by $\mathcal{G} \geq \mathcal{G}_c$ can be rewritten in terms of stress intensity factors under a pure mode I loading condition $K = K_c$. Equation (8) agrees with most of the experimental data for ceramics exhibiting SCG. These data were established on macrocracks under pure mode I, and therefore they did not experience kinking. Under mixed mode conditions however, kinking may take place and the previous laws may not be applicable anymore.

3.2 General Case and Approximations. In practice, most of the intrinsic flaws observed in ceramics are either cavities or inclusions of hard materials (Kingery et al., 1976). The most likely shape can be approximated by a sphere of radius a. Initiation is assumed to occur in a plane perpendicular to the direction of maximum principal stress, σ_I, and the initial flaw is assumed to be penny shaped. If the load history is simple (i.e., the direction of principal stresses does not change), then micro propagation happens in the same plane as micro initiation and no kinking is involved (Bilby and Cardew, 1975; Lemaitre, 1976; Wu, 1978; Amestoy et al., 1979). Consequently, the only morphological parameter needed is the radius of the crack in the considered plane, since the shape of the initial circle is not altered during micro propagation. The crack geometry is taken into account by a dimensionless factor Y so that the energy release rate $\mathcal{G}$ is given by

$$E\mathcal{G} = Y^2\|\underline{\sigma}\|^2 a \quad (9)$$

where $\|\underline{\sigma}\|$ denotes an equivalent uniaxial stress (here the maximum principal stress σ_I), and E the Young's modulus of the virgin material. The values of the parameter Y depend upon the geometry of the initial flaw and on the fact that this flaw intersects or not a free surface. The crack propagation law is assumed to be described by an expression similar to that of Eq. (8) written in terms of the energy release rate $\mathcal{G}$ instead of the stress intensity factor K

$$\frac{da}{dt} = C(E\mathcal{G})^{n/2}, \quad \mathcal{G}_{th} \leq \mathcal{G} \leq \mathcal{G}_c \quad (10)$$

and the parameters characterizing the crack propagation law are still C and n. Equation (10) is consistent with Eq. (8) in the case of pure mode I conditions.

Moreover, when the maximum principal stress σ_I is very large compared with the other two principal stresses σ_{II} and σ_{III}, the approximations made in this sub-section are not strong. The initial flaw size distribution to consider is denoted by $f_0(a)$. Because of the approximations made in this section, the general results derived in Section 2 can be simplified, and are studied in the following section by only considering the flaw size as a morphological parameter modeling the flaw distribution.

4 Simplified Reliability Analysis

In this Section, we assume that the flaw distribution is only dependent upon the size of the initial flaws and will be denoted by $f_0(a)$.

4.1 Expression for the Failure Probability. If the probability density function is assumed only to be dependent upon the flaw size, the failure probability, P_{F0}, of an RVE of volume V_0, is the probability of finding an initial flaw, whose size is larger than the critical flaw size. Rewriting Eq. (5) in the case of one parameter, the failure probability, P_{F0}, can be rewritten as (Hild and Roux, 1991)

$$P_{F0}(Q, \tau) = \int_{\psi[a_c(Q,\tau)]}^{+\infty} f_0(a)da \quad (11)$$

where $\psi(a_c)$ denotes the initial flaw size that, after a time τ, reaches the critical flaw size a_c obtained by integration of Eq. (9). It is referred to as *initial critical flaw size*. Its derivation is addressed in sub-Section 4.2. By means of Eq. (6), a simplified relationship between the initial flaw distribution and the failure probability of a structure Ω can be derived

$$P_F(Q, \tau) = 1 - \exp\left\{\frac{1}{V_0}\int_\Omega \ln\left(1 - \int_{\psi[a_c(Q,\tau)]}^{+\infty} f_0(a)da\right)dV\right\} \quad (12)$$

Equation (12) constitutes a unified expression for the failure probability with or without SCG. It relates the expression for the failure probability to the initial flaw size distribution f_0. In the next sub-section, expressions of the initial critical flaw size are derived.

4.2 Initial Critical Flaw Size. Expressions of the initial critical flaw size are derived under static (e.g. constant stress level) and dynamic conditions (e.g. linear stress level with time) by integration of Eq. (8)

$$\int_{\psi[a_c(Q,\tau)]}^{a_c(Q)} x^{-n/2}dx = \int_{t_I}^{t_F} CY^n\|\underline{\sigma}(Q, \tau)\|^n d\tau \quad (13)$$

where t_I denotes the initiation time ($Y^2\|\underline{\sigma}(Q(t_I), t_I)\|^2 a = E\mathcal{G}_{th}$) and t_F the failure time ($Y^2\|\underline{\sigma}(Q(t_F), t_F)\|^2 a = E\mathcal{G}_c$). These expressions enable to compute the failure probability of an RVE given in Eq. (11). In the following, σ_F denotes the value of the equivalent stress $\|\underline{\sigma}(Q(t_F), t_F)\|$ at failure. We define a scaling flaw size a_*, so that the scaling stress S_* corresponds to the failure stress of the scaling flaw: $Y^2 S_*^2 a_* = E\mathcal{G}_c$.

4.2.1 Static Conditions. Under static condition, the initiation time is equal to zero and integration of Eq. (13) shows that the normalized critical initial flaw size, $\psi(a_c)/a_*$ is related to the normalized failure stress σ_F/S_* and the time to failure under static condition t_{SF} by

$$\frac{\psi(a_c)}{a_*} = \left(\frac{S_*}{\sigma_F}\right)^2\left\{1 + \frac{n-2}{2}\left(\frac{\sigma_F}{S_*}\right)^2 \bar{t}_{SF}\right\}^{2/(2-n)}$$

$$\text{if} \quad \frac{\mathcal{G}_{th}}{\mathcal{G}_c} \leq \frac{\psi(a_c)}{a_*}\left(\frac{\sigma_F}{S_*}\right)^2 \leq 1 \quad (14)$$

with $\bar{t}_{SF} = CY^2(E\mathcal{G}_c)^{n/2-1}S_*^2 t_{SF}$.

4.2.2 Dynamic Conditions. When the stress evolution is linear with time, $\sigma = \dot{\sigma}t$, integration of Eq. (13) enables us to relate the normalized stress velocity $\dot{\sigma}/\dot{S}_*$ to the normalized failure stress σ_F/S_* by

$$\frac{2(n+1)}{(n-2)}\frac{\dot{\sigma}}{\dot{S}_*}\left(\frac{\sigma_F}{S_*}\right)^{-3} = \frac{\left(\dfrac{k}{\left\{\dfrac{\psi(a_c)}{a_*}\right\}^{1/2}\dfrac{\sigma_F}{S_*}}\right)^{n+1} - 1}{\left[1 - \left(\left\{\dfrac{\psi(a_c)}{a_*}\right\}^{1/2}\dfrac{\sigma_F}{S_*}\right)^{2-n}\right]} \quad (15)$$

with $\dot{S}_* = CY^2(E\mathcal{G}_c)^{n/2-1}S_*^3$, and $k = (\mathcal{G}_{th}/\mathcal{G}_c)^{1/2}$. The quantity $(\psi(a_c)/a_*)^{1/2}(\sigma_F/S_*)$ is bounded by k and 1. It is worth noting that when $Y\psi(a_c)^{1/2}\sigma_F$ approaches $(E\mathcal{G}_{th})^{1/2}$ the stress velocity $\dot{\sigma}$ approaches zero: this effect is due to the threshold energy release rate under which no SCG occurs. Conversely, when $Y\psi(a_c)^{1/2}\sigma_F$ approaches $(E\mathcal{G}_c)^{1/2}$ the stress velocity $\dot{\sigma}$ approaches infinity: there is no SCG phenomenon. Equation (15) constitutes an implicit relationship between the failure stress σ_F and the stress rate $\dot{\sigma}$. Figure 2 shows the evolution of the left-hand side of Eq. (15) as a function of normalized initial critical flaw size $(\psi(a_c)/a_*)^{1/2}(\sigma_F/S_*)$.

It is possible to relate the time to failure under static condition, t_{SF}, to the time to failure under dynamic condition, t_{DF}, and the time to initiation under dynamic conditions, t_{DI}, when the failure stress level is the same under static and dynamic conditions

$$t_{DF} = (n+1)t_{SF} + t_{DI}k^n\left(\frac{\psi(a_c)}{a_*}\right)^{-n/2}\left(\frac{\sigma_F}{S_*}\right)^{-n} \quad (16)$$

In most practical cases, Eq. (16) can be simplified: the parameter n has often a value between 10 and 30. Since the value of the ratio k is on the order of 0.5, the term $k^n(\psi(a_c)/a_*)^{-n/2}(\sigma_F/S_*)^{-n}$ is often very small compared to unity. Therefore the normalized critical initial flaw size, $\psi(a_c)/a_*$ is related to the normalized failure stress σ_F/S_* and to the time to failure t_{DF} by

$$\frac{\psi(a_c)}{a_*} = \left(\frac{S_*}{\sigma_F}\right)^2\left\{1 + \frac{n-2}{2(n+1)}\left(\frac{\sigma_F}{S_*}\right)^2\bar{t}_{DF}\right\}^{2/(2-n)} \quad (17)$$

with $\bar{t}_{DF} = CY^2(E\mathcal{G}_c)^{n/2-1}S_*^2t_{DF}$. The previous approximation is only valid when $(\psi(a_c)/a_*)(\sigma_F/S_*)^2$ is close to unity. In that case, the influence of the threshold energy release rate, $\mathcal{G}_{th}$ is negligible. When Eq. (17) is compared with Eq. (14), the well known relationship between the static life t_{DF} and the dynamic life t_{SF} is found: $t_{DF} = (n+1)t_{SF}$ (Davidge et al., 1973). On the other hand, when the ratio $(\psi(a_c)/a_*)(\sigma_F/S_*)^2$ is on the order of k, the previous approximation is not valid (Fig. 2). A series expansion about $(\psi(a_c)/a_*)(\sigma_F/S_*)^2 = k$ of Eq. (15) leads to the following result

$$\frac{\psi(a_c)}{a_*} \cong \left(\frac{kS_*}{\sigma_F}\right)^2 \times \left\{1 + \frac{1}{\dfrac{n-2}{2(k^{2-n}-1)}\left(\dfrac{\sigma_F}{S_*}\right)^2\bar{t}_{DF} + \dfrac{n-6+(n+2)k^{n-2}}{2(1-k^{n-2})}}\right\}^2 \quad (18)$$

When $k^{n-2} \ll 1$, Eq. (18) can be rewritten as

$$\frac{\psi(a_c)}{a_*} \cong \left(\frac{kS_*}{\sigma_F}\right)^2\left\{1 + \frac{1}{\dfrac{n-2}{2k^{2-n}}\left(\dfrac{\sigma_F}{S_*}\right)^2\bar{t}_{DF} + \dfrac{n-6}{2}}\right\}^2 \quad (19)$$

Figure 2 shows the two approximations about $(\psi(a_c)/a_*)(\sigma_F/S_*)^2 = k$ given by Eq. (18) and about $(\psi(a_c)/a_*)(\sigma_F/S_*)^2 = 1$ given by Eq. (17) compared with the exact solution given by Eq. (15). The approximation about $(\psi(a_c)/a_*)(\sigma_F/S_*)^2 = 1$ is valid in a very large interval, whereas the approximation about $(\psi(a_c)/a_*)(\sigma_F/S_*)^2 = k$ is valid only in a narrow interval.

4.3 Upper and Lower Bounds. By definition, Eq. (10) shows that $\psi(a_c)$ is greater than a_{th} (when $\mathcal{G} = \mathcal{G}_{th}$) and less than a_c (when $\mathcal{G} = \mathcal{G}_c$). This result can be extended to all initial flaws, i.e., to the initial flaw distribution, and two bounds can be obtained.

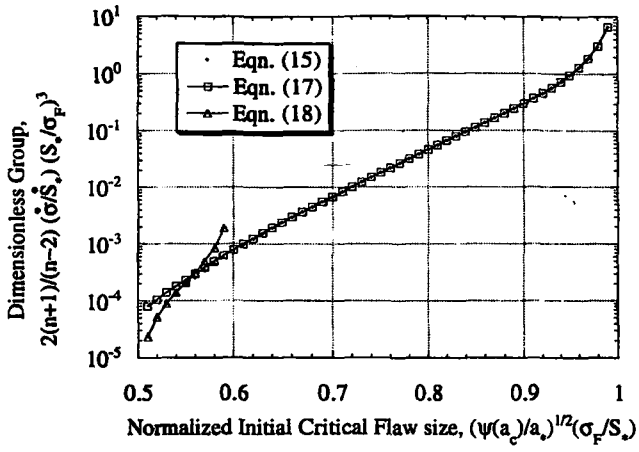

Fig. 2 Comparison of the evolution of a dimensionless group, $2(n+1)/(n-2)(\dot{\sigma}/\dot{S}_*)(S_*/\sigma_F)^3$, as a function of normalized initial critical flaw size, $(\psi(a_c)/a_*)^{1/2}(\sigma_F/S_*)$, by using Eqs. (15), (17), and (18). The parameter n is equal to 16, and the energy release rate ratio k is equal to 0.5.

In inert environment, i.e., when SCG does not occur, Eq. (11) holds with $\psi(a_c)$ equal to a_c. This particular case corresponds to an upper bound of the expression for the failure probability, denoted by $P_{F\text{-}UB}$

$$P_{F\text{-}UB}(Q) = 1 - \exp\left\{\frac{1}{V_0}\int_\Omega \ln\left(1 - \int_{a_c(Q)}^{+\infty} f_0(a)da\right)dV\right\} \quad (20)$$

On the other hand, $\psi(a_c)$ may be substituted into a_{th} defined as the initial threshold flaw size obtained when $\mathcal{G} = \mathcal{G}_{th}$. This particular case corresponds to another bound, viz. a lower bound of the failure probability, denoted by $P_{F\text{-}LB}$

$$P_{F\text{-}LB}(Q) = 1 - \exp\left\{\frac{1}{V_0}\int_\Omega \ln\left(1 - \int_{a_{th}(Q)}^{+\infty} f_0(a)da\right)dV\right\} \quad (21)$$

Equation (21) shows that a crucial material parameter is the threshold energy release rate, $\mathcal{G}_{th}$. This factor allows to derive an expression for a lower bound of the failure probability. A second crucial information is the flaw distribution. Because of linearity between external loads and stress field, and because $\mathcal{G}$ is a homogeneous function of degree 2 of the applied load Q, the following result applies

$$P_{F\text{-}LB}(kQ) = P_{F-UB}(Q) \quad (22)$$

This result shows that for a given failure probability, the failure stress corresponding to the lower bound is equal to the failure stress corresponding to the upper bound times the ratio k.

5 Correlation to a Weibull Law

This section is devoted to the analysis of a particular flaw size distribution. We assume that the initial flaw size distribution is approximated by a power law function for very large flaw sizes

$$f_0(a) \cong \frac{\kappa}{a_*}\left(\frac{a}{a_*}\right)^{-p} \quad (23)$$

where κ is a dimensionless constant. This function may correspond to the expression of a modified Gamma density function (Jayatilaka and Trustrum, 1977)

$$f_0(a) = \frac{1}{a_* \Gamma(p-1)} \left(\frac{a_*}{a}\right)^p \exp\left(-\frac{a_*}{a}\right) \quad (24)$$

where Γ represents the Euler integral of the second kind. When the ratio a/a_* becomes large, the function f_0 is proportional to a power law function with $\kappa = 1/\Gamma(p-1)$.

By using the previous assumption it is possible to correlate the failure probability of a structure to a Weibull law. In this section we assume that an initial flaw is only described by a flaw size. The failure probability, P_{F0}, is assumed to be very small as compared to unity. The initial flaw size distribution can therefore be approximated by a power law function. When the ratio $(\psi(a_c)/a_*)(\sigma_F/S_*)^2$ is close to unity, the failure probability of a single link, P_{F0}, can be rewritten as

$$P_{F0} \cong \frac{\kappa}{p-1}\left(\frac{\sigma_F}{S_*}\right)^{2(p-1)}\left\{1 + \frac{n-2}{2}\left(\frac{\sigma_F}{S_*}\right)^2 \bar{t}_F\right\}^{[2(p-1)/(n-2)]} \quad (25)$$

where $\bar{t}_F$ is either equal to $\bar{t}_{SF}$ or $\bar{t}_{DF}/(n+1)$. The failure probability of a structure, P_F, can then be rewritten as

$$P_F \cong 1 - \exp\left\{-\frac{1}{V_0}\int_\Omega P_{F0} dV\right\} \quad (26)$$

When the term $(\sigma_F/S_*)^2\bar{t}_F$ is very small compared with unity, i.e., $\psi(a_c)/a_*(\sigma_F/S_*)^2 \cong 1$, the expression for the failure probability, P_F, becomes

$$P_F \cong 1 - \exp\left\{-\frac{1}{V_0}\int_\Omega \frac{\kappa}{p-1}\left(\frac{\sigma_F}{S_*}\right)^{2(p-1)} dV\right\} \quad (27)$$

This expression is similar to a two-parameter Weibull law (Jayatilaka and Trustrum, 1977; Hild and Marquis, 1992). This case corresponds to fast fracture or fracture in an inert environment, and therefore gives an approximation of the upper bound of the failure probability given in Eq. (20). When the term $(\sigma_F/S_*)^2\bar{t}_F$ is very large compared to unity, i.e. $\psi(a_c)/a_*(\sigma_F/S_*)^2 \cong k$, the expression for the failure probability, P_F, can be rewritten as

$$P_F \cong 1 - \exp\left\{-\frac{1}{V_0}\int_\Omega \frac{\kappa}{p-1}\left(\frac{\sigma_F}{kS_*}\right)^{2(p-1)} dV\right\} \quad (28)$$

This expression again is similar to a two-parameter Weibull law in which the scale parameter becomes kS_* instead of S_* in Eq. (27). This modification can also be seen as a change in critical conditions: instead of the failure criterion ($\mathcal{G} = \mathcal{G}_c$), one uses the initiation criterion ($\mathcal{G} = \mathcal{G}_{th}$). This case gives an approximation of the lower bound of the failure probability given in Eq. (21). The result shown in Eq. (22) is also found when Eq. (28) is compared to Eq. (27). Lastly, when the two previous approximations are not valid, there is a coupling between the stress level and the time to failure (see for instance Eq. (25)) and it is not possible *a priori* to correlate the failure probability to a Weibull law.

6 Analysis of Four-Point Flexure Tests

In the following, we analyze the experimental results carried out on a spinel Mn Zn ferrite. One hundred machined rectangular-type specimens (45 mm × 4 mm × 8 mm) were subjected to four-point flexure in air at room temperature. The inner span was equal to 20 mm and the outer span was equal to 40 mm. Five different stress rates were applied (0.0975, 9.75, 48.75, 487.5, and 9750 MPa/s). In this analysis, for the sake of simplicity, only the part of the material within the inner span length is considered. Verifications on the whole structure have shown that this hypothesis was not too restrictive. In four-point flexure, the stress field is considered mainly one-dimensional. From post-mortem analyses, initiation occured within the volume and therefore the approximations made in Section 3 are consistent with these observations.

The flaw size distribution is first determined by analysis of the experimental data at the lowest stress rate. The identification procedure can be decoupled if the lowest stress rate corresponds to the lower bound described in Eq. (21). The flaw size distribution $f_0(a)$ is assumed to be described by a Gamma density function

$$f_0(a) = \frac{1}{a_* \Gamma(p)}\left(\frac{a}{a_*}\right)^{p-1} \exp\left(-\frac{a}{a_*}\right) \quad (29)$$

By using a least squares method, the following parameters are obtained: $p = 6.4$, $S_* = 160$ MPa, when $V/V_0 = 2400$ to fit the experimental results at the lowest stress rate. The values of the material parameters modeling SCG are then identified by using the experimental data at highest stress rate: $CY^2(E\mathcal{G}_c)^{n/2-1} = 3.2\ 10^{-3}\ \mathrm{m^2\ MPa^2\ s^{-1}}$, $n = 20$, $k = 0.625$. In Fig. 3 the identified curve is plotted and compared with the experimental data for the highest and the lowest stress rates. The value of the parameter n is consistent with that found in double torsion experiments on a sharp crack ($n = 20$). If the material parameters previously obtained are used, it is found that the lower bound given in Eq. (21) coincides with the failure probability computed by using Eq. (12). This result shows that the hypothesis made *a priori* to identify the flaw size distribution as well the parameters of the crack growth law, is satisfied *a posteriori*. In the same figure, the failure probability corresponding to the upper bound is plotted. The experiments almost all lie between the lower bound and the upper bound. Furthermore, the predictions of the highest stress level are quite close to the predictions of the upper bound.

In Fig. 4 the three other stress rates are analyzed. The same material parameters are used. The predictions are in reasonable agreement with the experiments. All these results show that Eq. (12) is capable of modeling a series of experiments performed at very different stress rates. In particular, the expressions of the lower and upper bounds are consistent with the experimental observations. The discrepancy observed for the intermediate stress levels can be explained at least by two reasons. First, the crack growth law parameters are identified at the highest stress

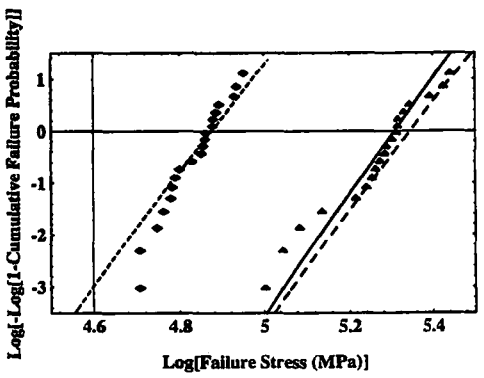

Fig. 3 Evolution of the failure probability, P_F, as a function of failure stress for a spinel Mn Zn ferrite subjected to dynamic fatigue in four-point flexure at two different stress rates (◆ = 0.0975 and ▲ = 9750 MPa/s), in air at room temperature. The solid line represents the identification at the highest stress level, and the dashed lines correspond to the identified upper and lower bounds.

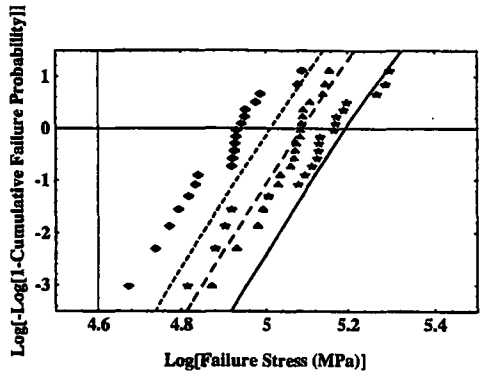

Fig. 4 Evolution of the failure probability, P_F, as a function of failure stress for a spinel Mn Zn ferrite subjected to dynamic fatigue in four-point flexure, in air at room temperature, at a stress rate equal to:

9.75 MPa/s (♦ = experiments, --- = identification),
48.75 MPa/s (▲ = experiments, – – = identification),
487.5 MPa/s (★ = experiments, —— = identification).

rate where the influence of the threshold is weak. Equation (10) overestimates the crack growth rate near the threshold energy release rate $\mathcal{G}_{th}$. The difficulty can be overcome by better accounting for the crack growth law near the threshold. Second, the flaw size distribution may vary from one set of specimens to another. This fact may explain the experimental observations for the first four failure probabilities when the stress rate is equal to 48.75 and 478.5 MPa/s. A post-inspection measuring the actual flaw size distributions could solve this problem.

7 Conclusion

An expression for the failure probability of a structure was derived in the framework of the weakest link theory and the independent events assumption. This expression models a brittle material subjected or not to Subcritical Crack Growth. The failure probability of a structure can be related to the initial flaw distribution through the evaluation of the set of initial critical flaws.

To assess the reliability of structures made of materials exhibiting Subcritical Crack Growth, one needs to devise a crack propagation law modeling the evolution and the possibility of crack kinking. Most of the data are obtained under pure mode I conditions, in which no kinking is involved. Under the assumption that all the flaws leading to the failure of a structure are initial sphere-like flaws, the crack propagation law is assumed to be similar to that in pure mode I condition. The consequence is that the only morphological parameter to consider is flaw size.

When the distribution is only a function of initial flaw size, a function ψ is used to find the initial critical flaw size: it depends upon the crack growth law that is used. Some simple results can be obtained at the level of a Representative Volume Element. Two bounds of the failure probability are obtained. The upper bound corresponds to the case where no Subcritical Crack Growth is involved. The failure conditions are then directly linked with a critical energy release rate. Conversely, the lower bound corresponds to initiation conditions related to a threshold energy release rate. These bounds can also be approximated by two different Weibull laws in which the shape parameters are the same, and the scale parameters are related by the energy release rate ratio.

Experiments on a spinel Mn Zn ferrite were performed at five different stress rates. The identifications of the parameters of the flaw size distribution give relatively good results by considering the highest and the lowest stress rates. The five sets of experiments show that Subcritical Crack Growth was involved at four stress rates. To avoid Subcritical Crack Growth the highest stress rate should have been at least one order of magnitude higher. On the other hand, the lowest stress rate coincides with the results given by the expression for a lower bound of the failure probability. This stress rate enables to get an information on the threshold energy release rate. The intermediate stress rates are relatively well described. These results show that the expression for the failure probability derived in this paper is able to account for Subcritical Crack Growth at low, medium and high stress rates. They also show that the expressions of an upper bound and a lower bound are consistent with experimental observations.

References

Amestoy, M., H. D. Bui, and K. Dang-Van, 1979, "Déviation infinitésimale d'une fissure dans une direction arbitraire," *C. R. Acad. Sci. Paris*, Vol. B t. 289, pp. 99–103.

Aoki, S., and M. Sakata, 1980, "Statistical Approach to Delayed Fracture of Brittle Materials," *Int. J. Fract.*, Vol. 16, pp. 459–469.

Aoki, S., I. Ohta, H. Ohnabe, and M. Sakata, 1983, "Statistical Approach to Time-Dependent Failure of Brittle Materials," *Int. J. Fract.*, Vol. 21, pp. 285–300.

Batdorf, S. B., and J. G. Crose, 1974, "A Statistical Theory for the Fracture of Brittle Structures Subjected to Polyaxial Stress States," ASME *Journal of Applied Mechanics*, Vol. 41, pp. 459–465.

Bilby, B. A., and G. E. Cardew, 1975, "The Crack with a Kinked Tip," *Int. J. Fract.*, Vol. 11, pp. 708–712.

Brinkman, C. R., and S. F. Duffy, 1994, "Life Prediction Methodologies and Data for Ceramic Materials (STP 1201)," ASTM, Philadelphia, PA.

Davidge, R. W., J. R. McLaren, and G. Tappin, 1973, "Strength-Probability-Time (SPT) Relationship in Ceramics," *J. Mat. Sci.*, Vol. 8, pp. 1699–1705.

Evans, A. G., 1972, "A Method for Evaluating the Time-Dependent Failure Characteristics of Brittle Materials—and its Application to Polycrystalline Alumina," *J. Mat. Sci.*, Vol. 7, pp. 1137–1146.

Evans, A. G., and S. M. Wiederhorn, 1974, "Crack Propagation and Failure Prediction in Silicon Nitride at Elavated Temperature," *J. Mat. Sci.*, Vol. 9, pp. 270–278.

Evans, A. G., 1978, "A General Approach for the Statistical Analysis of Multiaxial Fracture," *J. Am. Ceram. Soc.*, Vol. 61, pp. 302–308.

Freudenthal, A. M., 1968, *Statistical Approach to Brittle Fracture*, in Fracture (Liebowitz, H., ed.) Academic Press, Vol. 2 pp. 591–619.

Hild, F., and S. Roux, 1991, "Fatigue Initiation in Heterogeneous Brittle Materials," *Mech. Res. Comm.*, Vol. 18, pp. 409–414.

Hild, F., and D. Marquis, 1992, "A Statistical Approach to the Rupture of Brittle Materials," *Eur. J. Mech., A/Solids*, Vol. 11, pp. 753–765.

Hild, F., and D. Marquis, 1995, "Fiabilité de matériaux avec défauts en propagation stable," *C. R. Acad. Sci. Paris*, Vol. IIb t. 320, pp. 57–62.

Jayatilaka, A. D. S., and K. Trustrum, 1977, "Statistical Approach to Brittle Fracture," *J. Mat. Sci.*, Vol. 12, pp. 1426–1430.

Kadouch, O., 1993, "Rupture différée sous sollicitations mécaniques des ferrites spinelles NiZn et MnZn," PhD dissertation, École Nationale Supéricure des Mines de Paris.

Kingery, W. D., H. K. Bowen, and D. R. Uhlmann, 1976, *Introduction to Ceramics*, Wiley, NY.

Lamon, J., and A. G. Evans, 1983, "Statistical Analysis of Bending Strengths for Brittle Solids: a Multiaxial Fracture Problem," *J. Am. Ceram. Soc.*, Vol. 66, pp. 177–182.

Lamon, J., 1988, "Statistical Approaches to Failure for Ceramic Reliability Assement," *J. Am. Ceram. Soc.*, Vol. 71, pp. 106–112.

Lemaitre, J., 1976, "Extension de la notion de taux d'énergie de fissuration aux problèmes tridimensionnels et non linéaires," *C. R. Acad. Sci. Paris*, Vol. B t. 282, pp. 157–160.

Weibull, W., 1939, "A Statistical Theory of the Strength of Materials," Roy. Swed. Inst. Eng. Res., 151.

Wu, C.-H., 1978, "Fracture under Combined Loads by Maximum-Energy-Release-Rate Criterion," ASME *Journal of Applied Mechanics*, Vol. 45, pp. 553–558.

2.3.3 Rupture par fatigue de fontes GS

i Fontes GS à matrice bainitique

par F. HILD, A.-S. BÉRANGER et R. BILLARDON (1997).
Mech. of Mat., 22, pp. 11-21.

Fatigue failure maps of heterogeneous materials

François Hild[a,1], René Billardon[a] Anne-Sophie Béranger[b]

[a] *Laboratoire de Mécanique et Technologie -E.N.S. de Cachan / C.N.R.S. / Université Paris 6-61, avenue du Président Wilson F-94235 Cachan Cedex, France*

[b] *Renault - Direction de la Recherche - Service 0852-860, quai de Stalingrad, F-92109 Boulogne Billancourt, France*

Received 8 February 1995; revised version received 20 July 1995

Abstract

In this paper, so-called fatigue failure maps are studied as a function of initial flaw size distributions. The main cause of fatigue failure for brittle materials, and of fatigue initiation for ductile materials, is that initial flaws become critical. Fatigue failure maps where the number of cycles to initiation for a given failure probability is plotted for various flaw size distributions are a means of characterizing the influence of the initial flaw distribution on fatigue crack initiation. The results are applied to fatigue failure of austempered spheroidal graphite cast iron.

Keywords: High cycle fatigue; Failure probability; Flaw distribution; Heterogeneous materials; SG cast iron; Fatigue failure map

1. Introduction

The fatigue process in materials can be schematically divided into two stages. Initiation, which is often due to initial flaws, has to be considered for both brittle and ductile materials. Propagation is usually unstable for brittle materials (e.g. engineering ceramics, many metals in the domain of high cycle fatigue), while stable for ductile materials (e.g. many metals in the domain of low cycle fatigue). In this paper we will focus our attention on initiation in heterogeneous solids. The structure is supposed to remain macroscopically elastic whereas the microscopic evolution of the flaws is described according to a generalized Paris' law up to local failure. The macroscopic initiation corresponds to local failure.

In many heterogeneous materials, initial heterogeneities are mostly sphere-like cavities (e.g. intrinsic flaws in ceramics due to processing, flaws due to cooling down in S.G. cast iron), sphere-like brittle inclusions (e.g. spheroidal graphite), or sphere-like brittle inclusions with low interfacial strength (e.g. in ceramics). In all cases, micro crack initiation appears in planes perpendicular to the maximum principal stress. Furthermore, even though the initial nature of the flaws may be different, as soon as micro initiation occurs, most flaws behave like cracks of surface $\mathcal{A}$ with a normal aligned with the maximum principal stress direction (Clément, 1984). Consequently, in this paper only one flaw population is considered. During micro crack propagation, it is assumed that the surface increases with no morphological change, therefore the radius a of the surface is the only parameter to be accounted for, and the micro crack propagation law will be written in terms of this parameter. Initial heterogeneities are usually randomly distributed within heterogeneous materials, and are modeled by a flaw size distribution f, which is a

[1] Fax: (+33) 1-47-40-22-40; Email: hild@lmt.ens-cachan.fr

function of the size a. This function needs to be determined in order to assess the reliability of heterogeneous materials as shown in Section 2.

The flaws are supposed to be described by cracks whose geometry is taken into account by a dimensionless factor Y such that the energy release rate $\mathcal{G}$ is given by

$$\mathcal{G} = \frac{Y^2\sigma^2 a}{E}, \tag{1}$$

where σ stands for an equivalent uniaxial stress (for instance the maximum principal stress), and E the Young's modulus of the virgin material. It is worth noting that the values of the parameter Y depend upon the geometry of the initial defect and whether this flaw intersects a free surface. For instance, the distance of the flaws to the surface of the structure may be taken into account through the dimensionless parameter Y. Under monotonic and cyclic loading conditions, micro failure can be described by a criterion referring to a critical value of the energy release rate $\mathcal{G}_c$

$$\mathcal{G} \geq \mathcal{G}_c. \tag{2}$$

In order to take into account the localized non-linear behavior of the material in the vicinity of the crack tip under cyclic loading conditions, Elber (1970, 1971) has shown that crack propagation depends upon a so-called effective energy release rate density $\Delta\mathcal{G}_{\text{eff}} = \mathcal{G}_{\max} - \mathcal{G}_{\text{op}}$, where $\mathcal{G}_{\max}$ is the maximum energy release rate over one cycle and $\mathcal{G}_{\text{op}}$ the value of the energy release rate when crack opening occurs. Consequently, it is natural to define a crack initiation criterion as

$$\Delta\mathcal{G}_{\text{eff}} \geq 0. \tag{3}$$

In the following, micro crack initiation is described by a similar criterion postulated by Pellas et al. (1977)

$$\Delta\mathcal{G}_{\text{eff}} = [g(R)]^2\mathcal{G}_{\max} - \mathcal{G}_{\text{th}} \geq 0, \tag{4}$$

where $\mathcal{G}_{\text{th}}$ refers to a so-called threshold energy release rate and $g(R)$ an experimentally identified function of the load ratio R defined as

$$R = \frac{\min_{\text{cycle}}\sigma(t)}{\max_{\text{cycle}}\sigma(t)} = \frac{\sigma_{\min}}{\sigma_{\max}} = \sqrt{\frac{\mathcal{G}_{\min}}{\mathcal{G}_{\max}}}. \tag{5}$$

It is supposed that the load history is simple, i.e. the maximum principal stress direction is constant throughout the load history, and therefore bifurcation is not considered. The micro crack propagation law is assumed to be written as

$$\frac{da}{dN} = G(\Delta\mathcal{G}_{\text{eff}}) \quad \text{when } \Delta\mathcal{G}_{\text{eff}} \geq 0 \text{ and } \mathcal{G} \leq \mathcal{G}_c, \tag{6}$$

where G is a function of the effective energy release rate $\Delta\mathcal{G}_{\text{eff}}$. This function G is known and obtained for macro cracks by performing, for instance, experiments on CT specimens. However, the micro crack propagation law is, a priori, not known, since the average flaw size is, at least, one order of magnitude smaller than the macro crack used in CT specimens. The function G, in addition to the flaw size distribution f, is needed to fully assess the reliability of heterogeneous materials. The identification procedure is addressed in Section 3. The particular micro crack propagation law, as well as flaw size distribution are considered in Section 4 and used in Section 5 to analyze experimental data obtained on an austempered spheroidal graphite cast iron subjected to cyclic loading conditions.

The next step is to study the sensitivity of the failure probability to the flaw size distribution. This constitutes the main aim of this paper and is achieved by deriving so-called *fatigue failure maps* in Section 6. These fatigue failure maps give the number of cycles to initiation, for a given cumulative failure probability and for various flaw size distributions in the material. The approach presented herein may be applied to either brittle materials such as engineering ceramics, or ductile materials such as austempered spheroidal graphite cast iron.

2. Reliability of structures containing flaws

Statistical methods applied to predicting failure under monotonic conditions have been extensively used. The first attempt was made by Weibull (1939) and was based upon a statistical treatment of failure. Monotonic and cyclic loading conditions were analyzed. Batdorf and Crose (1974) modeled initial flaws by cracks whose size and orientation are randomly distributed. Evans and Lamon (1978, 1983, 1988) derived another model based upon similar assumptions. The drawback of these two last approaches is that they are not easily extendable to cases where stable crack

growth is possible (i.e. cyclic conditions). Attempts to model stable crack growth have been made by Sobczyk (1986) using stochastic crack growth equations. Statistical methods are also presently developed for Continuum Damage Mechanics (Krajcinovic, 1989).

In the framework of linear elastic fracture mechanics, Jayatilaka and Trustrum (1977) showed that under some simplifying assumptions the Weibull parameters can be related to the flaw distribution. These results have been extended in the framework of linear elastic fracture mechanics and continuum damage mechanics (Hild and Marquis, 1992). An expression for the cumulative failure probability was obtained in which the flaw distribution was directly considered. Under cyclic conditions, the initial flaw distribution evolves with the number of cycles; however, as shown in Hild and Roux (1991) and recalled in the following, the previous approach can still be used since it deals directly with the flaw distribution.

In the following, for the sake of simplicity, we shall consider only cases for which the load level is constant. Yet generalization to more complex load histories can easily be done by integration of Eq. (6). The cumulative initiation probability, P_{I0}, of a representative volume element (RVE) of volume V_0, is the probability of finding an initial flaw, whose size is larger than the critical flaw size a_c (determined from Eqs. (1) and (2)). In the case of monotonic loading conditions, the expression for P_{I0} is given by

$$P_{I0} = \int_{a_c}^{+\infty} f_0(a)\,\mathrm{d}a\,, \tag{7}$$

where f_0 stands for the initial flaw size distribution. In the case of cyclic loading conditions, the stable micro crack propagation leads to the evolution of the flaw size distribution. After N cycles, it is assumed that the flaw distribution is described by a function f_N. The expression for P_{I0} is then given by

$$P_{I0} = \int_{a_c}^{+\infty} f_N(a)\,\mathrm{d}a\,. \tag{8}$$

At this stage, it is useful to introduce a function ψ that relates the initial flaw size a_0 to the flaw size after N cycles a_N

$$a_0 = \psi(a_N)\,. \tag{9}$$

The function ψ is determined by integrating Eq. (6). Since the flaw size evolution is assumed to be deterministic, and if the only flaws to cause failure are those initially present within the material, the probability of finding a flaw of size a_N after N cycles is equal to the probability of finding an initial flaw of size $\psi(a_N)$. Thus, the function f_N can be related to the function f_0 by (Hild and Roux, 1991)

$$f_N(a) = f_0(\psi(a))\frac{\partial\psi}{\partial a}\,, \tag{10}$$

where the coefficient $(\partial\psi/\partial a)$ comes from the change of measure from $\mathrm{d}a$ to $\mathrm{d}\psi(a)$. Therefore P_{I0} can be rewritten as

$$P_{I0} = \int_{\psi(a_c)}^{+\infty} f_0(a)\,\mathrm{d}a\,, \tag{11}$$

where $\psi(a_c)$ denotes the initial flaw size that, after N cycles of loading with a maximum equivalent stress over one cycle σ_{max}, reaches the critical flaw size a_c. Eq. (11) constitutes a unified expression of the cumulative initiation probability in the case of monotonic and cyclic loading conditions. It relates the expression of the cumulative initiation probability to the initial flaw size distribution f_0.

If the interaction between defects is negligible, an independent events assumption can be made. The expression of the cumulative initiation probability, P_I of a structure Ω of volume V can be derived in the framework of the weakest link theory. In the case of monotonic and cyclic loading conditions, the expression of P_I can be related to the cumulative initiation probability, P_{I0}, of a link by (Freudenthal, 1968)

$$P_I = 1 - \exp\left\{\frac{1}{V_0}\int_{\Omega}\ln(1 - P_{I0})\,\mathrm{d}V\right\}\,. \tag{12}$$

By means of Eqs. (11) and (12), a general relationship between the initial flaw distribution and the cumulative initiation probability of a structure Ω can be derived

$$P_I = 1 - \exp\left\{\frac{1}{V_0}\int_{\Omega}\ln\left(1 - \int_{\psi(a_c)}^{+\infty} f_0(a)\,\mathrm{d}a\right)\mathrm{d}V\right\}\,. \tag{13}$$

For monotonic loading conditions, the same equation holds with a_c in place of $\psi(a_c)$. In the case of unstable macro propagation, the structural failure corresponds to the initiation and the expression of the cumulative failure probability P_F is given by

$$P_F = P_I \tag{14}$$

It is worth noting that in the case of high cycle fatigue, the propagation stage tends to become negligible when compared, in terms of number of cycles, with the initiation stage. In such circumstances, Eq. (14) can be applied to both brittle and ductile materials. In other words, since the propagation stage is neglected when Eq. (14) is used, this equation corresponds to a lower bound to the cumulative failure probability of the structure. Hence, in the following, "failure" refers to local failure, i.e. macroscopic initiation or lower bound to macroscopic failure.

Besides, Eqs. (13) and (14) show that the cumulative failure probability is a function of the applied load level, the volume of the structure, the stress field pattern as well as the number of cycles.

3. Identification from S–N curves

Standard macroscopic S–N curves can be interpreted as iso-failure probability plots. In particular, fatigue limits are defined for different values of the failure probability. In the following, an identification procedure is developed to determine the flaw size distribution f as well as micro crack propagation law modeled by the function G defined in Eq. (6).

When the fatigue limits are known, the identification can be performed in two different steps (Hild and Marquis, 1995). The first step consists in identifying the flaw size distribution f. A minimization scheme is used to determine the minimum error between all the available experimental data on fatigue limits. Such an error can be defined as

$$\mathrm{Err} = \frac{1}{N_e} \sum_{i=1}^{N_e} (P_{Fi} - P_{F\infty})^2 , \tag{15}$$

where N_e denotes the number of experimental data, P_{Fi} is the experimental cumulative failure probability and $P_{F\infty}$ is the predicted cumulative failure probability for an infinite number of cycles to failure. When the number of cycles to failure tends to infinity (i.e. the fatigue limit is reached), the cumulative failure probability can be rewritten as

$$P_{F\infty} = 1 - \exp\left\{ \frac{1}{V_0} \int_{\Omega} \ln\left(1 - \int_{a_{th}(\sigma_F, M)}^{+\infty} f_0(a)\, da \right) dV \right\} , \tag{16}$$

with

$$a_{th}(\sigma_F, M) = \frac{E\mathcal{G}_{th}}{Y^2 \sigma^2_{max}(\sigma_F, M) \left[g(R)\right]^2} , \tag{17}$$

derived from Eqs. (1) and (4), where $\sigma_{max}(\sigma_F, M)$ is the maximum applied equivalent stress level at a point M of Ω when the maximum equivalent stress level in the structure Ω is denoted by σ_F.

The second step of the identification concerns the parameters of the micro crack propagation law G. When the S–N curves used for the identification have been obtained in tension, this identification is straightforward: it consists of the analysis of a single iso-cumulative failure probability (e.g. 50%) since an iso-cumulative failure probability is described by a constant cumulative failure probability $P_{F0} = P_{I0}$, therefore $\psi(a_c)$ = const. (see Eq. (11)). When S–N curves used for the identification have been obtained for more complex stress fields (e.g. rotating flexure), an iso-cumulative failure probability is no longer associated to a constant cumulative failure probability P_{F0}. However, the identification is still possible by considering an iso-cumulative failure probability (e.g. 50%) defined for the testing specimen considered as a structure.

4. Particularization

In this section, the previous results are particularized to one type of micro crack propagation law as well as to one given flaw size distribution. It is assumed that the flaw size is bounded by a maximum value a_M. Two threshold stresses can be defined. A monotonic threshold stress (this quantity is only relevant in the case of monotonic brittle failure), S_u, may be defined as the lowest value of the stress level below which the monotonic failure probability has a zero value. From

Eqs. (1) and (2), the following expression for S_u can be derived

$$S_u = \frac{1}{Y}\sqrt{\frac{E\mathcal{G}_c}{a_M}}. \tag{18}$$

In other words, S_u denotes the minimum value of the applied local stress for which local failure is certain when a flaw of maximum size a_M is present in an RVE under monotonic loading condition.

In the case of cyclic loading, a cyclic threshold stress may be defined as the lowest value of the stress level below which the cyclic failure probability has a zero value. It is worth noting that this cyclic threshold stress depends upon the load ratio R (see Eq. (4)). For identification purposes, the cyclic threshold stress, S_{th}, is defined for $g(R) = 1$, and is related to the threshold energy release rate $\mathcal{G}_{th}$. Its expression can be derived from Eqs. (1) and (4)

$$S_{th} = \frac{1}{Y}\sqrt{\frac{E\mathcal{G}_{th}}{a_M}}. \tag{19}$$

In other words, S_{th} denotes the minimum value of the applied local stress for which local failure is certain when a flaw of maximum size a_M is present in an RVE under cyclic loading condition. It is worth noting that, combining Eqs. (18) and (19), there exists a simple linear relationship between the two threshold stresses

$$S_{th} = S_u k, \tag{20}$$

with

$$k = \sqrt{\frac{\mathcal{G}_{th}}{\mathcal{G}_c}}. \tag{21}$$

The results derived so far will be used to study the high cycle fatigue behavior of an austempered S.G. cast iron. It is assumed that the micro crack propagation law is a modified version of an Elber law (1970, 1971), and keeps the main features of the macro crack propagation law based upon a generalized Paris' law proposed by Pellas et al. (1977)

$$\frac{da}{dN} = C\left(\frac{\sqrt{\mathcal{G}_{max}}g(R) - \sqrt{\mathcal{G}_{th}}}{\sqrt{\mathcal{G}_c} - \sqrt{\frac{\mathcal{G}_{th}}{g(R)}}}\right)^n, \tag{22}$$

where N denotes the number of cycles, C and n are material parameters. The advantage of Eq. (22) is that it may be integrated explicitly (Hild and Roux, 1991). An expression for the function g has been proposed by Pellas et al. (1977)

$$g(R) = \frac{1-R}{1-mR} \quad \text{if}$$

$$R \le R_c = \frac{\sqrt{\mathcal{G}_{max}} - \sqrt{\mathcal{G}_{th}}}{\sqrt{\mathcal{G}_{max}} - m\sqrt{\mathcal{G}_{th}}}, \tag{23}$$

where m is a material parameter. The values of m are usually on the order of 0.5. The limit value R_c of the load ratio R corresponds to the initiation condition of Eq. (4),

$$\sqrt{\mathcal{G}_{max}}g(R_c) - \sqrt{\mathcal{G}_{th}} = 0, \tag{24}$$

so that

$$\frac{da}{dN} = 0 \quad \text{if } R \ge R_c \text{ and if } \mathcal{G}_{max} < \mathcal{G}_c. \tag{25}$$

For high values of the load ratio R such that $g(R) > k$, unstable propagation is deemed to occur. In practice, that means that when the maximum and minimum stresses over a cycle are of the same order, the initiation conditions correspond to the monotonic failure condition. On the other hand, when the load ratio R is negative, $g(R)$ remains close to unity. The approximation $g(R) \approx 1$ is usually sufficient to model the effects of negative load ratios.

By integration of Eq. (22) and recalling Eq. (1), the following closed form solution can be derived (Hild and Roux, 1991)

$$\varphi\left(\sqrt{\frac{a_N}{a_M}}\right) - \varphi\left(\sqrt{\frac{a_0}{a_M}}\right) = C^*\left(\frac{g(R)}{1 - \frac{\sqrt{\mathcal{G}_{th}}}{\sqrt{\mathcal{G}_c}g(R)}}\right)^n \left(\frac{\sigma}{S_u}\right)^n N, \tag{26}$$

where a_M denotes the maximum flaw size in the structure, a_0 the initial flaw size, and a_N the flaw size after N cycles. The dimensionless constant C^* is equal to C/a_M. When a_N is equal to the critical flaw size a_c determined from the failure criterion defined in Eq. (2), the initial flaw size is then equal to the initial critical flaw size $\psi(a_c)$ and Eq. (26) allows to relate $\psi(a_c)$ to a_c by

$$\varphi\left(\sqrt{\frac{a_c}{a_M}}\right) - \varphi\left(\sqrt{\frac{\psi(a_c)}{a_M}}\right) = C^* \left(\frac{g(R)}{1 - \frac{\sqrt{\mathcal{G}_{th}}}{\sqrt{\mathcal{G}_c} g(R)}}\right)^n \left(\frac{\sigma}{S_u}\right)^n N_F , \quad (27)$$

where N_F denotes the number of cycles to failure. The value of the function φ depends upon the power n. When $n \neq 1$ and $n \neq 2$, the function φ is given by

$$\varphi(x) = \varphi\left(\sqrt{\frac{a}{a_M}}\right) = 2\frac{(x - x_{th})^{1-n}(x_{th} - (n-1)x)}{(n-1)(n-2)}, \quad (28)$$

where x_{th} is the normalized threshold defect size obtained by using Eqs. (17) and (19)

$$x_{th} = \sqrt{\frac{a_{th}}{a_M}} = \frac{S_{th}}{\sigma g(R)} \quad (29)$$

At an RVE level, an iso-probability is defined as a curve σ–N such that the cumulative failure probability $P_{F0} = P_{I0}$ is constant. If the load history is proportional, it can be shown from Eq. (11) that this condition can be rewritten as

$$\frac{\psi(a_c)}{a_M} = B , \quad (30)$$

where the constant B depends upon the details of the flaw distribution and the value of the considered cumulative failure probability. By using Eqs. (27), (30) the normalized number of cycles to failure N^* is given by

$$N^* = +\infty \quad \text{if } \sigma\, g(R)\sqrt{B} < S_{th} \quad (31.1)$$

$$N^* = \left(\frac{1 - \frac{k}{g(R)}}{g(R)}\right)^n \left(\frac{\sigma}{S_u}\right)^{-n} \times \left\{\varphi(S_u/\sigma) - \varphi(\sqrt{B})\right\} \quad \text{if } \frac{S_{th}}{g(R)} \leq \sigma\sqrt{B} \leq S_u \quad (31.2)$$

$$N^* = 0 \quad \text{if } \sigma\sqrt{B} > S_u , \quad (31.3)$$

where the normalized number of cycles to failure is defined as

$$N^* = C^* N_F . \quad (31.4)$$

Eq. (31.1) corresponds to a case where no failure at all is possible. The limiting case is when $\sigma g(R)\sqrt{B} = S_{th}$, in other words, the "fatigue limit" is reached. The expression of the cumulative failure probability then only depends upon the initial flaw distribution and the value of the cyclic threshold stress S_{th}. This case allows an identification of the flaw size distribution independently of the crack growth law (as presented in Section 3). Eq. (31.2) corresponds to a case where fatigue failure occurs. For a given value of B (i.e. a given failure probability), the evolution of the number of cycles to failure mainly depends on the crack growth law. Therefore, the analysis of a constant failure probability allows to identify the parameters of the crack growth law, provided the flaw size distribution is known (i.e. the different values of the constant B have been identified). When this approach is still applicable to smaller number of cycles to failure, Eq. (31.3) corresponds to a case where monotonic failure occurs. The limiting case is when $\sigma\sqrt{B} = S_u$. The expression of the cumulative failure probability again only depends upon the initial flaw distribution, and the value of the monotonic threshold stress S_u.

Lastly, it is assumed that the flaw size distribution f_0 can be particularized as a beta distribution

$$f_0(a) = \frac{a_M^{-1-\alpha-\beta}}{B_{\alpha\beta}} a^\alpha (a_M - a)^\beta, \quad 0 < a < a_M, \quad \alpha, \beta > -1 , \quad (32)$$

where α and β are the parameters of the beta function, and $B_{\alpha\beta}$ is equal to $B(\alpha+1, \beta+1)$, where $B(.,.)$ is the Euler function of the first kind (Spanier and Oldham, 1987). In Fig. 1, the normalized beta density and cumulative beta density are plotted with $\alpha = 1.8$, $\beta = 17.5$ and are compared with the case when $\alpha = 1$, $\beta = 5$. Fig. 2 shows a Wöhler diagram when $\alpha = 1$, $\beta = 5$, $R = 0$, $n = 4$, and $k = 1/3$. It is recalled that $N^* = C^* N_F$ is the normalized number of cycles to failure. It is worth noting that when the ratio $\sigma/S_u < 1$, no failure occurs under monotonic condition while failure due to cyclic loading occurs when $\sigma/S_{th} \geq 1$, $\sigma/S_u \geq k = 1/3$. When $\sigma/S_{th} < 1$, no failure at all is possible. These results are consistent with the two

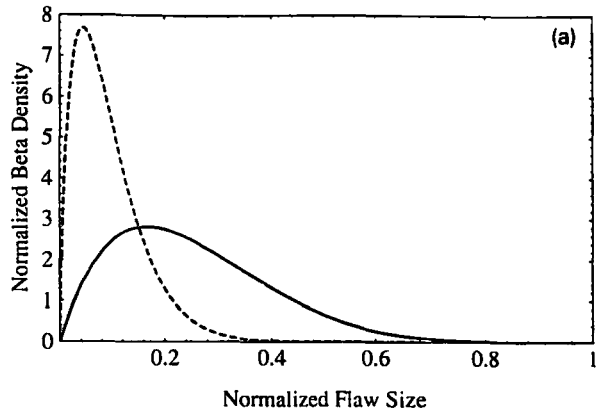

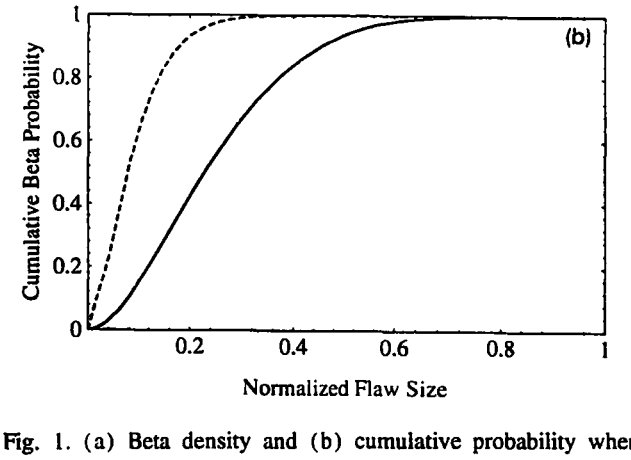

Fig. 1. (a) Beta density and (b) cumulative probability when $\alpha = 1$ and $\beta = 5$ (solid line), and $\alpha = 1.75$ and $\beta = 17.5$ (dashed line).

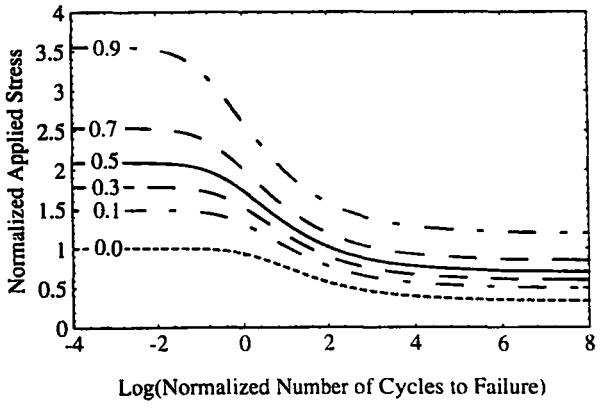

Fig. 2. Wöhler diagram when $\alpha = 1$, $\beta = 5$, $R = 0$, $n = 4$, and $k = 1/3$. Evolution of the normalized applied stress, σ/S_u, as a function of the normalized number of cycles, N^*, for different cumulative failure probabilities, P_{F0}.

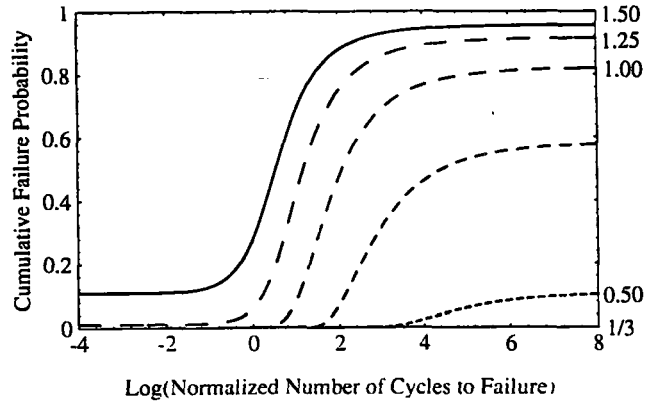

Fig. 3. Evolution of the cumulative failure probability, P_{F0}, as a function of the normalized number of cycles, N^*, for different values of the stress level, σ/S_u, when $\alpha = 1$, $\beta = 5$, $R = 0$, $n = 4$, and $k = 1/3$. Evolution of the cumulative failure probability, P_{F0}, as a function of the normalized number of cycles, N^*, for different values of the stress level, σ/S_u, when $\alpha = 1$, $\beta = 5$, $R = 0$, $n = 4$, and $k = 1/3$.

threshold stresses S_u and $S_{th} = kS_u$ defined in Eqs. (18) and (19).

By using Eq. (31.2), the equation of the median Wöhler curve ($P_{F0} = 50\%$), if $S_{th}/g(R) \leq \sigma\sqrt{B_{50}} \leq S_u$, is given by

$$N_{50}^* = \left(\frac{1 - \dfrac{\sqrt{\mathcal{G}_{th}}}{\sqrt{\mathcal{G}_c} g(R)}}{g(R)} \right)^n \left(\frac{\sigma}{S_u} \right)^{-n} \times \left\{ \varphi(S_u/\sigma) - \varphi(\sqrt{B_{50}}) \right\} , \tag{33}$$

where B_{50} denotes the value of B for which $P_{F0} = 50\%$. This equation can also be written in a format close to that suggested by Wöhler

$$\log(N_{50}^*) = \zeta\left(\frac{\sigma}{S_u}; R; n\right) - n\frac{\sigma}{S_u} , \tag{34}$$

where ζ is a function of the normalized stress level σ/S_u, the load ratio R, and n, the power of the crack growth law. The fatigue limit, S_{50}, defined as the smallest value of the stress level such that $P_{F0} = 50\%$

$$S_{50} = \frac{S_{th}}{g(R)\sqrt{B_{50}}} \tag{35}$$

In Fig. 3, the cumulative failure probability is plotted as a function of the normalized number of cycles to failure, N^*, for different stress levels when $R = 0$.

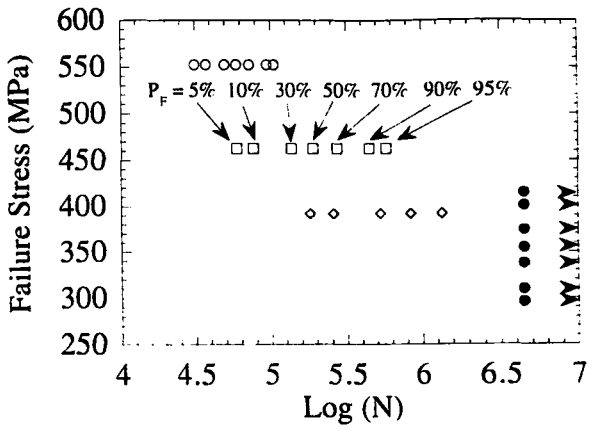

Fig. 4. Experimental data of austempered nodular graphite cast iron subjected to rotating flexure.

All these results show that the scatter observed in fatigue can be described by the introduction of a statistical flaw size distribution.

5. Analysis of fatigue tests on austempered S.G. cast iron

In this section, a series of experiments reported in Jokipii (1992) are analyzed in detail. These experiments have been carried out at different stress levels on Kymenite, which is an austempered S.G. cast iron, grade K-10005. The ratio between the threshold energy release rate and the critical energy release rate is of the order of 1/9 (i.e. $k = 1/3$). The specimens were subjected to rotating flexure with a test area diameter equal to 7.5 mm. Fig. 4 shows the experimental data obtained in rotating flexure. It is worth noting that there is information on both limited (open symbols) and unlimited (solid symbols) number of cycles to failure at different stress levels and for different cumulative failure probabilities.

In this case a two-step identification procedure can be carried out. The following values are identified by analyzing the fatigue limits: $\alpha = 1.8$, $\beta = 17.5$, $V/V_0 = 112$, $S_u = 520$ MPa. The result of the identification is shown in Fig. 5 in terms of cumulative failure probability versus fatigue limit. In flexure, because of the stress heterogeneity in the specimen, Eq. (30) is not equivalent to an iso-cumulative failure probability on a structural level. One single iso-cumulative failure probability is still sufficient to identify the two material parameters. The iso-cumulative failure probability

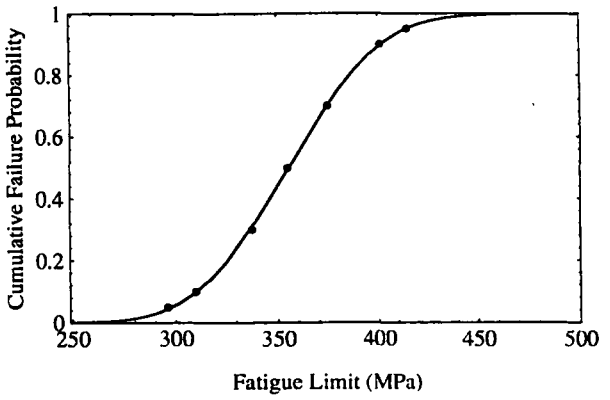

Fig. 5. Experiments and predictions of the fatigue limits for different cumulative failure probabilities ($\alpha = 1.75$, $\beta = 17.5$, $V/V_0 = 112$, $S_u = 520$ MPa, $k = 1/3$).

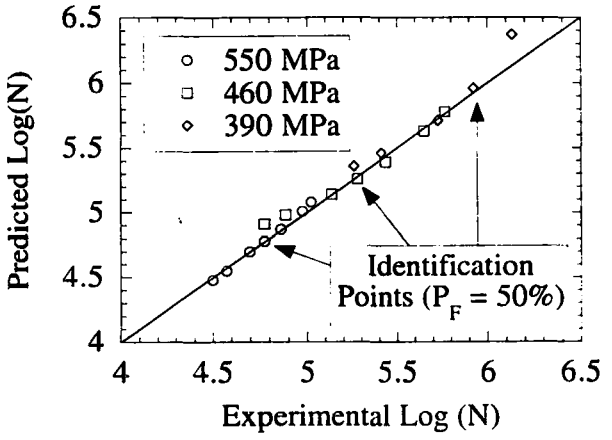

Fig. 6. Comparisons between experimental and predicted values of the number of cycles to failure when $k = 1/3$ ($n = 2.34$, and $C/a_M(1-k)^n = 1.3 \times 10^{-4}$). The identification points were taken for a cumulative failure probability equal to 50%.

of 50% is used to minimize an error similar to that defined in Eq. (15). The following values were obtained: $n = 2.34$, and $C/a_M(1-k)^n = 1.3 \times 10^{-4}$. In Fig. 6 the predictions of the number of cycles to failure are compared with the experimental observations. Three points were used for the identification and the remaining points are predictions. Out of 19 experimental data, 15 points exhibit a difference between experimental and predicted value of less than 15%, and the maximum difference is 75%. In Fig. 7 the cumulative failure probability is plotted as a function of the number of cycles to failure for the three different stress levels. It is worth noting that all the predictions are in good agreement with the experimental data.

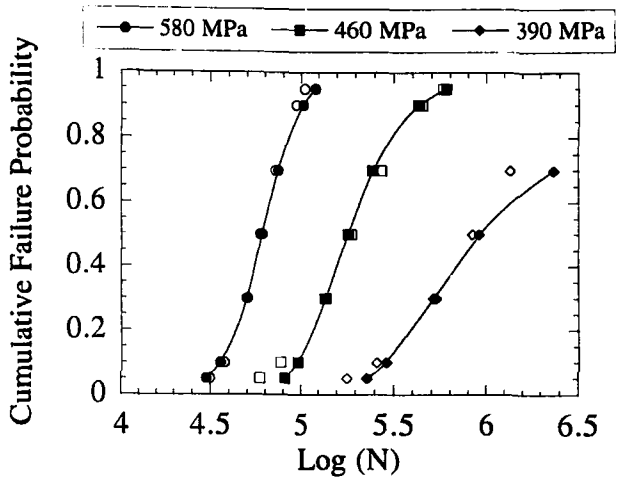

Fig. 7. Comparisons between experimental and predicted values of the cumulative failure probability for three different stress levels (550, 460, and 390 MPa), open symbols are experiments and solid symbols are the predictions.

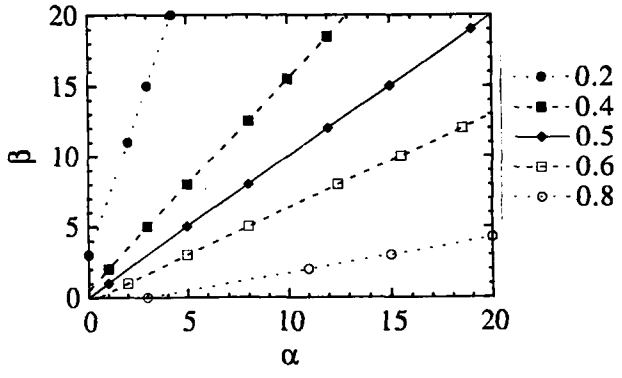

Fig. 8. Evolution of the average flaw size, $\bar{a}/a_M$, as a function of the parameters α and β.

6. Fatigue failure maps

The next question to address is the influence of the flaw size distribution upon failure properties. So-called fatigue failure maps are drawn for this purpose. By varying the values of α and β of the beta distribution given in Eq. (32), it is possible to vary the values of the average flaw size and the corresponding standard deviation. Fig. 8 shows the type of dependence of the average flaw size upon the values of the parameters α and β. For a beta density (Spanier and Oldham, 1987), the average flaw size, $\bar{a}$ is given by

$$\frac{\bar{a}}{a_M} = \frac{\alpha+1}{\alpha+\beta+2} \tag{36}$$

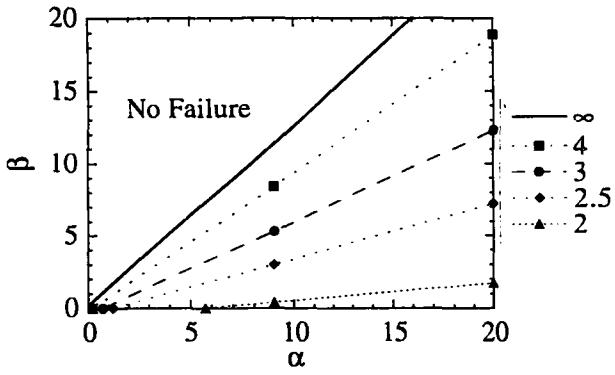

Fig. 9. Fatigue failure maps giving the logarithm of the normalized number of cycles to failure as a function of the parameters α and β, for a given cumulative failure probability $P_{F0} = 50\%$, and a given load level $\sigma/S_u = 0.5$, $R = 0$, $n = 4$, and $k = 1/3$.

and the corresponding standard deviation $\bar{\bar{a}}$

$$\frac{\bar{\bar{a}}}{a_M} = \sqrt{\frac{(\alpha+1)(\beta+1)}{(\alpha+\beta+2)^2(\alpha+\beta+3)}}. \tag{37}$$

Fatigue failure maps correspond to various contours of number of cycles to failure for a fixed stress level and are drawn for a given value of the cumulative failure probability $P_{F0} = P_{I0}$. Therefore they directly illustrate the relationship between the flaw size distribution in the material and the reliability of heterogeneous materials under cyclic loading conditions.

The first stage is to determine the values of the constants B for different values of α and β to plot such a map for a given value of P_{F0}, for instance, 50%. In the following, we shall consider cases for which $0 \leq \alpha, \beta \leq 20$, and all these results are given for $R = 0$, and are easily generalized to other cases. To obtain the number of cycles to failure when $P_{F0} = 50\%$, we use Eqs. (31.1), (31.2) and (31.3). One of these maps is drawn in Fig. 9 for a load level characterized by the ratio $\sigma/S_u = 0.5$. The boundary of the no-failure zone corresponds to $\sigma\sqrt{B_{50}} = S_{th}$ (since $g(R) = 1$). When the failure probability equals 50%, this boundary can be described by a straight line. Because initiation and final failure are assumed to be described by the same kind of criterion referring to the energy release rate $\mathcal{G}$, the boundaries can be drawn on one single map. These boundaries can be drawn for different stress levels, as shown in Fig. 10. Such a map can be used as follows. Below a given normalized stress level contour, σ/S_u, monotonic failure occurs when $P_{F0} = 50\%$ and Eq.

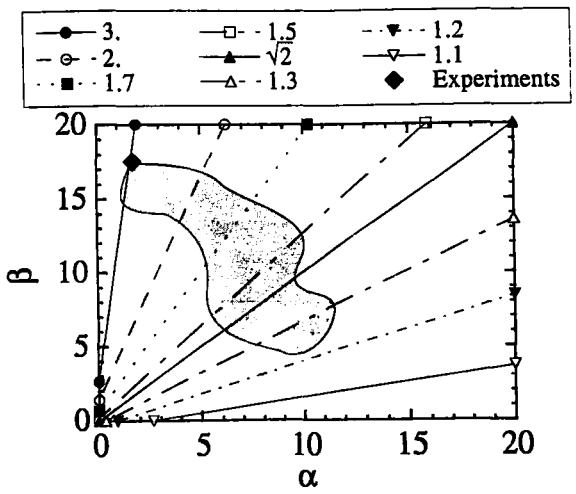

Fig. 10. Fatigue gfailure map giving the boundary of the monotonic failure and no-failure zones as a function of the parameters α and β when P_{F0} =50% for different normalized stress levels σ/S_u or $\sigma g(R)/S_{th}$.

(31.3) is satisfied. Above a given normalized stress level contour $\sigma g(R)/S_{th}$, no failure takes place when P_{F0} = 50% and Eq. (31.1) is satisfied.

When comparing Figs. 8, 9, and 10 it can be noticed that the iso-number of cycles to failure has the same shape as the average defect size curves; this can be explained by the fact that the iso-probability P_{F0} = 50% is approximately given by a constant value of $(\alpha+1)/(\alpha+\beta+2)$, i.e. $\bar{a}/a_M$ = const. (Eq. (36)). This also means that for this particular iso-probability the number of cycles to failure is weakly influenced by the standard deviation $\tilde{a}$.

Another feature of Eq. (12) is that the considered stress field is the macroscopic stress field since the interactions between defects are neglected. This approach can therefore be used as a post-processor to any classical structural analysis (performed on the structure without flaws). Phenomena such as volume effects and stress heterogeneity effects which have been modeled by Eq. (12) in the case of monotonic failure (Freudenthal, 1968; Hild et al., 1992), may also be modeled by this approach and applied to fatigue failure.

7. Conclusions

A reliability analysis taking account of flaw size distributions has been developed for solids subjected to cyclic loading conditions. Emphasis is put on the initiation stage, which is directly related to the evolution of initial flaws. A unified expression of the cumulative failure probability is derived for cyclic and monotonic failure within the framework of the weakest link theory and by assuming that flaws do not interact.

A two-step procedure is developed to identify the flaw distribution as well as the parameters of the micro crack propagation law. It is shown that the identification of the parameters related to flaw size distribution and crack growth law can be decoupled. In particular, the value of the parameters of the flaw size distribution can be determined from the fatigue limits at different failure probabilities. The identification of the parameters of the crack growth law can be obtained by the analysis of one single iso-cumulative failure probability (say 50%).

General features observed in the case of high cycle fatigue are modeled. For instance, a Wöhler diagram is drawn for different failure probabilities. Experiments on austempered S.G. cast iron are analyzed within the previous framework. The identification strategy is applied to experimental data in rotating flexure. The predictions of the whole set of data are in good agreement with the experimental number of cycles to failure. This last result shows that the expression of cumulative failure probability proposed herein is able to model fatigue data obtained on austempered S.G. cast iron.

To model the effect of initial flaw distributions on the fatigue behavior of heterogeneous materials, fatigue failure maps are introduced. They consist in plotting contours of constant number of cycles to failure in a space representative of the initial flaw distributions. Such maps are drawn at a given load level and for a given cumulative failure probability. When the initial flaw distribution is modeled by a beta distribution of exponents α and β, the maps are drawn in an α–β plane. The fatigue failure maps allow the extrapolation of the results obtained for a given flaw size distribution to other flaw size distributions.

Typical application of this approach concerns the reliability analysis of casted components. More and more tools are available to predict the different flaw size distributions from one point of a part of a cast to another, whereas the fatigue behavior of the material is in general merely derived from experiments performed on so-called flawless specimens. A fatigue failure map representative of the sensitivity of the material to flaws will enable a prediction of the reliability of the whole

component under cyclic loading conditions; in other words, it will enable the prediction of the number of cycles to macro crack initiation, or the probability of reaching a certain number of cycles without failure at every point of the component.

Acknowledgements

The authors gratefully acknowledge the financial support of Renault through contract CNRS/109 (H5-24-12) with the Laboratoire de Mécanique et Technologie, Cachan.

References

Batdorf, S. B. and J. G. Crose (1974), A statistical theory for the fracture of brittle structures subjected to polyaxial stress states, *J. Appl. Mech. 41*, 459-465.

Clément, P. (1984), Propagation par fatigue de petits défauts dans une fonte G.S., mémoire CNAM Paris.

Elber, W. (1970), Fatigue crack closure under cyclic tension, *Eng. Fract. Mech. 2*, 37-45.

Elber, W. (1971), *The Significance of Fatigue Crack Closure*, American Society for Testing and Materials, STP 486, Philadelphia, pp. 230-242.

Evans, A. G. (1978), A General approach for the statistical analysis of multiaxial fracture, *J. Am. Ceram. Soc. 61(7-8)*, 302-308.

Freudenthal, A. M. (1968), *Statistical Approach to Brittle Fracture*, Academic Press, pp. 591-619.

Hild, F. and S. Roux (1991), Fatigue initiation in heterogeneous brittle materials, *Mech. Res. Comm. 18 (6)*, 409-414.

Hild, F., R. Billardon and D. Marquis (1992), Hétérogénéité des contraintes et rupture des matériaux fragiles, *C.R. Acad. Sci. Paris, t. 315 (Série II)*, 1293-1298.

Hild, F. and D. Marquis (1992), A statistical approach to the rupture of brittle materials, *Eur. J. Mech. A 11(6)*, 753-765.

Hild, F. and D. Marquis (1995), Fiabilité de matériaux avec défauts en propagation stable, *C.R. Acad. Sci. Paris, t. 320 (Série IIb)*, 57-62.

Jayatilaka, A. D. S. and K. Trustrum (1977), Statistical approach to brittle fracture, *J. Mater. Sci. 12*, 1426-1430.

Jokipii, K., (1992), Kymenite, austempered ductile iron as material for various applications, in: *Eur. Meeting on Castings in Austempered Spheroidal Graphite Cast Iron*, Centre Technique des Industrie de la Fonderie, Sèvres (France).

Krajcinovic, D. (1989), Damage Mechanics, Mech. Mat., 8, 117-197.

Lamon, J. and A. G. Evans (1983), Statistical analysis of bending strengths for brittle solids: a multiaxial fracture problem, *J. Am. Ceram. Soc. 66*, 177-182.

Lamon, J. (1988), Statistical approaches to failure for ceramic reliability assessment, *J. Am. Ceram. Soc. 71(2)*, 106-112.

Pellas, J., G. Baudin and M. Robert (1977), Mesure et calcul du seuil de fissuration après surcharge, *Recherche aérospatiale 3*, 191-201.

Sobczyk, K. (1986), Modelling of random fatigue crack growth, *Eng. Fract. Mech. 24(4)*, 609-623.

Spanier, J. and K. B. Oldham (1987), *An Atlas of Functions*, Springer Verlag, New York.

Weibull, W. (1939), A statistical theory of the strength of materials, *Roy. Swed. Inst. Eng. Res.* 151.

ii Fontes GS à matrice ferritique

par H. YAACOUB AGHA, A.-S. BÉRANGER, R. BILLARDON et F. HILD (1998). *Fat. Fract. Eng. Mat. Struct.*, 21, pp. 287-296.

HIGH CYCLE FATIGUE BEHAVIOR OF SPHEROIDAL GRAPHITE CAST IRON

by

H. YAACOUB AGHA, A.-S. BÉRANGER, R. BILLARDON and F. HILD

Abstract – An expression for the cumulative failure probability of a structure is proposed for cyclic loading conditions. This expression is dependent on an initial flaw distribution and on a microcrack propagation law. Two sets of experiments were carried out on specimens made of spheroidal graphite cast iron. These specimens are tested under cyclic tension with two different load ratios. The initial flaw distribution is experimentally identified from microscopic observations. The crack propagation law parameters are identified from experimental results obtained with a load ratio $R = 0.1$. The expression for the failure probability is then used to predict experimental data obtained with a load ratio $R = -1$.

Keywords: probabilistic approach, initial defects, cast iron, high cycle fatigue

NOMENCLATURE

a	=	flaw size
a_c	=	critical flaw size
a_{c0}	=	initial flaw size that becomes critical after N_F cycles
a_M	=	maximum flaw size
a_{th}	=	threshold flaw size
b	=	constant
$B_{\alpha\beta}$	=	Euler function of the first kind
C, C^*, k, m, n	=	parameters of the crack propagation law
E	=	Young's modulus
Err	=	error
f	=	flaw size distribution
f_0	=	initial flaw size distribution
g	=	function

HV_{30} = hardness
K = stress intensity factor
K_c, K_{th} = critical and threshold stress intensity factors
K_{max}, K_{min} = maximum and minimum stress intensity factors
K_{op} = opening stress intensity factor
n_e = number of experiments
N, N_F = number of cycles (to failure)
N_{Fie}, N_{Fi} = experimental and predicted number of cycles to failure
P_F = cumulative failure probability of a structure
P_{F0} = cumulative failure probability of an element
R = load ratio ($= K_{min}/K_{max}$)
S_{th} = threshold stress
x = dimensionless flaw size
x_{th} = normalized threshold flaw size
V, V_0 = volumes of a structure and an element
Y = dimensionless parameter
α, β = parameters of a beta function
φ = function
σ = uniaxial equivalent stress (e.g., maximum principal stress)
σ_{max} = maximum equivalent stress
$\sigma_u, \sigma_{y0.2\%}$ = ultimate and yield stress
σ_∞ = fatigue limit

INTRODUCTION

Due to its good properties, Spheroidal Graphite (SG) cast iron is widely used in the automotive industry, in particular for safety components. For example, it is utilized in ground link elements such as steering knuckle holder, suspension arms [1]. These cast components are frequently subjected to high cycle fatigue conditions. The fatigue strength of components may be reduced by the presence of initial casting flaws randomly distributed within the material. Consequently, a life prediction method that accurately evaluates the effect of these casting flaws is required.

To study the fatigue failure of these materials, one needs information about the initial distribution of flaws and their evolution features. The fatigue process in materials can be schematically divided into two stages. Microcrack propagation, which is often due to initial flaws, has to be considered for both brittle and ductile materials.

Macrocrack propagation is usually unstable for brittle materials (e.g., engineering ceramics), while first stable and then unstable for ductile materials (e.g., many metals in the domain of low cycle fatigue). In this paper, we will focus our attention on SG cast iron subjected to high cycle fatigue. The structure is therefore assumed to remain macroscopically elastic whereas the microscopic evolution of the flaws is described according to a generalized Paris' law up to local failure. Macroscopic initiation corresponds to local failure and macrocrack propagation is not considered in this paper.

Probabilistic methods applied to predicting failure under monotonic conditions have been extensively used. The first attempt was made by Weibull [2] and was based upon a probabilistic treatment of failure. Monotonic and cyclic loading conditions were analyzed. Batdorf and Crose [3] modeled initial flaws by cracks whose sizes and orientations are randomly distributed. Evans and Lamon [4, 5, 6] derived another model based upon similar assumptions. Attempts to model stable crack growth have been made by Sobczyk [7] by using stochastic crack growth equations. In the framework of Linear Elastic Fracture Mechanics, Jayatilaka and Trustrum [8] showed that under some simple assumptions the Weibull parameters can be related to flaw distribution features. These results have been extended in the framework of Linear Elastic Fracture Mechanics and Continuum Damage Mechanics [9]. An expression for the cumulative failure probability was obtained, in which the flaw distribution was directly considered.

The aim of this paper is to apply the latter approach to the analysis of the failure of a ferritic SG cast iron by taking into consideration the initial flaw distribution. On the one hand, it is assumed that the defects are the only initiation sites so that discussing the stage I process is irrelevant in the present study. On the other hand, the stage II phase is referred to as *microcrack* propagation as opposed to *macrocrack* propagation, which corresponds to the minor part of the component life in high cycle fatigue. The flaw size distribution can be obtained from SEM observations coupled with image analysis. The crack propagation law can be obtained from conventional crack propagation experiments. In the first part of this paper, the crack propagation law is discussed with respect to the considered defects. The second part is concerned with an expression for the cumulative failure probability of a structure subjected to to high cycle fatigue. The third part deals with the analysis of uniaxial tensile tests performed on SG cast iron containing initial casting defects.

MICROCRACK PROPAGATION IN HIGH CYCLE FATIGUE

In some heterogeneous materials, initial heterogeneities are mostly sphere-like cavities (e.g., intrinsic flaws in ceramics due to processing, flaws due to cooling down in SG cast iron), or sphere-like brittle inclusions with low interfacial strength (e.g., graphite in cast iron). Under high cycle fatigue loadings, penny-shaped-like cracks propagate radially from these heterogeneities. As a first approximation, it is assumed that during microcrack propagation the surface of the defect increases with no morphological change. Therefore the radius a of the surface is the only parameter to be accounted for, and the microcrack propagation law will be written in terms of this parameter.

A number of studies have been focused on the crack propagation law. They show that short cracks tend to propagate faster than long cracks [10]. Furthermore, a crack arrest phenomenon was observed when specimens were tested below the endurance limit [11]. Experiments clearly showed that the propagation rate of artificial short cracks was larger than the value determined for long cracks [12]. In SG cast iron, there are four different defect populations that may lead to high cycle fatigue failure. First, pinholes are located at or close to the as-cast surface. These defects were not present in the experiments discussed herein since the studied batch of specimens was machined. Second, graphite nodules (see Fig. 1.1), especially when their geometry degenerates close to the as-cast surface, are potential initiation sites. Again the latter are not considered herein. Third, macro-shrinkage defects ($a > 0.5$ mm) are routinely detected visually or by NDE techniques and therefore are not present in the cast components used by the automotive industry. Fourth, microshrinkage porosities ($a \leq 0.5$ mm) are more difficult to detect and may be present in the components (see Fig. 1.2). The last class of defects is studied in this paper since they tend to be the micropropagation sites leading to final fracture. Their minimum size is generally greater than that of the graphite nodules (whose maximum size is of the order of a few tens of μm in radius).

The flaws are supposed to be described by cracks whose geometry is taken into account by a dimensionless factor Y such that a general stress intensity factor K is given by

$$K = Y\sigma\sqrt{a} \tag{1}$$

In this paper, only proportional loading conditions are considered (*i.e.*, the principal directions are independent of the number of cycles) and bifurcation of the crack is not considered. In the case of non-proportional loading conditions, the previous hypotheses need to be re-visited. It is worth noting that the values of the parameter Y

depend upon the geometry of the initial defect and the fact that this flaw intersects or not a free surface. For instance, the distance of the flaws to the surface of the structure may be taken into account through the dimensionless parameter Y.

To take into account the localized non-linear behavior of the material in the vicinity of the crack tip under cyclic loading conditions, Elber [13] has shown that crack propagation depends upon a so-called effective stress intensity factor $\Delta K_{\text{eff}} = K_{\max} - K_{\text{op}}$. In the following, the onset of microcrack propagation is described by a criterion postulated by Pellas et al. [14]

$$\Delta K_{\text{eff}} = g(R) K_{\max} - K_{\text{th}}(a) \geq 0 \tag{2}$$

where $K_{\text{th}}(a)$ is a function of the current crack size a [15]. The function g models the influence of load ratio R.

In many practical situations, it can be assumed that the flaw size is bounded by a maximum value a_{M}. In the case of cyclic loading, a cyclic threshold stress can be defined as the lowest value of the stress level below which no failure occurs (*i.e.*, the failure probability is equal to zero). The cyclic threshold stress, S_{th}, is related to the threshold stress intensity factor K_{th}. Its expression, when $g(R) = 1$, can be derived from Eqns. (1) and (2)

$$S_{\text{th}}(a_{\text{M}}) = \frac{K_{\text{th}}(a_{\text{M}})}{Y\sqrt{a_{\text{M}}}} \tag{3}$$

The results derived so far will be used to study high cycle fatigue of SG cast iron. It is assumed that the microcrack propagation law is a modified version of an Elber law [13], and keeps the main features of the macrocrack propagation law based upon the generalized Paris' law proposed by Pellas et al. [14]

$$\frac{da}{dN} = C \left[\frac{K_{\max}\, g(R) - K_{\text{th}}(a)}{K_{\text{c}} - \frac{K_{\text{th}}(a)}{g(R)}} \right]^{\text{n}} \tag{4}$$

This law has the advantage of a reasonable description of the near-threshold crack propagation rate: this is a key feature in the present case. In high cycle fatigue, during most part of the number of cycles leading to failure, the flaw size does not grow significantly. Therefore it is assumed that the evolution of the threshold stress intensity factor K_{th} is only dependent on the initial flaw size a_0. Furthermore, the flaw size usually varies between 10 μm and 500 μm, value for which K_{th} is only weakly dependent upon a_0 [15]. Hence, as a first approximation, the threshold stress intensity factor K_{th} will be taken as a constant. This hypothesis is consistent with experimental data obtained on SG cast iron (see below). The following closed-form solution can be derived by integration of Eqn. (4)

$$\varphi\left(\sqrt{\frac{a_c}{a_M}}\right) - \varphi\left(\sqrt{\frac{a_{c0}}{a_M}}\right) = C^* \left[\frac{g(R)\ K_{th}}{K_c - \frac{K_{th}}{g(R)}}\right]^n \left(\frac{\sigma_{max}}{S_{th}}\right)^n N_F \tag{5}$$

where a_{c0} denotes the initial flaw size that becomes critical (*i.e.*, equal to a_c, such that $K_{max}(a_c) = K_c$) after N_F cycles. The constant C^* is equal to C/a_M. The value of the function φ depends upon the power n of the microcrack propagation law

$$\varphi(x) = 2\frac{(x - x_{th})^{1-n}[x_{th} - (n-1)x])}{(n-1)(n-2)} \text{ when } n \neq 1 \text{ and } n \neq 2 \tag{6}$$

$$\varphi(x) = 2[x + x_{th}\ln(x - x_{th})] \text{ when } n = 1 \tag{7}$$

$$\varphi(x) = 2\ln(x - x_{th}) - \frac{2x}{x - x_{th}} \text{ when } n = 2 \tag{8}$$

where x_{th} is obtained by using Eqns (1) and (2)

$$x_{th} = \sqrt{\frac{a_{th}}{a_M}} = \frac{S_{th}}{\sigma_{max}\ g(R)} \tag{9}$$

The aim of the next section is to derive an expression for the cumulative failure probability when the material experiences cyclic loading conditions for which the defects are randomly distributed within the structure and can grow stably.

CUMULATIVE FAILURE PROBABILITY IN TENSION

In the following, for sake of simplicity, we shall consider only cases for which the tensile load level, σ_{max} is constant. Initial heterogeneities are assumed to be randomly distributed, and are modeled by a flaw size distribution f, which is a function of the size a. This function needs to be determined to assess the reliability of heterogeneous materials. The cumulative failure probability P_{F0} of an element Ω_0 is the probability of finding an initial flaw, whose size is larger than the critical flaw size a_{c0} [16]

$$P_{F0} = \int_{a_{c0}}^{+\infty} f_0(a)da \tag{10}$$

Equation (10) can be used when the flaw size evolution is deterministic, and if the only flaws to cause failure are those initially present within the material. The cumulative failure probability P_F of a structure Ω is related to the cumulative failure probability P_{F0} in the framework of the weakest link theory [17]. In pure tension or compression, the stress state is uniform and, provided that the flaw size distribution is uniform (*i.e.*, characterized by a unique function f over the whole body), the relationship between the two cumulative failure probabilities is given by

$$P_F = 1 - (1 - P_{F0})^{\frac{V}{V_0}} \tag{11}$$

Equation (11) is valid when the flaw interaction can be neglected. In SG cast iron the average distance between flaws is large compared with their size so that this hypothesis is very often fulfilled. It is worth noting that in high cycle fatigue, the propagation stage on a macroscopic scale tends to become negligible when compared, in terms of number of cycles, to the micropropagation stage. In such circumstances, Eqn. (11) can be applied to both brittle and ductile materials in high cycle fatigue. Since the propagation stage is neglected when Eqn. (11) is used, this equation corresponds to a lower bound to the cumulative failure probability of the structure. Hence, in the following, failure refers to local failure, *i.e.*, macroscopic initiation, which is a conservative estimate of the structural failure.

In the next section an identification procedure of the propagation law is proposed and applied to fatigue experiments performed on SG cast iron specimens. An experimental identification of the flaw distribution is performed on the same specimens.

ANALYSIS OF FATIGUE TESTS ON SG CAST IRON

In this section, a series of tension/compression experiments performed at LMT-Cachan and Renault are analyzed in details. These experiments have been carried out at different stress levels on specimens made of ferritic SG cast iron containing less than 5% of pearlite. The mechanical properties are the following: $\sigma_{y0.2\%} = 350$ MPa, $\sigma_u = 510$ MPa, $HV_{30} = 185$, and $E = 185$ GPa. The ratio between the threshold stress intensity factor and the critical stress intensity factor is of the order of 1/3 [15]. Cylindrical specimens (8 mm in diameter) are tested under cyclic tension with two different load ratios ($R = -1$ and $R = 0.1$).

Each curve in an S−N plot corresponds to a constant failure probability. It can be shown from Eqns. (10) and (11) that a constant failure probability can be rewritten in tension/compression as

$$\frac{a_{c0}}{a_M} = b(P_F) \tag{12}$$

where the constant b depends upon the details of the flaw distribution and the value of the considered cumulative failure probability. By using Eqns. (5) and (12) the number of cycles to failure is given by

$$N_F = +\infty \quad \text{if } \sigma_{max}\, g(R)\, \sqrt{b} \leq S_{th} \tag{13}$$

$$N_F = \left[\frac{K_c - \frac{K_{th}}{g(R)}}{K_{th} g(R)}\right]^n \left(\frac{\sigma}{S_{th}}\right)^{-n} \left[\varphi\left(\frac{S_{th} K_c}{\sigma_{max} K_{th}}\right) - \varphi\left(\sqrt{b}\right)\right] \quad \sigma_{max}\, g(R)\, \sqrt{b} > S_{th} \tag{14}$$

Equation (13) corresponds to a case where no failure at all is possible and the limiting stress case $\sigma\ g(R)\ \sqrt{b} = S_{\text{th}}$ corresponds to the 'fatigue limit' for a given cumulative failure probability. The expression for the cumulative failure probability then only depends upon the initial flaw distribution and the value of the cyclic threshold stress S_{th}. This case can allow an identification of the threshold stress S_{th} and the flaw size distribution independently of the crack growth law [18]. Equation (14) corresponds to higher stress states where fatigue failure occurs. For a given value of b (*i.e.*, a given failure probability), the evolution of the number of cycles to failure mainly depends on the crack growth law. Therefore the analysis of a constant failure probability enables to identify the parameters of the crack growth law, provided the flaw size distribution is known (*i.e.*, the different values of the constant b have been identified).

Lastly, it is assumed that the flaw size distribution f_0 can be modeled by a beta function

$$f_0(a) = \frac{a^{\alpha-1}\,(a_{\text{M}} - a)^{\beta-1}}{B_{\alpha\beta}\ a_{\text{M}}^{\alpha+\beta-1}} \quad \text{when} \quad 0 < a < a_{\text{M}}, \alpha > 0, \beta > 0 \tag{15}$$

This distribution possesses the key property of being bounded by 0 and a_{M}. In the present case, the only defects to be considered are microshrinkage cavities whose maximum size is given by the minimum detectable size by NDE techniques.

In the following, the flaw size distribution f and the microcrack propagation law parameters, C, n, m will be experimentally identified from the tests performed for a load ratio $R = 0.1$. Systematic microscopic observations of the fractured surfaces of 50 specimens subjected to high cycle fatigue tension/tension tests were performed by using a Scanning Electron Microscope to determine the initial flaw distribution. The initial defects on the fractured surfaces can be distinguished with no difficulty since the stable propagation area has different morphological characteristics as compared to those of the initial defects. Pictures of the fractured surfaces were stored in a SUN workstation and an image analysis program was used to determine the defect distribution. The size of the flaw is defined as the diameter of the smallest circle in which the flaw may be included (see Fig. 1.2). Flaws with a diameter less than 80 μm were not considered to avoid confusions with graphite nodules (with maximum size of the order of 60 μm in diameter). Since pores of small size ($a < 30$ μm) do not exist in the structure, we make the hypothesis that the probability of finding a defect of size equal to zero is zero. By taking into account this hypothesis, the parameters of the experimental flaw distribution α and β are identified. The following values are obtained: $\alpha = 2.3$, $\beta = 18.$ and the value chosen for a_{M} is 400 μm. This result shows that we are dealing with short cracks, and that the threshold stress intensity factor can be considered as a constant for flaws of this size as shown in Ref. [19].

It is assumed that $\frac{V}{V_0}$ is equal to 1 since the size of the specimens is small: 8 mm in diameter to be compared to $a_M = 400$ μm. The value of the threshold stress can then be deduced from Eqn. (3) by assuming that $Y \cong 2$ and $K_{th} = 4.2$ MPa$\sqrt{m}$ [19], $S_{th} = 105$ MPa. Figure 2 shows the identified flaw distribution. The values of flaw size corresponding to a failure probability 10%, 50%, and 90% are depicted in the same figure and given in Table 1. For a failure probability of 90% the critical flaw size has the same order of magnitude as the maximum size of nodular graphite.

Table 1: Values of the constant b for SG cast iron.

Failure probability	Constant b
10%	0.06
50%	0.14
90%	0.25

The second step of the identification is concerned with the parameters of the microcrack propagation law. Since the S−N curves used for the identification are obtained in tension, this identification is straightforward: it consists in the analysis of the constant cumulative failure probability $P_F = 50\%$, (*i.e.*, a_{c0} = constant, see Eqn. (12)). This failure probability is defined such that it minimizes the following error

$$\text{Err} = \frac{1}{n_e} \sum_{i=1}^{n_e} \left[N_{Fie} - N_{Fi} \left\{ b(P_F = 50\%), \frac{\sigma_{Fi}}{S_{th}}, n, C^*, R = 0.1 \right\} \right]^2 \tag{16}$$

where N_{Fi} is the number of cycles to failure predicted according to Eqn. (14). It can be noticed that Eqn. (16) corresponds to the assumption that the mean value of the number of cycles to failure experimentally measured for a given stress level coincides with a cumulative failure probability of 50%. Although this assumption is not fully consistent with other assumptions made to develop the approach discussed herein, it can be considered as a reasonable approximation.

An expression for the function g has been proposed by Pellas et al. [14]

$$g(R) = \frac{1 - R}{1 - mR} \tag{17}$$

where m is a material parameter. The values of m are usually of the order of 0.5. The approximation $g(R) \cong 1$ can be used when $R = 0.1$. The identification of the propagation law gives the following values: $n = 2$, and $C^* = 5.9 \times 10^{-5}$. In Fig. 3 the cumulative failure probabilities $P_F = 10\%$, $P_F = 50\%$, and $P_F = 90\%$ are plotted with the experimental results. It is assumed that the number of experiments is large enough to properly evaluate the failure probabilities 10% and 90%. This figure shows

that most experimental data lie between the two failure probabilities $P_F = 10\%$, and $P_F = 90\%$. Experimental observations of specimens where the corresponding point in the curve S-N is outside the zone between the failure probabilities $P_F = 10\%$, and $P_F = 90\%$ show that these specimens contain flaws of a size larger than a_M. Would such flaws be present in industrial cast components, they would have been detected by using NDE techniques.

Figure 4 shows the crack growth rate as a function of the stress intensity amplitude. The solid curve is identified from the analysis of a constant failure probability. The other points represent experimental results obtained on specimens made of SG cast iron. The solid squares concern an artificial short crack of initial length $a_0 = 240$ μm [20]. The open circles correspond to an artificial crack of initial length $a_0 = 1$ mm. The open squares concern an artificial long crack of initial length $a_0 = 6$ mm [20]. The identified curve is in good agreement with the experimental results especially for short cracks in the near-threshold regime. The discrepancy with the results for long cracks can be described by threshold differences.

The last parameter to be identified is m to model the load ratio effect (see Eqn. (17)). By comparing two fatigue limits (for $R = -1$ and $R = 0.1$) for the same available cumulative failure probability (50%), the parameter m is determined by using Eqn. (13)

$$\sigma_\infty(P_F = 50\%, R = 0.1)\; g(0.1) = \sigma_\infty(P_F = 50\%, R = -1)\; g(-1) \qquad (18)$$

The identified value is $m = 0.59$. Figure 5 shows the cumulative failure probabilities $P_F = 10\%$, $P_F = 50\%$, and $P_F = 90\%$ and the experimental results for $R = -1$. The same type of conclusion can be drawn for $R = -1$ as for $R = 0.1$. This result shows that the function g accounts for the influence of load ratio for different cumulative failure probabilities. All the material parameters identified for the material studied herein are gathered in Table 2.

CONCLUSIONS

A reliability analysis taking account of flaw size distributions has been developed for components subjected to cyclic loading conditions. Therefore, the underlying hypothesis is that the scatter in failure stress and number of cycles is entirely attributed to the random distribution of flaws. Emphasis is also put on the micro-propagation stage, which is directly related to the evolution of initial flaws. An expression for the cumulative failure probability is derived in the framework of the weakest link theory and by assuming that the flaw interaction can be neglected. The study is applied to SG cast iron where the maximum defect size is of the order of 400 μm. The crack

Table 2: Material parameters modeling high cycle fatigue of SG cast iron.

Parameter	Value (unit)
a_M	400. μm
Y	2.
S_{th}	105. MPa
α	2.3
β	18.
k	0.33
C^*	5.9×10^{-5}
n	2.0
m	0.59

propagation law is based on a modified Paris' law for this kind of flaws. The threshold stress intensity factor, which is dependent upon the current size of defect, is considered as a material constant for the described SG cast iron. A simplified expression for the cumulative failure probability is derived for cyclic failure in the case of tension. The analysis of a constant failure probability allows to identify the parameters of the microcrack propagation law.

Experimental data on SG cast iron in tension are analyzed within this framework for experiments with a load ratio $R = 0.1$. It is assumed that the flaw distribution is described by a beta probability density function. The flaw distribution is identified experimentally by using SEM observations and image analysis. The predictions of the failure probabilities for the two series of data ($R = 0.1$ and $R = -1$) are in good agreement with the experimental number of cycles to failure. This result shows that the influence of the load ratio is reasonably described by the model. Finally, the identified crack growth rate as a function of the stress intensity factor is in good agreement with experimental results, which indicates that the threshold stress intensity factor can be considered as a constant for small cracks. These results show that the expression for the cumulative failure probability proposed herein is able to model fatigue data obtained on SG cast iron. Extension to heterogeneous stress fields (such as bending) are under way to evaluate the predictive capabilities of the model.

ACKNOWLEDGMENTS

HYA, RB and FH gratefully acknowledge the financial support of Renault through contract CNRS/109 (H5−24−12) with LMT-Cachan.

References

[1] J. Le Gal (1994) Trends and Metallurgical Factors Involved in Automotive Cast Iron Parts. In: *Proceedings SCI 5* (in press).

[2] W. Weibull (1939) *A Statistical Theory of the Strength of Materials.* Roy. Swed. Inst. Eng. Res., 151.

[3] S. B. Batdorf and J. G. Crose (1974) A Statistical Theory for the Fracture of Brittle Structures Subjected to Polyaxial Stress States. *ASME J. Appl. Mech.* **41**, 459-465.

[4] A. G. Evans (1978) A General Approach for the Statistical Analysis of Multiaxial Fracture. *J. Am. Ceram. Soc.* **61**, 302-308.

[5] J. Lamon and A. G. Evans (1983) Statistical Analysis of Bending Strengths for Brittle Solids: a Multiaxial Fracture Problem. *J. Am. Ceram. Soc.* **66**, 177-182.

[6] J. Lamon (1988) Statistical Approaches to Failure for Ceramic Reliability Assessment. *J. Am. Ceram. Soc.* **71**, 106-112.

[7] K. Sobczyk (1986) Modelling of Random Fatigue Crack Growth. *Eng. Fract. Mech.* **24**, 609-623.

[8] A. de S. Jayatilaka and K. Trustrum (1977) Statistical Approach to Brittle Fracture. *J. Mater. Sci.* **12**, 1426-1430.

[9] F. Hild and D. Marquis (1992) A Statistical Approach to the Rupture of Brittle Materials. *Eur. J. Mech., A/Solids* **11**, 753-765.

[10] K. J. Miller (1982) The Short Crack Problem. *Fatigue Eng. Mater. Struct.* **5**, 223-232.

[11] D. Taylor and J. F. Knott (1982) Growth of Fatigue Cracks from Casting Defects in Nickel-Aluminum Bronze. *Met. Tech.* **9**, 221-228.

[12] J.-L. Bréat, F. Mudry and A. Pineau (1983) Short Crack Propagation and Closure Effects in a 508 Steel. *Fatigue Eng. Mat. Struct.* **6**, 349-358.

[13] W. Elber (1971) The Significance of Fatigue Crack Closure. In: *Damage Tolerance in Aircraft Structures*, ASTM, Philadelphia, PA (USA), STP 486, 230-242.

[14] J. Pellas, G. Baudin and M. Robert (1977) Mesure et calcul du seuil de fissuration après surcharge. *Recherche aérospatiale* **3**, 191-201.

[15] P. Clément, J.-P. Angeli and A. Pineau (1984) Short Crack Behavior in Nodular Cast Iron. *Fatigue Eng. Mater. Struct.* **7**, 251-265.

[16] F. Hild and S. Roux (1991) Fatigue Initiation in Heterogeneous Brittle Materials. *Mech. Res. Comm.* **18**, 409-414.

[17] A. M. Freudenthal (1968) Statistical Approach to Brittle Fracture. In: *Fracture*, H. Liebowitz, edt., Academic Press, New York, NY (USA), **2**, 591-619.

[18] H. Yaacoub Agha, A.-S. Béranger, R. Billardon and F. Hild (1997) Statistical Damage Tolerance for Cast Iron Under Fatigue Loadings. In: *Proceedings Third International Conference on Material Processing Defects*, M. Predeleanu and P. Gilormini, eds., Elsevier, Amsterdam (the Netherlands), 415-424.

[19] P. Clément and A. Pineau (1984) Amorçage et propagation de petites fissures dans la fonte à graphite spheroïdal. In: *Proceedings Journées internationales de printemps de la SFM*, SFM, Paris (France), 203-218.

[20] P. Clément (1984) *Propagation par fatigue de petits défauts dans une fonte GS.* CNAM report, CNAM Paris.

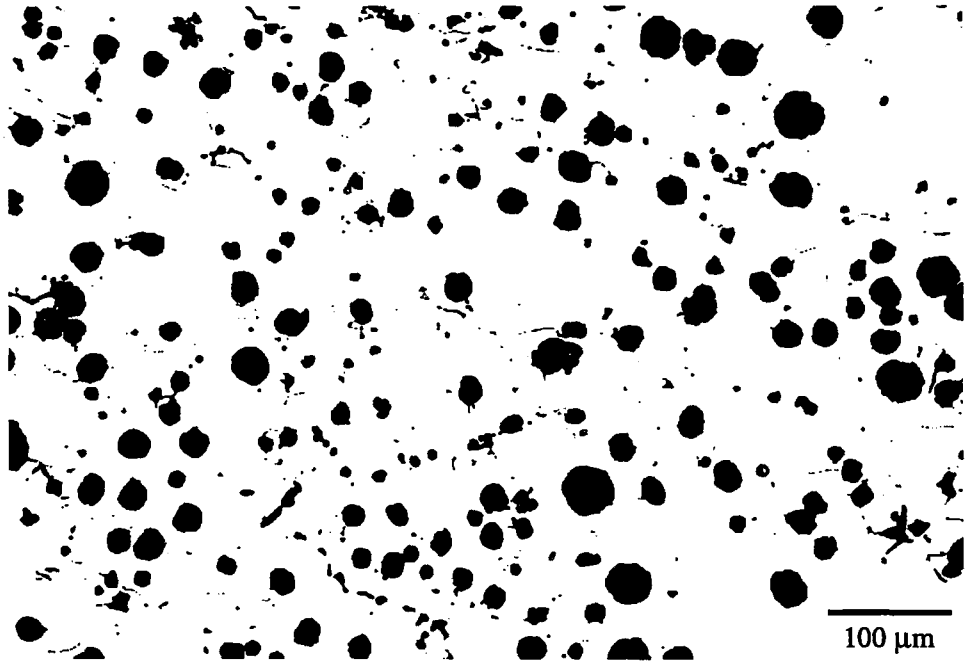

(a)

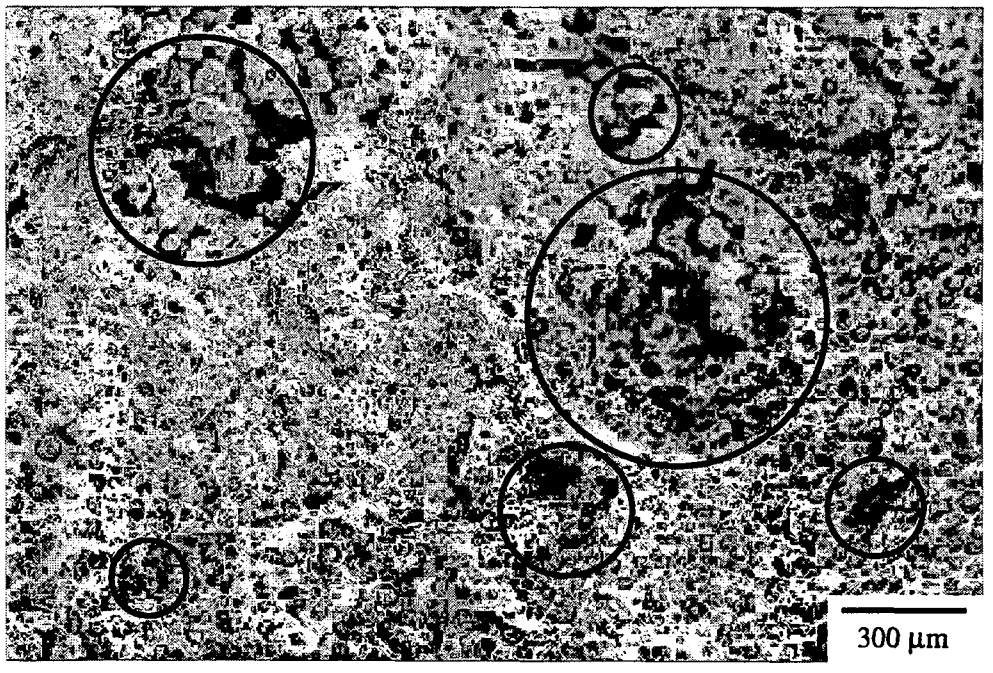

(b)

Figure 1: Microscopic observations of a fractured surface of an SG cast iron specimen submitted to high cycle fatigue tension/tension test: (a) Graphite nodules, (b) Microshrinkage cavities.

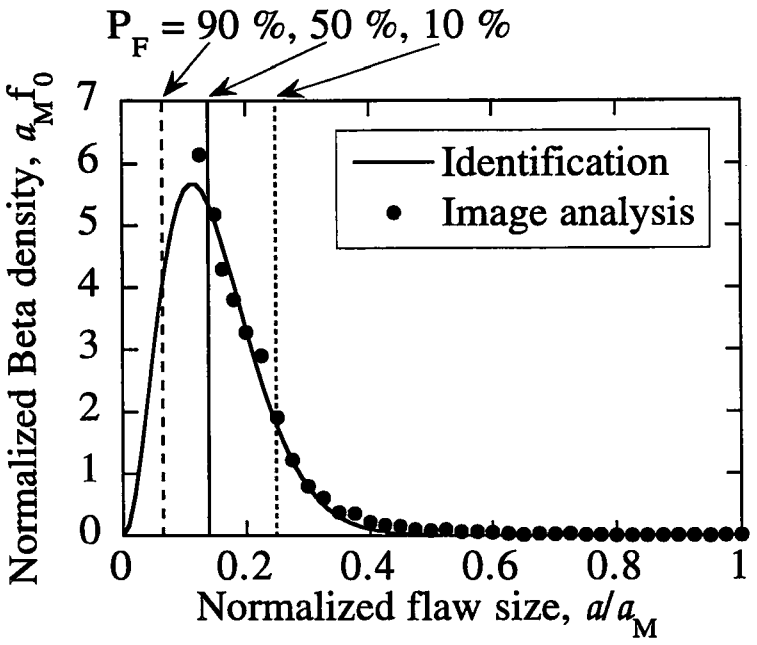

Figure 2: Identification of the initial flaw distribution of SG cast iron from image analysis.

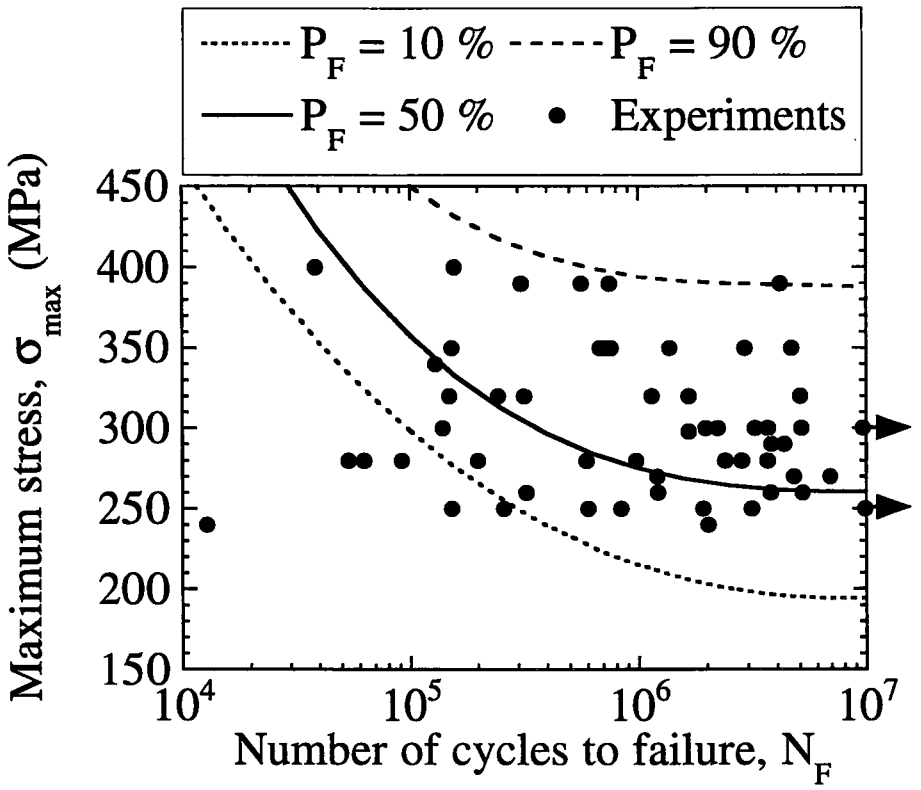

Figure 3: Predicted failure probabilities compared with experiments for $R = 0.1$.

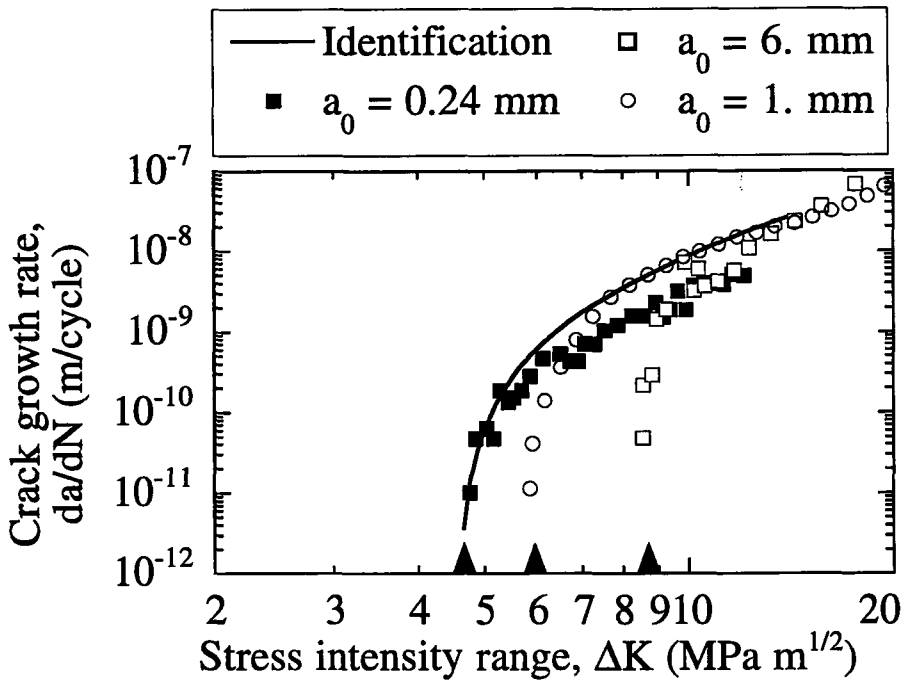

Figure 4: Crack growth rate as a function of stress intensity range for $R = 0.1$.

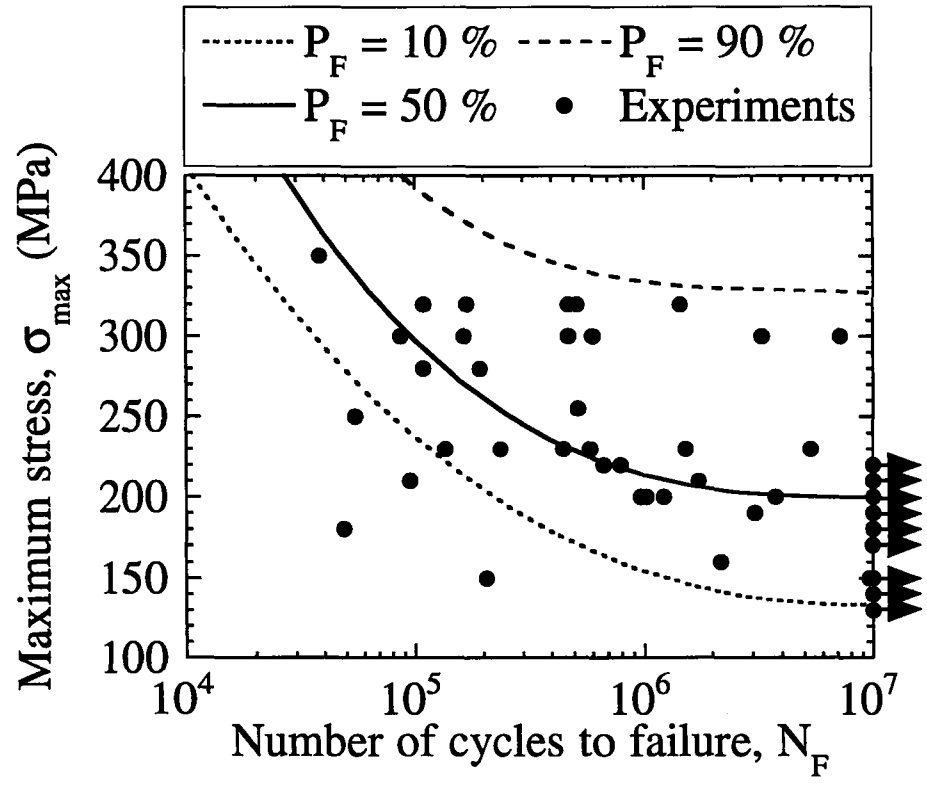

Figure 5: Predicted failure probabilities compared with experiments for $R = -1$.

2.4 Perspectives

Différents points abordés dans ce chapitre sont à compléter. Le premier d'entre eux concerne la notion de volume élémentaire dans le calcul de la probabilité de rupture. En effet, la définition proposée dans le cas de l'homogénéisation peut être transcrite au cas de la rupture fragile : « *ce volume élémentaire, grand par rapport à l'échelle des hétérogénéités de la microstructure, doit être suffisamment petit par rapport à celle de la structure macroscopique (en particulier du champ de contrainte appliqué) pour se prêter à un traitement continu* » [FRANÇOIS *et al.*, 1991]. Le fait qu'une microstructure puisse varier d'une zone à l'autre de la structure peut conduire à une expression différente de la probabilité de rupture d'une structure. Ceci peut se produire dans l'étude de pièces de fonderie pour lesquelles le procédé d'obtention implique des répartitions inhomogènes de défauts. Ce cas a été envisagé dans la rédaction du programme de calcul ASTAR de pièce de fonderie soumise à des sollicitations cycliques mais n'a pas encore été utilisé.

Les calculs de structure effectués avec ASTAR ont principalement montré la faisabilité d'un tel calcul (paragraphe 2.2.2). Restent toutes les validations à l'aide de comparaisons entre essais sur structure et prévisions numériques. Ce travail est en cours en collaboration avec Renault. Un des problèmes importants concerne les sollicitations multiaxiales dans lesquelles les critères simples discutés dans ce chapitre peuvent être mis en défaut. Des critères multiaxiaux existent dans la littérature (cf. par exemple [DANG VAN, 1973 ; DANG VAN *et al.*, 1984]). Cependant la plupart des critères prévoient les conditions d'amorçage sur matériau considéré comme sain (sans défaut) encore appelé stade I [MILLER, 1982 ; MILLER et DE LOS RIOS, 1986]. Or dans la majorité des cas des fontes GS, ce sont les défauts initiaux qui conduisent à la rupture par fatigue des pièces de fonderie. Le stade I ne se produit pratiquement pas car les défauts existent déjà et il s'agit à ce moment d'étudier le stade II (propagation en mode I prépondérant).

En fatigue, on parle souvent « d'effet de surface » ou « d'effet de sous-couche ». Les fissures sont plus nocives lorsqu'elles sont situées près de la surface. Ceci nécessite un traitement particulier des éléments de volume proches de la surface. La microstructure est souvent différente en sous-couche et en volume. Pour des fontes à graphite sphéroïdal, on peut observer des dégénérescences de nodules qui peuvent être catastrophique pour la tenue d'une structure comportant des surfaces brutes de fonderie [CHANTIER, 1997]. Dans ce cas, non seulement les populations de défauts peuvent être différentes mais également le comportement à la propagation du défaut. Enfin les effets DVH seront également différents : en particulier les différences entre des sollicitations cycliques de traction/compression et de flexion rotative ne conduiront pas aux mêmes différences

en termes de probabilité de rupture lorsque la rupture a lieu en volume ou en sous-couche.

Une autre voie de recherche concerne la prévision de l'apparition des défauts proprement dits. Ce type d'approche a été développé au LMT-Cachan durant les années 1980 dans le groupe « mise en forme » sous l'impulsion de M. PREDELEANU [PREDELEANU, 1987 ; GHOSH et PREDELEANU, 1992 ; 1995 ; PREDELEANU et GILORMINI, 1997] et J.-P. CORDEBOIS notamment. Plusieurs thèses (cf. par exemple [TARDIVEL, 1982 ; CORDEBOIS, 1983 ; BELKHIRI, 1985 ; FONTAINE, 1985 ; CHEVALIER, 1988 ; PIERRE, 1990 ; QUAEGEBEUR, 1990]) ont porté sur la prévision de l'endommagement dans la simulation de différents procédés de mise en forme. La corrélation avec des tailles et orientation de défauts ainsi formés reste cependant qualitative.

Ceci reste également vrai pour le procédé de fonderie. En effet, le savoir faire des fondeurs et les essais de fonderie ont constitué depuis longtemps un outil de prévision de l'état final du produit moulé. Le développement récent des moyens de calcul permet d'envisager aujourd'hui l'utilisation d'outils de simulation numérique pour modéliser le procédé de fonderie. La modélisation de ce procédé permet de prévoir l'état géométrique *et* métallurgique de la pièce moulée. Il doit aussi permettre d'avoir une idée des contraintes résiduelles et de la distribution de défauts dans la pièce finie [LESOULT et LACAZE, 1997]. Le procédé en tant que tel est assez complexe, il est constitué de trois phases principales : le remplissage du moule, la solidification et le refroidissement. Les codes industriels qui se trouvent actuellement sur le marché simulent le remplissage du moule en métal liquide et le refroidissement de la pièce du point de vue thermique seulement. Pour bien simuler le procédé de fonderie, il faut tenir compte d'abord des changements de phases qui se produisent dans la fonte au cours de son refroidissement et de l'interaction entre le métal et le moule en sable qui l'entoure. Au cours de son refroidissement, de la température de fusion à la température ambiante, la fonte GS subit une transformation de phase. Son comportement fait apparaître des interactions entre la réponse mécanique, la réponse thermique et le changement microstructural. La modélisation et la caractérisation de ce comportement ont été étudiées au LMT-Cachan par N. HAMATA [1992]. Les propriétés thermiques et mécaniques du moule influencent fortement les phases de solidification et de refroidissement. La géométrie finale de la pièce est liée à la rigidité du moule par exemple. Pour tenir compte de ce problème, le comportement thermo-hydro-mécanique anisotherme d'un sable à vert de moulage a été étudié au LMT-Cachan par F. AZZOUZ [1995]. Un programme complet de simulation du processus de fonderie devrait également inclure des critères d'apparition de défauts notamment lors de la solidification. Il semble ainsi raisonnable d'envisager qu'à moyen terme un outil de simulation du procédé de fonderie puisse être couplé à un calcul de tenue en fatigue de structures de fonderie.

Enfin, une des hypothèses fondamentales de ce chapitre a été celle du maillon le plus faible. Elle est sûrement applicable dans un ensemble de cas dont certains ont été exposés dans ce chapitre. Par contre, dans d'autres situations, cette hypothèse est beaucoup trop restrictive. En effet, même des matériaux à comportement fragile peuvent subir des ruptures multiples s'ils sont soumis à des sollicitations dynamiques ou s'ils sont renforcés. Dans ce cas, des lois de comportement (non-linéaires) peuvent être écrites. Elles sont étudiées dans le chapitre suivant.

Chapitre 3

Endommagement et rupture de matériaux à comportement quasi-fragile

C'est alors qu'apparut le renard :

— Bonjour, dit le renard.

— Bonjour, répondit poliment le petit prince, qui se retourna mais ne vit rien.

— Je suis là, dit la voix, sous le pommier...

A. DE SAINT-EXUPÉRY (1946), *Le Petit Prince*, Gallimard.

Dans ce chapitre, nous considérons des situations dans lesquelles les ruptures à l'échelle la plus « petite » (microscopique) sont nombreuses. Dans tous les cas, les mécanismes microscopiques sont identiques : c'est la fissuration (multiple). Localement, la rupture est brutale, mais le matériau est capable d'accommoder plusieurs ruptures. L'hypothèse du maillon le plus faible (du chapitre 2) ne s'appliquera plus à l'échelle mésoscopique. Le développement de cette fissuration sera désigné de manière générique par le terme « endommagement ».

La dégradation du matériau étant contrôlée et mesurable, elle se traduit par une non-linéarité du comportement mécanique. Sa détection est donc plus facile que dans le cas de la rupture fragile. C'est pourquoi on parlera de comportement quasi-fragile : les déformations resteront faibles mais les non-linéarités observables. Ceci a pour conséquence de rendre possible l'écriture de lois de comportement non-linéaires identifiables à l'échelle (mésoscopique) de l'élément de volume de la mécanique des milieux continus.

Différentes architectures de microstructures seront abordées dans ce chapitre. La première concerne des matériaux monolithiques identiques à ceux étudiés dans le chapitre 2 mais sollicités de manière à engendrer un endommagement diffus. C'est le cas des sollicitations par impact rencontrées dans l'étude des blindages légers (paragraphe 3.1). Des matériaux renforcés de fibres sont ensuite analysés. Deux mécanismes d'endommagement sont considérés. La fissuration matricielle est traitée dans le paragraphe 3.2 et la rupture de fibres dans le paragraphe 3.3. Dans tous les cas, les études sont effectuées à différentes échelles avec prise en compte de l'aspect aléatoire de la rupture à l'échelle la plus fine.

3.1 Endommagement de céramiques sous chargement dynamique

L'étude du comportement des blindages soumis à un impact constitue un des problèmes cruciaux pour les applications de défense. La protection d'un engin blindé –voire d'un aéronef de combat– se heurte toujours aux mêmes contraintes : résister à des menaces de plus en plus efficaces avec une masse la plus faible possible. En fonction du type de menace (projectiles de différents calibres), de la gamme de sollicitation (déterminée par la vitesse du projectile et les matériaux en présence) et de contraintes technologiques (encombrement, masse...) différentes solutions sont envisagées.

Les solutions classiques de blindage utilisent des aciers à haute limite d'élasticité (MARS 190, acier à double dureté) ou des alliages d'aluminium (AZ5G). Le comportement de tels blindages a été étudié très récemment, notamment en France au sein du GDR « Impact Matériaux », bien que de nombreux modèles, plus ou moins phénoménologiques, existent dans la littérature (cf. étude bibliographique de NÈME [1994] par exemple). Pour les véhicules modernes, la nécessité de diminuer la masse a entraîné les ingénieurs à se tourner vers des concepts de blindages bicouches, en remplacement de l'acier ou de l'alliage monolithique. Ce concept bicouche est particulièrement adapté à des menaces de type projectiles de faible calibre (éclats, balles perforantes de 12.7 mm). L'idée est d'associer un matériau dur en face avant à un matériau en face arrière susceptible d'emmagasiner de l'énergie en se déformant plastiquement (cf. figure 3.1). Le rôle principal du matériau en face avant est de briser ou d'émousser le projectile et de répartir l'énergie incidente sur une surface aussi large que possible. La face arrière assure la fonction de « structure » du blindé tout en arrêtant les débris venant de la face avant. La réponse du blindage à l'impact dépend non seulement du comportement individuel de ses constituants mais également des interactions entre eux. Il est par exemple possible de renforcer la tenue à l'impact de « carreaux » de céramique en les confinant dans une structure jouant aussi le rôle de face arrière.

Pour la face avant, le candidat le plus naturel est une céramique monolithique plus dure que l'acier et, en général, deux fois moins dense que ce dernier. De plus, sa résistance à la compression est très importante, ce qui est un atout pour ce type d'applications. Sa fragilité en traction oblige à l'associer à une face arrière faite d'un matériau souvent ductile (acier ou alliage d'aluminium). Des utilisations de composites à matrice céramique sont également envisagées [BRAS, 1996] notamment à proximité de zones chaudes (800 K).

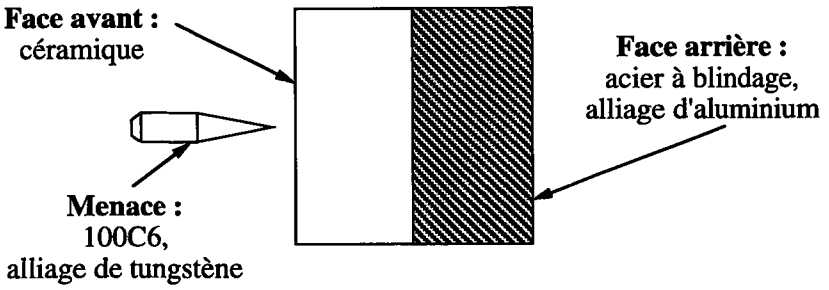

FIG. 3.1 - Principe du blindage bicouche.

Capacités à la fragmentation de céramiques

Afin de caractériser la tenue d'un revêtement en céramique, on peut mesurer le rapport entre la vitesse initiale (V_i) et la vitesse résiduelle (V_r) d'un projectile en fonction de la masse surfacique pour différents types de céramiques et différentes épaisseurs [ORSINI et COTTENOT, 1995]. La masse surfacique est définie comme la masse du blindage par unité de surface (et est donc égale au produit épaisseur × densité). La figure 3.2 résume différents essais réalisés pour une balle perforante de

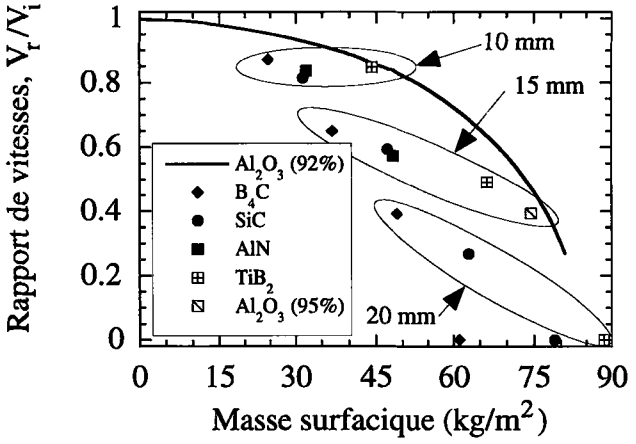

FIG. 3.2 - Propriétés balistiques pour différentes céramiques d'épaisseur 10, 15, 20 et 25 mm, $V_i = 800$ m/s, d'après ORSINI et COTTENOT [1995].

12.7 mm ayant une vitesse initiale $V_i = 800$ m/s. L'alumine (Al_2O_3) dite « 92% » est

considérée comme matériau de référence et a été étudiée de manière très importante [ORSINI et COTTENOT, 1995]. L'épaisseur de 10 mm est trop faible pour que la céramique puisse influencer de manière significative l'avancée du projectile. À partir de 15 mm, la céramique prend de plus en plus d'importance dans la réponse de la cible. Une compréhension complète de ce phénomène reste encore à développer et à valider. Le matériau le plus performant est le carbure de bore (B_4C) suivi du carbure de silicium (SiC) et du diborure de titane (TiB_2), puis du nitrure d'aluminium (AlN). Comparés à ses deux concurrents directs, le carbure de silicium est l'un des candidats les plus intéressants (si l'on tient compte du coût) par rapport à l'alumine « 92% ». C'est ce matériau qui sera étudié dans la suite. En parallèle à des céramiques monolithiques, différents composites à matrice céramique ont été analysés [ORSINI et COTTENOT, 1995]. Il ressort de ces études qu'il n'y a pas d'amélioration significative par rapport à une solution utilisant des céramiques monolithiques. On notera cependant que la configuration analysée dans ce paragraphe ne mesure que les capacités à la fragmentation de différentes céramiques car la face arrière a été retirée (et remplacée par un alliage d'aluminium en nid d'abeille). Par conséquent la céramique est peu sollicitée en compression. L'étude du comportement *in situ* d'une céramique dans un blindage bicouche demeure donc nécessaire et incontournable.

Comportement mécanique de céramiques au choc

Les différents mécanismes mis en jeu lors des tous premiers instants de l'interaction projectile/cible peuvent être mis en lumière par l'analyse d'une onde sphérique divergente [COSCULLUELA, 1992]. Suivant la microstructure de la céramique, différents mécanismes peuvent être actifs [COSCULLUELA, 1992 ; RIOU, 1996]. Par souci de concision, seuls deux mécanismes seront discutés. En se plaçant à un rayon fixé, on peut suivre l'état de contrainte dans un diagramme σ_{rr}-$\sigma_{\theta\theta}$. La figure 3.3 montre la réponse élastique pour différents rayons r d'une cavité de rayon a soumise à un échelon de pression p. On notera une décroissance de l'amplitude maximale de contrainte en $1/r$. Cette réponse peut schématiquement être décomposée en différentes étapes. La première étape consiste en une compression triaxiale induite par des déformations uniaxiales. Dans cette partie, le comportement en compression (compaction, plasticité et endommagement) doit être décrit. Le déplacement radial, induit par l'onde sphérique, produit une expansion du matériau conduisant à des contraintes orthoradiales positives. Ces dernières peuvent provoquer une fissuration de la céramique. Dans un dernier temps, il s'agit de modéliser la perforation éventuelle de la céramique par le projectile, ce qui nécessite une modélisation complète du blindage. Dans de nombreux cas, cette dernière étape peut être découplée de l'étude de la propagation de l'onde sphérique divergente et de

l'endommagement de la céramique [COSCULLUELA, 1992 ; DENOUAL *et al.*, 1996].

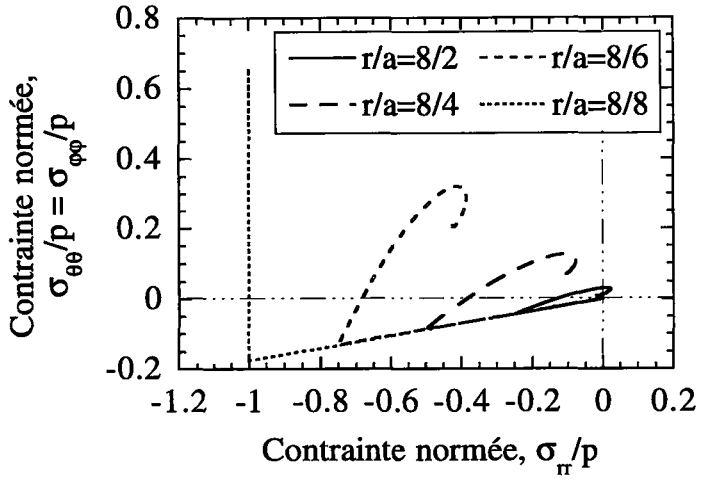

FIG. 3.3 - Trajet de chargement imposé par une onde sphérique divergente à un matériau élastique isotrope ($\nu = 0.15$).

Afin de caractériser le comportement mécanique de céramiques au choc, différentes techniques expérimentales sont utilisées. Citons la plus ancienne et la plus usitée : les barres de HOPKINSON [1914 ; KOLSKY, 1949]. Parallèlement à cette technique dont le dépouillement peut être délicat (cf. par exemple [GARY *et al.*, 1992]), des impacts de plaques ou des essais à l'explosif sont également conduits [COSCULLUELA, 1992]. Très récemment, des essais permettant de reproduire les configurations d'impact ont également été réalisés [STRASSBURGER et SENF, 1995 ; RIOU, 1996]. Ils font appel à des moyens d'observation ultra rapides (l'échelle de temps est la micro-seconde) et permettent d'effectuer des mesures de champs de fissuration dont les résultats peuvent être comparés qualitativement à des simulations numériques. Des informations plus globales telles que l'évolution de la vitesse du front de fissuration dans la céramique permettent de discriminer des modèles d'endommagement isotrope ou anisotrope. Cette étude est traitée dans le paragraphe 3.1.1. D'autres grandeurs telles que la densité locale de fissuration et la forme de la zone fissurée peuvent permettre de qualifier différents critères d'amorçage [RIOU, 1996] et les lois d'évolution de l'endommagement. Ces lois peuvent être, soit mésoscopiques [RIOU, 1996], soit issues d'une analyse probabiliste de la fragmentation de céramiques à l'échelle microscopique : cf. paragraphe 3.1.2. Dans le paragraphe 3.1.3, une première série d'applications est décrite. Enfin, à l'aide de techniques de Moiré [BERTIN-MOUROT *et al.*, 1997], on peut mesurer le champ de déplacement en surface à différents instants. Cette information est plus précise que les mesures locales de contrainte par jauge piézo-résistive et est directement exploitable pour une comparaison

quantitative avec des simulations par éléments finis. Ce travail est en cours dans le cadre de la thèse de C. DENOUAL.

3.1.1 Potentiel d'état - couplage d'état

par C. DENOUAL, C.E. COTTENOT et F. HILD (1996).
Actes 16th International Conference on BALLISTICS, APDS, Arlington, VA (USA), pp. 541-550.

16TH INTERNATIONAL SYMPOSIUM ON BALLISTICS

SAN FRANCISCO, CA, 23-28 SEPTEMBER, 1996

ON THE IDENTIFICATION OF DAMAGE DURING IMPACT OF A CERAMIC BY A HARD STEEL PROJECTILE

Christophe DENOUAL (1)*, Charles E. COTTENOT (1) and François HILD (2)

(1) DGA – CREA – Département Matériaux en Conditions Sévères
16 bis, avenue Prieur de la Côte d'Or, F–94114 Arcueil Cedex, France.

(2) Laboratoire de Mécanique et Technologie
E.N.S de Cachan / C.N.R.S / Université Paris 6
61, avenue du Président Wilson, F–94235 Cachan Cedex, France.

Impact produces high stress waves which lead to a complete fragmentation of brittle materials such as ceramics. Damage evolution during the first micro–seconds is an important mechanism of penetration. An edge–on impact configuration can be used to analyze damage state and evolution by an observation of the crack front pattern and velocity. A comparison is proposed between the experimental crack front velocities and the simulated ones obtained by a one–dimensional code with isotropic and anisotropic damage descriptions. It is shown that only the anisotropic damage description can produce a realistic crack front velocity.

INTRODUCTION

In most impact configurations, the stress field generated by a projectile in a ceramic can be assumed spherical and a comparison can be made between real impact failure morphology and soft recovery experiment of divergent spherical stress loads (Cosculluela, 1992). Stress waves can produce damage in both compressive and tension modes in two different locations in the ceramic. Damage in compression is produced near the impact surface when shear stresses reach a threshold value which can be dependent on pressure and strain rate. In the bulk of the ceramic, damage in tension is observed when the hoop stress induced by the radial motion of the impacted ceramic is sufficient to generate fracture in mode I initiating on micro defects such as porosities, inclusions. The complete perforation is dependent on the way the ceramic fractures in terms of damage location and evolution, and in terms of anisotropic behavior due to cracking. Damage evolution is then one of the main mechanisms to identify for numerical simulations of impacts. Most of the mechanisms initiated during impact (such as nucleation of flaws, propagation and interaction of cracks, stress release) can only be studied during dynamic tests, which have to be chosen to give reliable data on damage evolution.

One of the prevalent test configuration is the entire ceramic/steel specimen, which represents closely the real light bilayered armour concept. These perforation tests only give partial information, e.g. global displacements or some local stresses. The relative influence of the above–mentioned dynamic mechanisms on these results are often important and a good agreement between numerical simulations and experiment are usually obtained by tuning the material parameters.

Inverse determination of the evolution laws of internal variables (modeling damage, plasticity) using a structural simulation is delicate. Moreover, impact on bilayered configurations has several drawbacks, e.g. it is difficult to obtain direct observation of the damage zone evolution during impact and only post–mortem observations can give some indication on the crack density and orientation (Tranchet, 1994). The use of stress gauges is also difficult because of their sensitivity to the tensile stress that appears after the sign inversion of the stress component during the damage process. Another problem is the influence of the glue thickness (James, 1995) between the front and back layers which often modifies the local and global responses of the bilayered specimen.

EDGE–ON IMPACT CONFIGURATION

A quantitative information on the location and evolution of damage can be obtained by an "edge–on" impact configuration developed by E.M.I. (Straßburger and Senf, 1995). A 30 mm in diameter blunt projectile impacts a ceramic tile of 100x100x10 mm^3. The velocity of the impactor varies within the range [20m/s ; 1000m/s] and produces in the ceramic a zone of complete fragmentation. One can check after impact that the failure pattern of the complete armor and the edge–on impact configuration is comparable as shown in Fig. 1. Orientation of cracks and crack front propagation are consistent with a generation of damage by the tensile hoop stress that follows the longitudinal compressive wave (Riou, 1996).

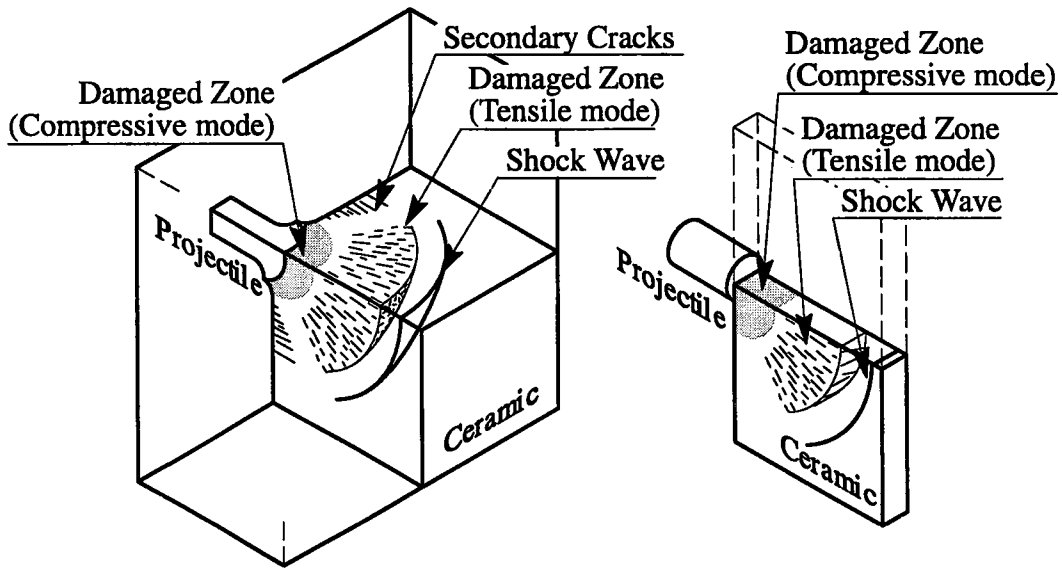

Fig. 1. Morphology of damage in a real configuration and in an edge–on impact specimen.

High speed camera pictures provide some indications on crack orientations and are helpful to understanding the damage evolution. This impact test can be used to identify damage mechanisms by a comparison of experimental and simulated values of the crack front velocity.

1D NUMERICAL SIMULATIONS WITH DAMAGE IN TENSION

To simplify the numerical simulations of edge–on impact, some stress components are not considered. First, the stress wave geometry is assumed to be cylindrical in the edge–on impact and spherical in the real impact in the bulk of the ceramic, even though a complex stress wave is observed near the impact surface as shown in Figs. 2 and 3. Second, the influence of stress propagation in the thickness of the edge–on impact is assumed to be weak (i.e. the tile is in equilibrium

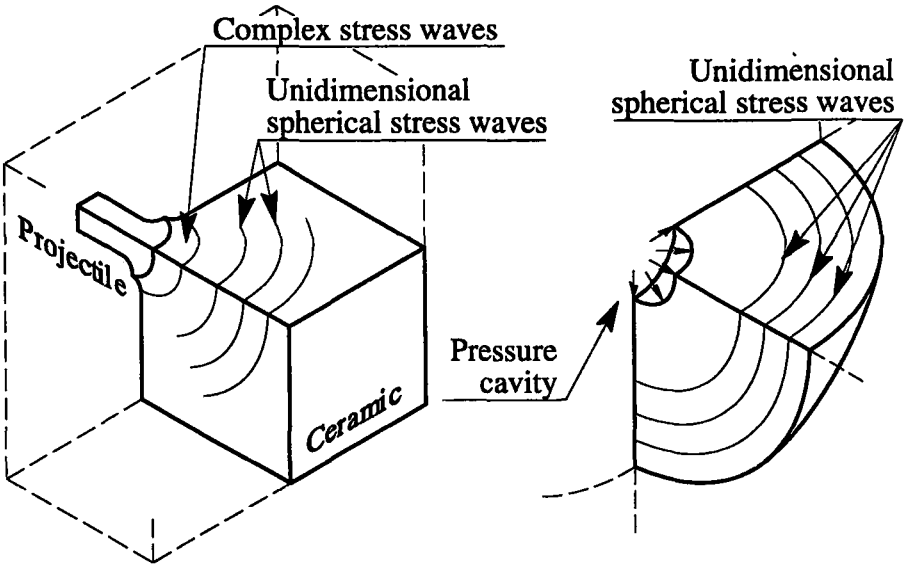

Fig. 2. Real and simulated stress wave geometry in an impact on a three dimensional structure.

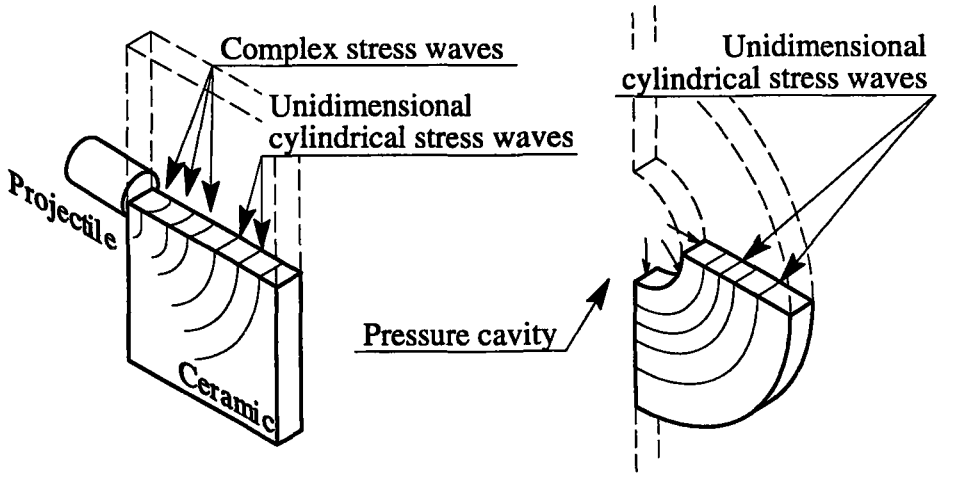

Fig. 3. Real and simulated stress wave geometry in an edge–on impact configuration.

in the thickness) and allows a one–dimensional description of impact. Since the stress which propagates in the thickness is proportional to the Poisson's ratio, this assumption is particularly good for low Poisson's ratio materials such as ceramics. Third, the stress reflections on the boundary of the specimen are not considered during the generation of damage. The simulated targets can then be described as semi–infinite volumes. The stress wave is assumed to be one–dimensional behind the pressure cavity and its radius can be approximated by the diameter of the impactor by analyzing EMI and CREA results (Riou, 1996). The pressure used in the 1D simulation can be defined in terms of magnitude and release time by a complex analysis of stress wave propagation near the projectile in the ceramic. This study is not the focus of the present paper and all the further computations will be performed with a constant pressure in order to give qualitative results.

The damage variable D due to cracking is dimensionless and lies within the range [0; 1]. It is assumed to follow the same evolution law both in cylindrical and spherical stress loading geometry and its description can be split in two parts. First, isotropic or anisotropic behavior for the dam-

aged material is chosen. Second, a damage evolution law developed in the framework of Continuum Damage Mechanics is proposed. Since a dimensionless description of impact is chosen, the above–mentioned law must be strain rate independent (Anderson *et al.*, 1993). If the material density ρ is assumed to be constant, the strain tensor ε and the the damage energy release rate Y can be derived from the Gibbs's specific enthalpy $\phi_e(\sigma,D)$

$$\rho\phi_e = \frac{1}{2}\,\sigma_{ij}\,S_{ijkl}(D)\,\sigma_{kl} \tag{1}$$

$$\varepsilon_{ij} = \rho\frac{\partial\phi_e}{\partial\sigma_{ij}} \quad ; \quad Y = \rho\frac{\partial\phi_e}{\partial D} \tag{2}$$

where S_{ijkl} is the four order compliance tensor, σ_{ij} the stress tensor, D the damage variable. Crack closure (D=0) is described by an activation–deactivation formulation. To give a description of this mechanism, the principal stress components σ_i can be split into positive and negative parts

$$\sigma_i = \langle\sigma_i\rangle - \langle-\sigma_i\rangle \quad with \quad \begin{cases}\langle x\rangle = x & \text{if} \quad x \geq 0\\ \langle x\rangle = 0 & \text{if} \quad x < 0\end{cases} \tag{3}$$

The enthalpy density $\phi_e(\sigma,D)$ can be written as follows (Lemaitre, 1992)

$$\rho\phi_e = \frac{1}{2E}\Big[(1+\nu)\langle\sigma_{ij}\rangle\langle\sigma_{ij}\rangle - \nu\langle\sigma_{kk}\rangle^2\Big] + \frac{1}{2E}\Big[(1+\nu)\langle-\sigma_{ij}\rangle\langle-\sigma_{ij}\rangle - \nu\langle-\sigma_{kk}\rangle^2\Big] \tag{4}$$

The stress wave propagation geometry implies that the shear stress components are equal to zero, i.e. only the radial stress σ_{rr} and hoop stress $\sigma_{\theta\theta}$ are used. For an isotropic damage description, Eqn. (4) becomes

$$\begin{aligned}\rho\phi_e = {} & \frac{1}{2E(1-D)}\Big[\langle\sigma_{rr}\rangle^2 + (1+\alpha)(1-\alpha\nu)\langle\sigma_{\theta\theta}\rangle^2 - 2(1+\alpha)\langle\sigma_{rr}\rangle\langle\sigma_{\theta\theta}\rangle\Big]\\ & + \frac{1}{2E}\Big[\langle-\sigma_{rr}\rangle^2 + (1+\alpha)(1-\alpha\nu)\langle-\sigma_{\theta\theta}\rangle^2 - 2(1+\alpha)\langle-\sigma_{rr}\rangle\langle-\sigma_{\theta\theta}\rangle\Big]\end{aligned} \tag{5}$$

and for an anisotropic description

$$\rho\phi_e = \frac{1}{2E}\left[\sigma_{rr}^2 + (1+\alpha)\left\{\left(\frac{1}{1-D} - \alpha\nu\right)\langle\sigma_{\theta\theta}\rangle^2 + (1-\alpha\nu)\langle-\sigma_{\theta\theta}\rangle^2\right\} - 2(1+\alpha)\sigma_{\theta\theta}\sigma_{rr}\right] \tag{6}$$

where α is equal to 1 for the spherical geometry and zero for the cylindrical one. The energy release rate density Y is derived from Eqns. (2), (5) and (6) and with an isotropic damage description is expressed as

$$Y = \frac{1}{2E}\frac{1}{(1-D)^2}\Big[\langle\sigma_{rr}\rangle^2 + (1+\alpha)(1-\alpha\nu)\langle\sigma_{\theta\theta}\rangle^2 - 2(1+\alpha)\langle\sigma_{rr}\rangle\langle\sigma_{\theta\theta}\rangle\Big] \tag{7}$$

and with an anisotropic damage description, the latter is given by

$$Y = \frac{(1+\alpha)}{2E}\frac{\langle\sigma_{\theta\theta}\rangle^2}{(1-D)^2} \tag{8}$$

Invoking the normality principle, the ratio of change for damage is

$$\dot{D} = \dot{\lambda}\frac{\partial f}{\partial Y} \tag{9}$$

where f is the damage criterion function and $\dot{\lambda} \geq 0$ is the damage multiplier. The loading/unloading conditions are formulated in Kuhn–Tucker form as

$$\dot{\lambda} \geq 0 \; ; \; f \leq 0 \; ; \; \dot{\lambda}f = 0 \tag{10}$$

where the actual value of $\dot{\lambda}$ is determined from the consistency requirement

$$\dot{\lambda}\dot{f} = 0 \tag{11}$$

An expression for the damage criterion function was proposed by Marigo (1981)

$$f = Y - Y_t(1 + mD) \tag{12}$$

where m is a strictly positive and dimensionless parameter and Y_t a threshold value. Equations (9), (11), (12) lead to

$$\dot{D} = \frac{\dot{Y}}{mY_t} \quad \text{if } f = 0 \tag{13}$$

When the value of m approaches zero, the damage evolution law can be associated to an instantaneous damage onset. If m approaches infinity, no damage occurs. The energy release rate density threshold is evaluated by means of a threshold stress σ_t obtained in a tensile test

$$Y_t = \frac{\sigma_t^2}{2E} \tag{14}$$

A 1D code for stress wave propagation both in spherical and cylindrical geometry of propagation is written to study damage descriptions and evolution laws. The code is based on a finite difference Lagrangian formulation and has been successfully validated by comparing the simulation with the analytical solution of a spherical cavity of radius a under rapid pressurization (Achenbach, 1993). The stability of the computation is obtained by a linear and quadratic viscosity described by Wilkins (1979).

SCALE DEPENDENCE

The damage constitutive law will be used for several scales and it is preferable to use normalized variables for simulations and experiments to analyze damage evolution laws. The target can be defined by many material or geometric parameters, e.g. diameter of impactor or tensile strength (as listed in Table 1) which are employed to normalize strain, stress, time and length variables.

Table 1. Reference parameters

Projectile diameter	2a
Sound celerity	C_L
Material density	ρ
Poisson's ratio	ν
Tensile strength	σ_t

The dimensionless variables used in the simulation are given in Table 2. The lengths are normalized with respect to the pressure cavity radius "a" which is estimated to be close to the projectile radius. To have comparable chronology while damage grows, the time is normalized wrt the propagation time of the longitudinal stress wave in the characteristic length. Since the same mechanisms are assumed to initiate for targets made of different materials, the stress is normalized by a characteristic stress, e.g. the tensile threshold stress σ_t. The Young's modulus E is calculated by employing the sound celerity, the Poisson's ratio and the material density. The characteristic strain is calculated using the hypothesis of 1D propagation geometry with $\alpha = 1$ for the spherical case and $\alpha = 0$ for the cylindrical one. The damage energy release rate is normalized by the threshold value Y_t.

In the area of compressive damage generation near the projectile, the stress can be assumed to be less than or equal to the compressive strength. In the simulation, the stress in the pressure cav-

ity (where no damage in compression can occur) is set to the maximum stress which can appear in this zone, i.e. to the compressive strength. Many ceramics have a compressive strength of one magnitude higher than their tensile strength. To give qualitative results, the compressive strength is assumed to be constant with pressure and the ratio between tensile and compressive strength of the impacted material is taken equal to one tenth.

Table 2. Dimensionless variables

Parameters	Characteristic Variables	Dimensionless Variables
Length	$L_c = a$	$\overline{L} = \frac{L}{a}$
Time	$T_c = \frac{a}{C_L}$	$\overline{T} = \frac{T}{a} C_L$
Stress	$\sigma_c = \sigma_t$	$\overline{\sigma} = \frac{\sigma}{\sigma_c}$
Strain	$\varepsilon_c = \varepsilon_t = \frac{(1+\nu)(1-2\nu)}{1-\nu+(a-1)\nu^2} \frac{\sigma_t}{E}$	$\overline{\varepsilon} = \frac{\varepsilon}{\varepsilon_t}$
Velocity	$V_c = \frac{L_c}{T_c} = C_L$	$\overline{V} = \frac{V}{C_L}$
Damage energy threshold	$Y_c = \frac{\sigma_t^2}{2E} = Y_t$	$\overline{Y} = \frac{Y}{Y_t}$

RESULTS

To compare the evolution of radial and hoop strains, a first result is given in a strain–time diagram at a constant location in the ceramic. The most interesting mechanisms can be studied in a diagram taken at a radius of two times the pressure cavity radius as shown in Fig. 4. Isotropic, anisotropic and undamaged behaviors are plotted using different values of the damage parameter m for a spherical geometry. All the variations between instantaneous damage generation for both isotropic and anisotropic descriptions and the elastic material can be obtained by changing the value of the damage parameter. In the isotropic case, it can be found that the damage increases in a smooth way only for values of m greater than 50. The evolution of the damaged zone radius versus time is shown in Fig. 5. The general shape of this curve is similar for spherical and cylindrical geometries even though the damage generation decreases more rapidly in the spherical case. One of the main result is the difference between isotropic and anisotropic damage evolutions. With an isotropic behavior, the damage zone increases by steps and an arrest time always follows a fast evolution time. Moreover, this evolution finally stopped not far from the pressure cavity. These curves can be opposed to the gradual evolution of the damaged zone with the anisotropic description of damage, which leads to a large damaged zone of many times the radius of the pressure cavity. The evolution of the crack front velocity is shown in Fig. 6 for several values of the damage parameter m with an anisotropic description. The results in the spherical and cylindrical geometry are bounded by the crack front velocity obtained with an instantaneous damage generation.

The damaged zone in the experimental edge–on impact is found to increase with a constant velocity during all the damage evolutions in a SiC–B supplied by Cercom ceramics (Straßburger, 1995). The crack front velocity depends on the impactor velocity and varies from 50% up to 90% of the sound celerity. One can notice that only the anisotropic damage description provides the

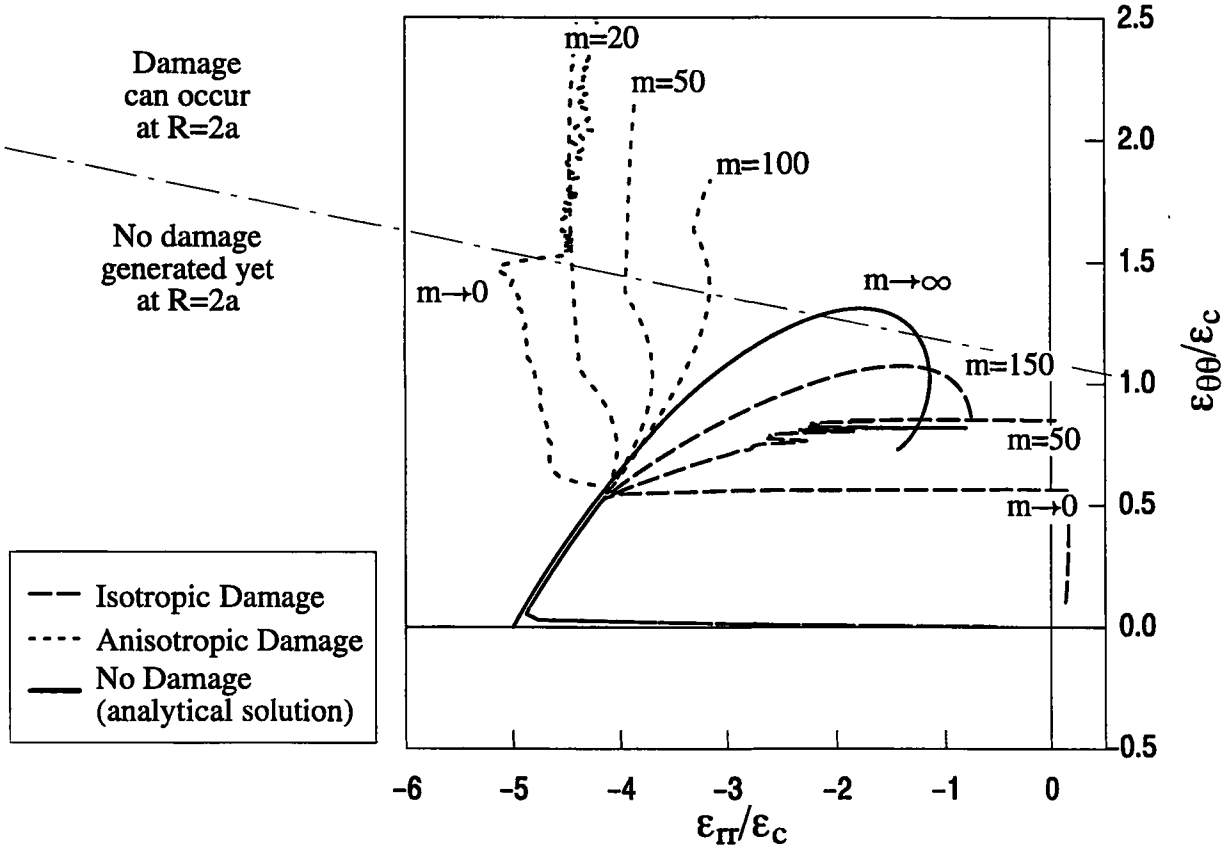

Fig. 4. Normalized radial and hoop strains for several damage parameter taken at a radius R=2a for a spherical geometry

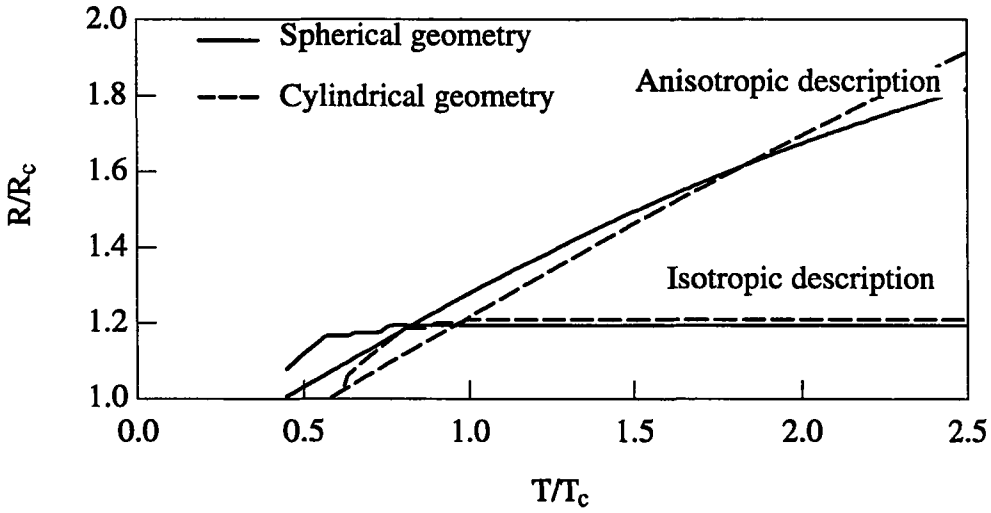

Fig. 5 Normalized damage zone size versus normalized time for m=20

same damaged zone evolution in the simulation, even though a large range of damage parameter values were tested.

DISCUSSION

Without any consideration on the damage evolution law, an important difference between isotropic and anisotropic behavior is found regarding the final damage zone size. In particular, the

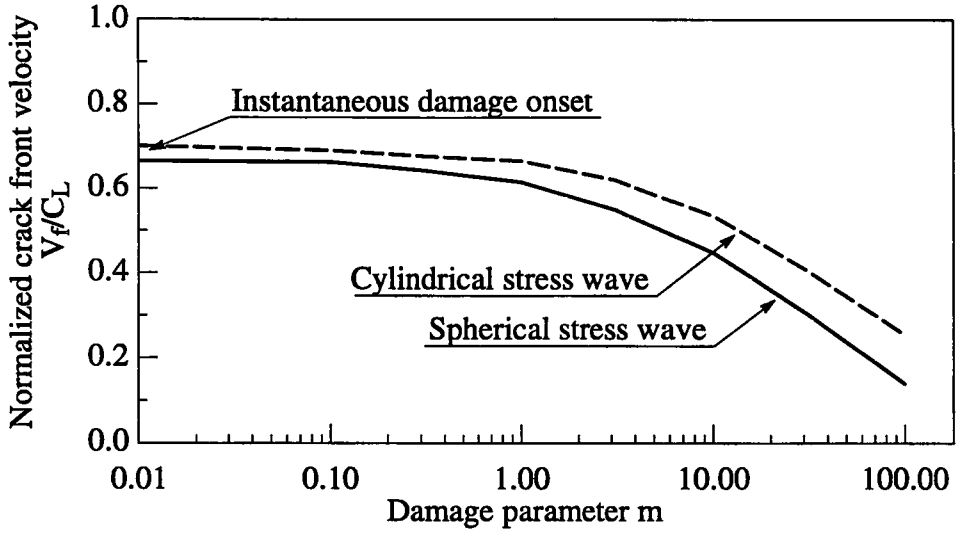

Fig. 6 Normalized crack front velocity versus damage parameter for an anisotropic description of damage.

isotropic description of the damaged material leads to an unrealistic cracked zone size. An explanation of the mechanism which makes the damaged zone grow or stop can be proposed using the radial–hoop stress diagram.

An evolution of strain before any damage generation can be observed for all the curves in Fig. 4. The stress evolutions can be explained in a two dimension graph by dividing the stresses into two components as shown in Fig. 7. A radial loading generated by the stress wave appears first and

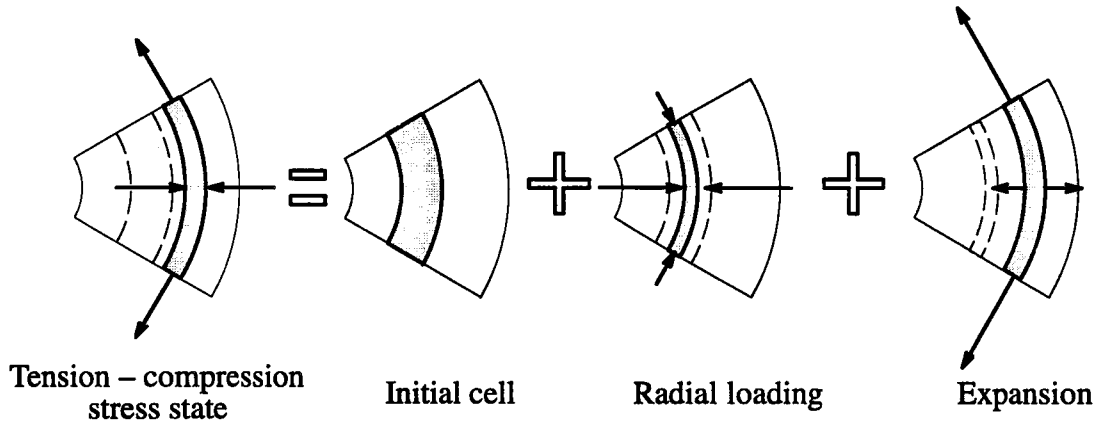

Fig. 7. The tension–compression stress state can described as a superposition of stress due to a radial expansion and stress due to a radial loading.

leads to radial strains only (the hoop strain remains equal to zero). Second, the radial motion induced by the stress wave produces a cylindrical (or spherical) expansion of the material and makes the hoop strain become positive. It can be noticed that both expansion and radial loading produce stresses in radial and hoop directions due to the coupling by the Poisson's ratio. Moreover, when isotropic damage occurs in a brittle material (i.e. with an instantaneous damage generation, $m \to 0$), the stress state can be described as the sum of stresses in the undamaged material, a radial unloading and a hoop loading as depicted in Fig. 8. The global stress evolution induced in the radial direction can then be described as a high radial stress unloading. Since the crack front velocity is less than the sound celerity in the undamaged material, the stress evolution in the dam-

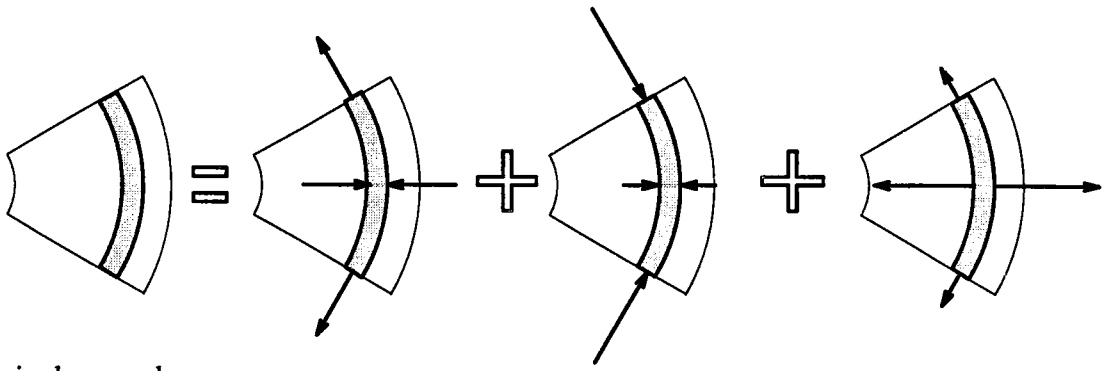

Fig. 8. The stress relaxation can be split into a fictitious hoop and radial loading.

aged material produces a stress modification in front of the damaged zone and a high unloading can be observed before any damage generation as it is shown in Fig. 4. If the relaxation wave is high enough to unload the hoop stress in the undamaged material, the damage generation is stopped (Fig. 5).

The previous feature cannot be observed with an anisotropic damage description. When damage occurs instantaneously, only the hoop stresses are released and the stress state can be described as the sum of the stress in the undamaged material and a hoop loading (Fig. 9). When damage

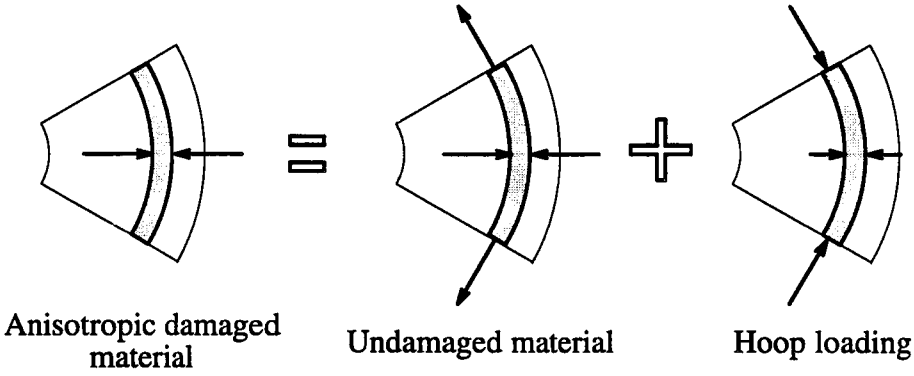

Fig. 9. The stress relaxation can be described as a hoop loading

occurs (i.e. when a hoop loading is added), the stress evolution in the radial direction is a slightly increased due to both the coupling of radial and hoop stresses through the Poisson's ratio and the projection of hoop stresses on the radial axis. The reloading intensifies the radial stresses and makes the hoop stresses increase more rapidly, i.e. damage onset amplifies the stresses, themselves increasing the damage generation. Therefore the damage generation is not stopped (Fig. 5).

CONCLUSIONS

A simple damage evolution law is proposed and allows to model a large range of damage generation, from a slow evolution to an instantaneous one. Isotropic and anisotropic damage descriptions are implemented and used in spherical and cylindrical stress wave geometries. It can be shown that only anisotropic damage descriptions can provide realistic crack front propagation.

An isotropic description leads to a rapid attenuation of the stress wave and prevents the damage propagation. In the anisotropic case, the stresses are amplified by a reloading due to damage onset. These results are obtained for a large range of damage parameters for cylindrical and spherical geometries.

ACKNOWLEDGMENT

This work was supported by DGA/DRET/STRDT (Délégation Générale pour l'Armement, Direction de la Recherche et de la Technologie, Service Technique des Recherches et Développements Technologiques).

REFERENCES

Achenbach, J. D. (1993). Wave Motions with Polar Symmetry. In: *Wave Propagation in Elastic Solids* (North Holland ed.), pp 129–132.

Anderson, C. E. Jr, S. A. Mullin and C. Kuhlman (1993). Computer Simulation of Strain–Rate Effects in Replica Scale Model Penetration Experiments. *Int. J. Impact Engng.*, **13** (1), pp 35–52.

Cosculluela, A. (1992). Plasticité, endommagements et ruptures des alumines sous sollicitations dynamiques triaxiales: influence de la taille des grains. PhD Dissertation, University of Bordeaux I.

James, J. (1995). Modification of Ceramic Failure in Impact by Stress Wave Management. In: Proc. Lightweight Armour Systems Symp., Session 3, paper 7, UK.

Lemaitre, J. (1992). A Course on Damage Mechanics. Springer–Verlag, Berlin.

Marigo, J. J. (1981). Formulation d'une loi d'endommagement d'un matériau élastique. C. R. Acad. Sci. Paris, t. 292, Série **II**, pp 1309–1312.

Riou, P. (1996). Contribution à l'étude de l'endommagement du Carbure de Silicium lors d'un impact basse énergie. PhD Dissertation, Ecole Nationale Supérieure des Mines de Paris.

Straßburger, E. and H. Senf (1995). Experimental Investigations of Wave and Fracture Phenomena in Impacted Ceramics and Glasses. Report, Army Research Laboratory, Aberdeen Proving Ground, MD 21005–5066.

Tranchet, J. Y. (1994). Comportement de deux matériaux fragiles polycritallins sous l'effet de la propagation d'une onde sphérique divergente. PhD Dissertation, University of Bordeaux I.

Wilkins, M. L. (1979). Use of Artificial Viscosity in Multidimensional Fluid Dynamic Calculations. *J. Comp. Phys.*, **36**, pp 281–303.

3.1.2 Fragmentation de céramiques sous impact

par C. DENOUAL, G. BARBIER et F. HILD (1997).
C. R. Acad. Sci. Paris, Série IIb (t. 325), pp. 685-691.

C. R. Acad. Sci. Paris, t. 325, Série II *b*, p. 685-691, 1997
Mécanique des solides et des structures/*Mechanics of solids and structures*

A probabilistic approach for fragmentation of brittle materials under dynamic loading

Christophe DENOUAL, Gilles BARBIER and François HILD

C. D. : Département Matériaux en Conditions Sévères, DGA/CREA, 16 bis, avenue Prieur de la Côte d'Or, 94114 Arcueil cedex ;

G. B. : Département MTC, EDF/DER, Centre des Renardières, BP 1, Écuelles, 77250 Moret-sur-Loing ;

F. H. : Laboratoire de Mécanique et Technologie, ENS de Cachan/CNRS/Université Paris-VI, 61, avenue du Président-Wilson, 94235 Cachan cedex, France.

Abstract. Dynamic loadings produce high stress waves leading to the fragmentation of brittle materials such as ceramics. The main mechanism used to explain the change of the number of fragments with stress rate is an obscuration phenomenon. After the presentation of a probabilistic approach, the evolution of the number of nucleated flaws and a damage model are derived.

Keywords: boolean random function / brittle materials / damage / fragmentation / impact / obscuration / probabilistic approach

Approche probabiliste de la fragmentation de matériaux fragiles sous chargement dynamique

Résumé. *Une sollicitation dynamique ou par explosions de matériaux fragiles conduit à leur fragmentation. Dans cette note, un modèle de fragmentation dynamique pour matériaux fragiles est proposé sur une base probabiliste. Un modèle d'endommagement est également discuté. Le principal mécanisme invoqué pour expliquer la variation en nombre de fragments est un phénomène d'occultation des défauts entre eux.*

Mots clés : *fonction booléenne aléatoire / matériaux fragiles / endommagement / fragmentation / impact / occultation / approche probabiliste*

Version française abrégée

La fragmentation est souvent observée dans les matériaux fragiles sollicités dynamiquement, soit par impact sur des blindages en céramique, soit par explosion de structures coques. Dans cette note, on s'intéresse à l'endommagement par fissuration en mode I de structures fragiles, en étudiant la probabilité de rupture des défauts en fonction des défauts environnants déjà rompus. En effet, la rupture d'un défaut entraîne une relaxation locale des contraintes (*fig. 1*) qui peut interdire la rupture (ou *occulter*) d'autres défauts. L'interaction entre les défauts susceptibles de rompre et cette zone d'occul-

Note présentée par André ZAOUI.

1251-8069/97/03250685

C. Denoual, G. Barbier and F. Hild

tation permet de comprendre pourquoi une fissure peut (ou ne peut pas) s'amorcer sur un défaut. Lorsque le défaut considéré est loin du défaut déjà rompu, la contrainte locale n'est pas affectée. En revanche, quand le défaut est dans la zone affectée par la nucléation du premier et que la contrainte locale est décroissante, aucun amorçage ne peut alors se produire dans cette zone. Ces interactions sont décrites dans un graphe « espace-temps » où l'on représente en abscisse l'espace (dont la dimension n est égale à 1, 2 ou 3) et où l'ordonnée représente le temps (*fig. 2*). Dans l'exemple proposé, les défauts 1 et 2 rompent et produisent des zones d'occultation qui interdisent la nucléation des défauts 3 et 4. Pour définir les zones dans lesquelles les défauts peuvent rompre, il est préférable d'*inverser* le problème en définissant les conditions de non-occultation pour un défaut donné, *i.e.* de regarder dans le passé d'un défaut susceptible de rompre si un défaut existe dans son *horizon* (*fig. 3*). Le nombre moyen de défauts susceptibles de rompre (noté μ_t et supposé poissonnien) peut être divisé en un ensemble de défauts occultés, noté μ_o, et un ensemble de défauts rompus, noté μ_b [éq. (1)]. La densité moyenne de défauts λ est définie par (2). L'équation différentielle (3) donne l'évolution de la variable λ_b en fonction de λ_t en connaissant la probabilité de non-occultation P_{no} (définie en (4), où $Z_i^{(n)}$ est une mesure de la zone d'interaction au temps t pour un défaut critique à T). La variable λ_b est proche de λ_t au début du chargement, mais devient par la suite très inférieure à λ_t pour T grand. Cette approche est confortée par l'existence d'une écriture identique utilisant le modèle d'*îles booléennes* (Serra, 1982 ; Jeulin, 1985). La probabilité d'être dans une zone non occultée s'exprime alors par l'intermédiaire de la taille moyenne des zones occultées au temps T, notée $\mathcal{M}^{(n)}(T)$ [éqs. (5) et (6)].

On suppose les zones d'interactions homothétiques (Bluhm, 1969 ; Freund, 1972) et être de la forme (7) avec $k \in]0,1]$ un paramètre de forme et C la célérité des ondes. La variable μ_t peut être estimée à partir d'une distribution en loi puissance à deux paramètres (8), où m est le module de Weibull et S_0 un paramètre d'échelle relatif à la zone de référence de mesure $Z_0^{(n)}$. Pour une vitesse de contrainte $\dot{\sigma}$ constante, une écriture adimensionnée de la densité de défauts $\bar{\lambda}$, du temps $\bar{T}$, de la mesure de zone $\bar{Z}^{(n)}$ et de la contrainte $\bar{\sigma}$ est proposée à l'aide de (9), où l'indice c indique une grandeur caractéristique.

Une première application est la densité de défauts rompus dont l'évolution est donnée en (10) dans le cas d'une vitesse de contrainte $\dot{\sigma}$ constante, où γ est la fonction gamma incomplète et $\binom{m+n}{m} = (m+n)!/(m!\,n!)$. Dans les résultats présentés sur la *figure 4*, le phénomène de saturation n'est dépendant que du module de Weibull m et de la dimension de l'espace n.

Une deuxième application est la définition d'une variable d'endommagement dans le cadre de la mécanique des milieux continus. En effet, sur une zone représentative, on peut écrire $D = 1 - P_{no}$. Il apparaît que l'équation différentielle proposée par Grady et Kipp (1980) pour décrire l'évolution de la variable d'endommagement est le premier ordre de l'équation (4). L'évolution de D est alors décrite par (11) en utilisant (4) et (7). En remarquant que l'évolution de D (de 0 à 1) est limitée à un intervalle de temps de t_c, la mesure de la zone représentative associée à D devient égale à la mesure de la zone caractéristique $Z_c^{(n)}$. Pour une vitesse de contrainte $\dot{\sigma}$ constante, une expression de D est définie par (12) à l'aide de (11) et (8). Une contrainte macroscopique Σ peut être définie (en opposition à la contrainte locale ou effective σ) par $\sigma = \Sigma/(1-D)$. Cette contrainte est maximale ($d\Sigma/d\sigma = 0$) pour la valeur donnée en (13).

---

1. Introduction

A probabilistic fragmentation analysis can be performed on brittle structures submitted to high tensile stress rate loading. Dynamic fragmentation occurs, for example, in an impacted ceramic. In the

bulk of the ceramic, damage in tension is observed when the hoop stress induced by the radial motion is sufficiently large to generate fracture in mode I initiating on micro-defects such as porosities or inclusions. Another situation is the explosion of 2D structures (impact on plate, exploding spherical shell) which generates a wide range of fragments. In this note, it is proposed to model fragmentation in brittle materials for which a time-dependent microscopic stress is applied. To study the fragmentation problem, it is assumed that the macroscopic stress state is homogeneous throughout the whole body. When a fracture is initiated in mode I, the local stress state is modified around the crack by a stress relief wave which is a complex function of time, crack velocity and stress wave celerity (*fig. 1*). To understand why a crack nucleates, one has to model the interaction of the zone (*i.e.*, volume, surface or length) affected by the stress relief and other defects that would nucleate. The behavior of a flaw around a nucleated one can be described by two different cases:

- the flaw is far from the nucleated one and the microscopic stress state is not affected;
- the flaw is in the interaction zone and the microscopic tensile stress is decreasing, *i.e.*, no cracks are emanating from this potential initiation site.

A third case may occur in which the flaw is in the affected zone but the local tensile stress increases, *i.e.*, initiation may occur. It is assumed that this case is insignificant in this problem.

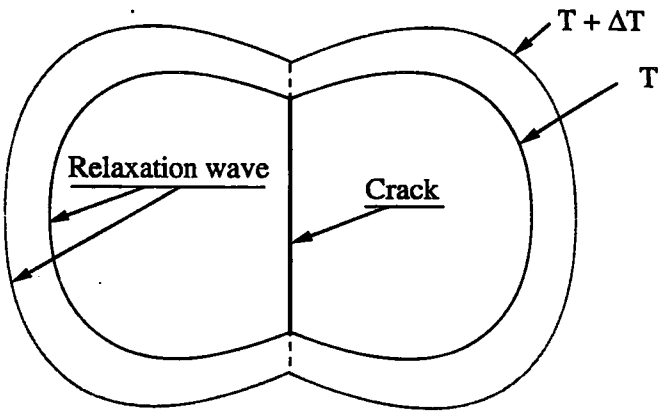

Fig. 1. – Relaxation around a propagating crack at time T and $T + \Delta T$.

Fig. 1. – Relaxation autour d'une fissure qui se propage à un instant T et $T + \Delta T$.

2. Probabilistic approach

The direction of the microscopic maximum principal stress is assumed to be constant, which allows to use $\sigma = \max [\sigma_1, \sigma_2, \sigma_3]$ instead of the stress tensor as an equivalent failure stress. The flaw nucleation can be represented on a space–time graph (*fig. 2*). The space locations of the defects are represented in a simple abscissa (instead of a three-, two- or one-dimensional representation) of an x–y graph where the y-axis represents the time (or stress) to failure of a given defect. The first crack nucleation occurs at time T_1 (corresponding to a stress $\sigma[T_1]$) at the space location M_1 and produces an 'obscured zone' $Z_i(T - T_1)$ increasing with time. At time T_2 (corresponding to a stress $\sigma[T_2] > \sigma[T_1]$) a second defect nucleates in a non-affected zone and produces its own obscured zone. The third and fourth defects do not nucleate because they are obscured by the first and both first and second defects, respectively. It is worth noting that the stress levels in overlapping obscured zones cannot be greater than the highest initiation stress associated to the considered obscured zones. The space–time graph is composed of the *union* of obscured zones in which no flaws can initiate and the complementary zone in which defects can nucleate. Because different obscured

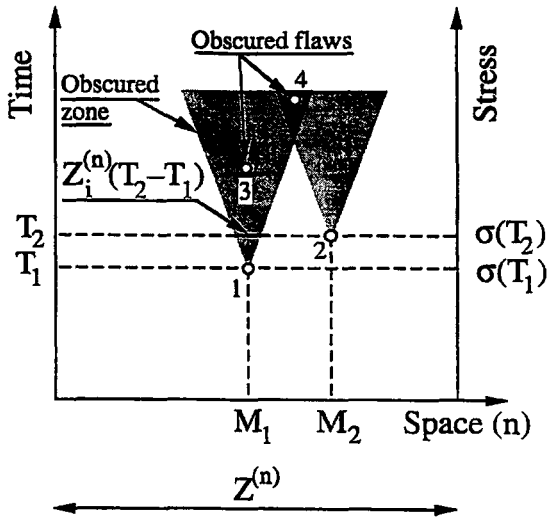

Fig. 2. – Fragmentation and obscuration phenomena.

Fig. 2. – Phénomènes de fragmentation et d'obscurcissement.

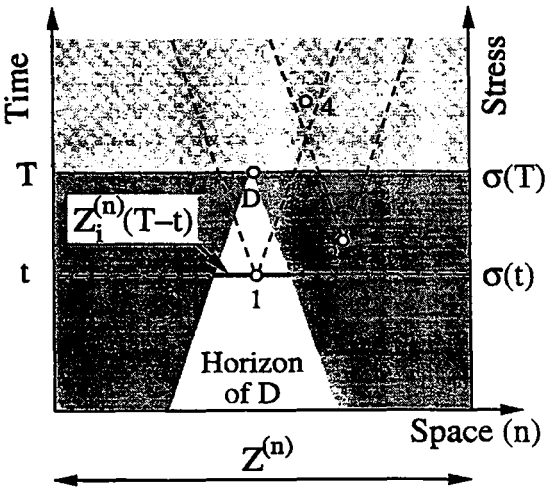

Fig. 3. – Schematic of the horizon of a defect D.

Fig. 3. – Schéma de l'horizon d'un défaut D.

zones may overlap (*i.e.*, a flaw can be obscured by one or more cracks), it is preferable to define the conditions of non-obscuration for a given defect by examining the *inverse* problem. It consists of considering the past history of a defect that would break at a time T. The defect will break if no defects exist in its *horizon*. For a given flaw D its horizon is defined as a space–time zone in which a defect will always obscure D (*fig. 3*). Outside the horizon a defect will never obscure D.

The flaw distribution can be split into two parts and the average number of broken flaws can be written as

$$\mu_b(T, Z^{(n)}) = \mu_t(T, Z^{(n)}) - \mu_o(T, Z^{(n)}) \tag{1}$$

where $\mu(T, Z^{(n)})$ denotes the mean number of flaws that may break in a zone of measure $Z^{(n)}$ (*i.e.*, volume ($n = 3$), surface ($n = 2$) or length ($n = 1$)) for a stress greater than or equal to $\sigma(T)$. The subscripts indicate the effectively broken flaws (b), the obscured flaws (o), and the total number of flaws able to break (t). The number of flaws μ is normalized by $Z^{(n)}$ to define the average flaw density $\lambda(T)$

$$\mu(T, Z^{(n)}) = Z^{(n)}\,\lambda(T). \tag{2}$$

Furthermore, we assume that the distribution of total flaws is modeled by a Poisson point process of intensity μ_t. New cracks will initiate only if the defect exists in the considered zone and if no defects exist in its horizon so that

$$\frac{d\lambda_b}{dt}(T) = \frac{d\lambda_t}{dt}(T)\,P_{no}(T) \quad \text{with} \quad \lambda_b(0) = \lambda_t(0) = 0 \tag{3}$$

where P_{no} is the probability that no defects exist in the horizon. An equivalent form for equation (3) can be found in Jeulin (1985). The variable P_{no} can be split into an infinity of events defined by the probability of finding at t a new defect during a time step dt in an interaction zone $Z_i^{(n)}(T-t)$.

This probability increment is written by using a Poisson point process of intensity $d\lambda_t/dt$. Those *independent events* can be used to provide an expression for P_{no}

$$P_{no}(T) = \exp\left[-\int_0^T \frac{d\lambda_t}{dt}(t)\, Z_i^{(n)}(T-t)\, dt\right] \tag{4}$$

where $Z_i^{(n)}(T-t)$ is the measure of the interaction zone at t for a defect that would break at T. At the beginning of loading, no interactions occur and $\lambda_b(T) \simeq \lambda_t(T)$ and as more and more defects nucleate $\lambda_b(T) << \lambda_t(T)$. It is expected that the density of broken flaws saturates when $T \to \infty$ even though the total density of flaws able to break may approach infinity. Equation (4) can be derived by using results of mathematical morphology. The probability of being in a non-obscured zone (P_{no}) is expressed through the mean obscuration zone $\mathcal{M}^{(n)}(T)$. This zone is calculated by averaging at time T the section of the obscured zones $Z_i^{(n)}(T-t)$ for a nucleation at time t and with density $\frac{1}{\lambda_t(T)}\frac{d\lambda_t}{dt}(t)$. The mean obscuration zone can then be expressed as

$$\mathcal{M}^{(n)}(T)\,\lambda(T) = \int_0^T \frac{d\lambda_t}{dt}(t)\, Z_i^{(n)}(T-t)\, dt \tag{5}$$

so that

$$P_{no}(T) = \exp[-\mathcal{M}^{(n)}(T)\,\lambda_t(T)]\,. \tag{6}$$

Equation (6) is the result obtained for the *boolean islands* model (Serra, 1982).

3. Applications

Usually, the interaction zone cannot be assumed as a time-constant variable and since no analytical expressions are available for $Z_i^{(n)}$, an approximation will be proposed. The shape of the interaction zone is supposed to be constant, *i.e.*, all the interaction zones are self-similar (Bluhm, 1969; Freund, 1972) and $Z_i^{(n)}$ can be written as

$$Z_i^{(n)}(T-t) = [kC(T-t)]^n \quad \text{with} \quad n = 1, 2, 3 \tag{7}$$

where $k \in\,]0, 1]$ is a shape parameter, C the longitudinal stress wave velocity so that $kC(T-t)$ is a representative length of the relaxation zone around a broken flaw. The static description of fracture in brittle materials can be given by a two-parameter Weibull model. The mean number of flaws able to break for a stress less than or equal to σ is then assumed to follow a power law function

$$\mu_t(T, Z^{(n)}) = \frac{Z^{(n)}}{Z_0^{(n)}}\left[\frac{\sigma(T)}{S_0}\right]^m \tag{8}$$

where m is the Weibull modulus and S_0 the scale parameter relative to the measure of a reference zone $Z_0^{(n)}$.

When dynamic loadings are considered with a constant stress rate $d\sigma/dt = \dot{\sigma}$, one can define a dimensionless flaw density ($\bar{\lambda} = \lambda/\lambda_c$), time ($\bar{T} = T/t_c$), space measure ($\bar{Z}^{(n)} = Z^{(n)}/Z_c^{(n)}$) and stress ($\bar{\sigma} = \sigma/\sigma_c$) from the condition

$$\lambda_c\, Z_c^{(n)} = 1 \quad \text{with} \quad \lambda_c = \lambda_t(t_c) \quad \text{and} \quad Z_c^{(n)} = Z_i^{(n)}(t_c) \tag{9}$$

where the subscript c denotes characteristic quantities. A characteristic stress can be defined by $\sigma_c = \dot{\sigma} t_c$. Equation (9) expresses the fact that the characteristic zone of measure $Z_c^{(n)}$ contains a unique flaw that may break at the characteristic time t_c.

3.1. *Fragmentation analysis*

By using equations (3), (4), (7) and (8) an analytical solution is proposed for the differential equation (3) in the case of a constant stress rate $\dot{\sigma}$:

$$\bar{\lambda}_b(\bar{T}) = \frac{m}{m+n}\binom{m+n}{m}\gamma\left[\frac{m}{m+n}, \frac{\bar{T}^{m+n}}{\binom{m+n}{m}}\right] \tag{10}$$

where γ is the incomplete gamma function and $\binom{m+n}{m}$ a binomial coefficient. The dimensionless density of broken flaws at saturation $\bar{\lambda}_b(\infty)$ can be derived from equation (10) and is only dependent on the Weibull modulus m and the space dimension n. *Figure 4* shows an increase of the number of broken flaws at saturation with the Weibull modulus m.

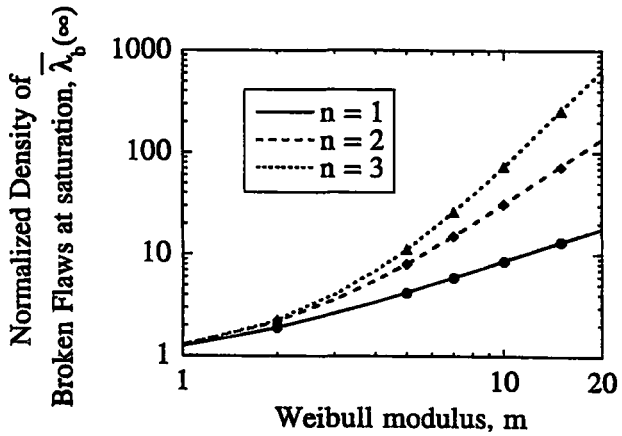

Fig. 4. – Normalized density of broken flaws at saturation versus Weibull modulus for different values of the space dimension n. The solid symbols show results obtained by Monte-Carlo simulations.

Fig. 4. – Évolution de la densité normée de défauts cassés en fonction du module de Weibull pour différentes valeurs de la dimension de l'espace n. Les symboles pleins correspondent à des résultats de simulations par la méthode de Monte-Carlo.

An explanation for this phenomenon can be proposed by using equation (3). With a high Weibull modulus m, the density of defects will increase dramatically in a small time step when the stress σ becomes larger than S_0. Because of the time dependence of the saturation mechanism, many defects nucleate before any significant saturation and the material will be fully fragmented. If m is small, there is much more time between two crack initiations. The first nucleated defects can then obscure others before their own nucleation and only few defects eventually nucleate. Lastly, the error between the Monte-Carlo simulations (300 realizations per computation) for a zone of measure $\bar{Z}^{(n)} = 100$ and the solution at saturation given in equation (10) is less than 0.5% (*fig. 4*).

3.2. *Damage evolution law*

The variable P_{no} can be used to define a damage variable in the framework of Continuum Damage Mechanics, even if P_{no} describes a non-homogeneous stress-field due to the randomness of fragmentation. By averaging over a representative zone (to be specified later), $1 - P_{no}$ is equal to

the damage variable D, with $D = 0$ for the virgin material and $D = 1$ for the fully broken one. It is interesting to notice that the first-order approximation of equation (4) leads to the differential equation proposed by Grady and Kipp (1980) to describe the evolution of a damage variable. By using equations (4) and (7), the evolution law of the damage variable D can be written as

$$\frac{d^{n-1}}{dt^{n-1}}\left(\frac{1}{1-D}\frac{dD}{dt}\right) = \lambda_t(t)\, n!\, (kC)^n . \tag{11}$$

An expression for the damage parameter D can be derived by integrating equation (11) in the case of a constant stress rate $\dot{\sigma}$:

$$D = 1 - \exp\left[-\frac{(\bar{\sigma})^{m+n}}{\binom{m+n}{m}}\right]. \tag{12}$$

Equation (12) shows that $D(\bar{T}=1) \cong 0$ and $D(\bar{T}=2) \cong 1$ (*i.e.*, most of the damage evolution occurs during a time interval equal to t_c). During t_c, the measure of the horizon is limited by $Z_i^{(n)}(t_c) = Z_c^{(n)}$ so that the *minimum* measure of the representative zone is $Z_c^{(n)}$. By noting that the applied stress Σ is related to the local (or effective) stress σ by $\sigma = \Sigma/(1-D)$, the ultimate strength ($d\Sigma/d\sigma = 0$) is denoted by Σ_{max} and is expressed as

$$\frac{\Sigma_{max}}{\sigma_c} = \left[\frac{\binom{m+n}{m}}{m+n}\right]^{\frac{1}{m+n}} \exp\left(-\frac{1}{m+n}\right). \tag{13}$$

It is worth noticing that the normalized ultimate strength only depends upon the Weibull parameter m and the space dimension n. The ultimate strength Σ_{max} is then proportional to $(\dot{\sigma})^{n/(m+n)}$.

Note remise le 2 octobre 1997, acceptée le 7 octobre 1997.

References

Bluhm J. I., 1969. Fracture Arrest, V, 1-63, in *Fracture*, H. Liebowitz (ed.), Academic Press, New York, USA.

Freund L. B., 1972. Crack Propagation in an Elastic Solid Subjected to General Loading – Constant Rate of Extension, *J. Mech. Phys. Solids*, 20, 129-140.

Grady D. E., Kipp M. E., 1980. Continuum Modeling of Explosive Fracture in Oil Shale, *Int. J. Rock Min. Sci. & Geomech. Abstr.*, 17, 147-157.

Jeulin D., 1985. Anisotropic Rough Surface Modeling by Random Morphological Functions, in *Proc. 4th Symp. on Stereology*, Göteborg (Sweden) and 1987, *Acta Stereol.*, 6, 183-189.

Serra J., 1982. *Image Analysis and Mathematical Morphology*, Academic Press, London (UK).

3.1.3 Lois d'évolution, identification et applications

i Analyse expérimentale de la multifragmentation dynamique

par C. DENOUAL, C.E. COTTENOT et F. HILD (1997).
Présenté à SCHOCK 97, Amherst, MA (USA), APS.
À paraître dans S.C. SCHMIDT, D.P. DANDEKAR et J.W. FORBES (eds.), *actes Shock Compression of Condensed Matter Conference*, API Press, New York, NY (USA).

ANALYSIS OF THE DEGRADATION MECHANISMS IN AN IMPACTED CERAMIC

C. DENOUAL,[1] C.E. COTTENOT[1] and F. HILD[2]

[1] *DGA/CREA-Département Matériaux en Conditions Sévères*
16 bis, Avenue Prieur de la Côte d'Or, F-94114 Arcueil Cedex, France.
[2] *Laboratoire de Mécanique et Technologie*
E.N.S. de Cachan / C.N.R.S. / Université Paris 6
61, Avenue du Président Wilson, F-94235 Cachan Cedex, France.

To analyze the degradation mechanisms in a natural sintered SiC (SSiC) ceramic during impact, three edge-on impact configurations are considered. First, the ceramic is confined by aluminum to allow a post–mortem analysis. In the second configuration, a polished surface of the ceramic is observed each micro-second by a high–speed camera to follow the damage generation and evolution. The third configuration uses a high–speed Moiré photography system to measure dynamic 2-D strain fields. Sequences of fringe patterns are analyzed.

INTRODUCTION

In many impact configurations, the stress field generated by a projectile in a ceramic can be assumed to be spherical and to produce damage in both compressive and tension modes in different locations within the ceramic. Damage in compression is generated near the impact surface when shear stresses reach a threshold value which can be dependent on pressure and strain rate. In the bulk of the ceramic, damage in tension is observed when the hoop stress induced by the radial motion of the impacted ceramic is sufficient to generate fracture in mode I initiating on micro–defects such as porosities or inclusions.

Most of the mechanisms initiated during impact (such as nucleation of flaws, propagation and interaction of cracks, stress release) can only be studied during dynamic tests, which have to be chosen to give reliable data on damage evolution.

A quantitative information on the location and evolution of damage can be obtained by an "edge-on" impact (EOI) configuration described in Ref. (1). These configurations are developed by the Ernst-Mach-Institut (EMI) and by the Centre de Recherches et d'Etudes d'Arcueil (CREA). In the latter configuration, a blunt projectile (11 mm in diameter and 20 mm in length) impacts a ceramic tile of size $100 \times 50 \times 10$ mm^3. The velocity of the impactor varies within the range [100 m/s; 330 m/s] and produces in the ceramic a zone of complete fragmentation. It can be shown that the same damage mechanism (*i.e.* damage in tension) is observed in EOI and in real impact configurations (2). The EOI can therefore be used to validate damage evolution laws for numerical simulations of the behavior of light armors.

Three different test configurations described in the following sections are used to understand the damage mechanisms. In all configurations, a nitrogen gas gun launches a steel cylinder which impacts a confined or unconfined SSiC tile with a velocity of 200 m/s or 330 m/s.

1 POST–MORTEM ANALYSIS

The first test is an EOI with an aluminum confinement presented in Fig. 1. A SSiC ceramic tile is impacted at a velocity of 330 m/s. The ceramic characteristics are given in Ref. (3). After impact,

the tile is coated in an epoxy resin and polished for macroscopic and microscopic analyses.

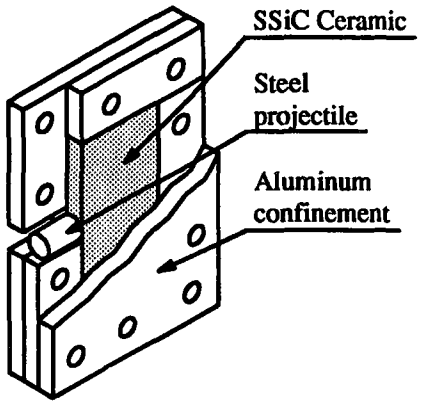

FIGURE 1. Schematic of the ceramic confinement. The tile is confined between two 10 mm thick aluminum plates. The edge confinement is obtained by aluminum tiles screwed on the plates.

The post–mortem crack pattern is presented in Fig. 2. Different zones can be separated with respect to the crack density and orientation. In front of the projectile, a small zone exhibits a randomly oriented crack pattern. In the bulk of the ceramic, one can observe long radial cracks with a second circumferential crack pattern superimposed on the first one.

In this last region, some radial cracks seem to kink in the circumferential direction, kink one more time and propagate in the radial direction. The kinked fractures are made of two small (and hardly visible, see Fig. 2) cracks linked by a small circumferential crack. This complex crack is then opened by the radial motion of the ceramic, widens and becomes a long macroscopic "kinked" fracture. This phenomenon shows that the radial cracks appear prior to the circumferential ones, since the latter do not go through the former. The maximum size of a fracture between two kinks in this zone does not exceed a few millimeters.

Near the tile rear face, a third zone exhibits a high density of cracks. This thin strip remains at a constant distance from the rear surface, like a spalling zone.

A microscopic analysis of the tile section along the projectile axis reveals the presence of some

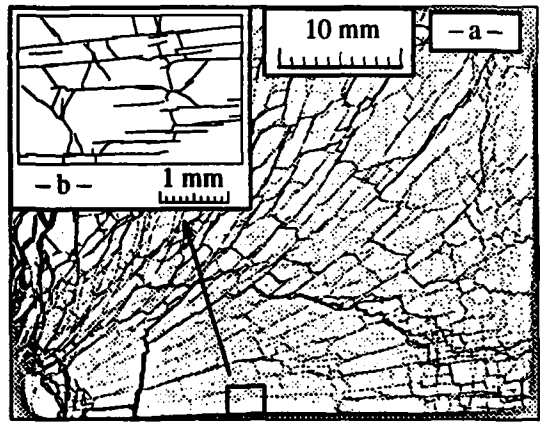

FIGURE 2. a–Half top view of tile impacted at a velocity of 330 m/s. b–The magnification shows many short radial cracks linked by short circumferential ones.

long cracks running through the whole specimen, from the projectile tip to the rear face of the tile. An explanation can be proposed by remembering that the stress field is modified during propagation by the tile edges. The first compressive wave is a uniaxial strain state (longitudinal wave) that is not compatible with the free edges of the tile. Two relaxation waves are therefore generated from both edges and interact with each other in the center of the tile. The stress state becomes tensile and crack nucleation occurs.

2 REAL–TIME VISUALIZATION OF CRACKS

The real–time visualization test is designed to provide an information on the chronology of damage onset. The ceramic target presents one mirror polished face illuminated by a flashlight. A high-speed camera records the reflected light. The pictures shown in Fig. 3 were obtained by Riou (4).

Most of the initiated cracks do not exceed a few millimeters in length (Figs. 3–a and 3–b). This leads to assume that the crack tip cannot follow the crack front, *i.e.* the velocity of the former is less than the velocity of the latter. A crack initiates when the tensile stress reaches a threshold value (depending on the size and shape of the defect) and stops because other defects nucleated in front of it and relaxed the hoop stress. No cir-

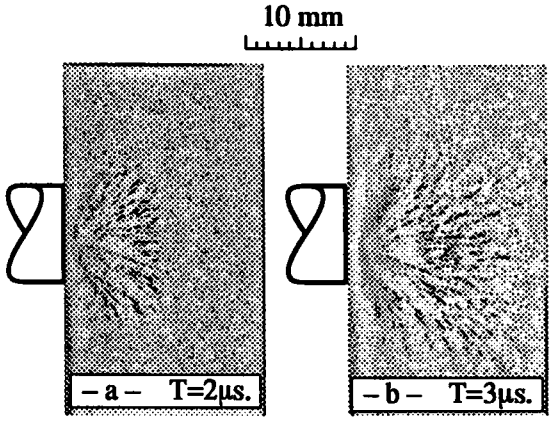

FIGURE 3. An example of pictures obtained by real–time visualization with a SSiC ceramic impacted at a velocity of 203 m/s.

cumferential cracks are visible in Fig. 3 but are clearly present in the last frame of the same shot (not presented in this paper, see Ref. (4)).

3 HIGH–SPEED PHOTOGRAPHY OF MOIRE FRINGES

Moiré photography is an optical technique that makes use of the geometric interferences occurring when two gratings are superimposed. The main difficulties to observe ceramic impact lie in the time range and the very high wave velocity (around 11,000 m/s). The simple and mobile Moiré optical set-up and the automated fringe pattern analysis are described in Ref. (5).

A typical result of the high–speed Moiré photography is presented in Fig. 4. The velocity of the impactor is equal to 330 m/s. The method used to analyze the fringes cannot give reliable data when they are blurred. To overcome this problem, the artifacts generated during the fringe pattern analysis are automatically reset to zero in a gray colored zone in Figs. 4–c and 4–d.

A set of twelve frames is taken. The first frame is recorded before any physical contact, is free of constrains and constitutes the reference Moiré pattern. The dynamic response of the specimen is recorded on eleven frames from 1 μs to 6.5 μs after impact with a 500 ns interframe time and a 40 ns exposure time.

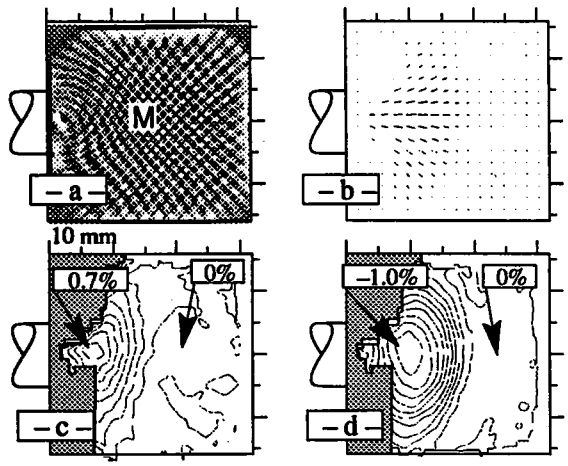

FIGURE 4. a–The initial frame (2 μs after impact). b–Third (negative) eigen direction c–and d–First and third eigen strains plotted with a 0.1% step between each contour.

Figure 4–a is the fringe pattern at $T = 2$ μs (the fourth frame of the whole sequence). Figure 4–b shows the eigen directions of the third (compressive) strain and confirms that the strain wave induced by an EOI has a circular geometry. The first and third eigen strains are given in Figs. 4–c and 4–d, respectively.

To compare the evolution of the radial and hoop strains, a typical result is given in Fig. 5. The strain diagram is plotted for a point M at a distance of 13 mm from the projectile tip (see Fig. 4–a). It can be noticed that the radial strain reaches an important value before any significant evolution of the hoop strain. This is consistent with a cylindrical stress wave in which the tensile strain is induced by the radial motion of the material.

A comparison with a numerical simulation is proposed with the model presented in Ref. (3). The general shape of the curve is very well reproduced by the model, with a tendency to under–estimate the compressive strain. A better modeling of the compressive behavior of the ceramic should improve the numerical/experimental agreement.

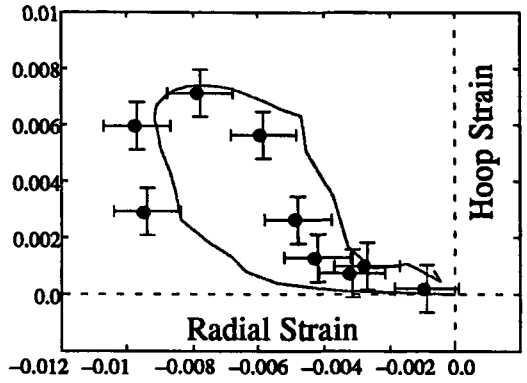

FIGURE 5. Typical example of strain evolution given by a Moiré technique (dots). A comparison (curve) is proposed with the model presented in Ref. (3).

DISCUSSION

A chronology of the damage onset can be proposed by using the results of the previous sections. The post–mortem analysis shows that the radial cracks are first generated and closely followed by the circumferential ones. The former damage is due to the divergent compressive wave that induces a tensile stress state. The latter crack pattern is due to the relaxation waves coming from the broken projectile and to the tensile stress wave emanating from the rear of the tile. When the two relaxation waves cross each other, another zone of dense crack nucleation can be observed and can be compared to a spall region.

The deformation in tension reaches a maximum value of 1% in the frame analyzed in Fig. 4. The ceramic in this zone cannot be undamaged and we can assume that cracks are present even if they are not visible. Moreover, the presence of cracks at $T = 2\ \mu s$ is compatible with the proposed chronology. In Fig. 4–a we can observe that the Moiré fringes are not blurred in the zone where cracks are assumed to nucleate. The local deformation induced by the crack nucleation is therefore sufficiently small not to blur the fringes, or, in other words, the nucleation is sufficiently dense so that the fringes location is not modified. This is not compatible with the results presented in Fig. 3 where macroscopic cracks would lead to a visible blur in the Moiré fringes.

The post–mortem analysis shows that many short cracks are nucleated and may be connected (at the end of the interaction) with the neighboring fracture to give macroscopic fractures. The initial short fractures are thus too small to be apparent in both real–time visualization of impact and Moiré photography and the previously estimated crack densities, far less than the real densities, have to be re–estimated. The main mechanism for the degradation of ceramic is therefore a very dense nucleation of cracks, some of them branching to provide macroscopic fracture.

CONCLUSION

Even if some damage mechanisms cannot be directly compared between real armor and EOI configurations, the EOI test can help to understand the ceramic degradation mechanisms during impact. First, the "powder" produced by impact is made of 3 anisotropic crack patterns, superimposing at different times to provide fragments of various shapes. Second, the very high density of nucleated cracks can only be established by using a fine microscopic analysis.

ACKNOWLEDGMENTS

This work was funded by DGA-DRET-STRDT. The authors wish to thank Ms. L. Riolacci for providing the picture of Fig. 2.

REFERENCES

1. Straßburger E., Senf H., Denoual C., Riou P., and Cottenot C.E., *"An Experimental Approach to Validate Damage Evolution Laws for Brittle Materials,"* To be presented at DYMAT 97, Toledo, Spain, Sept. 1997.
2. Denoual C., Cottenot C.E. and Hild F., *"On the identification of Damage During Impact of a Ceramic by a Hard Steel Projectile,"* Presented at the 16th Ballistic Symp., pp. 541–550, 1996.
3. Hild F. and Denoual C., *"A Probabilistic Model for the Dynamic Fragmentation of Brittle Solids,"* Presented at the APS Conference on Shock Compression of Condensed Matter, Amherst (MA), USA, 1997.
4. Riou P., PhD Dissertation, Ecole Nationale Supérieure des Mines de Paris, 1996.
5. Bertin-Mourot T., Denoual C., Deshors G., Louvigné P. F. and Thomas T., *"High Speed Photography of Moiré Fringes: Application to Ceramics under Impact,"* To be presented at DYMAT 97, Toledo, Spain, Sept. 1997.

ii Loi d'évolution

par F. HILD et C. DENOUAL (1997).
Présenté à SCHOCK 97, Amherst, MA (USA), APS.
À paraître dans S.C. SCHMIDT, D.P. DANDEKAR et J.W. FORBES (eds.), *actes Shock Compression of Condensed Matter Conference*, API Press, New York, NY (USA).

A PROBABILISTIC MODEL FOR THE DYNAMIC FRAGMENTATION OF BRITTLE SOLIDS

F. HILD[1] and C. DENOUAL[2]

[1] *Laboratoire de Mécanique et Technologie*
E.N.S. de Cachan / C.N.R.S. / Université Paris 6
61, Avenue du Président Wilson, F-94235 Cachan Cedex, France.
[2] *DGA/CREA-Département Matériaux en Conditions Sévères*
16 bis, Avenue Prieur de la Côte d'Or, F-94114 Arcueil Cedex, France.

Impact produces high stress waves leading to the fragmentation of brittle materials such as ceramics. The main mechanism used to explain the size variation of fragments with stress rate is an obscuration phenomenon. When a flaw initiates, the released stresses around the crack prevent other nucleations in an increasing zone. After a presentation of a probabilistic approach, a damage description and an evolution law are derived. Two numerical applications of the model are proposed.

INTRODUCTION

In the bulk of an impacted ceramic, damage in tension is observed when the hoop stress induced by the radial motion is sufficiently large to generate fracture in mode I initiating on micro-defects such as porosities or inclusions. When such a fracture is initiated, the zone affected by fracture is a complex function of time, crack velocity and stress wave celerity. In order to simplify the following development, the shape of the affected (or interaction) zone Z_i is supposed to be constant, *i.e.* all the interaction zones are self-similar and Z_i can be written as

$$Z_i(T-t) = S\,[kC(T-t)]^n \qquad (1)$$

where kC is the velocity of a propagating crack, S a shape parameter, C the longitudinal stress wave velocity so that $kC(T-t)$ is a representative length of the relaxation zone at time T around a broken flaw at time t. The parameter $n = 1, 2, 3$ is the space dimension. The shape parameter S is chosen in order to have $d\sigma/dt \leq 0$ in Z_i, *i.e.* no new nucleation can occur in Z_i.

To understand why a crack nucleates, one has to model the interaction of a nucleated defect and other defects that would nucleate. With a constant direction of the maximum principal stress and a small stress gradient, the space dimension can be uncoupled from the tensile stress (or time) dimension and the flaw nucleation can be represented on a space–time graph (Fig. 1). The space location of the defects is represented in a simple abscissa of an x-y graph where the y-axis represents time (or stress) to failure of a given defect. In this graph, a shaded cone represents the expansion of the interaction zone with time due to nucleation and propagation of a crack. A section Z (see Fig. 1) of a cone can be a volume, a surface or a length, depending on the space dimension n. The defects *outside* the shaded cones can nucleate and produce their own increasing interaction zone (*e.g.* defects No. 1 and No. 2). Inside the cones, the defects that should have broken do not nucleate (*e.g.* defects No. 3 and No. 4) since they are obscured.

Because different interaction volumes may overlap (a flaw can be obscured by one or more cracks), its preferable to define the conditions of non-obscuration for a given defect by examining the reverse problem (1). For a given flaw D, a non-interaction zone can be defined so that a de-

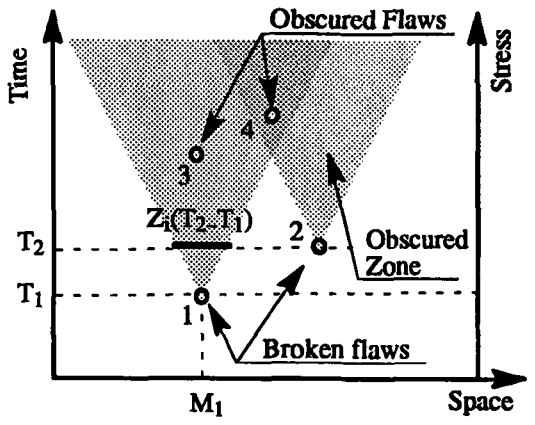

FIGURE 1. Depiction of obscuration phenomena.

fect cannot obscure D (Fig. 2) and the *horizon* of D in which a defect will always obscure D. The total

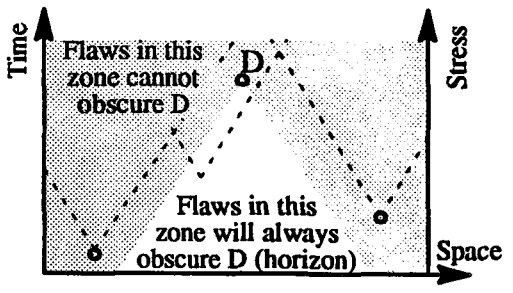

FIGURE 2. Schematic of the obscuration/non-obscuration zones for a defect D.

flaw density $\lambda_t(T)$ can therefore be split into two parts: $\lambda_b(T)$ (the broken flaws) and $\lambda_o(T)$ (the obscured flaws). Furthermore, we assume that the distribution of total flaws in a zone Z is modeled by a Poisson point process of intensity $Z\lambda_t(T)$. New cracks will initiate only if the defect exists in the considered zone and if no defects exist in its horizon so that

$$\frac{d\lambda_b}{dt}(T) = \frac{d\lambda_t}{dt}(T)P_{no}(T) \qquad (2)$$

where P_{no} is the probability of non-obscuration (no defects exist in the horizon). The variable P_{no} can be split into an infinity of events defined by the probability of finding at t a new defect during a time step dt in an interaction zone $Z_i(T-t)$. This probability increment is written by using a Poisson point process of intensity $d\lambda_t/dt$. Those *independent events* can be used to provide an expression for P_{no}

$$P_{no}(T) = \exp\left[-\int_0^T \frac{d\lambda_t}{dt}(t)Z_i(T-t)dt\right] \qquad (3)$$

where $Z_i(T-t)$ is the measure of the interaction zone at t for a defect that would break at T.

The static description of fracture in brittle materials can be modeled by a two-parameter Weibull law. The density of flaws able to break for a stress less than or equal to σ is then assumed to follow a power law function

$$\lambda_t(T) = \frac{1}{Z_0}\left[\frac{\sigma(T)}{S_0}\right]^m \qquad (4)$$

where m is the Weibull modulus and S_0 the scale parameter relative to the measure of a reference zone Z_0.

DAMAGE DESCRIPTION AND EVOLUTION LAW

One can notice that P_{no} is also the fraction of relaxed zones and can therefore be related to a damage variable D by the relation $1 - P_{no} = D$. This variable, defined in the framework of Continuum Damage Mechanics (CDM), evolves from zero to one when the initial material becomes more and more damaged. It is interesting to notice that the first order approximation of Eqn. (3) leads to the differential equation proposed by Grady and Kipp (2) to describe the evolution of a damage variable. The proposed damage variable is defined with the assumption that many cracks nucleate and propagate due to a tensile stress expressed in the direction of the maximum principal stress. Since the cracks will be strongly oriented, an anisotropic damage description is chosen (3).

This anisotropic description is expressed through a second order damage tensor. The tensor D_{ij} is diagonal in the eigen directions of $\underline{\underline{\sigma}}$ so that only 3 variables (D_1, D_2, D_3) have to be computed. The relationship between the microscopic principal stress σ_i and the macroscopic one (Σ_i) is

$$\Sigma_i = \frac{\sigma_i}{1-D_i} \text{ with } i = 1,3 \qquad (5)$$

This approach is useful when multiple crack patterns are superimposed (4).

The evolution of D is expressed in a differential form in order to be implemented in the FE code PamShock (5) by using Eqns. (2), (3) and (4)

$$\frac{d^{n-1}}{dt^{n-1}}\left(\frac{1}{1-D_i}\frac{dD_i}{dt}\right) = \lambda_t(\sigma_i)\, n!\, S\, (kC)^n \quad (6)$$

It is worth noting that D approaches smoothly 1 and does not need any cut-off. According to classical results of CDM, the evolution of D is stopped if $d\sigma/dt < 0$. The eigen directions ($\underline{d_1}$, $\underline{d_2}$, $\underline{d_3}$) associated to D_1, D_2 and D_3 may change at each time step until D_1 reaches a threshold value $D_{th} = 0.01$. Only the direction $\underline{d_1}$ is then locked, the other directions follow the eigen directions of $\underline{\underline{\sigma}}$, with the constraint to be perpendicular to $\underline{d_1}$. When D_2 reaches the threshold value, the whole directions are locked. Equations (2), (3) and (4) are also used to compute the density of broken flaws.

EXPERIMENTS AND COMPUTATIONS

In all the computations, $k = 0.38$, $S = 4\pi/3$ (spherical obscuration zones) and $n = 3$. The two materials used in this section are a natural sintered SiC (SSiC) processed by Céramique & Composites (France) and a SiC–B processed by CERCOM (USA) with the following characteristics

Property	SSiC	SiC–B
Young's mod.	410 GPa	450 GPa
Density	3.15	3.18
Weibull mod.	9.3	18
Mean strength	350 MPa	553 MPa
Effective vol.	1.25 mm^3	1.25 mm^3

The compressive behavior of both ceramics is not modeled in this study because of the very low impact velocities. To test the mesh sensitivity of the above described model, a plane shock wave spall configuration is analyzed. When a compressive stress pulse is generated in a plate, the reflected (tensile) pulse coming back from the free rear surface of the specimen is superimposed on the loading pulse. When the loading pulse duration is properly prescribed, a tensile stress is generated in the bulk of the specimen. The thickness of the damaged zone may strongly vary if the model is not mesh–independent. The shock wave spall simulation is therefore a severe test for damage evolution laws implemented in numerical codes.

A one dimensional code presented in Ref. (3) is used. The plate thickness is 10 mm and the imposed pressure is -1 GPa, for a duration of 10 μs. Four different mesh densities are tested: 20 el./mm, 40 el./mm, 80 el./mm, 160 el./mm. The numerical viscosity parameters are chosen so that they do not modify the loading pulse shape during propagation. The simulation is performed with the SSiC material. The results presented in Fig. (3) show no dependence of the size of the damaged zone on the mesh density. The second

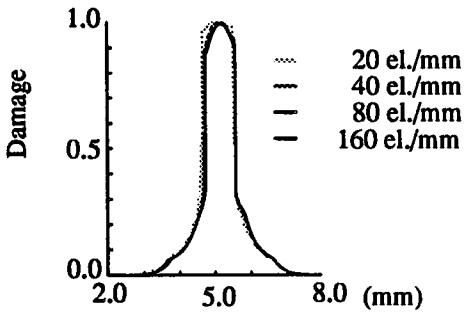

FIGURE 3. Damage location for 4 mesh densities in a plane shock wave spall configuration.

test concerns computational simulations of Edge-On Impacts (EOI) in two different configurations. The principle of EOI is detailed in Ref. (6) and typical results are presented in a companion paper (4). The first simulation is carried out on the configuration designed by the EMI on a SiC–B ceramic with a steel projectile of velocity 185 m/s and a tile of size 100 × 100 × 10 mm^3 (Fig. (4)).

Two differents zones can be depicted in the experimental result. The first one (say the *inner* zone) appears in front of the projectile. This zone widens progressively and finally becomes localized in thinner zones called corridors of varying locations. The second (*outer*) zone is generated at the projectile edges and can roughly be compared to a Herz cone crack. The damaged zone then splits into a thin part that stops at the edge of the tile,

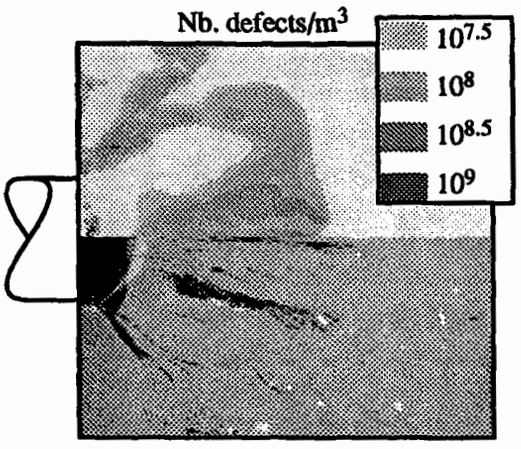

FIGURE 4. Simulated (top) and observed (bottom) crack pattern in an EOI test with a projectile velocity of 185 m/s, $T = 7.5$ μs.

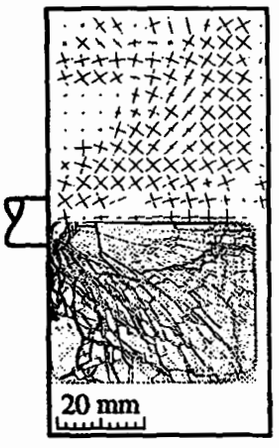

FIGURE 5. Simulated (top) and observed (bottom) crack directions in an EOI test with a projectile velocity of 330 m/s, $T = 15$ μs.

and a larger one that propagates through the ceramic at a constant distance from the edge.

The numerical simulation is in good accordance with the general shape of the damaged zone. The inner zone is well reproduced even if the corridors are generated too late and are not sufficiently extended. The simulated outer zone follows closely the observed one except for the bridge observed between the inner and the outer zones.

The second EOI test presented in Fig. (5) is performed with a steel projectile whose velocity is 330 m/s on a SSiC ceramic. The tile size is $100 \times 50 \times 10$ mm^3.

The inner/outer zones cannot be clearly defined because the whole specimen is fully broken at $T = 15$ μs. In both experiment and simulation, the ceramic is cracked in front of the projectile in radial and circumferential directions. It is worth mentioning that only an anisotropic damage model (in which the stiffness can be very small in one direction and unaltered in another direction) can provide such a crack pattern.

CONCLUSION

A probabilistic approach has been proposed to describe the stress rate dependence of the fragmentation mechanism. The proposed approach is used to develop a damage evolution law in tensile mode for impact simulations on ceramics. The model can provide an estimation of the number and the directions of activated flaws. Complex damage patterns, in which superposition of cracks of differents directions occurs, can be predicted.

ACKNOWLEDGMENTS

The authors wish to thank E. Straßburger and H. Senf from the EMI for providing the picture of Fig. (4). The authors wish also to thank A. Trameçon from ESI for his valuable help in implementing the model in PamShock. This work was funded by DGA-DRET-STRDT.

REFERENCES

1. Denoual C., Hild F. and Cottenot C.E., *"A Probabilistic Approach for Dynamic Fragmentation of Ceramics under impact Loading,"* Presented at ICF 9, Sydney, Australia, 6, pp. 2933–2940, 1997.
2. Grady D. E. and Kipp M. E. *Int. J. Rock Min. Sci. & Geomech. Abstr.*, 17, pp. 147-157, 1980.
3. Denoual C., Cottenot C.E. and Hild F., *"On the identification of Damage During Impact of a Ceramic by a Hard Steel Projectile,"* Presented at the 16th Ballistic Symp., pp. 541–550, 1996.
4. Denoual C., Cottenot C.E. and Hild F., *"Analysis of the Degradation Mechanisms in an Impacted Ceramic,"* Presented at the APS Conference on Shock Compression of Condensed Matter, Amherst (MA), USA, 1997.
5. Pamshock, Users' manual, ESI, 1997.
6. Straßburger E., Senf H., Denoual C., Riou P., and Cottenot C.E., *"An Experimental Approach to Validate Damage Evolution Laws for Brittle Materials,"* To be presented at DYMAT 97, Toledo, Spain, Sept. 1997.

3.2 Fissuration matricielle de composites sous chargement monotone

Dans ce paragraphe, des lois de comportement de composites sont écrites dans le cadre de la thermodynamique des milieux continus [GERMAIN *et al.*, 1983]. Le but est de décrire tous les mécanismes se produisant lorsqu'il y a fissuration matricielle. Dans la modélisation (cf. Chapitre 1), il s'agit d'introduire les variables internes qui décrivent le comportement de tels matériaux et le potentiel d'état associé $\overline{\psi}$. Le potentiel d'état est constitué d'une partie élastique récupérable $\overline{\psi}^{e}$ et d'une partie élastique irrécupérable $\overline{\psi}^{i}$. L'énergie irrécupérable correspond à la somme de toutes les densités d'énergies élastiques associées aux champs de contraintes résiduelles (cf. paragraphe 1.1).

Dans le paragraphe 3.2.1, on étudie le comportement de matrices fragiles renforcées par des fibres longues. Cette partie est consacrée à l'étude des mécanismes de fissuration matricielle, de décohésion et de glissement interfaciaux. Le champ de contraintes résiduelles lié à la dilatation différentielle entre fibre et matrice n'est pas considéré. On insistera sur les effets relatifs au caractère aléatoire de la rupture au niveau microscopique dans le cas de composites unidirectionnels.

Dans une seconde partie (paragraphe 3.2.2), des applications sont présentées. L'une concerne l'étude du comportement mécanique d'un composite unidirectionnel SiC/SiC. On notera que le même type d'approche peut être employé pour des composites stratifiés [HILD *et al.*, 1996]. Cette partie a notamment pour but de montrer que les modèles développés dans le cadre du Génie des Matériaux peuvent être inclus dans un formalisme couramment utilisé par les Mécaniciens des Matériaux. C'est pourquoi des formulations unidimensionnelles sont employées. Le même type d'approche sera utilisé pour étudier l'essai PIED (Pour Identifier l'Endommagement Diffus) développé en partie au LMT-Cachan [MAZARS et BERTHAUD, 1989 ; MAZARS *et al.*, 1990 ; RAMTANI, 1990]. En particulier, une analyse du comportement mécanique de l'interface entre les barrettes d'aluminium et le volume d'étude en ciment (renforcé ou non par des fibres courtes) est réalisée à l'aide du même modèle. L'effet de l'addition de fibres courtes sur la réponse de l'essai PIED est discuté. Une investigation plus complète peut être trouvée dans la thèse de D. BOUDON-CUSSAC [1996].

Enfin, une extension à des composites [0/90] est proposée (paragraphe 3.2.3). L'écriture du modèle de comportement est basée sur une généralisation bidimensionnelle des résultats obtenus lors de l'étude de la réponse de composites unidirectionnels [BURR *et al.*, 1995]. Une description plus détaillée des différentes étapes de calcul peut

être trouvée dans la thèse de A. BURR [1995].

3.2.1 Modèle de comportement de composites unidirectionnels

Ce paragraphe reprend les résultats publiés par BURR *et al.* [1996a] et les complète en discutant sur des cas simples quelques résultats liés à la prise en compte de distributions particulières de taille de fragments.

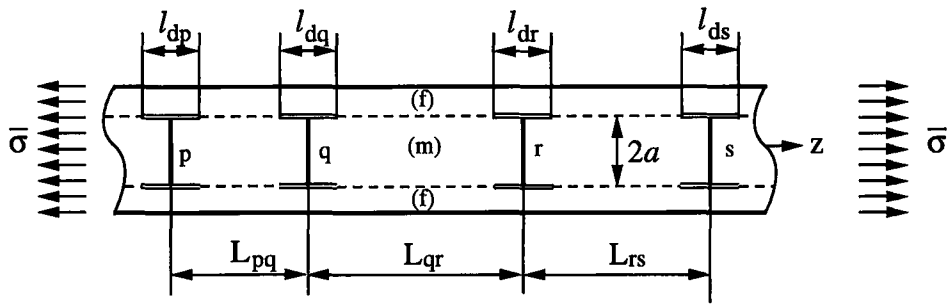

FIG. 3.4 - Distribution de distances L et de longueurs de décohésion l_d.

Lors d'un chargement, un composite renforcé par des fibres subit une multifissuration matricielle s'accompagnant de décohésion et de glissement à l'interface. La cellule élémentaire (figure 3.4), base de l'étude, contient des fissures matricielles distribuées de manière aléatoire et caractérisées par une densité de probabilité $F(L)$ qui évolue en fonction de la contrainte mésoscopique $\overline{\sigma}$. Les fissures matricielles engendrent un accroissement de densité d'énergie récupérable de GIBBS $\Delta\overline{\varphi}^{e}$ donné par

$$\Delta\overline{\varphi}^{e} = \frac{1}{\overline{L}} \int_0^{+\infty} \Delta\varphi^{e}(L) L F(L) dL \quad \text{avec} \quad \overline{L} = \int_0^{+\infty} L F(L) dL \tag{3.1}$$

où $\Delta\varphi^{e}(L)$ est la variation de densité d'énergie récupérable de GIBBS liée à la présence d'une fissure dans une cellule de longueur L. Cette écriture suppose que les interactions entre fissures sont *uniquement* données par les deux plus proches voisines. Les interactions à plus longue distance sont *négligées*. La décohésion et le glissement interfacial induisent des déformations inélastiques et des boucles d'hystérésis [AVESTON *et al.*, 1971]. Par application du principe des travaux virtuels (cf. équation (1.64)), la déformation inélastique mésoscopique (ou moyenne) $\overline{\epsilon}^{i}$ est donnée par

$$\overline{\epsilon}^{i} = \frac{1}{\overline{L}} \int_0^{+\infty} \left[\int_0^{L} \frac{\sigma_f^{r}(z,L)}{E_f} dz \right] F(L) dL \tag{3.2}$$

où $\sigma_f^{r}(z,L)$ est la contrainte résiduelle dans les fibres, z est la position courante dans une cellule de longueur L. Le champ de contrainte correspondant est auto-équilibré et

permet donc un stockage d'énergie $\overline{\psi}^{\mathrm{i}}$ (cf. équation (1.62))

$$\overline{\psi}^{\mathrm{i}} = \frac{EfE_{\mathrm{f}}}{2(1-f)E_{\mathrm{m}}\overline{L}} \int_0^{+\infty} \int_0^L \left[\frac{\sigma_{\mathrm{f}}^{\mathrm{r}}(z,L)}{E_{\mathrm{f}}}\right]^2 dz F(L)\, dL \tag{3.3}$$

où f est la fraction volumique de fibres, E_{f} et E_{m} sont les modules d'YOUNG respectifs de la fibre et de la matrice.

Les mécanismes élémentaires d'endommagement du composite sont décrits par des variables internes. La fissuration matricielle est modélisée par une variable d'endommagement D [LEMAITRE et DUFAILLY, 1977] définie par (cf. paragraphes 1.1.1 et 1.1.2.ii)

$$\Delta\overline{\varphi}^{\mathrm{e}} = \overline{\varphi}^{\mathrm{e}}(D) - \overline{\varphi}^{\mathrm{e}}(D=0) = \frac{\overline{\sigma}^2}{2E}\frac{D}{1-D} \tag{3.4}$$

Les équations (3.1) et (3.4) montrent que la variable d'endommagement D est fonction, *a priori*, de tous les moments de la distribution F des longueurs L. La déformation inélastique $\overline{\epsilon}^{\mathrm{i}}$ est une des variables internes modélisant l'endommagement interfacial (*i.e.*, la décohésion et le glissement). La seconde variable, d, est obtenue à partir de l'expression de la densité d'énergie irrécupérable $\overline{\psi}^{\mathrm{i}}$ (cf. paragraphe 1.1.2.iii)

$$\overline{\psi}^{\mathrm{i}} = \frac{E}{2}\frac{(\overline{\epsilon}^{\mathrm{i}})^2}{d} \tag{3.5}$$

Cette expression a également été introduite dans l'étude des bétons et des roches [ANDRIEUX, 1981 ; ANDRIEUX *et al.*, 1986]. La densité d'énergie libre $\overline{\psi}$ s'écrit

$$\overline{\psi} = \frac{E(1-D)}{2}\left(\overline{\epsilon} - \overline{\epsilon}^{\mathrm{i}}\right)^2 + \frac{E}{2}\frac{(\overline{\epsilon}^{\mathrm{i}})^2}{d} \tag{3.6}$$

et les forces associées aux quatre variables d'état sont définies par

$$\overline{\sigma} = \frac{\partial\overline{\psi}}{\partial\overline{\epsilon}} \quad , \quad Y = -\frac{\partial\overline{\psi}}{\partial D} \quad , \quad y = -\frac{\partial\overline{\psi}}{\partial d} \quad , \quad \overline{X} = -\frac{\partial\overline{\psi}}{\partial\overline{\epsilon}^{\mathrm{i}}} \tag{3.7}$$

L'équation (3.7.1) permet de définir la contrainte mésoscopique, l'équation (3.7.2) le taux de restitution de densité d'énergie de fissuration, l'équation (3.7.3) le taux de restitution de densité d'énergie d'auto-contrainte, et l'équation (3.7.4) la contrainte de rappel associée au mécanisme d'endommagement interfacial. Les lois d'évolution des variables internes peuvent être obtenues soit par analyse micromécanique (cf. exemple ci-dessous), soit par essais macroscopiques (figure 3.5). Cette dernière méthode sera utilisée dans le paragraphe suivant dans le cas d'un composite SiC/SiC. En particulier la mesure de la variable interne d passe par la quantification de la densité d'énergie

irrécupérable $\overline{\psi}^{\mathrm{i}}$: cf. [CHRYSOCHOOS, 1987] ou [CHO *et al.*, 1991].

À titre d'illustration, les résultats précédents vont être analysés dans deux cas particuliers pour lesquels des résultats simples peuvent être obtenus.

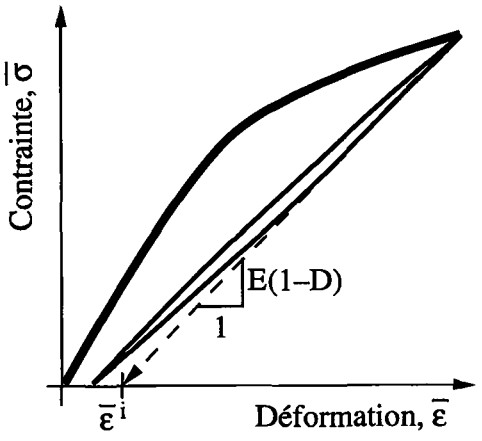

FIG. 3.5 - Courbe contrainte/déformation mésoscopiques.

Dans un premier temps, on ne considère que le mécanisme de fissuration matricielle. En utilisant le modèle de transfert de charge de COX [1952], on peut calculer (cf. paragraphe 1.1.2.ii) la variation de densité d'énergie récupérable $\Delta\varphi^{\mathrm{e}}(L)$

$$\Delta\varphi^{\mathrm{e}}(L) = \frac{\overline{\sigma}^2}{2E}\frac{(1-f)E_{\mathrm{m}}}{fE_{\mathrm{f}}}\frac{\tanh(\beta L)}{\beta L} \tag{3.8}$$

où β est une constante dépendant des propriétés élastiques et géométriques de la fibre et de la matrice (β est inversement proportionnel au rayon R de la fibre, $B = 2\beta$). On définit une longueur représentative $\overline{L}_{\mathrm{r}}$ de la fissuration à l'aide de la condition

$$\Delta\overline{\varphi}^{\mathrm{e}} = \Delta\varphi^{\mathrm{e}}(\overline{L}_{\mathrm{r}}) \tag{3.9}$$

Pour calculer $\Delta\overline{\varphi}^{\mathrm{e}}$, la densité de probabilité $F(L)$ est obtenue en supposant que les défauts sont distribués le long de la matrice à l'aide d'un processus ponctuel de POISSON. Ce modèle rentre dans un cadre beaucoup plus large [JEULIN, 1991] qui ne sera pas discuté dans ce document. Sous ces hypothèses, la fonction de répartition des fragments $F(L)$ s'écrit (cf. par exemple [GRADY, 1990])

$$F(L) = \lambda_{\mathrm{t}}(\sigma)\ \exp\left[-\lambda_{\mathrm{t}}(\sigma)L\right] \tag{3.10}$$

où $\lambda_{\mathrm{t}}(\sigma)$ désigne la densité de défauts rompus par unité de longueur. Si la densité $\lambda_{\mathrm{t}}(\sigma)$ est supposée décrite par une fonction puissance de la contrainte locale (ou microscopique)

σ, on retrouve alors les bases du modèle de WEIBULL. Le calcul de la longueur moyenne des fragments permet de lier $\overline{L}$ à $\lambda_t(\sigma)$

$$\overline{L} = \frac{1}{\lambda_t(\sigma)} \tag{3.11}$$

À l'aide des deux hypothèses précédentes, on peut évaluer la variation moyenne d'enthalpie libre

$$\Delta\overline{\varphi}^e = \frac{\overline{\sigma}^2}{2E}\frac{(1-f)E_m}{fE_f}\frac{1}{\beta\overline{L}}\left[\frac{1}{2\beta\overline{L}}G\left(\frac{1}{2\beta\overline{L}}\right)-1\right] \tag{3.12}$$

où G représente la fonction de Bateman, transformée de Laplace de la tangente hyperbolique [SPANIER et OLDHAM, 1987]. Le développement limité de l'équation (3.12) en $1/\beta\overline{L}$ au troisième ordre au voisinage de zéro s'écrit

$$\Delta\overline{\varphi}^e = \frac{\overline{\sigma}^2}{2E}\frac{(1-f)E_m}{fE_f}\frac{1}{\beta\overline{L}}\left[1-\frac{\ln(2)}{\beta\overline{L}}+\left(\frac{\pi}{\sqrt{24}\beta\overline{L}}\right)^2+O\left\{\frac{1}{(\beta\overline{L})^3}\right\}\right] \tag{3.13}$$

L'équation (3.12) montre que la variable d'endommagement D (cf. équation (3.4)) ainsi que la longueur représentative normée $\beta\overline{L}_r$ (cf. équation (3.9)) sont des fonctions non triviales de $\beta\overline{L}$

$$\frac{\tanh(\beta\overline{L}_r)}{\beta\overline{L}_r} = \frac{1}{\beta\overline{L}}\left[\frac{1}{2\beta\overline{L}}G\left(\frac{1}{2\beta\overline{L}}\right)-1\right] \tag{3.14}$$

En particulier, cette fonction est différente de celle obtenue en écrivant $\Delta\overline{\varphi}^e = \Delta\varphi^e(\overline{L})$ pour laquelle on obtient

$$\overline{L}_r \cong \overline{L} \tag{3.15}$$

La figure 3.6 montre l'évolution de l'erreur $\Delta\overline{L}$ définie par

$$\Delta\overline{L} = |\overline{L}_r - \overline{L}| \tag{3.16}$$

Pour de grandes valeurs de $\beta\overline{L}$, les deux longueurs sont quasiment identiques. Par contre lorsque $\beta\overline{L}$ diminue, il y a divergence entre les deux longueurs. En conséquence, la mesure de la longueur moyenne $\overline{L}$ n'est pas nécessairement la bonne quantité pour décrire la variable d'endommagement D.

Dans un deuxième temps, nous considérons que les mécanismes de fissuration et de décohésion/glissement sont découplés. Ceci revient à dire que les calculs précédents restent encore valables dans ce qui suit. En supposant que la ténacité interfaciale est faible et que le glissement interfacial est approximé par une résistance au cisaillement

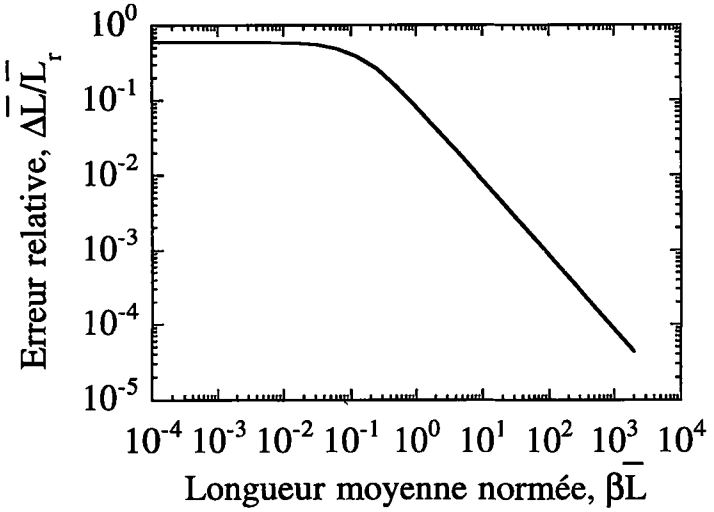

FIG. 3.6 - Évolution de l'erreur relative $\Delta\overline{L}/\overline{L}_r$ en fonction de la longueur moyenne normée $\beta\overline{L}$.

constante τ [KELLY et TYSON, 1965 ; AVESTON *et al.*, 1971], la longueur équivalente de décohésion $\bar{l}_d$ est définie à partir de l'expression de la déformation inélastique

$$\bar{\epsilon}^i = \frac{\tau \bar{l}_d^2}{2E_f R\overline{L}_r} \tag{3.17}$$

La déformation inélastique est ainsi une fonction des distributions de fissures matricielles et de longueurs de décohésion. Le calcul de la variable d'endommagement d'interface d est obtenu à partir du calcul de la densité d'énergie irrécupérable (cf. équation (3.3)). Dans le cas où la séparation minimale entre deux fissures est supérieure à la longueur de décohésion, celle-ci prend une valeur unique et la variable d'endommagement d s'écrit (cf. équation (1.75.1))

$$d = \frac{3(1-f)E_m}{4fE_f}\frac{\bar{l}_d}{\overline{L}_r} \tag{3.18}$$

Ce résultat n'est valable que lorsque le comportement interfacial vérifie les hypothèses de ce paragraphe. Lorsque le comportement interfacial est plus complexe, la variable d n'est proportionnelle au rapport $\bar{l}_d/\overline{L}_r$ qu'à la condition que le champ de contrainte à l'avant de la pointe de la fissure soit le champ de contrainte élastique du matériau sain.

Afin d'illustrer les résultats précédents, nous allons étudier le comportement d'un monofilament dans lequel la matrice est plus résistante que la fibre. Ceci constitue un test classique de caractérisation des propriétés d'interface, éventuellement des propriétés de rupture des fibres [BAXEVANAKIS *et al.*, 1993]. La particularité de cet essai est

que la courbe contrainte/déformation mésoscopique, est dominée par le phénomène de décohésion et de glissement. En effet, les distances moyennes entre fissures à saturation sont souvent de deux voire trois ordres de grandeur supérieurs au rayon de la fibre ($\beta\overline{L} \cong 10^2, 10^3$). Ceci a pour conséquence de conduire à des valeurs négligeables de la variable d'endommagement D, et à assimiler la longueur représentative $\overline{L}_r$ à la longueur moyenne $\overline{L}$. Ce cas correspond à une situation « en série ». Une situation « en parallèle » sera étudiée dans le paragraphe 3.3.1.

Pour déterminer l'expression de la longueur de décohésion $\bar{l}_d$, il s'agit d'obtenir l'évolution de la déformation inélastique $\overline{\epsilon}^i$ en fonction de la contrainte appliquée $\overline{\sigma}$. Dans le cas d'un modèle d'interface à cisaillement τ constant, deux voies sont possibles. La première voie consiste à étudier analytiquement le phénomène de multifissuration. En effet, le phénomène d'écran (ou d'exclusion) est écrit aisément pour un défaut isolé. Dans un cas unidimensionnel, la rupture ayant eu lieu pour $z = 0$, l'intervalle $]-l_R/2, l_R/2[$ est inaccessible (zone d'exclusion) à toute nouvelle rupture car la contrainte dans cette zone reste inférieure au niveau de contrainte atteint lors de la rupture à $z = 0$ (figure 3.7). La longueur l_R s'écrit

$$l_R(T) = \frac{RT}{\tau} \tag{3.19}$$

où T désigne la contrainte de traction qui existerait si aucune rupture n'avait eu lieu. On notera que par rapport à la multifragmentation des céramiques sous chargement dynamique, le phénomène d'exclusion est de nature similaire (cf. paragraphe 3.1.2).

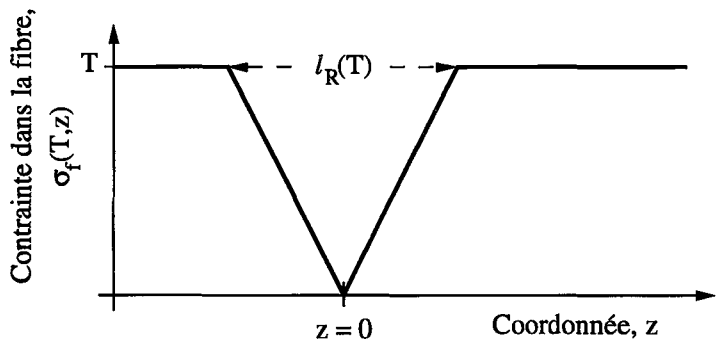

FIG. 3.7 - Zone d'exclusion pour toute nouvelle rupture.

GULINO et PHOENIX [1991] proposent une manière approchée d'étudier la fragmentation en supposant que le processus reste poissonien et en négligeant des défauts qui, cassés pour une contrainte locale t inférieure à la contrainte T, peuvent empêcher la

rupture ultérieure de défauts. L'inconvénient de ce modèle est que le phénomène de saturation (correspondant au cas où toute la longueur du composite est constituée de zones d'exclusions) n'est pas prévu. Pour améliorer ce modèle, on peut remarquer qu'un modèle d'îles booléennes [JEULIN et JEULIN, 1981 ; JEULIN, 1987 ; SERRA, 1988 ; 1989] constitue également une *borne inférieure* au nombre de défauts susceptibles d'être rompus. En effet, ce modèle ne prend pas en compte le phénomène d'exclusion et *surestime* donc la zone dans laquelle de nouvelles fissures ne peuvent plus s'amorcer. On suppose que la densité λ_t par unité de longueur est décrite par une fonction puissance de la contrainte locale T

$$\lambda_t(T) = \frac{1}{L_0}\left(\frac{T}{S_0}\right)^m \tag{3.20}$$

où m et $L_0 S_0^m$ sont les paramètres de WEIBULL. Deux grandeurs caractéristiques S_c et δ_c peuvent être définies [HENSTENBURG et PHOENIX, 1989 ; CURTIN, 1991] à l'aide de la relation $l_R(S_c)\lambda_t(S_c) = 1$, déjà utilisée dans le paragraphe 3.1.2

$$S_c^{m+1} = \frac{L_0 S_0^m \tau}{R} \quad \text{et} \quad \delta_c = l_R(S_c) \tag{3.21}$$

Ainsi, l'évolution du nombre de défauts effectivement rompus $\overline{\lambda}_b$ par unité de longueur caractéristique δ_c vérifie l'inéquation suivante

$$\overline{\lambda}_b(\overline{T}) \geq \frac{m}{m+1}\,\gamma\left[\frac{m}{m+1}, \overline{T}^{m+1}\right] \quad \text{avec} \quad \overline{T} = \frac{T}{S_c} \tag{3.22}$$

Ce résultat a la propriété intéressante de décrire la saturation de manière raisonnable (cf. tableau 3.1). D'autre part, l'expression de $F(L)$ obtenue lors de l'étude de la fragmentation matricielle pourra être employée en première approximation. Afin de calculer la déformation inélastique moyenne $\overline{\epsilon}^i$, l'équation (3.2) peut être réécrite comme suit

$$\overline{\epsilon}^i = \frac{1}{\overline{L}}\int_0^{+\infty} L\epsilon^i(L)F(L)dL \tag{3.23}$$

où $\epsilon^i(L)$ désigne la déformation inélastique d'une cellule de longueur L. Dans le cas d'un modèle d'interface à cisaillement τ constant, la déformation inélastique $\epsilon^i(L)$ s'exprime par

$$\epsilon^i(L) = \frac{f\tau}{(1-f)RE_m}\left(l_R - \frac{L}{2}\right) \quad \text{pour} \quad L < l_R \tag{3.24}$$

$$\epsilon^i(L) = \frac{f\tau l_R^2}{2(1-f)LRE_m} \quad \text{pour} \quad L \geq l_R \tag{3.25}$$

de telle manière que la déformation inélastique moyenne $\overline{\epsilon}^i$ devient

$$\overline{\epsilon}^{\mathrm{i}} = \frac{f\tau l_{\mathrm{R}}}{(1-f)RE_{\mathrm{m}}} - \frac{f\tau\overline{L}}{(1-f)RE_{\mathrm{m}}}\left[1-\exp\left(-\frac{l_{\mathrm{R}}}{\overline{L}}\right)\right] \tag{3.26}$$

En utilisant l'équation (3.17) et en remplaçant $\overline{l}_{\mathrm{d}}$ par $\overline{l}_{\mathrm{R}}$, fE_{f} par $(1-f)E_{\mathrm{m}}$ (le rôle de la matrice et de la fibre est échangé dans le test de multifragmentation), on obtient

$$\overline{l}_{\mathrm{R}}^{2} = 2\overline{L}l_{\mathrm{R}} - 2\overline{L}^{2}\left[1-\exp\left(-\frac{l_{\mathrm{R}}}{\overline{L}}\right)\right] \tag{3.27}$$

Expression qui, au premier ordre en $l_{\mathrm{R}}/\overline{L}$, devient

$$\overline{l}_{\mathrm{R}} \cong l_{\mathrm{R}} \tag{3.28}$$

Ce résultat montre à nouveau qu'au premier ordre la longueur représentative de glissement $\overline{l}_{\mathrm{R}}$ peut être approchée par l_{R} mais qu'elle diverge lorsque l'on s'approche de la saturation (figure 3.8).

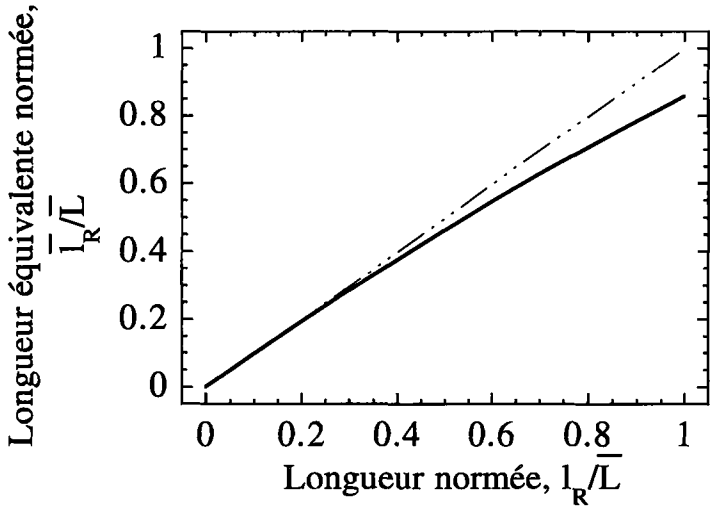

FIG. 3.8 - Évolution de la longueur équivalente de glissement normée $\overline{l}_{\mathrm{R}}/\overline{L}$ en fonction de la longueur de glissement normée $l_{\mathrm{R}}/\overline{L}$.

La densité d'énergie irrécupérable $\overline{\psi}^{\mathrm{i}}$ donnée par l'équation (3.3) peut être réécrite comme suit

$$\overline{\psi}^{\mathrm{i}} = \frac{1}{\overline{L}}\int_{0}^{+\infty} L\psi^{\mathrm{i}}(L)F(L)dL \tag{3.29}$$

où $\psi^{\mathrm{i}}(L)$ désigne la densité d'énergie irrécupérable d'une cellule de longueur L. Dans le cas d'un modèle d'interface à cisaillement τ constant, la densité d'énergie irrécupérable $\psi^{\mathrm{i}}(L)$ s'exprime par

$$\psi^{\mathrm{i}}(L) = \frac{fE\tau^2}{(1-f)E_{\mathrm{m}}E_{\mathrm{f}}R^2}\left(\frac{l_{\mathrm{R}}^2}{2} - \frac{l_{\mathrm{R}}L}{2} + \frac{L^2}{6}\right) \quad \text{pour} \quad L < l_{\mathrm{R}} \tag{3.30}$$

$$\psi^{\mathrm{i}}(L) = \frac{fE\tau^2}{(1-f)E_{\mathrm{m}}E_{\mathrm{f}}R^2}\frac{l_{\mathrm{R}}^3}{6L} \quad \text{pour} \quad L \geq l_{\mathrm{R}} \tag{3.31}$$

de telle manière que la densité d'énergie irrécupérable moyenne $\overline{\psi}^{\mathrm{i}}$ devient

$$\overline{\psi}^{\mathrm{i}} = \frac{fE\tau^2}{(1-f)E_{\mathrm{m}}E_{\mathrm{f}}R^2}\left[\frac{l_{\mathrm{R}}^2}{2} - \overline{L}l_{\mathrm{R}} + \overline{L}^2\left\{1 - \exp\left(-\frac{l_{\mathrm{R}}}{\overline{L}}\right)\right\}\right] \tag{3.32}$$

En utilisant l'équation (3.5), on obtient l'expression suivante pour la variable d'endommagement d

$$d = \frac{fE_{\mathrm{f}}}{(1-f)E_{\mathrm{m}}} \frac{\frac{1}{2}\left[l_{\mathrm{R}} - \overline{L}\left\{1 - \exp\left(-\frac{l_{\mathrm{R}}}{\overline{L}}\right)\right\}\right]^2}{l_{\mathrm{R}}^2 - 2\overline{L}l_{\mathrm{R}} + 2\overline{L}^2\left\{1 - \exp\left(-\frac{l_{\mathrm{R}}}{\overline{L}}\right)\right\}} \tag{3.33}$$

expression qui, au premier ordre en $l_{\mathrm{R}}/\overline{L}$ devient

$$d \cong \frac{3fE_{\mathrm{f}}}{4(1-f)E_{\mathrm{m}}}\frac{l_{\mathrm{R}}}{\overline{L}} \tag{3.34}$$

Ce résultat est identique à celui de l'équation (3.18) en intervertissant fE_{f} et $(1-f)E_{\mathrm{m}}$ (le rôle de la matrice et de la fibre est échangé dans le test de multifragmentation).

Si l'on veut rendre compte des phénomènes d'exclusion, surtout sensibles près de la saturation, on peut utiliser d'autres approches. Citons d'abord celle de CURTIN [1991] qui base son raisonnement sur l'empilement de sphères incompressibles le long d'une ligne [WIDOM, 1966]. Il a été montré que ce modèle n'était qu'une approximation de la solution dite « exacte » [HUI *et al.*, 1995]. Parallèlement à la démarche analytique, on peut également faire appel à une démarche numérique. Ces démarches font toutes appel à une méthode de Monte-Carlo. Dans le cas d'un modèle d'interface à contrainte de cisaillement τ constante, l'approche numérique n'est pas forcément nécessaire, bien qu'elle ait été employée [HENSTENBURG et PHOENIX, 1989]. On remarquera cependant que lorsque les phénomènes d'exclusion ne sont pas aussi simples que ceux évoqués précédemment, une méthode numérique s'impose assez naturellement [BAXEVANAKIS *et al.*, 1993 ; FEILLARD *et al.*, 1994 ; HILD et FEILLARD, 1997].

Pour étudier l'évolution de la longueur représentative de glissement $\overline{l}_{\mathrm{R}}$, nous allons faire appel à une méthode numérique, par souci de simplicité. Afin de vérifier les calculs, nous comparerons les résultats à saturation de la densité de défauts rompus $\overline{\lambda}_{\mathrm{b}}$ par unité de longueur caractéristique δ_{c} (tableau 3.1) à ceux obtenus par HUI *et*

al. [1995], CURTIN [1991] et HENSTENBURG et PHOENIX [1989]. Deux approches peuvent être utilisées. La première (appelée méthode 1), très proche du concept d'élément fini, consiste à discrétiser une longueur L_{tot} en N_{tot} éléments de longueur dz identique, chacun de ces éléments ne pouvant être le siège que d'une seule rupture. Si l'on suppose un processus de POISSON ponctuel, la probabilité de trouver un défaut rompu dans un élément de longueur $dz \ll L_{\text{tot}}$ est $dz\lambda_{\text{t}}$, que l'on peut aisément restituer en utilisant un générateur aléatoire de « bonne » qualité [PRESS *et al.*, 1992]. La séquence de chargement est alors obtenue en rangeant les contraintes de rupture par ordre croissant et en vérifiant que tout nouveau défaut susceptible de casser ne se trouve pas dans une zone d'exclusion. Le processus continue jusqu'à ce que soient « épuisées » toutes les contraintes de rupture. Cette méthode est très simple à programmer mais est très exigeante en place mémoire puisque toutes les contraintes de rupture doivent être stockées. Asymptotiquement, ce type de méthode tend vers un processus de POISSON ponctuel (cf. par exemple [GRADY, 1990]). La limitation de la méthode est le nombre d'éléments (de l'ordre de 10^5 dans notre cas). Les résultats de 10 réalisations par valeurs de module de WEIBULL analysées sont donnés en tableau 3.1. La longueur analysée est $L_{\text{tot}} = 10^3\delta_{\text{c}}$ et les éléments ont une longueur $dz = 10^{-2}\delta_{\text{c}}$.

TAB. 3.1 - Évolution du nombre de défauts rompus à saturation $\overline{\lambda}_{\text{b}}(\infty)$ en fonction du module de WEIBULL m à l'aide de différentes méthodes. Les nombres entre parenthèses donnent la valeur du coefficient de variation pour les méthodes numériques.

m	HENSTENBURG[♭]	CURTIN[♮]	HUI[♯]	Eq. (3.22)	Méth. 1	Méth. 2
3	1.03 (32.9%)	1.03	**1.05**	0.92	1.06 (1.0%)	1.05 (0.5%)
5	1.13 (29.4%)	1.15	**1.13**	0.94	1.14 (0.8%)	1.14 (0.8%)
10	1.24 (25.5%)	1.24	**1.24**	0.96	1.25 (0.6%)	1.24 (0.8%)
15	1.29 (24.0%)	1.30	**1.29**	0.98	1.30 (0.8%)	1.30 (0.4%)
∞	1.49[‡] (20.6%)	1.49[‡]	**1.50**	1.00	1.48[‡] (0.7%)	1.49[‡] (0.4%)

[♭] = [HENSTENBURG et PHOENIX, 1989], [♮] = [CURTIN, 1991], [♯] = [HUI *et al.*, 1995], [‡] : $m = 1000$.

La seconde approche (appelée méthode 2) est moins coûteuse en mémoire mais peut s'avérer plus longue que la précédente lorsque le nombre de défauts analysés croît. En effet, seuls les défauts qui ont cassé sont stockés. Les hypothèses de départ sont identiques à celles de la méthode précédente ($L_{\text{tot}} = N_{\text{tot}} \times dz$). La différence provient du fait que le pas de contrainte est calculé de manière à faire rompre, s'il n'est pas dans une zone d'exclusion, un seul défaut. Le pas de contrainte ΔT est déterminé de telle manière que : $dz\partial\lambda_{\text{t}}/\partial t(T)\Delta T = 1$; la position de ce nouveau défaut étant tirée à partir d'une distribution uniforme sur la longueur L_{tot}. Ce défaut cassera effectivement

s'il ne se trouve dans aucune zone d'exclusion des défauts déjà cassés. C'est cette condition qui peut s'avérer pénalisante à vérifier si le nombre de défauts déjà cassés devient grand car ce test doit être conduit à chaque fois qu'un nouveau défaut est généré. Asymptotiquement, ce type de méthode tend également vers un processus de POISSON ponctuel (cf. par exemple [GRADY, 1990]). Les résultats de 10 réalisations sont aussi donnés en tableau 3.1 pour une longueur $L_{\text{tot}} = 10^3\delta_c$ et des éléments de longueur $dz = 10^{-3}\delta_c$.

Les résultats du tableau 3.1 montrent que les deux méthodes conduisent à des résultats très proches de ceux obtenus par HUI *et al.* [1995]. Afin d'éviter les effets de bord, des conditions de périodicité sont imposées dans la recherche des zones d'exclusion. On peut remarquer que ces méthodes peuvent aussi être employées dans l'étude de la fragmentation dynamique avec des modifications minimes des conditions d'exclusion (cf. paragraphe 3.1.2).

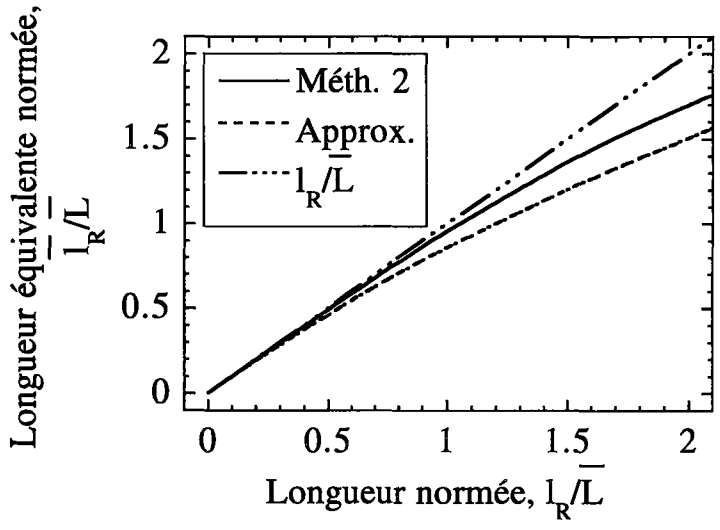

FIG. 3.9 - Évolution de la longueur équivalente de glissement normée $\bar{l}_R/\bar{L}$ en fonction de la longueur de glissement normée $l_R/\bar{L}$. Trois méthodes différentes sont utilisées ($m = 3$).

La figure 3.9 donne l'évolution de la longueur équivalente de glissement normée $\bar{l}_R/\bar{L}$ en fonction de la longueur de glissement normée $l_R/\bar{L}$ pour un module de WEIBULL $m = 3$. Toutes les trois approches conduisent au même résultat lorsque $l_R/\bar{L} \ll 1 : \bar{l}_R \cong l_R$. Par contre, on observe une divergence lorsque $l_R/\bar{L}$ croît. On a reporté les résultats d'une réalisation ($\bar{\lambda}_b(\infty) = 1.051$) avec la méthode 2 (notée Méth. 2), ceux donnés par l'approximation (notée Approx.) d'un processus poissonien (équation (3.27)) et enfin ceux pour lesquels on néglige les recouvrements de différentes

zones d'exclusion ($\bar{l}_R = l_R$). L'approximation d'un processus poissonien *surestime* le nombre de ruptures et sous-estime la déformation inélastique moyenne $\bar{\varepsilon}^i$, donc la longueur équivalente de glissement $\bar{l}_R$. Au contraire, l'égalité $\bar{l}_R = l_R$ constitue une borne supérieure car elle ne rend pas compte des recouvrements de zones d'exclusion et *surestime* la longueur équivalente de glissement $\bar{l}_R$.

Tous ces résultats montrent que le choix des longueurs équivalentes de fissuration et de glissement égales à la distance moyenne de fissuration et à la longueur moyenne de glissement ne sont valables qu'en première approximation. La signification de la taille d'une cellule élémentaire représentative ainsi que des longueurs à l'intérieur de celle-ci est donc à définir avec précaution. Si l'on veut caractériser la dégradation à partir d'observations microscopiques, une distance moyenne entre fissures, une longueur moyenne de décohésion sont des quantités pertinentes. Par contre, si on veut traduire l'effet de ces distributions aléatoires sur le comportement mécanique, ce sont d'autres éléments de la distribution qui peuvent s'ajouter à ceux que l'on considère assez systématiquement (moyennes, *i.e.*, moments d'ordre un). Les moments d'ordre un constituent une approximation au premier ordre pour les exemples traités ci-dessus. Une étude micromécanique est alors nécessaire pour connaître l'influence exacte associée à chaque distribution.

3.2.2 Applications à des composites unidirectionnels

par D. BOUDON-CUSSAC, A. BURR et F. HILD (1998).
G.Z. VOYADJIS, J.-W. W. JU et J.-L. CHABOCHE (eds.), *Damage Mechanics in Engineering Materials*, Studies in Applied Mechanics 46, pp. 303-320.

On the Continuum Description of Damage in Fiber-Reinforced Composites

D. Boudon-Cussac, A. Burr and F. Hild[a]

[a]Laboratoire de Mécanique et Technologie
ENS de Cachan / CNRS / Université Paris VI
61, avenue du Président Wilson, F-94235 Cachan Cedex, France

In this paper, the derivation of a mechanism-based constitutive law is presented to model the mechanical behavior of fiber-reinforced composites. It allows to account for matrix-cracking, interfacial debonding and sliding in the framework of Continuum Damage Mechanics. Applications are performed on a unidirectional SiC/SiC composite and on concrete specimens.

1. INTRODUCTION

The basic mechanisms related to the degradation of brittle matrices reinforced by continuous or discontinuous fibers and submitted to monotonic loading histories are matrix-cracking, interfacial debonding and sliding, and eventually fiber breakage and fiber pull-out. These mechanisms induce stiffness losses and inelastic strains. The latter are studied within the framework of Continuum Damage Mechanics (CDM) by using micromechanical analyses. An explicit expression of the Helmholtz free energy density is derived. In particular, internal variables are carefully chosen to describe the degradation mechanisms and written in an appropriate format to allow the derivation of constitutive equations applicable to structural calculations.

The model is used to analyze experimental data obtained on SiC matrices unidirectionally reinforced by continuous SiC fibers. The evolution laws are derived by using micromechanical parameters. The same model is used to study the behavior of an unreinforced concrete. To avoid localized damage, a prismatic concrete specimen is loaded by aluminum bars glued on two opposite lateral faces. In particular, the effect of glue between the aluminum bars and the concrete specimen is discussed and modeled. Furthermore, the model is utilized to study the behavior of concrete specimen reinforced by short fibers made of steel and aligned along the loading direction. This composite is loaded by using a similar technique as that used to analyze unreinforced concrete. The effect of the addition of short fibers is discussed.

2. PHYSICAL MODEL

Loading a composite consisting of a brittle matrix supported by stronger fibers, usually causes multiple matrix-cracking [1] accompanied by debonding and sliding at the

fiber-matrix interface. Because of stress redistribution between the fiber and matrix, the cracking density usually saturates. Matrix-cracking is responsible for the decrease of stiffness observed in experiments on Brittle Matrix Composites (BMCs), relief of residual stresses due to processing and sliding at the fiber-matrix interface are the source of irreversible strains.

2.1. The Unit Cell

The cell illustrated in Fig. 1 and first proposed by Aveston and Kelly [2] has stood the test of time with the introduction of a debond energy at the front of the slipping region [3]. This unit cell constitutes the basis for formulating constitutive equations suitable for finite element calculations used in design studies.

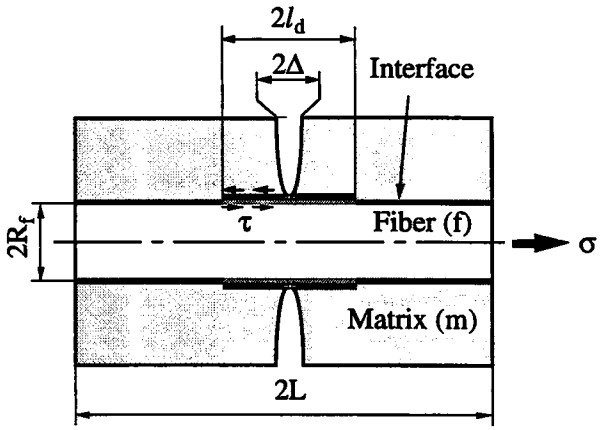

Figure 1. Elementary Cell.

In the unit cell shown in Fig. 1 the elastic moduli of the fiber and matrix are E_f and E_m respectively, the volume fraction of the fiber is f and R_f is the fiber radius. The elastic modulus of the undamaged composite is $E = fE_f + (1-f)E_m$. Matrix-cracking occurs when the matrix stress reaches a material value σ_{mc} [1,4] and the average distance between cracks is denoted by $2L$. The debond length at the fiber/matrix interface is $2l_d$, and the interface is assumed to have a constant shear strength τ. The critical energy release rate to extend an interface crack is $\mathcal{G}_d$. Following Hutchinson and Jensen [3], this critical energy release rate $\mathcal{G}_d$ can be represented as a debond strength σ_d which introduces simplicity in later calculations

$$\sigma_d = 2\sqrt{\frac{(1-f)E_m E_f \mathcal{G}_d}{R_f E}} \tag{1}$$

To define the state of the unit cell, the values for the crack spacing $2L$, the slip length $2l_d$ and the interface properties τ and σ_d must be known. The latter are unknown material parameters but are assumed to be constant. Residual stresses are introduced during processing so that the stress level in the matrix σ^*_{pm} is an additional unknown.

The statistical nature of the distribution of crack distances and debond lengths discussed in Ref. [5] is not considered herein. For the sake of simplicity, it is assumed that the average crack distance $2L$ and the corresponding debond length $2l_d$ are sufficient to characterize the state of the material.

2.2. Interrogation of First Loading Response

On first loading, the initial response of the composite is elastic when the modulus is E. On reaching the matrix-cracking stress σ_{mc}, matrix-cracking occurs which is accompanied by matrix-fiber interface debonding and slip. From the partial unloading tests shown in Fig. 2, it is possible to measure the current elastic modulus $E(1-D)$ and the total irreversible or inelastic strain. The relationship between the damage variable D and the crack spacing $2L$ may be estimated from micromechanics following the model of Cox [6] and Aveston and Kelly [2]

$$D = \frac{\Omega}{1+\Omega} \tag{2}$$

in which the dimensionless quantities are defined by

$$\Omega = \frac{\omega}{A}\tanh\left(\frac{1}{\omega}\right) \quad , \quad \omega = \frac{R_f}{\beta L} \quad , \quad A = \frac{fE_f}{(1-f)E_m} \quad , \quad \beta^2 = \frac{2G_m E}{(1-f)E_m E_f \ln\left(\frac{R_m}{R_f}\right)} \tag{3}$$

where G_m is the shear modulus of the matrix and $2R_m$ the average distance between fibers ($f = R_f^2/R_m^2$, see Fig. 1). Since the damage variable D is readily measured, Eqn. (2) provides a means of determining indirectly the crack spacing $2L$.

The crack opening displacement Δ_c following matrix-cracking consists of two contributions, viz. Δ_e is the elastic opening due to cracking, and Δ_p is the opening due to the relief of the residual stresses due to processing. The crack opening displacement Δ_e resulting from elastic deformations is given by the relationship [7,8]

$$\frac{(1-f)E_m}{E}\frac{\Delta_e}{L} = \frac{\sigma D}{E(1-D)} \tag{4}$$

By using the model of Cox [6] and Aveston and Kelly [2], the crack opening displacement Δ_p is accompanied by the irreversible strain ϵ_r

$$\epsilon_r = \frac{(1-f)E_m}{E}\frac{\Delta_p}{L} = \frac{\epsilon_{pm} D}{1-D} \quad \text{with } \epsilon_{pm} = \frac{\sigma^*_{pm}}{E_m} \tag{5}$$

and by the relief of initially stored energy

$$\psi_r = -\frac{E\epsilon_{pm}^2 D}{2(1-D)} = -\frac{1}{2}\epsilon_{pm} E \epsilon_r \tag{6}$$

When interface slip occurs, it is accompanied by an additional crack opening displacement Δ_s. The latter gives rise to a self-balancing stress field along the slip length $2l_F$ ($\leq 2l_d$) in the matrix, $\sigma_m(z)$ and in the fiber, $\sigma_f(z)$, for which the corresponding elastic

strains are denoted by $\epsilon_m(z)$ and $\epsilon_f(z)$, respectively. The self-balancing stress fields cause inelastic strains

$$\epsilon_i = \frac{(1-f)E_m}{E}\frac{\Delta_s}{L} = \frac{1}{L}\int_0^L \epsilon_f(z)dz \tag{7}$$

The total crack opening displacement Δ is the sum of three contributions

$$\Delta = \Delta_e + \Delta_p + \Delta_s \tag{8}$$

The crack closure condition is simply expressed as $\Delta = 0$. Debonding and friction also cause elastic energy to be stored in the material. The expression for the non-recoverable energy is found to be

$$\psi_d = \frac{EA}{2L}\int_0^L \epsilon_f^2(z)dz \tag{9}$$

The explicit calculation of the integral is left to a later stage. Equation (9) is concerned with the residual stress due to debonding and sliding. Normally there is an initial residual stress in many composite systems due to processing. The presence of the two residual stress fields induces a coupling term $\psi_{d|p}$ in the total non-recoverable energy density ψ_s. If the residual stress field due to processing is constant along the total length of the composite, the non-recoverable energy density $\psi_{d|p}$ can be expressed as

$$\psi_{d|p} = -\epsilon_i E \epsilon_{pm} \tag{10}$$

Equation (10) shows that the inelastic strain ϵ_i and the misfit strain ϵ_{pm} are sufficient to measure the energy resulting from the coupling.

3. THE CONTINUUM REPRESENTATION

Since the objective of the paper is to obtain mechanism-based constitutive equations which are suitable for finite element calculations, the results of the model are reformulated by using the techniques of Continuum Mechanics and the concept of state variables [9,10]. The model described in the preceding section helps to define the state variables and to calculate the free energy density (also called state potential) from which the corresponding forces can be deduced. Finally, the evolution laws have to be written.

3.1. State Potential for Unidirectional Composites

The free energy density for a given state is calculated by performing two elastic calculations following approaches introduced by Volterra [11], and used to analyze the elastic behavior of homogeneous and isotropic media [11,12], and the influence of inclusions in an infinite medium [13]. The first step consists of calculating the elastic energy when a crack is introduced and the unbroken part (f) is moved with respect to the broken part (m) by an additional amount Δ_s over a length $2l_F = 2l_d$ with no external load. The derivation of the non-recoverable energy ψ_s has been determined in the previous section and is rewritten as follows

$$\psi_s = \frac{E\epsilon_i^2}{2d} - \epsilon_i E \epsilon_{pm} - \frac{E\epsilon_{pm}^2 D}{2(1-D)} \tag{11}$$

where the general expression of the damage variable d is given by

$$d = \frac{1}{A}\left[\frac{1}{L}\int_0^L \epsilon_{\mathrm{f}}(z)dz\right]^2 / \left[\frac{1}{L}\int_0^L \epsilon_{\mathrm{f}}^2(z)dz\right] \tag{12}$$

By using the micromechanical model with a debond strength σ_{d} and a constant shear strength τ defined previously, the inelastic strain ϵ_{i} and the damage variable d are expressed as

$$\epsilon_{\mathrm{i}} = \lambda_{\mathrm{d}} T_{\mathrm{d}} (1 + \Sigma_{\mathrm{d}}) \quad , \quad d = \frac{\lambda_{\mathrm{d}}}{A}\left[1 + \frac{1}{3}(1 + \Sigma_{\mathrm{d}})^{-2}\right]^{-1} \tag{13}$$

where the dimensionless groups λ_{d}, T_{d} and Σ_{d} are given by

$$\lambda_{\mathrm{d}} = \frac{l_{\mathrm{d}}}{L} \quad , \quad T_{\mathrm{d}} = \frac{\tau l_{\mathrm{d}}}{R_{\mathrm{f}} E_{\mathrm{f}}} \quad , \quad \Sigma_{\mathrm{d}} = \frac{\sigma_{\mathrm{d}} R_{\mathrm{f}}}{\tau l_{\mathrm{d}}} \tag{14}$$

The value of the square bracket of Eqn. (13.2) varies between 1 and 4/3 for a high and low debond energy material [14] respectively, which means that the value of the dimensionless group Σ_{d} has little effect on d.

The second step consists of an elastic loading of a cracked system with friction prevented. The recoverable part of the Helmholtz free energy density becomes

$$\psi_{\mathrm{e}} = \frac{E(1-D)}{2}\left[\epsilon - \epsilon_{\mathrm{i}} - \frac{\epsilon_{\mathrm{pm}} D}{1-D}\right]^2 \tag{15}$$

The total free energy density is the sum of the two components (11) and (15) of energy density. The total free energy density can be expressed by using four state variables which are the total strain ϵ, and three internal variables, viz. the damage variable D modeling the loss of stiffness due to cracking, the inelastic strain ϵ_{i} due to debonding and sliding, the damage variable d measuring the amount of non-recoverable energy due to debonding and slip

$$\psi = \frac{E(1-D)}{2}\left[\epsilon - \epsilon_{\mathrm{i}} - \frac{\epsilon_{\mathrm{pm}} D}{1-D}\right]^2 + \frac{E\epsilon_{\mathrm{i}}^2}{2d} - \epsilon_{\mathrm{i}} E \epsilon_{\mathrm{pm}} - \frac{E\epsilon_{\mathrm{pm}}^2 D}{2(1-D)} \tag{16}$$

The forces associated with the state variables are given by

$$\sigma = \frac{\partial \psi}{\partial \epsilon} \quad , \quad Y = -\frac{\partial \psi}{\partial D} \quad , \quad X = -\frac{\partial \psi}{\partial \epsilon_{\mathrm{i}}} \quad , \quad y = -\frac{\partial \psi}{\partial d} \tag{17}$$

Equation (17.1) defines the macroscopic stress σ and Eqn. (17.2) the energy release rate density Y associated with matrix-cracking. The energy release rate density Y is proportional to the square of a modified 'effective stress' $(\sigma + E\epsilon_{\mathrm{pm}})/(1-D)$. Similarly, Eqn. (17.3) defines the back stress X associated with sliding whose exact value depends upon the interfacial properties. Equation (17.4) defines the energy release rate density y associated to the residual stresses due to debonding and sliding.

3.2. State Potential for 2D Composites

A 2D formulation requires an anisotropic damage description [15]. In the case of cracking perpendicular to the fiber direction, the generalization is straight forward since the only compliance change is given in the fiber direction, and therefore only one scalar anisotropic damage variable is needed and the previous 1D analysis is still relevant. For a 0/90 layered or woven composite, the Helmholtz free energy density depends upon the damage variables modeling matrix-cracking in the 0 and 90-degree 'layers'

$$\psi_{\mathrm{e}} = \frac{1}{2}\, \underline{\underline{\epsilon}}_{\mathrm{e}} : \underline{\underline{\underline{\underline{E}}}}(D^0_{\mathrm{m}}, D^{90}_{\mathrm{m}}) : \underline{\underline{\epsilon}}_{\mathrm{e}} \tag{18}$$

where $\underline{\underline{\epsilon}}_{\mathrm{e}}$ denotes the elastic strain tensor, ':' the contraction with respect to two indices, $\underline{\underline{\underline{\underline{E}}}}$ the elastic stiffness tensor of the damaged composite (i.e., it depends upon the matrix-cracking damage variables D^0_{m} and D^{90}_{m} [15]).

A second order tensor is needed to model the inelastic strains due to debonding and slip. In the case of a 2D composite, a first order approximation only requires the in-plane components (i.e., $\epsilon_{\mathrm{i}11}$, $\epsilon_{\mathrm{i}22}$, and $\epsilon_{\mathrm{i}12}$) of the inelastic strain tensor $\underline{\underline{\epsilon}}_{\mathrm{i}}$. Since each operative slip system can be integrated separately in terms of energetic contributions, the internal damage variables can be defined separately for each inelastic strain term. Therefore there are as many debond damage terms as non-vanishing inelastic strain components [15]

$$\psi_{\mathrm{d}} = \frac{E_{11}}{2}\frac{\epsilon^2_{\mathrm{i}11}}{d_{11}} + \frac{E_{22}}{2}\frac{\epsilon^2_{\mathrm{i}22}}{d_{22}} + \frac{G_{12}}{2}\frac{\epsilon^2_{\mathrm{i}12}}{d_{12}} \tag{19}$$

where E_{11}, E_{22}, are the Young's moduli along the 1- and 2-directions, respectively, and G_{12} is the shear modulus in the 1-2 plane. In the case of cracking perpendicular to the fiber direction, only one inelastic strain component is different from zero, viz. the normal component along the fiber direction. Similarly, only one scalar debond damage variable is needed.

Equation (10) is used to derive the generalized coupling term $\psi_{\mathrm{d|p}}$ for 2D composites

$$\psi_{\mathrm{d|p}} = -\,\underline{\underline{\epsilon}}_{\mathrm{i}} : \underline{\underline{\underline{\underline{E}}}} : \underline{\underline{\epsilon}}_{\mathrm{pm}} \tag{20}$$

where $\underline{\underline{\underline{\underline{E}}}}$ is the stiffness tensor of the undamaged material. It is worth noting that the misfit strain tensor $\underline{\underline{\epsilon}}_{\mathrm{pm}}$ is an average tensor on the composite level to be computed for each specific architecture. Lastly, the relief of initially stored energy by the residual stresses due to processing is expressed as a generalization of Eqn. (6)

$$\psi_{\mathrm{r}} = -\frac{1}{2}\, \underline{\underline{\epsilon}}_{\mathrm{pm}} : \underline{\underline{\underline{\underline{E}}}} : \underline{\underline{\epsilon}}_{\mathrm{r}} \left(\underline{\underline{\epsilon}}_{\mathrm{pm}}, D^0_{\mathrm{m}}, D^{90}_{\mathrm{m}}\right) \tag{21}$$

where the irreversible strain tensor $\underline{\underline{\epsilon}}_{\mathrm{r}}$ depends upon the misfit strain tensor $\underline{\underline{\epsilon}}_{\mathrm{pm}}$ and the damage state described by D^0_{m} and D^{90}_{m}.

The Helmholtz free energy density depends upon the damage variables modeling matrix-cracking, the inelastic strain tensor as well as the damage variables modeling debonding and sliding

$$\psi = \frac{1}{2}\underline{\underline{\epsilon}}_{\mathrm{e}} : \underline{\underline{\underline{\underline{E}}}}(D_{\mathrm{m}}^{0}, D_{\mathrm{m}}^{90}) : \underline{\underline{\epsilon}}_{\mathrm{e}} + \frac{E_{11}}{2}\frac{\overline{\epsilon}_{\mathrm{in}11}^{2}}{d_{11}} + \frac{E_{22}}{2}\frac{\overline{\epsilon}_{\mathrm{in}22}^{2}}{d_{22}} + \frac{G_{12}}{2}\frac{\overline{\epsilon}_{\mathrm{in}12}^{2}}{d_{12}} - \underline{\underline{\epsilon}}_{\mathrm{i}} : \underline{\underline{\underline{\underline{E}}}} : \underline{\underline{\epsilon}}_{\mathrm{pm}} - \frac{1}{2}\underline{\underline{\epsilon}}_{\mathrm{pm}} : \underline{\underline{\underline{\underline{E}}}} : \underline{\underline{\epsilon}}_{\mathrm{r}}\left(\underline{\underline{\epsilon}}_{\mathrm{pm}}, D_{\mathrm{m}}^{0}, D_{\mathrm{m}}^{90}\right) \quad (22)$$

with

$$\underline{\underline{\epsilon}}_{\mathrm{e}} = \underline{\underline{\epsilon}} - \underline{\underline{\epsilon}}_{\mathrm{i}} - \underline{\underline{\epsilon}}_{\mathrm{r}}\left(\underline{\underline{\epsilon}}_{\mathrm{pm}}, D_{\mathrm{m}}^{0}, D_{\mathrm{m}}^{90}\right) \quad (23)$$

where $\underline{\underline{\epsilon}}$ is the total strain tensor. The associated forces are defined by

$$\underline{\underline{\sigma}} = \frac{\partial \psi}{\partial \underline{\underline{\epsilon}}} \quad (24)$$

$$Y_{\mathrm{m}}^{0} = -\frac{\partial \psi}{\partial D_{\mathrm{m}}^{0}} \quad , \quad Y_{\mathrm{m}}^{90} = -\frac{\partial \psi}{\partial D_{\mathrm{m}}^{90}} \quad (25)$$

$$\underline{\underline{X}} = -\frac{\partial \psi}{\partial \underline{\underline{\epsilon}}_{\mathrm{i}}} \quad (26)$$

$$y_{11} = -\frac{\partial \psi}{\partial d_{11}} \quad , \quad y_{22} = -\frac{\partial \psi}{\partial d_{22}} \quad , \quad y_{12} = -\frac{\partial \psi}{\partial d_{12}} \quad (27)$$

Equations (24), (25), (26) and (27) constitute a generalization of Eqns. (17.1), (17.2), (17.3) and (17.4).

3.3. The Evolution Laws

The final step in establishing the model is to determine the growth laws $F_{\mathrm{D}}, F_{\mathrm{i}}, F_{\mathrm{d}}$ which relate the state variables $(D, \epsilon_{\mathrm{i}}, d)$ to their associated forces (Y, X, y)

$$D = F_{\mathrm{D}}(Y) \quad , \quad \epsilon_{\mathrm{i}} = F_{\mathrm{i}}(X) \quad , \quad d = F_{\mathrm{d}}(y) \quad (28)$$

To be thermodynamically admissible, the intrinsic dissipation $\mathcal{D}$ must be positive

$$\mathcal{D} = Y\,\dot{D} + X\,\dot{\epsilon}_{\mathrm{i}} + y\,\dot{d} \geq 0 \quad (29)$$

It can be shown that this condition is satisfied in the present case.

The evolution laws will be identified for two different BMCs, viz. a unidirectional SiC/SiC composite and a reinforced concrete. The identification procedure is based upon the experimental results of a loading/partial unloading test (Fig. 2) from which the current value of the elastic modulus $E(1-D)$ and the total inelastic strain $\epsilon_{\mathrm{i}} + \epsilon_{\mathrm{r}}$ can be measured. A similar approach is used to identify the parameters of the evolution laws of 2D composites. A detailed description of the procedure can be found in Ref. [16].

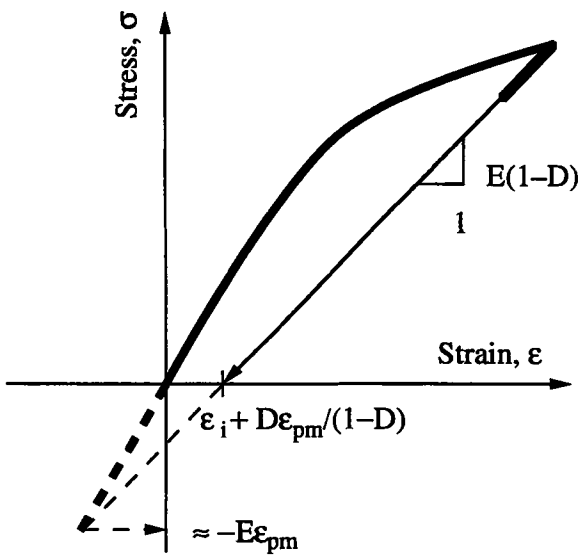

Figure 2. Schematic stress/strain curve with partial unloading.

4. SiC/SiC COMPOSITE

The first material to be analyzed is a unidirectional SiC/SiC composite. This material has been extensively studied so that many experimental data are available. In particular, the change of the average crack density with the applied stress has been measured [17] even though the task is tedious and needs special care to get reliable data [18]. The initial cracking condition can be written as

$$Y = Y_c \tag{30}$$

From Eqns. (17.2) and (30), the matrix-cracking stress σ_{mc} is found to be

$$\frac{\sigma_{mc}}{E} + \epsilon_{pm} = \sqrt{\frac{2Y_c}{E}} \tag{31}$$

This relationship is a transcription in the framework of CDM of the well-known expression derived in Linear Elastic Fracture Mechanics [4]. The Cox' Model (see Eqns. (2) and (3), $1 > 2.5\ \omega$) predicts that there is a linear relationship between the damage quantity $D/(1-D)$ and the average crack density ω

$$\frac{D}{1-D} = \frac{\omega}{A} \tag{32}$$

The micromechanics associated with crack spacing is complex and involves statistical calculations [19]. Instead of following this route, use is made of the experimental observation of Domergue [17] that the crack density ω satisfies the following evolution law

$$\omega = \frac{\sigma - \sigma_c}{\sigma_0} \quad \text{with} \quad \sigma_0 = \frac{(\sigma_F - \sigma_{mc})\,\beta L_F}{R_f} \tag{33}$$

The normalizing constants L_F and σ_F are the values of L and σ at failure before saturation occurs. If saturation occurs, the previous constants are the values of L and σ at saturation. By eliminating the crack density ω from the last two equations and by using Eqn. (17.2) for Y in Eqn. (33) combined to Eqn. (32), the evolution law for D in terms of Y becomes

$$D = \frac{2\sqrt{Y} + \sqrt{Y_0} - \sqrt{Y_c} - \sqrt{\left(2\sqrt{Y} + \sqrt{Y_0} - \sqrt{Y_c}\right)^2 - 4\sqrt{Y}\left(\sqrt{Y} - \sqrt{Y_c}\right)}}{2\sqrt{Y}}$$

$$\text{with} \quad \sqrt{2EY_0} = A\sigma_0 \tag{34}$$

To get the onset of interfacial debonding (when $l_d = 0$), the dependence of the dimensionless group T_d with the applied stress σ is needed

$$T_d = \frac{1}{2A}\left(\frac{\sigma - \sigma_{id}}{E}\right) \tag{35}$$

where the stress σ_{id} describing the onset of interfacial debonding can be calculated

$$\frac{\sigma_{id}}{E} + \epsilon_{pm} = \frac{A\sigma_d}{E_f} \tag{36}$$

The growth law for the inelastic strain ϵ_i has been defined by Eqn. (28.2) with the definition of the back stress X given in Eqn. (17.3). By eliminating the debond length l_d between Eqns. (13) and (35), and the crack spacing $2L$ (Eqns. (3.2) and (33)), the relationship between ϵ_i and the applied stress σ becomes

$$\epsilon_i = \frac{B(\sigma - \sigma_{mc})}{4A^2\sigma_0}\left[\left(\frac{\sigma}{E} + \epsilon_{pm}\right)^2 - \left(\frac{A\sigma_d}{E_f}\right)^2\right] \quad \text{with} \quad B = \frac{\beta E_f}{\tau} \tag{37}$$

It is possible formally to develop the relationship (28.2), but from a computation point of view, it is easier to use directly the result of the micromechanics given in Eqn. (37).

The growth law of the interfacial damage d can be written as a function of its associated force y. Instead, the evolution law is given as a function of the applied stress σ

$$d = \frac{B(\sigma - \sigma_{mc})(\sigma - \sigma_{id})}{2A^2\sigma_0 E}\left[1 + \frac{1}{3}\left\{1 + 2\frac{A\sigma_d}{E_f}\left(\frac{\sigma - \sigma_{id}}{E}\right)^{-1}\right\}^{-2}\right]^{-1} \tag{38}$$

The first key parameter to determine is the misfit strain ϵ_{pm}. Usually at the onset of matrix-cracking, the inelastic strains are very small so that the value of the misfit stress $E\epsilon_{pm}$ is obtained by searching the intersection of the unloading line with the elastic response of the material (see Fig. 2). The accuracy of the measurement of this quantity can be checked by using the first partial unloadings. In the present case, the following estimate is found

$$\epsilon_{pm} = 5.8 \times 10^{-4} \pm 4 \times 10^{-5} \tag{39}$$

The value of the misfit strain is in good agreement with that obtained by using an identification technique based upon the analysis of hysteresis loops [14]. The difference in coefficients of thermal expansion is then on the order of $\Delta\alpha \cong 1.5 \times 10^{-6} \pm 10^{-7}$ K^{-1} when the temperature variation $\Delta T = 1000$ K. The value of $\Delta\alpha$ is expected for SiC/SiC composites obtained by CVI [17].

The experimental relationship observed between D and Y is shown in Fig. 3. From this curve the values of the dimensionless parameters $\sqrt{2Y_c/E}$ and $\sqrt{2Y_0/E}$ can be obtained

$$\sqrt{\frac{2Y_c}{E}} = 1.07 \times 10^{-3} \pm 3 \times 10^{-6} \quad \text{and} \quad \sqrt{\frac{2Y_0}{E}} = 3.7 \times 10^{-4} \pm 8 \times 10^{-6} \tag{40}$$

from which the matrix-cracking stress σ_{mc} can be derived immediately and has the value 275 ± 1 MPa, which is in good agreement with experimental observations [17].

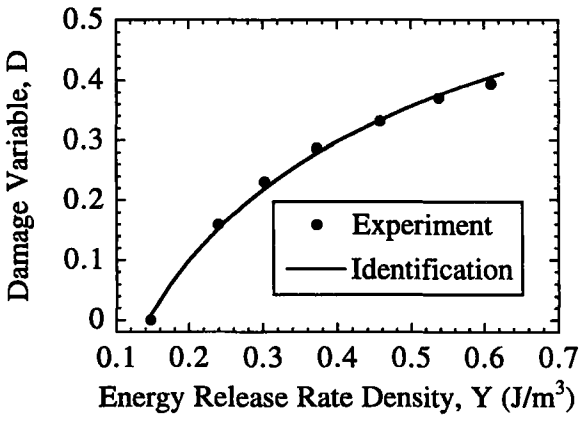

Figure 3. Damage variable D versus its associated force Y for a SiC/SiC composite.

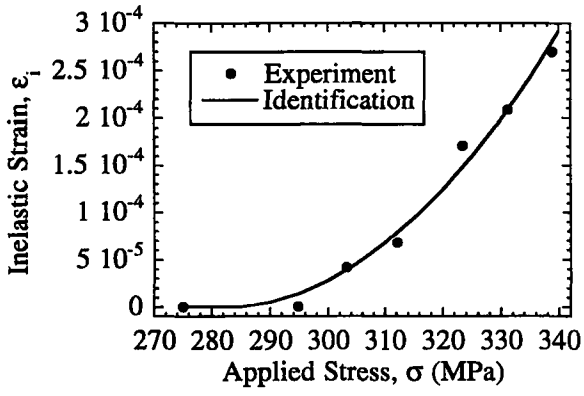

Figure 4. Inelastic strain ϵ_i versus applied stress σ for a SiC/SiC composite.

Equations (37) and (38) contain the dimensionless parameters $B/4A^2$ and $A\sigma_d/E_f$. They are identified by using the inelastic strain due to debonding and sliding alone. By fitting the experimental data of Fig. 4, the values of the dimensionless parameters are

$$\frac{B}{4A^2} = 73 \times 10^3 \pm 9 \times 10^3 \quad \text{and} \quad \frac{A\sigma_d}{E_f} = 1.7 \times 10^{-3} \pm 2 \times 10^{-5} \tag{41}$$

Since all the dimensionless parameters have been identified, the value of the dimensionless group λ_d can be computed

$$\lambda_d = \frac{l_d}{L} = B\omega T_d \tag{42}$$

At saturation, λ_d is equal to unity so that the value for the saturation stress σ_{sat} is

$$\sigma_{sat} = 490 \text{ MPa} > \sigma_F = 340 \text{ MPa} \tag{43}$$

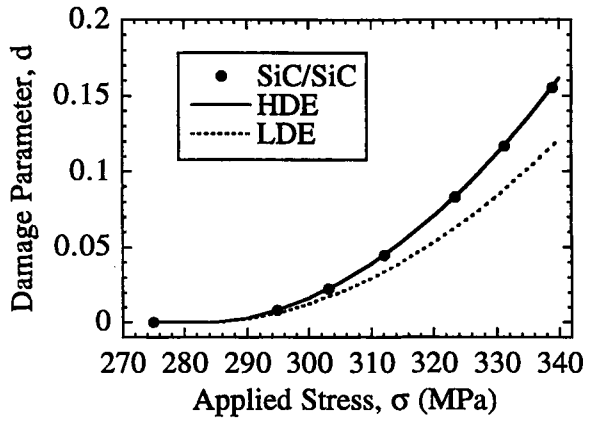

Figure 5. Damage variable d versus applied stress σ for a SiC/SiC composite.

Another output of the identification is the variation of the damage variable d with the applied stress σ. Figure 5 compares the response of a high debond energy (HDE) material, a low debond energy (LDE) material and the analyzed SiC/SiC composite. The behavior of the SiC/SiC composite coincides with the response given by an HDE material. This result was also found by Evans et al. [14]. On the other hand, it has been shown that layered alumina with carbon/epoxy prepregs is an LDE composite [20].

In the previous sections, the only discussed features were associated with monotonic loading conditions. As a consequence of the previous identification, the inelastic strains upon complete unloading (referred to as permanent strains and denoted by ϵ_p) are predictions since they were not used to tune the model. Unloading from the maximum stress σ_{max} to a stress $\sigma_{max} - \Delta\sigma$ is accompanied by reverse slip from the extremity of the debonded region (the reverse slip length is $2l_u$). The expressions of the inelastic strain $\Delta\epsilon_i$ decrement is given by

$$\Delta\epsilon_i = -2\lambda_u T_u \tag{44}$$

where the dimensionless group T_u measures the average strain due to reverse slip over a distance l_u

$$T_u = \frac{\tau l_u}{E_f R_f} = \frac{\Delta\sigma}{4EA} \tag{45}$$

and λ_u is defined as

$$\lambda_u = \frac{l_u}{L} = B\omega T_u \tag{46}$$

Equation (44) is valid provided the reverse slip length l_u is less than the debond length l_d. When the reverse slip length l_u is equal to the debond length l_d, reverse slip no longer evolves. If $\Delta\sigma_a$ denotes the stress decrement at which slip arrest occurs then

$$\frac{\Delta\sigma_a}{E} = 4AT_d \tag{47}$$

When $\Delta\sigma \geq \Delta\sigma_a$, the inelastic strain decrement is

$$\Delta\epsilon_i = -2\lambda_d T_d - \frac{\Delta\sigma - \Delta\sigma_a}{AE}\lambda_d \tag{48}$$

When the material behaves in an HDE regime, slip arrest is very likely to occur. This property can be noticed when the hysteresis loops have a parabolic and a subsequent linear portion. In the present case, slip arrest was always involved. Figure 6 shows that the predicted values of the permanent strains are in good agreement with the measured ones.

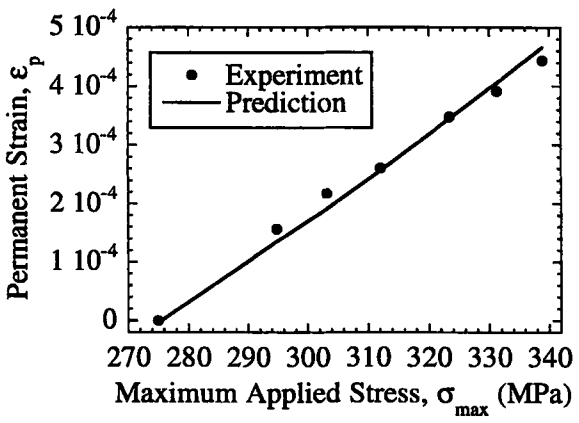

Figure 6. Permanent strain ϵ_p versus maximum applied stress σ_{max} for a SiC/SiC composite.

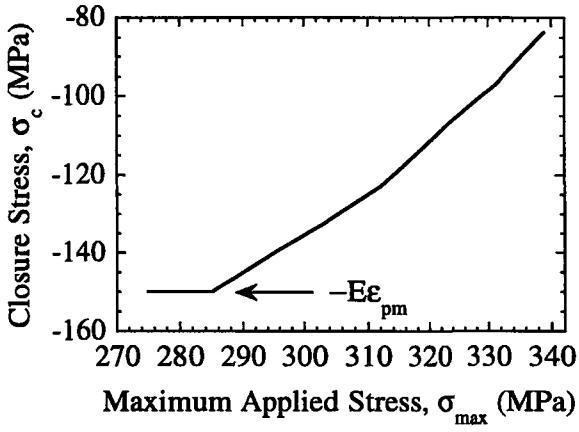

Figure 7. Crack closure stress σ_c versus maximum applied stress σ_{max} for a SiC/SiC composite.

Lastly, the crack closure condition is analyzed. No data are available to compare the predictions with experimental data. By using Eqns. (4), (5), (7) and (8), the crack closure condition $\Delta = 0$ can be rewritten as

$$\epsilon_i(\sigma_c) + \frac{(\sigma_c + E\epsilon_{pm})\,D}{E(1-D)} = 0 \tag{49}$$

where σ_c denotes the closure stress, $\epsilon_i(\sigma_c)$ the inelastic strain at the current stress level and D the damage variable at the maximum stress level σ_{max}. Geometrically, this condition is given by the intersection of the stress/strain curve with the elastic response ($\sigma = E\epsilon$) of the material: see Fig. 2. Equation (49) shows that the crack closure condition depends upon all the active mechanisms. In particular, when friction is prevented (i.e., $\epsilon_i = 0$), the closure stress ($\sigma_c = -E\epsilon_{pm}$) is independent of the damage variable D. This result was used to identify the misfit strain ϵ_{pm} (see Fig. 2). Furthermore, the crack closure stress only vanishes when the misfit strain vanishes. Under this hypothesis, the closure condition reduces to the two equivalent conditions: $\sigma_c = 0$ and $\epsilon_c = 0$, where ϵ_c is the closure strain.

In Fig. 7, the predicted values of the closure stress are plotted. When the maximum stress is less than the debond stress (i.e., $\sigma_{id} = 285$ MPa) the closure stress is equal to $-E\epsilon_{pm} = -150$ MPa as expected by the model. As the maximum stress increases, the closure stress increases too.

5. CONCRETE SPECIMEN

The identification of the constitutive law of monolithic as well as fiber-reinforced concrete in tension is difficult from a direct uniaxial test. Early localization occurs and leads to the formation of one macrocrack. A special tension test allowing the Identification of Diffuse Damage (referred to as 'ID2') was first proposed by L'Hermite [21], then devised by Bazant and Pijaudier-Cabot [22], Mazars et al. [23,24]. This technique consists of gluing 8 × 8 × 250 mm^3 aluminum bars on 38 × 80 × 160 mm^3 concrete prismatic specimens (Fig. 8) to avoid the formation of a single crack. In the identification procedure, the previous authors assume that the interface between the aluminum bars and the concrete specimen is infinitely strong ($\sigma_d \to \infty$) and that the strain is uniform in the bars. Under these assumptions, the underlying behavior of concrete is deduced in a straight forward manner [22–24]. In the present case, the effect of the interface will be explicitly considered and discussed.

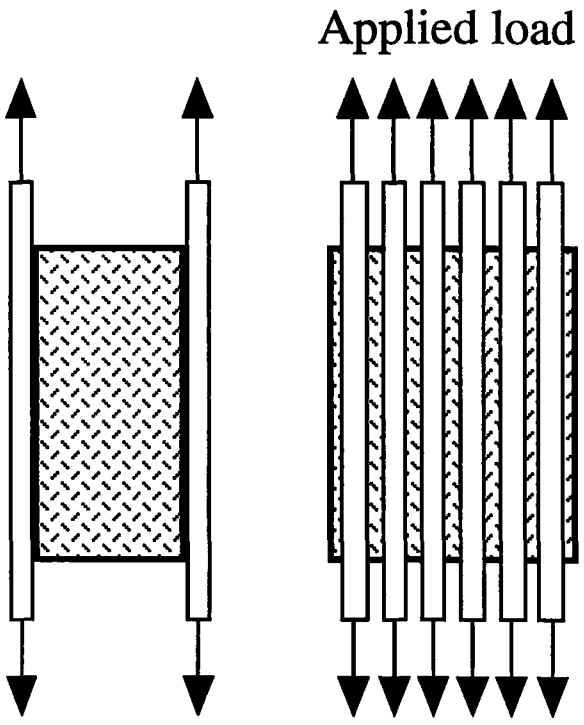

Figure 8. Schematic of an ID2 specimen.

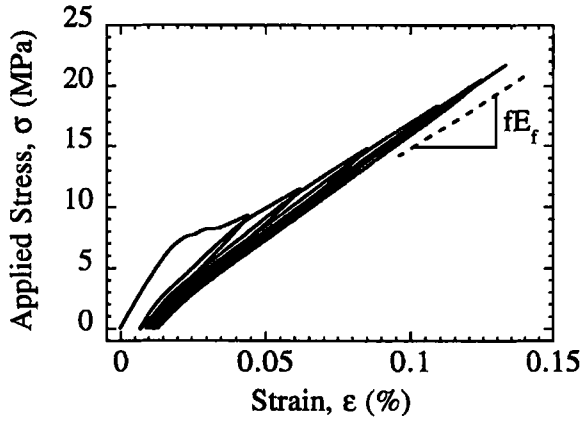

Figure 9. Stress/strain response of an ID2 concrete specimen ($f_{sf} = 0.\%$) loaded in tension.

The aim of this section is to analyze this experimental technique by using the model of Section 3. The effect of short fibers added in a concrete matrix is also discussed. In

the tested concrete specimens, four different volume fractions (f_{sf}) of short steel fibers are considered: 0., 0.1, 0.3 and 0.6%. The fibers are aligned along the loading direction.

5.1. Analysis of Unreinforced Concrete

In this subsection, experimental data obtained for two ID2 specimens made of unreinforced concrete ($f_{sf} = 0.\%$) are analyzed. As a first approximation, this specimen can be described by the unit cell introduced in Section 2. In the present case however, the residual stresses due to processing can be neglected. The state variables still are ϵ, D, ϵ_i and d on a macroscopic scale and the associated forces are σ, Y, X and y, respectively. Unload/reload sequences in tension (Fig. 9) are performed. The damage variable D, the inelastic strain ϵ_i as well as the permanent strain ϵ_p are measured as a function of the applied stress σ.

Figure 9 shows that at the end of the test, the composite behavior approaches that of the volume fraction of aluminum bars (denoted by fE_f in the figure). It is therefore expected that, contrary to the analyzed SiC/SiC composite, saturation occurs. This feature will be discussed later on.

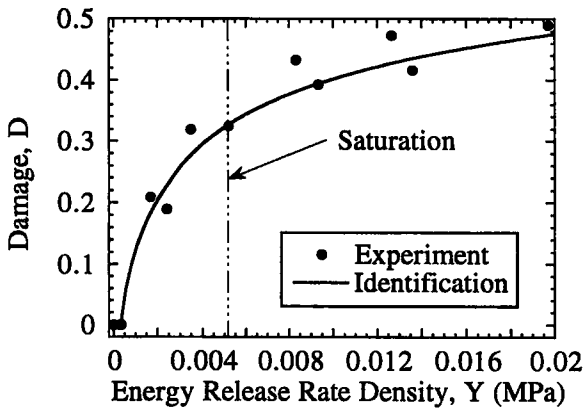

Figure 10. Damage variable D versus its associated force Y for two ID2 concrete specimens ($f_{sf} = 0.\%$).

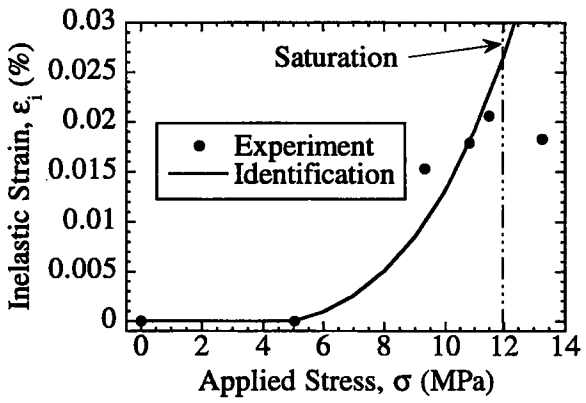

Figure 11. Inelastic strain ϵ_i versus applied stress σ for two ID2 concrete specimens ($f_{sf} = 0.\%$).

The identification procedure uses the same information as that used in the analysis of the unidirectional SiC/SiC composite (viz. the damage variable D and the inelastic strain ϵ_i). The experimental relationship observed between D and Y is given in Fig. 10. From this curve the values of the following dimensionless parameters can be obtained

$$\sqrt{\frac{2Y_c}{E}} = 1.3 \times 10^{-3} \pm 10^{-5} \quad \text{and} \quad \sqrt{\frac{2Y_0}{E}} = 4.4 \times 10^{-4} \pm 6 \times 10^{-5} \tag{50}$$

from which the matrix-cracking stress σ_{mc} can be derived immediately and has the value 5.1 ± 0.4 MPa, which is in good agreement with the experimental observations of Fig. 9.

The dimensionless parameters $B/4A^2$ and $A\sigma_d/E_f$ are identified by using the inelastic strain due to debonding and sliding. By fitting the experimental results of Fig. 11, the values of the dimensionless parameters are

$$\frac{B}{4A^2} = 12 \times 10^3 \pm 10^3 \quad \text{and} \quad \frac{A\sigma_d}{E_f} \cong 0 \tag{51}$$

The fact that σ_d is vanishingly small indicates that the specimen behaves in a low debond energy (LDE) regime. Therefore, the usual assumptions made to identify the underlying behavior of concrete (i.e., $\sigma_d \to \infty$) cannot be used in the present case. The analysis of the change of the inelastic strain shows that there is a change in the evolution pattern for a stress greater than 12 MPa, indicating the onset of cracking saturation.

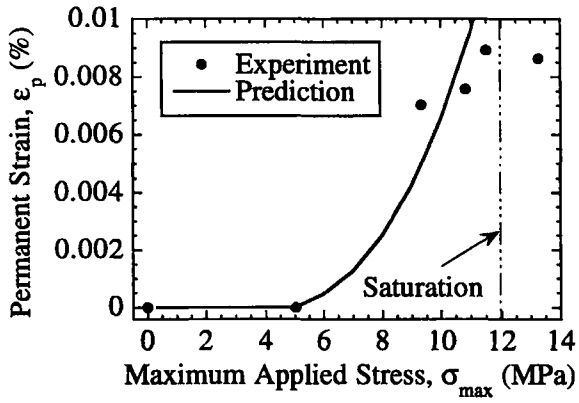

Figure 12. Permanent strain ϵ_p versus maximum applied stress σ_{max} for two ID2 concrete specimens ($f_{sf} = 0.\%$).

When the composite behaves in an LDE regime and the residual stresses are negligible, there exists a very simple relationship between the inelastic strain ϵ_i and the corresponding permanent strain ϵ_p

$$\epsilon_i = 2\epsilon_p \tag{52}$$

Figure 12 shows that the predictions of the change of the permanent strain with the applied stress is in reasonable agreement with the experiments. Figures 11 and 12 consistently show that the saturation stress is equal to 12 MPa. On the other hand, Fig. 10 shows that the prediction, *a priori* only valid up to saturation, can be further extended. Beyond the saturation level, the behavior of the ID2 specimen is mainly driven by the aluminum bars and the interface between the bars and the concrete parallelepiped (Fig. 9). It is worth remembering that the interface is weak (indicated by the LDE regime): the underlying behavior of concrete is very difficult to deduce since the stress state in concrete is not uniform along the loading direction.

5.2. Analysis of Reinforced Concrete

The effect of the addition of short fibers is discussed in this subsection by comparing the response of specimens with and without short fibers.

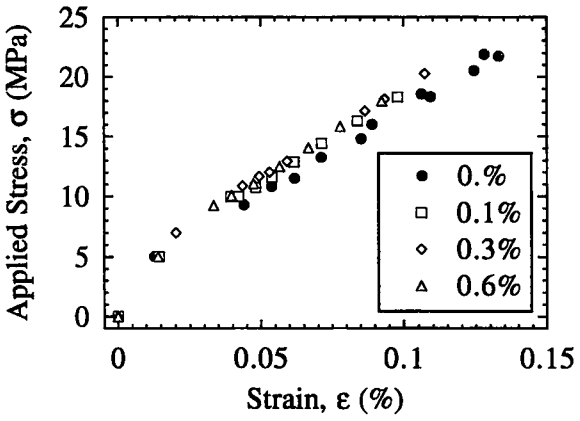

Figure 13. Comparison of stress/strain responses of ID2 concrete specimens loaded in tension when $f_{sf} = 0., 0.1, 0.3$ and 0.6%.

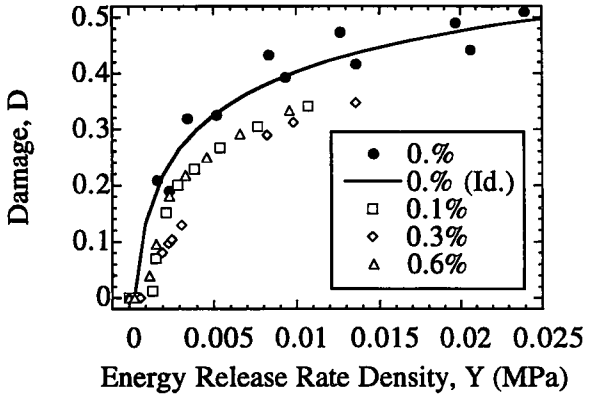

Figure 14. Damage variable D versus its associated force Y for ID2 specimens ($f_{sf} = 0., 0.1, 0.3$ and 0.6%). The symbols are experimental data and the solid line is the identification when $f_{sf} = 0.\%$.

The comparison at a purely macroscopic level consists of plotting the stress/strain responses for different volume fractions of short fibers ($f_{sf} = 0., 0.1, 0.3$ and 0.6%). Figure 13 shows that the volume fraction $f_{sf} = 0.\%$ constitutes a lower bound to the stress/strain behavior. However the effect of the volume fraction is not very important.

The experimental relationship observed between D and Y is shown in Fig. 14. The effect of the addition of short fibers becomes more significant. However, the most important feature is the presence of short fibers but not their relative volume fraction. This result indicates that the cracks are probably bridged but by very few short fibers so that the actual value of the volume fraction is unimportant.

Similarly, Fig. 15, shows that the overall inelastic strain is more influenced by the presence of short fibers rather than their respective volume fraction. Lastly, Fig. 16 shows the prediction of the change of the permanent strain with the maximum stress. A similar effect of the short fiber volume fraction can be observed. The prediction is in reasonable agreement with all the experimental data up to the saturation level (i.e., 12 MPa).

6. SUMMARY

A Continuum Damage Mechanics formulation has been applied to fiber-reinforced Composites. In addition to the total strain, the internal variables which define the state of the material have been identified. Matrix-cracking is described by one damage variable,

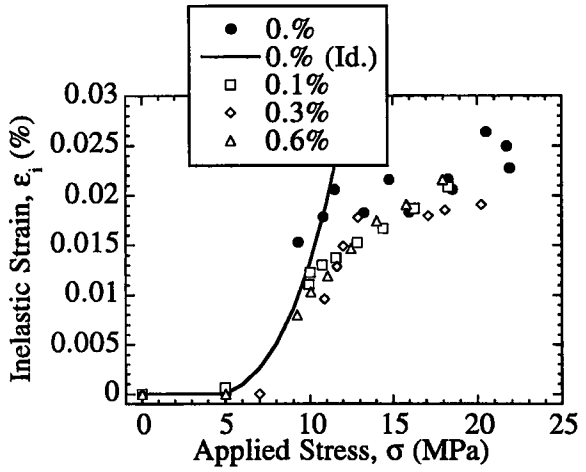

Figure 15. Inelastic strain ϵ_i versus applied stress σ for ID2 specimens ($f_{sf} = 0., 0.1, 0.3$ and 0.6%).The symbols are experimental data and the solid line is the identification when $f_{sf} = 0.\%$.

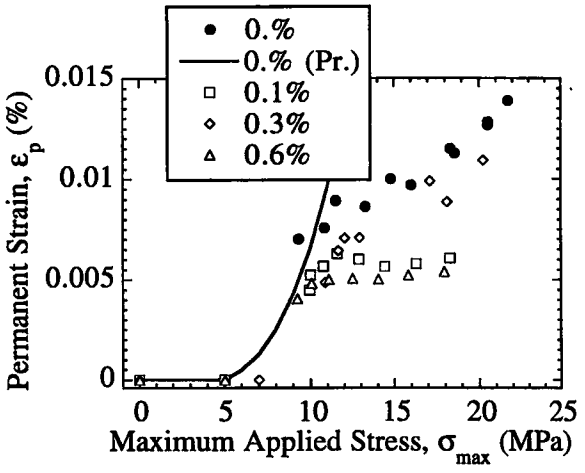

Figure 16. Permanent strain ϵ_p versus maximum applied stress σ_{max} for ID2 specimens $f_{sf} = 0., 0.1, 0.3$ and 0.6%.The symbols are experimental data and the solid line is the prediction when $f_{sf} = 0.\%$

debonding and sliding are modeled by an inelastic strain and another damage variable measuring the amount of non-recoverable energy. These variables are related to microscopic quantities introduced to analyze the degradation mechanisms of BMCs.

Micromechanical parameters are exhibited to model matrix-cracking, interfacial debonding and sliding. Their identification is discussed by analyzing the mechanical behavior of a unidirectional SiC/SiC composite. This composite behaves in a large debond energy regime in which the stress levels related to the debond strength are significantly higher than those related to sliding.

Conversely, concrete specimens reinforced by aluminum bars exhibit a low debond energy regime. The classical identification procedure cannot be used to infer the behavior of concrete from the response of the composite system. Furthermore, this type of experiment is more sensitive to the presence or the lack of short fibers in concrete than the actual volume fraction (up to 0.6%). However, in some other cases, the effect of fiber volume fraction can be more significant (e.g., three point flexure tests [25]).

The framework presented in this paper has been extended to model layered as well as woven fiber-reinforced composites. The nature of the different internal variables have been discussed. The same formalism can also be used to model high temperature applications in which the change of residual stresses as well as creep mechanisms need to be incorporated [26]. This work is still in progress.

REFERENCES

1. J. Aveston, G. A. Cooper and A. Kelly, in Proceedings National Physical Laboratory: Properties of Fiber Composites, IPC Science and Technology Press, Surrey (UK), (1971) 15.
2. J. Aveston and A. Kelly, J. Mater. Sci. 8 (1973) 352.
3. J. W. Hutchinson and H. M. Jensen, Mech. Mater. 9 (1990) 139.
4. B. Budiansky, J. W. Hutchinson and A. G. Evans, J. Mech. Phys. Solids 34 [2] (1986) 167.
5. A. Burr, P. Feillard and F. Hild, C. R. Acad. Sci. Paris Série IIb [t. 323] (1996) 377.
6. H. L. Cox, Br. J. Appl. Phys. 3 (1952) 72.
7. A. A. Vakulenko and M. L. Kachanov, Izv. AN SSSR, Mekh. Tverdogo Tela 4 (1971) 159.
8. A. C. F. Cocks and F. A. Leckie, in Advances in Applied Mechanics, Academic Press, New-York (USA), (1987), 239.
9. J. R. Rice, J. Mech. Phys. Solids 19 (1971) 433.
10. P. Germain, Q. S. Nguyen and P. Suquet, ASME J. Appl. Mech. 50 (1983) 1010.
11. V. Volterra, Annales Scientifiques de l'Ecole Normale Supérieure, Paris (France) 24 [3] (1907) 401.
12. A. E. H. Love, Cambridge University Press, Cambridge (UK), 1927.
13. J. D. Eshelby, Proc. Roy. Soc. London A 241 (1957) 376.
14. A. G. Evans, J.-M. Domergue and E. Vagaggini, J. Am. Ceram. Soc. 77 [6] (1994) 1425.
15. A. Burr, F. Hild and F. A. Leckie, Arch. Appl. Mech. 65 [7] (1995) 437.
16. A. Burr, F. Hild and F. A. Leckie, Eur. J. Mech. A/Solids 16 [1] (1997) 53.
17. J.-M. Domergue, PhD dissertation, University of California, Santa Barbara, 1995.
18. S. Jansson and F. A. Leckie, Acta Metall. Mater. 40 [11] (1993) 2967.
19. W. A. Curtin, Acta Metall. Mater. 41 [5] (1993) 1369.
20. F. Hild, A. Burr and F. A. Leckie, Int. J. Solids Struct. 33 [8] (1996) 1209.
21. S. L'Hermite, in Proceedings 4th International Symposium on the Chemistry of Cement, Washington DC (USA), (1960) 659.
22. Z. P. Bazant and G. Pijaudier-Cabot, ASCE J. Eng. Mat. 115 [4] (1989) 755.
23. J. Mazars and Y. Berthaud, C. R. Acad. Sci. Paris Série II [t. 308] (1989) 579.
24. J. Mazars, Y. Berthaud and S. Ramtani, Eng. Fract. Mech. 35 [4/5] (1990) 629.
25. D. Boudon-Cussac, PhD dissertation, University Paris VI, 1996.
26. A. Burr, F. Hild and F. A. Leckie, in Proceedings JNC10, D. Baptiste and A. Vautrin (eds.), AMAC, Paris (France), (1996) 1275.

3.2.3 Application à un composite SiC/SiC [0/90]

par A. BURR, F. HILD et F.A. LECKIE (1997).
Eur. J. Mech. A/Solids, 16 (1), pp. 53-78.

Continuum description of damage in ceramic-matrix composites

A. BURR *, F. HILD *[1] and F. A. LECKIE **

ABSTRACT. – A constitutive law is proposed for Ceramic-Matrix Composites which models matrix-cracking, interface debonding and sliding, fiber-breakage, and fiber pull-out. These different mechanisms induce loss of stiffness, inelastic strains, hysteresis loops, and crack closure. The features are analyzed within the framework of Continuum Damage Mechanics by the introduction of physical internal variables identified previously in material science investigations. The procedure is applied to a SiC/SiC [0/90] laminate composite using the results of pure tension tests of two laminate orientations. Each test involves a series of loading and unloading sequences. In order to verify the material description the behavior of an Iosipescu shear test is predicted using a Finite Element calculation and the results are compared with experiment.

Nomenclature

a	crack size
α	inelastic strain
$\underline{\underline{\alpha}}$	inelastic strain tensor
α_i	inelastic strain component in the i-direction (i = 11 or 22)
α_{11}, α_{22}, α_{12}	components of the inelastic strain tensor $\underline{\underline{\alpha}}$ in 1-2 frame
d	damage variable due to debonding and slip
$\underline{\underline{d}}$	debonding and sliding damage tensor
d_{11}, d_{22}, d_{12}	components of the debonding and sliding damage tensor $\underline{\underline{d}}$ in 1-2 frame
D, D_m, D_{my}, D_{my}^{00}, D_{my}^{90}	damage variables modeling matrix-cracking
$\overline{D}$, $\overline{D}^{00}$, $\overline{D}^{45}$	macroscopic damage variables
D_f, D_{f1}, D_{f1}^{00}, D_{f1}^{90}	damage variables modeling fiber-breakage
D_i	set of damage variables
D_{sat}, Y_{mth}, Y_{m0}, m_m	parameters of the evolution law of matrix-cracking damage
Δ_S	crack opening displacement due to slip
$\delta\bar{\varepsilon}$, $\delta\bar{\varepsilon}^{00}$, $\delta\bar{\varepsilon}^{45}$	maximum hysteresis loop widths
E, E_1, E_2, E_m, E_f	Young's moduli
E^{00}	Young's modulus of the 0-degree layer in the fiber direction
E^{90}	Young's modulus of the 90-degree layer in the fiber direction
$\overline{E}$	equivalent Young's modulus
$\tilde{E}$	Young's modulus of a damaged material

* Laboratoire de Mécanique et Technologie, ENS de Cachan/CNRS/Université Paris-VI, 61, avenue du Président Wilson, 94235 Cachan Cedex, France.

** Department of Mechanical and Environmental Engineering, College of Engineering, University of California, Santa Barbara CA 93106-5070, U.S.A.

[1] To whom correspondence should be addressed.

$\underline{\underline{\underline{\underline{E}}}}\left(D_{my}, D_{f1}^{00}, D_{f1}^{90}\right)$	fourth order elastic tensor on the composite level of a woven composite
$\underline{\underline{\underline{\underline{E}}}}\left(D_{my}^{00}, D_{my}^{90}, D_{f1}^{00}, D_{f1}^{90}\right)$	fourth order elastic tensor on the composite level
$\underline{\underline{\underline{\underline{E}}}}^{L}(D_{my}, D_{f1})$	fourth order elastic tensor on the layer level
$\underline{\underline{\underline{\underline{E}}}}^{00}\left(D_{my}^{00}, D_{f1}^{00}\right)$	fourth order elastic tensor of the 0-degree layer
$\underline{\underline{\underline{\underline{E}}}}^{90}\left(D_{my}^{90}, D_{f1}^{90}\right)$	fourth order elastic tensor of the 90-degree layer
$\overline{\varepsilon}$	macroscopic strain
$\underline{\underline{\varepsilon}}$	overall strain tensor
$\varepsilon_{11}, \varepsilon_{22}, \varepsilon_{12}$	component of the strain tensor $\underline{\underline{\varepsilon}}$ in 1-2 frame
$\underline{\underline{\varepsilon}}_f^i$	strain tensor in the fiber aligned along the i-direction
$\varepsilon_{f11}, \varepsilon_{f22}, \varepsilon_{f12}$	component of the strain tensor $\underline{\underline{\varepsilon}}_f$ of the fiber in 1-2 frame
$\overline{\varepsilon}_{in}$	inelastic strain upon complete unloading ($\overline{\sigma} = 0$)
$\overline{\varepsilon}_{in}^{00}, \overline{\varepsilon}_{in}^{45}$	macroscopic inelastic strain upon complete unloading
$\underline{\underline{\varepsilon}}^{L}, \underline{\underline{\varepsilon}}^{00}, \underline{\underline{\varepsilon}}^{90}$	strain tensor on a layer level
$\varepsilon_{mxx}, \varepsilon_{myy}, \varepsilon_{mxy}$	components of the strain tensor $\underline{\underline{\varepsilon}}_m$ of the matrix in x-y frame
$\varepsilon_{m11}, \varepsilon_{m22}, \varepsilon_{m12}$	components of the strain tensor $\underline{\underline{\varepsilon}}_m$ of the matrix in 1-2 frame
$\overline{\varepsilon}_M, \overline{\varepsilon}_M^{00}, \overline{\varepsilon}_M^{45}$	maximum applied strain
f, f_f	fiber volume fraction
f_m	matrix volume fraction
f^{00}, f^{90}	volume fraction of the 0-degree and the 90-degree layer
F	set of associated forces
$\mathcal{G}$	energy release rate
$\overline{G}$	equivalent shear modulus
$\tilde{G}_f$	shear modulus of the damaged fiber embedded in the matrix
$G_m, \tilde{G}_m$	shear modulus of the undamaged and damaged matrix
G^{00}	shear modulus of the 0-degree layer
G^{90}	shear modulus of the 90-degree layer
L	crack spacing
l_F	friction length (assumed to be equal to debond length l_d)
ν_m	Poisson's ratio of the matrix
R	fiber radius
S	set of state variables
ψ	Helmholtz free energy density (state potential)
ψ^D	elastic energy density on the composite level
ψ^e	elastic (or reversible) free energy density
ψ_f	elastic energy density of the fiber
ψ^s	stored free energy density
ψ^S	stored energy density due to debonding and sliding of a composite
ψ^L	elastic energy density on the layer level
ψ_m	elastic energy density of the matrix
ψ^{00}	free energy density of the layer at 0 degree
ψ^{90}	free energy density of the layer at 90 degrees
ρ_1	residual stress in the matrix
ρ_1^{00}	residual stress in the broken part of the 0-degree layer
σ	effective (or microscopic) stress
$\overline{\sigma}$	macroscopic stress
$\underline{\underline{\sigma}}$	overall stress tensor
$\sigma_{11}, \sigma_{22}, \sigma_{12}$	components of the stress tensor $\underline{\underline{\sigma}}$ in 1-2 frame
$\underline{\underline{\sigma}}_f$	stress tensor of the fiber
$\underline{\underline{\sigma}}_f^i$	stress tensor in the fiber aligned along the i-direction
σ_i	stress applied to the composite in the i-direction (i = 11 or 22)
$\underline{\underline{\sigma}}^{L}, \underline{\underline{\sigma}}^{00}, \underline{\underline{\sigma}}^{90}$	stress tensor on a layer level

$\underline{\underline{\sigma}}_m$	stress tensor of the matrix
$\overline{\sigma}_M$, $\overline{\sigma}_M^{00}$	maximum applied stress
σ_{th}, σ_0, τ_{th}, τ_0	parameters of the evolution law of the inelastic strains
τ_{eq}	equivalent shear stress
W	width
X	back-stress
$\underline{\underline{X}}$	back-stress tensor
X_{11}, X_{22}, X_{12}	components of the back-stress tensor $\underline{\underline{X}}$ in 1-2 frame
y	debonding and friction energy release rate density
$\underline{\underline{y}}$	energy release rate density tensor due to debonding and friction
y_{11}, y_{22}, y_{12}	components of the energy release rate density tensor $\underline{\underline{y}}$ in 1-2 frame
Y	cracking energy release rate density
Y_f, Y_{fl}	energy release rate densities associated with fiber-breakage
Y_{f0}, m_f	parameters of the evolution of fiber-breakage damage
Y_i	set of energy release rate densities
Y_m, Y_{my}	energy release rate densities associated with matrix-cracking
:	contraction wrt. two indices

1. Introduction

This study is concerned with the behavior of ceramics reinforced by continuous ceramic fibers. It has been demonstrated by Averston *et al.* (1971) that following matrix-cracking, sliding occurs at the fiber-matrix interface which causes inelastic deformations. The presence of matrix cracks and inelastic deformations may impart to the material the ability to redistribute stresses. In fact the results of experiments on notched panels on SiC/CAS composites (Cady *et al.*, 1995b) suggest the capacity of the material to redistribute stresses is sufficiently high for this material to be notch-insensitive. The ability to redistribute stress is an important property since design studies indicate that working stresses are sufficiently high for matrix-cracking to be unavoidable in regions of stress concentration.

The micromechanics which describes interface debonding and sliding has been established by Hutchinson and Jensen (1990) and Evans *et al.* (1994). In contrast to the early phenomenological studies (Ladevèze, 1983) the intention of the present study is to develop a continuum description of the damage processes which is mechanism-based and which may be used to describe the behavior of Ceramic-Matrix Composites (CMCs) under the conditions of multiaxial stress occurring in practice. Since crack spacing at saturations is small (Beyerley *et al.*, 1992) in most CMCs, Continuum Damage Mechanics is an appropriate means of describing degradation since changes in elastic moduli measured on a macroscopic level provide a simpler and more robust means of measuring damage than does microscopic measurement of crack density, which requires the average of many readings before reliable values are established (Jansson and Leckie, 1993).

By combining Continuum Damage Mechanics (CDM) (Lemaitre, 1992) with the micromechanical studies referred to previously, constitutive equations are developed

which lend themselves to the finite element procedures commonly used in practice (Zienkievicz and Taylor, 1989; Hibbitt *et al.*, 1995). The CDM formulation applied to reinforced composites is written within the framework of the Thermodynamics of Irreversible Processes (Coleman and Gurtin, 1967; Rice, 1971; Germain *et al.*, 1983). The first step in establishing such a model is to identify the internal variables which define the state of the material. The second step is to determine the expression of the state potential in terms of the state variables and the third one to define the evolution laws of the internal variables.

The model is developed along the lines described, for instance, by Ashby (1992). As mentioned earlier, the aim of the model is to be applied to structural applications. The degradation mechanisms are first determined by analyzing unidirectional CMCs in Section 2. The model is then extended to multidirectional systems in Section 3 by modeling the same mechanisms. The procedure described in the previous paragraph constitutes the general framework in which the model is written. In Section 4, the model identification is developed. In particular the number of tests constitutive of the input to the parameter tuning are discussed. The procedure is applied to continuous fiber SiC/SiC composites in a [0/90] lay-up for which suitable experimental data are available (Pluvinage, 1991). Section 5 is concerned with the prediction of a Iosipescu shear experiment. The results are compared with experimental data. This last section constitutes a first validation of the model.

2. The tensile stress-strain relationship for unidirectional CMCs

Post-mortem analyses of broken specimens indicate the presence of arrays of microcracks in the matrix which are accompanied by debonding and friction at the fiber-matrix interface. Hutchinson and Jensen (1990) and Evans *et al.* (1994) have analyzed the behavior of unidirectional CMCs in tension by considering the unit cell shown in Figure 1, when matrix-cracking of spacing $2L$ is accompanied by debonding and sliding at the interface over a friction length $2l_F$. The micromechanics analysis can predict the one-dimensional macroscopic stress-strain response shown in Figure 2. The microcracks are usually aligned with the principal stress or strain directions. By studying a cracked panel with crack of length $2a$ in a cell of area $4LW$ *(Fig. 3)*, the reduction in stiffness may be estimated. If the initial behavior of the elementary cell is isotropic and elastic, and Young's modulus is E, it can be shown that the stiffness loss depends on the crack density defined as $\pi a^2/4LW$. By assuming plane stress conditions, and that the crack interactions can be neglected, a first approximation for the reduced elastic modulus $\widetilde{E}$ can be written as

$$\frac{\widetilde{E}}{E} = \frac{1}{1 + 2\frac{\pi a^2}{4LW}} \tag{1}$$

The relationship can be recast in framework of CDM (Lemaitre and Chaboche, 1978) as

$$\frac{\widetilde{E}}{E} = 1 - D \tag{2}$$

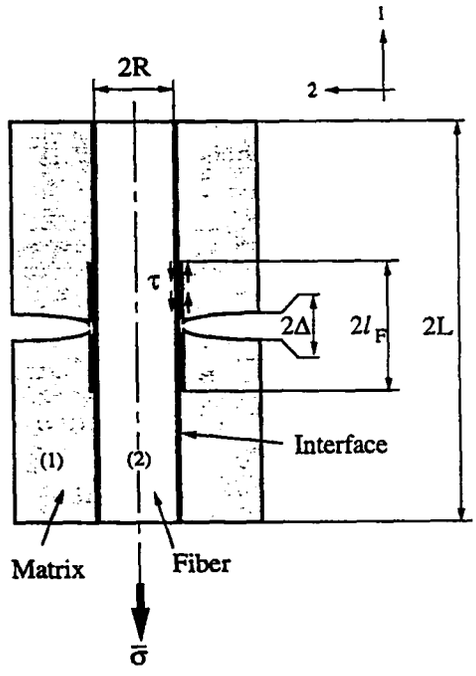

Fig. 1. – Elementary cell containing a crack. A debond zone is characterized by the debond length $2l_F$, and the average crack spacing is $2L$.

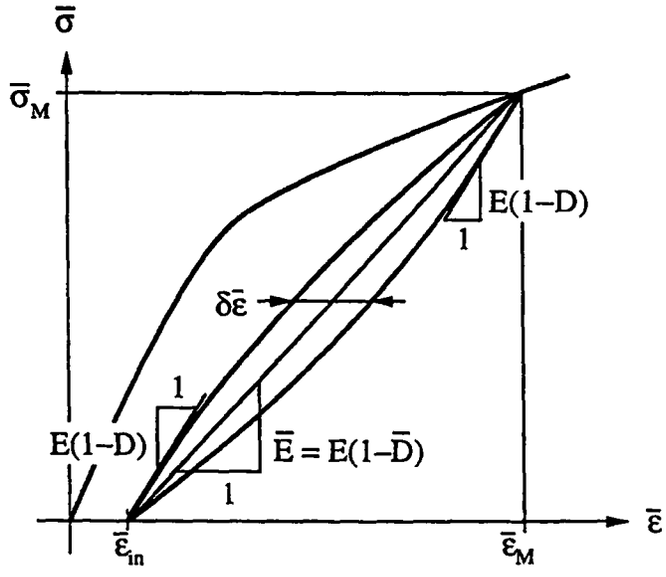

Fig. 2. – Stress, $\bar{\sigma}$, *versus* strain, $\bar{\varepsilon}$, during a loading-unloading-reloading sequence.

where

(3) $$D = \frac{2\frac{\pi a^2}{4LW}}{1 + 2\frac{\pi a^2}{4LW}}$$

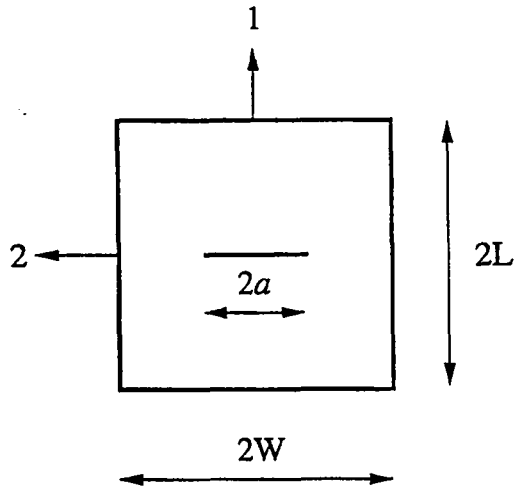

Fig. 3. – Elementary cell of size $2L \times 2W$ containing a crack of size $2a$.

is the damage variable associated with the crack density. When D is small, a first order solution to Eq. (3) is given by

$$D \simeq 2\frac{\pi a^2}{4LW} \tag{4}$$

so that the damage variable is proportional to the crack density. In the case of constituents with different elastic properties, D depends upon the elastic properties of the two constituents, as well as on the geometry (*i.e.*, the ratios a/R and a/L, see *Fig.* 1, where R is the fiber radius). The uniaxial stress-strain relationship becomes

$$\sigma = \frac{\overline{\sigma}}{1-D} = E\,\overline{\varepsilon} \tag{5}$$

The elementary cell illustrated in Figure 1 has been analyzed by various authors (Hutchinson and Jensen, 1990; Evans *et al.*, 1994), but a different analytic approach is now used which follows the thermodynamic developments of Rice (1971) and Germain *et al.* (1983) and which can be formulated conveniently in one and three dimensions alike. This is done by calculating the internal elastic energy density in the unit cell (Hild *et al.*, 1996) caused by matrix-cracking, debonding and sliding at the interface. Two "cut and paste" steps are used to evaluate the elastic energies following approaches introduced by Volterra (1907), and applied to the analysis the elastic behavior of homogeneous and isotropic media by considering the elastic properties of a cut cylinder (Volterra, 1907; Love, 1927), as well as inclusions in an infinite medium (Eshelby, 1957), or to the study creeping materials (Cocks and Leckie, 1987). The first step consists in moving the unbroken part (2) with respect to the broken part (1) with no external load by an amount Δ_s over a length l_F (*Fig.* 4). Because of interfacial sliding, this displacement Δ_s gives rise to a self-balanced linear stress field along a length l_F in parts (1) and (2) when the interfacial behavior is assumed to be characterized by a constant shear strength. By

integration over l_F and then averaging over the total length L, the elastic energy density associated with this process is given by

$$\psi^s = \frac{2}{3}\frac{fE_1(1-f)E_2}{E}\left\{\frac{\Delta_s}{l_F}\right\}^2\frac{l_F}{L} \tag{6}$$

The crack opening displacement Δ_s due to slip induces are irreversible or inelastic strain α expressed as

$$\alpha = \frac{(1-f)E_1}{E}\frac{\Delta_s}{L} \tag{7}$$

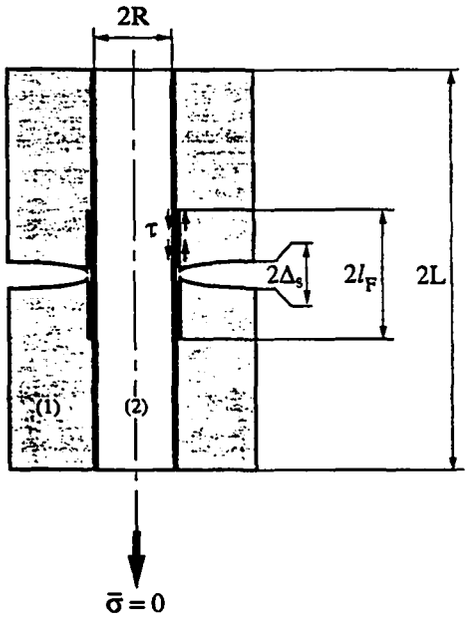

Fig. 4. – Motion of the unbroken part (2) with respect to the broken part (1) with no external load by an amount Δ_s over a length l_F.

The second step consists of an elastic loading of the damaged system so that the elastic energy density is given by

$$\psi^e = \frac{1}{2}E(1-D)(\bar{\varepsilon}-\alpha)^2 \tag{8}$$

The total elastic energy density is the sum of the two elements of the energy densities and that associated with the residual stresses due to processing

$$\psi = \frac{1}{2}E(1-D)(\bar{\varepsilon}-\alpha)^2 + \frac{2}{3}\frac{fE_1(1-f)E_2}{E}\left\{\frac{\Delta_s}{l_F}\right\}^2\frac{l_F}{L} + \rho_1\,\alpha \tag{9}$$

where $-\rho_1 E_1/E$ is the residual stress in the broken layer (1). For convenience the energy density can be expressed in a more compact form by using state variables which

are the total strain $\overline{\varepsilon}$, the damage variable D modeling the loss of stiffness due to the cracking mechanism, the inelastic strain α derived previously (Eq. (7)), and the damage variable $d = 3(1-f)E_1 l_F/4fE_2 L$ which defines the size of the slip zone related to the average crack spacing. The friction length saturates when the cracking process stops ($L = l_F$) along with cracking damage D. Upon loading, all the internal variables vary (since L, l_F and Δ_s evolve), whereas upon unloading, the only variables to vary are the inelastic strain α and d (only Δ changes), D is constant. The elastic energy density in terms of the new internal variables is (Hild *et al.*, 1996)

$$\psi = \frac{1}{2}E(1-D)(\overline{\varepsilon}-\alpha)^2 + \frac{1}{2}E\left(\frac{\alpha^2}{d}\right) + \rho_1\,\alpha. \tag{10}$$

The forces associated with the state variables $(\overline{\varepsilon}, D, d, \alpha)$ are respectively given by

$$\overline{\sigma} = \frac{\partial\psi}{\partial\overline{\varepsilon}} = E(1-D)(\overline{\varepsilon}-\alpha) \tag{11.1}$$

$$Y = -\frac{\partial\psi}{\partial D} = \frac{E}{2}(\overline{\varepsilon}-\alpha)^2 \tag{11.2}$$

$$y = -\frac{\partial\psi}{\partial d} = \frac{E}{2}\left(\frac{\alpha}{d}\right)^2 \tag{11.3}$$

$$X = \frac{\partial\psi}{\partial\alpha} = -\overline{\sigma} + E\frac{\alpha}{d} + \rho_1 \tag{11.4}$$

These associated forces are useful in particular to determine the relevant forces driving each mechanism. Matrix-cracking is assumed to be driven by Y, which plays an identical role as the energy release rate $\mathcal{G}$ in the framework of Linear Elastic Fracture Mechanics. From a micromechanical analysis (Hild *et al.*, 1996), it can be shown that the back-stress is dependent on the applied stress $\overline{\sigma}$, therefore the driving force of the inelastic strains can be taken as the stresses acting in the same direction. The same assumption can be made when the evolution of the damage variable d related to sliding is analyzed, *i.e.* the driving force of d can be chosen to be its associated force y, or the applied stress $\overline{\sigma}$.

In the present approach the growth laws of the internal variables (D, d, α) are established from macroscopic quantities measured in the course of unloading and reloading sequences. To this end use is made of the solution of the response of the unit cell (*Fig.* 1) when subjected to an unloading/reloading sequence during which the magnitude of the shear stress remains constant.

The expressions obtained from the analysis for the residual stress ρ_1 and the internal variables D, d, α in terms of the macroscopic quantities shown in Figure 2 are given respectively by (Hild *et al.*, 1996).

$$\frac{-\rho_1}{E} = \left(\sqrt{\frac{\overline{\varepsilon}_{\text{in}} + 2\delta\overline{\varepsilon}}{4\delta\overline{\varepsilon}}} - 1\right)(\overline{\varepsilon}_M - \overline{\varepsilon}_{\text{in}} - 2\delta\overline{\varepsilon}) \tag{12.1}$$

$$D = \frac{\overline{\varepsilon}_M\overline{D} - \overline{\varepsilon}_{\text{in}}\overline{D} - 2\delta\overline{\varepsilon}}{\overline{\varepsilon}_M - \overline{\varepsilon}_{\text{in}} - 2\delta\overline{\varepsilon}} \tag{12.2}$$

$$\frac{d}{4} = \frac{\sqrt{(\overline{\varepsilon}_{\text{in}} + 2\delta\overline{\varepsilon})\delta\overline{\varepsilon}}}{\overline{\varepsilon}_M - \overline{\varepsilon}_{\text{in}} - 2\delta\overline{\varepsilon}} \tag{12.3}$$

$$\alpha = \frac{d}{2}\frac{\overline{\sigma}_M - \rho_1(1-D)}{E(1-D)} \tag{12.4}$$

Equations (12) are only valid when a constant shear strength characterizes the interfacial behavior, and lastly Eqs. (12.3) and (12.4) are only valid for monotonic loading conditions.

By performing a series of unloading/reloading sequences the internal variables can be determined from experiment using Eqs. (12). The residual stress ρ_1 is calculated from Eq. (12.1) and it is a test of the effectiveness of the model that the same value of the residual stress is obtained for each loading sequence. The values of D and d are given by applying Eqs. (12.2) and (12.3) respectively. The information is now available to complete the calculation for Eq. (12.4). The corresponding associated forces are obtained by the expressions givens in Eqs. (11). The relationship between the internal variables and the associated forces can then be investigated by knowing the driving forces of each state variable. This method is proposed to model the behavior of CMC laminates.

3. CMCs with multidirectional fiber systems

The one-dimensional investigation is now extended to a [0/90] laminate composite and to a [0/90] woven composite subjected to multiaxial plane stress states. In this paper, only monotonic loading conditions are analyzed, even though the present framework can be easily extended to cyclic loading conditions and to non-proportional loading conditions. Following established procedures, the properties of each layer are first determined and those of the composite are then calculated by ensuring compatibility conditions.

The components of each layer consist of the matrix, the fiber and the interface, with f being the fiber volume fraction. The fiber direction defines the 1-2 axes. The axes x-y correspond to the principal axes of the strains in the ceramic matrix. The definition of the axes used at the constituent, layer and composite levels are shown in Figure 5. Following Section 2, the loss of stiffness due to matrix-cracking and fiber-breakage is first established and this is followed by the influence of the slip at the interfaces.

3.1. Elastic energies of the composite associated with matrix-cracking and fiber-breakage

3.1.1. *Constituent level: matrix and fiber*

The initial behavior of the matrix is assumed to be isotropic. The presence of cracks leads the behavior to become anisotropic. The assumption is made that cracking occurs normal to the y-direction (e.g. maximum principal strain direction) in the matrix. Under the hypothesis of monotonic loading condition, only one damage variable is needed to

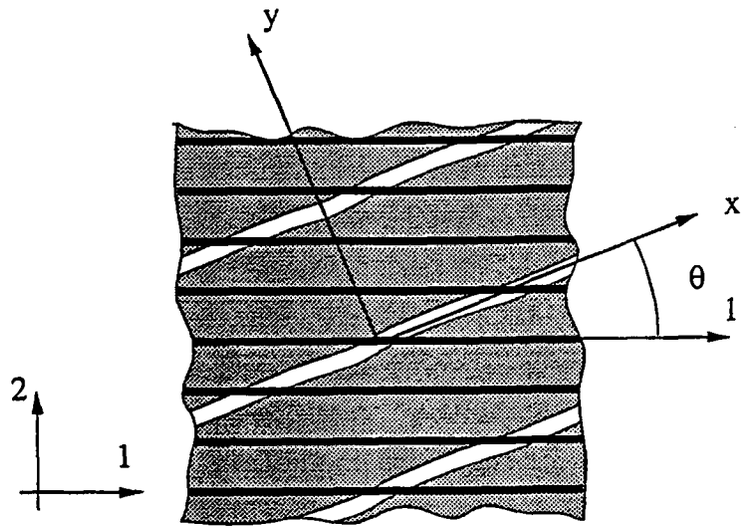

Fig. 5. – The initial principal directions of orthotropy, or material directions, 1 and 2 often do not coincide with the loading directions x and y. The angle θ measures their respective orientation.

model matrix-cracking, and is denoted by D_{my}. The study of a cracked system normal to one direction shows that the Young's modulus along that direction as well as the shear modulus are altered (Budiansky and O'Connell, 1976; Chaboche, 1982) and that the expression of the elastic energy density of the matrix is

$$\psi_m = \frac{1}{2}\frac{E_m(\varepsilon_{mxx}^2 + 2\nu_m(1-D_{my})\varepsilon_{mxx}\varepsilon_{myy} + (1-D_{my})\varepsilon_{myy}^2)}{1-\nu_m^2(1-D_{my})} + 2\tilde{G}_m(D_{my})\varepsilon_{mxy}^2 \tag{13.1}$$

and

$$\tilde{G}_m(D_{my}) = \frac{G_m}{1+\left(\frac{D_{my}}{1-D_{my}}\right)\frac{1}{2(1+\nu_m)}}$$

It is assumed that the fibers are aligned along the 1-direction and that fiber-breakage is perpendicular to the fiber direction. Therefore the elastic energy density is given by

$$\psi_f = \frac{1}{2}(E_f(1-D_{f1})\varepsilon_{f11}^2 + E_f\varepsilon_{f22}^2) + 2\tilde{G}_f(D_{f1})\varepsilon_{f12}^2 \tag{13.2}$$

The expression of the stresses in the matrix $\underline{\underline{\sigma}}_m$ and in the fibers $\underline{\underline{\sigma}}_f$ are obtained by partial differentiation of the elastic energy density with respect to the strain tensors $\underline{\underline{\varepsilon}}_m$ and $\underline{\underline{\varepsilon}}_f$ respectively

$$\underline{\underline{\sigma}}_m = \frac{\partial \psi_m}{\partial \underline{\underline{\varepsilon}}_m} \tag{14.1}$$

$$\underline{\underline{\sigma}}_f = \frac{\partial \psi_f}{\partial \underline{\underline{\varepsilon}}_f} \tag{14.2}$$

and the associated forces to the damage variables are defined as

$$Y_{my} = -\frac{\partial \psi_m}{\partial D_{my}} \tag{14.3}$$

$$Y_{f1} = -\frac{\partial \psi_f}{D_{f1}} \tag{14.4}$$

These generalized forces are the energy release rate densities associated with matrix-cracking and fiber-breakage, respectively. They play similar roles as the force Y introduced in Section 2, and therefore are assumed to be the driving forces of the damage variables.

3.1.2. *Layered composite*

When the composite consists of layers of unidirectional fibers with different orientations, the laminate properties are determined by applying laminate theory to the properties of individual layers.

3.1.2.1. Layer level

A layer consists of fibers aligned along one orientation (the 1-direction) embedded in a matrix. To determine the behavior of this layer, micro-interface compatibility conditions are written in terms of the strains $\underline{\underline{\varepsilon}}^L$ and stresses $\underline{\underline{\sigma}}^L$ on the layer level. These conditions are the compatibility and the equilibrium between a fiber (tensors $\underline{\underline{\varepsilon}}_f$ and $\underline{\underline{\sigma}}_f$) and the surrounding matrix (tensors $\underline{\underline{\varepsilon}}_m$ and $\underline{\underline{\sigma}}_m$), which takes place in that system. Therefore, it is more convenient to write the conditions in the 1-2 material frame as follows,

$$\varepsilon_{m11} = \varepsilon_{f11} = \varepsilon_{11}^L \tag{15.1}$$

$$f_m \sigma_{m11} + f_f \sigma_{f11} = \sigma_{11}^L \tag{15.2}$$

$$f_m \varepsilon_{m22} + f_f \varepsilon_{f22} = \varepsilon_{22}^L \tag{15.3}$$

$$\sigma_{m22} = \sigma_{f22} = \sigma_{22}^L \tag{15.4}$$

$$f_m \varepsilon_{m12} + f_f \varepsilon_{f12} = \varepsilon_{12}^L \tag{15.5}$$

$$\sigma_{m12} = \sigma_{f12} = \sigma_{12}^L \tag{15.6}$$

When the principal strain directions do not coincide with the material frame, Eqs. (14.1-14.2) have to be rewritten in the 1-2 frame. The application of Eqs. (15) then defines

the elastic properties of the layer

$$\underline{\underline{\sigma}}^L = \underline{\underline{\underline{\underline{E}}}}^L\left(D_{my}, D_{f1}\right) : \underline{\underline{\varepsilon}}^L \tag{16.1}$$

From Eq. (16.1), the elastic energy density ψ^L associated with matrix-cracking and fiber-breakage on the layer level can be written as

$$\psi^L = \frac{1}{2}\,\underline{\underline{\varepsilon}}^L : \underline{\underline{\underline{\underline{E}}}}^L\left(D_{my}, D_{f1}\right) : \underline{\underline{\varepsilon}}^L \tag{16.2}$$

Matrix-cracking and fiber-breakage are dissipative mechanisms which do not store energy. Therefore they influence only the reversible (*i.e.*, elastic) part of the free energy density.

3.1.3. *Composite level*

For simplicity, the case of two layers at 0 and 90 degrees are considered. The micromechanical quantities associated with the 0 degree layer are superscripted by ^{00}, and those at 90 degrees by ^{90}. The elastic behavior of the composite system is determined by applying classical laminate theory. The compatibility condition and global equilibrium allow to get the overall stresses $\underline{\underline{\sigma}}$ and strains $\underline{\underline{\varepsilon}}$

$$\underline{\underline{\varepsilon}} = \underline{\underline{\varepsilon}}^{00} = \underline{\underline{\varepsilon}}^{90} \tag{17.1}$$

$$\underline{\underline{\sigma}} = f^{00}\underline{\underline{\sigma}}^{00} + f^{90}\underline{\underline{\sigma}}^{90} \tag{17.2}$$

By solving Eqs. (17) and using Eq. (16.1), the overall behavior of the composite is defined as

$$\underline{\underline{\sigma}} = \underline{\underline{\underline{\underline{E}}}}\left(D_{my}^{00}, D_{my}^{90}, D_{f1}^{00}, D_{f1}^{90}\right) : \underline{\underline{\varepsilon}} \tag{18.1}$$

with

$$\underline{\underline{\underline{\underline{E}}}}\left(D_{my}^{00}, D_{my}^{90}, D_{f1}^{00}, D_{f1}^{90}\right) = f^{00}\underline{\underline{\underline{\underline{E}}}}\left(D_{my}^{00}, D_{f1}^{00}\right) + f^{90}\underline{\underline{\underline{\underline{E}}}}\left(D_{my}^{90}, D_{f1}^{90}\right)$$

From Eq. (18.1), the elastic energy density ψ^D associated with matrix-cracking and fiber-breakage on the composite level can be written as

$$\psi^D = f^{00}\psi^{00} + f^{90}\psi^{90} \tag{18.2}$$

with

$$\psi^{00} = \frac{1}{2}\underline{\underline{\varepsilon}} : \underline{\underline{\underline{\underline{E}}}}^{00}\left(D_{my}^{00}, D_{f1}^{00}\right) : \underline{\underline{\varepsilon}} \tag{18.3}$$

$$\psi^{90} = \frac{1}{2}\underline{\underline{\varepsilon}} : \underline{\underline{\underline{\underline{E}}}}^{90}\left(D_{my}^{90}, D_{f1}^{90}\right) : \underline{\underline{\varepsilon}} \tag{18.4}$$

3.1.2. *Woven composite*

Woven composites are another architecture commonly used. Equations (16) can be used also for woven architectures. This approximation is relevant when two different damage mechanisms can be exhibited in the tows at 0 and 90 degrees. Also, the effects due to fiber cross-over are neglected. Therefore the results developed so far can be extended to woven architectures.

However, there may be some situations in which the distinction between the matrix of the tows at 0 and 90 degrees is more difficult to make because there is only one matrix-cracking mechanism. In place of Eq. (16) for the single layer, the equilibrium and compatibility conditions are given by the following equations written in the 1-2 frame

$$\varepsilon_{m11} = \varepsilon_{f11}^{1} = \varepsilon_{11} \tag{19.1}$$

$$\sigma_{m11} = \sigma_{f11}^{2} \tag{19.2}$$

$$(1 + f_m)\sigma_{m11} + f_f\sigma_{f11}^{1} = 2\sigma_{11} \tag{19.3}$$

$$\varepsilon_{m22} = \varepsilon_{f22}^{2} = \varepsilon_{22} \tag{19.4}$$

$$\sigma_{m22} = \sigma_{f22}^{1} \tag{19.5}$$

$$(1 + f_m)\sigma_{m22} + f_f\sigma_{f22}^{2} = 2\sigma_{22} \tag{19.6}$$

$$f_m\varepsilon_{m12} + f_f\varepsilon_{f12}^{1} = \varepsilon_{12} \tag{19.7}$$

$$\sigma_{m12} = \sigma_{f12}^{1} = \sigma_{f12}^{2} = \sigma_{12} \tag{19.8}$$

By solving Eqs. (19) and noting that there exists only one degradation mechanism taking place in the matrix characterized by one damage variable D_{my} and two

degradation mechanisms associated with fiber-breakage in the 0 and 90 degrees directions $\left(D_{f1}^{00}, D_{f1}^{90}\right)$, the overall behavior of the composite is defined as

$$\underline{\underline{\sigma}} = \underline{\underline{\underline{\underline{E}}}}\left(D_{my}, D_{f1}^{00}, D_{f1}^{90}\right) : \underline{\underline{\varepsilon}} \tag{20.1}$$

The elastic energy density ψ^D associated with matrix-cracking and fiber-breakage on the composite level can be written as

$$\psi^D = \frac{1}{2}\,\underline{\underline{\varepsilon}} : \underline{\underline{\underline{\underline{E}}}}\left(D_{my}, D_{f1}^{00}, D_{f1}^{90}\right) : \underline{\underline{\varepsilon}} \tag{20.2}$$

3.2. State potential associated with debonding and fiber pull-out

Inelasticity is essentially due to sliding at the interface between the fiber and the matrix. Sliding is involved in debonding as well as fiber pull-out. From a micromechanical point of view, this sliding can take place as soon as a crack is bridged by fibers. In a CDM formulation, only the equivalent homogenous sliding and the associated forces are considered. By considering equivalent homogeneous sliding on the composite level, there is no way to distinguish the contributions due to fiber/matrix debonding and sliding, and inter-layer delamination. However, in most CMCs delamination is not as critical as in polymeric matrix composites for which the Young's moduli differences are far more important. Therefore, the cell model used to describe cracking and sliding is that shown in Figure 1. The analysis that has been done on a 1-D model (given in Section 2) can be formally extended to give the expression of the elastic energy density due to sliding of a layered composite along the 1-2 directions (Burr *et al.*, 1995)

$$\psi^S\left(\underline{\underline{\alpha}}, \underline{\underline{d}}\right) = \frac{1}{2}\,\overline{E}\left(\frac{\alpha_{11}^2}{d_{11}} + \frac{\alpha_{22}^2}{d_{22}}\right) + \frac{1}{2}\,\overline{G}\left(\frac{\alpha_{12}^2}{d_{12}}\right) \tag{21}$$

with

$$\overline{E} = \frac{f^{00}E^{00}f^{90}E^{90}}{f^{00}E^{00} + f^{90}E^{90}}$$

$$\overline{G} = \frac{f^{00}G^{00}f^{90}G^{90}}{f^{00}G^{00} + f^{90}G^{90}}$$

3.2.1. *State laws*

The following development deals with layered CMCs. By using the results of Section 2, the total elastic energy density of the composite is the sum of the elastic energy density of the damaged composite ψ^D and the elastic energy density due to debonding and sliding ψ^S

$$\psi = \frac{1}{2}\left(\underline{\underline{\varepsilon}} - \underline{\underline{\alpha}}\right) : \underline{\underline{\underline{\underline{E}}}}\left(D_{my}^{00}, D_{my}^{90}, D_{f1}^{00}, D_{f1}^{90}\right) : \left(\underline{\underline{\varepsilon}} - \underline{\underline{\alpha}}\right) + \psi^S\left(\underline{\underline{\alpha}}, \underline{\underline{d}}\right) \tag{22}$$

The force associated with total strain is

$$\underline{\underline{\sigma}} = \frac{\partial \psi}{\partial \underline{\underline{\varepsilon}}} = \underline{\underline{\underline{\underline{E}}}}\left(D_{my}^{00}, D_{my}^{90}, D_{f1}^{00}, D_{f1}^{90}\right) : \left(\underline{\underline{\varepsilon}} - \underline{\underline{\alpha}}\right) \tag{23.1}$$

and corresponds to the macrocsopic stress. The associated force to the damage variables modeling matrix-cracking and fiber-breakage are

$$Y_i = -\frac{\partial \psi}{\partial D_i} \tag{23.2}$$

where $D_{i=1;4} = \left\{D_{my}^{00}; D_{my}^{90}; D_{f1}^{00}; D_{f1}^{90}\right\}$, and $Y_{i=1;4} = \left\{Y_{my}^{00}; Y_{my}^{90}; Y_{f1}^{00}; Y_{f1}^{90}\right\}$ represent the corresponding energy release rate densities due to matrix-cracking and fiber-breakage. The associated force to the damage variables modeling sliding are

$$\underline{\underline{y}} = -\frac{\partial \psi}{\partial \underline{\underline{d}}} = -\frac{\partial \psi^S}{\partial \underline{\underline{d}}} \tag{23.3}$$

where $\underline{\underline{d}} = \{d_{11}; d_{22}; d_{12}\}$, and $\underline{\underline{y}}$ correspond to the energy release rate densities due to debonding and sliding. The associated forces to the inelastic strains $\underline{\underline{\alpha}}$ are

$$\underline{\underline{X}} = \frac{\partial \psi}{\partial \underline{\underline{\alpha}}} = -\underline{\underline{\sigma}} + \frac{\partial \psi^S}{\partial \underline{\underline{\alpha}}} \tag{23.4}$$

and represent the back-stresses in the sliding zone. It is worth noting that in this section the residual stresses are not accounted for. Otherwise there would have been an additional term in Eqs. (23.4) and (22).

3.2.2. *Evolution laws*

The identification procedure is performed on a $[0/90]_s$ laminate architecture of CMCs. The first step is to define all the internal state variables needed to model the material behavior. The three total strain variables, (e.g., $\varepsilon_{11}, \varepsilon_{22}, \varepsilon_{12}$), are given either from experiment or as input from a F.E. calculation. The four damage variables $D_{i=1;4} = \left\{D_{my}^{00}; D_{my}^{90}; D_{f1}^{00}; D_{f1}^{90}\right\}$ are used to define the change in the elastic properties, with $D_m = \left\{D_{my}^{00}; D_{my}^{90}\right\}$ is the set of damage variables modeling matrix-cracking, and $D_f = \left\{D_{f1}^{00}; D_{f1}^{90}\right\}$ is the set of damage variables modeling fiber-breakage. Assuming the damage evolution laws, $D_m(Y_m)$ and $D_f(Y_f)$ are functions of the associated forces $Y_m = \left\{Y_{my}^{00}; Y_{my}^{90}\right\}$, and $Y_f = \left\{Y_{f1}^{00}; Y_{f1}^{90}\right\}$ respectively, then only two evolution laws, one for each mechanism, are sufficient to compute the four components or damage. The three damage variables, $\{d_{11}; d_{22}; d_{12}\}$, define the sliding distances, with d_{11} or d_{22} being associated with sliding in the fiber directions and d_{12} associated with shear sliding. Consequently only two evolution laws are needed, $d_{11}(y_{11})$ or $d_{22}(y_{22})$, and $d_{12}(y_{12})$.

For the same reasons, two evolution laws for the inelastic strains, $\alpha_{11}(X_{11})$ or $\alpha_{22}(X_{22})$, and $\alpha_{12}(X_{12})$ define the evolution of the three inelastic strains, $\{\alpha_{11}; \alpha_{22}; \alpha_{12}\}$. In conclusion, the model has 13 state variables, three of which are

TABLE I. – Thermodynamic variables modeling elasticity, matrix cracking, debonding and sliding, fiber breakage and pull-out.

Mechanism	State variables			Associated forces	
		Observable	Internal		
Elasticity	Total strain	$\underline{\underline{\varepsilon}}$		$\underline{\underline{\sigma}}$	Stress
Matrix-cracking	Damage variables		D_m^{00} D_m^{90}	Y_m^{00} Y_m^{90}	Energy release rate densities
Fiber-breakage	Damage variables		D_f^{00} D_f^{90}	Y_f^{00} Y_f^{90}	Energy release rate densities
Debonding and sliding	Inelastic strain		$\underline{\underline{\alpha}}$	$\underline{\underline{X}}$	Back-stress
	Damage variables		d_{11} d_{22} d_{12}	y_{11} y_{22} y_{12}	Energy release rate densities

strain inputs and the remaining 10 micromechanical internal variables are derived from 6 evolution laws. Therefore, the set S of state variables is (*Table* 1)

$$S = \left\{\underline{\underline{\varepsilon}}; \underline{\underline{\alpha}}; D_{i=1;4}; \underline{\underline{d}}\right\} \tag{24.1}$$

and the associated forces F are (*Table* 1)

$$F = \left\{\underline{\underline{\sigma}}; \underline{\underline{X}}; Y_{i=1;4}; \underline{\underline{y}}\right\} \tag{24.2}$$

The second step is to define the relevant tests required to identify the growth of the six internal variables. This is achieved from unloading/reloading tests performed at regular intervals and measuring the macroscopic inelastic strain upon complete unloading, $\overline{\varepsilon}_{\text{in}}$, the macroscopic damage of the composite, $\overline{D}$, and the maximum hysterisis loop width, $\delta\overline{\varepsilon}$ (*Fig.* 2). Using Eqs. (12), the internal variables can be calculated.

When tension is applied at 45 degrees on a $[0/90]_s$ layered composite, the macroscopic damage variable, $\overline{D}^{45}$, is related to the microscopic damage variables taking place in the matrix alone, $\{D_{my}^{00}, D_{my}^{90}\}$, by using the transformation rules given in the Appendix. Moreover, in this particular case, the two damage variables D_{my}^{00} and D_{my}^{90} have the same value. Therefore, the evolution law, $D_m(Y_m)$, is directly given by the evolution of the macroscopic damage of the composite $\overline{D}^{45}$ (*Fig.* 6).

The evolution law of the damage variable associated with fiber-breakage, $D_f(Y_f)$, is found from measurement of the macroscopic damage $\overline{D}^{00}$ (*Fig.* 6) in a tension test at 0 degree on the [0/90] which has been compensated by the contribution matrix-cracking which is calculated from the results of the first test.

Similarly, the evolution laws of the state variables related to sliding, $\alpha_{11}(X_{11})$ or $\alpha_{22}(X_{22})$, and $d_{11}(y_{11})$ or $d_{22}(y_{22})$ are known from the evolution of the macroscopic

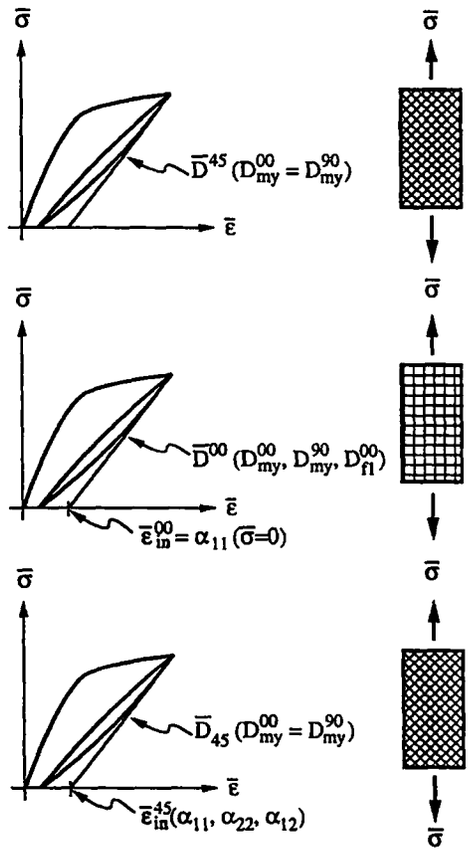

Fig. 6. – Flow chart of the identification procedure.

inelastic strain upon complete unloading $\bar{\varepsilon}^{00}_{\text{in}} = \alpha_{11}(\bar{\sigma}_{11} = 0)$, the macroscopic damage of the composite, $\bar{D}^{00}$, and the maximum hysteresis loop width, $\delta\bar{\varepsilon}^{00}$, using generalized micromechanics relations (Eqs. 12)

$$\frac{-\rho_1^{00}}{E^{00}} = \left(\sqrt{\frac{\bar{\varepsilon}^{00}_{\text{in}} + 2\delta\bar{\varepsilon}^{00}}{4\delta\bar{\varepsilon}^{00}}} - 1\right)(\bar{\varepsilon}^{00}_{m} - \bar{\varepsilon}^{00}_{\text{in}} - 2\delta\bar{\varepsilon}^{00}) \tag{25.1}$$

$$D^{00} = \frac{\bar{\varepsilon}^{00}_{M}\bar{D}^{00} - \bar{\varepsilon}^{00}_{\text{in}}\bar{D}^{00} - 2\delta\bar{\varepsilon}^{00}}{\bar{\varepsilon}^{00}_{M} - \bar{\varepsilon}^{00}_{\text{in}} - 2\delta\bar{\varepsilon}^{00}} \tag{25.2}$$

$$\frac{d_{11}}{4} = \frac{\sqrt{(\bar{\varepsilon}^{00}_{\text{in}} + 2\delta\bar{\varepsilon}^{00})\delta\bar{\varepsilon}^{00}}}{\bar{\varepsilon}^{00}_{M} - \bar{\varepsilon}^{00}_{\text{in}} - 2\delta\bar{\varepsilon}^{00}} \tag{25.3}$$

$$\alpha_{11} = \frac{d_{11}}{2}\,\frac{\bar{\sigma}^{00}_{M} - \rho_1^{00}(1 - D^{00})}{E^{00}(1 - D^{00})} \tag{25.4}$$

Finally, returning to the results of the tension test at 45 degrees on a $[0/90]_s$ layered composite (*Fig.* 6), the evolution laws of the state variables related to sliding, $\alpha_{12}(X_{12})$

and $d_{12}(y_{12})$ are given by the following relationships similar to those calculated by the micromechanical analysis

$$\frac{d_{12}}{4} = \frac{\overline{\varepsilon}_{\text{in}}^{45}}{\overline{\varepsilon}_{M}^{45} - 2\overline{\varepsilon}_{\text{in}}^{45}} \tag{26.1}$$

$$\alpha_{12} = \frac{d_{12}}{2} \frac{\overline{\varepsilon}_{M}^{45}}{1 + \frac{d_{12}}{2}} \tag{26.2}$$

In this analysis, it can be noticed that the residual stress $-\rho_1^{45}$ in the tension direction is equal to zero, and therefore $\overline{\varepsilon}_{\text{in}}^{45} = 2\delta\overline{\varepsilon}^{45}$, which leads to the above results. Equations (25) and (26) can be used to predict the overall behavior of the analyzed CMC. However, they are valid provided the interfacial behavior can solely be modeled by a constant interfacial shear strength. This is not the only model available to study CMCs. Therefore the evolution laws of the damage variables as well as the inelastic strains are determined by direct measurement of their values at different stress levels. The drawback of this approach is that the model is not completely identified since the damage variables related to debonding and sliding are not identified. Therefore the part of the free energy that is stored is not fully determined since it depends upon the details of the interfacial behavior. The stress/strain relationship however is known and thus a structural analysis can be performed.

In summary, only two tests, on the same architecture, enable us to extract all six evolution laws that define the behavior of the material (see *Fig.* 6). Two tensile tests are sufficient when the back-stresses are computed (therefore the damage variables related to debonding and sliding). In the following it will be shown that two tests are still sufficient as long as the evolution of the inelastic strain α_{12} can be obtained by the analysis of one of the tensile tests.

4. Model identification

The identification is performed on a $[0/90]_s$ laminate architecture of a SiC/SiC composite using the experimental results of Pluvinage (1991). Only two tension tests are used to establish the evolution laws of the damage quantities and the inelastic strains. The first step is to consider the elastic properties. Inspection of the composite (Pluvinage, 1991) indicates the presence of porosity in the matrix. Because the model is mechanism-based, the only means of accounting for this porosity is by an initial non-zero matrix damage quantity, D_{m0}. The measurement of Young's Moduli E^{00} and E^{45} respectively for a 0 degree and $\pm$ 45 degree tension tests combined with their analytic expressions gives the value of the initial non-zero isotropic damage quantity, $D_{m0} = 0.7$, which affects *only the initial elastic properties*. This damage value is consistent with experimental observations of initial porosities due to the Chemical Vapor Infiltration technique used to process these materials (Pluvinage, 1991).

The evolution laws of the state variables are written in terms of the associated forces. Therefore, the evolution of the damage variables is written as a function of the strain energy release rate densities. The evolution of the inelastic strains is written in terms of the corresponding back-stresses. It can be shown that the back-stresses are linearly proportional to the macroscopic stresses as shown in Eqs. (23.4) and (25.4). For the sake of simplicity, the evolution of the inelastic strains is thus written in terms of the macroscopic stresses. Lastly, the evolution of the damage variable $\underline{\underline{d}}$ is not explicitly needed in the present approach since only monotonic loading conditions are considered (*see* Section 2) and no particular statement is made concerning the interfacial behavior (*see* Section 3).

From the analysis of a tension test at 0 degree, the maximum hysteresis loop width is close to half of the corresponding inelastic strain upon complete unloading. It is concluded from Eq. (25.1) that the macroscopic residual stresses are very small and will therefore be neglected.

The variation of D_m with Y_m obtained from the experimental data is shown in Figure 7 a. Since matrix cracking is related to the presence of randomly distributed flaws, an appropriate form of evolution law which can fit the data shown in Figure 7 a is given by a Weibull law (1939; 1951)

$$D_m = D_{sat}\left(1 - \exp\left[-\left(\frac{Y_m - Y_{mth}}{Y_{m0}}\right)^{m_m}\right]\right) \tag{27}$$

The values that fit the data of Figure 7 a are

$$D_{sat} = 1.0 \quad Y_{mth} = 0\,\mathrm{Jm}^{-3} \quad Y_{m0} = 0.6\,\mathrm{Jm}^{-3} \quad m_m = 1.2 \tag{28}$$

The threshold energy release rate density Y_{mth} has a zero value in accordance with the hypothesis of no macroscopic residual stresses. The parameters Y_{m0} and m_m are directly related to the evolution of cracking density as a function of applied stress. The damage parameter at saturation has a very high value in agreement with the fact that average crack spacing is very small for these composites (Pluvinage, 1991). The evolution laws for matrix damage having been determined, the fiber-breakage damage D_f can be plotted, as a function of Y_f. Using Curtin's relationship (1991) for fiber damage, the evolution law is given by

$$D_f = 1 - \exp\left[-\left(\frac{Y_f}{Y_{f0}}\right)^{(m_f+1)/2}\right] \tag{29}$$

In the following computations, it was assumed that during the matrix-cracking process, only few fibers break. Therefore, no attempt was made to identify the previous parameters.

Lastly, the expression used to fit the evolution laws for the inelastic strains shown in Figures 7 b and 7 c are

$$\alpha_i = \frac{\langle \sigma_i - \sigma_{th} \rangle}{\sigma_0} \tag{30}$$

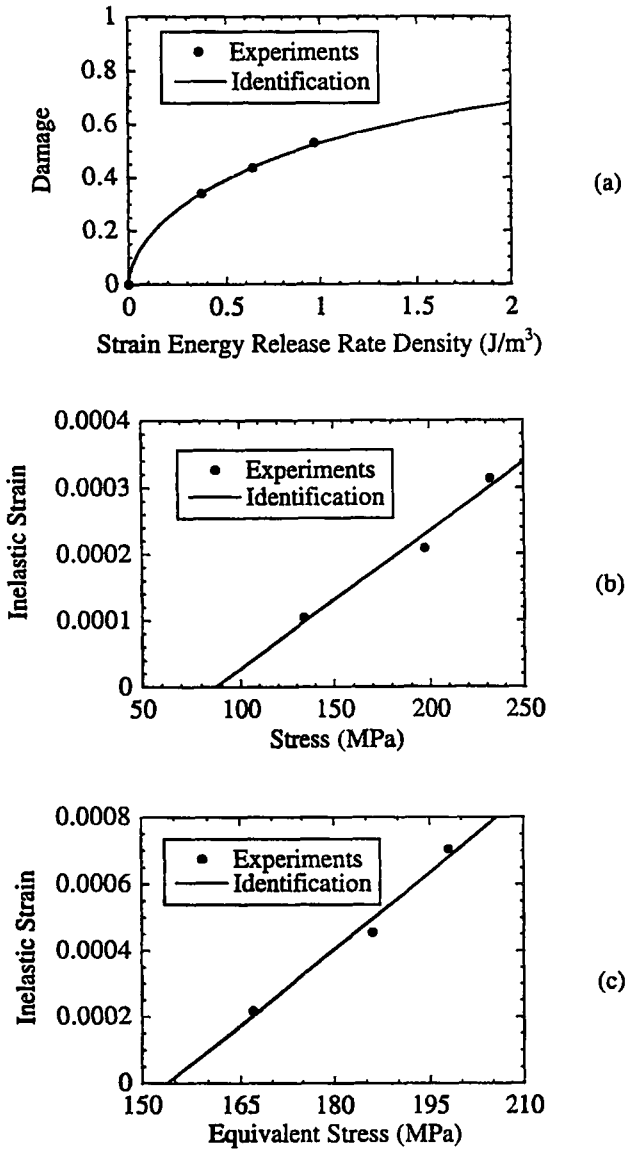

Fig. 7. – Experimental and identified evolution of:
(a) the matrix-cracking damage variable D_m as a function of the strain energy release rate density associated with matrix-cracking Y_m;
(b) the inelastic strains α_{11} (or α_{22}) as a function of the stress σ_{11} (or σ_{22});
(c) the inelastic strains α_{12} as a function of the equivalent stress τ_{eq}.

$$\alpha_{12} = \frac{\langle \tau_{eq} - \tau_{th} \rangle}{\tau_0} \mathrm{Sign}(\sigma_{12}) \tag{31}$$

The material parameters of Eqs. (30) and (31) are related to the interfacial behavior.

The introduction of the expression for τ_{eq} comes from the observation that the stress/strain curves obtained for tensile tests at ± 45 degrees and shear tests at 0 degree almost coincide for CMC systems. This observation appears to apply for a whole class of materials: SiC/SiC, SiC/CAS, SiC/C, C/C composites (Cady *et al.*, 1995*a*), and

presumably SiC/Al_2O_3 composites (Heredia *et al.*, 1995). One choice for τ_{eq} which satisfies this requirement is given by

$$\tau_{eq} = \sqrt{\left| \sigma_{12} \left[\sigma_{12} + \frac{3}{2}(\sigma_{11} + \sigma_{22}) \right] \right|} \tag{32}$$

Similar behavior is observed in concrete for which both the hydrostatic and shear stress states influence the inelastic deformations (Drucker and Prager, 1956). The definition of the equivalent shear stress given in Eq. (32) enables us to identify all the evolution laws by analyzing two tensile tests. This hypothesis is crucial and will be checked in Section 5. The constants in Eqs. (30) and (31) which define the inelastic strains are given by (see *Fig.* 7 b and 7 c).

$$\begin{aligned} \sigma_{th} &= 88\,\text{MPa} \quad \sigma_0 = 480\,\text{GPa} \\ \tau_{th} &= 154\,\text{MPa} \quad \tau_0 = 64.8\,\text{GPa} \end{aligned} \tag{33}$$

This model is implemented in the industrial Finite Element code ABAQUS (Hibbit *et al.*, 1995) via a user material (UMAT) routine. This allows to investigate more complex loading conditions on a structural level. The Finite Element procedure was checked by analyzing pure tension tests at 0 and ± 45 degrees. The comparisons in terms of stress-strain between the experiments and the computations are shown in Figure 8. There is a good agreement between the model and the experiments used to identify the model.

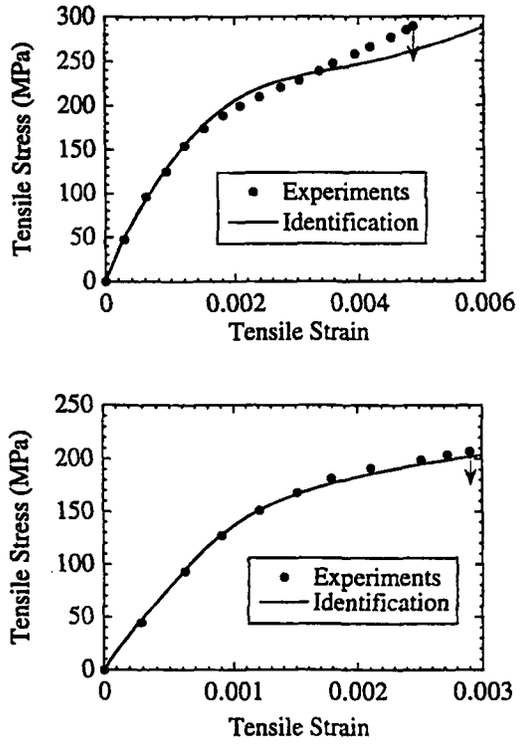

Fig. 8. – Experimental and identified evolution of the tensile stresses σ_{yy} as a function of the tensile strains ε_{yy} in
(a) a tension test on a [0/90] SiC/SiC lay-up at 0 degree,
(b) a tension test on a [0/90] SiC/SiC lay-up at ± 45 degrees.

5. Analysis of experiments on SiC/SiC composites

When the availability of materials is restricted to planar form, the most usual means of obtaining shear data is to subject the Iosipescu specimen (Iosipescu, 1967) to shear force (Pluvinage, 1991). In order to investigate the suitability of the Iosipescu test as a means of obtaining shear data, a Finite Element analysis has been performed using the constitutive equations described and identified previously. The Iosipescu specimen shown in Figure 9 is subjected to shear loading and measurement of the shear properties of the material are obtained by plotting the average stress at the minimum section against the shear strain measured by strain gauges placed at the center of the specimen. It is known that the shear stress at the minimum section of this specimen is sensibly constant when the material is elastic and isotropic, but is is not known if the constant shear stress assumption is valid when cracking occurs. In addition to verifying the suitability of the Iosipescu specimen, the tests provide an opportunity to measure the ability of the constitutive equations to predict the behavior of a component in which the stress state is different from those used in the identification procedure.

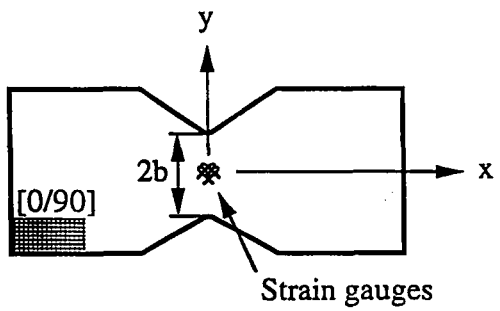

Fig. 9. – Iosipescu specimen configuration.

The plot of the average stress against the strain at the center of the specimen is shown in Figure 10. This prediction agrees with the experimental observations to within 5%. The stress-strain shear curve at the center of the ligament is also shown in Figure 10. It can be seen that the average stress-strain shear curve *underestimates* the actual stresses. The difference, which is not large, is the result of the assumption that the shear stress and strain are almost uniform across the minimum section. The results of the finite element analysis shown in Figure 11 indicate that the shear stress at the minimum section is essentially constant therefore justifying the use of the Iosipescu specimen as a means of obtaining shear data. Lastly, the hypothesis made to write the evolution of the inelastic strain α_{12} (Eq. (31)) as a function of the equivalent shear stress τ_{eq} (Eq. (32)) seems reasonable when the results of prediction of the Iosipescu test is compared with the experiments. Figure 11 also compares the shear stress profile for the linear elastic and non-linear calculations when the external load level is identical. The effect of non-linear stress/strain behavior allows the stresses to be redistributed when compared to a purely linear elastic calculation. This effect can be measured by the ratio of the average to maximum shear stresses in the elastic calculation (0.93) and in the non-linear analysis

(0.95). This difference is not important since the shear stress profile is almost constant in the ligament even for a linear elastic computation.

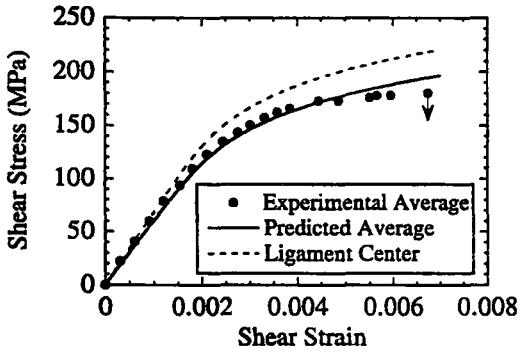

Fig. 10. – Experimental and predicted evolution of the average shear stresses σ_{xy} as a function of the shear strains γ_{xy} in a Iosipescu test on a [0/90] SiC/SiC lay-up. This evolution is compared with the evolution of the shear stresses σ_{xy} as a function of the shear strains γ_{xy} in the center of the specimen.

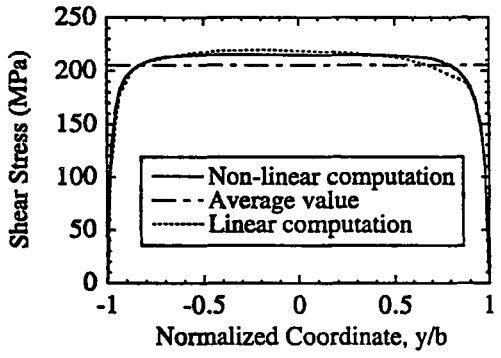

Fig. 11. – Shear stress profile in the ligament of the Iosipescu specimen when the shear strain γ_{xy} in the center of the specimen is equal to 0.007 as a function of the relative distance y/b from the center of the ligament for a linear and non-linear computation.

6. Conclusions

A CDM model is proposed for CMCs which is mechanisms-based. The laws which relate the growth of the internal state variables to their associated forces have been derived from the unloading-reloading paths during tensile experiments for two different directions. The ability of the model to predict the response to another state of stress suggests the advantage of a mechanisms-based approach.

When applied to SiC/SiC [0/90] lay-ups, the present model has ten internal variables, viz. three inelastic strains modeling sliding, three damage variables describing the amount of debonding and four damage variables accounting for matrix-cracking and fiber-breakage in the two plies. It is shown that only two different experiments in tension are needed to identify the growth laws of the ten internal variables. The

model has the potential to be applied to other material configurations (e.g., SiC/CAS, SiC/C, C/C, and presumably SiC/Al_2O_3 composites) and architectures (e.g., woven configurations). Furthermore, the general framework presented herein has been applied to room temperature configurations and monotonic loading conditions. However extensions to cyclic load histories as well as high temperature applications can be included with minimal change to the state potential formulations. Evolution laws will have to be modified slightly.

The reliability of the Iosipescu test is confirmed as a means of average stress-strain shear data, and the constitutive equations are able to predict the shear properties correctly. However, it is shown that the average shear properties may be slightly different from the actual stress-strain shear data in the center of the ligament. Therefore the identification of the shear properties based upon the measurements on a Iosipescu test are, strictly speaking, only an approximation of the actual response in pure shear.

The ability of stress redistribution due to the non-linearity of the stress/strain curve has been shown in the case of the Iosipescu experiment. Stress redistribution is important for structural applications and needs to be further studied on other types of structures and load configurations (e.g., plates with holes, notches, pin-loaded structures). This work is still under way.

Acknowledgments

This work was supported by the Advanced Research Project Agency through the University Research Initiative under Office of Naval Research Contract No. N-00014-92-J-1808.

APPENDIX

Let us consider a lamina with initial principal directions of orthotropy given by 1 and 2. The initial principal directions of orthotropy, or material directions, often do not coincide with the loading directions given by x and y (*Fig.* 5). The z-axis is perpendicular to the plan (1-2) and (x-y).

Under plane stress conditions, an elastic stress-strain relation in the material directions can be written in terms of the compliance matrix $\{S\}$.

$$\text{(A1.1)} \qquad \begin{pmatrix} \varepsilon_{11} \\ \varepsilon_{22} \\ \gamma_{12} \end{pmatrix} = \begin{pmatrix} S_{11} & S_{12} & 0 \\ S_{12} & S_{22} & 0 \\ 0 & 0 & S_{66} \end{pmatrix} \begin{pmatrix} \sigma_{11} \\ \sigma_{22} \\ \sigma_{12} \end{pmatrix}$$

or in terms of the stiffness matrix $\{Q\}$

$$\text{(A1.2)} \qquad \begin{pmatrix} \sigma_{11} \\ \sigma_{22} \\ \sigma_{12} \end{pmatrix} = \begin{pmatrix} Q_{11} & Q_{12} & 0 \\ Q_{12} & Q_{22} & 0 \\ 0 & 0 & Q_{66} \end{pmatrix} \begin{pmatrix} \varepsilon_{11} \\ \varepsilon_{22} \\ \gamma_{12} \end{pmatrix}$$

If we now consider the same expression written in the loading directions, the general stress-strain relation leads to a full compliance matrix $\{\overline{S}\}$

$$\text{(A2.1)} \qquad \begin{pmatrix} \varepsilon_{xx} \\ \varepsilon_{yy} \\ \gamma_{xy} \end{pmatrix} = \begin{pmatrix} \overline{S}_{11} & \overline{S}_{12} & \overline{S}_{16} \\ \overline{S}_{12} & \overline{S}_{22} & \overline{S}_{26} \\ \overline{S}_{16} & \overline{S}_{26} & \overline{S}_{66} \end{pmatrix} \begin{pmatrix} \sigma_{xx} \\ \sigma_{yy} \\ \sigma_{xy} \end{pmatrix}$$

or to a full compliance matrix $\{\overline{Q}\}$

$$\text{(A2.2)} \qquad \begin{pmatrix} \sigma_{xx} \\ \sigma_{yy} \\ \sigma_{xy} \end{pmatrix} = \begin{pmatrix} \overline{Q}_{11} & \overline{Q}_{12} & \overline{Q}_{16} \\ \overline{Q}_{12} & \overline{Q}_{22} & \overline{Q}_{26} \\ \overline{Q}_{16} & \overline{Q}_{26} & \overline{Q}_{66} \end{pmatrix} \begin{pmatrix} \varepsilon_{xx} \\ \varepsilon_{yy} \\ \gamma_{xy} \end{pmatrix}$$

The relationship between the compliance matrix in the material directions, $\{S\}$, and in the loading directions, $\{\overline{S}\}$ can be written as follows

$$\text{(A3.1)} \qquad \{\overline{S}\} = \{T\}^T \{S\} \{T\}$$

and the relationship between the stiffness matrix in the material directions, $\{Q\}$, and in the loading directions, $\{\overline{Q}\}$ can be written as follows

$$\text{(A3.2)} \qquad \{\overline{Q}\} = \{T\}^{-1} \{Q\} \{T\}^{-T}$$

where the superscript ^{T} denotes the matrix transpose, and $\{T\}$ the transformation matrix associated with a positive rotation of angle θ of principal axes about z from material axes (*Fig.* 1)

$$\text{(A4)} \qquad \{T\} = \begin{pmatrix} \cos^2\theta & \sin^2\theta & -2\sin\theta\cos\theta \\ \sin^2\theta & \cos^2\theta & 2\sin\theta\cos\theta \\ \sin\theta\cos\theta & -\sin\theta\cos\theta & \cos^2\theta - \sin^2\theta \end{pmatrix}$$

REFERENCES

ASHBY M. F., 1992, Physical Modeling of Materials Problems, *Mat. Sci. Tech.*, **8**, 102-111.

AVESTON J., COOPER G. A., KELLY A., 1971, *Single and Multiple Fracture, National Physical Laboratory: Properties of Fiber Composites*, IPC Science and Technology Press, Surrey (UK), 15-26.

BEYERLEY D., SPEARING S. M., ZOK F. W., EVANS A. G., 1992, Damage, Degradation and Failure in a Unidirectional Ceramic-Matrix Composite, *J. Am. Ceram. Soc.*, **75**, n° 10, 2719-2725.

BUDIANSKY B., O'CONNELL R. J., 1976, Elastic Moduli of a Cracked System, *Int. J. Solids Struct.*, **12**, 81-97.

BURR A., HILD F., LECKIE F. A., 1995, Micro-Mechanics and Continuum Damage Mechanics, *Arch. Appl. Mech.*, **65**, n° 7, 437-456.

CADY C., HEREDIA F. E., EVANS A. G., 1995*a*, In-Plane Mechanical Properties of Several Ceramic-Matrix Composites, *J. Am. Ceram. Soc.*, **78**, n° 8, 2065-2078.

CADY C., MAKIN T. J., EVANS A. G., 1995*b*, Silicon Carbide Calcium Aluminosilicate – A Notch-Insensitive Ceramic-Matrix Composite, *J. Am. Ceram. Soc.*, **78**, n° 1, 77-82.

CHABOCHE J. L., 1982, Le concept de contrainte effective appliqué à l'élasticité et à la viscoplasticité en présence d'un endommagement anisotrope, *Colloque international du CNRS*, **295**, 31-43.

COCKS A. C. F., LECKIE F. A., 1987, Creep Constitutive Equations for Damaged Materials, in *Advances in Applied Mechanics*, Academic Press, New York, **25**, 239-294.

COLEMAN D. B., GURTIN M. E., 1967, Thermodynamics with Internal Variables, *J. Chem. Phys.*, **47**, 597-613.

CURTIN W. A., 1991, Exact Theory of Fiber Fragmentation in Single-Filament Composite, *J. Mat. Sci.*, **26**, 5239-5253.

DRUCKER D. C., PRAGER W., 1956, Soil Mechanics and Plastic Analysis of Limit Design, *Quat. of Appl. Math.*, **14**.

ESHELBY J. D., 1957, The Determination of the Elastic Field of an Ellipsoidal Inclusion and Related Problems, *Proc. Roy. Soc. London*, **A241**, 376-396.

EVANS A. G., DOMERGUE J. M., VAGAGGINI E., 1994, Methodology for Relating the Tensile Constitutive Behavior of Ceramic matrix Composites to Constituent Properties, *J. Am. Ceram. Soc.*, **77**, n° 6, 1425-1435.

GERMAIN P., NGUYEN Q. S., SUQUET P., 1983, Continnum Thermodynamics, *J. Appl. Mech.*, **50**, 1010-1020.

HEREDIA F. E., EVANS A. G., ANDERSON C. A., 1995, Tensile and Shear Properties of Continuous Fiber-Reinforced SiC/Al_2O_3 Composites Processed by Melt Oxidation, *J. Am. Ceram. Soc.*, **78**, n° 10, 2790-2800.

HIBBITT H. D., KARLSSON B. I., SORENSEN P., 1995, *Abaqus, version 5.5.*

HILD F., BURR A., LECKIE F. A., 1996, Matrix-Cracking and Debonding in Ceramic-Matrix Composites, *Int. J. Solids Struct.*, **33**, n° 8, 1209-1220.

HUTCHINSON J. W., JENSEN H. M., 1990, Models for Fiber Debonding and Fiber Pull-Out in Brittle Composites with Friction, *Mech. Mat.*, **9**, 139-163.

IOSIPESCU N., 1967, New Accurate Procedure for Single Shear Testing of Metals, *J. Mater.*, **2**, 537-566.

JANSSON S., LECKIE F. A., 1993, The Mechanics of Failure of Silicon Carbide Fiber-Reinforced Glass-Matrix Composites, *Acta Metall. Mat.*, **40**, n° 11, 2967-2978.

LADEVÈZE P., 1983, *Sur une théorie de l'endommagement anisotrope*, LMT Cachan, Report N° 34.

LEMAITRE J., 1992, *A Course on Damage Mechanics*, Springer-Verlag, Berlin (Germany).

LEMAITRE J., CHABOCHE J.-L., 1978, Aspect phénoménologique de la rupture par endommagement, *J. Méc. Appl.*, **2**, n° 3, 317-365.

LOVE A. E. H., 1927, *The Mathematical Theory of Elasticity*, Cambridge University Press, Cambridge (UK).

PLUVINAGE P., 1991, *Étude expérimentale et simulation numérique du comportement mécanique de matériaux composites SiC/SiC, Influence des paramètres de stratification et d'élaboration*, Thèse d'Université, Bordeaux-I.

RICE J. R., 1971, Inelastic Constitutive Relations for Solids: An Internal Variable Theory and its Application to Metal Plasticity, *J. Mech. Phys. Solids*, **19**, 433-455.

VOLTERRA V., 1907, Sur l'équilibre des corps élastiques multiplement connexes, *Annales Scientifiques de l'École Normale Supérieure*, **24**, n° 3, 401-518.

WEIBULL W., 1939, A Statistical Theory of the Strength of Materials, *Roy. Swed. Inst. Eng. Res.*, **151**.

WEIBULL W., 1951, A Statistical Distribution Function of Wide Applicability, *J. Appl. Mech.*, **18**, n° 3, 293-297.

ZIENKIEVICZ O. C., TAYLOR R. L., 1989, *The Finite Element Method*, McGraw-Hill, London (UK), 4th edition.

(Manuscript received August 8, 1995;
revised April 1996;
accepted June 6, 1996.)

3.3 Rupture de fibres sous chargement monotone

Le mécanisme de rupture des fibres est souvent celui qui conduit à la ruine complète d'un composite renforcé de fibres longues. Leur petit diamètre (de quelques μm à quelques centaines de μm) leur confère une résistance de l'ordre de quelques GPa (l'effet de volume, discuté dans le chapitre 2 est mis à profit pour atteindre ces valeurs importantes de résistance). Lorsque le composite est dans une configuration favorable (caractéristiques mécaniques de l'interface optimales [HILD, 1997]), la rupture de fibre ne s'effectue pas forcément dans le plan de la fissure matricielle et un deuxième mécanisme devient actif : c'est l'arrachement (ou « *pull-out* »). Il permet aux fibres de « ponter » la fissure matricielle et ainsi de rester actives mécaniquement bien qu'elles soient rompues.

La prise en compte de l'aspect aléatoire de la rupture locale des fibres (qui obéit aux mêmes hypothèses que celles du chapitre 2) est possible dans le cas d'hypothèses simples développées dans le paragraphe 3.3.1.i à partir d'une écriture de lois de comportement très similaires à celle développée dans le paragraphe 3.2.1 dans l'étude de la fissuration matricielle. Les conditions d'amorçage macroscopique (*i.e.*, les conditions de localisation décrites dans le chapitre 1) sont obtenues dans la première partie du paragraphe 3.3.1.ii dans le cas d'une écriture unidimensionnelle. Une généralisation est développée dans le paragraphe 3.3.1.iii. Enfin, une extension à des architectures [0/90] est proposée dans le paragraphe 3.3.2 en vue d'applications à des structures tournantes.

La redistribution des efforts au voisinage d'une rupture de fibre est fondamentale pour la tenue du composite. Différents régimes extrêmes ont été analysés [GÜCER et GURLAND, 1962]. Ils partent du concept de matériaux à fonctionnement « en série » où la charge supportée par la fibre est redistribuée sur ses plus proches voisins (*i.e.*, partage local d'effort). À l'opposé, un système « en parallèle » (*i.e.*, partage global d'effort) consiste à supposer que la charge supportée par la fibre qui vient de casser est redistribuée de manière uniforme à toutes les fibres non rompues. Bien entendu, des régimes intermédiaires, plus ou moins compliqués, peuvent être imaginés [ZWEBEN et ROSEN, 1970 ; NEUMEISTER, 1993]. La deuxième partie du paragraphe 3.3.1.ii en discute différentes applications pour différents types de matrices renforcées par des fibres en carbure de silicium.

3.3.1 Endommagement et rupture de composites unidirectionnels

i Loi de comportement

par F. HILD, A. BURR et F.A. LECKIE (1994).
Eur. J. Mech. A/Solids, 13 (6), pp. 731-749.

Fiber breakage and fiber pull-out of fiber-reinforced ceramic-matrix composites

F. HILD*, **, A. BURR*, ** and F. A. LECKIE*

ABSTRACT. – Fiber breakage and fiber pull-out induce loss of stiffness, anelastic strains, hysteresis loops, and crack closure. Ultimate strength properties of fiber-reinforced composites are derived and compared with results related to localization. These features are analyzed in the framework of Continuum Mechanics through the introduction of internal variables. Three models which are progressively more faithful to the micromechanical analysis are studied. They provide guidance on the choice of the relevant internal variables to model the mechanical behavior of unidirectional fiber-reinforced composites.

1. Introduction

Ceramic-Matrix Composites (CMC's) are potential candidates to meet the new goals of high performance structures, especially when the elements are subjected to high mechanical and thermal load histories [URI, 1994]. Their low density combined with high strength and good performance at high temperature are appealing features in the design of new generation jet engines.

This paper is part of an effort to derive constitutive equations which describe the behavior of CMC's within the context of Continuum Damage Mechanics (CDM). The approach makes use of the micromechanical analyses of the degradation mechanisms occurring in CMC's. The degradation mechanisms include matrix cracking and fiber breakage both of which are accompanied by slip at the fiber/matrix interface. Matrix cracking which first forms at quite low stresses continues to grow with increasing stress until saturation is reached when the application of increased stress does not increase the crack density. The saturation is usually the consequence of the shear induced by the interface between fibers and matrix [Aveston *et al.*, 1971]. Starting from a material which is assumed free from any initial macro defect, the mechanical behavior is predicted by using Continuum Damage Mechanics. The results presented herein are valid when the steady matrix cracking stress [Budiansky *et al.*, 1986] is less than the ultimate strength of a fiber-reinforced composite [Budiansky, 1993]. When this hypothesis is satisfied, the key

* Department of Mechanical and Environmental Engineering, University of California, Santa Barbara CA 93106-5070, U.S.A.

** Also at Laboratoire de Mécanique et Technologie, E.N.S. de Cachan/C.N.R.S./Université Paris-VI, 61, avenue du Président-Wilson, F-94235 Cachan Cedex, France.

mechanism leading to final failure is fiber breakage. For this reason no attempt is made to model the growth of matrix craking and saturation conditions are assumed. The fiber breakage mechanism is accompanied by distributed fiber pull-out when broken fibers pulling out of the matrix introduce shear stresses along the interface. This mechanism distinguishes the behavior of fiber-reinforced CMC's from that of the classical dry fiber bundle [Coleman, 1958].

The ultimate tensile strength at localization of strain is calculated for unidirectional composites and a micromechanics analysis of unloading-reloading sequences is developed, when hysteresis loops are formed. The micromechanics models are used to evaluate three different constitutive laws which are progressively more faithful to the micromechanical analysis. It is shown in practice that it is not always necessary to model all the details revealed by micromechanics. Previous studies by Hild *et al.* [Hild *et al.*, 1994 *b*] indicate that by identifying the relevant internal variables of a Continuum Damage Mechanics description the studies of unidirectional composites can be extended readily to the 2-*D* constitutive laws applicable to multidirectional lay ups under complex loading conditions.

2. Expression of the ultimate tensile strength

A unit cell of length L_R (*Fig.* 1 *a*) is considered where the matrix cracks are saturated with spacing L_m. The length L_R is the *recovery* length and refers to twice the longest fiber that can be pulled out and cause a reduction in the load carrying capacity. Away from a fiber break, as in the case of matrix cracking, the fiber stress builds up through the stress transfer across the sliding fiber-matrix interface. If the interfacial shear stress τ is assumed to be constant, the recovery length is related to the maximum stress in the fiber by [Curtin, 1991]

$$L_R = \frac{RT}{\tau} \tag{1}$$

where the reference stress T is the fiber stress in the plane of the matrix crack, R is the fiber radius. Generally, $L_m \ll L_R$ and the stress field in the intact fibers [Cox, 1952; Kelly, 1973] for $0 \leq x \leq \frac{L_m}{2}$ is (*Fig.* 1 *b*)

$$\sigma_F(T, x) = T - \frac{2\tau}{R} x \tag{2}$$

If the fibers exhibit a statistical variation of strength that obeys a two-parameter Weibull law [Weibull, 1939], then the probability that a fiber would break anywhere within the recovery length L_R at or below a reference stress T is given by

$$P_F(T) = 1 - \exp\left\{-\frac{2}{L_0}\int_0^{L_R/2}\left\{\frac{\sigma_F(T, x)}{S_0}\right\}^m dx\right\} \tag{3}$$

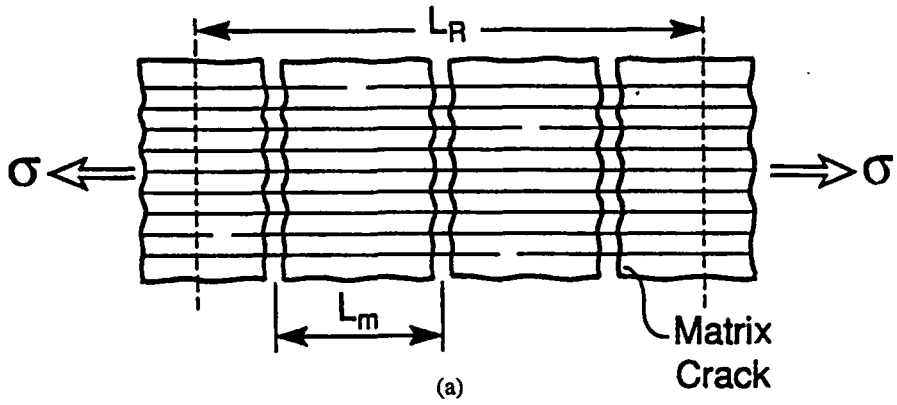

(a)

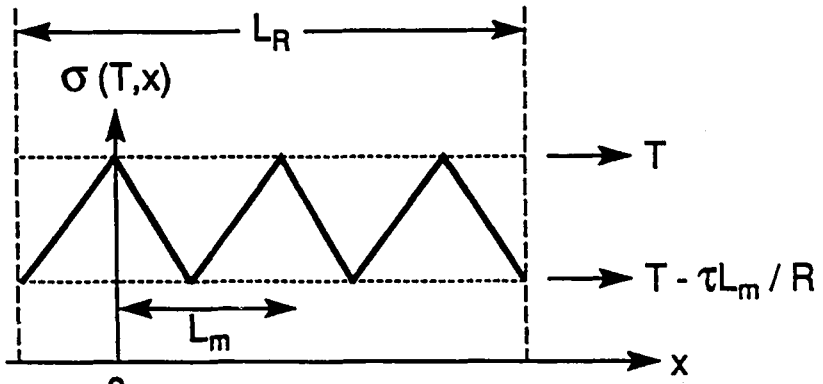

(b)

Fig. 1 *a*. – Depiction of the recovery length L_R when the density of matrix cracks (characterized by L_m) reaches saturation.

Fig. 1 *b*. – Fiber stress field $\sigma_F\,(T,\,x)$ along a length L_R for a reference stress T when the fibers are intact.

where m is the shape parameter, S_0 is the stress scale parameter, and L_0 a reference length. Eqn. (3) can be simplified when $L_m/L_R \ll 1$ to become

$$P_F\,(T) = 1 - \exp\left\{-\left(\frac{T}{S_c}\right)^{m+1}\right\} \tag{4}$$

where S_c denotes the *characteristic strength* [Henstenburg & Phoenix, 1989]

$$S_c^{m+1} = \frac{L_0\,S_0^m\,\tau}{R} \tag{5}$$

The relevant length to consider is the recovery length instead of the total length of the composite [Cao & Thouless, 1990]. The cumulative failure probability is thus *independent* of the total length of the composite, provided the total length of the composite is greater than the recovery length [Hild *et al.*, 1994 *a*]. The average stress $\bar{\sigma}$ applied to the composite is related to the reference stress T by

$$\bar{\sigma} = f\,T\,\{1 - P_F\,(T)\} + \bar{\sigma}_{FP}\,(T) = \bar{\sigma}_{FB}\,(T) + \bar{\sigma}_{FP}\,(T) \tag{6}$$

where f is the fiber volume fraction, $\bar{\sigma}_{FB}\,(T)$ denotes that component of the stress provided by *unbroken fibers*, and $\bar{\sigma}_{FP}\,(T)$ denotes that component of the stress provided

by *failed fibers* as they pull out from the matrix. For global load sharing [Curtin, 1993], the pull-out stress is given is given by

$$\bar{\sigma}_{FP}(T) = f\, P_F(T)\, \bar{\sigma}_b(T) \tag{7}$$

where $\bar{\sigma}_b(T)$ denotes the average stress at a plane of matrix crack $x = 0$ when a fiber breaks at location $x = t$, and at the reference stress level T. When the load is assumed to be homogeneous over the entire composite length, the average pull-out stress $\bar{\sigma}_b(T)$ reduces to $T/2$, and the external stress takes the form

$$\bar{\sigma} = f\, T\, \{1 - P_F(T)\} + f\, \frac{T}{2}\, P_F(T) \tag{8}$$

In Figure 2, the contributions of the two mechanisms are plotted for $m = 4$. The pull-out stress is a strictly increasing function, whereas the stress in the unbroken fibers reaches a maximum value. Because of the decrease of the stress $\bar{\sigma}_{FB}$, an ultimate stress exists. This decrease leads to a loss of uniqueness of the stress-strain relationship. Indeed, elastic unloading of the unbroken fibers may arise in one part of the composite and further fiber breakage in another part. Consequently localization appears and Eqn. (8) after that point corresponds to the homogeneous solution, which usually cannot be reached [Hild & Burr, 1994]. The applied stress level corresponding to the onset of localization will be referred to as localization tensile strength, and will be denoted by $\bar{\sigma}_{LTS}$. In the framework of CDM, the initiation of a macrocrack is described as a localization of the deformations [Billardon & Doghri, 1989], which corresponds to the onset of a surface across which the velocity gradient is discontinuous. Physically, it corresponds to localized pull-out,

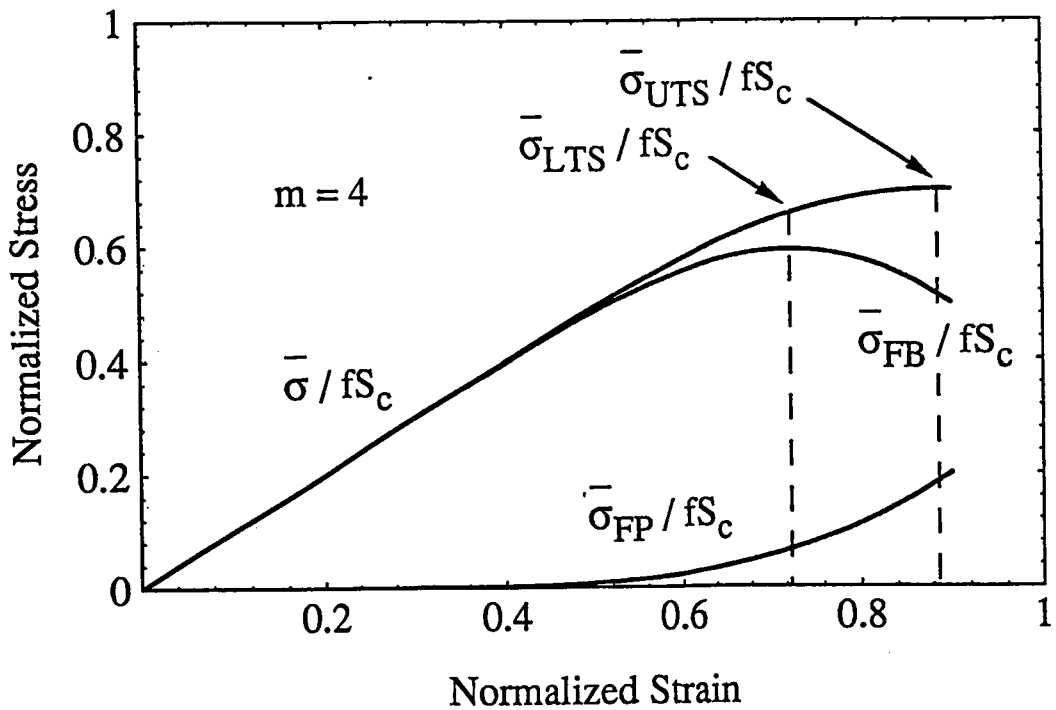

Fig. 2. – Normalized stresses, $\bar{\sigma}/f\,S_c$, $\bar{\sigma}_{FB}/f\,S_c$, $\bar{\sigma}_{FP}/f\,S_c$ versus normalized strain, $\bar{\varepsilon}\,E_F/S_c$.

whereby one macrocrack develops and pull-out continues to evolve in the vicinity of that macrocrack only. This phenomenon leads to a different behavior as compared to the homogeneous solution for which damage is still evolving in a diffusive manner. Under small deformations assumption, localization is mainly driven by the damage mechanism that causes strain softening [Lemaitre, 1992]. The localization tensile strength of the composite is defined by the condition

$$d\bar{\sigma}_{FB}/d\bar{\varepsilon} = 0 \tag{9}$$

or

$$d\bar{\sigma}_{FB}/dT = 0 \tag{10}$$

because the reference stress T is proportional to the average strain on the composite according to the relation,

$$\bar{\varepsilon} = \frac{2}{L_m}\int_0^{L_m/2} \frac{\sigma_F(T, x)}{E_F}\, dx \cong \frac{T}{E_F} \tag{11}$$

where E_F denotes the Young's modulus of the *unbroken* fibers. Consequently, the localization tensile strength becomes

$$\bar{\sigma}_{LTS} = \frac{f S_c}{2}\left(\frac{1}{m+1}\right)^{1/(m+1)}\left\{1+\exp\left(-\frac{1}{m+1}\right)\right\} \tag{12}$$

The ultimate tensile strength of the composite is defined by the condition

$$d\bar{\sigma}/d\bar{\varepsilon} = 0 \tag{13}$$

This equation cannot be solved analytically. A first order solution of the ultimate tensile strength, $\bar{\sigma}_{UTS}$, is predicted to be [C, 1991]

$$\bar{\sigma}_{UTS} = f S_c\left(\frac{2}{m+2}\right)^{1/(m+1)}\frac{m+1}{m+2} \tag{14}$$

3. Unloading-reloading sequence

The consequences of unloading followed by a reloading sequence are now investigated. Reversed motion of fibers relative to the matrix has been studied by numerous authors [Marshall & Oliver, 1987; McMeeking & Evans, 1990]. After reaching a maximum value characterized by T_M (less than the localization level), and by the maximum friction length L_{FM}, which is equal to half the maximum recovery length, L_{RM}, the load is reversed (*Fig.* 3). The maximum friction length is therefore related to the maximum reference stress T_M by

$$L_{FM}(T_M) = \frac{RT_M}{2\tau} \tag{15}$$

Upon unloading, in the range, $0 \leq |z| \leq L_{FU}$, there is a reversal of both the relative sliding direction and the frictional shear stress (*Fig.* 3). For $L_{FU} \leq |z| \leq L_{FM}$, the shear stress there remains unchanged from that prevailing during the loading process. The actual load level is characterized by the reference stress $T = T_M - \Delta T_U$, and the unloading friction length L_{FU} is related to ΔT_U by

$$L_{FU} = \frac{R\,\Delta T_U}{4\tau} = L_{FM}\left(\frac{\Delta T_U}{2}\right) \tag{16}$$

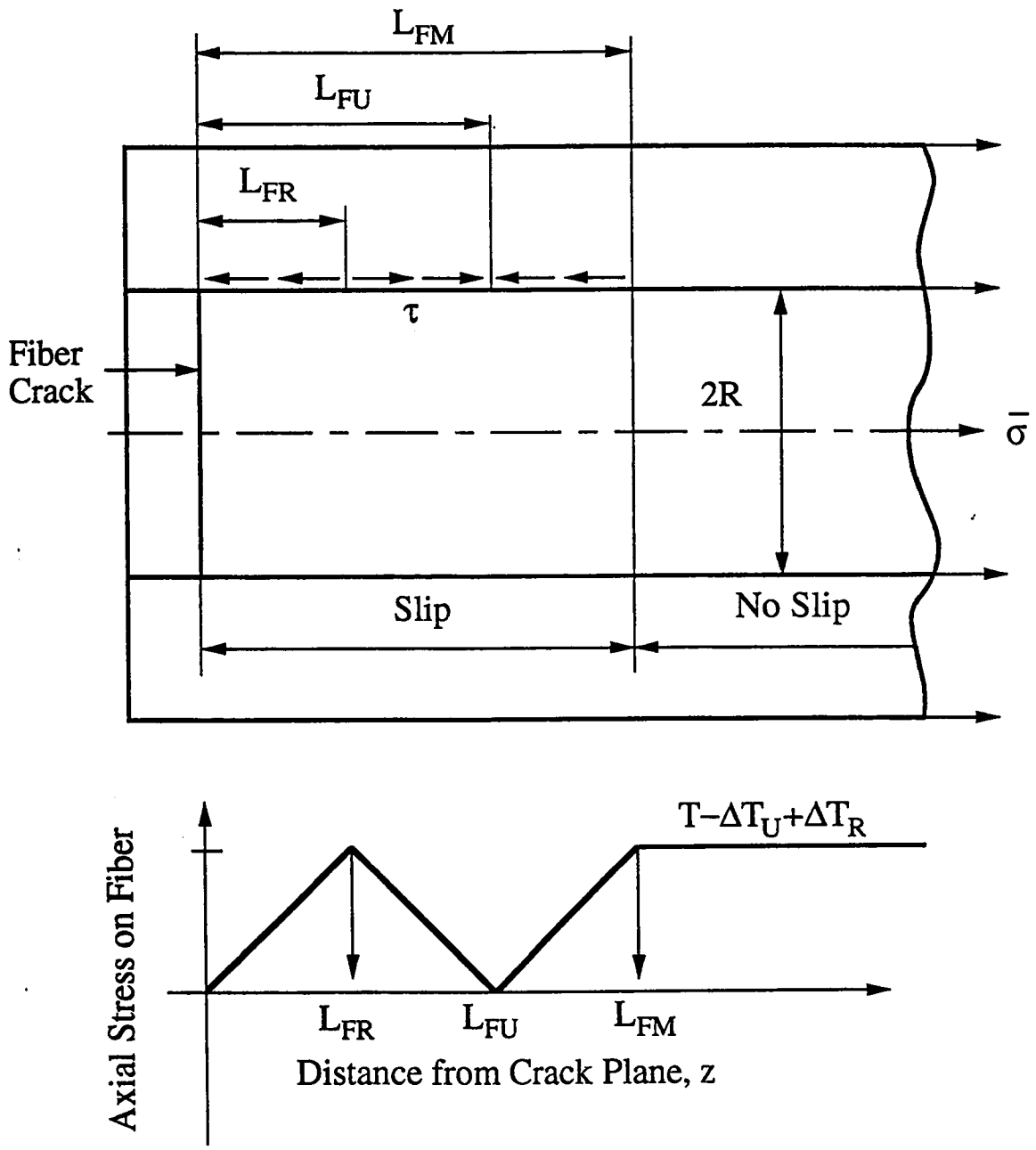

Fig. 3. – Depiction of the friction length, L_F, upon loading, the unloading friction length, L_{FU}, the reloading friction length, L_{FR}, and the corresponding axial stress on a broken fiber embedded in matrix.

Then, the external stress takes the form

$$\frac{\bar{\sigma}}{f} = (T_M - \Delta T_U) - \frac{P_F(T_M)}{4}\,\frac{2T_M^2 - \Delta T_U^2}{T_M} \tag{17}$$

Because of fiber pull-out, anelastic strains exist after complete unloading ($\bar{\sigma} = 0$). When $\bar{\sigma} = 0$, the expression of the unloading amplitude $\Delta T_U = T_M$ is

$$T_m = \frac{2T_M - \sqrt{2}T_M\sqrt{1 + (1 - P_F(T_M))^2}}{P_F(T_M)} \tag{18}$$

for which, the corresponding anelastic strains are given by

$$\bar{\varepsilon}_{\text{an}} = \frac{T_M - T_m}{E_F} \tag{19}$$

The anelastic strains depend upon the maximum load level, and the percentage of broken fibers, $P_F(T_M)$, within the recovery length L_{RM}. In Figure 4 the anelastic strains are plotted as a function of the maximum load level T_M. Their evolution which is a non-linear function of the maximum applied strains indicates that the anelastic strains are an order of magnitude smaller than the maximum total applied strain.

If unloading continues below T_m, there is closure of the fiber cracks when $\Delta T_U = T_c$ given by

$$T_c = \sqrt{2}T_M \tag{20}$$

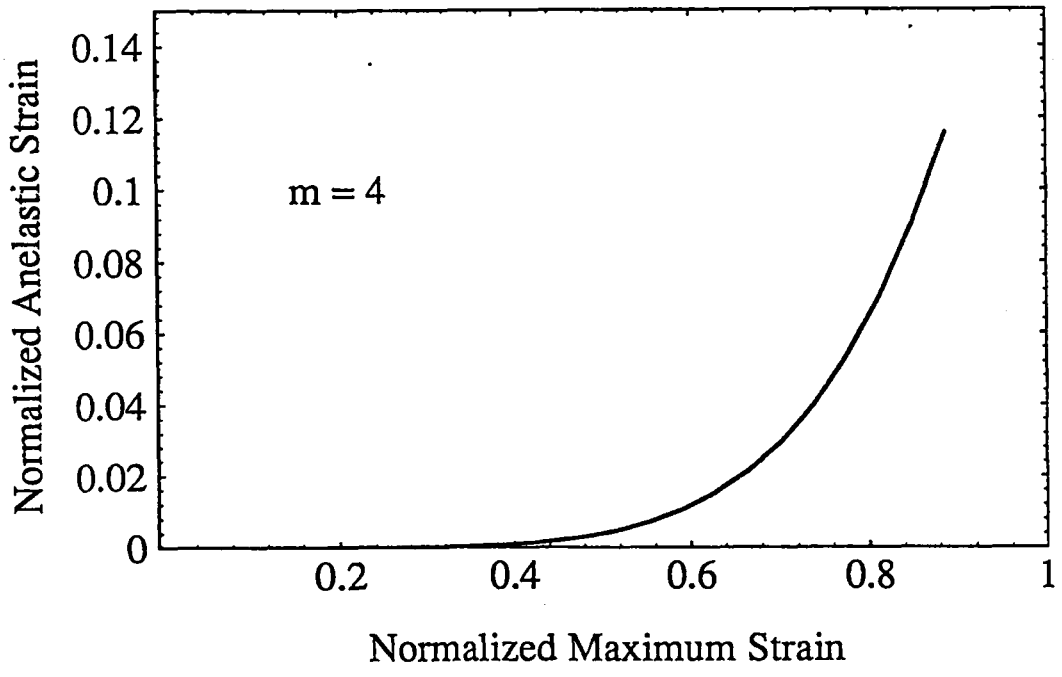

Fig. 4. – Normalized anelastic strain, $\bar{\varepsilon}_{\text{an}}$ ($\bar{\sigma} = 0$) E_F/S_c as a function of normalized strain, $\bar{\varepsilon}\,E_F/S_c$.

The unloading and the closure phenomenon can be described in terms of the difference in displacement between a broken face and an adjacent unbroken fiber, measured by δ (*Fig.* 5). The displacement δ is referred to as crack opening displacement. When δ is positive, there is pull-out, when δ is equal to zero, there is no pull-out since closure takes over. During the unloading sequence, the expression of the crack opening is given by

$$\delta(T_M, \Delta T_U) = \frac{R(2T_M^2 - \Delta T_U^2)}{8\tau E_F} \tag{21}$$

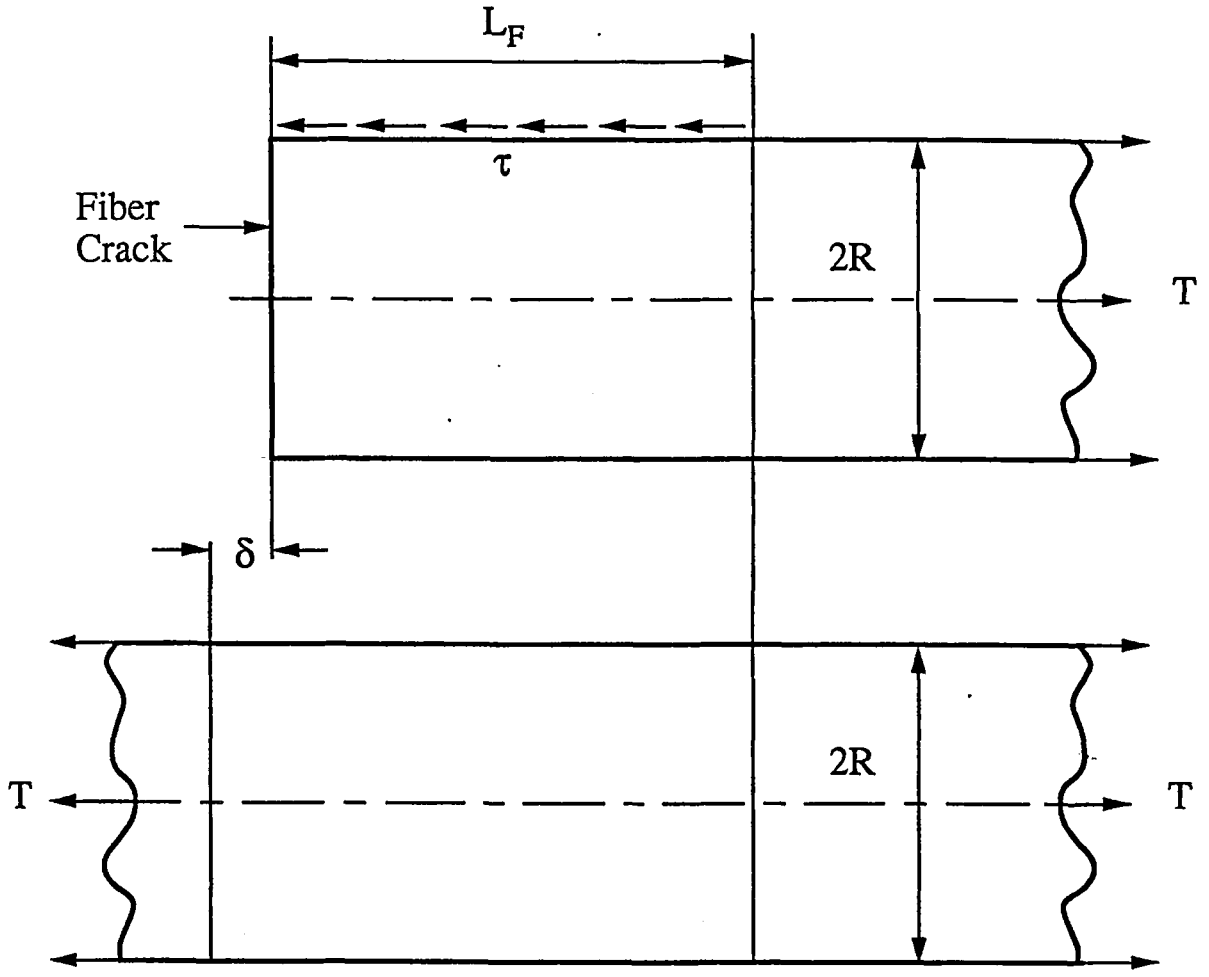

Fig. 5. – Depiction of the opening displacement δ.

After reaching a minimum value characterized by the amplitude T_m of the reference stress, and by the reverse friction length L_{Fm}, the load is reversed again (*Fig.* 3). It then leads to a reloading process. Upon reloading, characterized by $T = T_M - T_m + \Delta T_R$, sliding is confined to $0 \leq |z| \leq L_{FR}$,

$$L_{FR} = \frac{R\Delta T_R}{4\tau} \tag{22}$$

Then, the external stress takes the form

$$\frac{\bar{\sigma}}{f} = (T_M - T_m + \Delta T_R) - \frac{P_F(T_M)}{4}\,\frac{2T_M^2 - T_m^2 + \Delta T_R^2}{T_M} \tag{23}$$

In Figure 6 a loading-unloading-reloading sequence is plotted. The non-linear effects are the consequence of fiber breakage leading to a reduced Young's modulus, and fiber pull-out inducing friction and anelastic strains. If no wear mechanisms is involved, this first cycle corresponds to the steady state cycle. One way of characterizing the hysteresis loops is to measure their maximum width, $\delta\bar{\varepsilon}$. In Figure 7 the maximum hysteresis loop width is plotted as a function of maximum strain. Again, the evolution is non-linear wrt. the maximum applied strains.

Lastly it is possible to calculate the evolution of the crack opening during the reloading sequence to give

$$\delta(T_M,\, \Delta T_m,\, \Delta T_R) = \frac{R(2T_M^2 - T_m^2 + \Delta T_R^2)}{8\tau E_F} \tag{24}$$

During a loading-unloading-reloading sequence, the pull-out stress, $\bar{\sigma}_{FP}(T_M, T_m, \Delta T_R)$, is related to the crack opening displacement measured during the sequence, $\delta(T_M, T_m, \Delta T_R)$, by

$$\bar{\sigma}_{FP}(T_M, T_m, \Delta T_R) = \left(\bar{\varepsilon} - \frac{\delta(T_M, T_m, \Delta T_R)}{L_{FM}}\right) f E_F P_F(T_M) \tag{25}$$

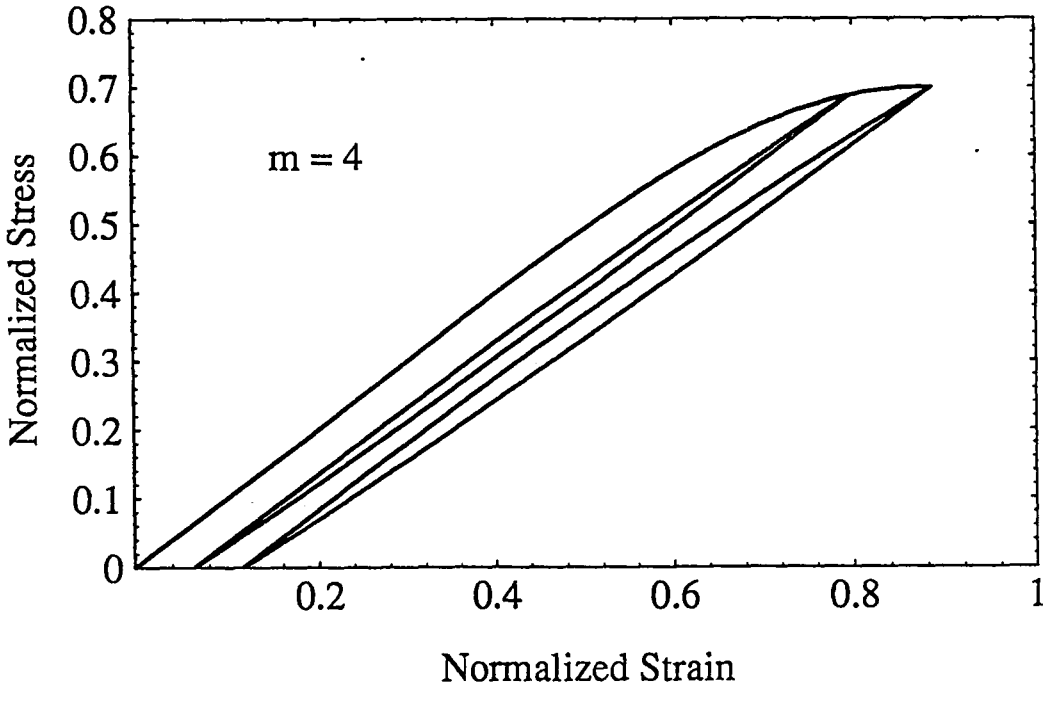

Fig. 6. – Normalized stress, $\bar{\sigma}/f\,S_c$, versus normalized strain, $\bar{\varepsilon}\,E_F/S_c$, during a loading-unloading-reloading sequence.

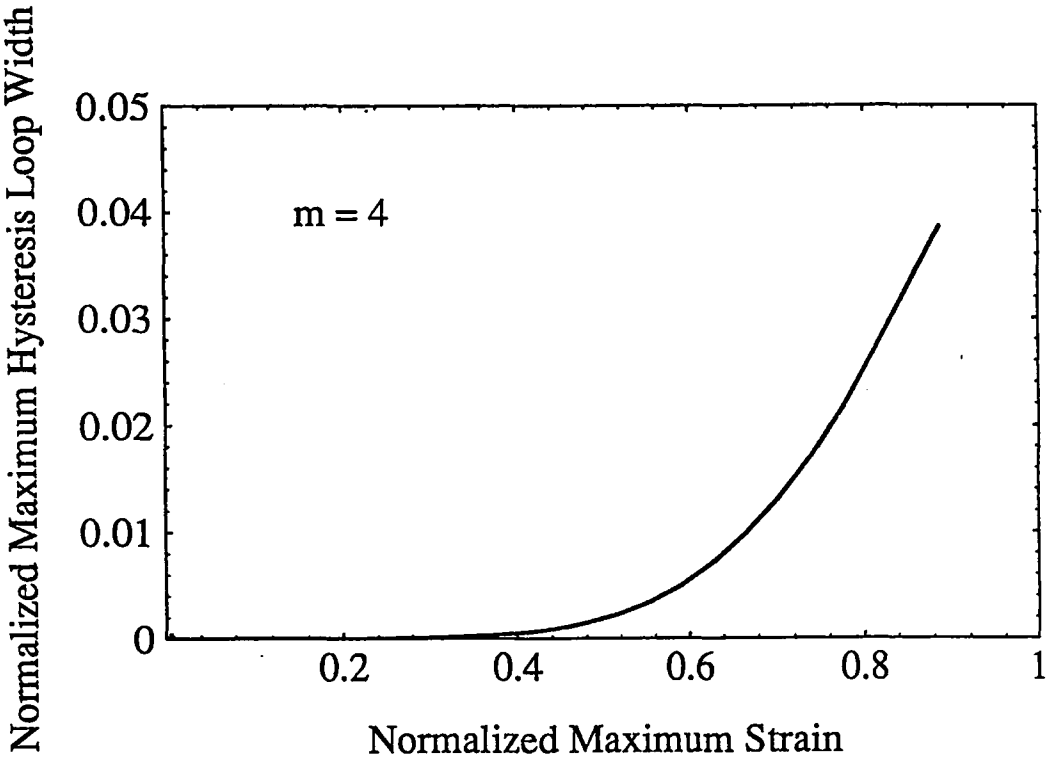

Fig. 7. – Normalized maximum hysteresis loop width, $\delta\bar{\varepsilon}\, E_F/S_c$ as a function of maximum normalized strain, $\bar{\varepsilon}\, E_F/S_c$.

This micromechanical analysis enabled us to study loading and unloading sequences when fiber breakage and fiber pull-out are considered. In the next Section, the previous results will be modeled in the framework of Continuum Mechanics.

4. Continuum mechanics modeling

The micromechanical analysis shows that fiber breakage induces a reduction in stiffness, anelastic strains due to slipping at the matrix/fiber interface of broken fibers, and hysteresis loops due to reverse slipping upon unloading-reloading. In the following development, three different approaches are considered within the framework of Continuum Mechanics which model some or all of the features of the micromechanical model, depending on the degree of accuracy desired.

Within the framework of the thermodynamics of irreversible process [Bataille & Kestin, 1979; Germain *et al.*, 1983], the first step is to determine the state variables which describe the internal mechanisms which define the behavior of a material. The second step is to determine the state potential in terms of the state variables and the third step is to write the evolution laws of the internal variables. For the sake of simplicity, a one dimensional description will follow.

4.1. First model – fiber breakage

In this simplest model, only fiber breakage is considered and the effects of slip are neglected. This model predicts a reduction in stiffness as fibers break, but is unable to

model anelastic strains and hysteresis loops (*Fig.* 8). Because fiber breakage is a softening mechanism localization is possible (Section 2). In this case, the microscopic description of damage is the percentage of broken fibers in a cell of length $2L_F = L_R$ and is identical to the change of macroscopic stiffness. The damage variable D is therefore equal to $P_F(\bar{\varepsilon})$, and the stress strain relationship can be written as follows

$$\bar{\sigma} = f E_F (1 - D) \bar{\varepsilon} \tag{26}$$

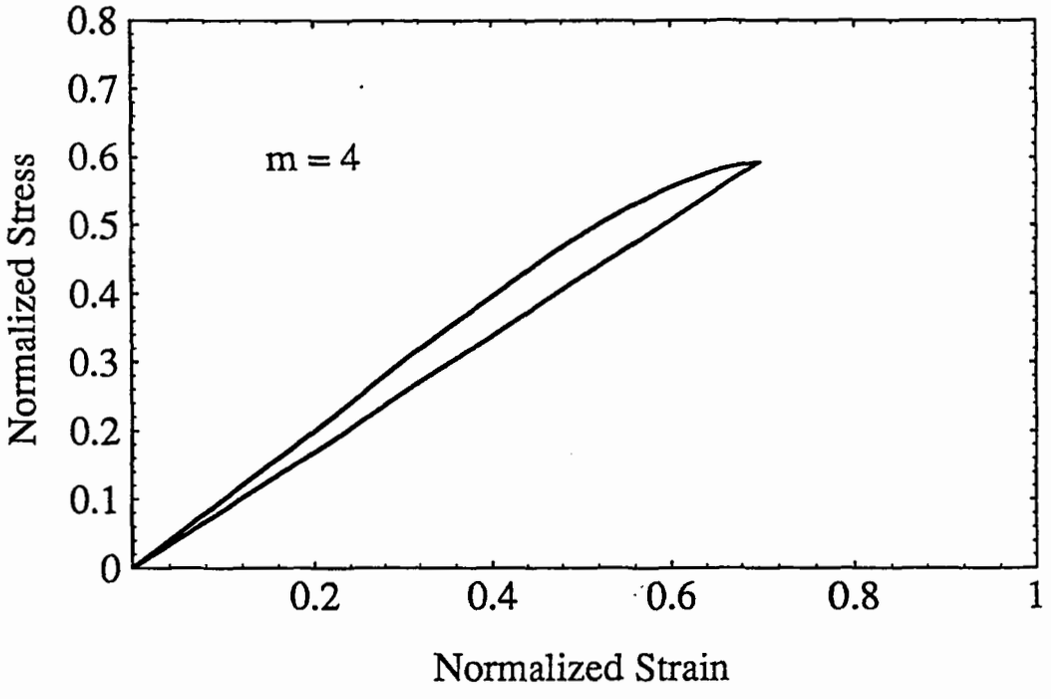

Fig. 8. – Normalized stress, $\bar{\sigma}/f S_c$, versus normalized strain, $\bar{\varepsilon} E_F / S_c$, during a loading-unloading-reloading sequence for model No. 1.

The damage variable D evolves as the maximum value of $\bar{\varepsilon}$ increases during a loading sequence $0 \leq \xi \leq t$. On the other hand, when $\bar{\varepsilon}$ decreases, the percentage of broken fibers remains constant. Furthermore, only positive strains (or stresses) lead to fiber breakage

$$D = P_F \left(\underset{0 \leq \xi \leq t}{\text{Max}} \langle \bar{\varepsilon}(\xi) \rangle \right) \tag{27}$$

where $\langle \cdot \rangle$ denotes the Macauley brackets. This latter condition can be rewritten as

$$\overset{\circ}{D} = \begin{cases} \dfrac{dP_F(\bar{\varepsilon})}{d\bar{\varepsilon}} \overset{\circ}{\bar{\varepsilon}} & \text{if } \dfrac{d}{dt} \underset{0 \leq \xi \leq t}{\text{Max}} \langle \bar{\varepsilon}(\xi) \rangle > 0 \\ 0 & \text{otherwise} \end{cases} \tag{28}$$

The above results can also be derived by using two potentials following the procedure described by Lemaitre and Chaboche [Lemaitre & Chaboche, 1985]. The first potential

is the Helmholtz free energy density, ψ. The second potential is the pseudo-potential of dissipation, F, which defines the growth rate of the state variables. Since no friction is involved when fiber break the elastic energy density is written as

$$\psi = \frac{f E_F}{2} (1 - D) \bar{\varepsilon}^2 \tag{29}$$

The expression of the external applied stress is given by the partial derivation of ψ wrt. $\bar{\varepsilon}$ which gives the same result as Eqn. (26). The thermodynamic force associated with the damage variable D is defined as the partial derivative of ψ wrt. the damage variable D. If Y denotes the associated thermodynamic force then

$$Y = -\frac{\partial \psi}{\partial D} = \frac{f E_F}{2} \bar{\varepsilon}^2 \tag{30}$$

In the framework of Continuum Damage Mechanics, Y is refered to as the damage energy release rate density [Chaboche, 1978]. The evolution law satisfies the second principle of thermodynamics since the dissipation Φ is positive

$$\Phi = Y \overset{\circ}{D} \geq 0 \tag{31}$$

Since Y is positive definite, $\overset{\circ}{D}$ is positive, *i.e.* damage always increases and therefore accounts only for deterioration of materials (here fiber breakage). Let us now postulate that the kinetic laws are derived from a pseudo-potential of dissipation, F. The function F is a scalar continuous function of the dual variables (here Y), the state variables having the possibility to act as parameters (here D). If the function F is a convex function, and if the kinetic laws are derived by means of a positive scalar multiplier, $\overset{\circ}{\lambda}$, then the second principle of thermodynamics is always satisfied. Within the so-called normality rule of generalized standard materials, the kinetic law is selected to be

$$\overset{\circ}{D} = \begin{cases} \overset{\circ}{\lambda} \dfrac{\partial F}{\partial Y} & \text{if} \quad F = 0 \quad \text{and} \quad \overset{\circ}{F} = 0 \\ 0 & \text{if} \quad F < 0 \quad \text{or} \quad \overset{\circ}{F} < 0 \end{cases} \tag{32}$$

with

$$F = 1 - \exp\left\{ -\left(\frac{Y}{Y_c} \right)^{(m+1)/2} \right\} - D \qquad \text{and} \qquad Y_c = \frac{1}{2} \frac{f S_c^2}{E_F}$$

The value of the multiplier $\overset{\circ}{\lambda}$ is determined by using the consistency condition $\overset{\circ}{F} = 0$. The expression of the multiplier is here given by

$$\overset{\circ}{\lambda} = \overset{\circ}{Y} \tag{33}$$

It is worth noting that Eqn. (32) which is written in terms of Continuum Damage Mechanics is completely equivalent to Eqns. (27) and (28).

4.2. Second model – fiber breakage and pull-out

This second model introduces the contribution of fiber breakage and fiber pull-out, but neglects hysteresis loops (*Fig.* 9). The features that are modeled are the reduction in stiffness due to fiber breakage and the anelastic strains due to fiber pull-out. It is assumed that the unloading process is linear, and is characterized by the damage $\bar{D}$. Therefore, the expression of the state potential ψ is written as [L & C, 1985]

$$\psi = \frac{f E_F}{2} (1 - \bar{D}) (\bar{\varepsilon} - \bar{\varepsilon}_{\text{an}})^2 \tag{34}$$

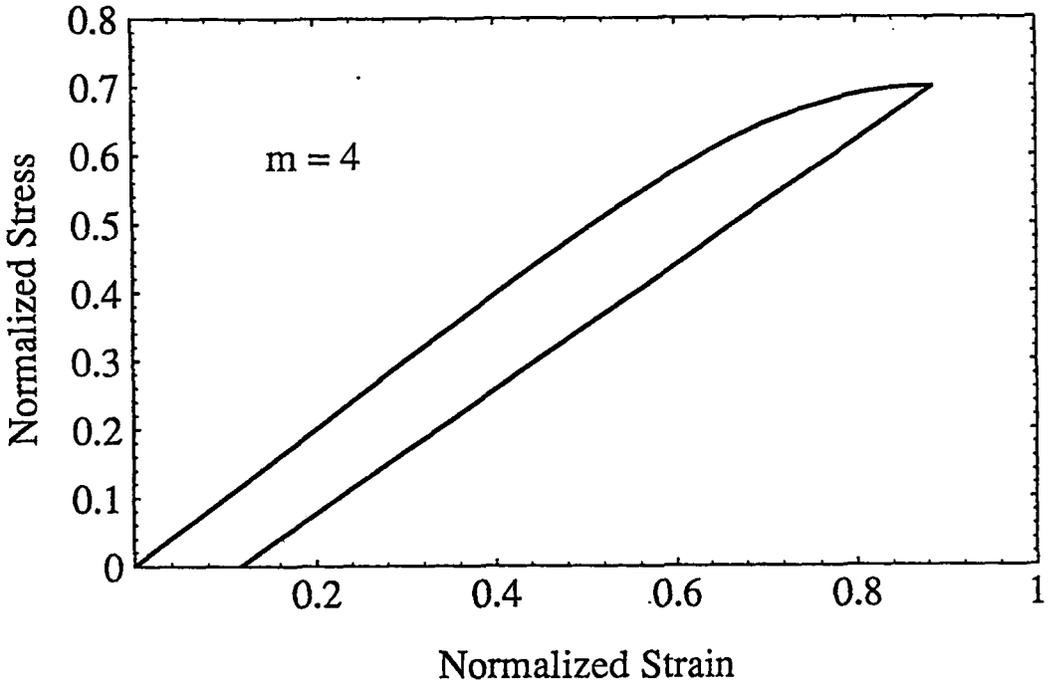

Fig. 9. – Normalized stress, $\bar{\sigma}/f S_c$, versus normalized strain, $\bar{\varepsilon} E_F / S_c$, during a loading-unloading-reloading sequence for model No. 2.

The state laws are obtained by partial differentiation of ψ wrt. the state variables

$$\begin{cases} \bar{\sigma} = \dfrac{\partial \psi}{\partial \bar{\varepsilon}} = f E_F (1 - \bar{D}) (\bar{\varepsilon} - \bar{\varepsilon}_{\text{an}}) \\ \bar{\sigma} = -\dfrac{\partial \psi}{\partial \bar{\varepsilon}_{\text{an}}} \\ \bar{Y} = -\dfrac{\partial \psi}{\partial \bar{D}} = \dfrac{f E_F}{2} (\bar{\varepsilon} - \bar{\varepsilon}_{\text{an}})^2 \end{cases} \tag{35}$$

Using Eqns. (18) and (19) of the micromechanical model, the anelastic strains are related to the maximum strain level, $\bar{\varepsilon}_M = \underset{0 \le \xi \le t}{\text{Max}} \langle \bar{\varepsilon} (\xi) \rangle$, and to the cumulative failure probability $P_F (\bar{\varepsilon}_M)$ by

$$\bar{\varepsilon}_{\text{an}} = \bar{\varepsilon}_M \left(1 - \frac{2 - \sqrt{2} \sqrt{1 + (1 - P_F (\bar{\varepsilon}_M))^2}}{P_F (\bar{\varepsilon}_M)} \right) \tag{36}$$

The damage variable $\bar{D}$ corresponding to the unloading modulus and is related to the cumulative failure probability by

$$\bar{D} = 1 - \frac{P_F(\bar{\varepsilon}_M)\left(1 - \dfrac{P_F(\bar{\varepsilon}_M)}{2}\right)}{2 - \sqrt{2}\sqrt{1 + (1 - P_F(\bar{\varepsilon}_M))^2}} \tag{37}$$

Eqn. (37) gives the relationship between the microscopic damage variable, $D = P_F(\bar{\varepsilon}_M)$, defined in the previous sub-Section and the macroscopic damage variable, $\bar{D}$. The evolution laws of the anelastic strains and the macroscopic damage variables derived in the micromechanical model are defined in Eqns. (36) and (37).

The dissipation Φ is now

$$\Phi = \bar{\sigma}\ \overset{\circ}{\bar{\varepsilon}}_{an} + \bar{Y}\ \overset{\circ}{\bar{D}} \geq 0 \tag{38}$$

and is positive. It is not easy to derive a simple expression for F and this has not been attempted. The evolution laws are written in terms of the maximum strains reached during the loading history. These laws are therefore directly integrated laws.

In this sub-Section, the approach was from a macroscopic point of view. Here we can see some apparent differences between the quantities at a micro level and macro level. These quantities are of course related but their significance is different, depending on the scale at which the observations are made. For example, the macroscopic damage variable $\bar{D}$ is related to the microscopic damage variable D by Eqn. (37). Furthermore, as shown in Section 2, localization predicted by this model (leading to the ultimate tensile stress) arises later than localization at a micro scale (localization tensile strength). This is due to the fact the softening mechanism at a micro scale is counter-balanced by the strengthening mechanism due to fiber pull-out up to the ultimate point. This law corresponds to the homogeneous solution after localization at the micro level.

4.3. Third model - micro mechanics based model

The model now discussed takes account of all three features induced by fiber breakage and fiber pull-out, viz. the reduction in stiffness due to fiber breakage, the anelastic strains due to fiber pull-out, and the hysteresis loops. The model is based on the micro mechanical study described previously (*Fig.* 6). The details of the unloading and reloading process are complex and to avoid this difficulty it is useful to introduce the crack opening displacement δ, which characterizes the material state related to the reverse friction. The crack opening displacement δ is also useful in determining the conditions when closure occurs. To characterize the state of the composite, four quantities are required. These are the overall strain $\bar{\varepsilon}$, the friction length L_F, the percentage of broken fibers, P_F, within the recovery length $L_R = 2L_F$, and the crack opening displacement, δ. To derive the free energy density associated to a loading sequence, we consider two different elastic steps to reach the same state. The first step consists in moving the unbroken fibers wrt.

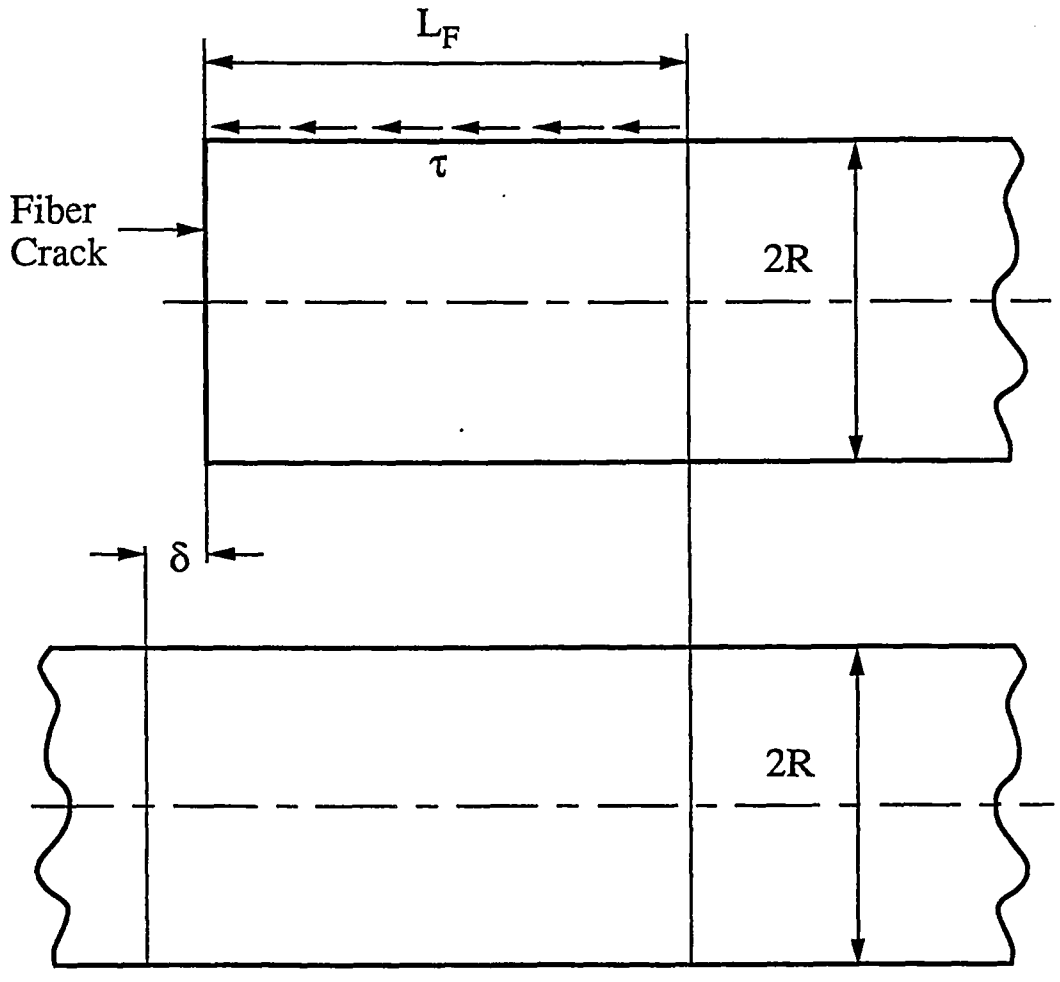

Fig. 10. – Motion of the unbroken fibers wrt. the broken fibers with no external load by an amount δ over a length L_F.

the broken fibers with no external load by an amount δ over a length L_F (*Fig.* 10). The elastic energy density associated with this process is given by

$$\psi^s = \frac{f E_F}{2} \left(\frac{\delta}{L_F} \right)^2 P_F \frac{4 - 3 P_F}{3} \tag{39}$$

The opening displacement δ induces an overall anelastic strain α

$$\alpha = \frac{\delta}{L_F} P_F \tag{40}$$

It is worth noting that $\bar{\varepsilon}_{an} = \alpha$ when $\bar{\sigma} = 0$. The second step, during which no friction occurs, consists in adding an elastic loading from the previous state. It involves an additional elastic energy density given by

$$\psi^e = \frac{f E_F}{2} (\bar{\varepsilon} - \alpha)^2 \tag{41}$$

The total free energy density is then sum of the two energies. A more convenient expression for the free energy density is obtained by using state variables in a modified

form. The state variables are the total strain, $\bar{\varepsilon}$, the damage variable modeling the percentage of broken fibers, $D = P_F$, and the anelastic strains α due to the crack opening displacement δ modeling the fiber pull-out mechanism. The opening strain α is similar to a kinematic hardening variable, and the associated force corresponds to the back-stress induced by the slipping mechanism. The free energy density ψ can then be written in terms of the new internal variables

$$\psi = \frac{f E_F}{2} (\bar{\varepsilon} - \alpha)^2 + \frac{f E_F}{2} \frac{4 - 3D}{3D} \alpha^2 \tag{42}$$

The thermodynamic forces associated with the new state variables are respectively given by

$$\begin{cases} \bar{\sigma} = \dfrac{\partial \psi}{\partial \bar{\varepsilon}} = f E_F (\bar{\varepsilon} - \alpha) & (43.1) \\ Y = -\dfrac{\partial \psi}{\partial D} = \dfrac{2 f E_F}{3} \left(\dfrac{\alpha}{D}\right)^2 & (43.2) \\ X = \dfrac{\partial \psi}{\partial \alpha} = f E_F \left(\dfrac{4\alpha}{3D} - \bar{\varepsilon}\right) & (43.3) \end{cases}$$

The evolution laws of the damage variable is directly given by the evolution of the cumulative failure probability P_F

$$D = P_F \left(\underset{0 \le \xi \le t}{\text{Max}} \langle \bar{\varepsilon}(\xi) \rangle \right) \tag{44}$$

The evolution law of the internal variable α uses the results derived during the loading-unloading-reloading sequence. Upon loading, the evolution of α is given by

$$\alpha = \frac{1}{2} \underset{0 \le \xi \le t}{\text{Max}} \langle \bar{\varepsilon}(\xi) \rangle \, P_F \left(\underset{0 \le \xi \le t}{\text{Max}} \langle \bar{\varepsilon}(\xi) \rangle \right) \tag{45.1}$$

The variation of α, $\Delta\alpha = \alpha - \alpha_0$, wrt. minimum or maximum value, α_0 (corresponding to a maximum loading or minimum unloading level characterized by $\bar{\varepsilon}_0$) is related to the strain variation, $\Delta\bar{\varepsilon} = \bar{\varepsilon} - \bar{\varepsilon}_0$, by

$$\Delta\alpha = \frac{1}{4} \frac{(\Delta\bar{\varepsilon})^2}{\underset{0 \le \xi \le t}{\text{Max}} \langle \bar{\varepsilon}(\xi) \rangle} \text{Sign}(\Delta\bar{\varepsilon}) \, P_F \left(\underset{0 \le \xi \le t}{\text{Max}} \langle \bar{\varepsilon}(\xi) \rangle \right) \tag{45.2}$$

Instead of the complicated pattern of friction and reverse friction descrided in the micro mechanical analysis, a single macroscopic variable is introduced. This is the opening strain which corresponds to the crack opening displacement. It is worth remembering that this last model captures the essential features related to fiber breakage and fiber pull-out and that it is able to predict the localization tensile strength. Furthermore,

the crack closure condition can be obtained by computing that α vanishes, *i.e.* when $\Delta\bar{\varepsilon} = \sqrt{2} \underset{0\leq\xi\leq t}{\text{Max}} \langle \bar{\varepsilon}(\xi) \rangle$. This last result shows that α cannot be negative. Moreover, the free energy density catches this crack closure phenomenon, and does not correspond to a partition in positive/negative strains or positive/negative stresses as is usually assumed [L, 1992]. The dissipation Φ

$$\Phi = -X \overset{\circ}{\alpha} + Y \overset{\circ}{D} \geq 0 \tag{46}$$

is positive during a loading sequence. The condition given in Eqn. (46) is strong [Onat & Leckie, 1988] and is not satisfied during part of the unloading or reloaging sequence. On the other hand, during a complete unloading-reloading sequence, the dissipated energy over one cycle is given by

$$\Delta\Phi = \frac{f E_F}{2} \left\{ \frac{P_F(\bar{\varepsilon}_M)}{6} \frac{(\bar{\varepsilon}_M - \bar{\varepsilon}_m)^3}{\bar{\varepsilon}_M} \right\} \tag{47}$$

which is a positive quantity, in accordance with the second principle of thermodynamics.

5. Conclusions

In this paper models have been developed which describe the mechanisms of fiber breakage and fiber pull-out. Upon loading, fiber breakage induces a softening behavior whereas fiber pull-out induces strengthening. Because of fiber breakage, loss of uniqueness and localization appear before the peak of the macroscopic stress/strain response in tension.

A micromechanical model is derived which describes the loading and unloading-reloading sequences. These sequences induce slip and reverse slip. Because of fiber pull-out, permanent strains appear upon complete unloading. Moreover, hysteresis loops are observed upon unloading and reloading. These hysteresis loops characterize the amount of energy that is dissipated during one unloading-reloading cycle. A convenient means of characterizing the sequences is to introduce the crack opening displacement between broken and unbroken fibers.

In the framework of Continuum Mechanics, three models have been studied. The first model was concerned with fiber breakage modeled by an internal variable called damage and corresponding to the percentage of broken fibers within a relevant length, the recovery length. This model is able to predict loss of stiffness and localization, but not anelastic strains nor hysteresis loops. The second model was based on the loss of stiffness and the anelastic strains. It was able to model the loading portion, anelastic strains, but not localization on a microscopic level nor hysteresis loops. The third model considered two internal variables, which are the damage at a microscopic level, and an opening strain proportional to the crack opening displacement divided by the friction. This model was able to capture all the details of the microscopic study with only two internal variables.

This last model will constitute the basis of a constitutive law applied to Ceramic-Matrix Composites subject to complex loading conditions. In particular the knowledge of the free energy density, the internal variables and their associated forces are crucial. These laws have to be generalized under more complex loading conditions, as well as composite architectures. In the case of more complex architectures, the interaction between fibers in different directions has to be assessed, especially in the case of woven configurations.

Acknowledgments

This work was supported by the Defense Advanced Research Project Agency through the University Research Initiative under Office of Naval Research Contract No. N-00014-92-J-1808.

REFERENCES

AVESTON J., COOPER G. A., KELLY A., 1971, Single and Multiple Fracture, in *Conference Proceedings of the National Physical Laboratory: Properties of Fiber Composites,* IPC Sciences and Technologie Press, Surrey, England, 15-26.

BATAILLE J., KESTIN J., 1979, Irreversible Processes and Physical Interpretations of Rational Thermodynamics, *J Non Equil. Thermodynamics,* **4**, 229-258.

BILLARDON R., DOGHRI I., 1989, Prévision de l'amorçage d'une macro-fissure par la localisation de l'endommagement, *C. R. Acad. Sci., Paris,* **308**, Series II, 347-352.

BUDIANSKY B., 1993, Tensile Strength of Aligned-Fiber Composites, *University Research Initiative,* Winter Study Group, University of California, Santa Barbara.

BUDIANSKY B., HUTCHINSON J. W., EVANS A. G., 1986, Matrix Fracture in Fiber-Reinforced Ceramics, *J. Mech. Phys. Solids,* **34**, 167-189.

CAO H. C., THOULESS M. D., 1990, Tensile Tests of Ceramic-Matrix Composites: Theory and Experiments, *J. Am. Ceram. Soc.,* **73**, [7], 2091-2094.

CHABOCHE J.-L., 1978, Description thermodynamique et phénoménologique de la viscoplasticité cyclique avec endommagement, *Thèse de doctorat de l'État,* Université Paris-VI.

COLEMAN B. D., 1958, On the Strength of Classical Fibers and Fibers Bundles, *J. Mech. Phys. Solids,* **7**, 60-70.

COX H. L., 1952, The elasticity and the strength of paper and other fibrous Materials, *Br. J. Appl. Phys.,* **3**, 72-79.

CURTIN W. A., 1991, Theory of Mechanical Properties of Ceramic Matrix Composites, *J. Am. Ceram. Soc.,* **74**, [11], 2837-2845.

CURTIN W. A., 1993, The "Tough" to Brittle Transition in Brittle Matrix Composites, *J. Mech. Phys. Solids,* **41**, [2], 217-245.

GERMAIN P., NGUYEN Q. S., SUQUET P., 1983, Continuum Thermodynamics, *J. Appl. Mech.,* **50**, 1010-1020.

HENSTENBURG R. B., PHOENIX, 1989, Interfacial Shear Strength Using Single-Filament-Composite Test. Part II: A Probability Model and Monte Carlo Simulations, *Polym. Comp.,* **10**, [5], 389-406.

HILD F., BURR A., 1994, Localization and Ultimate Strength of Fiber-Reinforced Ceramic-Matrix Composites, *Mech. Res. Comm.,* 21, [4], 297-302.

HILD F., DOMERGUE J.-M., EVANS A. G., LECKIE F. A., 1994 *a*, Tensile and Flexural Ultimate Strength of Fiber Reinforced Ceramic-Matrix Composites, *Int. J. Solids Struct.,* **31**, [7], 1035-1045.

HILD F., LARSSON P.-L., LECKIE F. A., 1994 *b*, Localization due to Damage in two Direction Fiber-Reinforced Composites, *J. Appl. Mech.,* accepted.

KELLY A., 1973, Chapter 5, in *Strong Solids,* Oxford University Press, 2nd edn.

LEMAITRE J., 1992, *A Course on Damage Mechanics,* Springer-Verlag, Berlin.

LEMAITRE J., CHABOCHE J.-L., 1985, *Mécanique des matériaux solides,* Dunod, Paris. English translation: *Mechanics of Solid Materials,* Cambridge University Press, Cambridge, 1990.

MARSHALL D. B., OLIVIER W. C., 1987, Measurement of Interfacial Mechanical Properties in Fiber-Reinforced Ceramic Composites, *J. Am. Ceram. Soc.,* **70**, 542-548.

McMeeking R. M., Evans A. G., 1990, Matrix Fatigue Cracking in Fiber Composites, *Mech. Mat.*, **9**, 217-227.
Onat E. T., Leckie F. A., 1988, Representation of Mechanical Behavior in the Presence of Changing Internal Structure, *J. Appl. Mech.*, **55**, 1-10.
URI, 1994, Winter Study Group, University of California, Santa Barbara (USA).
Weibull W., 1939, A Statistical Theory of the Strength of Materials, 151, *Royal Swed. Inst. For Eng. Res.*

(Manuscript received November 8, 1993;
accepted June 28, 1994.)

ii Etude unidimensionnelle des conditions de rupture

Localisation microscopique et mésoscopique

par F. HILD et A. BURR (1994).
Mech. Res. Comm., 21 (4), pp. 297-302.

LOCALIZATION AND ULTIMATE TENSILE STRENGTH OF FIBER-REINFORCED CERAMIC-MATRIX COMPOSITES

François Hild and Alain Burr

Laboratoire de Mécanique et Technologie,
E.N.S. de Cachan / C.N.R.S. URA 860 / Université Paris 6
61 avenue du Président Wilson, F-94235 Cachan Cedex, France.

(Received 31 August 1993; accepted for print 10 February 1994)

Introduction

The stress–strain behavior of ceramic–matrix composites (CMCs) is often non–linear. The loading of such composites results in two *independent* damage mechanisms: fiber failure and matrix cracking. Furthermore, the fibers are supposed to be subject to global load sharing, whereby the load transmitted from each failed fiber is shared equally among the intact fibers. Some aspects of the associated fiber failure stochastics have already been addressed [1-4]. The results usually overestimate the ultimate tensile strength observed experimentally. Moreover, the non–linearity is overestimated as well [5]. In this paper, the problem is analyzed in the light of results related to strain localization [6]: by strain localization we mean the localization of fiber breakage and fiber pull–out into *one* plane of matrix crack.

Expression of the Ultimate Tensile Strength

A composite with a saturation density of matrix cracks is considered, spacing L_m, within a unit cell of length L_R. The length L_R is the *recovery length* and refers to the longest fiber ($L_R/2$) that can be pulled out and cause a reduction in the load carrying capacity. The recovery length is thus related to the reference tensile stress T in unbroken fibers by

$$L_R = \frac{RT}{t} \tag{1}$$

where τ is the interfacial shear resistance, and R the fiber radius.

If the fibers exhibit a statistical variation of strength that obeys a two–parameter law, then the probability that a fiber would break anywhere within the recovery length L_R at or below a reference stress T can be written as

$$P_F(T) = 1 - \exp\left\{ - \left(\frac{T}{S_c}\right)^{m+1} \right\} \tag{2}$$

with

$$S_c^{m+1} = \frac{L_0 S_0^m \tau}{R}$$

where S_c is the characteristic strength [7], m the shape parameter, S_0 the stress scale parameter, and L_0 a reference length.

The average tensile stress $\bar{\sigma}$ applied to the composite is related to the reference stress T by

$$\bar{\sigma}(T) = f\,T \left\{ 1 - P_F(T) \right\} + \bar{\sigma}_{FP}(T) = \bar{\sigma}_{UF}(T) + \bar{\sigma}_{FP}(T) \tag{3}$$

where $\bar{\sigma}_{FP}(T)$ denotes that component of the stress provided by *failed fibers* as they pull out from the matrix. It has been shown that $\bar{\sigma}_{FP}(T)$ is an increasing function and then saturates [8]. A first approximation [1] is given by $\bar{\sigma}_{FP}(T) \approx f\,T\,P_F(T) / 2$.

In Fig. 1, the contributions of the two mechanisms, viz. fiber breakage and fiber pull–out, are plotted when m = 4. It is worth noting that the contribution of the unbroken fibers, $\bar{\sigma}_{UF}(T)$, reaches a maximum value prior to reaching the ultimate point. This result shows that a softening

mechanism on a microscale takes place prior to the softening mechanism on a macroscale. This decrease leads to a loss of uniqueness and localization on a microscale beyond that point.

Since $\bar{\sigma}_{UF}(T)$ decreases, there are two alternatives. The first one, referred to as *homogeneous solution*, corresponds to the case where fiber breakage continues to evolve uniformly in the whole specimen. This is only possible if the strains can be prescribed over the whole specimen. The second one, referred to as *localized solution*, consists in elastic unloading of the unbroken fibers in one part of the specimen, and further fiber breakage in the other part (whose size is on the order of the characteristic length $\delta_c = RS_c/\tau$). This localized solution appears as soon as the overall strain cannot be controlled on a microscopic scale. Otherwise, the homogeneous solution is the only solution to this problem. Consequently Eqn. (3) after the localization point corresponds to the homogeneous solution, which usually cannot be reached.

The applied stress level corresponding to the onset of localization will be referred to as localization tensile strength, and will be denoted by $\bar{\sigma}_{LTS}$. In most cases, this stress level corresponds to the ultimate tensile strength of a CMC. The aim of the remainder of this Section is to derive this stress level and to compare it with the ultimate tensile strength given by the homogeneous solution.

In fiber–reinforced composites, broken fibers cannot control the strains: only unbroken fibers within the recovery length control the strains. As soon as $\bar{\sigma}_{UF}(T)$ reaches a maximum, the overall strains cannot be controlled on a microscale. Therefore, a localized solution appears when $\bar{\sigma}_{UF}(T)$ achieves its maximum. The localization tensile strength of the composite is thus given by

$$\bar{\sigma}_{LTS} = \bar{\sigma}\left(S_c\left\{\frac{1}{m+1}\right\}^{1/(m+1)}\right) = \bar{\sigma}(T_L) \tag{4}$$

where T_L is the value of the stress in the unbroken fibers when $\bar{\sigma}_{UF}(T)$ achieves its maximum. At localization, the tangent modulus at the onset of localization on a microscale is still positive

$$\frac{d\bar{\sigma}(T_L)}{d\bar{\varepsilon}} = \frac{d\bar{\sigma}_{FP}(T_L)}{d\bar{\varepsilon}} > 0 \tag{5}$$

By using the previous approximation of the pull–out stress, the localization tensile strength becomes

$$\bar{\sigma}_{LTS} = \frac{fS_c}{2}\left(\frac{1}{m+1}\right)^{1/(m+1)}\left\{1+\exp\left(-\frac{1}{m+1}\right)\right\} \tag{6}$$

On the other hand, the ultimate tensile strength, corresponding to the response of the homogeneous solution, is given by

$$\bar{\sigma}_{UTS} = \mathrm{Max}\{\bar{\sigma}(T);\, T\geq 0\} \tag{7}$$

This equation cannot be solved analytically. A first order solution of the ultimate tensile strength is given by [1]

$$\bar{\sigma}_{UTS} = fS_c\left\{\frac{2}{m+2}\right\}^{1/(m+1)}\frac{m+2}{m+1} \tag{8}$$

In Fig. 2, the ultimate tensile strength is compared with the localization tensile strength for different values of m. It is worth noting that in terms of stress levels, the two strengths are very close. However, in terms of failure strains, and ductility, the two differ more significantly (Fig. 1). More importantly, as mentioned earlier, the tangent modulus is equal to zero when the ultimate tensile strength is reached whereas it is still positive when the localization on a microscale sets in. In the following, the tensile strength derived from Eqn. (8) is compared with the localization tensile strength given by Eqn. (6) in the case of carbon–matrix composites.

Comparison with Experiment

Experiments performed on two carbon–matrix composites (material A and C) reinforced by SiC (Nicalon) fibers [9] are summarized in Table 1: $L_0 = 25$ mm, $R = 6.5$ μm. The predictions agree well with experiments (Table 2). In particular, in these experiments, the stress–strain response does not show that the tangent modulus at the ultimate is vanishing. This is consistent with Eqn. (5): the onset of localization on a microscale sets in when the tangent modulus is still positive. This last result has been observed in various fiber–reinforced composites [5].

EXPERIMENTAL RESULTS

Material	f	S_0 (MPa)	m	τ (MPa)	$\bar{\sigma}_{TS}$ (MPa)
A	0.2	1165	4.5	10	290
C	0.2	1140	4.5	14	345

Table 1: Experimental results for carbon–matrix composites.

PREDICTIONS

Material	$\bar{\sigma}_{LTS}$ (MPa)	$\bar{\sigma}_{UTS}$ (MPa)
A	295	310
C	310	325

Table 2: Predictions of the tensile strength for carbon–matrix composites.

Acknowledgments

The authors are indebted to Prof. Frederick A. Leckie for valuable discussions. This work has been supported by the Defense Advanced Research Project Agency through the University Research Initiative under Office of Naval Research Contract No. N–00014–92–J–1808.

References

1. W.A. Curtin, J. Am. Ceram. Soc., **74** (11), 2837–2845 (1991).
2. S.L. Phoenix and R. Raj, Acta Metall. Mater., **40** (11), 2813-2828 (1992).
3. W.A. Curtin, J. Mech. Phys. Solids, **41** (1), 35-53 (1993).
4. S.L. Phoenix, Comp. Sci. Tech., **48**, 65-80 (1993).
5. U.R.I., Winter Study Group, University of California, Santa Barbara (U.S.A.) (1994).
6. F. Hild et al., Int. J. Solids Struct., **29** (24), 3221-3238 (1992).
7. R.B. Henstenburg and S.L. Phoenix, Polym. Comp., **10** (5), 389-406 (1989).
8. W.A. Curtin, J. Mat. Sci., **26**, 5239-5253 (1991).
9. F.E. Heredia et al., J. Am. Ceram. Soc., **75** (11), 3017-3025 (1992).

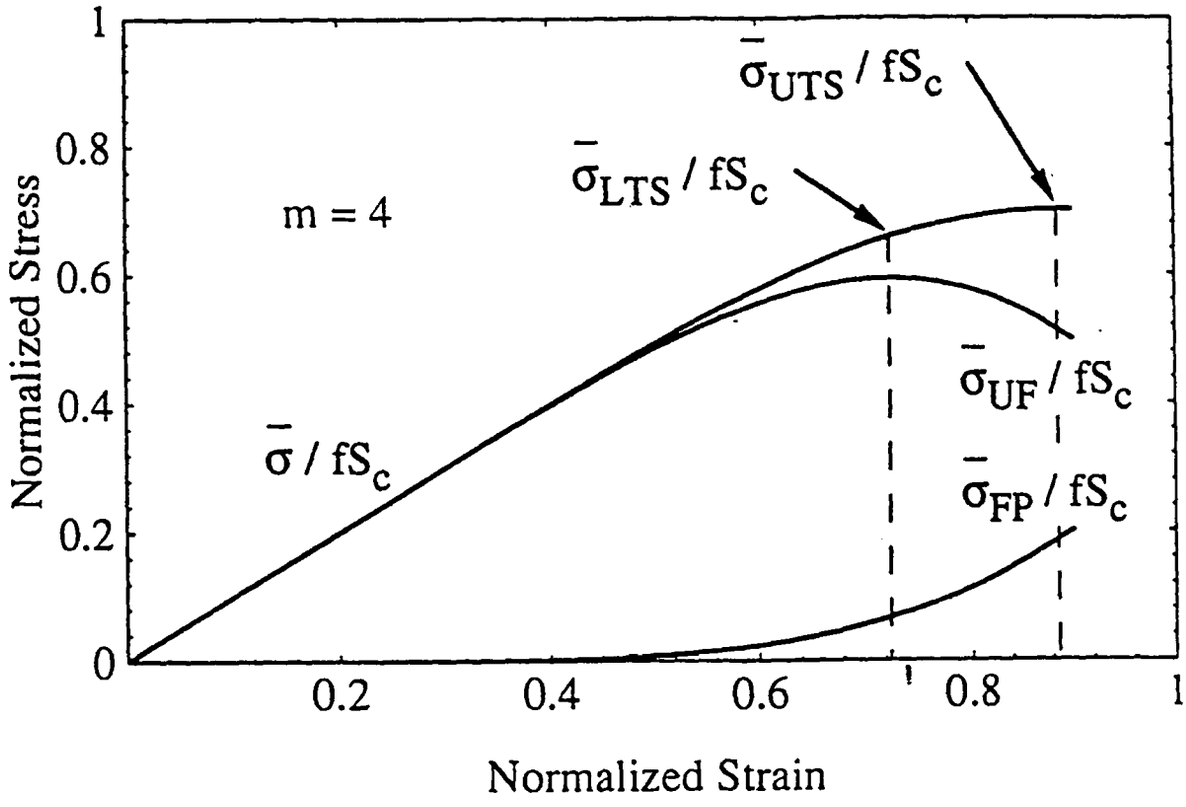

Figure 1: Normalized stresses, $\bar{\sigma} / fS_c$, $\bar{\sigma}_{UF} / fS_c$, $\bar{\sigma}_{FP} / fS_c$ vs. normalized strain, T / S_c.

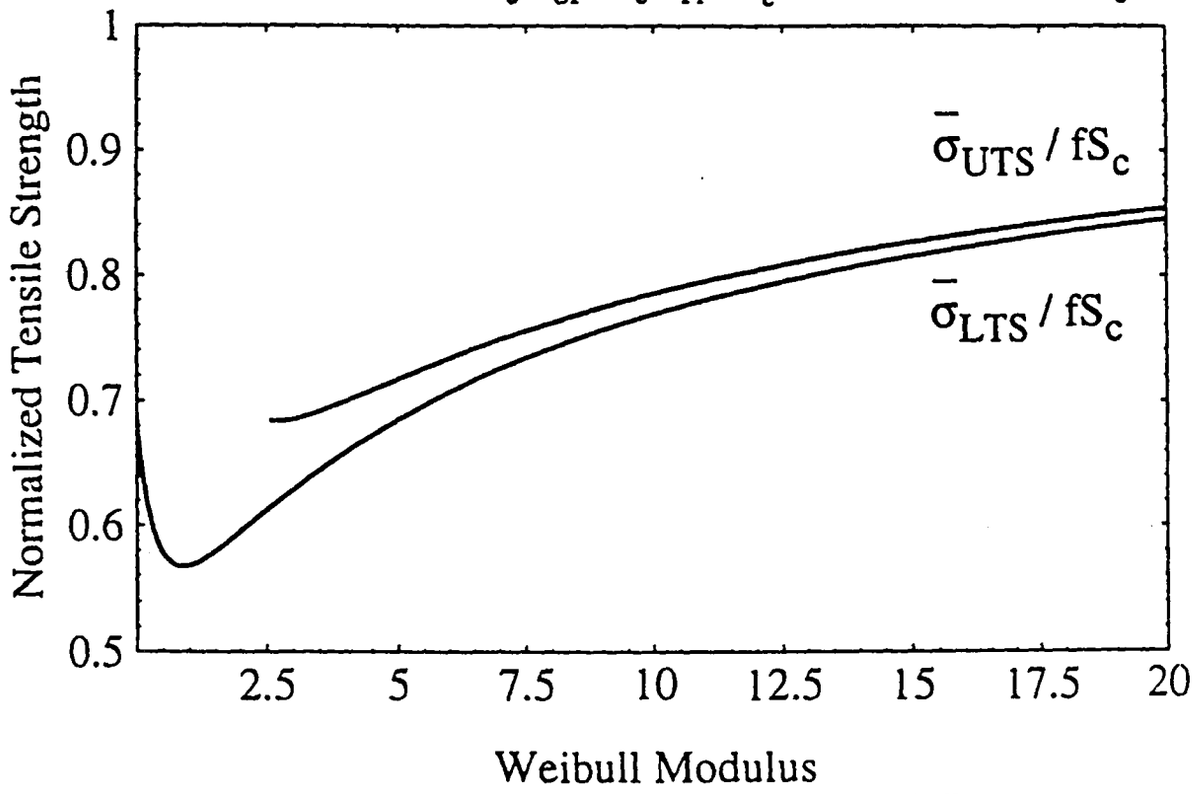

Figure 2: Normalized tensile strengths, $\bar{\sigma}_{LTS} / fS_c$, $\bar{\sigma}_{UTS} / fS_c$ vs. Weibull parameter, m.

Applications

par F. HILD et P. FEILLARD (1997).
Rel. Eng. Sys. Saf., 56 (3), pp. 225-235.

Ultimate strength properties of fiber-reinforced composites*

François Hild & Pascal Feillard

Laboratoire de Mécanique et Technologie, ENS Cachan/CNRS/Université Paris VI, 61 avenue du Président Wilson, F-94235 Cachan Cedex, France

The volume effect and stress heterogeneity effect (i.e., the effect of loading type) on the ultimate strength are analyzed for fiber-reinforced composites. The main failure mechanisms are assumed to be fiber breakage and fiber pull-out. Depending on the load redistribution around a broken fiber, two different regimes can be obtained. The results are applied to the prediction of ultimate strengths of SiC fiber-reinforced composites subjected to tension, pure flexure and three-point flexure.

1 INTRODUCTION

In spite of the fact that Fiber-Reinforced Composites (FRCs) are made of brittle fibers, the composites can exhibit a fracture resistance behavior [1, 2]. The origin of the fracture resistance is the consequence of the statistical failure strength of fibers (i.e., all the fibers do not break at the same load level and they can be subject to multiple breakage) and of sliding which occurs between broken fibers and the surrounding matrix. The non-linearity of a stress/strain curve close to the ultimate point is one of the indications of multiple fragmentation of fibers [3]. In this paper we study the case where the ultimate strength of FRCs is dictated by fiber breakage and fiber pull-out. The multiple fragmentation of fibers depends upon the statistical nature of fiber breakage as well as the load redistribution around a fiber break. Two extreme regimes (or modes) can be exhibited as described in an earlier analysis by Gücer and Gurland [4]. The first, referred to as a *global load sharing* regime assumes that the load carried by a fiber at failure is equally shared by all the unbroken fibers. This hypothesis was also used to model dry fiber bundles [5–7]. Global load sharing is an important assumption that allows us to relate the fragmentation analysis of a single fiber composite to fiber breakage and fiber pull-out in a multi-fiber composite. On the other hand, a *local load sharing* regime assumes that there exists a weakest zone in the material where the onset of a failure mechanism leads to the failure of the composite (e.g., a fiber adjacent to a previously broken fiber breaks because of the stress concentration induced by the initially broken fiber [8] bundle pull-out [9]). Because of localized load shedding from a broken fiber on to the nearest neighboring fibers, localized breaks induce the final failure of the composite.

The assessment of ultimate strengths of FRCs is mainly based upon the assumption of a constant interfacial sliding stress in the case of ceramic matrices [10–13] or ductile matrices [14–16] in the global load sharing regime although the same assumption can be used to describe bundle pull-out [9]. A constant interfacial sliding stress is also assumed to study multiple fragmentation taking place in polymeric- as well as ceramic-matrix composites [17–20]. To carry out the analysis, an elementary cell can be considered whose size, the *recovery length*, is directly related to the longest fiber that can be pulled out and cause a reduction in load carrying capacity [10, 13]. In the case of polymeric matrices other models have been used [21] based upon more refined mechanical models of the interfacial behavior [22]. The latter studies deal with the distribution of fragment length and therefore one relevant length to consider is the average fragment length. This length can be used to derive ultimate strengths of FRCs, regardless of the details of the mechanical behavior of the interface. From a design point of view, it is important not only to evaluate the ultimate tensile strength of FRCs but to model the stress/strain response of the composite so that the capacity of the components subjected to multiple loadings can be estimated [23]. We focus our attention on determining the strength of rectangular

*This work was partially supported by the Advanced Research Projects Agency through the University Research Initiative, ONR Contract N00014-12-J-1808.

beams made of unidirectional composites subjected to a combination of tension and flexure so that closed-form solutions can be obtained. In the first part it is shown that the ultimate tensile strength can be derived by considering an elementary cell of size equal to the average fragment length. The second part is concerned with a constitutive law derived in tension and compression to analyze the pure flexural loadings discussed in the third part. In pure flexure, the failure mode is assumed to be identical to that in tension (i.e., no compressive mode is considered in the present analysis). The fourth part establishes the interaction between tensile and flexural loadings and the fifth is concerned with the study of the ultimate strength in three-point flexure. Experimental data are compared with predictions and the two load transfer regimes are discussed.

2 ULTIMATE TENSILE STRENGTH

In this section, expressions of the ultimate tensile strength of FRCs are derived. The key mechanism leading to final failure of the considered FRC is assumed to be fiber breakage. This mechanism is usually characterized by the fact that a fiber undergoes multiple fragmentation until final fracture. The matrix contribution is supposed to be negligible compared to that of the fibers. Depending on the analyzed system, different models are used to describe the behavior of the fiber/matrix interface. The simplest assumption is to consider a constant interfacial shear stress τ [24, 25]. Other models have been proposed [26, 22] in which the debonding propagation is based upon a shear lag analysis limited by an interfacial shear strength and a Coulomb friction law which models the load transfer along the debond length. In both cases, expressions of the average fragment length are derived numerically [17, 27] as well as analytically [19, 28]. The latter quantity will be used to assess the ultimate tensile strength of FRCs.

In the first part a global load sharing regime is supposed to occur. By assuming that the fibers do not interact, a single fiber system is then representative of the whole composite behavior [18, 11, 16]. Let us consider an elementary cell of size equal to the average fragment length $\bar{L}$. The average fragment length is defined as the ratio of the total composite length L divided by the average number of fiber breaks $\bar{N}(T)$ in a single fiber

$$\bar{L}(T) = \frac{L}{\bar{N}(T)} \tag{1}$$

where T is the reference stress equal to the stress level in an unbroken fiber for the same macroscopic strain $\bar{\epsilon}$. Furthermore, the average stress $\bar{\sigma}$ is related to the stress field along the fibers in the elementary cell $\sigma_F(T,z)$ by

$$\bar{\sigma}(T) = \frac{f}{\bar{L}(T)} \int_{-\bar{L}(T)/2}^{\bar{L}(T)/2} \sigma_F(T,z)\mathrm{d}z \tag{2}$$

where z is the current position along the fiber direction, and f the fiber volume fraction. Since the reference stress T is directly proportional to the macroscopic strain $\bar{\epsilon}$, the ultimate tensile strength is reached when

$$\frac{\partial \bar{\sigma}(T = T_u)}{\partial T} = 0 \tag{3}$$

where the reference stress corresponding to the ultimate tensile strength is denoted by T_u. If we assume that the interfacial shear resistance is modeled by a constant shear stress τ, the average stress is given by

$$\bar{\sigma}(T) = fT\left[1 - \frac{L_R(T)}{2\bar{L}(T)}\right] \tag{4}$$

where L_R is the so-called recovery length. The latter is related to the reference stress by

$$L_R(T) = \frac{RT}{\tau} \tag{5}$$

where R is the fiber radius. The recovery length refers to twice the longest fiber that can be pulled out and cause a reduction of the load carrying capacity (Fig. 1).

It is worth noting that eqn (4) can be used in the case of a constant interfacial shear stress when the ratio $L_R(T)/\bar{L}(T)$ is approximated by the cumulative failure probability $P_r(T)$ of a piece of composite of length $L_R(T)$ [13]. As long as the interaction between

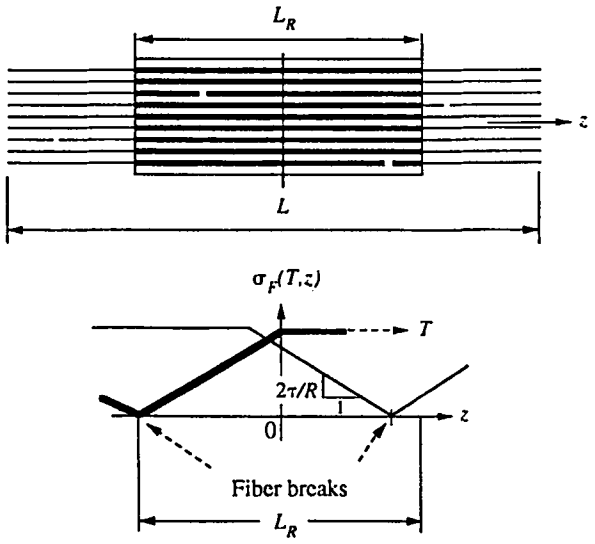

Fig. 1. Distribution of the fiber stress field $\sigma_F(T,z)$ for a given value of the reference stress T in the case of a constant interfacial shear stress τ. Two different fibers are considered.

fiber breaks is negligible (i.e., $L_R(T)/\bar{L}(T) \ll 1$), the evolution of the average fragment length is given by [10, 13]

$$\frac{L_R(T)}{\bar{L}(T)} = 1 - \exp\left[-\left(\frac{T}{S_c}\right)^{m+1}\right] \tag{6}$$

where m is the Weibull modulus [29] modeling fiber failure, and S_c is the characteristic strength [17] defined as

$$S_c = \left(\frac{S_0^m L_0 \tau}{R}\right)^{\frac{1}{m+1}} \tag{7}$$

where S_0 is the scale parameter and L_0 the corresponding gauge length of the Weibull law modeling fiber failure. Equation (6) neglects the fragments of size less than or equal to $L_R(T)$ (i.e., it is assumed that there are no over-lapping recovery regions). This assumption is not very strong since the strain levels at the ultimate point are significantly lower than those at fiber breakage saturation [13]. A first order solution of the ratio $L_R(T)/\bar{L}(T)$ is found to be

$$\frac{L_R(T)}{\bar{L}(T)} \cong \left(\frac{T}{S_c}\right)^{m+1} \tag{8}$$

and the corresponding ultimate strength $\bar{\sigma}_{UTS}$ is given by

$$\bar{\sigma}_{UTS} \cong f S_c \left(\frac{2}{m+2}\right)^{\frac{1}{m+1}} \frac{m+1}{m+2}. \tag{9}$$

This expression is rigorously identical to that found by Curtin [10]. Equation (9) shows that the characteristic strength is the scaling stress needed to derive the ultimate tensile strength. Furthermore, eqn (9) is valid provided the composite length L is greater than the recovery length at the ultimate $L_R(T_u)$, which is proportional to the reference length δ_c defined by [19]

$$\delta_c = \frac{R S_c}{\tau}. \tag{10}$$

The characteristic strength S_c can be reinterpreted as the average strength of a fiber of length δ_c. When the previous condition is not met, the ultimate tensile strength is length-dependent and the dry fiber bundle strength [6, 7] is a good approximation of the ultimate tensile strength [30, 13]

$$\frac{\bar{\sigma}_{UTS}}{f S_0} \cong \left(\frac{L_0}{Lme}\right)^{\frac{1}{m}}. \tag{11}$$

Equations (9) and (11) show that the volume effect is different from that of purely brittle materials or FRCs exhibiting a local load sharing regime for which the ultimate tensile strength, defined as the average failure stress, $\bar{\sigma}_{FT}$ is proportional to $V^{-1/m}$, for any composite volume V

$$\frac{\bar{\sigma}_s}{S_s} = \left(\frac{V_s}{V}\right)^{\frac{1}{m_s}} \Gamma\left(1 + \frac{1}{m_s}\right) \tag{12}$$

where $\Gamma(.)$ is the Euler function of the second kind (also called gamma function), S_s is the Weibull scale parameter, V_s is the reference volume and m_s is the Weibull shape parameter modeling the onset of localized failure.

If debonding propagation is based upon a shear lag analysis limited by an interfacial shear strength, and a Coulomb friction law modeling the load transfer along the debond length [26, 22], the exclusion zones where no additional fiber breakage is possible are not as easily determined as previously (since the recovery length is of statistical nature). However, the general formalism of eqns (2) and (3) still applies. Instead of one quantity modeling the interfacial behavior, i.e., τ, two quantities are used, viz. the friction coefficient μ defining the shear stress level $\tau_f = -\mu\sigma_{rr}$ in the debond zone, which is dependent upon the radial stresses σ_{rr}, and the maximum shear strength τ_d. The expression of the friction stress τ_f shows that the Poisson effect as well as the residual stresses are accounted for in this model [31]. An expression of the average fragment length has to be derived numerically [31] for any combination of τ_d, μ and initial residual stresses in the composite. The distribution of fragments can be approximated by a Weibull distribution and the average fragment length is therefore given by

$$\beta\bar{L}(T) = \beta L_1(T)\Gamma\left(1 + \frac{1}{m_1(T)}\right) \tag{13}$$

where $L_1(T)$ and $m_1(T)$ are the Weibull scale and shape parameters, respectively. The parameters model the fragment length distribution, are identified from the numerical simulations and depend upon the reference stress level T. The parameter β is a function of the elastic properties of the matrix and the fiber as well as the fiber volume fraction [32]

$$\beta = \sqrt{\frac{2G_m}{E_f R^2 \ln\left(\frac{\bar{R}}{R}\right)}} \tag{14}$$

where E_f is the Young's modulus of the fibers, G_m is the shear modulus of the matrix, $2\bar{R}$ is the average distance between fibers. When fiber breakage saturates, the parameters $L_1(T)$ and $m_1(T)$ saturate as well (see Fig. 2 in the case of a unidirectional SiC/LAS composite). The numerical computations are performed on a single filament representative of the composite. The results of Fig. 2 were obtained with an analysis of a fiber containing 500,000 elements of length 20 μm whose strength is randomly distributed

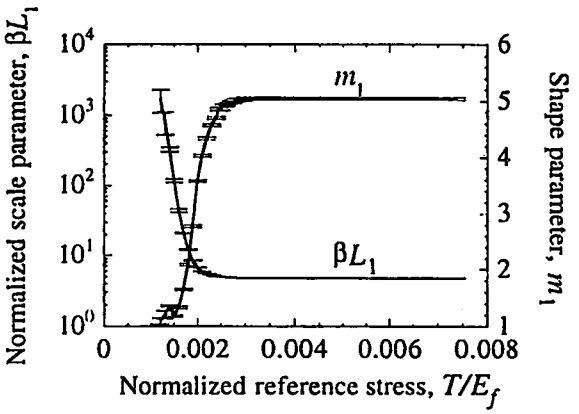

Fig. 2. Shape and scale parameters of the fiber fragment distribution as a function of normalized reference stress for a SiC/LAS composite ($f = 0{\cdot}5$, $\beta = 50\ \text{mm}^{-1}$, $S_0 = 1500$ MPa, $L_0 = 10$ mm, $m = 4$, $\mu = 0{\cdot}16$, $\tau_d = 50$ MPa).

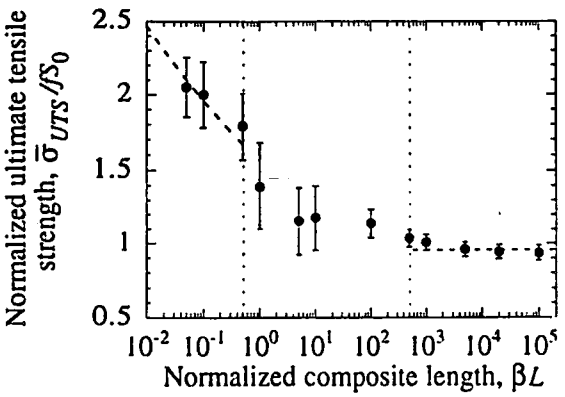

Fig. 4. Normalized ultimate tensile strength of an E Glass/Epoxy composite as a function of normalized composite length ($\beta = 10\ \text{mm}^{-1}$, $fS_0 = 900$ MPa, $L_0 = 10$ mm, $m = 10$, $\mu = 0{\cdot}9$, $\tau_d = 80$ MPa, $R = 5{\cdot}5\ \mu$m).

according to a Weibull law. Because of the statistical distribution of fragment lengths, the debond lengths are also of statistical nature. A more detailed presentation of the numerical analysis used to predict the present results can be found in [31, 33].

The fragmentation model can be utilized to model matrix cracking as well as fiber breakage. If matrix cracking saturates, the interfacial shear stress τ_f does not evolve significantly when the reference stress increases. Under these circumstances, the results obtained by a model with a constant shear strength are expected to be close to those obtained by the above-discussed model. In particular the evolution of the ultimate tensile strength as a function of the composite length is identical as shown in Fig. 3 when $\tau = \tau_f$. Each simulation of Fig. 3 is the result of 1,000 realizations for the same fiber length.

Before saturation, however, the previous results do not apply and a constant shear strength hypothesis can be a crude approximation of the actual interfacial behavior. In the following, the ultimate tensile strength of an Epoxy matrix reinforced by E Glass fibers is analyzed. Figure 4 shows the evolution of the ultimate tensile strength as a function of the composite length. Each simulation of Fig. 4 is again the result of 1,000 realizations for the same fiber length. Three different regimes can be exhibited.

First, for very small composite lengths (i.e., $\beta L < 0{\cdot}5$) the first break is fatal to the composite and the whole composite length containing a fiber break is debonded (see Fig. 5). In that case a constant interfacial shear stress hypothesis is admissible. Since the composite length is less than the characteristic length ($\delta_c \beta \cong 1$) a length-dependent regime is expected and actually observed. The length dependence is shown to be proportional to $L^{-0.1}$ in accordance with $L^{-1/m}$ when $m = 10$ (value of the Weibull shape parameter of E Glass fibers).

Second, for large composite lengths (i.e., $\beta L > 500$) the onset of debonding signals final failure of the composite (see Fig. 5). The number of breaks is not on the order of unity as in the case of small composite

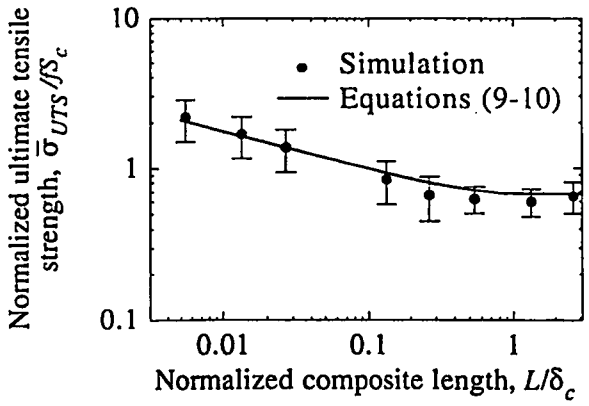

Fig. 3. Normalized ultimate tensile strength of a SiC/LAS composite as a function of normalized composite length ($f = 0{\cdot}5$, $S_c = 2500$ MPa, $m = 4$).

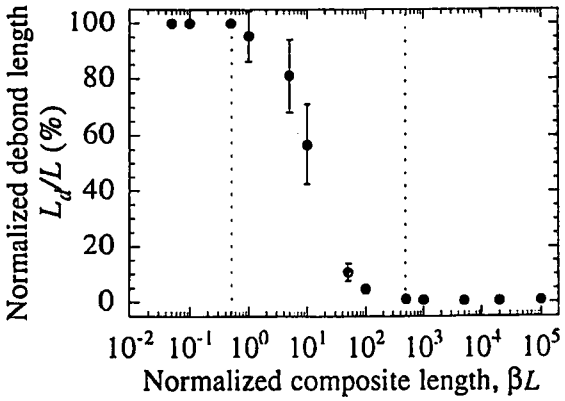

Fig. 5. Normalized debond length of an E Glass/Epoxy composite as a function of normalized composite length ($\beta = 10\ \text{mm}^{-1}$, $fS_0 = 900$ MPa, $L_0 = 10$ mm, $m = 10$, $\mu = 0{\cdot}9$, $\tau_d = 80$ MPa, $R = 5{\cdot}5\ \mu$m).

lengths. According to the Cox model [32], the onset of debonding is given by the condition [31]

$$2\tau_d = T_u \beta R \tanh\left(\frac{\beta \bar{L}(T_u)}{2}\right). \quad (15)$$

When the average fiber fragment length $\bar{L}(T_u)$ is greater than $3/\beta$, the previous condition can simplified to become $2\tau_d \cong T_u \beta R$. This criterion is deterministic so that the ultimate tensile strength can be expressed as

$$\bar{\sigma}_{UTS} = fT_u \left[1 - \frac{\tanh\left(\frac{\beta \bar{L}(T_u)}{2}\right)}{\frac{\beta \bar{L}(T_u)}{2}}\right]. \quad (16)$$

It is worth noting that the format of eqn (16) is identical to that of eqn (4). Furthermore, when $\beta \bar{L}(T_u) > 100$ the previous expression can be simplified so that the ultimate tensile strength can be approached by

$$\bar{\sigma}_{UTS} \cong fT_u \quad (17)$$

In the present case, the ultimate tensile strength is equal to $0{\cdot}96\, fS_0$. This value is in good agreement with the numerical simulations shown in Fig. 4. Third, for composites of intermediate lengths (i.e., $0{\cdot}5 < \beta L < 500$) the onset of debonding is not fatal to the composite (see Fig. 5). On the other hand, there is no complete debonding so none of the two previous regimes is relevant. Moreover, the number of fiber breaks increases as the composite length increases. In the case of the present simulations, the number of breaks for intermediate lengths was less than 10. Lastly, the ultimate tensile strength decreases with the total length to approach the length-independent regime when the length of the composite increases (see Fig. 4).

These simulations show that the features exhibited by a model assuming a constant interfacial shear stress can be obtained by different models even when matrix cracking is not involved. However there is (are) some additional regime(s) in-between. Moreover the length-independent regime can be explained by different reasons as shown by the two ultimate strength studies within the global load sharing framework.

3 CONSTITUTIVE EQUATION

In this section the behavior of FRCs is studied from a macroscopic point of view. Therefore we will only consider the average stress, or macroscopic stress $\bar{\sigma}$ and the corresponding macroscopic strain $\bar{\epsilon}$, or, equivalently, the reference stress T/E_f. The constitutive equations will be derived using the microscopic approach of Section 2. It is worth remembering that a constitutive equation modeling gradual fiber breakage can be written only in the global load sharing regime for which the composite behavior is length-independent.

In the following, it is assumed that the stress/strain behavior can be characterized by a series expansion of the macroscopic stress $\bar{\sigma}$ as a function of the reference stress T modeling the gradual degradation of the material (i.e., fiber breakage, debonding and pull-out)

$$\frac{\bar{\sigma}(T)}{fS_c} = \frac{T}{S_c} + \sum_{n \geq 1} \psi_n \left(\frac{T}{S_c}\right)^{\beta(n)} \quad (18)$$

where ψ_n are the coefficients of the series expansion, and $\beta(n)$ is a linear combination of the power n. Equation (18) will be used later to predict the ultimate flexural strength.

If the ultimate point is reached when $T = T_u = AS_c$, where A is a constant, the ultimate tensile strength can be rewritten as

$$\frac{\bar{\sigma}_{UTS}}{fS_c A} = 1 + \sum_{n \geq 1} \psi_n A^{\beta(n)-1}. \quad (19)$$

For example, in the case of a constant interfacial shear stress, the parameters in eqn (18) are such that $\psi_n = -\delta_{mn}/2$, where δ_{mn} denotes the Kronecker symbol, $\beta(n) = \delta_{mn}(m+2)$, S_c is given by eqn (7) and $A = (2/(m+2))^{\frac{1}{m+1}}$. Another application can be found in [13].

The constitutive eqn (18) is only valid in the tensile part, and does not take into account matrix cracking since the initial Young's modulus is assumed to be the Young's modulus of the unbroken fibers fE_f. In the compressive part we assume that the behavior is unaltered upon loading and is given by the behavior of the virgin material. Therefore the compressive behavior is defined by the Young's modulus of the composite $\bar{E}$. No compressive failure mechanism is considered herein. A damage variable, D_1, is introduced to measure the difference in Young's modulus in tension ($T/S_c \ll 1$) and compression

$$D_1 = 1 - \frac{fE_f}{\bar{E}}. \quad (20)$$

In the next sections, this constitutive law will be used to determine ultimate strengths in pure and three-point flexure.

4 ULTIMATE FLEXURAL STRENGTH

This section is devoted to the determination of the ultimate strength of rectangular beams under pure flexure by making use of the model derived in tension and compression. The beam is made of one layer whose fibers are aligned along the z-direction. It is

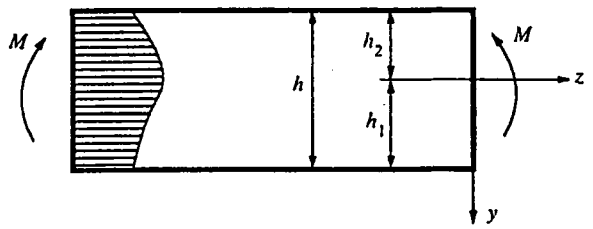

Fig. 6. Definition of the beam geometry in the case of pure flexure.

assumed that there is a sufficient number of fibers in the width of the beam so that a global load sharing hypothesis is made for each height y. The Bernoulli kinematic condition [34] leads to

$$\bar{\epsilon} = \mathcal{R}y \tag{21}$$

where $\mathcal{R}$ is the curvature, and y the height ordinate measured from the neutral axis (see Fig. 6).

Using eqn (18), we obtain the variation of the normalized tensile stress

$$\bar{\Sigma} = Y + \sum_{n\geq 1} \psi_n Y^{\beta(n)} \tag{22}$$

with

$$\bar{\Sigma} = \frac{\bar{\sigma}}{fS_c} \text{ and } Y = \frac{E_f}{S_c}\mathcal{R}y.$$

The position of the neutral axis h_1 (see Fig. 6) is determined from the force balance equation. The ultimate flexural strength is reached when $\bar{\sigma}(h_1) = \bar{\sigma}_{UTS}$ and the position of the neutral axis is given by

$$\frac{h}{h_1} = 1 + \sqrt{(1-D_1)\left\{1 + 2\sum_{n\geq 1} \frac{\psi_n A^{\beta(n)-1}}{\beta(n)+1}\right\}}. \tag{23}$$

Using the moment equation, the ultimate flexural strength $\bar{\sigma}_{UFS}$ is given by

$$\frac{\bar{\sigma}_{UFS}}{fS_cA} = 2\left(\frac{h_1}{h}\right)^2\left\{\frac{1}{1-D_1}\left(\frac{h}{h_1}-1\right)^3 + 1 + 3\sum_{n\geq 1}\frac{\psi_n A^{\beta(n)-1}}{\beta(n)+2}\right\}. \tag{24}$$

The ratio of the ultimate flexural strength to the ultimate tensile strength is then given by

$$\frac{\bar{\sigma}_{UFS}}{\bar{\sigma}_{UTS}} = \frac{2\left(\frac{h_1}{h}\right)^2\left\{\frac{1}{1-D_1}\left(\frac{h}{h_1}-1\right)^3 + 1 + 3\sum_{n\geq 1}\frac{\psi_n A^{\beta(n)-1}}{\beta(n)+2}\right\}}{1 + \sum_{n\geq 1}\psi_n A^{\beta(n)-1}}. \tag{25}$$

Equation (25) shows that the ultimate strength ratio $\bar{\sigma}_{UFS}/\bar{\sigma}_{UTS}$ is independent of the composite length, but depends upon the damage parameter D_1 in addition to the parameters ψ_n, $\beta(n)$ and A. This result constitutes a second difference with a weakest link hypothesis for which the average strength ratio $\bar{\sigma}_{FF}/\bar{\sigma}_{FT}$ for *the same volume* loaded in pure flexure and in tension is given by

$$\frac{\bar{\sigma}_{FF}}{\bar{\sigma}_{FT}} = [2(m_s+1)]^{\frac{1}{m_s}} \tag{26}$$

where $\bar{\sigma}_{FF}$ is the average failure stress in pure flexure. To illustrate the previous results, a constant interfacial shear strength is assumed in the framework of global load sharing. By using the approximations to derive eqn (8), the position of the neutral axis is given by

$$\frac{h}{h_1} = 1 + \sqrt{(1-D_1)\frac{(m+1)(m+4)}{(m+2)(m+3)}} \tag{27}$$

and the ultimate flexural strength $\bar{\sigma}_{UFS}$ becomes

$$\frac{\bar{\sigma}_{UFS}}{fS_c} = 2\left(\frac{h_1}{h}\right)^2\left(\frac{2}{m+2}\right)^{\frac{1}{m+1}}\left[\frac{1}{1-D_1}\left(\frac{h}{h_1}-1\right)^3 + \frac{(m+1)(m+5)}{(m+2)(m+4)}\right]. \tag{28}$$

In Fig. 7 the evolution of the normalized flexural strength is plotted as a function of the Weibull parameter m and the damage parameter D_1. The lower the value of the Weibull parameter, the higher the normalized flexural strength. On the other hand, the higher the value of the damage parameter, the higher the normalized flexural strength. These results have been obtained differently in [13] but are very close to those presented herein.

Lastly, when the only difference in the tension/compression behavior is given by the Young's modulus difference ($m \to +\infty$) modeled by the damage variable D_1, eqns (27) and (28) show that ratio of the ultimate flexural strength to the ultimate tensile strength approaches $2/(1+\sqrt{1-D_1})$.

5 INTERACTION BETWEEN FLEXURE AND TENSION

In this section we will study stress states where we combine tensile and flexural loads. The beam characteristics are the same as those used in the previous section. We still assume a Bernoulli hypothesis [34]. The kinematic condition leads to a linear strain field in the beam of height h such that (see Fig. 8)

$$\bar{\epsilon}(y) = \frac{T_c}{E_f} Y(y) \tag{29}$$

with

$$Y(y) = \frac{1+\alpha}{2} + \frac{1-\alpha}{h}y \quad -\frac{h}{2} \leq y \leq \frac{h}{2}.$$

The variable y now denotes the height ordinate measured from the mid-plane of the beam, and the

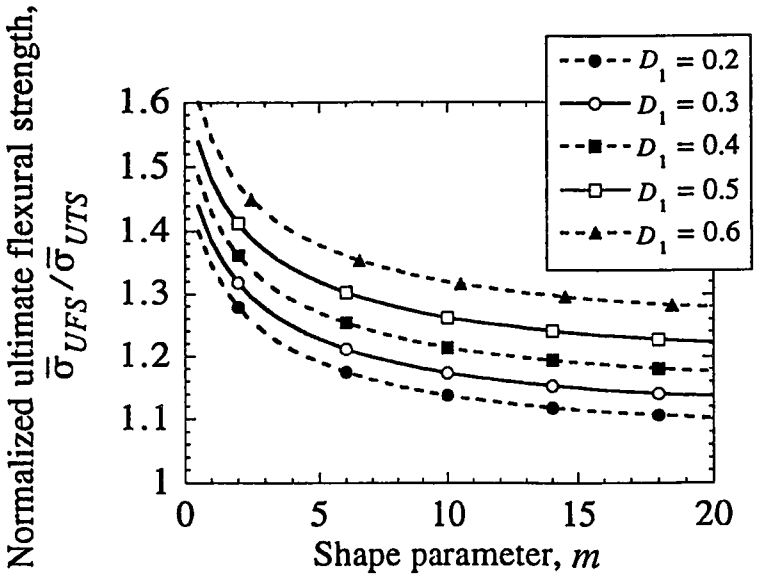

Fig. 7. Evolution of the normalized flexural strength as a function of the Weibull parameter m and the damage parameter D_1.

constant α, which is less than or equal to 1, measures the ratio of $\bar{\epsilon}(-h/2)$ to $\bar{\epsilon}(h/2)$

$$\alpha = \frac{\bar{\epsilon}(-h/2)}{\bar{\epsilon}(h/2)}. \tag{30}$$

When α lies between 0 and 1 then the whole beam undergoes tensile stresses, whereas negative values of α lead to a mixed tensile/compressive mode. The tensile strength is obtained from a force balance equation and is defined as

$$\bar{\sigma}_T = \frac{N[\bar{\sigma}(h/2) = \bar{\sigma}_{UTS}]}{bh} \tag{31}$$

where N denotes the resultant force, and b the width of the beam. The flexural strength is obtained from a moment balance and is defined as

$$\bar{\sigma}_F = \frac{6M[\bar{\sigma}(h/2) = \bar{\sigma}_{UTS}]}{bh^2}. \tag{32}$$

where M denotes the resultant moment. When α is

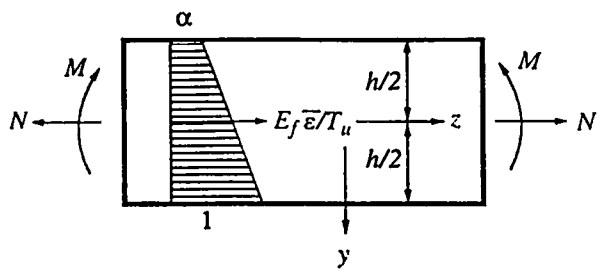

Fig. 8. Definition of the beam geometry in the case of flexure combined with tension.

positive, the beam is in a pure tensile mode. Therefore the results are *independent* of the variable D_1. The resultant force equation yields

$$\bar{\sigma}_T = \frac{fS_cA}{1-\alpha}\left\{\frac{1-\alpha^2}{2} + \sum_{n\geq 1}\frac{\psi_n A^{\beta(n)-1}}{\beta(n)+1}(1-\alpha^{\beta(n)+1})\right\}. \tag{33}$$

The moment equation enables us to derive the flexural strength to be

$$\bar{\sigma}_F = -\frac{3(1+\alpha)}{1-\alpha}\bar{\sigma}_T + \frac{2fS_cA}{(1-\alpha)^2} \times\left\{1-\alpha^3+3\sum_{n\geq 1}\frac{\psi_n A^{\beta(n)-1}(1-\alpha^{\beta(n)+2})}{\beta(n)+2}\right\}. \tag{34}$$

When α is negative, a part of the beam is in compression. In that case the results *depend* on the damage variable D_1. The resultant force equation allows us to get the tensile strength

$$\bar{\sigma}_T = \frac{fS_cA}{1-\alpha}\left\{\frac{1}{2} - \frac{\alpha^2}{2(1-D_1)} + \sum_{n\geq 1}\frac{\psi_n A^{\beta(n)-1}}{\beta(n)+1}\right\} \tag{35}$$

and the moment equation enables us to derive the flexural strength

$$\bar{\sigma}_F = -\frac{3(1-\alpha)}{1-\alpha}\bar{\sigma}_T + \frac{2fS_cA}{(1-\alpha)^2} \times\left[1-\frac{\alpha^3}{1-D_1}+3\sum_{n\geq 1}\frac{\psi_n A^{\beta(n)-1}}{\beta(n)+2}\right]. \tag{36}$$

To illustrate the previous results, a constant interfacial shear strength is assumed. By using the approximations discussed to derive eqn (8), the

following results are obtained. When α is positive, the resultant force equation leads to

$$\bar{\sigma}_T = \frac{fS_c}{1-\alpha}\left(\frac{2}{m+2}\right)^{\frac{1}{m+1}}\left[\frac{1-\alpha^2}{2} - \frac{1-\alpha^{m+3}}{(m+2)(m+3)}\right] \quad (37)$$

and the moment equation

$$\bar{\sigma}_F = -\frac{3(1+\alpha)}{1-\alpha}\bar{\sigma}_T + \frac{2fS_c}{(1-\alpha)^2}\left(\frac{2}{m+2}\right)^{\frac{1}{m+1}} \times\left[1-\alpha^3 - \frac{3(1-\alpha^{m+4})}{(m+2)(m+4)}\right]. \quad (38)$$

When α is negative, the resultant force equation allows us to get the tensile strength

$$\sigma_T = \frac{fS_c}{(1-\alpha)}\left(\frac{2}{m+2}\right)^{\frac{1}{m+1}} \times\left[\frac{(m+1)(m+4)}{2(m+2)(m+3)} - \frac{\alpha^2}{2(1-D_1)}\right] \quad (39)$$

and the moment equation enables us to derive the flexural strength

$$\bar{\sigma}_F = -\frac{3(1+\alpha)}{1-\alpha}\bar{\sigma}_T + \frac{2fS_c}{(1-\alpha)^2}\left(\frac{2}{m+2}\right)^{\frac{1}{m+1}} \times\left[\frac{(m+1)(m+5)}{(m+2)(m+4)} - \frac{\alpha^3}{1-D_1}\right]. \quad (40)$$

In Fig. 9 an interaction diagram is plotted when $m=4$, and $D_1 = 2/7$ for a constant interfacial shear strength. The interaction diagram is also compared to a linear prediction: in that particular case a straight line describes very well the interaction line (see dotted line in Fig. 9). This is one difference when we compare to the interaction diagram of an elastic-perfectly plastic material. In that case the interaction is given by a quarter of an ellipse.

Lastly, when the only difference in the tension/compression behavior is given by the Young's modulus difference ($m \to +\infty$) modeled by the damage variable D_1, the interaction diagram is only a function of the parameter D_1 (see Fig. 9). This last result constitutes a lower bound in the interaction diagram.

In a local load sharing regime, an interaction diagram has no meaning. However, one can study the combined effect of tension and pure flexure. The strain field defined in eqn (29) is used. The average failure stress ratio for *the same volume* is given by

$$\frac{\bar{\sigma}_F}{\bar{\sigma}_{FT}} = (H_{m_s})^{-\frac{1}{m_s}} \quad (41)$$

where $\bar{\sigma}_F$ is the average failure stress under combined loading conditions, and H_{m_s} is the Weibull stress heterogeneity factor [35] defined as

$$H_{m_s} = \frac{1-\alpha^{m_s}}{(1-\alpha)(m_s+1)} \text{ when } \alpha \geq 0 \quad (42)$$

$$H_{m_s} = \frac{1}{(1-\alpha)(m_s+1)} \text{ when } \alpha < 0. \quad (43)$$

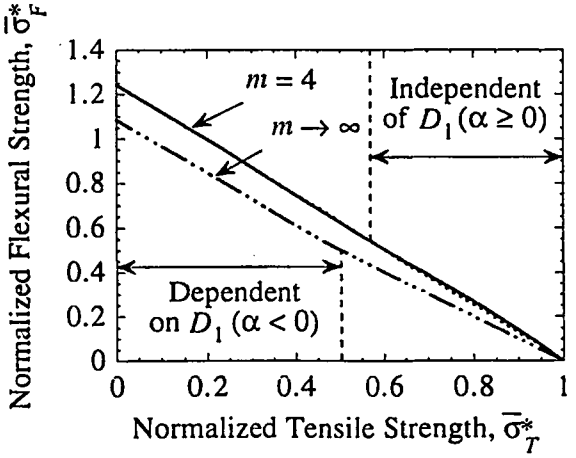

Fig. 9. Interaction diagram (solid line) between tension and flexure when $m=4$, and $D_1 = 2/7$ giving the normalized flexural strength $\bar{\sigma}_F^* = \bar{\sigma}_F/\bar{\sigma}_{UTS}$ vs the normalized tensile strength $\bar{\sigma}_T^* = \bar{\sigma}_T/\bar{\sigma}_{UTS}$. The dotted line gives a linear interaction. The dashed line shows the interaction diagram when $m \to +\infty$.

6 ULTIMATE THREE-POINT FLEXURAL STRENGTH

The aim of this section is to derive the ultimate strength of rectangular beams loaded in three-point flexure. The tensile and compressive behavior follows the same hypotheses as those made in the previous sections. However, in three-point flexure the stress field profile along the fiber direction is no longer uniform. Therefore, eqn (4) cannot be used. Throughout this section, the longitudinal stress field, $\sigma(T,z)$, is assumed to be symmetric about $z=0$ and maximum at $z=0$. Depending on the position of the fiber along the y-axis, the stress field will vary. In the first part of the section, only a set of fibers is analyzed for which the position along the y-axis is the same. A global load sharing regime is assumed in a plane normal to the y-axis, for each value of y. Furthermore, the beam length is assumed to be sufficiently large with respect to the beam height and width so that the shear stresses can be neglected. For the sake of simplicity, the interfacial sliding resistance is assumed constant. The contribution of the broken fibers within the recovery length or pull-out stress, $\bar{\sigma}_{po}$, at $z=0$ is written as

$$\frac{\bar{\sigma}_{po}(T)}{f} = \int_0^T \bar{\sigma}_p(t)\frac{dP_F(t,L_R(t))}{dt}dt \quad (44)$$

where $\bar{\sigma}_p(t)$ denotes the average stress at $z = 0$ when a fiber breaks at a location z, and at a reference stress level t, and $P_F(t,L_R(t))$ is the failure probability that a fiber break within the recovery length $L_R(t)$ at or below a reference stress t. In tension, the probability density of fracture locations is uniform, therefore $\bar{\sigma}_p(t) = t/2$. On the other hand, when the stress field along the fiber direction is not homogeneous, the previous result does not apply, and one needs to determine the average fracture location to estimate the pull-out stress. The average stress $\bar{\sigma}$ applied to the composite at the plane $z = 0$, is given by [10]

$$\frac{\bar{\sigma}}{f} = T\{1 - P_F(T,L_R(T))\} + \frac{2\tau}{R}\langle h(T)\rangle P_F(T,L_R(T)). \quad (45)$$

The first term of the right hand side of eqn (45) corresponds to the contribution of the unbroken fibers, and the second term is the pull-out contribution (stress $\bar{\sigma}_{po}(T)$). The quantity $\langle h(T)\rangle$ represents the average pull-out length, or average fracture location in $L_R(T)/2$ when the reference stress is less than or equal to T. The aim of the present calculation is to evaluate the average fracture location $\langle h(T)\rangle$ when the stress filed along the fiber direction is not homogeneous.

Oh and Finnie [36] derived the average fracture location of a brittle material. In that case the considered volume is constant. In the present case, the length to consider (i.e., the recovery length) is varying with the stress level measured by T. Therefore the results need to be generalized. By recasting the cumulative failure probability $P_F(T,L_R(T))$ of a fiber part of length $L_R(T)$, useful functions are exhibited to determine the average fracture location. Under the weakest link assumption and the independent events hypothesis, the cumulative failure probability $P_F(T,L_R(T))$ of a piece of fiber of length $L_R(T)$ is expressed as

$$P_F(T,L_R(T)) = 1 - \exp\left[\frac{2}{L_0}\int_0^{L_R(T)/2} \ln\{1 - P_{F0}(T,z)\}\mathrm{d}z\right] \quad (46)$$

where $P_{F0}(T,z)$ denotes the cumulative failure probability of a single link of length L_0 whose mid-section is located at z. The failure probability density is obtained by differentiation of eqn (46) with respect to T

$$\frac{\mathrm{d}P_F(T,L_R(T))}{\mathrm{d}T} = \int_0^{L_R(T)/2} 2\Phi(T,z)\mathrm{d}z + 2\Psi(T) \quad (47)$$

so that eqn (46) can be rewritten as

$$P_F(T,L_R(T)) = \int_0^T 2\left\{\int_0^{L_R(t)/2} \Phi(t,z)\mathrm{d}z + \Psi(t)\right\}\mathrm{d}t \quad (48)$$

where $\Phi(t,z)$ corresponds to the failure probability density for a reference stress varying between T and $T + dT$, of an element of length $\mathrm{d}z$ centered at z, and $\Psi(T)$ is the failure probability density associated with the length increase from $L_R(T)$ to $L_R(T) + L_R'(T)\mathrm{d}T$. The first term is identical to that given in [36, 37, 18] when using a Weibull law, the second term is due to the load dependence of the recovery length $L_R(T)$. By using eqns (46) and (47), the expressions of the functions Φ and Ψ are, respectively, given by

$$\Phi(T,z) = -\{1 - P_F(T,L_R(T))\}\frac{1}{L_0} \times \frac{\partial}{\partial T}[\ln\{1 - P_{F0}(T,z)\}] \quad (49)$$

$$\Psi(T) = -\{1 - P_F(T,L_R(T))\}\frac{L_R'(T)}{2L_0} \times \left[\ln\left\{1 - P_{F0}\left(T, \frac{L_R(T)}{2}\right)\right\}\right]. \quad (50)$$

When $L_R(T)$ is independent of T, or $P_{F0}(T,L_R(T)/2)$ vanishes, $\Psi(T)$ vanishes as well, and the results given in [37] still apply in the case of a Weibull law. By dimensional analysis and by inspection of eqn (47), the average $\langle h(T)\rangle$ of the fracture location $h(T)$ for a piece of composite of length $L_R(T)$ at a reference stress T is [38]

$$\langle h(T)\rangle = \frac{\displaystyle\int_0^T 2\left\{\int_0^{L_R(t)/2} z\Phi(t,z)\mathrm{d}z + \frac{1}{4}L_R(t)\Psi(t)\right\}\mathrm{d}t}{\displaystyle\int_0^T 2\left\{\int_0^{L_R(t)/2} \Phi(t,z)\mathrm{d}z + \Psi(t)\right\}\mathrm{d}t}. \quad (51)$$

This expression of the average fracture location does not consider the fibers that originally broke outside the recovery length but were brought into it as the load level increased. The approximation made here is worst when the stress field is constant over the whole length (i.e., pure tension). In that case, however, it can be shown that this hypothesis is not very strong [13]. Equation (45) is used for each height y to determine the global stress state of the composite in three-point flexure. By studying the most loaded fibers in the tensile part, it can be shown that when the specimen length is greater than 5 times the characteristic length δ_c, the gradient effect in three-point flexure along the fiber direction is negligible when compared to the one due to load recovery in the vicinity of a fiber break [39]. Under these circumstances the ultimate strength in three-point flexure $\bar{\sigma}_{U3F}$ is on the same order of magnitude as the ultimate flexural strength $\bar{\sigma}_{UFS}$

$$\bar{\sigma}_{U3F} \cong \bar{\sigma}_{UFS} \text{ when } L > 5\delta_c. \quad (52)$$

This result constitutes a major difference with materials for which a weakest link concept can be used. In that case the ratio of the ultimate strength in three-point flexure is greater than that in pure flexure.

Table 1. Comparison between experimental (Exp.) and predicted (Pred.) ultimate strengths expressed in MPa for three composites reinforced by SiC fibers

Loading Material	Tension		Pure Flexure		Three-point Flexure	
	Exp.	Pred.	Exp.	Pred.	Exp.	Pred.
SiC/LAS[40]	790	850	1050	1080	1180	1090
SiC/C[41]	345	340	455	430	455	435
SiC/Al[42]	700	690	815	820	930	930

When the *two volumes are identical*, the average failure stress ratio is given by

$$\frac{\bar{\sigma}_{F3}}{\bar{\sigma}_{FF}} = (m_s + 1)^{\frac{1}{m_s}} \tag{53}$$

where $\bar{\sigma}_{F3}$ is the average failure stress in three-point flexure.

The previous results are applied to three composites reinforced by SiC fibers (Table 1). Two of the three composites have ultimate strengths following a global load sharing hypothesis (LAS and C matrices). This result is related to the fact that matrix cracking has saturated and that the interfacial shear strength is small (on the order of a few MPa). On the other hand, the aluminum matrix leads to ultimate strengths described by a local load sharing hypothesis ($m_s = 7$). This matrix is more sensitive to localized fiber failures and to higher values of the interfacial shear strength.

7 CONCLUSIONS

A unified approach to the prediction of the ultimate tensile strength of FRCs has been proposed. The key quantity to consider is the average fragment length. Expressions of the ultimate tensile strength are derived within this general framework and compared with other existing theories. In particular, in the global load sharing regime it is shown that the ultimate tensile strength is mostly length-independent. Conversely, in the local load sharing regime, the ultimate tensile strength is always length-dependent. A description of the behavior of these FRCs up to the ultimate tensile point has been derived in the framework of Continuum Mechanics.

A generalization to pure flexural modes is proposed to derive the ultimate flexural strength. In the global load sharing regime, the increase in terms of ultimate flexural strength is due to the conjunction of two phenomena: difference in elastic moduli in tension and in compression, and 'ductility' due to fiber breakage and fiber pull-out. It has been shown that the 'ductility' contributes substantially to this increase.

An interaction between tension and flexure is studied. Although some differences are noticed when compared to an elastic perfectly plastic behavior, some similar features can be shown, in particular the increase in terms of normalized ultimate strength. This case corresponds to a situation where the 'ductility' is distributed within a large region of the structure. On the other hand, when the 'ductility' is confined within a very small area of the structure, the increase in terms of the ultimate strength is expected to be less important, though the gradients along the fiber direction could play a role and increase it again.

Lastly, in the case of three-point flexure, the ultimate strength has the same order of magnitude as that in pure flexure within the framework of global load sharing. On the other hand, in the local load sharing regime, the ultimate strength in three-point flexure increases as compared with pure flexure when the two volumes are identical. The three-point flexure experiments therefore allow to discriminate the two load transfer regimes when compared with the pure flexure case. This result can be observed when ultimate strengths of LAS and C matrix composites (exhibiting a global load sharing regime) are compared with Al matrix composites (exhibiting a local load sharing regime) subjected to pure tension, pure flexure and three-point flexure.

REFERENCES

1. Netravali, A.N., Henstenburg, R.B., Phoenix, S.L. and Schwartz, P., Interfacial shear strength studies using the single-filament-composite test. Part I: Experiments on graphite fibers in epoxy. *Polymer Composites*, 1989, **10**, 226–241.
2. Thouless, M.D., Sbaizero, O., Sigl, L.S. and Evans, A.G., Effect of interface mechanical properties on pullout in a SiC-fiber-reinforced lithium aluminium silicate glass-ceramic. *Journal of the American Ceramic Society*, 1989, **72**, 525–532.
3. Heredia, F.E., Spearing, S.M., Evans, A.G., Mosher, P. and Curtin, W.A., Mechanical properties of carbon matrix composites reinforced with nicalon fibers. *Journal of the American Ceramic Society*, 1992, **75**, 3017–3025.
4. Gücer, D.E. and Gurland, J., Comparison of the statistics of two fracture models. *Journal of the Mechanics and Physics of Solids*, 1962, **10**, 365–373.
5. Pierce, F.T., Tensile tests for cotton yarns V: The 'weakest link' theorems on the strength of long and of composite specimens. *Journal of the Textile Institute*, 1926, **17**, T355–T368.
6. Daniels, H.E., The statistical theory of the strength of

bundles of threads. *Proceedings of the Royal Society of London*, 1944, **183**, 405–429.
7. Coleman, B.D., On the strength of classical fibers and fiber bundles. *Journal of the Mechanics and Physics of Solids*, 1958, **7**, 60–70.
8. Zweben, C. and Rosen, B.W., A statistical theory of material strength with application to composite materials. *Journal of the Mechanics and Physics of Solids*, 1970, **18**, 189–206.
9. Neumeister, J.M., Bundle pullout—a failure mechanism limiting the tensile strength of continuous fiber reinforced brittle matrix composites and its implications for strength dependence on volume and type of loading. *Journal of the Mechanics and Physics of Solids*, 1993, **41**, 1405–1424.
10. Curtin, W.A., Theory of mechanical properties of ceramic matrix composites. *Journal of the American Ceramic Society*, 1991, **74**, 2837–2845.
11. Phoenix, S.L. and Raj, R., Scalings in fracture probabilities for a brittle matrix fiber composite. *Acta Metallica Materiala*, 1992, **40**, 2812–2828.
12. Neumeister, J.M., A constitutive law for continuous fiber reinforced brittle matrix composites with fiber fragmentation and stress recovery. *Journal of the Mechanics and Physics of Solids*, 1993, **41**, 1383–1404.
13. Hild, F., Domergue, J.-M., Evans, A.G. and Leckie, F.A., Tensile and flexural ultimate strength of fiber-reinforced ceramic-matrix composites. *International Journal of Solids and Structures*, 1994, **31**, 1035–1045.
14. Kelly, A. and Davies, G.J., The principles of the fiber reinforcement of metals. *Metallurgy Review*, 1965, **10**, 1–11.
15. Jansson, S., Mechanical characterization and modeling of non-linear deformation and fracture of a fiber reinforced metal matrix composite. *Mechanics of Materials*, 1991, **12**, 47–62.
16. Curtin, W.A., Ultimate strength of fiber-reinforced ceramics and metals. *Composites*, 1993, **24**, 98–102.
17. Henstenburg, R.B. and Phoenix, S.L., Interfacial shear strength studies using the single-filament-composite test, Part II: A probability model and Monte Carlo simulations. *Polymer Composites*, 1989, **10**, 389–406.
18. Sutcu, M., Weibull statistics applied to fiber failure in ceramic composites and work of fracture. *Acta Metallica*, 1989, **37**, 651–661.
19. Curtin, W.A., Exact theory of fiber fragmentation in single-filament composite. *Journal of Materials Science*, 1991, **26**, 5239–5253.
20. Hui, C.Y., Phoenix, S.L., Ibnabdeljalil, M. and Smith, R.L., An exact closed form solution for fragmentation of Weibull fibers in a single filament composite with applications to fiber-reinforced ceramics. *Journal of the Mechanics and Physics of Solids*, 1995, **43**, 1551–1585.
21. Feillard, P., Rouby, D., Désarmot, G. and Favre, J.-P., Limits of conventional micromechanical analysis of interface properties in glass/epoxy model composites. *Materials Science Engineering*, 1994, **A188**, 159–166.
22. Nairn, J.A., A variational mechanics analysis of the stresses around breaks in embedded fibers. *Mechanics of Materials*, 1992, **13**, 131–157.
23. Hild, F., Larsson, P.-L. and Leckie, F.A., Uncoupled and fully coupled approaches to predict macro-initiation in fiber-reinforced ceramic-matrix composites. *Composite Structures*, 1994, **29**, 365–377.
24. Kelly, A. and Tyson, W.R., Tensile properties of fibre-reinforced metals: copper/tungsten and copper/molybdenum. *Journal of the Mechanics and Physics of Solids*, 1965, **13**, 329–350.
25. Aveston, J., Cooper, G. A. and Kelly, A., Single and multiple fracture. In *Proceedings National Physical Laboratory: Properties of Fiber Composites*, IPC Science and Technology Press, Surrey, UK, 1971, pp.15–26.
26. Hutchinson, J.W. and Jensen, H.M., Models for fiber debonding and fiber pull-out in brittle composites with friction. *Mechanics of Materials*, 1990, **9**, 139–163.
27. Feillard, P., Désarmot, G. and Favre, J.-P., A critical assessment of fragmentation test with glass/epoxy systems. *Composite Science Technology*, 1993, **49**, 109–119.
28. Gulino, R. and Phoenix, S.L., Weibull strength statistics for graphite fibres measured from the break progression in a model graphite/glass/epoxy microcomposite. *Journal of Materials Science*, 1991, **26**, 3107–3118.
29. Weibull, W., *A statistical theory of the strength of materials*. vol. 151, Roy. Swed. Inst. Engng Res., Stockholm, 1939.
30. Curtin, W.A., Strength versus gauge length in ceramic-matrix composites. *Journal of the American Ceramic Society*, 1994, **77**, 1072–1074.
31. Feillard, P., Désarmot, G. and Favre, J.-P., Theoretical aspects of the fragmentation test. *Composite Science Technology*, 1994, **50**, 265–279.
32. Cox, H.L., The elasticity and the strength of paper and other fibrous materials. *British Journal of Applied Physics*, 1952, **3**, 72–79.
33. Favre, J.-P., Sigety, P. and Jacques, D., Stress transfer by shear in carbon fibre model composites, Part 2: Computer simulation of the fragmentation test. *Journal of Materials Science*, 1991, **26**, 189–195.
34. Timoshenko, S. P. and Goodier, J. N., *Theory of Elasticity*, 3rd edition, McGraw-Hill, NY, 1970.
35. Hild, F., Billardon, R. and Marquis, D., Hétérogénéité des contraintes et rupture des matériaux fragiles. *C. R. Acad. Sci. Paris*, 1992, **t315**, 1293–1298.
36. Oh, H.L. and Finnie, I., On the location of fracture in brittle solids-I due to static loading. *International Journal of Fracture Mechanics*, 1970, **6**, 287–300.
37. Thouless, M.D. and Evans, A.G., Effects of pull-out on the mechanical properties of ceramic-matrix composites. *Acta Metallica*, 1988, **36**, 517–522.
38. Hild, F., On the average pull-out length of fiber-reinforced composites. *C. R. Acad. Sci. Paris*, 1994, **t319**, 1123–1128.
39. Hild, F., Ultimate strength of structures made of fiber-reinforced ceramic-matrix composites. PhD dissertation, University of California, Santa Barbara, USA, 1995.
40. Jansson, S. and Leckie, F.A., The mechanics of failure of silicon carbide fiber-reinforced glass-matrix composites. *Acta Metallica Materiala*, 1993, **40**, 2967–2978.
41. Schwartz, S., Lee, S. and Mosher, P., Properties of silicon carbide fiber reinforced composites. In *Proc. 15th Ann. Conf. Composite Materials and Structures, ACerS*, Cocoa Beach, FL, 14–18 January 1994.
42. Leckie, F. A., Ultimate strength properties of SiC/Al composites. University of California, Santa Barbara, Report, 1995.

iii Etude bidimensionnelle des conditions de rupture

par F. HILD, P.-L. LARSSON et F.A. LECKIE (1994).
Comp. Struct., 29, pp. 365-377.

Uncoupled and coupled approaches to predict macrocrack initiation in fiber reinforced ceramic matrix composites

François Hild,* Per-Lennart Larsson,‡ & Frederick A. Leckie
Department of Mechanical and Environmental Engineering, University of California, Santa Barabara, CA 93106, USA

Localized fiber pull-out is one of the fracture features of fiber reinforced ceramic matrix composites. The onset of this mechanism is predicted by using Continuum Damage Mechanics, and corresponds to a localization of the deformations. After deriving two damage models from a uni-axial bundle approach, and criteria at localization, different axisymmetric configurations are analyzed through two different approaches to predict macrocrack initiation.

1 INTRODUCTION

To achieve the new goals of high performance structures, Ceramic Matrix Composites (CMCs) become a suitable candidate, especially when the elements are subjected to high mechanical and thermal load histories.[1] Indeed, their low density combined with high strength and good performances at high temperature are appealing features. For example, in the design of the new generation of jet engines, CMCs will be used in the combuster, the turbine disks and the nozzle section.[1]

In this paper we will focus our attention on rotating parts, i.e. an element in the turbine stages where angular rotation induces mechanical loading. To simplify the analysis, we will consider axisymmetric structures. The structures are assumed to be reinforced by fibers in the circumferential direction. The main goal of this paper is to predict the initiation of a macrocrack in the structure, which often constitutes the early stages of the final failure by fracture of the structure. Starting from a material which is assumed free from any initial macro defect, the initiation can be predicted using Continuum Damage Mechanics (CDM). In this paper we will neglect the matrix cracking process. This degradation takes place at an early stage of loading and often does not lead to final failure of a structure. Matrix cracks gradually develop as the load level increases. They usually saturate because of the shear effects induced by the interface between fibers and matrix.[2] The results presented herein are valid when the steady matrix stress[3] is less than the ultimate strength of a fiber reinforced composite.[4] When that hypothesis is satisfied, the key mechanism leading to a final failure is fiber breakage. The fiber breakage mechanism is accompanied by distributed fiber pull-out; a broken fiber pulls out of the matrix and involves shear stresses along the interface to recover its original load level. This mechanism distinguishes the behavior of fiber reinforced CMCs from classical fiber-bundle behavior.[5] From a design point of view it is interesting to evaluate their differences, especially in terms of load levels.

The degradation mechanism will be described by an internal variable called *damage*. In the framework of CDM, the initiation of a macrocrack corresponds to a localization of the deformations, which corresponds to the onset of a surface across which the velocity gradient is discontinuous. Physically, it corresponds to localized pull-out, whereby one macrocrack develops and pull-out continues to evolve in the vicinity of that macrocrack only. This phenomenon leads to a different behavior, compared to the homogeneous solution for which damage is still evolving in a diffusive manner. Under a small-deformations

*Laboratoire de Mécanique et Technologie, E.N.S. de Cachan/C.N.R.S./Université Paris 6, 61 avenue du Président Wilson, F-94235 Cachan Cedex, France.

‡Department of Solid Mechanics, Royal Institute of Technology, S-100 44 Stockholm, Sweden.

assumption, localization is mainly driven by the damage mechanism that causes strain softening.[6]

In Section 2, the main results concerning loss of uniqueness and localization will be recalled. In particular a property giving a necessary and sufficient condition of loss of uniqueness and localization will be proven and will be applied in Section 3. Section 3 deals with two constitutive laws modeling fiber breakage. The condition of localization and loss of uniqueness will be studied, and general criteria may be derived using the property given in Section 2. Section 4 presents two strategies to predict the initiation of a macrocrack. The first one, which is referred to as *fully coupled* approach, consists of calculating the stresses and strains evolution in elasticity coupled with damage; therefore the damage evolution is *fully coupled* with the evolution of the stresses and the strains. The second approach, which is referred to as *decoupled* approach and which is an easier calculation more amenable to design, consists of an elastic computation and the use of the failure criterion derived from the localization analysis in Section 3. The differences between the two approaches are analyzed. The results, in terms of loads at localization, are also compared to the corresponding cumulative failure probability when the structure is assumed to be made of a brittle material.

2 LOCALIZATION AND LOSS OF UNIQUENESS

2.1 General theory

The failure at a *meso*-level, which corresponds to the initiation of a macrocrack, is defined as the bifurcation of the rate problem in certain modes, viz. the appearance of a surface across which the velocity gradient is discontinuous.[7] This phenomenon is referred to as *localization*, and corresponds to the failure of the ellipticity condition.[8] The condition of localization can also be compared to the loss of uniqueness of the rate problem.

Stationary waves were studied by Hadamard[9] in elasticity and by Hill[10] and Mandel[11] in elasto-plasticity. Rice[12] related the localization of plastic shear bands to jumps of the velocity gradient. Borré and Maier,[13] who extended the results given by Rice[12] and Rice and Rudnicki,[14,15] have given necessary and sufficient conditions for the onset of modes inside the body.

Under the small strains assumption and in elasticity coupled with damage, the behavior of a material is assumed to be described by the following piece-wise linear rate constitutive law

$$\dot{\sigma}=\begin{cases}\mathbf{E}:\dot{\varepsilon} \text{ if } \dot{D}=0\\ \mathbf{H}:\dot{\varepsilon} \text{ if } \dot{D}\neq 0\end{cases} \tag{1}$$

where $\dot{\sigma}$ and $\dot{\varepsilon}$ denote the stress and strain rates, respectively, $\mathbf{E}$ and $\mathbf{H}$ are fourth-rank tensors, $\mathbf{E}$ is assumed to be positive, definite, and D is either a single damage variable or a set of damage variables.

Localization occurs *inside* the body, *if and only if*[13,14]

$$\mathrm{Det}(\mathbf{n}\cdot\mathbf{H}\cdot\mathbf{n})=0 \tag{2}$$

for any vector $\mathbf{n}\neq 0$ and at any point inside a structure Ω.

This criterion corresponds to the failure of the ellipticity condition of the rate equilibrium equation; it also can be used as an indicator of the local failure of the material, at a *meso*-scale.[7]

Furthermore, any loss of uniqueness, considered as bifurcation of the rate boundary value problem, is excluded provided the operator

$$\mathbf{H}_S=\frac{1}{2}(\mathbf{H}+\mathbf{H}^T) \tag{3}$$

is strictly positive-definite everywhere within the structure (where ^{T} denotes the Euclidean transposition). This condition is equivalent to the condition of hardening

$$\dot{\sigma}:\dot{\varepsilon}>0. \tag{4}$$

Equations (2) and (3) show that the quantity that defines loss of uniqueness and localization is the linear tangent modulus $\mathbf{H}$. In the following, we analyze loss of uniqueness and loss of ellipticity (i.e. localization) for plane states when

$$\begin{cases}\varepsilon_{11}=\alpha\varepsilon_{22} \text{ with } \alpha\in\mathbb{R}\\ \varepsilon_{12}=0.\end{cases} \tag{5}$$

The parameter α is referred to as strain ratio. These particular states only are considered since the computations will deal with shear-free states. These states lead to a tangent modulus that takes the following form

$$\mathbf{H}=\begin{Bmatrix}H_{1111} & H_{1122} & 0\\ H_{2211} & H_{2222} & 0\\ 0 & 0 & H_{1212}\end{Bmatrix} \tag{6}$$

where $H_{ijkl}=\partial\sigma_{ij}/\partial\varepsilon_{kl}$ are the components of the tangent modulus H defined in eqn (1). For problems under hypothesis (5), the non-vanishing components of vector n are n_1 and n_2, and the matrix $A=\mathbf{n}\cdot H\cdot\mathbf{n}$ reduces to[16]

$$A=\begin{Bmatrix} n_1^2H_{1111}+n_2^2H_{1212} & n_1n_2(H_{1212}+H_{1122}) \\ n_1n_2(H_{1212}+H_{2211}) & n_1^2H_{1212}+n_2^2H_{2222} \end{Bmatrix}. \tag{7}$$

We rewrite $(n_1,n_2)=(\cos\theta,\sin\theta)$, let X be equal to $\tan^2\theta$, and let Y be equal to $1/X$. The localization condition (eqn (2)) can be written in terms of X or Y

$$aX^2+bX+c=0,\ a\neq 0 \tag{8.1}$$

$$cY^2+bY+a=0,\ c\neq 0 \tag{8.2}$$

with

$$a=H_{1212}H_{2222} \tag{9.1}$$

$$b=H_{1111}H_{2222}-H_{1122}H_{2211}-H_{1122}H_{1212}-H_{2211}H_{1212} \tag{9.2}$$

$$c=H_{1212}H_{1111}. \tag{9.3}$$

If real positive roots are found, then the localization direction is perpendicular to the vector $(n_1, n_2, 0)=(\cos\theta,\sin\theta,0)$, characterized by the angle θ (Fig. 1). The values of H_{1111}, H_{2222}, H_{1122}, H_{2211} and H_{1212} are model-dependent.

2.2 Necessary and sufficient condition at localization

In this section, general results concerning localization are analyzed. A necessary and sufficient condition at localization *and* loss of uniqueness will be derived under the following conditions. Let us assume that $H_{1122}=H_{2211}=\nu H_{2222}$ $(\nu<\sqrt{2})$, that H_{1111} and H_{1212} are positive numbers and that H_{2222} can become negative (H_{ijkl} are the components of the tangent operator H). This condition will be satisfied in the models used later. It can be seen from eqns (3) and (6) that there is no loss of uniqueness, provided

$$\lambda>0 \tag{10.1}$$

where

$$2\lambda=H_{1111}-H_{2222}+\sqrt{(H_{1111}-H_{2222})^2+2\nu^2(H_{2222})^2}. \tag{10.2}$$

Furthermore, it is noticed that when H_{2222} is equal to zero, λ is equal to zero (loss of uniqueness) and the coefficients a, b, and c of eqns (9) reduce to

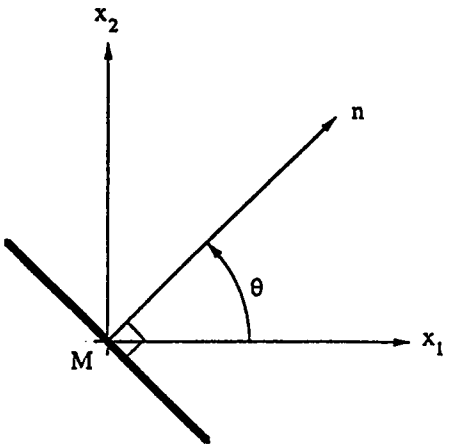

Fig. 1. Localization mode.

$$a=0,\quad b=0,\quad c=H_{1111}H_{1212}>0. \tag{11}$$

Localization occurs since it is possible to find Y satisfying eqn (8.2): $Y=0$, and the localization direction is given by $\theta=\pi/2$. Therefore a *sufficient* condition of loss of uniqueness *and* localization is that H_{2222} should be equal to zero.

Since localization corresponds to a particular mode of all of the solutions after loss of uniqueness, it suffices to show that H_{2222} equal to zero is a sufficient condition for loss of uniqueness. Using the triangular inequality, we have

$$\frac{2-\nu\sqrt{2}}{2}H_{2222}\leq\lambda. \tag{12}$$

Loss of uniqueness corresponds to λ equal to zero, and therefore $H_{2222}\leq 0$. Since it has been shown that H_{2222} equal to zero is sufficient to define localization and loss of uniqueness, we have the following property: *a necessary and sufficient condition to have localization and loss of uniqueness is H_{2222} equal to zero. The angle at localization is equal to $\pi/2$.*

Conversely, under the conditions $H_{1122}=H_{2211}=\nu H_{1111}(\nu<\sqrt{2})$, H_{2222} and H_{1212} are positive numbers and H_{1111} can become negative, *a necessary and sufficient condition to have localization and loss of uniqueness is H_{1111} equal to zero. The angle at localization is equal to 0.* The proof is the same as previously when studying eqn (8.1).

3 CONSTITUTIVE LAWS

This section is concerned with the development of two constitutive laws in the case of CMCs rein-

forced in one direction. Since these models will be used to study spinning structures, we choose a cylindrical coordinate system (r, φ) as shown in Fig. 2(a). We assume a plane stress hypothesis. This hypothesis is consistent with the results derived in Section 2: eqn (6) is still valid. The fibers are assumed to be in the hoop direction, and the two analyzed geometries are a disk of outer radius a, and a ring of outer radius a and inner radius b $(a=2b)$ shown in Figs 2(b) and 2(c). We let ω denote the angular rotation speed. Since the structure, the boundary conditions and the loading are axisymmetric, the problem is axisymmetric, and the only non-zero stresses are related to the corresponding strains by[17]

$$\sigma_{rr}=\frac{E_\varphi}{k\{1-\nu_{r\varphi}^2(1-D_\varphi)k\}} \times\{\varepsilon_{rr}+\nu_{r\varphi}(1-D_\varphi)k\varepsilon_{\varphi\varphi}\} \tag{13}$$

$$\sigma_{\varphi\varphi}=\frac{E_\varphi(1-D_\varphi)}{1-\nu_{r\varphi}^2(1-D_\varphi)k}(\varepsilon_{\varphi\varphi}+\nu_{r\varphi}\varepsilon_{rr}) \tag{14}$$

where E_φ denotes the Young's modulus in the hoop direction, $\nu_{r\varphi}$ denotes the Poisson's ratio, k denotes the ratio of the Young's modulus in the fiber direction (E_φ) to the Young's modulus in the radial direction (E_r), and D_φ denotes the damage variable modeling the fiber degradation. The damage variable can be defined as the percentage of broken fibers.[18-20] The percentage of broken fibers is given by the corresponding cumulative failure probability which will be modeled by a Weibull expression.[21] A first expression of the damage variable can be obtained[20] by extending a study of fiber-bundle to 2D configurations, and will be referred to as model No. 0

$$D_\varphi^{(0)}=1-\exp\left\{-\frac{r}{r_0}\left\{\frac{\sigma_{\varphi\varphi}}{(1-D_\varphi^{(0)})f\sigma_0}\right\}^m\right\}$$
$$\text{if } \varepsilon_{\varphi\varphi}>0 \text{ and } \dot{\varepsilon}_{\varphi\varphi}>0 \tag{15}$$

where m and σ_0 are the shape and scale parameters of a Weibull law, $2\pi r_0$ is the corresponding gauge length, r is the fiber radius (since the fiber length is $2\pi r$) and f is the volume fraction of fibers in the hoop direction. This first expression corresponds to a generalization of the behavior of a fiber-bundle in the hoop direction embedded in a matrix. This means that if a fiber breaks, it will not be able to carry any load (i.e. no distributed pull-out takes place) and therefore this model constitutes a *lower* bound of the expected behavior of the composite.

On the other hand, it has been proven[22] that due to distributed pull-out, the evolution of fiber breakage is *not* dictated by the length of the fiber (here $2\pi r$) *but* by the length over which the tensile stress field recovers its original level. Using a shear lag approach[23-24] with constant interfacial shear stress τ, this length, also called *recovery length*, L_{rec}, is given by (Fig. 3)

$$L_{rec}=\frac{RT}{\tau} \tag{16}$$

where R is the fiber radius, T is the tensile stress in the unbroken fibers. In this case, the relevant length to consider is the recovery length L_{rec}. By equilibrium considerations, the tensile stress T is related to the external applied stress $\sigma_{\varphi\varphi}$ by

$$fT=\frac{\sigma_{\varphi\varphi}}{(1-D_\varphi)}. \tag{17}$$

Therefore, instead of r in eqn (15), we will consider L_{rec}. We then end up with a second type of damage evolution which will be referred to as model No. 1

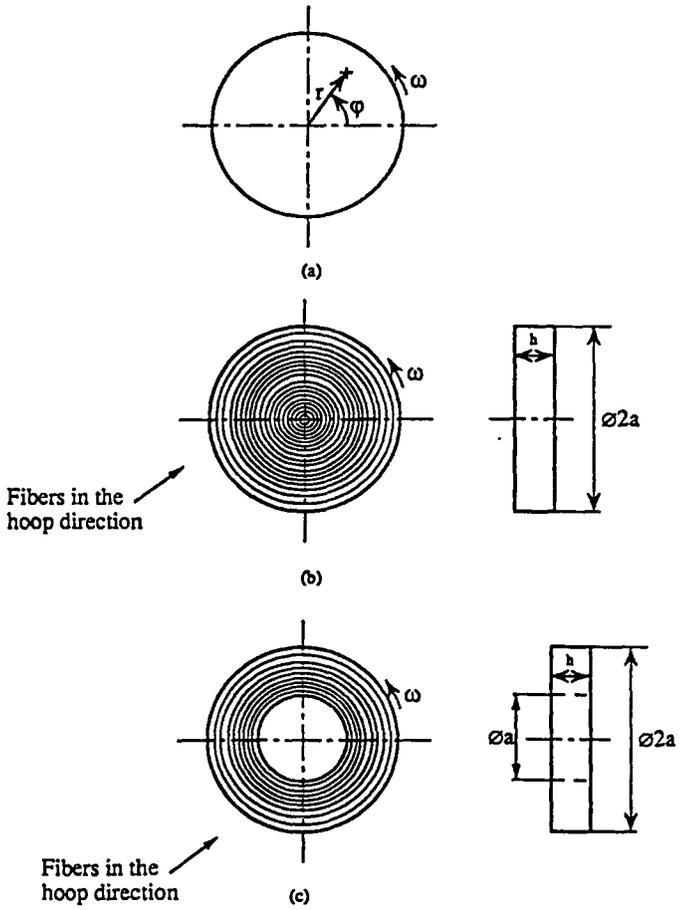

Fig. 2. Analyzed structures. The quantity ω represents the angular velocity: (a) coordinate system; (b) spinning disk; (c) spinning ring.

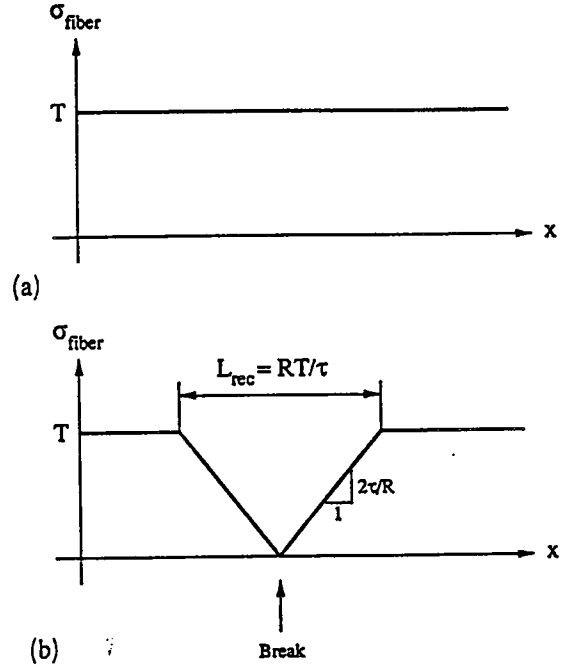

Fig. 3. Definition of the recovery length. Stress in the fiber against fiber axis x: (a) just before the break; (b) just after the break.

$$D_{\varphi}^{(1)} = 1 - \exp\left[-\left\{ \frac{\sigma_{\varphi\varphi}}{(1 - D_{\varphi}^{(1)}) f \sigma_c} \right\}^{m+1} \right]$$

$$\text{if } \varepsilon_{\varphi\varphi} > 0 \text{ and } \dot{\varepsilon}_{\varphi\varphi} > 0 \qquad (18.1)$$

where the expression of the scaling σ_c stress is given by

$$\sigma_c = \left(\frac{\sigma_0^m 2\pi r_0 \tau}{R} \right)^{1/m+1}. \qquad (18.2)$$

This stress has been previously used by Phoenix *et al.*,[25-26] and by Curtin[27] and is referred to as characteristic strength. It can also be noted that this expression is valid under a global load-sharing hypothesis, i.e. when a fiber breaks, the load it was carrying is evenly distributed to the unbroken fibers. Although shear is involved on a microscale, we assume that the macroscopic stress state is shear-free so that eqn (5) still applies. Therefore, all of the results derived in Section 2.2 can be used.

With these two models the ultimate tensile strength in the fiber direction is given by

$$\sigma_{\varphi\varphi} = \sigma_u = \begin{cases} f\sigma_0 \left(\dfrac{r_0}{e m r} \right)^{1/m} & \text{for model No. 0} \\ f\sigma_c \left(\dfrac{1}{e(m+1)} \right)^{1/m+1} & \text{for model No. 1.} \end{cases} \qquad (19)$$

It is worth noting that the ultimate tensile strength in the fiber direction *does* depend on the fiber length for model No. 0, whereas it is *independent* of the fiber length for model No. 1. Equation (19) shows that the characteristic strength σ_0 corresponds to the scaling stress of the ultimate tensile strength in the fiber direction. In particular, this result shows that the ultimate strength is independent of the total length of the fiber. Instead it depends on the recovery length at the ultimate, which is proportional to the characteristic length[27] $L_c = R\sigma_c/\tau$. Furthermore, in this paper *only* the fiber breakage mechanism is taken into account since it is the most important mechanism compared to the pull-out mechanism in terms of the contribution to the stress levels.[22-29] The damage level at the ultimate tensile point is given by

$$D_{\varphi} = D_c = \begin{cases} 1 - \exp\left(\dfrac{-1}{m} \right) & \text{for model No. 0} \\ 1 - \exp\left(\dfrac{-1}{m+1} \right) & \text{for model No. 1.} \end{cases} \qquad (20)$$

In both models it can be noticed that the percentage of broken fibers at the ultimate tensile point (D_c) is independent of all material parameters but the Weibull modulus.

For both models the tangent operator H takes the form

$$H_{rrrr} = F_1 - \frac{F_2 F_4 F_3^{(i)}}{1 + F_5 F_3^{(i)}} \qquad (21.1)$$

$$H_{\varphi\varphi\varphi\varphi} = \frac{F_6}{1 + F_5 F_3^{(i)}} \qquad (21.2)$$

$$H_{rr\varphi\varphi} = H_{\varphi\varphi rr} = \nu_{r\varphi} H_{\varphi\varphi\varphi\varphi} \qquad (21.3)$$

$$H_{r\varphi r\varphi} = 2G_{r\varphi} > 0 \qquad (21.4)$$

where $G_{r\varphi}$ corresponds to the shear modulus of the composite (assumed to be constant), the explicit expressions for F_j are given in Appendix 1; the superscript (i) refers to either model No. 0 (0) or model No. 1 (1). It is worth noting that all conditions presupposed in the property derived in Section 2 are satisifed. Furthermore, it is easily seen that when D_{φ} is equal to D_c then $F_3^{(i)}$ tends to infinity, and thus $H_{\varphi\varphi\varphi\varphi}$ vanishes. On the other hand, H_{rrrr} and $H_{r\varphi r\varphi}$ remain positive. Consequently, localization *and* loss of uniqueness

occur if and only if

$$D_\varphi = D_c \tag{22.1}$$

$$\sigma_{\varphi\varphi} = \sigma_u \,. \tag{22.2}$$

These two criteria are easier to compute than the general criteria of localization and loss of uniqueness. Moreover, the criterion refers to a maximum critical stress which does not need a computation when elasticity is coupled with damage. Indeed, an elastic computation can use criterion (22.2), whereas a computation where elasticity is coupled with damage can use both criteria. Therefore a post-processing approach described by Lemaitre[30] is not necessary, in this particular case, since criterion (22.2) does not refer to damage variables. On the other hand, as it will be shown in the next section, the damaged zone is not small compared to the dimensions of the structures. Therefore a *locally coupled* approach[30] is not very interesting in this particular case.

It is also worth noting that criteria (22) are independent of the strain ratio α (5) and therefore the knowledge of the ultimate tensile strength is particularly crucial. The angle at localization is equal to $\pi/2$, i.e. perpendicular to the fiber direction (Fig. 4(a)).

If the fibers are in the radial direction, then using the corollary of the property derived in Section 2, we find that localization and loss of uniqueness can be characterized by

$$D_r = D_c \tag{23.1}$$

$$\sigma_{rr} = \sigma_u \tag{23.2}$$

where D_r denotes the damage variable modeling the degradation of the fibers in the radial direction. The angle at localization is equal to 0, i.e. again perpendicular to the fiber direction (Fig. 4(b)).

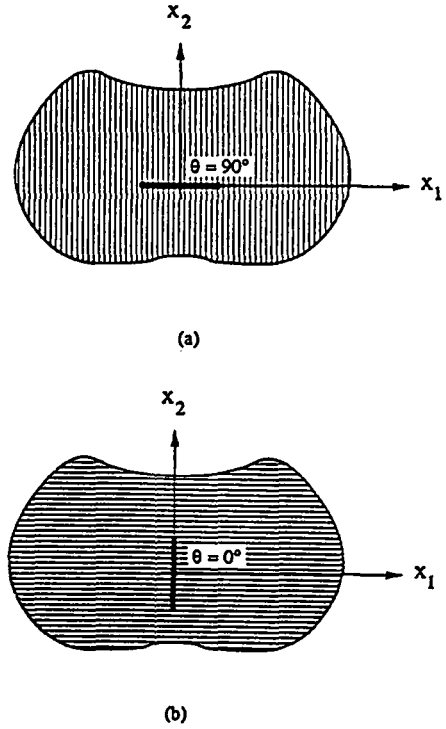

Fig. 4. Localization angles θ for: (a) fibers parallel to the 2-axis ($\theta = \pi/2$); (b) fibers parallel to the 1-axis ($\theta = 0$).

4 INITIATION OF MACROCRACKS IN SPINNING STRUCTURES

As mentioned earlier, we will apply these results to two spinning geometries (Figs 2(b) and 2(c)). In each case, the external boundaries are supposed to be traction-free. The first part of this section is devoted to the direct application with the two models presented in Section 3. The second part deals with a simplified approach using elastic computations. The third part is concerned with the comparisons between the previous computations and the assessment of the reliability of those structures using a Weibull-type approach.

4.1 Fully coupled computations

When the constitutive equations presented in Section 3 are considered, it proved impossible to derive a closed-form solution for the stress state and the damage state. Instead, the problem is solved using the Finite Element Method. Constitutive laws (13)–(15), and (18) are implemented into a standard finite element code ABAQUS,[31] and a solution is sought for by discretizing the problem using two-node axisymmetric shell elements. Since the linear tangent modulus H had to be implemented into the finite element code, the load (i.e. the angular rotation speed) required for loss of uniqueness and localization could be conveniently calculated using ABAQUS through a UMAT routine. In summary, the complete constitutive equations given by damage coupled with elasticity were implemented. Therefore these computations will be referred to as *fully coupled.*

It should be noted that due to the non-explicit expression for the damage parameter given in (15) and (18), an iterative procedure had to be outlined to determine the damage state characterized by D_φ at every time the calculated strain field changed at a certain Gauss point. This was done by using a standard bisection method. A test of

mesh dependence of the numerical results is also performed. The number of elements proves to have a very weak influence on the solution, and satisfactory results for the stress and state variable can be obtained by modeling the disk with only 20 elements.

The material analyzed herein is a CMC defined in Appendix 2. The numerical values are close to those found by Jansson and Leckie[32] for a lithium alumino-silicate (LAS) matrix reinforced with silicon carbide fibers (commercial name Nicalon).

In Fig. 5, the stress field in the hoop direction obtained with a fully coupled computation is compared to the elastic stress field at the same load level. It can be noted that the load level corresponds to the localization speed for the ring with model No. 1. Due to the damage coupling, a redistribution takes place. In particular it is worth noting that the stress levels in the most loaded part ($r \geq 0{\cdot}23$ m) are larger in the elastic computation. This trend is the same for both models and both structures.

In Fig. 6, the outer displacement of the ring obtained by an elastic computation and a fully coupled computation (model No. 1) are compared. Due to the gradual distribution of the damage all over the structure, the 'global' stiffness of the damaged structure softens as the applied load increases. The higher the load, the higher the softening.

In terms of load levels at localization, Table 1*a* summarizes the results. Note that model No. 1 gives much higher load levels than model No. 0. This is mainly due to the radial dependence of the ultimate tensile strength (19) of model No. 0, compared to the radial independence of model No. 1. In Figs 7 and 8 where the stresses in the hoop direction are plotted against the radius, the stress levels at localization (i.e. when the curve $\sigma_{\varphi\varphi}(r)$ intersects the curve σ_u: criterion (22.2)) are in the same ratio as the load levels. It is worth noting that, as mentioned earlier, the ultimate tensile strength is r-dependent for model No. 0 (Fig. 7) and r-independent for model No. 1 (Fig. 8). Crite-

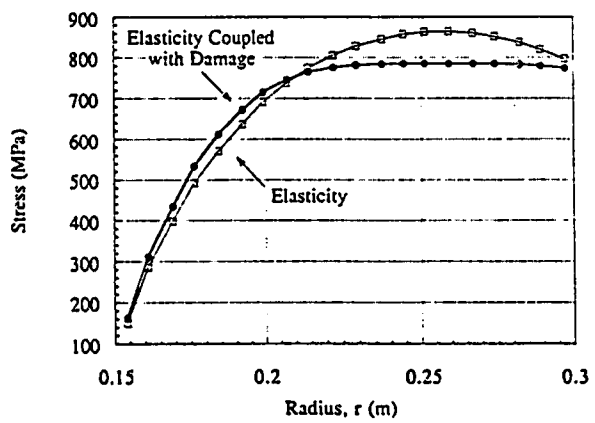

Fig. 5. Hoop stress $\sigma_{\varphi\varphi}(r)$ as a function of the radius obtained by fully coupled computation and a decoupled computation at localization ($\rho\omega^2 = 2{\cdot}26\ 10^{10}$ kg m^{-3} s^{-2}) for the ring wih model No. 1. Note the stress redistribution.

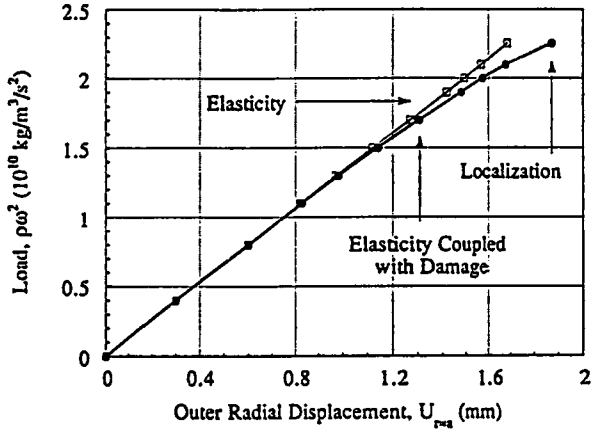

Fig. 6. Outer radial displacement as a function of the applied load ($\rho\omega^2$) obtained by a fully coupled computation and a decoupled computation up to localization ($\rho\omega^2 = 2{\cdot}26\ 10^{10}$ kg m^{-3} s^{-2}) for the ring with model No. 1. Note the stiffness softening.

Table 1a. Load levels ($\rho\omega^2$) at localization for the two structures and the two models predicted by the fully coupled approach

$\rho\omega^2$ (10^{10} kg m^{-3} s^{-2})	Disk	Ring
Model No. 0	0·59	0·71
Model No. 1	1·87	2·26

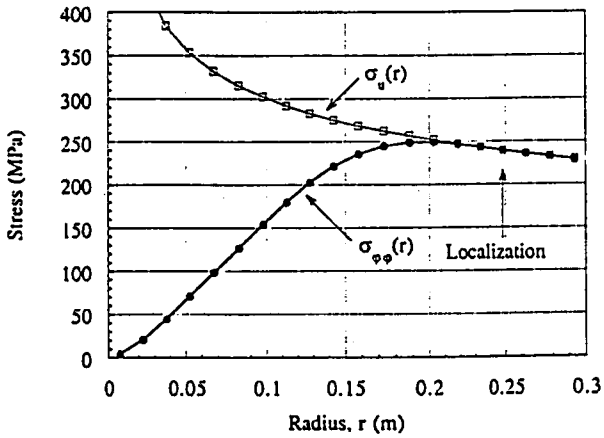

Fig. 7a. Hoop stress $\sigma_{\varphi\varphi}(r)$ as a function of the radius intersecting (see the arrow) the r-dependent ultimate tensile strength $\sigma_u(r)$ at localization ($\rho\omega^2 = 0{\cdot}59\ 10^{10}$ kg m^{-3} s^{-2}) for a fully coupled computation applied to the disk with model No. 0. Note the r-dependence of the ultimate tensile strength.

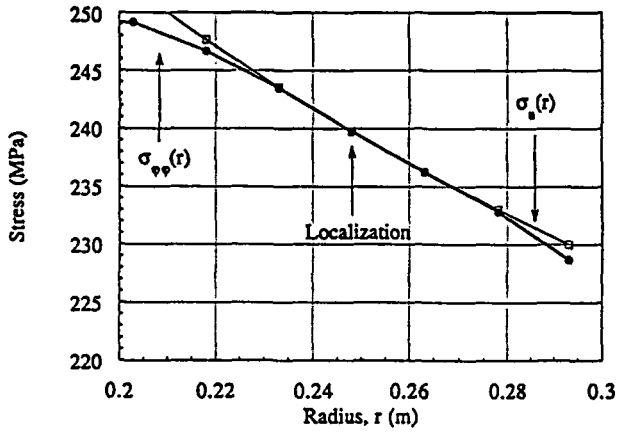

Fig. 7b. Zoom around the radius at localization of the hoop stress $\sigma_{\varphi\varphi}(r)$ as a function of the radius intersecting (see the arrow) the r-dependent ultimate tensile strength $\sigma_u(r)$.

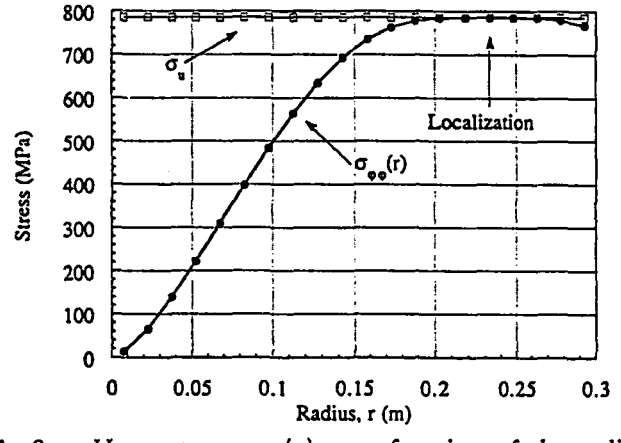

Fig. 8a. Hoop stress $\sigma_{\varphi\varphi}(r)$ as a function of the radius intersecting (see the arrow) the r-independent ultimate tensile strength σ_u at localization ($\rho\omega^2 = 1{\cdot}87$ kg m^{-3} s^{-2}) for a fully coupled computation applied to the disk with model No. 1. Note the r-independence of the ultimate tensile strength.

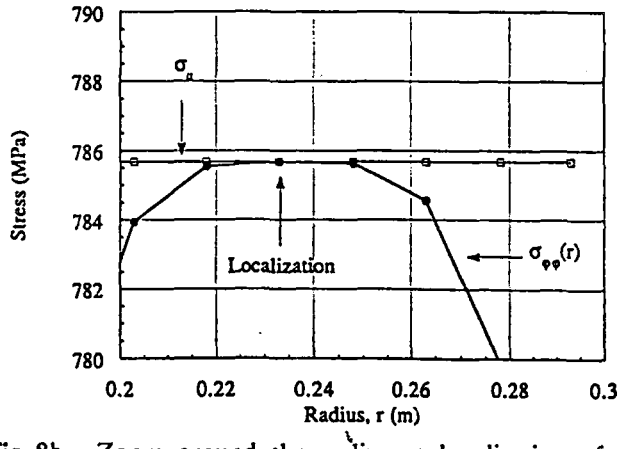

Fig. 8b. Zoom around the radius at localization of the hoop stress $\sigma_{\varphi\varphi}(r)$ as a function of the radius intersecting (see the arrow) the r-independent ultimate tensile strength σ_u.

rion (22.1) is shown in Figs 9 and 10 for model No. 0 and No. 1, respectively; note the different values for critical damage. In this case the localization point is very easy to spot compared to Figs 7 and 8.

Although the load levels in terms of $\rho\omega^2$ at localization are very different for model No. 0 and 1, it can be noticed that when the dimensionless parameter $\rho\omega^2 a^2/\sigma_u(r_{loc})$ is studied (where $\sigma_u(r_{loc})$ denotes the ultimate tensile strength at the localization radius) the results between model No. 0 and No. 1 come close together and the main change is given by the ratio b/a (Table 1b). In first approximation, a good estimate for the dimensionless parameter $\rho\omega^2 a^2/\sigma_u(r_{loc})$ is 2.1 for the disk ($b/a = 0{\cdot}0$) and 2·6 for the ring ($b/a = 0{\cdot}5$).

Finally, the accuracy of the numerical investigations is addressed. Figure 11 shows that the radius

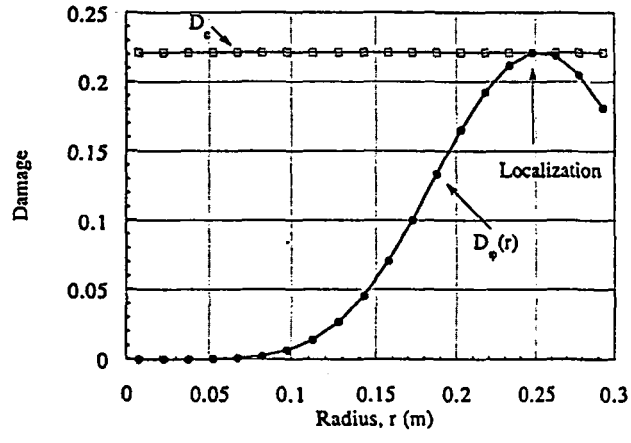

Fig. 9. Damage variable $D_\varphi(r)$ as a function of the radius intersecting (see the arrow) the critical damage value at localization ($\rho\omega^2 = 0{\cdot}59\ 10^{10}$ kg m^{-3} s^{-2}) for a fully coupled computation applied to the disk with model No. 0.

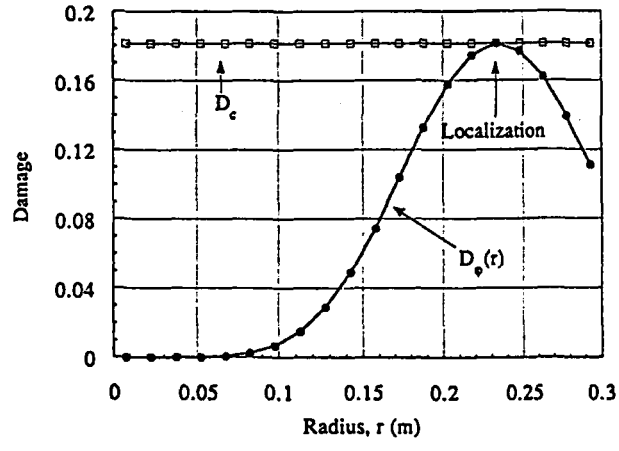

Fig. 10. Damage variable $D_\varphi(r)$ as a function of the radius intersecting (see the arrow) the critical damage value at localization ($\rho\omega^2 = 1{\cdot}87\ 10^{10}$ kg m^{-3} s^{-2}) for a fully coupled computation applied to the disk with mode No. 1.

at localization is well characterized over the range of loads exceeding the localization load level. On the other hand, in terms of damage at localization (Fig. 12) and hoop stress at localization (Fig. 13), localization needs to be spotted more precisely. This phenomenon is more important in terms of angle at localization (Fig. 14). In this case, the number of decimal positions to get an angle at localization of 89° (instead of 90°) is equal to 8!

In summary, from a numerical perspective, localization needs to be spotted very accurately,

Table 1b. Normalized load levels ($\rho\omega^2 a^2/\sigma_u(r_{loc})$) at localization of the two structures and the two models predicted by the fully coupled approach

$\rho\omega^2 a^2/\sigma_u(r_{loc})$	Disk	Ring
Model No. 0	2·2	2·7
Model No. 1	2·1	2·6

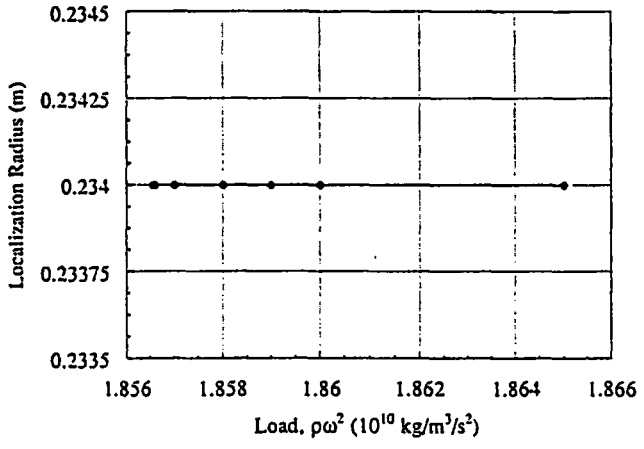

Fig. 11. Localization radius as a function of the load level, for a fully coupled computation applied to the disk with model No. 1.

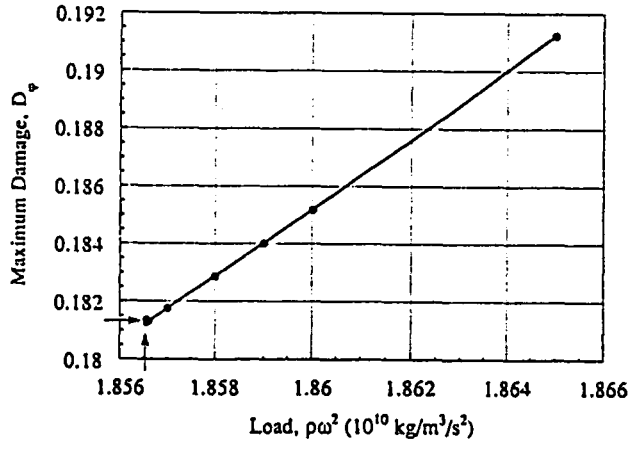

Fig. 12. Maximum damage at localization as a function of the load level, for a fully coupled computation applied to the disk with model No. 1.

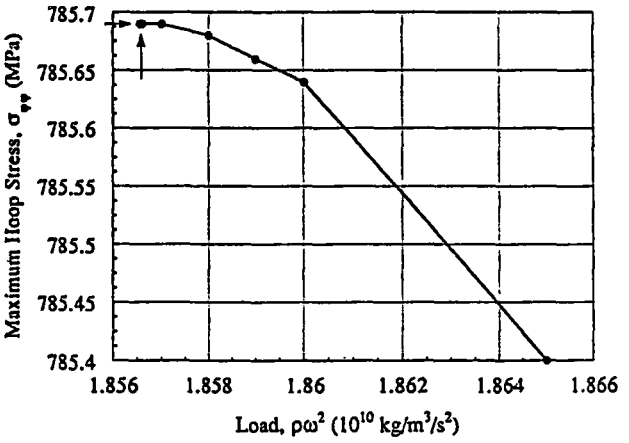

Fig. 13. Maximum hoop stress at localization as a function of the load level, for a fully coupled computation applied to the disk with model No. 1.

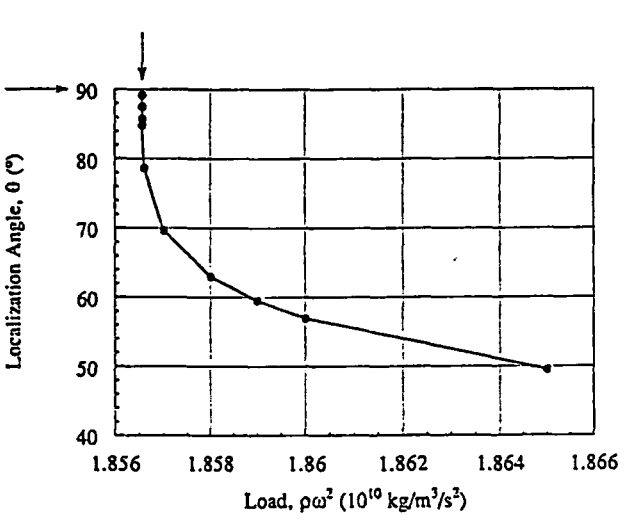

Fig. 14. Localization angle as a function of the load level, for a fully coupled computation applied to the disk with model No. 1.

especially in terms of angle at localization. This phenomenon is only due to numerical accuracy. Statistical fluctuations do not enter this problem since the constitutive laws (on a macroscale) are deterministic, although they are based upon statistical information (on a microscale). On a microscale, however, there will be statistical fluctuations leading to a post-localization behavior, strongly dependent on these fluctuations, whereas the pre-localization behavior will not lead to fluctuations.

4.2 Decoupled computations

In this sub-section, we will take advantage of the criterion (22.2) which does not require a fully coupled computation. Therefore a purely elastic set of computations has been carried out. The aim of this section is to compare the load levels predicted by the two types of approach. The results

are summarized in Table 2*a*. It can be noticed that all of the load levels at localization are lower for the decoupled analysis. This is due to redistribution, noticed earlier in Figs 7 and 8. Moreover, the error measured as the ratio of the difference between the decoupled angular speed and the fully coupled angular speed to the fully coupled angular speed is lower in the case of model No. 1. This is due to a lower stress redistribution at localization for model No. 1 since the value of critical damage is equal to 0·181 ($=1-\exp(-1/5)$) compared to model No. 0 for which the critical damage is equal to 0·221 ($=1-\exp(-1/4)$).

Again the load levels in terms of $\rho\omega^2$ at localization are very different for model No. 0 and No. 1, but in terms of the dimensionless parameter $\rho\omega_i^2a^2/\sigma_u(r_{loc})$, the results are very close and the main change is given by the ratio b/a (Table 2*b*). In first approximation, a good estimate for the dimensionless parameter $\rho\omega^2a^2/\sigma_u(r_{loc})$ is 2·0 ($b/a=0·0$) for the disk and 2·5 for the ring ($b/a=0·5$). These results constitute a lower bound when compared to the fully coupled results.

The maximum difference between the two models approaches is −6·1%, which is not significant. Therefore a decoupled computation gives good information of the loads that these kind of structures can support. Furthermore, due to the stress field redistribution, the decoupled approach gives conservative results of all of the analyzed cases. Therefore it constitutes a 'good' lower bound approximation of the models No. 0 and No. 1.

Table 2a. Load levels ($\rho\omega^2$) at localization for the two structures and the two models predicted by the decoupled approach, in parenthesis () is the difference in terms of angular velocity with the fully coupled approach

	$\rho\omega^2$ (10^{10} kg m^{-3} s^{-2})	
	Disk	Ring
Model No. 0	0·53 (−4·6%)	0·62 (−6·1%)
Model No. 1	1·75 (−3·1%)	2·05 (−4·5%)

Table 2b. Normalized load levels ($\rho\omega^2a^2/\sigma_u(r_{loc})$) at localization for the two structures and the two models predicted by the decoupled approach

	$\rho\omega^2a^2/\sigma_u(r_{loc})$	
	Disk	Ring
Model No. 0	2·1	2·5
Model No. 1	2·1	2·5

4.3 Comparison with a Weibull-type of analysis

In this sub-section we compare the load levels at localization, obtained by both approaches, to the cumulative failure probability obtained by modeling the material as an elastic brittle material. The conditions for first failure are determined at the load levels obtained previously. We assume that the disk and the ring are made of a monolithic ceramic whose characteristics are identical to that of the fibers (i.e. same m, σ_0, and r_0). This kind of analysis may be used to assess the reliability of these spinning structures, supposedly made of brittle material. In the framework of the weakest link assumption, the expression of the cumulative failure probability P_F is given by a Weibull expression[21]

$$P_F=1-\exp\left\{-\frac{h}{V_0}\int_S\left\{\frac{\sigma_{\varphi\varphi}}{\sigma_0}\right\}^m dA\right\} \tag{24}$$

where V_0 is the gauge volume ($V_0=h\pi r_0^2$), and h the disk or ring thickness. Using the same normalization as in the previous sections, the elastic stress field can be scaled by writing the hoop stress as follows

$$\sigma_{\varphi\varphi}(r)=(\rho\omega^2a^2)f(r) \tag{25}$$

where the function f is a dimensionless function. Since the function f depends only on the shape of the stress field and not on its level, it can characterize the stress field heterogeneity, and the cumulative failure probability can be rewritten as

$$P_F=1-\exp\left\{-\frac{A}{A_0}H_m\left(\frac{\rho\omega^2a^2}{\sigma_0}\right)^m\right\} \tag{26a}$$

where H_m is a generalized definition of the stress heterogeneity factor[33] associated with a Weibull law, and is defined as

$$H_m=\frac{1}{a^2-b^2}\int_b^a 2r\{f(r)\}^m dr. \tag{26b}$$

Note that if the hoop stress is homogeneous then H_m is equal to 1; otherwise, as the stress field gets more heterogeneous, H_m gets closer to zero. In the case of the disk $H_m=0·04$ and in the case of the ring $H_m=0·02$. The stress heterogeneity factors fully characterize the elastic stress field in terms of cumulative failure probability, i.e. in terms of reliability of these structures.

The results of cumulative failure probability for the same load levels as those predicted by the fully

coupled approach are summarized in Table 3. It can be noticed that the cumulative failure probabilities are very high. Therefore a design strategy using this kind of reliability assessment can expect quite high value in terms of the cumulative failure probability corresponding to the load levels at localization.

5 CONCLUSIONS

In the framework of Continuum Damage Mechanics, a localization criterion corresponds to the initiation of a macrocrack. Under certain hypotheses, the localization criterion can be rewritten in terms of a necessary and sufficient condition in terms of one component of the tangent operator. This result is applied to derive criteria at localization in terms of a critical damage value and a maximum normal stress for constitutive laws modeling the fiber breakage for unidirectionally reinforced ceramic matrix composites.

The constitutive laws are used to study axisymmetric spinning structures made of CMCs. Two approaches are analyzed. The fully coupled approach where the complete constitutive law is implemented in a FE code is compared to the decoupled approach, that consists of using an elastic computation. Indeed, one of the previous criteria can be used in an elastic computation. The result predicting localization are of the same order of magnitude. Furthermore, the decoupled approach gives conservative results in terms of load at localization, and the results in the analyzed structures are very close to those predicted by a fully coupled method. The fact that the decoupled approach gives conservative results is due to a stress redistribution when the fully coupled approach is used.

This kind of approach will also be carried out in the case of structures reinforced by fibers in two perpendicular directions. This enables us to look for an optimum volume fraction of fibers in terms of load at localization.

Table 3. Cumulative failure probability corresponding to the localization load levels obtained by the decoupled and fully coupled approaches

	P_F	
	Disk	Ring
Model No. 0	0·60	0·53
Model No. 1	1·00	1·00

ACKNOWLEDGEMENTS

The authors gratefully acknowledge the financial support of the US Air Force, through contract AFOSR-90-0132 with the Department of Mechanical and Environmental Engineering, University of California at Santa Barbara, and the support by the Advanced Research Project Agency, through the University Research Initiative.

REFERENCES

1. U.R.I., Proceedings University Research Initiative, University of California, Santa Barbara (1992).
2. Aveston, J., Cooper, G. A. & Kelly, A., Single and multiple fracture. In *Conf. Proceedings of the National Physical Laboratory: Properties of Fiber Composites*. IPC Science and Technology Press, Surrey, UK (1971).
3. Budiansky, B., Hutchinson, J. W. & Evans, A. G., Matrix fracture in fiber-reinforced ceramics. *J. Mech. Phys. Solids*, 34 (1986) 167–89.
4. Budiansky, B., Tensile strength of aligned-fiber composites. Proceedings University Research Initiative, Winter Study Group, University of California, Santa Barbara (1993).
5. Coleman, B. D., On the strength of classical fibers and fiber bundles. *J. Mech. Phys. Solids*, 7 (1958) 60–70.
6. Lemaitre, J., *A Course on Damage Mechanics*. Springer-Verlag, Berlin (1992).
7. Billardon, R. & Doghri, I., Prévision de l'amorçage d'une macro-fissure par la localisation de l'endommagement. *C. R. Acad. Sci. Paris*, 308 (II) (1989) 347–52.
8. Benallal, A., Billardon, R. & Geymonat, G., Localization phenomena at the boundaries and interfaces of solids. *Proc. 3rd Conf. on Constitutive Laws for Engineering Materials: Theory and Applications*, Tucson, AZ (1991).
9. Hadamard, J., *Leçon sur la propagation des ondes et les équations de l'hydrodynamique*, Paris (1903).
10. Hill, R., Acceleration waves in solids. *J. Mech. Phys. Solids*, 10 (1962) 1–16.
11. Mandel, J., Ondes plastiques dans un millieu indéfini à trois dimensions. *J. de Mécanique*, 1 (1) (1962) 3–30.
12. Rice, J. R., The localization of plastic deformations. *Proc. Theoretical and Applied Mechanics*, Koiter, W. T. (1976).
13. Borré, G. & Maier, G., On linear versus nonlinear flaw rules in strain localization analysis. *Meccanica*, 24 (1989) 36–41.
14. Rudnicki, J. W. & Rice, J. R., Conditions for localization of deformation in pressure-sensitive dilatant materials. *J. Mech. Phys. Solids*, 23 (1975) 371–94.
15. Rice, J. R. & Rudnicki, J. W., A note on some features of the theory of localization of deformation. *Int. J. Solids Struct.*, 16 (1980) 597–605.
16. Ortiz, M., Leroy, Y. & Needelman, A., A finite element method for localized failure analysis. *Comput. Meths Appl. Engng.*, 61 (1987) 189–214.
17. Hild, F., Larsson, P.-L. & Leckie, F. A., Localization due to damage in fiber reinforced composites. *Int. J. Solids Struct.*, 29 (24) (1992) 3221–38.

18. Krajcinovic, D. & Silva, M. A. G., Statistical aspects of the continuous damage theory. *Int. J. Solids Struct.*, **18** (7) (1982) 551–62.
19. Hult, J. & Travnicek, L., Carrying capacity of fiber bundles with varying strength and stiffness. *J. de Mécanique Théorique et Appliquée*, **2** (2) (1983) 643–57.
20. Hild, F., Larsson, P.-L. & Leckie, F. A., Localization due to damage in two-direction fiber-reinforced composites. *J. Appl. Mech.* (1992) accepted.
21. Weibull, W., A statistical theory of the strength of materials. *Ing. Vetenskap. Akad.*, **15** (1939).
22. Curtin, W. A., Theory of mechanical properties of ceramic matrix composites. *J. Am. Ceram. Soc.*, **74** (11) (1991) 2837–45.
23. Cox, H. L., The elasticity and the strength of paper and other fibrous materials. *Br. J. Appl. Phys.*, **3** (1952) 72–9.
24. Kelly, A., In *Strong Solids*. Oxford University Press, 2nd edn, Oxford University Press (1973).
25. Henstenburg, R. B. & Phoenix, S. L., Interfacial shear strength using single-filament-composite test. Part II: A probability model and Monte Carlo simulations. *Polym. Comp.*, **10** (5) (1989) 389–406.
26. Phoenix, S. L. & Raj, R., Scalings in fracture probabilities for a Brittle matrix fiber composite. *Acta Metall. Mater.*, **40** (11) (1992) 2813–28.
27. Curtin, W. A., Exact theory of fiber fragmentation in single-filament composite. *J. Mat. Sci.*, **26** (1991) 5239–53.
28. Hild, F., Domergue, J.-M., Evans, A. G. & Leckie, F. A., Tensile and flexural ultimate strength of fiber reinforced ceramic matrix composites. *Int. J. Solids Struct.*, **31** (7) (1994) 1035–45.
29. Phoenix, S. L., Statistical issues in the fracture of brittle matrix fibrous composites. *Comp. Sci. Tech.*, **48** (1993) 65–80.
30. Lemaitre, J., Micro-mechanics of crack initiation. *Int. J. Fract.*, **42** (1990) 87–99.
31. Hibbitt, H. D., Karlsson, B. I. & Sorenson, P., ABAQUS, version 5.2 (1992).
32. Jansson, S. & Leckie, F. A., The mechanics of failure of silicon carbide fiber-reinforced glass-matrix composites. *Acta Metall.*, **40** (11) (1993) 2967–78.
33. Hild, F., Billardon, R. & Marquis, D., Stress heterogeneity influence on failure of brittle materials. *C. R. Acad. Sci. Paris*, **315** (II) (1992) 1293–8.

APPENDIX 1

Model	No. 0	No. 1
F_1	$\dfrac{E_\varphi}{k(1-\nu_{r\varphi}^2(1-D_\varphi)k)}$	
F_2	$\dfrac{E_\varphi \nu_{r\varphi}(\nu_{r\varphi}\varepsilon_{rr}+\varepsilon_{\varphi\varphi})}{(1-\nu_{r\varphi}^2(1-D_\varphi)k)^2}$	
F_4	$\dfrac{E_\varphi \nu_{r\varphi}(1-D_\varphi)}{1-\nu_{r\varphi}^2(1-D_\varphi)k}$	
F_5	$\dfrac{E_\varphi(\nu_{r\varphi}\varepsilon_{rr}+\varepsilon_{\varphi\varphi})}{(1-\nu_{r\varphi}^2(1-D_\varphi)k)^2}$	
F_6	$\dfrac{E_\varphi(1-D_\varphi)}{1-\nu_{r\varphi}^2(1-D_\varphi)k}$	
$F_3^{(0)}$	$\dfrac{\dfrac{m}{f\sigma_0}\left\{\dfrac{\sigma_{\varphi\varphi}}{(1-D_\varphi^{(0)})f\sigma_0}\right\}^{m-1}}{1-m\left\{\dfrac{\sigma_{\varphi\varphi}}{(1-D_\varphi^{(0)})f\sigma_0}\right\}^{m}}$	
$F_3^{(1)}$		$\dfrac{\dfrac{m+1}{f\sigma_c}\left\{\dfrac{\sigma_{\varphi\varphi}}{(1-D_\varphi^{(1)})f\sigma_c}\right\}^{m}}{1-(m+1)\left\{\dfrac{\sigma_{\varphi\varphi}}{(1-D_\varphi^{(1)})f\sigma_c}\right\}^{m+1}}$

APPENDIX 2

Material parameters for the ceramic matrix fiber composite analyzed in the finite element calculations are:

$E_r = 20{\cdot}0$ GPa

$E_\varphi = 140{\cdot}0$ GPa

$G_{r\varphi} = 13{\cdot}0$ GPa

$\nu_{r\varphi} = 0{\cdot}0214$

$m = 4{\cdot}0$

$f\sigma_0 = 1450{\cdot}0$ MPa

$r_0 = 0{\cdot}002$ m

$f\sigma_c = 1300{\cdot}0$ MPa

$a = 0{\cdot}3$ m, $b = 0{\cdot}15$ m.

3.3.2 Endommagement et rupture de composites [0/90]

i Rupture des composites

par F. HILD, P.-L. LARSSON et F.A. LECKIE (1996).
ASME J. Appl. Mech., 63 (2), pp. 321-326.

F. Hild[1]
Department of Mechanical and Environmental Engineering, University of California, Santa Barbara, CA 93106-5070

P.-L. Larsson
Department of Solid Mechanics, Royal Institute of Technology, S-100 44 Stockholm, Sweden

F. A. Leckie
Department of Mechanical and Environmental Engineering, University of California, Santa Barbara, CA 93106-5070
Mem. ASME

Localization due to Damage in Two-Direction Fiber-Reinforced Composites

Fiber pull-out is one of the fracture features of fiber-reinforced ceramic matrix composites. The onset of this mechanism is predicted by using continuum damage mechanics, and corresponds to a localization of deformation. After deriving two damage models from a uniaxial bundle approach, different configurations are analyzed through numerical methods. For one model some very simple criteria can be derived, whereas for the second one none of these criteria can be derived and the general criterion of localization must be used.

1 Introduction

Ceramic matrix composites (CMCs) can either be reinforced by fibers in one direction or by fibers in two directions. The aim of this paper is to study composites reinforced with fibers in two perpendicular directions by extending a previous study on CMCs with fibers in one direction (Hild et al., 1992).

The rupture of most of the CMCs involves two separate failure mechanisms. The first mechanism is matrix cracking. The matrix cracks develop and their density saturates as the load level increases. The second mechanism is fiber breakage accompanied by fiber pull-out. Eventually, the final rupture will take place around one of the matrix cracks: it corresponds to *localized* fiber pull-out due to fiber breakage. The occurrence of this mechanism corresponds to the appearance of a macrocrack and will be described by a localization of deformation. The initiation of macrocracks in a structure during service often constitutes the early stage of the final failure of the structure. Starting from a material that is assumed free from any initial defect, the initiation of macrocracks can be predicted using continuum damage mechanics. The driving force is fiber breakage, which is accompanied by *distributed* pull-out. The approach using localization has successfully been used for ductile materials (Billardon and Doghri, 1989a, b; Doghri, 1989). The initiation stage is considered as the onset of a surface across which the velocity gradient is discontinuous. Under small deformation assumptions, this phenomenon is mainly driven by the damage mechanism that causes strain softening. For CMCs, the damage mechanism is related to fiber breakage, and the damage variable describes the percentage of broken fibers (Hild et al., 1992).

Although localization can be studied at the scale of fibers bonded to a matrix through an interface (Benallal et al., 1991a), i.e., at a micro level, localization also can be analyzed at a mesolevel, when the material is assumed to be homogeneous. Continuum damage mechanics, which represents a local approach to fracture (Benallal et al., 1991b), constitutes an efficient tool for this purpose. The progressive deterioration of the material is modeled by internal variables defined at the meso level. These variables are called *damage* variables. The damage state and the evolution of these variables is obtained through a uniaxial study based on fiber breakage (Coleman, 1958; Curtin, 1991). A two-dimensional plane-stress analysis is performed based on an extended model. The loss of uniqueness and the localization are studied for shear free states. A criterion referring to a critical value of the damage or to a maximum normal stress can describe the localization, which constitutes an objective criterion, from a design point of view.

2 Localization and Loss of Uniqueness

The failure at a meso level, with the initiation of a macrocrack, is defined as the bifurcation of the rate problem in certain modes, viz. the appearance of a surface across which the velocity gradient is discontinuous (Billardon and Doghri, 1989a). This phenomenon is referred to as *localization*, and corresponds to the failure of the ellipticity condition. The condition of localization can also be compared to the loss of uniqueness of the rate problem.

Stationary waves were studied by Hadamard (1903) in elasticity and by Hill (1962) and Mandel (1962) in elastoplasticity. Rice (1976) related the localization of plastic shear bands to jumps of the velocity gradient. Borré and Maier (1989) have given necessary and sufficient conditions for the onset of modes inside the body, and extended the results given by Rice (1976) and Rice and Rudnicki (1975, 1980).

Under small strain assumption and in elasticity coupled with damage, the behavior of a material is assumed to be described by the following piece-wise linear rate constitutive law:

$$\dot{\boldsymbol{\sigma}} = \begin{cases} \mathbf{E} : \dot{\boldsymbol{\epsilon}} & \text{if} \quad \dot{D} = 0 \\ \mathbf{H} : \dot{\boldsymbol{\epsilon}} & \text{if} \quad \dot{D} \neq 0 \end{cases} \tag{1}$$

where $\dot{\boldsymbol{\sigma}}$ and $\dot{\boldsymbol{\epsilon}}$, respectively, denote the stress and strain rates, $\mathbf{E}$ and $\mathbf{H}$ are fourth rank tensors, $\mathbf{E}$ is assumed to be positive definite, and D is either a single damage variable or a set of damage variables.

Localization occurs *inside* the body, *if and only if* (Rudnicki and Rice, 1975; Borré and Maier, 1989; Benallal et al., 1991a)

$$\text{Det}\,(\boldsymbol{n} \cdot \mathbf{H} \cdot \boldsymbol{n}) = 0 \quad \text{for a vector } \boldsymbol{n} \neq 0 \quad \text{and at a point inside a structure } \Omega. \tag{2}$$

[1] Visiting Postgraduate Researcher, also at the Laboratoire de Mécanique et Technologie, E.N.S. de Cachan/C.N.R.S./Universite Paris 6, 61 avenue du Président Wilson, F-94235 Cachan Cedex, France.

Contributed by the Applied Mechanics Division of THE AMERICAN SOCIETY OF MECHANICAL ENGINEERS for publication in the ASME JOURNAL OF APPLIED MECHANICS.

Discussion on this paper should be addressed to the Technical Editor, Professor Lewis T. Wheeler, Department of Mechanical Engineering, University of Houston, Houston, TX 77204-4792, and will be accepted until four months after final publication of the paper itself in the ASME JOURNAL OF APPLIED MECHANICS.

Manuscript received by the ASME Applied Mechanics Division, Feb. 25, 1992; final revision, Oct. 8, 1993. Associate Technical Editor: G. J. Dvorak.

This criterion corresponds to the failure of the ellipticity condition of the rate equilibrium equation; it also can be used as an indicator of the local failure of the material, at a meso scale (Billardon and Doghri, 1989a).

Furthermore, any loss of uniqueness, considered as bifurcation of the rate boundary value problem, is excluded provided

$$\dot{\boldsymbol{\sigma}} : \dot{\boldsymbol{\epsilon}} > 0. \tag{3}$$

In this study, the quantity that defines loss of uniqueness and localization is the linear tangent modulus $\mathbf{H}$. In the following, we analyze loss of uniqueness and loss of ellipticity (i.e., localization) for states when

$$\begin{cases} \epsilon_{11} = \alpha \epsilon_{22} \\ \epsilon_{12} = 0. \end{cases} \tag{4}$$

The parameter α is referred to as the strain ratio and its inverse is denoted by β. These particular states only are considered. When the hypothesis of Eq. (4) is satisfied, the nonvanishing components of the vector $\boldsymbol{n}$ are n_1 and n_2, and the matrix $\mathbf{A} = \boldsymbol{n} \cdot \mathbf{H} \cdot \boldsymbol{n}$ reduces to (Ortiz et al., 1987)

$$\mathbf{A} = \begin{bmatrix} n_1^2 H_{1111} + n_2^2 H_{1212} & n_1 n_2 (H_{1212} + H_{1122}) \\ n_1 n_2 (H_{1212} + H_{2211}) & n_1^2 H_{1212} + n_2^2 H_{2222} \end{bmatrix}. \tag{5}$$

If we rewrite $(n_1, n_2) = (\cos\theta, \sin\theta)$, $X = \tan^2\theta$, then the localization condition is equivalent to finding real positive roots of the following equation:

$$aX^2 + bX + c = 0 \tag{6}$$

with

$$\begin{aligned} a &= H_{1212} H_{2222} \\ b &= H_{1111} H_{2222} - H_{1122} H_{2211} - H_{1122} H_{1212} - H_{2211} H_{1212} \\ c &= H_{1212} H_{1111}. \end{aligned} \tag{7}$$

If real positive roots are found, then the localization direction is perpendicular to the vector $(n_1, n_2, 0) = (\cos\theta, \sin\theta, 0)$, characterized by the angle θ (Fig. 1). The values of H_{1111}, H_{2222}, H_{1122}, H_{2211} and H_{1212} are model dependent and specific models are now developed.

3 Constitutive Laws

This section is concerned with the development of two constitutive laws in the case of CMCs reinforced in two perpendicular directions. At constant temperature, the behavior of a CMC reinforced by unidirectional fibers in the x_2-direction (see Fig. 1) can be characterized by the Helmholtz free energy density ψ_2, which is a function of the state variables ϵ_{11}, ϵ_{22}, ϵ_{12}, and the damage variable D_2 in the x_2-direction

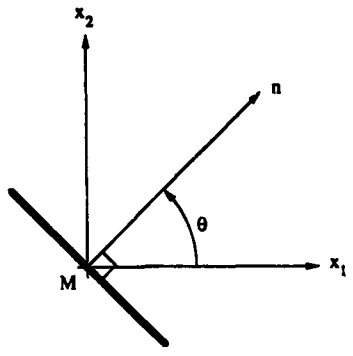

Fig. 1 Localization mode

$$\rho\psi_2 = \rho\psi(\epsilon_{11}, \epsilon_{22}, \epsilon_{12}, D_2, f_2, k_2), \tag{8}$$

where D_2 represents the fiber degradation in the x_2-direction, E_2 the Young's modulus in the x_2-direction, ν_{12} the Poisson's ratio, k_2 the ratio of the Young's modulus in the fiber direction (E_2) to the Young's modulus in the transverse direction (E_1), and G_{12} the shear modulus. It is worth noting that the elastic quantities depend on the volume fraction of fibers. The expression for the general Helmholtz free energy density ψ is given by

$$\rho\psi(x, y, z, d, f, k) = \frac{E_2(f)}{2}\left[\frac{x^2 + 2\nu_{12}k(1-d)xy + ky^2}{k\{1 - \nu_{12}^2 k(1-d)\}}\right] + 2G_{12}z^2 \tag{9}$$

where ρ is the material density, x, y, z are dummy variables representing strains, d damage, f volume fraction, and k Young's moduli ratio. The stresses and the thermodynamic force Y_2 associated to the damage variable D_2 are derived from the Helmholtz free energy density ψ_2 as follows:

$$\sigma_{11} = \rho\frac{\partial\psi_2}{\partial\epsilon_{11}} \quad \sigma_{22} = \rho\frac{\partial\psi_2}{\partial\epsilon_{22}} \quad 2\sigma_{12} = \rho\frac{\partial\psi_2}{\partial\epsilon_{12}}$$

$$Y_2 = \rho\frac{\partial\psi_2}{\partial D_2}. \tag{10}$$

The explicit expressions for the stresses related to the strains and the damage variable modeling the fiber degradation in the x_2-direction are given by

$$\begin{aligned} \sigma_{11} &= \frac{E_2}{k_2[1 - \nu_{12}^2(1-D_2)k_2]}[\epsilon_{11} + \nu_{12}(1-D_2)k_2\epsilon_{22}] \\ \sigma_{22} &= \frac{E_2(1-D_2)}{1 - \nu_{12}^2(1-D_2)k_2}(\epsilon_{22} + \nu_{12}\epsilon_{11}) \\ \sigma_{12} &= 2G_{12}\epsilon_{12}. \end{aligned} \tag{11}$$

The damage state of fibers in the x_2-direction, D_2 can be related to the stress (and is denoted by $D_2^{(1)}$) or strain state (and is denoted by $D_2^{(2)}$). The relationship is either implicit in terms of the normal stress in the x_2-direction (model #1)

$$D_2^{(1)} = 1 - \exp\left[-\left\{\frac{\sigma_{22}}{(1 - D_2^{(1)})f_2\sigma_c}\right\}^{m+1}\right]$$

$$\text{if} \quad \epsilon_{22} > 0 \quad \text{and} \quad \dot{\epsilon}_{22} > 0 \tag{12}$$

where m is the shape parameter of a Weibull law (Weibull, 1939), σ_c the characteristic strength (Henstenburg and Phoenix, 1989), and f_2 is the volume fraction of fibers in the x_2-direction; or explicit in terms of the normal strain in the x_2-direction (model #2)

$$D_2^{(2)} = 1 - \exp\left[-\left(\frac{\epsilon_{22}}{\epsilon_c}\right)^{m+1}\right]$$

$$\text{if} \quad \epsilon_{22} > 0 \quad \text{and} \quad \dot{\epsilon}_{22} > 0 \tag{13}$$

where ϵ_c is related to the characteristic strength σ_c by $\sigma_c = E_F\epsilon_c$ (E_F is the Young's modulus of the fibers). Both models describe the same material behavior when subjected to uniaxial tension. However, the models give different predictions for multiaxial loading states (Hild et al., 1992). It is worth noting that the damage evolution laws are a priori independent of the volume, since we assume that the local behavior of the fiber degradation is not dependent on the total length of the fiber (Curtin, 1991). This type of behavior is observed when *distributed* pull-out happens in conjunction with fiber breakage, and it can be shown that in most practical cases, the statistics driving the fiber breakage is independent of the total length of the composite. On the

other hand, if the composite length becomes very small, a length dependence is found again (Hild et al., 1994), and in this case the evolution of the damage variable is mainly given by a fiber-bundle-type of behavior, which leads to replacing $m + 1$ by m, the characteristic strength σ_c by $\sigma_0(L/L_0)^{-1/m}$, where σ_0 is the scale parameter of a Weibull law, and the scale strain ϵ_c by $\epsilon_0(L/L_0)^{-1/m}$, where L_0 is the gauge length at which the scale parameter has been identified, and $\sigma_0 = E_f\epsilon_0$. Since the results are the same for both damage evolution laws when the previous permutation is used, we will just express them in the case when the model is length independent, which is the most relevant in practice.

If the fibers are in the x_1-direction then the breakage can be modeled by a damage variable denoted by D_1. Using Eq. (9), the Helmholtz free energy density $\rho\psi_1$ is given by

$$\rho\psi_1 = \rho\psi(\epsilon_{22}, \epsilon_{11}, \epsilon_{12}, D_1, f_1, k_1). \tag{14}$$

If the fibers are in both x_1 and x_2-directions, then we assume as a first approximation that the total specific Helmholtz free energy $\rho\psi_{12}$ is given by a law of mixture of the Helmholtz free energy densities in the x_1 and in the x_2-directions

$$\rho\psi_{12} = (1 - f)\rho\psi_1 + f\rho\psi_2 \tag{15}$$

where f is the fraction of fibers in the x_2-direction ($f = f_2/(f_1 + f_2)$, and where f_1 and f_2 are the volume fraction of fibers in the x_1 and x_2-direction, respectively). This assumption also corresponds to a Lin-Taylor Hypothesis. The evolution of the stresses is given by

$$\sigma_{11} = \rho\frac{\partial\psi_{12}}{\partial\epsilon_{11}} = (1 - f)S_{11} + fS_{12}$$

$$\sigma_{22} = \rho\frac{\partial\psi_{12}}{\partial\epsilon_{22}} = (1 - f)S_{21} + fS_{22}$$

$$\sigma_{12} = \frac{1}{2}\rho\frac{\partial\psi_{12}}{\partial\epsilon_{12}} = 2G_{12}\epsilon_{12} \tag{16}$$

where the explicit expression for S_{ij} is given in Appendix A, and the corresponding thermodynamic forces associated to the two *independent* damage variables D_1 and D_2 are

$$Y_1 = \rho\frac{\partial\psi_{12}}{\partial D_1} = (1 - f)\rho\frac{\partial\psi_1}{\partial D_1}$$

$$Y_2 = \rho\frac{\partial\psi_{12}}{\partial D_2} = f\rho\frac{\partial\psi_2}{\partial D_2}. \tag{17}$$

Again, the evolution of the damage variables can either be implicit in terms of the respective normal stresses (model #1)

$$D_1^{(1)} = 1 - \exp\left[-\left\{\frac{\sigma_{11}}{(1 - D_1^{(1)})f_1\sigma_c}\right\}^{m+1}\right]$$

$$\text{if} \quad \epsilon_{11} > 0 \quad \text{and} \quad \dot{\epsilon}_{11} > 0$$

$$D_2^{(1)} = 1 - \exp\left[-\left\{\frac{\sigma_{22}}{(1 - D_2^{(1)})f_2\sigma_c}\right\}^{m+1}\right]$$

$$\text{if} \quad \epsilon_{22} > 0 \quad \text{and} \quad \dot{\epsilon}_{22} > 0 \tag{18}$$

or explicit in terms of the respective normal strains (model #2)

$$D_1^{(2)} = 1 - \exp\left[-\left(\frac{\epsilon_{11}}{\epsilon_c}\right)^{m+1}\right] \quad \text{if} \quad \epsilon_{11} > 0 \quad \text{and} \quad \dot{\epsilon}_{11} > 0$$

$$D_2^{(2)} = 1 - \exp\left[-\left(\frac{\epsilon_{22}}{\epsilon_c}\right)^{m+1}\right]$$

$$\text{if} \quad \epsilon_{22} > 0 \quad \text{and} \quad \dot{\epsilon}_{22} > 0. \tag{19}$$

It is worth noting that we assume that the statistical properties of the fibers are supposed to be identical in both directions. This hypothesis will be maintained throughout the paper since generalization would be straightforward. Both models are studied for shear free states when the strain ratio α (see Eq. (4)), and thus its inverse β are given.

3.1 Failure Criteria for Model #1. For model #1, the evolution of the damage variables is implicit in the sense that $D_1^{(1)}$ (respectively $D_2^{(1)}$) is a function of the normal stress σ_{11} (respectively σ_{22}) *and* the damage variable $D_2^{(1)}$ (respectively $D_2^{(1)}$) itself. The evolution is therefore computed by a numerical scheme based upon a Newton method. To study localization and loss of uniqueness, we need to compute the tangent operator, which takes the following form:

$$H_{1111} = \frac{[(1 - f)F_{11} + fF_{12}](1 + fF_{52}F_{72}) - fF_{22}F_{72}[(1 - f)F_{41} + fF_{42}]}{[1 + fF_{21}F_{72}](1 + fF_{52}F_{72}) - f(1 - f)F_{22}F_{72}F_{51}F_{71}}$$

$$H_{2222} = \frac{[(1 - f)F_{61} + fF_{62}][1 + (1 - f)F_{21}F_{71}] - (1 - f)F_{51}F_{71}[(1 - f)F_{41} + fF_{42}]}{[1 + fF_{21}F_{72}](1 + fF_{52}F_{72}) - f(1 - f)F_{22}F_{72}F_{51}F_{71}}$$

$$H_{1122} = \frac{[(1 - f)F_{41} + fF_{42}](1 + fF_{52}F_{72}) - fF_{22}F_{72}[(1 - f)F_{61} + fF_{62}]}{[1 + fF_{21}F_{72}](1 + fF_{52}F_{72}) - f(1 - f)F_{22}F_{72}F_{51}F_{71}}$$

$$H_{2211} = \frac{[(1 - f)F_{41} + fF_{42}][1 + (1 - f)F_{21}F_{71}] - (1 - f)F_{51}F_{71}[(1 - f)F_{11} + fF_{12}]}{[1 + fF_{21}F_{72}](1 + fF_{52}F_{72}) - f(1 - f)F_{22}F_{72}F_{51}F_{71}}$$

$$H_{1212} = 2G_{12} \tag{20}$$

where the explicit expressions for F_{ij} are given in Appendix B.

The loss of uniqueness and localization are investigated when the fiber fraction f and the strain ratio α vary. Although analytical results cannot be derived from criterion (2) in the general case, some simple results can be found when f is equal to 0 or 1. In these cases, the criteria derived by Hild et al. (1992) apply. If f is equal to 0 (fibers only in the x_1-direction), then localization and loss of uniqueness occur at the same load level when

$$D_1^{(1)} = D_c = 1 - \exp\left(\frac{-1}{m + 1}\right)$$

$$\sigma_{11} = \sigma_{u1} = f_1\sigma_c\left(\frac{1}{(m + 1)e}\right)^{1/(m+1)}$$

$$Y_1 = Y_c = \frac{\sigma_{u1}^2}{2E_1(1 - D_c)^2} \tag{21}$$

where the stress σ_{u1} corresponds to the ultimate tensile strength in the x_1-direction. It is worth noting that the three previous criteria are easier to compute than the general criterion (2). The direction of localization is $\theta = 0$ deg, i.e., a localization surface perpendicular to the fiber direction.

If f is equal to 1, the same kind of result apply and the direction of localization is $\theta = 90$ deg, i.e., a localization surface again perpendicular to the fiber direction. When $f \neq 0$ and $f \neq 1$, these results cannot be proved. However the computations show that loss of uniqueness and localization can be described very accurately by the two following criteria:

$$\text{Max}(D_1^{(1)}, D_2^{(1)}) = D_c = 1 - \exp\left(\frac{-1}{m+1}\right) \quad (22)$$

$$\sigma_{11} = \sigma_{u1} \quad \text{or} \quad \sigma_{22} = \sigma_{u2} \quad (23)$$

when the fiber properties are the same in the two directions. The maximum error is .5 percent in terms of criteria (22) and (23).

Criterion (22) shows that for model #1, maximum damage at localization depends only on the Weibull exponent of the fibers. Furthermore, criterion (23) shows that the maximum normal stress σ_{11} (respectively σ_{22}) depends only on the volume fraction of fibers in the x_1 (respectively x_2-) direction and on the fiber characteristics. This result is consistent with some experimental observations on woven carbon matrix composites reinforced with SiC (Nicalon) fibers (Heredia et al., 1992). On the other hand, the localization angle is dependent on the fiber percentage f (see Fig. 2). When the fiber percentage f and the sign of the strains ϵ_{11} and ϵ_{22} are constant, the variation of the localization angle is due to the fact that the maximum tensile stress is either reached in the x_1 or in the x_2-direction.

Moreover, if the strain ratio α is different from 0 and 1 then there is a complete symmetry of the results. If the strain ratio α is positive, the strains ϵ_{11} and ϵ_{22} are positive, changing α into β, f_2 into f_1, changes f into $1 - f$, and alters the absolute value of the localization angle $|\theta|$ into $\pi/2 - |\theta|$ and keeps the maximum stresses and damage levels constant. These two properties are referred to as *symmetry properties*, and are mainly due to the features of Eqs. (4), (8), (14), and (15).

When the strain ratio α is equal to 1 and the fiber percentage f is equal to .5, the localization angle is undetermined. This is due to the vanishing of the three constants a, b, and c in Eq. (6), for $H_{1111} = H_{1122} = H_{2211} = H_{2222} = 0$. Any value of the angle θ satisfies Eq. (6). This phenomenon can be observed when the fiber percentage f is different from 1: if $\sigma_{11} = \sigma_{u1}$ and $\sigma_{22} = \sigma_{u2}$ simultaneously, then $D_1^{(1)} = D_2^{(1)} = D_c$, and $H_{1111} = H_{1122} = H_{2211} = H_{2222} = 0$. This particular result shows that in terms of this model, for a given strain ratio α, it is possible to optimize locally a CMC reinforced by fibers in two perpendicular directions. Indeed, in terms of fiber breakage, a condition $\sigma_{11} = \sigma_{u1}$ and $\sigma_{22} = \sigma_{u2}$ leads to an optimum of the fiber behavior in both directions.

Model #1 constitutes a straightforward generalization of the fiber bundle models studied by Krajcinovic and Silva (1982), and Hult and Travnicek (1983). Finally, a shear stress has no influence on all the previous results since we assumed no coupling between the damage variables and the shear strain or stress for both model #1 and #2.

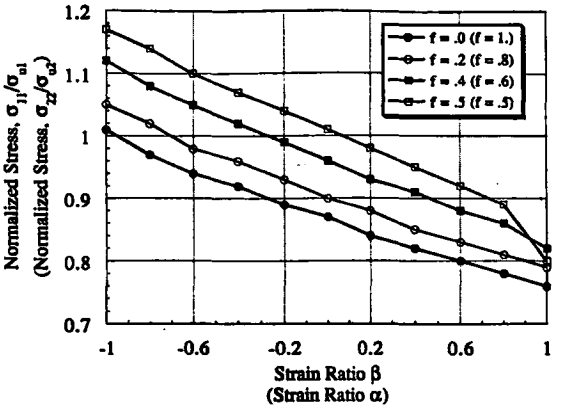

Fig. 3 Normalized maximum stress at localization for model #2, the main caption of the axes corresponds to the case where $f_2 = .5$, $f_1 = .0$, .125, .333, .5, and the captions in brackets correspond to the cases where $f_1 = .5$, $f_2 = .0$, .125, .333, .5

3.2 Study of Localization With Model #2. For model #2, the evolution of the damage variables is explicit and therefore is easier to compute. The tangent operator takes the form

$$H_{1111} = (1-f)(F_{11} - F_{21}F_{31}) + fF_{12}$$
$$H_{2222} = (1-f)F_{62} + f(F_{42} - F_{52}F_{32})$$
$$H_{1122} = (1-f)F_{41} + f(F_{42} - F_{22}F_{32})$$
$$H_{2211} = (1-f)(F_{41} - F_{21}F_{31}) + fF_{42}$$
$$H_{1212} = 2G_{12} \quad (24)$$

where the explicit expressions for F_j are given in Appendix B. As shown in the case of fibers in only one direction (Hild et al., 1992), the localization criterion cannot be described by some simple criteria as those given by model #1. When fibers are in both directions the latter results are confirmed. A first consequence is that an optimization procedure can be performed since the maximum stress at localization, and the maximum damage at localization are dependent on both the strain ratio α and on the fiber percentage f.

Since the elastic law given in Eqs. (16) is identical for both models, the symmetry properties apply also for model #2 (see Figs. 3, 4, and 5). It can also be noticed that the maximum stress at localization varies with the fiber fraction f and with the strain ratio α.

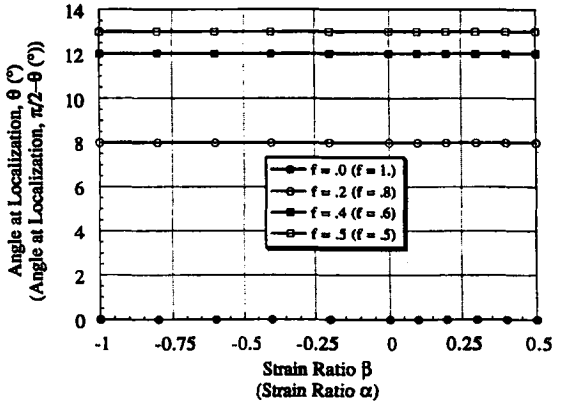

Fig. 2 Absolute value of the localization angle in degrees at localization for model #1, the main caption of the axes corresponds to the case where $f_2 = .5$, $f_1 = .0$, .125, .333, .5, and the captions in brackets correspond to the cases where $f_1 = .5$, $f_2 = .0$, .125, .333, .5

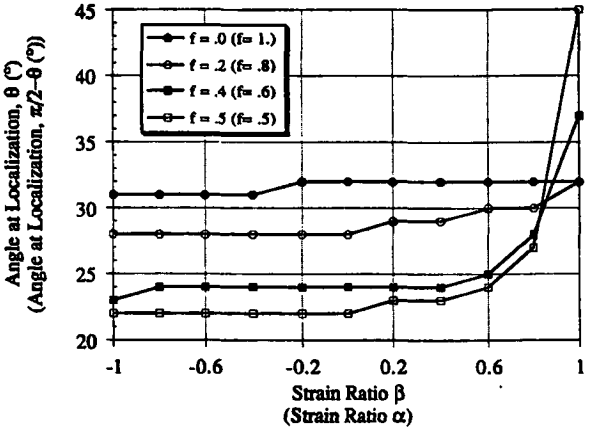

Fig. 4 Absolute value of the localization angle in degrees for model #2, the main caption of the axes corresponds to the case where $f_2 = .5$, $f_1 = .0$, .125, .333, .5, and the captions in brackets correspond to the cases where $f_1 = .5$, $f_2 = .0$, .125, .333, .5

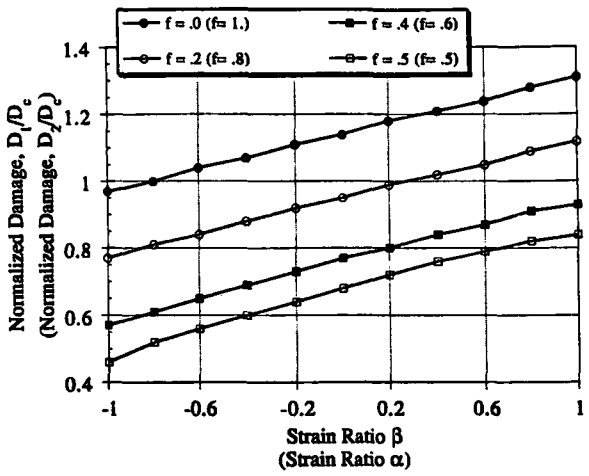

Fig. 5 Maximum normalized damage value at localization (m = 4.) for model #2, the main caption of the axes corresponds to the case where f_2 = .5, f_1 = .0, .125, .333, .5, and the captions in brackets correspond to the cases where f_1 = .5, f_2 = .0, .125, .333, .5

In the experiments reported by Heredia et al. (1992) the stress at localization was given by the ultimate tensile strength corresponding to the volume fraction of fibers in the same direction. This is not found by using model #2. Indeed, in a tensile test, when $f_1 = f_2 = .5$ the maximum stress σ_{22} normalized by the ultimate tensile strength σ_{u2} is given by .63, whereas the same tensile test when $f_1 = .0$ and $f_2 = .5$ would give a normalized tensile strength σ_{22}/σ_{u2} equal to 1. On the other hand, the damage at localization D_2 normalized by the critical damage D_c is equal to 1.04 when $f_1 = .5$ and $f_2 = .5$ and is equal to 1. when $f_1 = .0$ and $f_2 = .5$.

It is too early to draw a final conclusion, but it seems that the predictions of model #1 correspond more to reality than those of model #2. On the other hand, model #2 turned out to give results very close to model #1 when applied to structures with fibers in one direction (Hild et al., 1992). This will be addressed in the case of structures with fibers in two perpendicular directions such as spinning disks.

4 Conclusions

Using a one-dimensional study of fiber breakage modeled by a single damage variable, two models are derived. Both of them are then generalized to a two-dimensional plane stress analysis, with fibers in two perpendicular directions. Whereas model #1 constitutes a straightforward generalization of the elementary study, model #2 exhibits different features. Indeed, loss of uniqueness and localization can be described by some very simple criteria referring to Continuum Damage Mechanics for model #1. Conversely, these simple criteria do not apply for model #2. Physically, model #1 gives a better description of some experimental trends observed in the case of a carbon matrix reinforced with silicon carbide (Nicalon) fibers in two perpendicular directions. On the other hand, model #2 is easier to compute, and when applied to the study of spinning disc with fibers in one direction, it leads to load levels at localization of the same order of magnitude as model #1 (Hild et al., 1992).

Lastly, this study shows that the localization for model #1 can be described by using criterion (23) derived from the general criterion of localization (2). This criterion can also be used for a computation in elasticity and may turn out to be sufficient in first approximation to predict load levels at which a macrocrack initiates, instead of using a computation in elasticity coupled with damage.

5 Acknowledgments

The authors gratefully acknowledge the financial support of the U.S. Air Force through contract AFOSR-90-0132 with the Department of Mechanical and Environmental Engineering, University of California at Santa Barbara, and the DARPA University Research Initiative with the University of California at Santa Barbara (ONR contract N00014-86-K0753).

References

Benallal, A., Billardon, R., and Geymonat, G., 1991a, "Localization Phenomena at the Boundaries and Interfaces of Solids," *3rd Conference on Constitutive Laws for Engineering Materials: Theory and Applications*, C. S. Desai and G. Franlziskonis, eds., Tucson, AZ, Jan.

Benallal, A., Billardon, R., and Lemaitre, J., 1991b, "Continuum Damage Mechanics and Local Approach to Fracture: Numerical Procedures," *Comp. Meth. in Appl. Mech. and Eng.*, Vol. 92, pp. 141–155.

Billardon, R., and Doghri, I., 1989a, "Prévision de l'amorçage d'une macrofissure par la localisation de l'endommagement," *C. R. Acad. Sci. Paris*, Vol. 308, Serie II, pp. 347–352.

Billardon, R., and Doghri, I., 1989b, "Localization Bifurcation Analysis for Damage Softening Elasto-Plastic Materials," *Strain Localization and Size Effect due to Cracking and Damage*, J. Mazars and Z. P. Bazant eds., Elsevier, New York, pp. 295–307.

Borré, G., and Maier, G., 1989, "On Linear versus Nonlinear Flaw Rules in Strain Localization Analysis," *Meccanica*, Vol. 24, 36–41.

Coleman, B. D., 1958, "On the Strength of Classical Fibers and Fiber Bundles," *J. Mech. Phys. Solids*, Vol. 7, pp. 60–70.

Curtin, W. A., 1991, "Theory of Mechanical Properties of Ceramic-Matrix Composites," *J. Am. Ceram. Soc.*, Vol. 74, No. 11, pp. 2837–2845.

Doghri, I., 1989, "Etude de la localisation de l'endommagement," Thèse de l'Université Paris 6, May.

Hadamard, J., 1903, *Leçon sur la propagation des ondes et les équations de l'hydrodynamique*, Librairies scientifiques A. Hermann, Paris.

Heredia, F. E., Spearing, S. M., Evans, A. G., Mosher, P., and Curtin, W. A., 1992, "Mechanical Properties of Carbon Matrix Composites Reinforced with Nicalon Fibers," *J. Am. Ceram. Soc.*, Vol. 75, No. 11, pp. 3017–3025.

Henstenburg, R. B., and Phoenix, S. L., 1989, "Interfacial Shear Strength Studies Using the Single-Filament-Composite Test. Part II: A Probability Model and Monte-Carlo Simulations," *Polym. Comp.*, Vol. 10, No. 5, pp. 389–406.

Hild, F., Larsson, P.-L., and Leckie, F. A., 1992, "Localization Due to Damage in Fiber Reinforced Composites," *Int. J. Solids Struct.*, Vol. 29, No. 4, pp. 3221–3238.

Hild, F., Domergue, J.-M., Evans, A. G., and Leckie, F. A., 1994, "Tensile and Flexural Ultimate Strength of Fiber Reinforced Ceramic-Matrix Composites," *Int. J. Solids Struct.*, Vol. 31, No. 7, pp. 1035–1045.

Hill, R., 1962, "Acceleration Waves in Solids," *J. Mech. Phys. Solids*, Vol. 10, pp. 1–16.

Hult, J., and Travnicek, L., 1983, "Carrying Capacity of Fiber Bundles with Varying Strength and Stiffness," *Journal de Mécanique Théorique et Appliquée*, Vol. 2, No. 2, pp. 643–657.

Krajcinovic, D., and Silva, M. A. G., 1982, "Statistical Aspects of the Continuous Damage Theory," *Int. J. Solids Struct.*, Vol. 18, No. 7, pp. 551–562.

Mandel, J., 1962, "Ondes Plastiques dans un Milieu Indéfini à Trois Dimensions," *J. de Mécanique* Vol. 1, No. 1, pp. 3–30.

Ortiz, M., Leroy, Y., and Needelman, A., 1987, "A Finite Element Method for Localized Failure Analysis," *Comput. Meths. Appl. Eng.*, Vol. 61, pp. 189–214.

Rice, J. R., 1976, "The Localization of Plastic Deformations," *Theoretical and Applied Mechanics*, W. T. Koiter, ed., Elsevier, New York, pp. 207–220.

Rice, J. R., and Rudnicki, J. W., 1980, "A Note on Some Features of the Theory of Localization of Deformation," *Int. J. Solids Struct.*, Vol. 16, pp. 597–605.

Rudnicki, J. W., and Rice, J. R., 1975, "Conditions for Localization of Deformation in Pressure-Sensitive Dilatant Materials," *J. Mech. Phys. Solids*, Vol. 23, pp. 371–394.

Weibull, W., 1939, "A Statistical Theory of the Strength of Materials," *Ingeniörsvetenskapakademiens*, Handlingar Nr 151.

Appendix A

$$k_1 = \frac{E_2(f_1)}{E_1}$$

$$k_2 = \frac{E_2(f_2)}{E_1}$$

$$S_{11} = \frac{E_2(f_1)(1 - D_1)}{1 - \nu_{12}^2(1 - D_1)k_1}(\epsilon_{11} + \nu_{12}\epsilon_{22})$$

$$S_{12} = \frac{E_2(f_2)}{k_2[1 - \nu_{12}^2(1 - D_2)k_2]}[\epsilon_{11} + \nu_{12}(1 - D_2)k_2\epsilon_{22}]$$

$$S_{21} = \frac{E_2(f_1)}{k_1[1 - \nu_{12}^2(1 - D_1)k_1]}[\epsilon_{22} + \nu_{12}(1 - D_1)k_1\epsilon_{11}]$$

$$S_{22} = \frac{E_2(f_2)(1 - D_2)}{1 - \nu_{12}^2(1 - D_2)k_2}(\epsilon_{22} + \nu_{12}\epsilon_{11})$$

Appendix B

$$F_{11} = \frac{E_2(f_1)(1 - D_1)}{1 - \nu_{12}^2(1 - D_1)k_1}$$

$$F_{12} = \frac{E_2(f_2)}{k_2(1 - \nu_{12}^2(1 - D_2)k_2)}$$

$$F_{21} = \frac{E_2(f_1)(\nu_{12}\epsilon_{11} + \epsilon_{22})}{(1 - \nu_{12}^2(1 - D_1)k_1)^2}$$

$$F_{22} = \frac{E_2(f_2)\nu_{12}(\nu_{12}\epsilon_{11} + \epsilon_{22})}{(1 - \nu_{12}^2(1 - D_2)k_2)^2}$$

$$F_{41} = \frac{E_2(f_1)\nu_{12}(1 - D_1)}{1 - \nu_{12}^2(1 - D_1)k_1}$$

$$F_{42} = \frac{E_2(f_2)\nu_{12}(1 - D_2)}{1 - \nu_{12}^2(1 - D_2)k_2}$$

$$F_{51} = \frac{E_2(f_1)\nu_{12}(\nu_{12}\epsilon_{11} + \epsilon_{22})}{(1 - \nu_{12}^2(1 - D_1)k_1)^2}$$

$$F_{52} = \frac{E_2(f_2)(\nu_{12}\epsilon_{11} + \epsilon_{22})}{(1 - \nu_{12}^2(1 - D_2)k_2)^2}$$

$$F_{61} = \frac{E_2(f_1)}{k_1(1 - \nu_{12}^2(1 - D_1)k_1)}$$

$$F_{62} = \frac{E_2(f_2)(1 - D_2)}{1 - \nu_{12}^2(1 - D_2)k_2}$$

$$F_{31} = \frac{m + 1}{\epsilon_c}\left(\frac{\epsilon_{11}}{\epsilon_c}\right)^m \exp\left[-\left(\frac{\epsilon_{11}}{\epsilon_c}\right)^{m+1}\right]$$

$$F_{32} = \frac{m + 1}{\epsilon_c}\left(\frac{\epsilon_{22}}{\epsilon_c}\right)^m \exp\left[-\left(\frac{\epsilon_{22}}{\epsilon_c}\right)^{m+1}\right]$$

$$F_{71} = \frac{\dfrac{m + 1}{f_1\sigma_c}\left[\dfrac{\sigma_{11}}{(1 - D_1)f_1\sigma_c}\right]^m}{1 - (m + 1)\left[\dfrac{\sigma_{11}}{(1 - D_1)f_1\sigma_c}\right]^{m+1}}$$

$$F_{72} = \frac{\dfrac{m + 1}{f_2\sigma_c}\left[\dfrac{\sigma_{22}}{(1 - D_2)f_2\sigma_c}\right]^m}{1 - (m + 1)\left[\dfrac{\sigma_{22}}{(1 - D_2)f_2\sigma_c}\right]^{m+1}}$$

ii Applications à des structures tournantes

par F. HILD et F.A. LECKIE (1995).
Actes ASME TURBO EXPO '95, Houston, TX (USA), ASME.

FIBER DISTRIBUTION IN REINFORCED CERAMIC ROTATING DISCS

Francois Hild
Laboratoire de Mécanique et Technologie
E.N.S. Cachan
Cachan Cedex, France

Frederick A. Leckie
Department of Mechanical and Environmental Engineering
University of California, Santa Barbara
Santa Barbara, California

ABSTRACT

Fiber pull-out of fiber reinforced brittle matrix composites is an indication of final failure. The onset of this failure mechanism can be predicted using Continuum Damage Mechanics. After deriving a damage model from a uniaxial approach, different configurations are analyzed through analytical and numerical (F.E. calculations) methods. An extension to fibers in two perpendicular directions is proposed and the failure strength of a rotating disc structure is estimated. The results of the calculations are used to define an optimal fiber distribution in the radial and circumferential directions.

1. INTRODUCTION

The aim of this paper is to study the failure by fracture of fiber reinforced brittle matrix composites and to analyze an optimal fiber distribution. One of the features of the behavior of these composites is fiber pull-out due to fiber breakage. The occurrence of this mechanism is assumed to be described by the appearance of a macro-crack and will be described by a localization of the deformations. The initiation of macro-cracks in a structure during service often constitutes the early stage of the final failure of the structure. Starting from a material that is assumed free from any macro initial defect, the initiation of macro-cracks can be predicted using Continuum Damage Mechanics. The initiation stage is considered as the onset of a surface across which the velocity gradient is discontinuous. Under small deformations assumption, this phenomenon is mainly driven by the damage mechanism that causes strain-softening. For ceramic matrix composites, the damage mechanism is related to the percentage of broken fibers.

Although localization can be studied at the scale of fibers bonded to a matrix through an interface [1], i.e., at a micro-level, localization can also be analyzed at a meso-level, where the material behavior is homogenized. Continuum Damage Mechanics, which represents a local approach to fracture, constitutes an efficient tool for this purpose. The progressive deterioration of the material is modeled by an internal variable defined at the meso-level. This variable is called *damage*. The damage state and the evolution of this variable are obtained through a uniaxial study based on fiber breakage [2]. A 2-D plane stress analysis is performed based on an extended model. A criterion referring to a critical value of the damage can describe the failure which constitutes an objective criterion, from a design point of view. An extension to the case of fibers in two directions is proposed, based on a law of mixture in terms of the specific Helmholtz free energy.

This approach is also used to study a spinning disc made of a fiber reinforced ceramic matrix composite. The same criterion is implemented and studied through Finite Element computations. An extension to fibers in two perpendicular directions is proposed and an optimal fiber distribution is discussed in the case of the spinning structure.

2. UNIAXIAL BEHAVIOR

This section is concerned with the development of a single damage variable model for tensile behavior of unidirectional fiber reinforced ceramic matrix composites. A schematic stress-strain diagram is shown in Fig. 1 for such a specimen. The micro-structural phenomena responsible for the features of curve 0ABC are now discussed. On initial loading from point 0 to A of Fig. 1 the

Presented at the International Gas Turbine and Aeroengine Congress and Exposition
Houston, Texas - June 5-8, 1995

composite behaves as a virgin, i.e. undamaged, elastic material with modulus E. Further loading from point A to B causes cracking of the matrix. The cracks traverse the entire load bearing section within the homogeneously stressed region. Further loading along BC involves further development of matrix cracks, which involves two processes. First the process of fiber debond, both at the front of the crack and in its wake, which is necessary to cause the stresses to redistribute. The second process is fiber failure, which precedes the process of fiber pull-out.

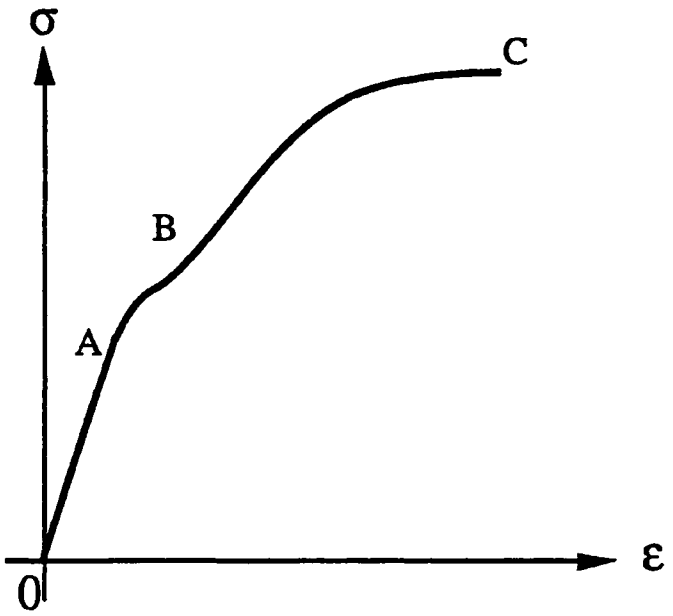

FIGURE 1. SCHEMATIC UNIAXIAL STRESS-STRAIN CURVE OF A FIBER REINFORCED BRITTLE MATRIX COMPOSITE.

The characteristics of fiber failure are determined by a statistical distribution of fiber strength [2]. This single mechanism is the *only* one considered in this study. Future development can be carried out by modeling the matrix cracking process and the fiber pull-out mechanism.

The model is based upon the assumption that the nominal stress applied to a bundle of fibers in parallel can be expressed in terms of a damage variable, denoted by D = r/n, where r is the number of failed fibers and n is the total number contained within the load bearing cross-section. This type of approach has been applied to perfectly brittle fiber systems [3-4]. It is shown that the nominal applied stress s is related to the uniaxial strain ε by

$$s = E\,(1-D)\,\varepsilon = \tilde{E}\,\varepsilon \qquad (1)$$

where E is the Young's modulus of each unbroken fiber and $\tilde{E}$ the Young's modulus of the damaged bundle. If the nominal stress is the total current load divided by the total initial fiber area, then the average stress in the unbroken fibers is

$$\tilde{\sigma} = \frac{\sigma}{1-D} \qquad (2)$$

This later expression refers to the concept of effective stress [5-6]. Although the nominal stress does not always increase with the applied strain ε, the stress in the unbroken fibers, $\tilde{\sigma}$, does increase whatever the applied strain, ε. Two regimes can be exhibited depending on the fiber length , and we are going to study both of them. We assume that the fiber failure probability, $P_F(\tilde{\sigma})$, at a stress $\tilde{\sigma}$ is given by a Weibull distribution [7]

$$P_F(\tilde{\sigma}) = 1 - \exp\left[-\frac{L}{L_0}\left(\frac{\tilde{\sigma}}{\sigma_0}\right)^m\right] \qquad (3.1)$$

where σ_0 is the scale parameter of the in-situ fibers, m is the shape parameter, L is the fiber length, and L_0 is a gauge length for which m and σ_0 were identified. This first expression corresponds to the behavior of a fiber bundle, and will be referred to as model #0. On the other hand, due to interfacial sliding characterized by a shear stress t, the fiber failure probability can be written as

$$P_F(\tilde{\sigma}) = 1 - \exp\left[-\left(\frac{\tilde{\sigma}}{\sigma_1}\right)^{m+1}\right] \qquad (3.2)$$

where σ_1 is the characteristic strength multiplied by the fiber volume fraction [8]. This second expression takes consideration of the interfacial properties between fibers and matrix, and will be referred to as model #1. The ratio r/n characterized by damage variable D is

$$r/n = D = P_F(\tilde{\sigma}) \qquad (4)$$

This definition is consistent with the bounded values of D for which D=0 for no failed fiber and D=1 for complete failure of all fibers. The damage is thus related to the nominal stress by

$$D = 1 - \exp\left[-\frac{L}{L_0}\left\{\frac{\sigma}{(1-D)\sigma_0}\right\}^m\right] \text{ if } \varepsilon>0 \text{ and } \dot{\varepsilon}>0 \quad \text{(model \#0)} \qquad (4.1)$$

$$D = 1 - \exp\left[-\left\{\frac{\sigma}{(1-D)\sigma_1}\right\}^{m+1}\right] \text{ if } \varepsilon > 0 \text{ and } \dot{\varepsilon} > 0 \quad \text{(model \#1)} \qquad (4.2)$$

The peak in the stress-strain plane (σ,ε) coincides with a critical value of damage

$$D = D_C = 1 - \exp(-1/m) \quad \text{(model \#0)} \quad (5.1)$$
$$D = D_C = 1 - \exp(-1/(m+1)) \quad \text{(model \#1)} \quad (5.2)$$

It can be noticed that the critical value of the damage is always *independent of* the fiber length, L. Conversely, the maximal nominal stress σ_{0M} may *depend upon* the length L for small volumes

$$\sigma_{0M} = \sigma_0 \left(\frac{L_0}{meL}\right)^{1/m} \quad \text{(model \#0)} \quad (6.1)$$
$$\sigma_{0M} = \sigma_1 \left[\frac{1}{e(m+1)}\right]^{1/(m+1)} \quad \text{(model \#1)} \quad (6.2)$$

The critical value of damage, D_C, is *only* related to the shape parameter m by Equ. (5) and is therefore a material dependent parameter. Conversely, σ_{0M} may depend upon the length of the fibers, so that it is not a material parameter.

Finally, as it has been underlined above, this model does not consider fiber pull-out. Thus this model constitutes a *lower* bound estimate up to the maximal nominal stress is reached, for a strain-controlled test. If the test is stress-controlled, then the point for which $\sigma = \sigma_{0M}$ constitutes the ultimate stable point.

3. 2-D STUDY WITH FIBERS IN ONE DIRECTION

This section deals with the study of a 2-D model extending the ideas of the previous section. The fibers are assumed to be parallel to the 2-direction. An analytical and numerical approach is studied.

3.1. Analytical study

In elasticity, under the plane stress hypothesis, with the small strain assumption, the relationship between stresses and strains is given by

$$\begin{bmatrix}\varepsilon_{11}\\ \varepsilon_{22}\\ \varepsilon_{12}\end{bmatrix} = \begin{bmatrix} 1/E_1 & -\nu_{21}/E_2 & 0 \\ -\nu_{12}/E_1 & 1/E_2 & 0 \\ 0 & 0 & 1/2G_{12}\end{bmatrix}\begin{bmatrix}\sigma_{11}\\ \sigma_{22}\\ \sigma_{12}\end{bmatrix} \quad (7)$$

When fiber breaking in the 2-direction is considered, the damage state is described by damaged elastic constants $\tilde{E}_1$, $\tilde{E}_2$, ν_{12}, $\tilde{\nu}_{21}$, $\tilde{G}_{12}$ instead of E_1, E_2, ν_{12}, ν_{21}, G_{12} respectively. The Young's modulus E_2 is no longer constant but depends upon the degradation of the fibers characterized by D_2 to become $\tilde{E}_2 = E_2(1-D_2)$: it is a straightforward extension of Equ. (2). Since the effect of pulling in the 1-direction is unaltered by the presence of the breaks in the fiber in the 2-direction, ν_{12} is equal to ν_{12}. Finally we assume that $\tilde{E}_1 = E_1$ (no effect of the damage D_2 in the 1-direction) and that $\tilde{G}_{12} = G_{12}$ (the shear properties are slightly altered by fiber failure).[9] We suppose also that the material is hyperelastic so that

$$\frac{\tilde{\nu}_{21}}{\tilde{E}_2} = \frac{\tilde{\nu}_{12}}{\tilde{E}_1} \quad (8)$$

It can then be shown that $\tilde{\nu}_{21} = \nu_{21}(1-D_2)$, and if $D_2 = 0$ then the behavior is purely elastic and is described by Equ. (8). if there is a damage evolution then the relationships between strains and stresses are given by

$$\sigma_{11} = \frac{E_2}{k[1-\nu_{12}^2(1-D_2)k]}[\varepsilon_{11}+\nu_{12}(1-D_2)k\varepsilon_{22}] \quad (9.1)$$
$$\sigma_{22} = \frac{E_2(1-D_2)}{1-\nu_{12}^2(1-D_2)k}(\nu_{12}\varepsilon_{11}+\varepsilon_{22}) \quad (9.2)$$
$$\sigma_{12} = 2G_{12}\varepsilon_{12} \quad (9.3)$$

where $k = E_2/E_1$ is referred to as the Young's moduli ratio. As mentioned in section 2, the damage state of fibers in the 2-direction, D_2, can be related to the stress state through an implicit relationship

$$D_2 = 1 - \exp\left[-\frac{L}{L_0}\left\{\frac{\sigma_{22}}{(1-D_2)\sigma_0}\right\}^m\right] \text{ if } \varepsilon_{22} > 0 \text{ and } \dot{\varepsilon}_{22} > 0$$
(model \#0) (9.4.1)

$$D_2 = 1 - \exp\left[-\left\{\frac{\sigma_{22}}{(1-D_2)\sigma_1}\right\}^{m+1}\right] \text{ if } \varepsilon_{22} > 0 \text{ and } \dot{\varepsilon}_{22} > 0$$
(model \#1) (9.4.2)

The initiation criterion is given by

$$D_2 = D_C \quad (10.1)$$

Since Equ. (10.1) implies that σ_{22} is constant and equals σ_{0M}, another criterion may be

$$\sigma_{22} = \sigma_{0M} \quad (10.2)$$

This model gives the same results as those found in a uniaxial approach and constitutes a straightforward generalization to 2-D cases.

3.2. F.E.M. analysis: spinning disc

The geometry of the problem is shown in Fig. 2. Here ω represents the angular rotation speed, with dimension rad/s. In the present setting, the stress state is axisymmetric, at least up to the point where localization occurs, and hence a cylindrical coordinate system is introduced in Fig. 2 It is

assumed that the fibers are oriented in the circumferential direction and coordinates x_1 and x_2 in the previous section are replaced with r and φ, respectively. The stress-strain relationship becomes

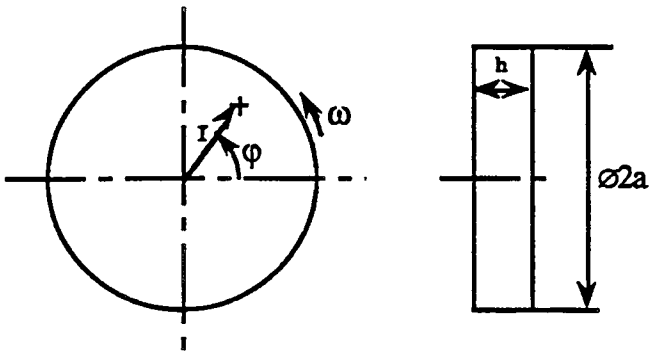

FIGURE 2. THE GEOMETRY OF THE CIRCULAR DISC (a = .3 m, h = .01 m).

$$\sigma_r = \frac{E_\varphi}{k[1-\nu_{r\varphi}^2(1-D_\varphi)k]}[\varepsilon_r+\nu_{r\varphi}(1-D_\varphi)k\varepsilon_\varphi] \qquad (11.1)$$

$$\sigma_\varphi = \frac{E_\varphi(1-D_\varphi)}{1-\nu_{r\varphi}^2(1-D_\varphi)k}(\nu_{r\varphi}\varepsilon_r+\varepsilon_\varphi) \qquad (11.2)$$

in obvious notations. It should be remembered that no shear stress $\sigma_{r\varphi}$ is present due to axisymmetry. The expression for the damage parameter, D_φ, in the circumferential direction is in this problem either r-dependent (model #0)

$$D_{\varphi 0} = 1- \exp\left[-\frac{r}{L_0}\left\{\frac{\sigma_\varphi}{(1-D_\varphi)\sigma_0}\right\}^m\right] \text{ if } \varepsilon_{\varphi\varphi} > 0$$

$$\text{and } \dot{\varepsilon}_{\varphi\varphi} > 0 \qquad (12.1)$$

or r-independent (model #1)

$$D_{\varphi 1} = 1- \exp\left[-\left\{\frac{\sigma_\varphi}{(1-D_\varphi)\sigma_1}\right\}^{m+1}\right] \quad \text{if } \varepsilon_{\varphi\varphi} > 0$$

$$\text{and } \dot{\varepsilon}_{\varphi\varphi} > 0 \qquad (12.2)$$

In the relation (12.1), L_0 is a material constant representing the length dependence of the problem, while all the other parameters are defined earlier.

To describe completely the axisymmetric boundary value problem, small strains kinematics and equilibrium equations have also to be introduced. At this stage, it proved impossible to derive a closed-form solution for the stress state and for the damage variable. Instead the problem was solved using the finite element method. The constitutive relations were implemented into a standard finite element code ABAQUS [10], and a solution was sought for by discretizing the problem using 2-node axisymmetric shell elements.

The material analyzed is a ceramic matrix composite with E_r = 20 GPa, E_φ = 140 GPa, $G_{r\varphi}$ = 13 GPa, $\nu_{r\varphi}$ = .0214, m = 4 for model 0 and σ_0 = 1450 MPa, m = 3, σ_1 = 1293 MPa, L_0 = .002 m for model 1, and the geometry of the disc is chosen with practical applications in mind, namely a = .3 m and h = .01 m.

In Fig. 3 the stress field is plotted as a function of the radial coordinate r at failure when $\rho\omega^2 = .55\ 10^{10}$ kg/m^3/s^2. A comparison is made with an elastic solution when the effect of damage is ignored. As could be expected, the introduction of damage reduces the maximum nominal stress acting within the disc and causes a redistribution of the whole stress field. Similar results are obtained for model 1.

Failure occurs when r has the approximate value .248 m for model #0, and .234 m for model #1. The failure speeds are

$$\rho\omega_0^2 = .58598\ 10^{10} \text{ kg/m}^3/\text{s}^2$$

$$\rho\omega_1^2 = 1.7076\ 10^{10} \text{ kg/m}^3/\text{s}^2$$

It can be observed from the results the strong role played by the constitutive equations.

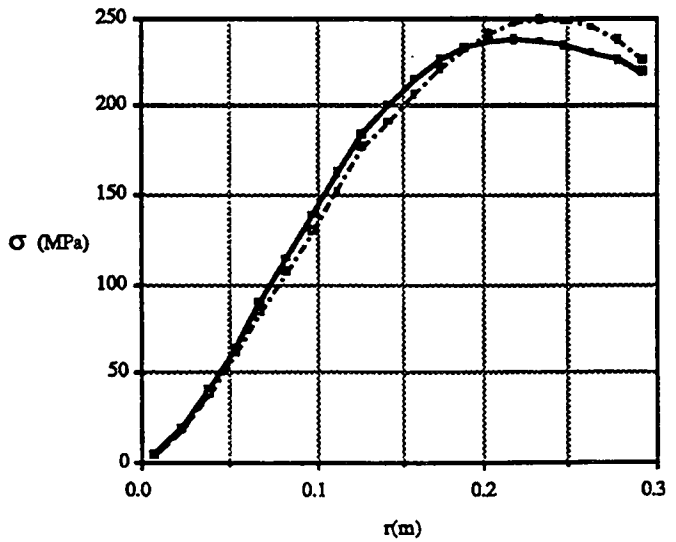

FIGURE 3. HOOP STRESS, Σ_ϑ, AS A FUNCTION OF THE RADIAL COORDINATE R, $P\Omega^2 = .55\ 10^{10}$ KG/M^3/S^2, (——▫——) DAMAGE MODEL #0, AND (·-·-▪-·-·) LINEAR ELASTIC MODEL WHEN $D_\vartheta = 0$.

4. 2-D STUDY WITH FIBERS IN TWO PERPENDICULAR DIRECTIONS

In this section the composite consists of a brittle matrix reinforced by fibers in two perpendicular directions. The constitutive equations for materials reinforced in two directions have been derived in Ref. 9 and contain damage in the radial and circumferential directions. The same structure and material as in section 3.2 are analyzed (E_M = 20 GPa, E_F = 140. GPa, G_{MF} = 13 GPa, ν_{MF} = .0214, m = 4 for model 0 and σ_0 = 1450 MPa, m = 3, σ_1 = 1293 MPa, L_0 = .002 m for model 1, a = .3 m, and h = .01 m). In the present setting, the stress state is axisymmetric, at least up to the point where failure occurs, and hence a cylindrical coordinate system is introduced. It is assumed that the fibers are oriented in the radial and circumferential directions, and coordinates x_1 and x_2 in the previous section are replaced with r and φ respectively. The volume fraction of fibers in the ϕ direction is f of the total number of fibers. In this first analysis, we assume that there is an r-dependence in the hoop direction, which corresponds to the length of the fiber. Strictly speaking, the damage law in the r direction should be dependent on an integral length, and whilst it is possible for this effect to be included, the calculations are much more complex and it is assumed that the length is a. The expression for the damage variables D_r and D_φ are given by (model #0)

$$D_{r0} = 1 - \exp\left[-\frac{a}{L_0}\left\{\frac{\sigma_r}{(1-D_r)\sigma_0}\right\}^m\right] \text{ if } \varepsilon_{rr} > 0 \text{ and } \dot{\varepsilon}_{rr} > 0$$

$$D_{\varphi 0} = 1 - \exp\left[-\frac{r}{L_0}\left\{\frac{\sigma_\varphi}{(1-D_\varphi)\sigma_0}\right\}^m\right] \text{ if } \varepsilon_{\varphi\varphi} > 0 \text{ and } \dot{\varepsilon}_{\varphi\varphi} > 0$$

To describe completely the axisymmetric boundary value problem, small strains kinematics and equilibrium equations have also to be introduced. Again, it proved impossible to derive a closed-form solution for the stress state and for the damage variable. Instead the problem was solved using the finite element code ABAQUS [10]. The results of the computations are given in table 1.

TABLE 1
COMPUTATIONS FOR THE CIRCULAR DISC WITH DIFFERENT VOLUME FRACTION RATIOS (MODEL #0)

Volume fraction ratio f	1.	.9	.8	.7	.6	.55
$\rho\omega_0^2$ at failure (10^{10} kg/m^3/s^2)	.586	.672	.747	.817	.883	.914
$f\rho\omega_0^2 a^2/\sigma_{0M}$ (r_{loc})	2.2	2.2	2.2	2.0	1.8	1.7

In this part, the strength is independent in the r direction according to model #1.

$$D_{r1} = 1 - \exp\left[-\left\{\frac{\sigma_r}{(1-D_r)\sigma_1}\right\}^m\right] \text{ if } \varepsilon_{rr} > 0 \text{ and } \dot{\varepsilon}_{rr} > 0$$

$$D_{\varphi 1} = 1 - \exp\left[-\left\{\frac{\sigma_\varphi}{(1-D_\varphi)\sigma_1}\right\}^m\right] \text{ if } \varepsilon_{\varphi\varphi} > 0 \text{ and } \dot{\varepsilon}_{\varphi\varphi} > 0$$

The results of the computations are given in Table 2.

TABLE 2.
COMPUTATIONS FOR THE CIRCULAR DISC WITH DIFFERENT VOLUME FRACTION RATIOS (MODEL #1)

Volume fraction ratio f	1.	.9	.8	.7	.6	.55
$\rho\omega_1^2$ at failure (10^{10} kg/m^3/s^2)	1.708	1.918	2.080	2.194	2.234	2.202
$f\rho\omega_1^2 a^2/\sigma_{0M}$ (r_{loc})	2.2	2.2	2.1	1.9	1.7	1.5

The strong dependence of the form of the constitutive law on the failure speed is then evident with the failure speed being increased by a factor of 150%. This illustrates the importance of using the correct model. Model 0 is likely to be appropriate when the fiber matrix interface is strong and model 1 when the interface is weak. The optimum volume fraction f is 0.6.

5. CONCLUSIONS

Using a one-dimensional study of fiber breaking modeled by a single damage variable, a one-dimensional model is derived. This model is then generalized to a 2-D plane stress analysis with fibers in two directions. The model has been applied to determining the strength of spinning discs.The constitutive models for which the strength is independent of length predict failure speeds which are 50% higher than those calculated assuming that the fiber strength is length dependent. The optimal distribution of fibers is that 60% of the total fibers should be in the circumferential direction

6. ACKNOWLEDGMENTS

The authors gratefully acknowledge the financial support of the U.S. Air Force through contract AFOSR-90-0132 with the Department of Mechanical and Environmental Engineering, University of California, Santa Barbara.

7. REFERENCES

1. Benallal, A., Billardon, R., and Geymonat, G., 3rd Conference on Constitutive Laws for Engineering Materials: Theory and Applications, Tucson, AZ, January 1991.
2. Coleman, B.D., *J. Mech. Phys. Solids* 7, pp. 60-70 (1958).
3. Krajcinovic, D., and Silva, M.A.G., *Int. J. Solids Structures* **18** [7], pp. 551-562 (1982).
4. Hult, J., and Travnicek, L., *Journal de Mécanique Théorique et Appliquée* 2 [2], pp. 643-657 (1983).
5. Rabotnov, Y.N., in *Progress in Applied Mechanics*, Prager Anniversary Vol., McMillan, New-York, 307 (1963).
6. Lemaitre, J., and Chaboche, J.-L., in *Mechanics of Solid Materials*. Cambridge University Press. Cambridge (1990).
7. Weibull, W., *Ing. Vetens. Akad.*, Handlingar Nr 151 (1939).
8. Curtin, W.A., *J. Am. Ceram. Soc.*, **74** [11], pp. 2837-2845 (1991).
9. Hild, F., Larsson, P.L. and Leckie, F.A., *Int. J. Solids Struct.*, 31 [7] 1035–45 (1994).
10. ABAQUS, Hibitt, H.D., Karlsson, B.I. and Sorenson, P., Inc., version 4.8 (1989).

3.4 Perspectives

Tous les exemples traités dans ce chapitre montrent que, bien que les modèles développés soient obtenus par des dialogues entre différentes échelles, la phénoménologie garde une place importante. L'utilisation de la phénoménologie est déplacée mais n'est pas absente. Ceci est vrai pour les matériaux monolithiques (céramiques techniques) mais également pour les composites à fibres longues ou courtes. En particulier, le comportement de l'interface fait appel à des modèles tout aussi phénoménologiques que la plasticité mésoscopique par exemple. Certains parallèles sont d'ailleurs assez frappants.

En ce qui concerne la modélisation du comportement mécanique à l'impact de céramiques, le modèle proposé reste à valider sur différentes configurations. Ce travail est en cours et constitue une partie de la thèse de C. DENOUAL. D'autre part, la base probabiliste présentée ici peut constituer un complément au modèle « d'endommagement retardé » développé au LMT-Cachan dans l'étude du comportement au choc de matériaux composites [LADEVÈZE, 1995 ; DEÜ, 1997]. La partie liée à la dégradation en compression reste à écrire. La difficulté liée à ce comportement est que plusieurs mécanismes peuvent être actifs. Le premier mécanisme est la fissuration sous-critique en compression qui conduit à la rupture finale en compression [LANKFORD, 1981 ; 1991]. Cependant, suivant la microstructure de la céramique (et plus précisément le type de joint de grain rencontré et la taille des grains), on peut observer de la microplasticité dans le cas d'alumines [LONGY et CAGNOUX, 1989 ; COSCULLUELA, 1992] ou de nitrure de silicium [LANKFORD, 1996]. Quant au carbure de silicium, plus particulièrement analysé dans le paragraphe 3.1, il semblerait que la plasticité ne puisse pas se développer de manière significative, même pour des niveaux de contrainte rencontrés dans le cas d'impacts sur structures. Des concepts développés dans le paragraphe 3.1.2 devraient pouvoir être étendus au cas de la compression.

Les composites à matrice fragile tels que ceux étudiés dans ce document n'auront d'intérêt que s'ils peuvent être utilisés à des hautes températures. Un des problèmes est alors de connaître et surtout de modéliser leur comportement au fluage. Une première application, non développée dans ce document, a été menée pour l'étude du comportement mécanique à haute température de composites à base de carbure de silicium [BURR *et al.*, 1996b]. On notera qu'une autre approche a été développée au LMT-Cachan en faisant appel à la notion, plus mésoscopique, de « visco-endommagement » [ROSPARS *et al.*, 1997]. Ce type d'analyse devra également être élargi aux composites, plus prometteurs, à base d'oxydes [COX et ZOK, 1996] qui ne subissent pas de

fragilisation provoquée par l'oxydation à des températures intermédiaires de l'ordre de 600-800 degrés CELSIUS [HEREDIA *et al.*, 1995]. Le modèle développé ici devra être adapté aux particularités de ce type de matériaux dont les caractéristiques mécaniques se rapprochent de celles observées pour des composites C/C. Un premier modèle mécanique est présenté dans [DUPÉ, 1997].

La seconde propriété importante des matériaux composites est leur tenue sous sollicitations cycliques. Dans ce cas, on observe des phénomènes de « rochet inélastique » liés à l'usure des interfaces [ROUBY et REYNAUD, 1993]. Ce mécanisme de dégradation interfaciale peut être intégré dans le formalisme général développé dans le paragraphe 3.2 dans un cadre unidimensionnel [BURR *et al.*, 1997a] ou bidimensionnel [BURR *et al.*, 1997b]. Il peut aussi être intégré dans le cas de ruptures de fibres (analysées dans le paragraphe 3.3) par l'obtention de cartes donnant l'évolution de la résistance au cisaillement de l'interface en fonction du nombre de cycles et de l'amplitude du chargement [BURR et HILD, 1995].

Une autre direction d'étude concerne les composites à matrice métallique (titane ou aluminium par exemple) pour lesquelles une hypothèse du maillon le plus faible permet de prévoir les variations de résistance (par exemple en traction, flexion 4 points et flexion 3 points [HILD et FEILLARD, 1997]). Un module de WEIBULL « apparent » de 7 est trouvé, mais sa signification en terme de mécanisme de rupture n'a pas été expliquée (cf. paragraphe 3.3.1.ii). Pour ce type de matériau, les interactions très locales entre un lieu de rupture de fibre et les fibres avoisinantes sont très vraisemblablement la cause de la rupture. Une meilleure compréhension de ce phénomène passe par des études expérimentales et numériques de ce type de situations.

La plupart des études relatives aux composites renforcés par des fibres continues concerne des matrices céramiques (plus particulièrement le carbure de silicium) et des fibres céramiques (en carbure de silicium également). D'autres composites, à bas coût, sont actuellement analysés en vue de leur éventuelle utilisation dans les véhicules urbains de demain. Ils sont souvent à base de fibres de verre et de matrices résines. Leur particularité est la fabrication à partir de trames de fibres orientées de manière aléatoire (figure 3.10). La répartition (aléatoire) de fibres leur confère un comportement mécanique [CHANTIER, 1997 ; COLLIN, 1997] complètement différent de celui observé pour les composites SiC/SiC (paragraphe 3.2.3). Les mécanismes de dégradations microscopiques sont identiques à ceux des composites à matrice céramique, c'est-à-dire fissuration matricielle, décohésion et glissement interfacial et rupture de fibres. Le modèle présenté ici peut être modifié pour tenir compte de l'orientation aléatoire de

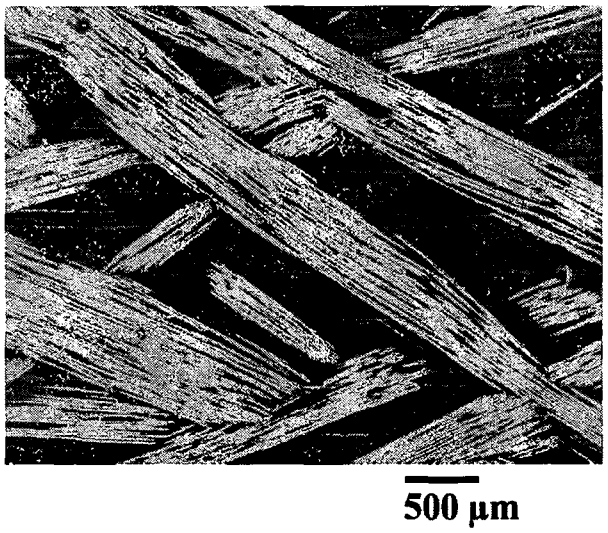

FIG. 3.10 - Microstructure particulière de matrices vinylester renforcée par des fibres de verre.

fibres [CHANTIER, 1997]. La formulation bidimensionnelle reste à écrire.

Une autre classe de matériaux étudiés concerne les matrices cimentaires renforcées par des fibres courtes en acier. Ces composites ont été étudiés dans le cadre de la thèse de D. BOUDON-CUSSAC [1996] et caractérisés en utilisant l'essai PIED (discuté dans le paragraphe 3.2.2). Une prise en compte complète de la texture de ce type de matériaux est possible dans le cadre développé dans ce document. On peut même envisager une étape d'optimisation de celle-ci en fonction des sollicitations mécaniques que subit ce type de composites.

Contrairement aux aciers et alliages métalliques, des règles de conception sont encore balbutiantes pour les matériaux composites à matrices céramiques (ou métalliques). Leur comportement mécanique très particulier, leur aptitude à redistribuer les contraintes au voisinage de concentrations de contraintes macroscopiques (trous, entailles...) n'a pas encore été étudiée de manière très intensive. Le modèle unidimensionnel du paragraphe 3.2.1 a servi de base à l'étude simplifiée de la capacité à redistribuer les contraintes à l'aide d'un modèle à deux barres [BURR *et al.*, 1997a]. Cette étude est en cours de généralisation à l'aide du modèle bidimensionnel du paragraphe 3.2.3 [BURR *et al.*, 1997b].

Enfin, le formalisme des « milieux standard généralisés » n'a été que très peu employé dans ce chapitre (cf. paragraphe 3.3.1.i). La positivité de la dissipation intrinsèque a cependant été vérifiée pour les lois d'évolution introduites dans ce chapitre. L'écriture

des lois d'évolution dans ce cadre reste donc à traiter. En particulier, les lois d'évolution du paragraphe 3.1 nécessitent un traitement particulier du fait de leur caractère « non-local » en espace et en temps.

Postface

"What was this new method?"

"Mainly it was a process of investigating nature with our own senses. Since the fourteenth century there had been an increasing number of thinkers who warned against blind faith in old authority, be it religious doctrine or the natural philosophy of Aristotle. There were also warnings against the belief that problems can be solved purely by thinking. An exaggerated belief in the importance of reason had been valid all through the Middle Ages. Now [during the Renaissance] it was said that every investigation of natural phenomena must be based on observation, experience, and experiment. We call this empirical method."

"Which means?"

"It only means that one bases one's knowledge of things on one's own experience—and not on dusty parchments or figments of the imagination. Empirical science was known in the antiquity, but systematic experiments *were something quite new."*

"I guess they didn't have any of the technical apparatus we have today."

"Of course they had neither calculators nor electronic scales. But they had mathematics and they had scales. And it was now above all imperative to express scientific observations in precise mathematical terms. 'Measure what can be measured, and make measurable what cannot be measured,' said the Italian Galileo Galilei..."

J. GARDNER (1991), *Sophie's World*, Berkeley.

Les analyses présentées dans ce mémoire ont porté sur l'endommagement et la rupture de matériaux hétérogènes pour lesquels une approche probabiliste s'avère être un outil efficace (voire indispensable). Le mécanisme principal de dégradation est la fissuration à l'échelle la plus petite (*i.e.*, microscopique ou mésoscopique selon le problème traité). Ceci concerne des matériaux à comportement fragile (céramiques, fontes GS sous sollicitation cyclique) ou quasi-fragile (céramiques monolithiques impactées ou renforcées par des fibres longues, ciments renforcés par des fibres longues ou courtes). Le dialogue entre les différentes échelles a d'une part permis de construire des modèles de prévision de l'endommagement et de la rupture de ces matériaux. D'autre part, diverses stratégies d'identification des paramètres du matériau ont été mises en oeuvre tout au long de ce travail.

Le passage « macro-méso » (*i.e.*, identification de la distribution de défauts à partir des probabilités de rupture), initialement appliqué à la prévision de la rupture dans le cas d'une propagation instable de défauts a été généralisé à la fatigue à grand nombre de cycles de fontes GS et à la fissuration sous-critique de céramiques monolithiques. Il permet d'accroître le domaine de validité de l'identification par rapport à l'utilisation d'une loi de WEIBULL qui doit être déterminée à *tous* les niveaux de contrainte envisagés (en fatigue à grand nombre de cycles) ou à *toutes* les vitesses de contrainte (fissuration sous-critique). Cette démarche n'est cependant valable que si l'on est en présence d'une seule population de défauts. Dans le cas contraire, il faut faire appel à un passage « méso-macro » qui détermine *a priori* toutes les populations de défauts par observations directes pour prévoir la probabilité de rupture. Ceci sera particulièrement important dans l'étude quantitative de la probabilité de rupture du bras de suspension (cf. paragraphe 2.2.2).

L'écriture d'une loi de comportement bénéficie également du dialogue entre les échelles microscopique et mésoscopique. Le calcul du potentiel d'état a été conduit à partir d'un passage « micro-méso » : que ce soit pour des matériaux monolithiques ou renforcés par des fibres. Les mécanismes de dégradation sont ainsi pris en compte de manière totalement explicite. Quant aux lois d'évolution, différentes procédures d'écriture et d'identification ont été appliquées. Un passage « micro-méso » a été utilisé pour décrire les effets d'interaction de plusieurs fissures dans des cas de sollicitations statiques (paragraphes 3.2.1 et 3.3.1) ou dynamiques (paragraphe 3.1.2). Les stratégies d'identification proprement dites ont utilisé, la plupart du temps, des passages « méso-micro » (*i.e.*, utilisation d'un essai de traction pour déterminer les paramètres des lois d'évolution écrites à l'échelle microscopique) ; le passage inverse nécessitant des observations (délicates) sur des matériaux non disponibles. Dans le cas de composites

unidirectionnels SiC/SiC, des comparaisons entre les deux approches montrent qu'un passage « méso-micro » est suffisant et permet également d'exhiber les groupes adimensionnels pertinents pour l'étude du comportement mécanique (cf. paragraphe 3.2.2). Dans d'autres situations, un passage « micro-méso » a pu être employé car les paramètres de WEIBULL des fibres et les propriétés d'interface étaient disponibles à l'échelle microscopique [HILD *et al.*, 1994]. Enfin, pour des composites bidirectionnels SiC/SiC une identification à l'échelle mésoscopique s'est avérée suffisante vu le faible nombre de données disponibles. Les validations sur des essais non homogènes n'ont pas nécessité une identification plus poussée.

Des passages d'échelles permettent également de mettre en évidence des paramètres d'adimensionnement. Le plus naturel d'entre eux est une longueur (caractéristique). C'est le cas de la multifragmentation de céramiques monolithiques (paragraphe 3.1.2) ou de fibres (paragraphe 3.3.1). À l'aide de ces grandeurs on peut distinguer différents régimes de comportement suivant la taille de l'élément de volume (mésoscopique). Des contraintes caractéristiques ont également été identifiées : elles sont toujours le résultat d'une combinaison entre espace (longueur) et temps ou contrainte conduisant à une rupture locale (ou microscopique). La démarche d'adimensionnement va ainsi de pair avec un passage d'échelle et est un des gains importants que l'on peut escompter en utilisant le dialogue entre deux échelles consécutives.

Enfin les études à des échelles relativement petites nécessitent des moyens d'observation adaptés. On peut citer la microscopie optique ou électronique qui fait maintenant partie intégrante des laboratoires qui s'intéressent à la Mécanique des Matériaux. Les moyens d'analyse d'image sont souvent couplés à l'observation microscopique. L'observation *in situ* (machine d'essai dans un microscope ou microscope monté sur une machine d'essai) est également de plus en plus employée. Enfin, des mesures de champs de déplacement [COLLIN *et al.*, 1998] ou de température par différentes techniques permettent de tester la validité d'hypothèses faites lors d'analyses à différentes échelles. Tous ces équipements constituent autant de compléments modernes aux analyses expérimentales classiques qui s'enrichissent d'informations, d'observations et de mesures plus précises et plus nombreuses, en vue, éventuellement de discriminer différents modèles d'endommagement et/ou de rupture de matériaux hétérogènes.

Bibliographie

Il se trouvait dans la région des astéroïdes 325, 326, 327, 328, 329, 330. Il commença donc par les visiter pour y chercher une occupation et pour s'instruire...
A. DE SAINT-EXUPÉRY (1946), *Le Petit Prince*, Gallimard.

Les publications insérées dans le mémoire sont en **gras** *dans la liste qui suit. Les paragraphes dans lesquels ils se trouvent sont également donnés.*

Introduction

BUI H.D. (1969). *Étude de l'évolution de la frontière du domaine élastique avec l'écrouissage et relations de comportement élasto-plastique des métaux cubiques*, thèse d'État, Faculté des Sciences de l'Université de Paris.

CAILLETAUD G. (1987). *Une approche micromécanique phénoménologique du comportement inélastique des métaux*, thèse d'État, Université Paris 6.

CHABOCHE J.-L. (1978). *Description thermodynamique et phénoménologique de la viscoplasticité cyclique avec endommagement*, thèse d'État, Université Paris 6.

CORDEBOIS J.-P. (1976). *Comportement et résistance des milieux métalliques et multi-perforés*, thèse de troisième cycle, Université Paris 6.

DUFAILLY J. (1980). *Modélisation mécanique et identification de l'endommagement plastique des métaux*, thèse de troisième cycle, Université Paris 6.

GILORMINI P. (1995). Insuffisance de l'extension classique du modèle auto-cohérent au comportement non linéaire, *C. R. Acad. Sci. Paris*, Série IIb (t. 320), pp. 115-122.

KACHANOV L.M. (1958). Time of the Rupture Process under Creep Conditions, *Bull. SSR Acad. Sci., Division of Techical Sciences*, 8, pp. 26-31.

KACHANOV L.M. (1961). Rupture Time under Creep Conditions, RADOK J.M.R. (ed.), *actes Problems of Continuum Mechanics*, SiAM, Philadelphia, PA (USA), pp. 202-218.

KRAJCINOVIC D. et LEMAITRE J. (eds.) (1987). Continuum Damage Mechanics: Theory and Applications, Springer Verlag, Wien (Austria).

LECKIE F.A. et HAYHURST D.R. (1974). Creep Rupture of Structures, *Proc. Roy. Soc. London*, A340, pp. 323-347.

MAZARS J. (1984). *Application de la mécanique de l'endommagement au comportement non linéaire et à la rupture du béton de structure*, thèse d'État, Université Paris 6.

ODQVIST F.K.G. (1966). *The Mathematical Theory of Creep and Creep Rupture*, Clarendon Press, Oxford (UK).

ODQVIST F.K.G. et HULT J. (1961). Some Aspects of Creep Rupture, *Arkiv for Fysik*, 19 (26), pp. 379-382.

PILVIN P. (1990). *Approches multiéchelles pour la prévision du comportement anélastique des métaux*, thèse d'Université, Université Paris 6.

PILVIN P. (1995). *Contribution de la simulation numérique au développement*

de relations de comportement en mécanique des matériaux, habilitation à diriger des recherches, Université Paris 6.

RABOTNOV Y.N. (1969). *Creep Problems in Structural Members*, North-Holland, Amsterdam (the Netherlands).

SUQUET P. (ed.) (1996). Continuum Micromechanics, International Center for Mechanical Sciences, Udine (Italy).

WEBER J. (1996). Le développement durable, *actes VIe rencontres Sciences et Citoyens*, Journal du CNRS, décembre, p. 14.

ZAOUI A. (1970). *Effets de la désorientation des grains sur le comportement viscoplastique de métaux polycristallins (système CFC)*, thèse d'État, Faculté des Sciences de l'Université de Paris.

ZARKA J. (1968). *Sur la viscoplasticité des métaux*, thèse d'État, Faculté des Sciences de l'Université de Paris.

Chapitre 1

ANDRIEUX S. (1981). Un modèle de matériau microfissuré avec frottement, *C. R. Acad. Sci. Paris*, Série II (t. 293), pp. 329-332.

ANDRIEUX S., BAMBERGER Y. et MARIGO J.-J. (1986). Un modèle de matériau microfissuré pour les bétons et les roches, *J. Méc. Th. Appl.*, 5 (3), pp. 471-513.

ARAVAS N., KIM K.-S. et LECKIE F.A. (1990). On the Calculations of the Stored Energy of Cold Work, *ASME J. Eng. Mat. Tech.*, 112, pp. 465-470.

AVESTON J., COOPER G.A. et KELLY A. (1971). Single and Multiple Fracture, *actes National Physical Laboratory: Properties of Fiber Composites*, IPC Science and Technology Press, Surrey (UK), pp. 15-26.

BARENBLATT G.I. (1962). The Mathematical Theory of Equilibrium of Crack in Brittle Fracture, *Adv. Appl. Mech.*, 7, pp. 55-129.

BAZANT Z.P. (1986). Mechanics of Distributed Cracking, *Appl. Mech. Rev.*, 39 (5), pp. 673-705.

BEGLEY M.R., EVANS A.G. et MCMEEKING R.M. (1995). Creep Rupture in Ceramic Matrix Composites with Creeping Fibers, *J. Mech. Phys. Solids*, 43 (5), pp. 727-740.

BENALLAL A., BILLARDON R., DOGHRI I. et MORET-BAILLY L. (1987). Crack Initiation and Propagation Analyses Taking into Account Initial Strain Hardening and Damage Fields, LUXMORE A. (ed.), *actes Numerical Methods in Fracture Mechanics*, Pineridge Press, pp. 337-351.

BILLARDON R. et DOGHRI I. (1989). Prévision de l'amorçage d'une macro-fissure par la localisation de l'endommagement, *C. R. Acad. Sci. Paris*, t. 308 (Série II), pp. 347-352.

BORRÉ G. et MAIER G. (1989). On Linear versus Nonlinear Flaw Rules in Strain Localization Analysis, *Meccanica*, 24, pp. 36-41.

BUDIANSKY B. (1965). On the Elastic Moduli of Some Heterogeneous Materials, *J. Mech. Phys. Solids*, 13, pp. 223-227.

BUDIANSKY B., HUTCHINSON J.W. et EVANS A.G. (1986). Matrix Fracture in Fiber-Reinforced Ceramics, *J. Mech. Phys. Solids*, 34 (2), pp. 167-189.

BUDIANSKY B. et O'CONNELL R.J. (1976). Elastic Moduli of a Cracked System, *Int. J. Solids Struct.*, 12, pp. 81-97.

BUI H.D. (1973). Dualité entre les intégrales indépendantes de contour, *C. R. Acad. Sci. Paris*, t. 276.

BUI H.D. (1978). *Mécanique de la rupture fragile*, Masson, Paris (France).

BUI H.D., DANG VAN K. et STOLZ C. (1981a). Formulations variationnelles du problème en vitesse pour le solide élastique-fragile ayant des zones endommagées, *C.*

R. Acad. Sci. Paris, série II (t. 292), pp. 251-254.

BUI H.D., DANG VAN K. et STOLZ C. (1981b). Relations entre les grandeurs macroscopiques et microscopiques pour un solide élastique-fragile ayant des zones endommagées, *C. R. Acad. Sci. Paris*, série II (t. 292), pp. 863-866.

BUI H.D., DANG VAN K. et STOLZ C. (1982). Relations entre grandeurs microscopiques et macroscopiques pour un solide anélastique ayant des zones endommagées, *C. R. Acad. Sci. Paris*, série II (t. 294), pp. 1155-1158.

BURR A., HILD F. et LECKIE F.A. (1995). Micro-Mechanics and Continuum Damage Mechanics, *Arch. Appl. Mech.*, 65 (7), pp. 437-456.

CHABOCHE J.-L. (1977). Sur l'utilisation des variables d'état interne pour la description du comportement viscoplatique et de la rupture par endommagement, *actes Problemes non-linéaires de mécanique*, Symposium franco-polonais, Cracovie (Pologne), pp. 137-159.

CHABOCHE J.-L. (1992). Une nouvelle condition unilatérale pour décrire le comportement des matériaux avec dommage anisotrope, *C. R. Acad. Sci. Paris*, t. 314 (Série II), pp. 1395-1401.

COCKS A.C.F. et LECKIE F.A. (1987). Creep Constitutive Equations for Damaged Materials, in : HUTCHINSON J.W. et WU T.Y. (eds.), *Advances in Applied Mechanics*, Academic Press, New York, NY (USA), pp. 239-294.

COLLOMBET F. (1985). *Modélisation de l'endommagement anisotrope, application au comportement du béton sous compression triaxiale*, thèse de troisième cycle, Université Paris 6.

CORDEBOIS J.-P. (1979). Comportement et résistance des milieux métalliques et multi-perforés, *J. Méc. Appl.*, 3 (1), pp. 119-142.

CORDEBOIS J.-P. et SIDOROFF F. (1982). Endommagement anisotrope en élasticité et plasticité, *J. Méc. Th. Appl.*, Numéro spécial, pp. 45-60.

COX H.L. (1952). The Elasticity and the Strength of Paper and other Fibrous Materials, *Br. J. Appl. Phys.*, 3, pp. 72-79.

DELOBELLE P. (1997). Caractérisation et modélisation des matériaux en faibles épaisseurs pour des applications microtechniques, *actes Colloque National MECAMAT Mécanismes et Mécanique des Matériaux multifonctionnels*, Aussois (France).

DOGHRI I. (1989). *Étude de la localisation de l'endommagement*, thèse d'Université, Université Paris 6.

DRAGON A. et HALM D. (1995). A Model of Anisotropic Damage by Macrocrack Growth; Unilateral Effect, JEULIN D. (ed.), *actes Workshop on the 'Mechanical Behavior of Damaged Solids'*, Fontainebleau (France).

DRAGON A. et HALM D. (1996). A Model of Damage by Mesocrack Growth - Unilateral Behavior and Induced Anisotropy, *C. R. Acad. Sci. Paris*, série IIb (322),

pp. 275-282.

DUFAILLY J. (1980). *Modélisation mécanique et identification de l'endommagement plastique des métaux*, thèse de troisième cycle, Université Paris 6.

DUFAILLY J. (1995). *Identification des lois de comportement à variables internes*, habilitation à diriger des recherches, Université Paris 6.

DUGDALE D.S. (1960). Yielding of Steel Sheets Containing Slits, *J. Mech. Phys. Solids*, 8, pp. 100-104.

ESHELBY J.D. (1956). The Continuum Theory of Lattice Defect, in : SEITZ F. et TURNBULL D. (eds.), *Solid State Physics*, Academic Press, New York, NY (USA), pp. 79-141.

ESHELBY J.D. (1957). The Determination of the Elastic Field of an Ellipsoidal Inclusion and Related Problems, *Proc. Roy. Soc. London*, A 241, pp. 376-396.

ESHELBY J.D. (1959). The Elastic Field Outside an Ellipsoidal Inclusion, *Proc. Roy. Soc. London*, A 252, pp. 561-569.

FRANÇOIS M. (1995). *Identification des symétries matérielles de matériaux anisotropes*, thèse d'Université, Université Paris 6.

GERMAIN P., NGUYEN Q.S. et SUQUET P. (1983). Continuum Thermodynamics, *ASME J. Appl. Mech.*, 50, pp. 1010-1020.

GILETTA D. (1985). *Modélisation mécanique et identification de la couche élémentaire*, thèse de docteur ingénieur, Université Paris 6.

GRIFFITH A.A. (1921). The Phenomenon of Rupture and Flow in Solids, *Phil. Trans. Roy. Soc. London*, A221, pp. 163-197.

GRIFFITH A.A. (1924). The Theory of Rupture, *actes First International Conference of Applied Mechanics*, Delft (the Netherlands), pp. 55-63.

HACHICH M. (1994). *Conditions de bifurcation dans les solides*, thèse d'Université, Université Paris 6.

HADAMARD J. (1903). *Leçon sur la propagation des ondes et les équations de l'hydrodynamique*, Librairies scientifiques A, Hermann, Paris (France).

HALPHEN B. et NGUYEN Q.S. (1975). Sur les matériaux standard généralisés, *J. Méc.*, 14, pp. 39-63.

HILD F. (1992). *De la rupture des matériaux à comportement fragile*, thèse d'Université, Université Paris 6.

HILD F. (1997). *Exercice long 1996/97 - Première partie : Composites renforcés de fibres*, DEA Mécanique & Matériaux, rapport de correction.

HILL R. (1950). *The Mathematical Theory of Plasticity*, Oxford University Press, Oxford (UK).

HILL R. (1958). A General Theory of Uniqueness and Stability in Elasto-Plastic Solids, *J. Mech. Phys. Solids*, 6, pp. 236-249.

HILL R. (1961). Bifurcation and Uniqueness in Non-Linear Mechanics of Continua, LAVRENTIEV M.A. (ed.), *actes Problems of Continuum Mechanics*, SIAM, Philadelphia, PA (USA), p. 155.

HILL R. (1962). Acceleration Waves in Solids, *J. Mech. Phys. Solids*, 10, pp. 1-16.

HUTCHINSON J.W. (1974). Plastic Buckling, YIH C.S. (ed.), *actes Advances in Applied Mechanics*, Academic Press, New York, NY (USA), pp. 67-144.

IRWIN G.R. (1957). Analysis of the Stresses and Strains near the End of a Crack Traversing a Plate, *ASME J. Appl. Mech.*, 24, pp. 361-364.

KACHANOV M. (1994). Elastic Solids with Many Cracks and Related Problems, *Adv. Appl. Mech.*, 30, pp. 259-445.

KANNINEN M.F. et POPELAR C.H. (1985). *Advanced Fracture Mechanics*, Oxford University Press, New York, NY (USA).

KELLY A. et TYSON W.R. (1965). Tensile Properties of Fibre-Reinforced Metals: Copper/Tungsten and Copper/Molybdenum, *J. Mech. Phys. Solids*, 13, pp. 329-350.

KRAJCINOVIC D. (1987). Micromechanical Basis of Phenomenological Models, in : KRAJCINOVIC D. et LEMAITRE J. (eds.), *Continuum Damage Mechanics: Theory and Applications*, Springer Verlag, Wien (Austria), pp. 195-206.

KRAJCINOVIC D. (1989). Damage Mechanics, *Mech. Mater.*, 8, pp. 117-197.

KRAJCINOVIC D. et SUMARAC D. (1987). Micromechanics of the Damage Processes, in : KRAJCINOVIC D. et LEMAITRE J. (eds.), *Continuum Damage Mechanics: Theory and Applications*, Springer Verlag, Wien (Austria), pp. 135-194.

LA BORDERIE C. (1991). *Phénomènes unilatéraux dans un matériau endommageable : application à l'analyse de structures en béton*, thèse d'Université, Université Paris 6.

LADEVÈZE P. (1983). *Sur une théorie de l'endommagement anisotrope*, LMT-Cachan, rapport interne n°34.

LADEVÈZE P., GASSER A. et ALLIX O. (1994). Damage Mechanisms Modeling for Ceramic Composites, *ASME J. Eng. Mater. Tech.*, 116, pp. 331-336.

LADEVÈZE P. et LEMAITRE J. (1984). Damage Effective Stress in Quasi-Unilateral Conditions, *actes IUTAM Congress*, Lyngby (Denmark).

LECKIE F.A. et ONAT E.T. (1980). Tensorial Nature of Damage Measuring Internal Variables, HULT J. et LEMAITRE J. (eds.), *actes IUTAM Symposium on Physical Nonlinearities in Structures*, Springer-Verlag, pp. 140-155.

LEMAITRE J. (1978). Théorie mécanique de l'endommagement isotrope appliqué à la fatigue des métaux, HALPHEN B. et NGUYEN Q.S. (eds.), *actes Matériaux et structures sous chargement cyclique*, Association Amicale des Ingénieurs Anciens Elèves de l'ENPC, pp. 133-144.

LEMAITRE J. (1984). How to Use Damage Mechanics, *Nucl. Eng. Design*, 80,

pp. 233-245.

LEMAITRE J. (1992a). *A Course on Damage Mechanics*, Springer-Verlag, Berlin (Germany).

LEMAITRE J. (1992b). Histoire des essais mécaniques, *Journée 3D au LMT-Cachan.*

LEMAITRE J. et CHABOCHE J.-L. (1985). *Mécanique des matériaux solides*, Dunod, Paris (France).

LEMAITRE J. et DUFAILLY J. (1977). Modélisation et identification de l'endommagement plastique des métaux, *actes 3e congrès français de mécanique*, Grenoble (France).

LEMAITRE J. et DUFAILLY J. (1987). Damage Measurements, *Eng. Fract. Mech.*, 28 (5-6), pp. 643-661.

LIÉNARD C. (1989). *Plasticité couplée à l'endommagement en conditions quasi-unilatérales pour la prévision de l'amorçage de fisures*, thèse d'Université, Université Paris 6.

LOVE A.E.H. (1927). *The Mathematical Theory of Elasticity*, Cambridge University Press, Cambridge (UK).

MANDEL J. (1962). Ondes plastiques dans un milieu indéfini à trois dimensions, *J. de Mécanique*, 1 (1), pp. 3-30.

MANDEL J. (1966). *Cours de mécanique des milieux continus. Tome I : Généralités, Mécanique des fluides*, Gauthier-Villars, Paris (France).

MANDEL J. (1977). Equations de comportement d'un système élastoviscoplastique dont l'écrouissage est dû à des contraintes résiduelles, *C. R. Acad. Sci. Paris*, Série A (t. 284), pp. 257-260.

MANDEL J. (1978a). Modèle élastoplastique, in : *Propriétés mécaniques des matériaux*, Eyrolles, Paris (France), pp. 208-211.

MANDEL J. (1978b). *Propriétés mécaniques des matériaux*, Eyrolles, Paris (France).

MARQUIS D. (1989). *Phénoménologie et thermodynamique : couplages entre thermoélasticité, plasticité, vieillissement et endommagement*, thèse d'État, Université Paris 6.

MARSHALL D.B., COX B.N. et EVANS A.G. (1985). The Mechanics of Matrix Cracking in Brittle-Matrix Fiber Composites, *Acta Metall.*, 33 (11), pp. 2013-2021.

MAZARS J. (1984). *Application de la mécanique de l'endommagement au comportement non linéaire et à la rupture du béton de structure*, thèse d'État, Université Paris 6.

MAZARS J. (1989). L'effet d'échelle dans les structures en béton, *Rev. Franç. Géotech.*, 49, pp. 15-24.

MAZARS J., BERTHAUD Y. et RAMTANI S. (1990). The Unilateral Behavior of Damaged Concrete, *Eng. Fract. Mech.*, 35 (4/5), pp. 629-635.

ONAT E.T. (1984). Effective Properties of Elastic Materials that Contain Penny Shaped Voids, *Int. J. Eng. Sci.*, 22 (8-10), pp. 1013-1021.

ONAT E.T. et LECKIE F.A. (1988). Representation of Mechanical Behavior in the Presence of Changing Internal Structure, *ASME J. Appl. Mech.*, 55, pp. 1-10.

PERRIN G. et LEBLOND J.-B. (1993). Rudnicki and Rice's Analysis of Strain Localization Revisited, *ASME J. Appl. Mech.*, 60, pp. 842-846.

PIJAUDIER-CABOT G. (1985). *Caractérisation et modélisation du comportement de béton par un essai multiaxial automatique*, thèse de troisième cycle, Université Paris 6.

POSS M. (1982). *Endommagement et rupture des matériaux composites Carbone-Carbone*, thèse de troisième cycle, Université Paris 6.

RABOTNOV Y.N. (1969). *Creep Problems in Structural Members*, North-Holland, Amsterdam (the Netherlands).

RAMTANI S. (1990). *Contribution à la modélisation du comportement multiaxial du béton endommagé avec description du caractère unilatéral*, thèse d'Université, Université Paris 6.

RICE J.R. (1968). A Path Independent Integral and Approximate Analysis of Strain Concentrations by Notches and Cracks, *ASME J. Appl. Mech.*, 35, pp. 379-386.

RICE J.R. (1976). The Localization of Plastic Deformations, in : KOITER W.T. (ed.), *Theoretical and Applied Mechanics*, North-Holland, pp. 207-220.

RICE J.R. et RUDNICKI J.W. (1980). A Note on Some Features of the Theory of Localization of Deformation, *Int. J. Solids Struct.*, 16, pp. 597-605.

RUDNICKI J.W. et RICE J.R. (1975). Conditions for Localization of Deformation in Pressure-Sensitive Dilatant Materials, *J. Mech. Phys. Solids*, 23, pp. 371-394.

SIDOROFF F. (1997). Aspects mécaniques des nanotechnologies optoélectroniques pour les composants III-V, *actes Colloque National MECAMAT Mécanismes et Mécanique des Matériaux multifonctionnels*, Aussois (France).

SUO Z. (1992). *Advanced Fracture Mechanics*, UCSB, graduate course.

SUQUET P. (1982). *Plasticité et Homogénéisation*, thèse d'État, Université Paris 6.

SURESH S. et BROCKENBROUGH J.R. (1990). A Theory for Creep by Interfacial Flaw Growth in Ceramics and Ceramic Composites, *Acta Metall. Mater.*, 38 (1), pp. 55-68.

VAKULENKO A.A. et KACHANOV M.L. (1971). Continuum Theory of Medium with Cracks, *Mekh. Tverdogo Tela*, 4, pp. 159-166.

VOLKERSEN O. (1938). Die Nietkraftverteilung in zugbeanspruchten Ni-

etverbindungen mit konstanten Laschenquerschnitten, *Luftfahrtforschung*, 15 (1/2), pp. 41-47.

VOLTERRA V. (1907). Sur l'équilibre des corps élastiques multiplement connexes, *Annales Scientifiques de l'École Normale Supérieure, Paris (France)*, 24 (3), pp. 401-518.

WEBER C.H., LÖFVANDER J.P.A. et EVANS A.G. (1994). The Creep Anisotropy of a Continuous-Fiber-Reinforced Silicon Carbide Calcium Aluminosilicate Composite, *J. Am. Ceram. Soc.*, 77 (7), pp. 1745-1752.

YAACOUB AGHA H. et HILD F. (1995). Influence of Initial Damage on the Failure of Brittle Materials, LEMAIRE M., FAVRE J.-P. et MEBARKI A. (eds.), *actes ICASP7, Applications of Statistics and Probability*, Balkema, Rotterdam (the Netherlands), pp. 225-232.

Chapitre 2

AZZOUZ F. (1995). *Modélisation du comportement thermo-hydro-mécanique d'un sable de fonderie*, thèse d'Université, Université Paris 6.

BASTENAIRE F. (1960). *Étude statistique et physique de la dispersion des résistances et des endurances à la fatigue*, thèse d'État, Université de Paris.

BATDORF S.B. (1977). Fundamentals of the Statistical Theory of Fracture, in : BRADT R.C., HASSELMAN D.P.H. et LANGE F.F. (eds.), *Fracture mechanics of ceramics*, pp. 1-30.

BATDORF S.B. et CROSE J.G. (1974). A Statistical Theory for the Fracture of Brittle Structures Subjected to Polyaxial Stress States, *ASME J. Appl. Mech.*, 41, pp. 459-465.

BATDORF S.B. et NEINISCH JR. H.L. (1978). Weakest Link Theory Reformulated for Arbitrary Fracture Criterion, *J. Am. Ceram. Soc.*, 61 (7-8), pp. 355-358.

BELKHIRI L. (1985). *Étude de la déformabilité des métaux lors de l'écrasement à froid*, thèse de troisième cycle, Université Paris 6.

BENALLAL A., BILLARDON R. et LEMAITRE J. (1991). Continuum Damage Mechanics and Local Approach to Fracture: Numerical Procedures, *Comp. Meth. Appl. Mech. Eng.*, 92, pp. 141-155.

BÉRANGER A.-S., BILLARDON R., HILD F. et YAACOUB AGHA H. (1997). Effect of Initial Flaws in High Cycle Fatigue of SG Cast Iron, WANG R. (ed.), *actes IUTAM Symposium on Rheology of Bodies with Defects*, Kluwer, Dordrecht (the Netherlands), (soumis).

BERDIN C. (1989). *Evaluation des modèles de rupture pour matériaux fragiles*, Centre des matériaux, ENSMP, mémoire de DEA.

BERDIN C. (1993). *Étude expérimentale et numérique de la rupture des matériaux fragiles*, thèse de l'ENSMP, École Nationale Supérieure des Mines de Paris.

BEREMIN F.M. (1983). A Local Criterion for Cleavage Fracture of a Nuclear Pressure Vessel Steel, *Metallurgical Transactions A*, 14A, pp. 2277-2287.

BILLARDON R. (1997). Relationship Between Mechanics and Physics through Internal State Variables and State Couplings, *ESMC3 Conference (Keynote lecture)*, Stockholm (Sweden).

BILLARDON R., HILD F. et YAACOUB AGHA H. (1996). *Modélisation de la rupture de la fonte G.S. sous sollicitations cycliques*, LMT-Cachan, rapport final d'avenant.

BILLARDON R. et HIRSINGER L. (1997). Modeling and Numerical Simulation of the Magneto-Elastic Behavior of Magnetostrictive Solids, *actes École CEA-EDF-INRIA, Matériaux intelligents et structures adaptatives.*

BOMPARD P. (1996). *Exercice long 1995/96 : Fontes à graphite sphéroïdal*, DEA Mécanique & Matériaux, rapport de correction.

BRINKMAN C.R. et DUFFY S.F. (eds.) (1994). *Life Prediction Methodologies and Data for Ceramic Materials (ASTM STP 1201)*, ASTM, Philadelphia, PA (USA).

BUI H.D. (1978). *Mécanique de la rupture fragile*, Masson, Paris (France).

CARRÉ H. (1996). *Étude de la rupture d'un matériau précontraint : le verre trempé*, thèse de l'ENPC, École Nationale des Ponts et Chaussées.

CHANTIER I. (1997). *Introduction de l'effet de surface sur la rupture d'une fonte à graphite sphéroïdal*, LMT-Cachan, mémoire de DEA.

CHAO L.Y. et SHETTY D.K. (1990). Equivalence of Physically Based Statistical Fracture Theories for Reliability Analysis of Ceramics in Multiaxial Loadings, *J. Am. Ceram. Soc.*, 73 (7), pp. 1917-1921.

CHEVALIER L. (1988). *Étude des caractéristiques des matériaux tréfilés après l'opération de tréfilage*, thèse d'Université, Université Paris 6.

CLÉMENT P. (1984). *Propagation par fatigue de petits défauts dans une fonte GS*, CNAM Paris, rapport CNAM.

CLÉMENT P., ANGELI J.-P. et PINEAU A. (1984). Short Crack Behavior in Nodular Cast Iron, *Fatigue Eng. Mater. Struct.*, 7 (4), pp. 251-265.

CLÉMENT P. et PINEAU A. (1984). Amorçage et propagation de petites fissures dans la fonte à graphite spheroïdal, *actes Journées internationales de Printemps de la SFM*, pp. 203-218.

CORDEBOIS J.-P. (1983). *Critères d'instabilité plastique et endommagement ductile en grande déformation, application à l'emboutissage*, thèse d'État, Université Paris 6.

COSTER M. (1974). *Application des méthodes quantitatives et stéréologiques à l'étude de la croissance et des caractéristiques mécaniques d'échantillons polyphasés*, thèse d'État, Université de Caen.

COSTER M. et CHERMANT J.-L. (1989). *Précis d'analyse d'image*, Editions du CNRS, Paris (France).

DANG VAN K. (1973). Sur la résistance à la fatigue des métaux, *Sciences et Techniques de l'armement*, 47 (3e fassicule), pp. 641-722.

DANG VAN K., LE DOUARON A. et LIEURADE H.P. (1984). Multiaxial Fatigue Limit: a New Approach, VALLURI S.R., TAPLIN D.M.R., RAMA RAO P., KNOTT J.F. et DUBEY R. (eds.), *actes ICF6*, Pergamon Press, Oxford (UK), pp. 1879-1885.

DAVIES D.G.S. (1973). The Statistical Approach to Engineering Design in Ceramics, *Proc. Brit. Ceram. Soc.*, 22, pp. 429-452.

EVANS A.G. (1972). A Method for Evaluating the Time-Dependent Failure Characteristics of Brittle Materials - and its Application to Polycrystalline Alumina, *J.*

Mater. Sci., 7, pp. 1137-1146.

EVANS A.G. (1978). A General Approach for the Statistical Analysis of Multiaxial Fracture, *J. Am. Ceram. Soc.*, 61 (7-8), pp. 302-308.

EVANS A.G. et WIEDERHORN S.M. (1974). Proof Testing of Ceramic Materials-An Analytical Basis for Failure Prediction, *Int. J. Fract.*, 10, pp. 379-392.

FOND C. (1992). *Interaction entre fissures et cavités circulaires dans des milieux élastiques plans*, thèse d'Université, Université Paris 6.

FONTAINE (1985). *Contribution à l'étude de l'aptitude au formage à froid des métaux*, thèse de troisième cycle, Université Paris 6.

FRANÇOIS D., PINEAU A. et ZAOUI A. (1991), *Comportement mécanique des matériaux (volume 1)*, Hermes, Paris (France).

FREUDENTHAL A.M. (1968). Statistical Approach to Brittle Fracture, in : LIEBOWITZ H. (ed.), *Fracture*, Academic Press, New York, NY (USA), pp. 591-619.

FURGIUELE F.M. et LAMBERTI A. (1991). On the Equivalence of Two Weakest-Link Fracture Statistics Formulations, *Int. J. Fract.*, 51, pp. R15-R20.

GHOSH S.K. et PREDELEANU M. (eds.) (1992). Proceedings of the Second International Conference on Materials Processing Defects, *J. Mater. Proc. Tech.*, 32 (1-2), pp. 1-530.

GHOSH S.K. et PREDELEANU M. (eds.) (1995). Materials Processing Defects, Elsevier, Amsterdam (the Netherlands).

GOURDIN C., HIRSINGER L., BARBIER G. et BILLARDON R. (1997). Experimental Identification of the Coupling Between the Anhysteretic Magnetic and Magnetostrictive Behaviors, *actes International Conference on Magnetism*, (accepté).

GRENET L. (1899). Mechanical Strength of Glass, *Bull. Soc. Enc. Nat. Paris (Ser. 5)*, 4, pp. 838-848.

GUMBEL E.J. (1954). Statistical Theory of Extreme Values and Some Practical Applications, *National Bureau of Standards Appl. Math. Series*, 33.

HACHICH M. (1990). *Comportement de matériaux fragiles soumis à des sollicitations de fatigue*, LMT-Cachan, mémoire de DEA.

HAMATA N. (1992). *Modélisation du couplage entre l'élasto-viscoplasticité anisotherme et la transformation de phase d'une fonte G.S. ferritique*, thèse d'Université, Université Paris 6.

HIBBITT H.D., KARLSSON B.I. et SORENSEN P. (1995). *Abaqus*, version 5.5.

HILD F. (1990). *Dispositif de traction-compression d'une éprouvette*, ENS de Cachan/Renault Brevet français n°90 06848 (Bulletin Officiel de la propriété industrielle, 92/33 14 août 1992, n° de publication 2 662 801), 1er juin 1990.

HILD F. (1992). *De la rupture des matériaux à comportement fragile*, thèse d'Université, Université Paris 6.

HILD F. (1996). *Approches statistiques de la rupture : application aux matériaux fragiles*, LMT-Cachan, rapport interne n°168.

HILD F., BILLARDON R. et MARQUIS D. (1992). Hétérogénéité des contraintes et rupture des matériaux fragiles, *C. R. Acad. Sci. Paris*, t. 315 (Série II), pp. 1293-1298.

HILD F. et MARQUIS D. (1990). Corrélation entre la distribution des défauts et la distribution de la contrainte à rupture pour des matériaux à comportement fragile, *C. R. Acad. Sci. Paris*, t. 311 (Série II), pp. 573-578.

HILD F. et MARQUIS D. (1992). A Statistical Approach to the Rupture of Brittle Materials, *Eur. J. Mech., A/Solids*, 11 (6), pp. 753-765.

HILD F. et MARQUIS D. (1994). Influence of Subcritical Propagation of Initial Flaws on the Reliability of Brittle Structures, *ESMC2 Conference*, Genoa (Italy).

HILD F. et MARQUIS D. (1995). Fiabilité de matériaux avec défauts en propagation stable, *C. R. Acad. Sci. Paris*, t. 320 (Série IIb), pp. 57-62.

HILD F. et ROUX S. (1991). Fatigue Initiation in Heterogeneous Brittle Materials, *Mech. Res. Comm.*, 18 (6), pp. 409-414.

HIRSINGER L. (1994). *Étude des déformations de magnéto-élastiques dans les matériaux ferromagnétiques doux. Application à l'étude des déformations d'une structure de machine électrique*, thèse d'Université, Université Paris 6.

JAYATILAKA A. DE S. et TRUSTRUM K. (1977). Statistical Approach to Brittle Fracture, *J. Mater. Sci.*, 12, pp. 1426-1430.

JEULIN D. (1991). *Modèles morphologiques de structures aléatoires et changement d'échelle*, thèse d'État, Université de Caen.

JOKIPII K. (1992). Kymenite, Austempered Ductile Iron as Material for Various Applications, *actes European Meeting on Castings in Austempered Spheroidal Graphite Cast Iron*, CTIF, Sèvres (France).

KACHANOV M. (1994). Elastic Solids with Many Cracks and Related Problems, *Adv. Appl. Mech.*, 30, pp. 259-445.

KADLECEK V. et SPETLA Z. (1967). Effect of Size and Shape of Test Specimens on the Direct Tensile Strength of Concrete, *Bull. RILEM*, 36, pp. 175-184.

KADOUCH O. (1993). *Rupture différée sous sollicitations mécaniques des ferrites spinelles NiZn et MnZn*, thèse de l'ENSMP, École Nationale Supérieure des Mines de Paris.

KATAMAYA Y. et HATTORI Y. (1982). Effects of Specimen Size on Strength of Sintered Silicon Nitride, *C. of J. Am. Ceram. Soc.*, 65, pp. C-164/C-165.

L'HERMITE S. (1973). Influence de la dimension absolue sur la résistance de flexion, *Annales de l'ITBTB*, 309-310, pp. 39-41.

LAMON J. (1988). Statistical Approaches to Failure for Ceramic Reliability Assessment, *J. Am. Ceram. Soc.*, 71 (2), pp. 106-112.

LAMON J. et EVANS A.G. (1983). Statistical Analysis of Bending Strengths for Brittle Solids: a Multiaxial Fracture Problem, *J. Am. Ceram. Soc.*, 66 (3), pp. 177-182.

MARQUIS D. (1989). *Phénoménologie et thermodynamique : couplages entre thermoélasticité, plasticité, vieillissement et endommagement*, thèse d'État, Université Paris 6.

MCCLINTOCK F.A. et ZAVERL JR F. (1979). An Analysis of the Mechanics and Statistics of Brittle Crack Initiation, *Int. J. Fract.*, 15 (2), pp. 107-118.

MILLER K.J. (1982). The Short Crack Problem, *Fatigue Eng. Mater. Struct.*, 5, pp. 223-232.

MILLER K.J. et DE LOS RIOS E.R. (eds.) (1986). The Behavior of Short Fatigue Cracks, MEP, London (UK), pp. 223-232.

PARIS P.C., GOMEZ M.P. et ANDERSON W.P. (1961). A Critical Analysis of Crack Propagation Laws, *The Trend in Engineering*, 13, pp. 9-14.

PIERCE F.T. (1926). Tensile Tests for Cotton Yarns, V. The 'Weakest Link' Theorems on the Strength of Long and of Composite Specimens, *J. Text. Inst.*, 17, pp. T355-T368.

PIERRE P. (1990). *Critères d'instabilité plastique. Influence de gradients de contraintes dans l'épaisseur des tôles embouties*, thèse d'Université, Université Paris 6.

PIJAUDIER-CABOT G. et BAZANT Z.P. (1987). Nonlocal Damage Theory, *ASCE J. Eng. Mech.*, 113 (10), pp. 1512-1533.

PIJAUDIER-CABOT G. et BERTHAUD Y. (1990). Damage and Interactions in a Microcracked Medium. Non-Local Formulation, *C. R. Acad Sci. Paris*, t. 310 (Série II), pp. 1577-1582.

PREDELEANU M. (ed.) (1987). Computational Methods for Predicting Material Processing Defects, Elsevier, Amsterdam (the Netherlands).

PREDELEANU M. et GILORMINI P. (eds.) (1997). Third International Conference on Material Processing Defects, Elsevier, Amsterdam (the Netherlands).

QUAEGEBEUR P. (1990). *Étude de l'influence des paramètres rhéologiques des matériaux sur la capacité de déformation des tôles minces*, thèse d'Université, Université Paris 6.

ROUX S. (1990). *Structures et Désordre*, thèse de l'ENPC, École Nationale des Ponts et Chaussées.

SURESH S. (1991). *Fatigue of Materials*, Cambridge University Press, Cambridge.

TARDIVEL F. (1982). *Sur la détermination des caractéristiques mécaniques d'un embouti*, thèse de troisième cycle, Université Paris 6.

TUCKER W.T. et JOHNSON C.A. (1994). The Multiaxial Equivalent of Stressed Volume, BRINKMAN C.R. et DUFFY S.F. (eds.), *Life Prediction Methodologies and Data for Ceramic Materials (ASTM STP 1201)*, ASTM, Philadelphia, PA (USA),

pp. 265-279.

WANG R. (ed.) (1997). *Proceedings of IUTAM Symposium on Rheology of Bodies with Defects*, Kluwer, Dordrecht (the Netherlands).

WEIBULL W. (1939a). *The Phenomenon of Rupture in Solids*, Roy. Swed. Inst. Eng. Res. 153.

WEIBULL W. (1939b). *A Statistical Theory of the Strength of Materials*, Roy. Swed. Inst. Eng. Res. 151.

WEIBULL W. (1951). A Statistical Distribution Function of Wide Applicability, *ASME J. Appl. Mech.*, 18 (3), pp. 293-297.

WEIBULL W. (1952). A Survey of 'Statistical Effects' in the Field of Material Failure, *Appl. Mech. Rev.*, 5 (11), pp. 449-451.

WIEDERHORN S.M. (1967). Influence of Water Vapor on Crack Propagation in Soda-Lime-Silicate Glass, *J. Am. Ceram. Soc.*, 50 (8), pp. 407-417.

YAACOUB AGHA H. (1996). *Tolérance aux défauts initiaux : application à une fonte G.S. en fatigue*, thèse d'Université, Université Paris 6.

YAACOUB AGHA H., BÉRANGER A.-S., BILLARDON R. et HILD F. (1997). Statistical Damage Tolerance for Cast Iron Under Fatigue Loadings, PREDELEANU M. et GILORMINI P. (eds.), *actes Third International Conference on Material Processing Defects*, Elsevier, Amsterdam (the Netherlands), pp. 415-424.

Chapitre 3

ANDRIEUX S. (1981). Un modèle de matériau microfissuré avec frottement, *C. R. Acad. Sci. Paris*, Série II (t. 293), pp. 329-332.

ANDRIEUX S., BAMBERGER Y. et MARIGO J.-J. (1986). Un modèle de matériau microfissuré pour les bétons et les roches, *J. Méc. Th. Appl.*, 5 (3), pp. 471-513.

AVESTON J., COOPER G.A. et KELLY A. (1971). Single and Multiple Fracture, *actes National Physical Laboratory: Properties of Fiber Composites*, IPC Science and Technology Press, Surrey (UK), pp. 15-26.

BAXEVANAKIS C., JEULIN D. et VALENTIN D. (1993). Fracture Statistics of Single-Fiber Composite Specimens, *Comp. Sci. Tech.*, 48, pp. 47-56.

BERTIN-MOUROT T., DENOUAL C., DEHORS G., LOUVIGNÉ P.-F. et THOMAS T. (1997). High Speed Photography of Moiré Fringes - Application to Ceramics under Impact, *J. Phys. IV, Coll. C3, Suppl. III aug. 1997*, pp. 311-316.

BOUDON-CUSSAC D. (1996). *De l'anisotropie des bétons renforcés de fibres courtes en acier*, thèse d'Université, Université Paris 6.

BRAS F. (1996). *Étude et modélisation de l'endommagement de composites stratifiés SiC-SiC : exploitation d'essais statiques et de type Hopkinson*, thèse de l'ENSC, École Normale Supérieure de Cachan.

BURR A. (1995). *Micromécanique et comportement de matériaux hétérogènes*, thèse d'Université, Université Paris 6.

Burr A., Feillard P. et Hild F. (1996a). Identification of a Potential to Model the Behavior of Fiber-Reinforced Composites, *C. R. Acad. Sci. Paris*, Série IIb (t. 323), pp. 377-383.

Paragraphe 3.2.1

BURR A. et HILD F. (1995). Ultimate Tensile Strength during Fatigue of Fiber-Reinforced Ceramic-Matrix Composites, *Mech. Res. Comm.*, 22 (4), pp. 401-406.

BURR A., HILD F. et LECKIE F.A. (1995). Micro-Mechanics and Continuum Damage Mechanics, *Arch. Appl. Mech.*, 65 (7), pp. 437-456.

BURR A., HILD F. et LECKIE F.A. (1996b). Comportement sous chargement thermomécanique cyclique de composites à matrice céramique, BAPTISTE D. et VAUTRIN A. (eds.), *actes JNC10*, AMAC, pp. 1275-1284.

BURR A., HILD F. et LECKIE F.A. (1996c). Damage, Fatigue and Failure of Ceramic-Matrix Composites, in : MCDOWELL D. (ed.), *Application of Damage Mechanics in Fatigue and Fracture (ASTM STP 1315)*, ASTM, Philadelphia, PA (USA).

BURR A., HILD F. et LECKIE F.A. (1997). On the Mechanical Behaviour under Cyclic Loading of Ceramic-Matrix Composites, *Mater. Sci. Eng.*, A (accepté).

CHANTIER I. (1997). *Loi de comportement de composites à matrice polyester*, DEA Mécanique & Matériaux, projet numérique.

CHO C., HOLMES J.W. et BARBER J.R. (1991). Estimation of Interfacial Shear in Ceramic Composites from Frictional Heating Measurements, *J. Am. Ceram. Soc.*, 74 (11), pp. 2802-2808.

CHRYSOCHOOS A. (1987). *Dissipation et blocage d'énergie lors d'un écrouissage en traction simple*, thèse d'État, Université Montpellier II.

COLLIN F. (1997). *Étude du comportement mécanique d'un composite vinylester renforcé de fibres de verre*, ISMCM/CESTI, rapport de stage de fin d'études.

COSCULLUELA A. (1992). *Plasticité, endommagements et ruptures des alumines sous sollicitations dynamiques triaxiales : influence de la taille de grain*, thèse d'Université, Université de Bordeaux I.

COX B.N. et ZOK F.W. (1996). Advances in Ceramic Composite Reinforced by Continuous Fibers, *Current Opinion in Solid State and Material Science*, 1, pp. 666-673.

COX H.L. (1952). The Elasticity and the Strength of Paper and other Fibrous Materials, *Br. J. Appl. Phys.*, 3, pp. 72-79.

CURTIN W.A. (1991). Exact Theory of Fiber Fragmentation in Single-Filament Composite, *J. Mater. Sci.*, 26, pp. 5239-5253.

Denoual C., Cottenot C.E. et Hild F. (1996). On the Identification of Damage during Impact of a Ceramic by a Hard Projectile, *actes 16th International Conference on BALLISTICS*, APDS, Arlington, VA (USA), pp. 541-550.

Paragraphe 3.1.1

DEÜ J.-F. (1997). *Rupture de composites stratifiés sous chargement dynamique : apports des méso-modèles avec endommagement retardé*, thèse de l'ENSC, École Normale Supérieure de Cachan.

DUPÉ F. (1997). *Étude du comportement mécanique de composites à base d'oxyde*, LMT-Cachan, mémoire de DEA.

FEILLARD P., DÉSARMOT G. et FAVRE J.-P. (1994). Theoretical Aspects of the Fragmentation Test, *Comp. Sci. Tech.*, 50, pp. 265-279.

GARY G., KLEPACZKO J. et ZHAO H. (1989). Corrections for Wave Dispersion and Analysis of Small Strain with Split Hopkinson Bars, *actes Int. Conf. Imp. Eng.*, Sendai (Japan).

GERMAIN P., NGUYEN Q.S. et SUQUET P. (1983). Continuum Thermodynamics, *ASME J. Appl. Mech.*, 50, pp. 1010-1020.

GRADY D.E. (1990). Particle Size Statistics in Dynamic Fragmentation, *J. Appl. Phys.*, 68 (12), pp. 6099-6105.

GÜCER D.E. et GURLAND J. (1962). Comparison of the Statistics of Two

Fracture Models, *J. Mech. Phys. Solids*, 10, pp. 365-373.

GULINO R. et PHOENIX S.L. (1991). Weibull Strength Statistics for Graphite Fibres Measured from the Break Progression in a Model Graphite/Glass/Epoxy Microcomposite, *J. Mater. Sci.*, 26 (11), pp. 3107-3118.

HENSTENBURG R.B. et PHOENIX S.L. (1989). Interfacial Shear Strength Studies Using the Single-Filament-Composite Test. Part II: A Probability Model and Monte Carlo Simulations, *Polym. Comp.*, 10 (5), pp. 389-406.

HEREDIA F.E., MCNULTY J.C., ZOK F.W. et EVANS A.G. (1995). Oxidation Embrittlement Probe for Ceramic-Matrix Composites, *J. Am. Ceram. Soc.*, 78, pp. 2097-2000.

HILD F. (1997). *Exercice long 1996/97 - Première partie : Composites renforcés de fibres*, DEA Mécanique & Matériaux, rapport de correction.

HILD F., BURR A. et LECKIE F.A. (1996). Matrix Cracking and Debonding in Ceramic-Matrix Composites, *Int. J. Solids Struct.*, 33 (8), pp. 1209-1220.

Hild F. et Feillard P. (1997). Ultimate Strength Properties of Fiber-Reinforced Composites, *Rel. Eng. Sys. Saf.*, 56 (3), pp. 225-235.

Paragraphe 3.3.1.ii

HOPKINSON D. (1914). A Method of Measuring the Pressure Produced in the Detonation of High Explosives or by the Impact of Bullets, *Phil. Trans. Roy. Soc.*, A 213, pp. 437.

HUI C.Y., PHOENIX S.L., IBNABDELJALIL M. et SMITH R.L. (1995). An Exact Closed Form Solution for Fragmentation of Weibull Fibers in a Single Filament Composite with Applications to Fiber-Reinforced Ceramics, *J. Mech. Phys. Solids*, 43 (10), pp. 1551-1585.

JEULIN D. (1987). Anisotropic Rough Surface Modeling by Random Morphological Functions, *Acta Stereol.*, 6, pp. 183-189.

JEULIN D. (1991). *Modèles morphologiques de structures aléatoires et changement d'échelle*, thèse d'État, Université de Caen.

JEULIN D. et JEULIN P. (1981). Synthesis of Rough Surfaces by Random Morphological Functions, *actes 3rd European Symposium of Stereology*, Stereol. Iugosl., 3 (1), pp. 239-246.

KELLY A. et TYSON W.R. (1965). Tensile Properties of Fibre-Reinforced Metals: Copper/Tungsten and Copper/Molybdenum, *J. Mech. Phys. Solids*, 13, pp. 329-350.

KOLSKY H. (1949). An Investigation of the Mechanical Properties of Materials at Very High Rates of Loading, *Proc. Phys. Soc. London*, 62b, pp. 676-700.

LADEVÈZE P. (1995). A Damage Computational Approach for Composites: Basic Aspects and Micromechanical Relations, *Comp. Mech.*, 17, pp. 142-150.

LANKFORD J. (1981). Mechanisms Responsible for Strain-Rate-Dependent

Compressive Strength in Ceramic Materials, *J. Am. Ceram. Soc.*, 64 (2), pp. C33-C34.

LANKFORD J. (1991). The Compressive Strength of Strong Ceramics: Microplasticity versus Microfracture, *J. Hard Mat.*, 2 (1-2), pp. 55-77.

LANKFORD J. (1996). High Strain Rate Compression and Plastic Flow of Ceramics, *J. Mat. Sci. Letters*, 15, pp. 745-750.

LEMAITRE J. et DUFAILLY J. (1977). Modélisation et identification de l'endommagement plastique des métaux, *actes 3e congrès français de mécanique*, Grenoble (France).

LONGY F. et CAGNOUX J. (1989). Plasticity and Microcracking in Shock-Loaded Alumina, *J. Am. Ceram. Soc.*, 72 (6), pp. 971-979.

MAZARS J. et BERTHAUD Y. (1989). Une technique expérimentale appliquée au béton pour créer un endommagement diffus et mettre en évidence son caractère unilatéral, *C. R. Acad. Sci. Paris*, Série II (t. 308), pp. 579-584.

MAZARS J., BERTHAUD Y. et RAMTANI S. (1990). The Unilateral Behavior of Damaged Concrete, *Eng. Fract. Mech.*, 35 (4/5), pp. 629-635.

NÈME A. (1994). *Comportement de plaques épaisses à l'impact de cylindres. Modélisation du comportement de la plaque*, thèse de l'ENSC, École Normale Supérieure de Cachan.

NEUMEISTER J.M. (1993). Bundle Pullout-A Failure Mechanism limiting the Tensile Strength of Continuous Fiber Reinforced Brittle Matrix Composites and its Implications for Strength Dependence on Volume and Type of Loading, *J. Mech. Phys. Solids*, 41 (8), pp. 1405-1424.

ORSINI H. et COTTENOT C. (1995). Specific Test to Evaluate Intrinsic Ballistic Properties of Ceramic Materials Against an AP 12.7 mm Projectile. Application to Improve Ceramic Materials, *actes 15th International Symposium on Ballistics*, Jerusalem (Israël).

PRESS W.H., TEUKOLSKY S.A., VETTERLING W.T. et FLANNERY B.P. (1992). *Numerical Recipes in Fortran*, Cambridge University Press, Cambridge (USA).

RAMTANI S. (1990). *Contribution à la modélisation du comportement multiaxial du béton endommagé avec description du caractère unilatéral*, thèse d'Université, Université Paris 6.

RIOU P. (1996). *Contribution à l'étude de l'endommagement du carbure de silicium lors d'un impact de basse énergie : application aux blindages*, thèse de l'ENSMP, École Nationale Supérieure des Mines de Paris.

ROSPARS C., CHERMANT J.-L. et LADEVÈZE P. (1997). On a Possible Creep Model for a 2D SiC/SiC Composite, *Mat. Sci. Eng.*, A (accepté).

ROUBY D. et REYNAUD P. (1993). Fatigue Behaviour Related to Interface Modification During Load Cycling in Ceramic-Matrix Fibre Composites, *Comp. Sci.*

Tech., 48, pp. 109-118.

SERRA J. (ed.) (1988). Image Analysis and Mathematical Morphology, Volume 2: Theoretical Advances, Academic Press, London.

SERRA J. (1989). Boolean Random Functions, *J. Microscopy*, 156, pp. 41-63.

SPANIER J. et OLDHAM K.B. (1987). *An Atlas of Functions*, Springer Verlag, New York.

STRASSBURGER E. et SENF H. (1995). *Experimental Investigations of Wave and Fracture Phenomena in Impacted Ceramics and Glasses*, ARL, Report ARL-CR-214.

WIDOM B. (1966). Random Sequential Addition of Hard Spheres to a Volume, *J. Chem. Phys.*, 44 (10), pp. 3888-3894.

ZWEBEN C. et ROSEN B.W. (1970). A Statistical Theory of Material Strength with Application to Composite Materials, *J. Mech. Phys. Solids*, 18, pp. 189-206.

Postface

COLLIN F., BERTHAUD Y. et HILD F. (1998). Visualisation par analyse d'images de la répartition des déformations et de l'amorçage dans un matériau composite, BERTHAUD Y., COTTRON M., MORESTIN F., MOUCHERONT P. et TARONI M. (eds.), *actes Photomécanique 98*, Sirocco, Marne-la-Vallée (France), pp. 241-248.

HILD F., DOMERGUE J.-M., EVANS A.G. et LECKIE F.A. (1994). Tensile and Flexural Ultimate Strength of Fiber-Reinforced Ceramic-Matrix Composites, *Int. J. Solids Struct.*, 31 (7), pp. 1035-1045.